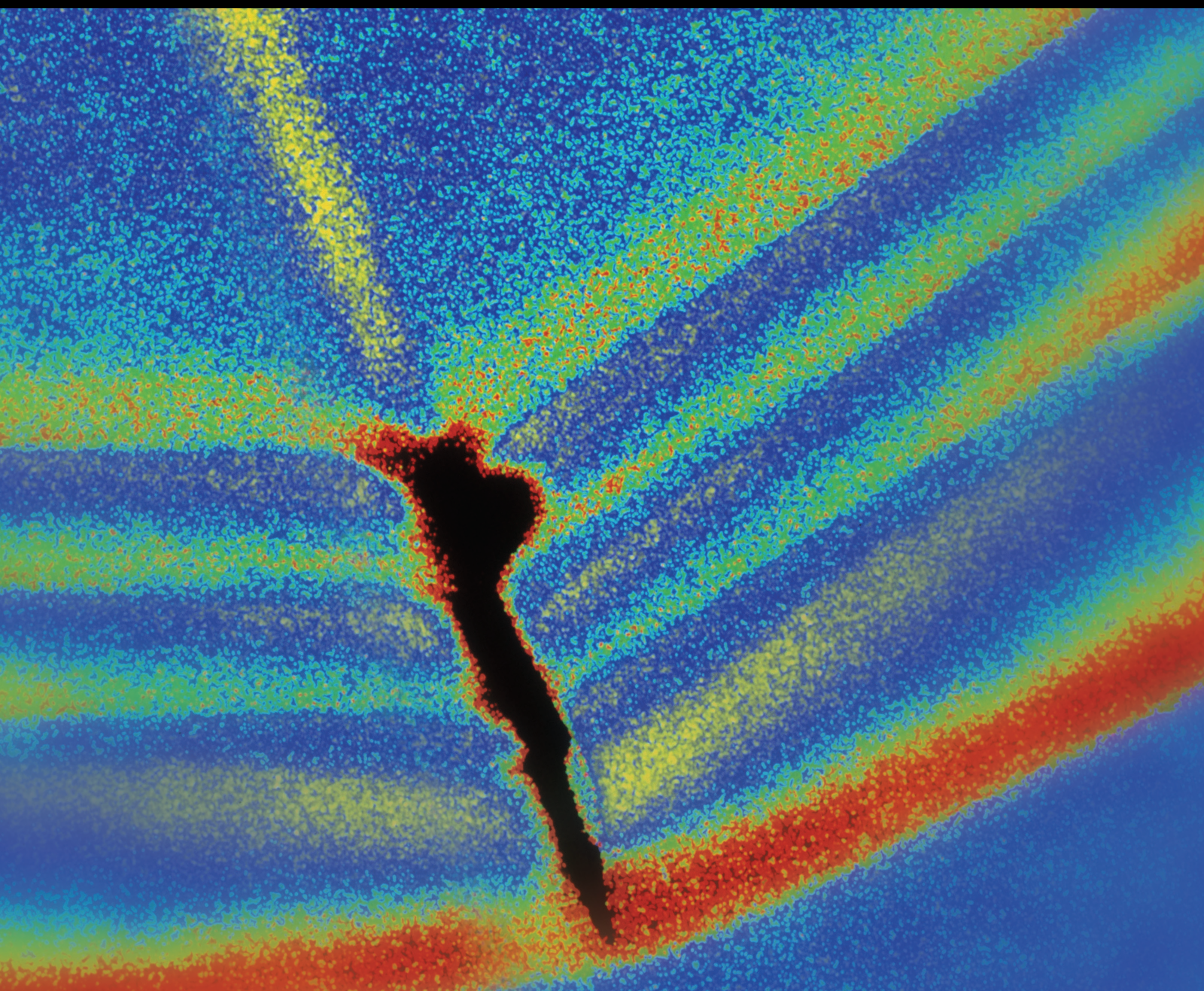


Shock and Vibration

# Geotechnical Earthquake Engineering and Geodynamics

Lead Guest Editor: Honglue Qu

Guest Editors: Changwei Yang, Chuanbin Zhu, Gang Fan, Jianbo Zhu, and  
Jianjing Zhang





---

# **Geotechnical Earthquake Engineering and Geodynamics**

Shock and Vibration

---

## **Geotechnical Earthquake Engineering and Geodynamics**

Lead Guest Editor: Honglue Qu

Guest Editors: Changwei Yang, Chuanbin Zhu,  
Gang Fan, Jianbo Zhu, and Jianjing Zhang



---

Copyright © 2021 Hindawi Limited. All rights reserved.

This is a special issue published in “Shock and Vibration.” All articles are open access articles distributed under the Creative Commons Attribution License, which permits unrestricted use, distribution, and reproduction in any medium, provided the original work is properly cited.

# Chief Editor

Huu-Tai Thai , Australia

## Associate Editors

Ivo Calìo , Italy  
Nawawi Chouw , New Zealand  
Longjun Dong , China  
Farzad Ebrahimi , Iran  
Mickaël Lallart , France  
Vadim V. Silberschmidt , United Kingdom  
Mario Terzo , Italy  
Angelo Marcelo Tusset , Brazil

## Academic Editors

Omid A. Yamini , Iran  
Maher Abdelghani, Tunisia  
Haim Abramovich , Israel  
Desmond Adair , Kazakhstan  
Manuel Aenlle Lopez , Spain  
Brij N. Agrawal, USA  
Ehsan Ahmadi, United Kingdom  
Felix Albu , Romania  
Marco Alfano, Italy  
Sara Amoroso, Italy  
Huaming An, China  
P. Antonaci , Italy  
José V. Araújo dos Santos , Portugal  
Lutz Auersch , Germany  
Matteo Aureli , USA  
Azwan I. Azmi , Malaysia  
Antonio Batista , Brazil  
Mattia Battarra, Italy  
Marco Belloli, Italy  
Francisco Beltran-Carbajal , Mexico  
Denis Benasciutti, Italy  
Marta Berardengo , Italy  
Sébastien Besset, France  
Giosuè Boscato , Italy  
Fabio Botta , Italy  
Giuseppe Brandonisio , Italy  
Francesco Bucchi , Italy  
Rafał Burdzik , Poland  
Salvatore Caddemi , Italy  
Wahyu Caesarendra , Brunei Darussalam  
Baoping Cai, China  
Sandro Carbonari , Italy  
Cristina Castejón , Spain

Nicola Caterino , Italy  
Gabriele Cazzulani , Italy  
Athanasios Chasalevris , Greece  
Guoda Chen , China  
Xavier Chimentin , France  
Simone Cinquemani , Italy  
Marco Civera , Italy  
Marco Cocconcelli , Italy  
Alvaro Cunha , Portugal  
Giorgio Dalpiaz , Italy  
Thanh-Phong Dao , Vietnam  
Arka Jyoti Das , India  
Raj Das, Australia  
Silvio L.T. De Souza , Brazil  
Xiaowei Deng , Hong Kong  
Dario Di Maio , The Netherlands  
Raffaella Di Sante , Italy  
Luigi Di Sarno, Italy  
Enrique Lopez Droguett , Chile  
Mădălina Dumitriu, Romania  
Sami El-Borgi , Qatar  
Mohammad Elahinia , USA  
Said Elias , Iceland  
Selçuk Erkaya , Turkey  
Gaoliang Fang , Canada  
Fiorenzo A. Fazzolari , United Kingdom  
Luis A. Felipe-Sese , Spain  
Matteo Filippi , Italy  
Piotr Fołga , Poland  
Paola Forte , Italy  
Francesco Franco , Italy  
Juan C. G. Prada , Spain  
Roman Gabl , United Kingdom  
Pedro Galvín , Spain  
Jinqiang Gan , China  
Cong Gao , China  
Arturo García García-Perez, Mexico  
Rozaimi Ghazali , Malaysia  
Marco Gherlone , Italy  
Anindya Ghoshal , USA  
Gilbert R. Gillich , Romania  
Antonio Giuffrida , Italy  
Annalisa Greco , Italy  
Jiajie Guo, China

Amal Hajjaj , United Kingdom  
Mohammad A. Hariri-Ardebili , USA  
Seyed M. Hashemi , Canada  
Xue-qiu He, China  
Agustin Herrera-May , Mexico  
M.I. Herreros , Spain  
Duc-Duy Ho , Vietnam  
Hamid Hosano , Japan  
Jin Huang , China  
Ahmed Ibrahim , USA  
Bernard W. Ikuu, Kenya  
Xingxing Jiang , China  
Jiang Jin , China  
Xiaohang Jin, China  
MOUSTAFA KASSEM , Malaysia  
Shao-Bo Kang , China  
Yuri S. Karinski , Israel  
Andrzej Katunin , Poland  
Manoj Khandelwal, Australia  
Denise-Penelope Kontoni , Greece  
Mohammadreza Koopialipour, Iran  
Georges Kouroussis , Belgium  
Genadijus Kulvietis, Lithuania  
Pradeep Kundu , USA  
Luca Landi , Italy  
Moon G. Lee , Republic of Korea  
Trupti Ranjan Lenka , India  
Arcanjo Lenzi, Brazil  
Marco Lepidi , Italy  
Jinhua Li , China  
Shuang Li , China  
Zhixiong Li , China  
Xihui Liang , Canada  
Tzu-Kang Lin , Taiwan  
Jinxin Liu , China  
Ruonan Liu, China  
Xiuquan Liu, China  
Siliang Lu, China  
Yixiang Lu , China  
R. Luo , China  
Tianshou Ma , China  
Nuno M. Maia , Portugal  
Abdollah Malekjafarian , Ireland  
Stefano Manzoni , Italy






Stefano Marchesiello , Italy  
Francesco S. Marulo, Italy  
Traian Mazilu , Romania  
Vittorio Memmolo , Italy  
Jean-Mathieu Mencik , France  
Laurent Mevel , France  
Letícia Fleck Fadel Miguel , Brazil  
FuRen Ming , China  
Fabio Minghini , Italy  
Marco Miniaci , USA  
Mahdi Mohammadpour , United Kingdom  
Rui Moreira , Portugal  
Emiliano Mucchi , Italy  
Peter Múčka , Slovakia  
Fehmi Najar, Tunisia  
M. Z. Naser, USA  
Amr A. Nassr, Egypt  
Sundararajan Natarajan , India  
Toshiaki Natsuki, Japan  
Miguel Neves , Portugal  
Sy Dzung Nguyen , Republic of Korea  
Trung Nguyen-Thoi , Vietnam  
Gianni Niccolini, Italy  
Rodrigo Nicoletti , Brazil  
Bin Niu , China  
Leilei Niu, China  
Yan Niu , China  
Lucio Olivares, Italy  
Erkan Oterkus, United Kingdom  
Roberto Palma , Spain  
Junhong Park , Republic of Korea  
Francesco Pellicano , Italy  
Paolo Pennacchi , Italy  
Giuseppe Petrone , Italy  
Evgeny Petrov, United Kingdom  
Franck Poisson , France  
Luca Pugi , Italy  
Yi Qin , China  
Virginio Quaglini , Italy  
Mohammad Rafiee , Canada  
Carlo Rainieri , Italy  
Vasudevan Rajamohan , India  
Ricardo A. Ramirez-Mendoza , Mexico  
José J. Rangel-Magdaleno , Mexico

Didier Rémond , France  
Dario Richiedi , Italy  
Fabio Rizzo, Italy  
Carlo Rosso , Italy  
Riccardo Rubini , Italy  
Salvatore Russo , Italy  
Giuseppe Ruta , Italy  
Edoardo Sabbioni , Italy  
Pouyan Roodgar Saffari , Iran  
Filippo Santucci de Magistris , Italy  
Fabrizio Scozzese , Italy  
Abdullah Seçgin, Turkey  
Roger Serra , France  
S. Mahdi Seyed-Kolbadi, Iran  
Yujie Shen, China  
Bao-Jun Shi , China  
Chengzhi Shi , USA  
Gerardo Silva-Navarro , Mexico  
Marcos Silveira , Brazil  
Kumar V. Singh , USA  
Jean-Jacques Sinou , France  
Isabelle Sochet , France  
Alba Sofi , Italy  
Jussi Sopanen , Finland  
Stefano Sorace , Italy  
Andrea Spaggiari , Italy  
Lei Su , China  
Shuaishuai Sun , Australia  
Fidelis Tawiah Suorineni , Kazakhstan  
Cecilia Surace , Italy  
Tomasz Szolc, Poland  
Iacopo Tamellini , Italy  
Zhuhua Tan, China  
Gang Tang , China  
Chao Tao, China  
Tianyou Tao, China  
Marco Tarabini , Italy  
Hamid Toopchi-Nezhad , Iran  
Carlo Trigona, Italy  
Federica Tubino , Italy  
Nerio Tullini , Italy  
Nicolò Vaiana , Italy  
Marcello Vanali , Italy  
Christian Vanhille , Spain


Dr. Govind Vashishtha, Poland  
F. Viadero, Spain  
M. Ahmer Wadee , United Kingdom  
C. M. Wang , Australia  
Gaoxin Wang , China  
Huiqi Wang , China  
Pengfei Wang , China  
Weiqiang Wang, Australia  
Xian-Bo Wang, China  
YuRen Wang , China  
Wai-on Wong , Hong Kong  
Yuanping XU , China  
Biao Xiang, China  
Qilong Xue , China  
Xin Xue , China  
Diansen Yang , China  
Jie Yang , Australia  
Chang-Ping Yi , Sweden  
Nicolo Zampieri , Italy  
Chao-Ping Zang , China  
Enrico Zappino , Italy  
Guo-Qing Zhang , China  
Shaojian Zhang , China  
Yongfang Zhang , China  
Yaobing Zhao , China  
Zhipeng Zhao, Japan  
Changjie Zheng , China  
Chuanbo Zhou , China  
Hongwei Zhou, China  
Hongyuan Zhou , China  
Jiaxi Zhou , China  
Yunlai Zhou, China  
Radoslaw Zimroz , Poland

## Contents


### **Spatiotemporal Evolution of Earthquakes in Longmenshan Fault and Adjacent Area, before and after the 2008 Wenchuan Earthquake**

Gang Fan , Jun Wang , Shunchao Qi , Gongda Lu, Xingguo Yang , and Jiawen Zhou   
Research Article (13 pages), Article ID 9400276, Volume 2021 (2021)




### **Research on Intelligent Evaluation Model of Railway Internationalized Earthquake Emergency Rescue Talents Based on Analytic Hierarchy Process and Fuzzy Theory**

Jin Jing , Yang Yu, and Jiang Yuxin  
Research Article (9 pages), Article ID 6862306, Volume 2021 (2021)





### **Study on Dynamic Response Characteristics and Damage Mechanism of Tunnel Lining at Entrance of Shallow Bias Tunnel**

Lin Li, Xiaodan Guo, Zuyin Zou , Zhanyuan Zhu, Zihong Guo, Weimin Xiao, and Deping Guo  
Research Article (15 pages), Article ID 8930560, Volume 2021 (2021)




### **Research on Deep-Site Failure Mechanism of High-Steep Slope under Active Fault Creeping Dislocation**

Yang Liu , Kaiwen Zhang , Denghang Tian , Liming Qu , and Yang Liu  
Research Article (12 pages), Article ID 4482523, Volume 2021 (2021)

### **Failure Characteristics and Mechanism of Multiface Slopes under Earthquake Load Based on PFC Method**

Tao Yang , Yunkang Rao , Huailin Chen , Bing Yang , Jiangrong Hou , Zihong Zhou , and Haojiang Ding   
Research Article (11 pages), Article ID 9329734, Volume 2021 (2021)





### **Analysis of Tunnel Lining Failure Mechanism under the Action of Active Fault**

Sujian Ma , Liang Zhang , Dong Wang, XinRong Tan, Sifeng Li , and Yang Liu  
Research Article (11 pages), Article ID 9918021, Volume 2021 (2021)

### **Influence of Two Cooling Methods on Dynamic Mechanical Properties of High Temperature Sandstone**

Qi Ping , Qi Diao, Dezhi Qi, Chen Wang, and Chuanliang Zhang  
Research Article (12 pages), Article ID 2667182, Volume 2021 (2021)

### **Experimental Study on Seismic Response of Buried Oil and Gas Pipeline Soil Layers under Lateral Multipoint Excitation**

Jianbo Dai , Li Wang , Chengtao Hu , and Guidi Zhang   
Research Article (11 pages), Article ID 9887140, Volume 2021 (2021)

### **Push Plate Test of CRTS II Slab Ballastless Track: Theoretical Analysis, Experiments, and Numerical Simulation**

Yu Liu , Qianqi Xu , Xiaodan Sun , Guotao Yang , and Guotang Zhao   
Research Article (12 pages), Article ID 1945385, Volume 2021 (2021)



**Dynamic Response of Parallel Overlapped Tunnel under Seismic Loading by Shaking Table Tests**

Tao Yang , Yunkang Rao , Honggang Wu , Junyun Zhang , Hao Lei , and Haojiang Ding   
Research Article (15 pages), Article ID 2535762, Volume 2021 (2021)






**Vibration Response Characteristics and Application of Existing Railway Subgrade**

Junyun Zhang , Zhuoling He , Siyuan Chen , and Le Zhang   
Research Article (10 pages), Article ID 9926980, Volume 2021 (2021)

**Rapid Assessment and Classification for Seismic Damage of Mountain Tunnel Based on Concentric Circle Method**

Hua Xu , Jingsong Xu, Runfang Sun, Hefu Pu, and Yin Cheng  
Research Article (16 pages), Article ID 9944797, Volume 2021 (2021)

**Shaking Table Test on the Seismic Responses of a Slope Reinforced by Prestressed Anchor Cables and Double-Row Antisliding Piles**

Zuo-ju Wu , Zhi-jia Wang , Jun-wei Bi , Xiao Fu , and Yong Yao   
Research Article (13 pages), Article ID 9952380, Volume 2021 (2021)

**Dynamic Response and Failure Characteristics of Slope with Weak Interlayer under Action of Near-Fault Ground Motion**

Bing Yang , Jiangrong Hou , Yifei Liu , and Zihong Zhou   
Research Article (18 pages), Article ID 5595278, Volume 2021 (2021)

## Research Article

# Spatiotemporal Evolution of Earthquakes in Longmenshan Fault and Adjacent Area, before and after the 2008 Wenchuan Earthquake

Gang Fan <sup>1,2</sup>, Jun Wang <sup>3</sup>, Shunchao Qi <sup>1</sup>, Gongda Lu,<sup>1</sup> Xingguo Yang <sup>1</sup>,  
and Jiawen Zhou <sup>1</sup>

<sup>1</sup>College of Water Resource and Hydropower, Sichuan University, Chengdu 610065, Sichuan, China

<sup>2</sup>State Key Laboratory of Geohazard Prevention and Geoenvironment, Chengdu University of Technology, Chengdu 610059, Sichuan, China

<sup>3</sup>Sichuan Highway Planning Survey Design and Research Institute Ltd., Chengdu 610041, Sichuan, China

Correspondence should be addressed to Jiawen Zhou; [jwzhou@scu.edu.cn](mailto:jwzhou@scu.edu.cn)

Received 5 June 2021; Revised 15 October 2021; Accepted 10 November 2021; Published 24 November 2021

Academic Editor: Annalisa Greco

Copyright © 2021 Gang Fan et al. This is an open access article distributed under the Creative Commons Attribution License, which permits unrestricted use, distribution, and reproduction in any medium, provided the original work is properly cited.

Seismicity sequence following a main earthquake usually contains much meaningful information for unveiling the focal mechanism and predicting the reoccurrence interval of large earthquakes. The spatiotemporal evolution of earthquakes before and after the 2008 Wenchuan earthquake ( $M_s$  8.0) is analysed comprehensively in this study. The frequency-magnitude relation of the 3493 earthquake events retrieved from the database of the International Seismological Centre indicates that the adopted catalogue is complete for magnitudes  $\geq M_s$  3.4. The seismicity during the 10 years before the Wenchuan earthquake remained stable, including the magnitudes and focal depths. However, seismicity attenuated sharply in the year following the Wenchuan earthquake, and the magnitude of earthquakes before the Wenchuan earthquake decreased gradually. The area of the seismogenic zone of the 2008 Wenchuan earthquake was smaller than the earthquake stricken area. The earthquakes that occurred in the Longmenshan fault area and adjacent area in the study period were mainly shallow earthquakes. The focal depths of earthquakes in the study area became stable gradually after the Wenchuan earthquake, mainly within the range from 10 to 16 km. The earthquakes in the study area were mainly distributed with an along-dip distance of 0–20 km, and the seismicity was distributed uniformly along the fault strike.

## 1. Introduction

The 12 May 2008  $M_s$  8.0 Wenchuan earthquake and the 20 April 2013  $M_s$  7.0 Lushan earthquake, which both occurred on the Longmenshan fault, caused great losses of human lives and to the economy. The Longmenshan fault is an active fault in southwest China [1]. Since the Wenchuan earthquake and the Lushan earthquake both occurred on the Longmenshan fault, the Longmenshan fault has received much attention in recent years. Historically, a total of 25 destructive earthquakes have been recorded in the Longmenshan fault area since 1169. Before the Wenchuan earthquake, studies on the Longmenshan fault mainly focused on the fault slip rates [2]. After the Wenchuan earthquake, studies on the Longmenshan fault

mainly concentrated on the seismogenic process [3, 4], stress state [5, 6], coseismic surface rupture [7], kinematic characteristics [8–11], and deep tectonic environment [12–15] of the fault area. Liu et al. [16] and Yin et al. [17] analysed the spatiotemporal distribution of the early aftershocks following the Wenchuan earthquake. Wu et al. [18] performed a comprehensive detection of early aftershocks following the Lushan earthquake using events 2 days before and 3 days after the main shock. Huang et al. [19] and Fang et al. [20] also relocated the aftershocks of the 2008 Wenchuan and 2013 Lushan earthquakes. The existing studies unveiled the Longmenshan fault. However, the considered temporal scale is limited. The geologic structure of the Longmenshan fault and adjacent area is significantly complicated; therefore, more

studies are needed to deepen the understanding of the destructive Longmenshan fault.

Large shallow earthquakes are generally followed by abundant seismicity that decays with time according to a power law, typically known as Omori's law [21]. The earthquake events with typical foreshock, main shock, and aftershock are the most promising type to achieve short-impending prediction of strong earthquakes, so it has attracted much attention [22]. However, due to its rarity, the understanding of foreshock activity of this type of earthquake is still very shallow. Seismicity following a main earthquake carries useful information regarding the triggering mechanism of earthquakes [23–28]. In recent years, many studies have focused on the historical earthquake sequence, including the Landers earthquake [29, 30], the Chi-Chi earthquake [31], the mid-Niigata Prefecture earthquake [32], the Tohoku earthquake [33], and the Rigan earthquake [34]. These studies promoted the understanding of the focal mechanisms of large earthquakes and offered engineering geologists a reference for making seismic hazard maps.

In this study, earthquake records with a temporal scale from 1 January 1900 to 31 December 2017 are adopted to reveal the spatiotemporal evolution of earthquakes in the Longmenshan fault area and adjacent area. The aims are to obtain innovative findings on the focal mechanism of the fault and to provide meaningful information for earthquake disaster prevention and mitigation in the Longmenshan fault area and adjacent area.

## 2. Geological Background of the Study Area

Earthquake events are complex geological phenomenon, they mainly occurred on the fault belts and also can affect the adjacent fault belts. The destructive 2017 Jiuzhaigou earthquake occurred in the adjacent area of the Longmenshan fault area. For these two reasons, the study area was defined as a rectangle with longitude ranging from 102.101°E to 106.397°E and latitude ranging from 29.790°N to 33.365°N, which covers the Longmenshan fault belt and adjacent area, as illustrated in Figure 1. The Longmenshan fault belt is approximately 500 km long and 30–50 km wide, striking north-northeast and dipping west to steep faults beneath. The Longmenshan fault area is the boundary tectonic belt between the Qinghai-Tibet Plateau and the South China block. The elevation of the eastern margin of the Tibetan Plateau rises steeply westward from 500 m to 4000 m. The Longmenshan fault area has become active since the late Cenozoic. It is composed of three main faults with strong seismic capacities, i.e., the west Wenchuan-Maoxian Fault, the central Yingxiu-Beichuan Fault, and the east Guanxian-Jiangyou Fault. Among these faults, no rupture was found on the Wenchuan-Maoxian Fault during the Wenchuan earthquake. A rupture approximately 240 km long was detected on the Yingxiu-Beichuan Fault, which was the main surface rupture of the Wenchuan earthquake [35]. A rupture approximately 70 km long was observed on the Guanxian-Jiangyou Fault. The faulting geometry along the rupture appears to be complex. Focal mechanism analysis and GPS observation

results show that the Longmenshan fault has vertical uplift and northeast horizontal movement relative to the Sichuan Basin [36].

The Wenchuan earthquake was attributed to the strain accumulated in the Longmenshan fault area and caused by the collision between the Indian and Eurasian Plates along the Himalayan front and the uplift of the Qinghai-Tibet Plateau [8]. The 2008 Wenchuan earthquake was followed by an abundant amount of seismicity, providing an opportunity to analyse the spatiotemporal evolution of seismicity and the triggering mechanisms of great earthquakes.

## 3. Data and Completeness Analysis

The study period is from 1 January 1900 to 31 December 2017. The adopted earthquake catalogue in this study was retrieved from the database of the International Seismological Centre (ISC, <https://www.isc.ac.uk>). The earthquake catalogue provided by the ISC includes 3493 events in the study area, with magnitude  $M_s$  ranging from 1.6 to 8.0. The earthquake distribution and magnitude included in the adopted catalogue are plotted in Figure 1.

The completeness analysis of the adopted earthquake catalogue is a fundamental issue for the study of earthquake sequences. It has long been observed that the sizes of any randomly chosen group of tectonic earthquakes adhere to an inverse power law magnitude-frequency distribution known as the Gutenberg-Richter distribution [37, 38]. The cumulative form of the Gutenberg-Richter relationship can be written as

$$\ln n(M) = a - b \cdot M, \quad (1)$$

where  $n(M)$  is the cumulative number of earthquakes with magnitudes greater than or equal to  $M$ ,  $M$  is the earthquake magnitude,  $a$  and  $b$  are constants, and the surface wave magnitude  $M_s$  is used in this study.

The Gutenberg-Richter relationship has generally been regarded as universal. It is applicative globally, in smaller regions and on individual faults [39, 40]. The completeness of seismicity can be quantitatively represented by the magnitude of completeness, i.e.,  $M_c$ . Figure 2 is the Gutenberg-Richter plot of the cumulative number of events  $N$  versus  $M_s$  for the earthquake catalogue adopted in this study, with  $a = 6.81$  and  $b = 0.90$ . An obvious curvature is detected in Figure 2. The magnitude of completeness,  $M_c$ , can be defined as the magnitude at the maximum curvature [41]. According to its definition,  $M_c = 3.4$  in this study, as illustrated in Figure 2. The linear representation of the Gutenberg-Richter relationship in the segment with magnitude  $M_s \geq 3.4$  indicates that the adopted earthquake catalogue is complete above magnitude  $M_s$  3.4. Numerous earthquake events are often missing in earthquake catalogues following large events due to a large number of events occurring in a short time interval and to the coda noise generated by the large events [42]. This absence may be the reason for the flattening of the curve for  $M_s < 3.4$ . A deviation is observed in the high-magnitude segment in Figure 2, which is due to the shortage of samples with high magnitude.

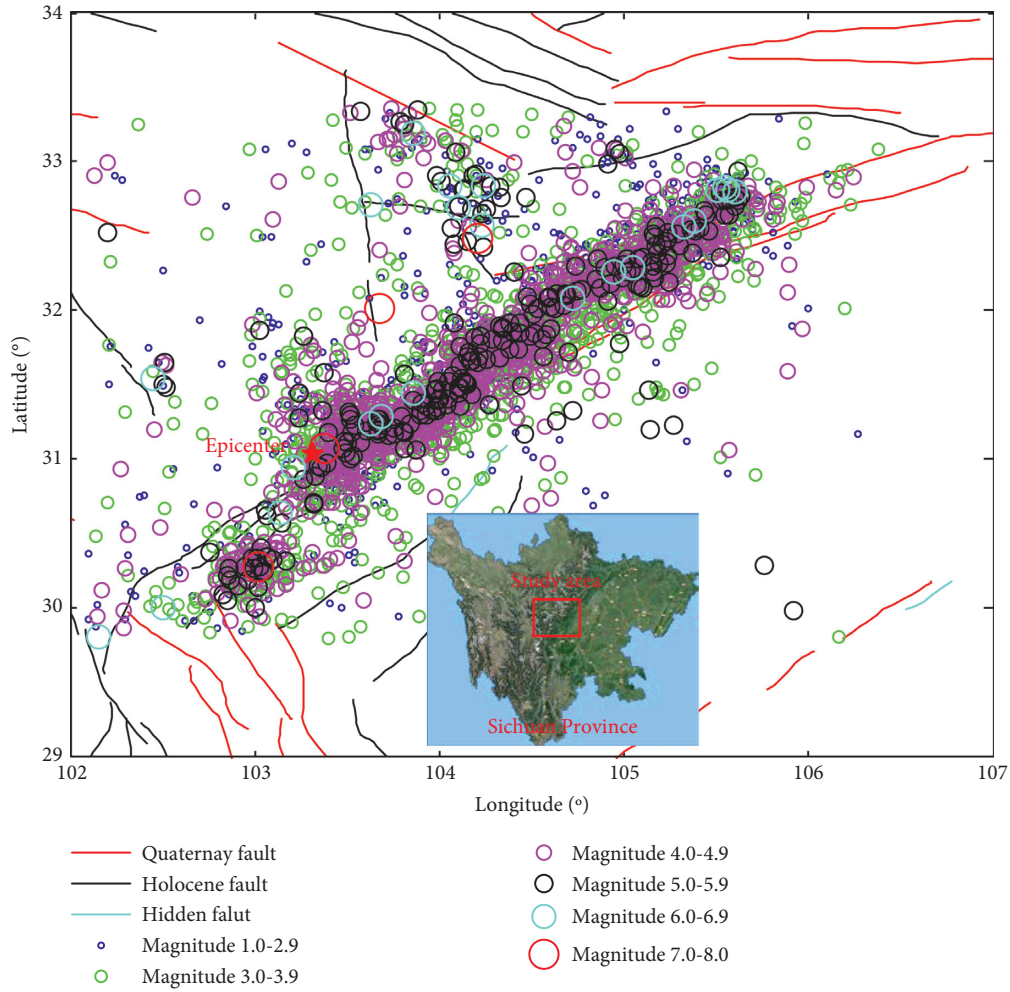


FIGURE 1: Earthquake distribution in the Longmenshan fault area and adjacent area. The scale and color of the circles represent the magnitude of earthquake events used in this study; the red star represents the epicentre of the 2008 Wenchuan earthquake.

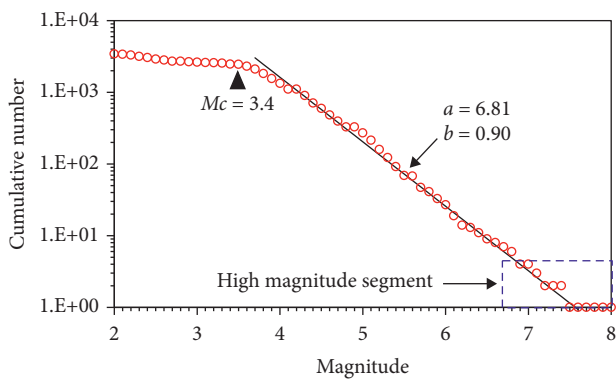


FIGURE 2: Gutenberg–Richter magnitude–frequency relationship from 1 January 1900 to 31 December 2017 in the Longmenshan fault area.

#### 4. Spatiotemporal Evolution Analysis

In the past decade, two catastrophic earthquakes have occurred in the Longmenshan fault area and adjacent area, i.e., the 12 May 2008 Wenchuan earthquake ( $M_s$  8.0) and the 20

April 2013 Lushan earthquake ( $M_s$  7.0). These two catastrophic earthquakes have some mechanical effects on the following seismicity in the study area [43, 44]. Although the adopted catalogue includes earthquake events recorded from 1 January 1900 to 31 December 2017, this study mainly focuses on the spatiotemporal evolution of the earthquake events in approximately 10 years following the 2008 Wenchuan earthquake in the Longmenshan fault area and adjacent area, i.e., from 12 May 2008 to 31 December 2017.

**4.1. Temporal Sequence.** Not all following seismicity happens immediately following a main earthquake. Rather, the seismicity frequency decays like a diffusive process. According to the adopted catalogue of earthquake events, before the Wenchuan earthquake, the seismicity of the Longmenshan fault area and adjacent area was low. The slip rate of the Longmenshan fault, obtained by geologic observations and GPS, is very small (1–3 mm/a) [45]. In contrast, many earthquake events were recorded after the 2008 Wenchuan earthquake. The temporal distribution of the earthquake events in 20 years before (i.e., from 1 January 1988 to 11 May 2008) and 10 years after the 2008 Wenchuan

earthquake (i.e., from 12 May 2008 to 31 December 2017) is plotted in Figure 3. Since the earthquake catalogue is incomplete below  $M_s$  3.4, only the earthquake records with  $M_s$  larger than 3.4 are plotted in Figure 3. To clearly present the historical earthquake events, only the earthquake events in the 20 years before the Wenchuan earthquake are plotted. In the near 20 years before the Wenchuan earthquake, the magnitudes of the earthquake events that occurred in the Longmenshan fault area and adjacent area were mainly less than  $M_s$  5.0. The moving average curve shows that the magnitudes of the earthquake events before the Wenchuan earthquake decreased gradually, while the seismicity in the 10 years before the Wenchuan earthquake remained stable. The magnitude of the earthquakes that occurred in the Longmenshan fault area and adjacent area in 2016 and 2017 increased obviously, as shown in Figure 3. The number of earthquake events with magnitudes exceeding  $M_s$  5.0 is limited, as shown in Figure 4. It can be found from Figure 4 that only 15 earthquake events with magnitudes of  $M_s$  5 or greater were recorded in the 20 years before the Wenchuan earthquake, and only 1 event with magnitude larger than 6 ( $M_s$  6.4) was recorded in this period. Then, the 2008 Wenchuan earthquake triggered an abundance of earthquakes in the Longmenshan fault area and adjacent area, including many earthquake events with magnitudes  $M_s \geq 5.0$ . Figure 4 shows that a total of 1208 earthquakes with magnitude  $M_s \geq 4.0$  and 226 earthquakes with magnitude  $M_s \geq 5.0$  were recorded in 10 years following the Wenchuan earthquake.

To clarify the temporal evolution of seismicity following the Wenchuan earthquake, the number of earthquakes ( $M_s \geq 3.4$ ) in each year and cumulative number are illustrated in Figure 5. Figure 5(a) shows that the number of earthquakes in 2009 is much smaller than that in 2008, implying a sudden attenuation of earthquakes. Then, the number of earthquakes decreases gradually from 2009 to 2012. Due to the occurrence of the 2013 Lushan earthquake, which was also located in the Longmenshan fault area, the number of earthquakes increased suddenly and then decreased gradually from 2013 to 2016. The increase in the number in 2017 may have been due to the occurrence of the Jiuzhaigou earthquake ( $M_w$  6.5), which occurred near the Longmenshan fault zone. In this study, the modified Omori-Ustu formula  $n(t) = K(t+c)^{-p}$  was adopted to predict the attenuation of the seismicity of the 2008 Wenchuan earthquake [46]. Figure 5(b) shows that the Omori-Ustu law could predict the attenuation of seismicity approximately, and the deviation in 2013 was caused by the Lushan earthquake.

To reveal the seismogenic environment of the earthquake events in the Longmenshan fault area, the earthquake events in the study area in different periods were analysed. The analysis period (1 January 1900 to 31 December 2017) was divided into three stages: 1 January 1900 to 12 May 2008 Wenchuan earthquake, 12 May 2008 Wenchuan earthquake to 20 April 2013 Lushan earthquake, and 20 April 2013 Lushan earthquake to 31 December 2017. The earthquake events in these three stages are plotted in Figure 6. The earthquake events in the

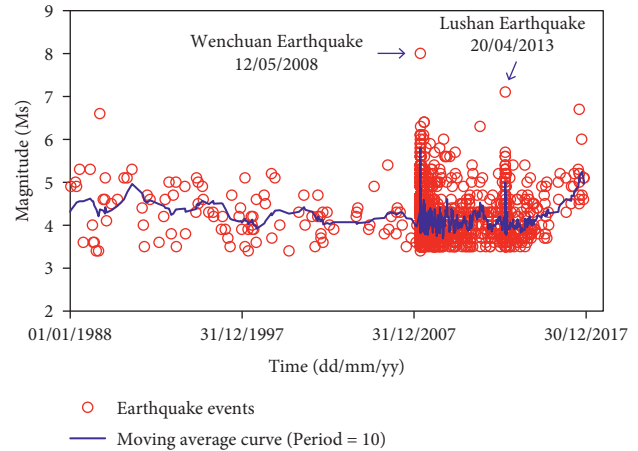


FIGURE 3: Temporal sequence of earthquake events ( $M_s \geq 3.4$ ) 20 years before and 10 years following the 2008 Wenchuan earthquake.

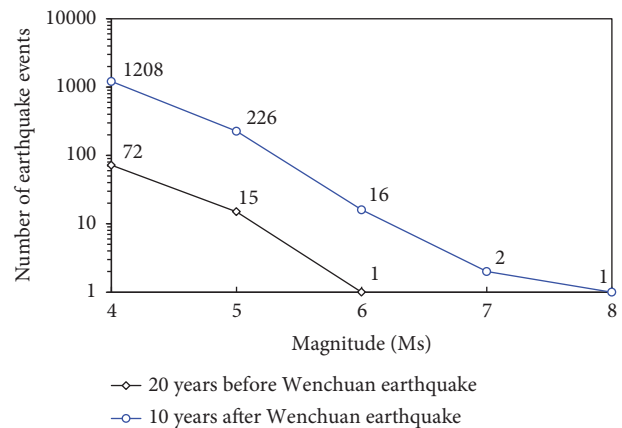


FIGURE 4: Number of earthquake events with magnitude not less than a certain value in 20 years before and 10 years following the 2008 Wenchuan earthquake. The numbers of earthquake events with magnitude not less than  $M_s$  4, 5, 6, 7, and 8 are illustrated.

Longmenshan fault area and adjacent area in the study period were mainly distributed in three segments, i.e., the Lushan segment, Yingxiu segment, and Beichuan-Guangyuan segment, as illustrated in Figure 6. Before the Wenchuan earthquake, there were many microearthquakes with magnitudes  $M_s < 3.0$  in the Lushan segment and the Yingxiu segment. However, few earthquakes were recorded in the northeast Beichuan-Guangyuan segment, as illustrated in Figure 6(a). The northern section of the Longmenshan fault belt had almost no movement before 2007, and the shortening rate and the right-lateral slip rate were 0.2 mm/a and 0.18 mm/a, respectively [36]. The movement of the south section of the Longmenshan fault was small, and the shortening rate and the right-lateral slip rate were 1.8 mm/a and 1.6 mm/a, respectively [36]. These data indicate that the Yingxiu segment experienced intense extrusional strain dominated by fragmentation in the seismogenic period and that the Wenchuan earthquake was the result of rapid dislocation in the Yingxiu segment of the Longmenshan fault.

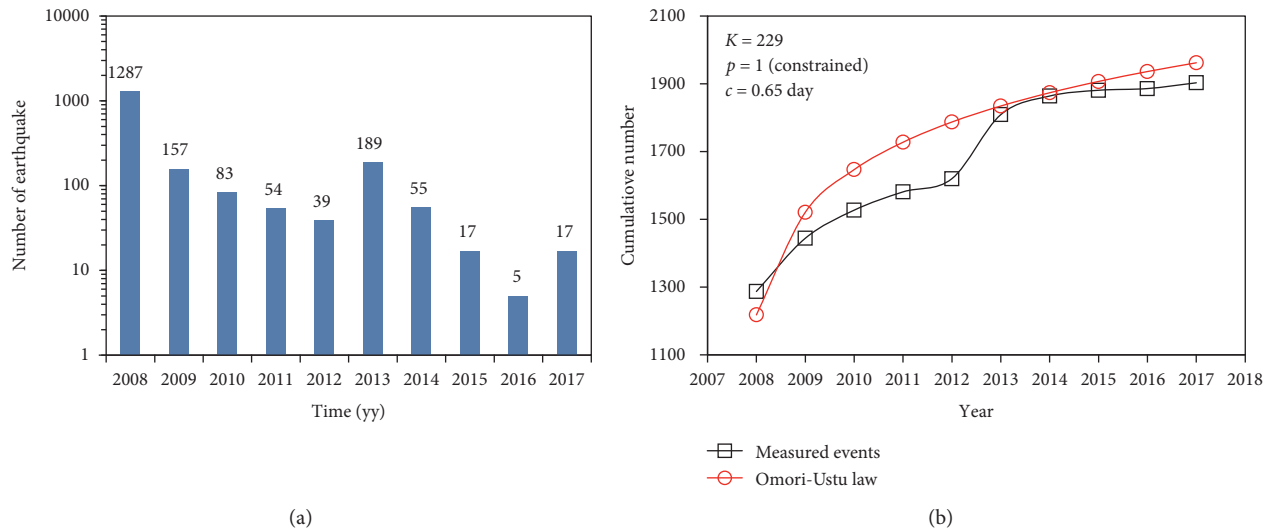


FIGURE 5: Attenuation of seismicity sequence: (a) number of earthquakes ( $M_s \geq 3.4$ ) in each year after the 2008 Wenchuan earthquake, and (b) cumulative number of earthquakes.

When the Wenchuan earthquake occurred in 2008, the seismicity extended to the Beichuan-Guangyuan segment immediately, and a number of earthquakes were recorded in the Beichuan-Guangyuan segment, including many earthquakes with magnitude  $M_s > 4.0$ . Nevertheless, the seismicity did not extend to the Lushan segment, and the seismic density in the Lushan segment did not change very much before and after the Wenchuan earthquake, as shown in Figure 6(b). A comparison of Figures 6(a) and 6(b) implies that the area of the seismogenic zone of the Wenchuan earthquake was smaller than the earthquake stricken area, denoting that, in the rapid rupture process of a seismogenic fault, other seismogenic faults can connect and expand to form a larger catastrophic fault. The seismogenic zone is the depth interval of unstable (stick-slip) behavior where earthquakes can nucleate and slip coseismically.

When the Lushan earthquake occurred in 2013, the seismicity in the Lushan segment was activated, and many seismicity events were recorded in this segment between 20 April 2013 and 31 December 2017, as illustrated in Figure 6(c). To reveal the influence of the Lushan earthquake on the seismicity in the Lushan segment, the seismicity distributions for one year before and one year following the Lushan earthquake are illustrated in Figure 7. Figure 7 shows that only two earthquake events were recorded in the Lushan segment one year before the Lushan earthquake. However, many earthquake events were recorded in the Lushan segment one year following the Lushan earthquake. By comparing the seismic density in the study area one year before and one year following the 2013 Lushan earthquake, it could be found that the seismic density in the Longmenshan fault area increased slightly due to the Lushan earthquake, as shown in Figures 7(a) and 7(b). The number of earthquakes with magnitudes  $M_s$  3.0–3.9 clearly increased. The Lushan earthquake motivated stress release in the Yingxiu segment and the Beichuan-Guangyuan segment, leading to an increase in seismic density in these two segments.

The distribution of the seismicity of the Wenchuan earthquake indicates an asymmetric bilateral rupture of the Longmenshan fault and adjacent area. The rupture extended to the northeast immediately after the Wenchuan earthquake, and the rupture was hindered to the southwest due to a blocking body. The delayed rupture of the blocking body triggered the 2013 Lushan earthquake, as illustrated in Figure 6(c), and increased the seismicity in the Yingxiu segment and the Beichuan-Guangyuan segment slightly, as illustrated in Figure 7.

**4.2. Attenuation of Seismicity.** The seismicity number decays over time, depending on several parameters peculiar to each seismogenic region, including main shock magnitude, crustal rheology, and stress changes along the fault. However, the exact roles of these parameters in controlling the duration of the earthquake sequence are still unknown [24]. The fast decay of seismicity following large earthquakes has been widely reported by researchers. The attenuations of seismicity of the Wenchuan earthquake and the Lushan earthquake are compared in Figure 8, although the relationship between the Wenchuan earthquake and the Lushan earthquake is still a controversial topic. Figure 8 shows that the number of seismicity events of the Wenchuan earthquake is much larger than that of the Lushan earthquake. In the first month following the Wenchuan earthquake, nearly 1179 earthquakes with magnitudes  $M_s \geq 3.4$  were recorded. However, only 179 earthquakes with magnitude  $M_s \geq 3.4$  were recorded in the first month following the Lushan earthquake. The number of earthquake events of the Wenchuan earthquake with magnitude  $M_s \geq 5.0$  (109 recorded events) is also much larger than that of the Lushan earthquake (20 recorded events) in the first month. Figure 8 also shows that the earthquakes attenuated quickly after the main shocks of the Wenchuan and Lushan earthquakes. Two months after the main shocks of the Wenchuan earthquake

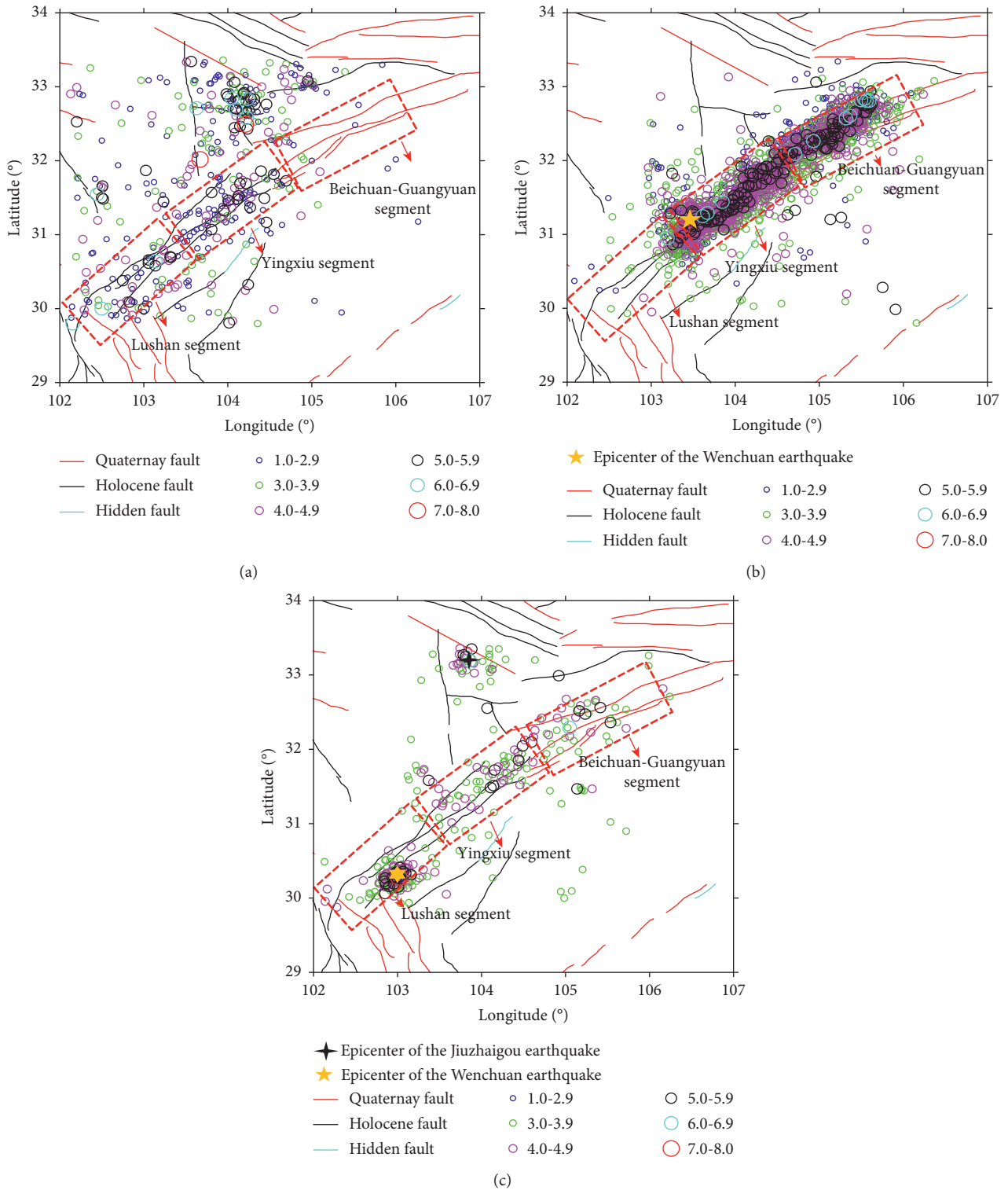


FIGURE 6: Earthquake catalog in the Longmenshan fault area and adjacent area. (a) From 1 January 1900 to 12 May 2008 Wenchuan earthquake, (b) from 12 May 2008 Wenchuan earthquake to 20 April 2013 Lushan earthquake, and (c) from 20 April 2013 Lushan earthquake to 31 December 2017.

and the Lushan earthquake, the number of earthquakes decreased sharply and then became stable gradually. One year after the main shocks of the Wenchuan and Lushan earthquakes, the seismicity was extremely low, and no earthquake

with magnitude  $M_s \geq 5.0$  occurred in the Longmenshan fault area. The reported fast decay of the seismicity following the Wenchuan earthquake is in accordance with the 1999 earthquake and the 2011 Tohoku earthquake [31, 33].

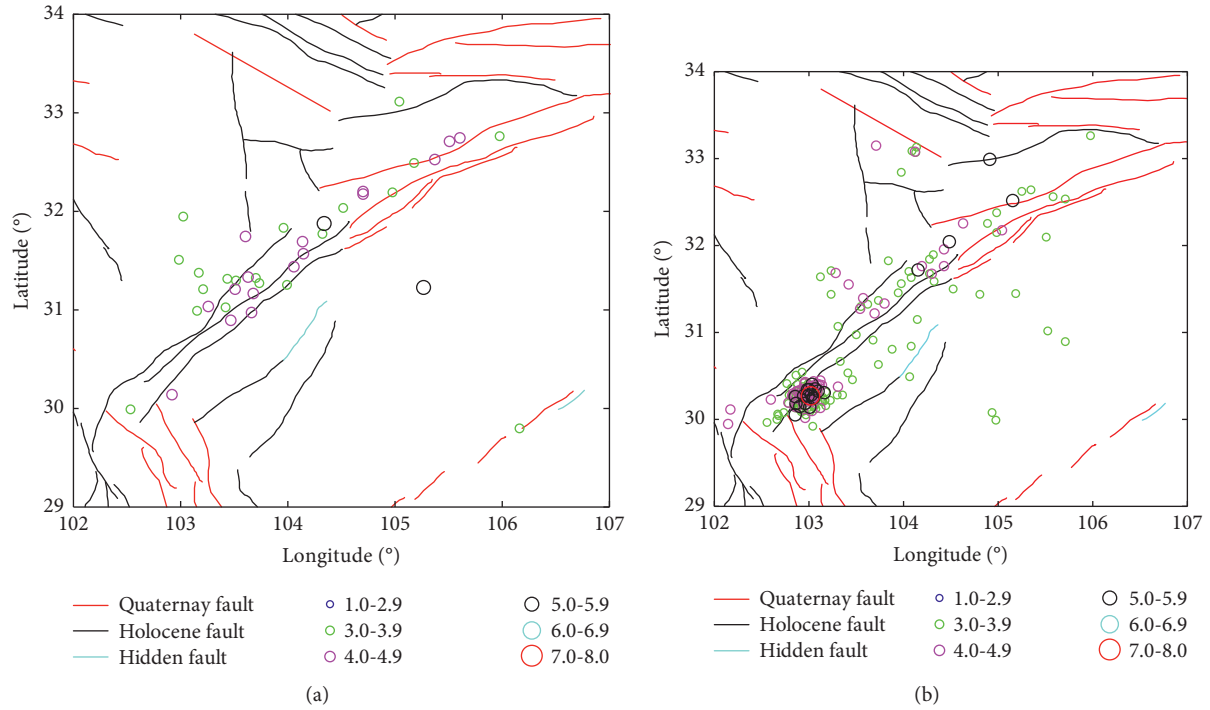


FIGURE 7: Seismicity distribution in one year. (a) Before the Lushan earthquake and (b) one year following the Lushan earthquake.

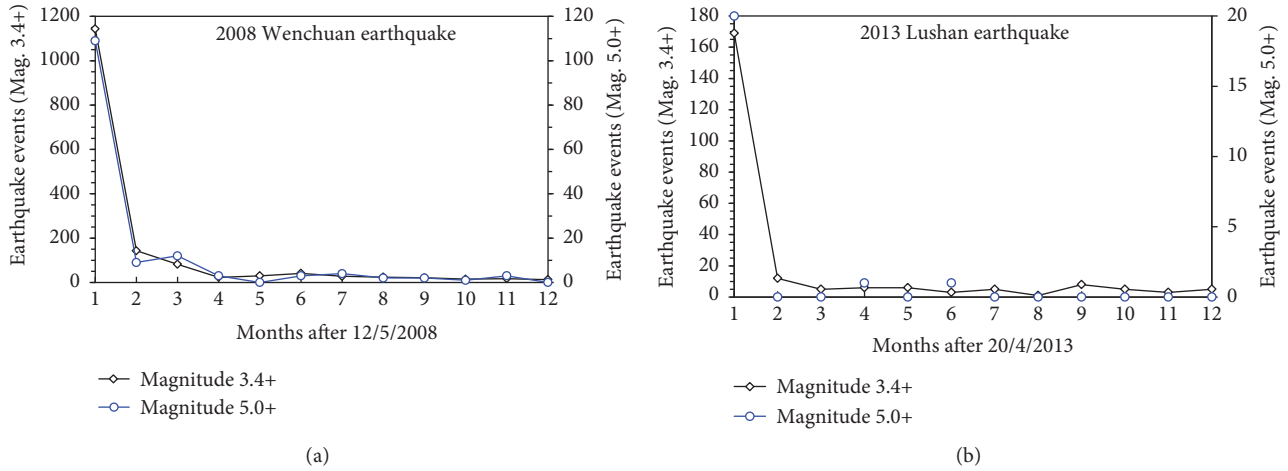


FIGURE 8: Number of seismicity events with magnitude ( $M_s$ ) not less than 3.4 and 5.0 in one year following (a) the 2008 Wenchuan earthquake and (b) one year following the 2013 Lushan earthquake. Magnitude 3.4+ and magnitude 5.0+ represent magnitude not less than  $M_s$  3.4 and  $M_s$  5.0, respectively.

**4.3. Focal Depth.** Focal depth is one of key parameters for earthquake early warning; combined with the crustal velocity model of the fault belt, the focal depth can provide meaningful information for earthquake early warning. Focal depth analysis can be used to unveil the spatial characteristics of the fault belt and the mechanism of great earthquakes in the Longmenshan fault area. In this study, the focal depth of earthquakes before the Wenchuan earthquake during the 10 years before the Wenchuan earthquake and the seismicity during the 10 years following the Wenchuan earthquake are analysed separately, as shown in Figure 9.

This figure implies that the earthquakes that occurred in the Longmenshan fault area and the adjacent area in the past 20 years were mainly shallow earthquakes. Almost all the earthquake events occurred at depths less than 60 km. Figure 9(a) shows that the focal depth of the earthquakes in the study area before the Wenchuan earthquake remained stable in the 10 years before the Wenchuan earthquake, mainly changing in the range of 10–30 km. In the 6 months following the Wenchuan earthquake, the focal depth of the seismicity fluctuated dramatically within the depth range of 0–30 km. An abundance of seismicity occurred at shallow



focal depths above 10 km. The moving average curve shows that the focal depth of the seismicity became stable gradually in the period before the Lushan earthquake (i.e., from 12 May 2008 to 20 April 2013), mainly within the depth range of 10–16 km. When the Lushan earthquake occurred on 20 April 2013, the moving average curve suffered a sudden fluctuation and then became stable quickly. As time passed, the focal depths of the seismicity became stable gradually. It should be pointed out that despite the uncertainties of focal depth of the earthquakes in the ISC catalog, many researchers have paid attention to the identification of focal depth, and the identification accuracy of focal depth has been improved [47, 48]. The uncertainty of focal depth in the ISC catalog remains indistinct; however, with the increasing accuracy of interpretation on focal depth, a better understanding and application of focal depth can be expected.

#### 4.4. Along-Dip and Along-Strike Evolution of Seismicity.

The along-dip and along-strike evolution of seismicity are analysed in this study to reveal the spatiotemporal distribution of seismicity in the study area. The directional study of seismicity can help engineering geologists unveil the distribution characteristics of earthquake-induced landslides. The Gaussian projection is adopted to locate the epicentres of the earthquake events in plane coordinates before the analysis. Here, the along-dip distance is defined as the perpendicular distance from the epicentre of each earthquake to the central Yingxiu-Beichuan Fault. The along-strike distance is defined as the perpendicular distance from the epicentre of each earthquake to the normal line, which crosses through the epicentre of the Wenchuan earthquake on the central Yingxiu-Beichuan Fault. One limitation of this analysis is that we simply assign the location from the recorded catalogue; in reality, the true locations of the earthquake events could be different [5, 49]. Because this study mainly focuses on the overall evolution of seismicity following the Wenchuan main shock, such a difference should not produce any crucial bias to the overall conclusion of this study.

The temporal distribution of seismicity versus along-dip distance in the 10 years following the Wenchuan earthquake is illustrated in Figure 10. The seismicity mainly occurred in the area with along-dip distances less than 20 km. The range of the along-dip distance increased gradually with time. Postearthquake investigations show that more than 70% of the landslides triggered by the Wenchuan earthquake were located within 3 km from seismic faults and 80% within 5 km [50]. Hence, the spatiotemporal evolutions of seismicity within along-dip distances of 0–3 km and 0–5 km are detected in this study. In addition, since Figure 10 indicates that the earthquakes are mainly distributed in the area with along-dip distances less than 20 km, the spatiotemporal evolutions within 0–10 km and 0–20 km are also analysed. The earthquakes with magnitude  $M_s$  3.4 to 5.0 and magnitude  $M_s$  5.0 to 8.0 are analysed separately, as illustrated in Figures 11 and 12, respectively.

It is clear that, within the along-dip distances of 0–3 km, 0–5 km, and 0–10 km, the earthquake events in the study

area with magnitude  $M_s$  3.4 to 5.0 and  $M_s$  5.0 to 8.0 are distributed uniformly along the distance, as shown in Figures 11(a)–11(c) and 12(a)–12(c). However, Figures 11(d) and 12(d) show that when the along-dip distance exceeds 10 km, the seismic density of seismicity decreases gradually with increasing along-dip distance. The seismic density with an along-dip distance of 0–10 km is larger than that with an along-dip distance of 10–20 km. Figure 11 also shows that the seismicity with small magnitudes (green circles and light green circles in Figure 11) mainly occurred 100 days after the main shock of the Wenchuan earthquake. The earthquakes with magnitudes  $M_s$  4.0 to 5.0 (the red circles and light red circles in Figure 11) occurred uniformly with a logarithmic time scale as time passed in the 10 years after the Wenchuan earthquake. Figure 12 shows that the earthquakes with magnitudes of  $M_s$  5.0 to 8.0 are also distributed uniformly with a logarithmic time scale in the 10 years following the Wenchuan earthquake.

The above analysis indicates that the earthquakes of the Wenchuan earthquake were mainly distributed with along-dip distances of 0–20 km, and the earthquakes occurred uniformly with a logarithmic time scale in the 10 years following the Wenchuan earthquake.

The Longmenshan fault is a banded fault, and most of the earthquakes after the Wenchuan earthquake in the study area occurred along the fault strike. Hence, the study on the along-strike distance of earthquakes is more meaningful than the relative distance between the earthquakes and the epicentre of the main shock of the Wenchuan earthquake. The spatiotemporal evolution of earthquakes along the fault strike is illustrated in Figure 13. It shows that the earthquakes in the study area are distributed uniformly along the fault strike, which can also be found in Figure 1. The length of the Longmenshan fault is approximately 240 km. In the study area, the farthest earthquake event along the fault strike is approximately 250 km from the epicentre of the Wenchuan earthquake.

The surface rupture of Wenchuan earthquake near the epicentre mainly extended towards the northeast direction and did not extend towards the southwest direction. The 2013 Lushan earthquake occurred on the south segment of the Longmenshan fault belt, the epicentre of which is approximately 87 km from the epicentre of the Wenchuan earthquake. A seismic gap approximately 45 km long was observed between the Lushan earthquake and the Wenchuan earthquake. However, earthquake-generated stress changes may enhance the tectonic load applied to another fault, moving it closer to failure [29]. Hence, the 2008 Wenchuan earthquake may have motivated the occurrence of the 2013 Lushan earthquake [43, 51, 52].

## 5. Discussion

This study shows that the earthquake sequence of the Wenchuan earthquake has not ended and that the seismicity will continue for years. The relationship between the Wenchuan earthquake and the Lushan earthquake is still under debate [41, 46, 48].

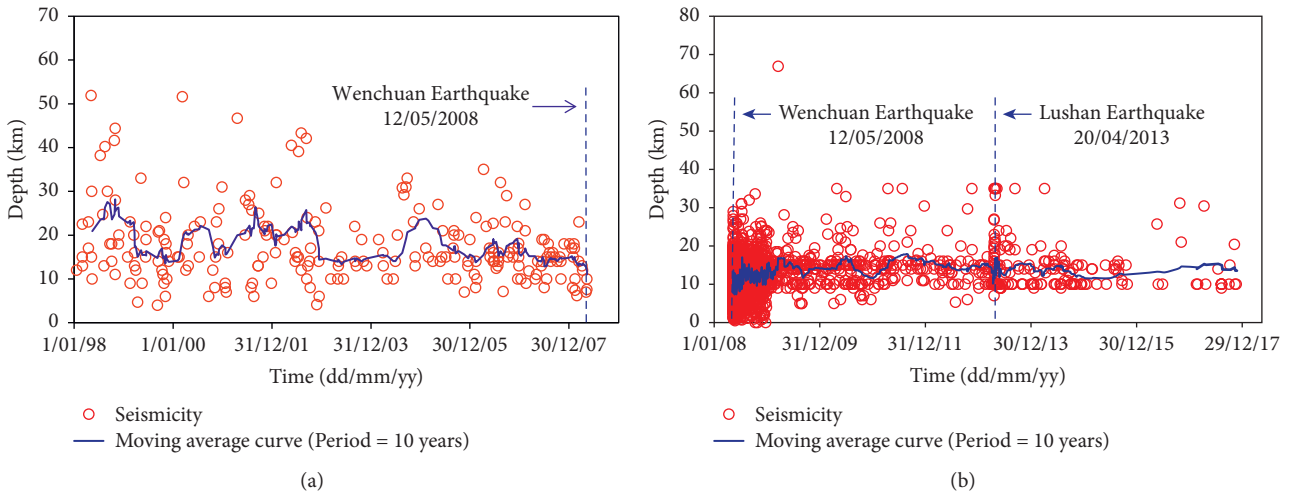


FIGURE 9: Focal depth of (a) earthquakes in 10 years before the Wenchuan earthquake and (b) earthquakes in 10 years following the 2008 Wenchuan earthquake in the Longmenshan fault area.

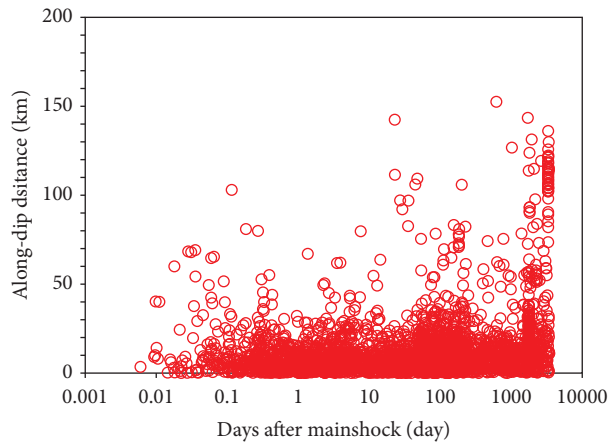


FIGURE 10: Distribution of seismicity with along-dip distance in 10 years following the Wenchuan earthquake.

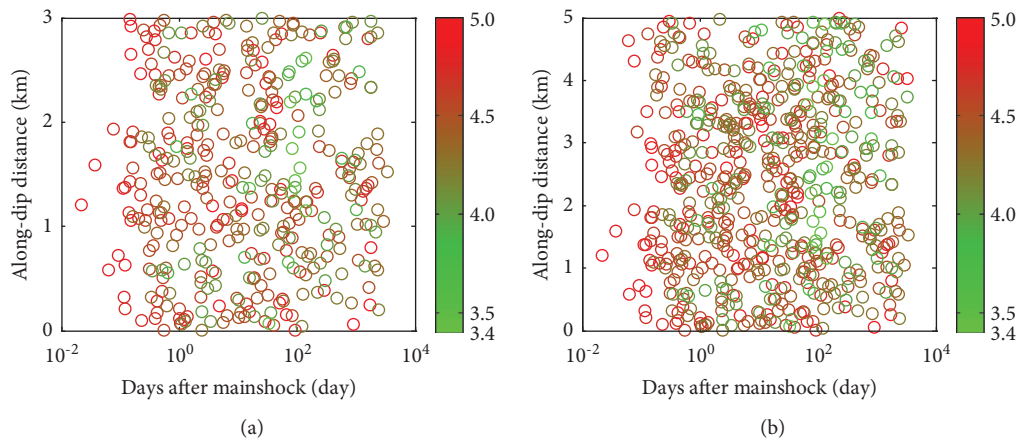


FIGURE 11: Continued.

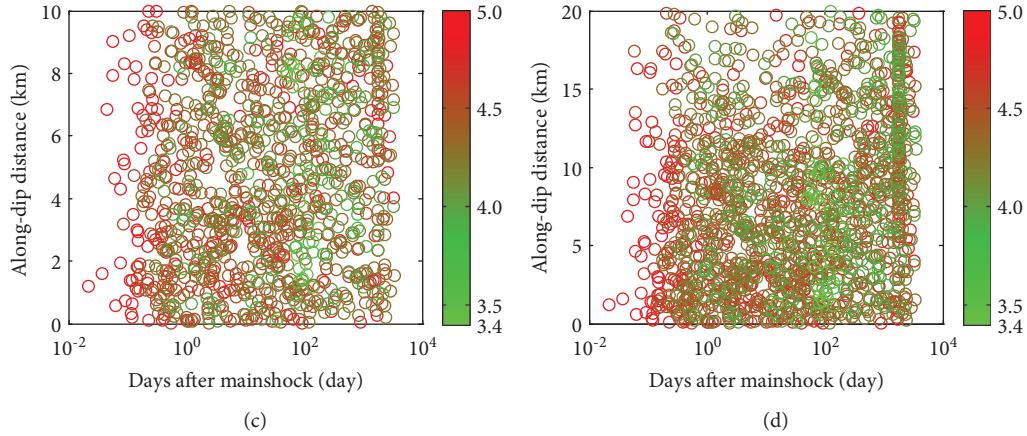


FIGURE 11: Spatiotemporal evolution of seismicity with magnitude  $M_s$  3.4 to 5.0 along the fault dip with logarithmic time since the main shock, projection within (a) 3 km, (b) 5 km, (c) 10 km, and (d) 20 km of the perpendicular to strike distance. The colors of the circles represent the magnitude of earthquake events.

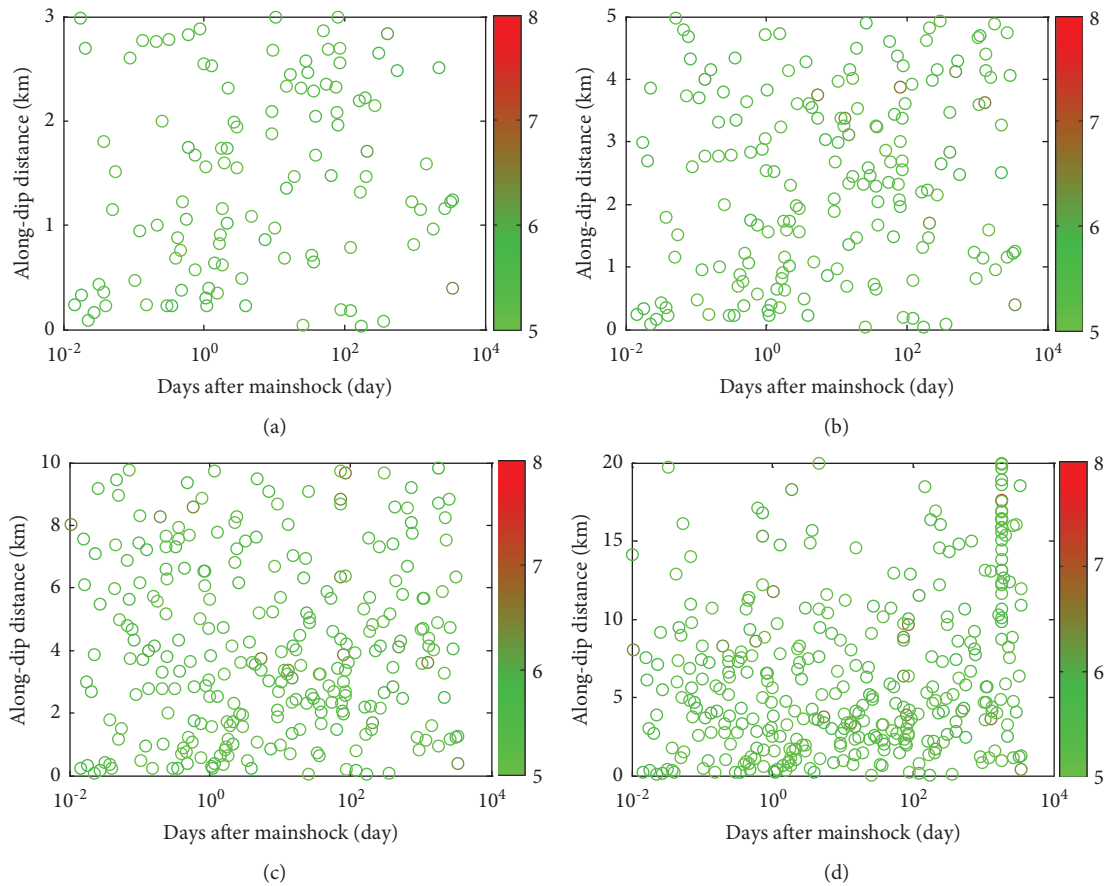


FIGURE 12: Spatiotemporal evolution of seismicity with magnitude  $M_s$  5.0 to 8.0 along the fault dip with logarithmic time since the main shock; projection within (a) 3 km, (b) 5 km, (c) 10 km, and (d) 20 km of the perpendicular to strike distance. The colors of the circles represent the magnitude of earthquake events.

The occurrence of the next strong earthquake in the Longmenshan fault belt and adjacent area is of great concern to many scientists and millions of Chinese people. The Wenchuan earthquake now marks a new beginning for strain to build up for another great earthquake caused by

dextral-slip thrust offset in the Longmenshan Mountains [48]. Studies have been conducted on the prediction of recurrence interval in the Longmenshan fault belt. The recurrence interval is estimated to be 3000–6000 years by offset landforms, 5000–5500 years by earthquake moment rate,

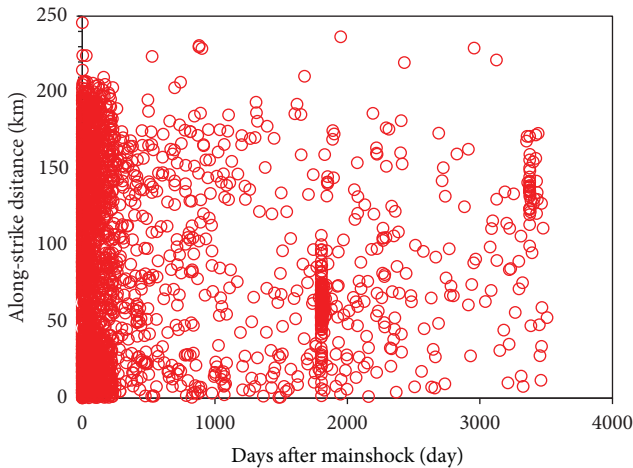


FIGURE 13: Spatiotemporal evolution of seismicity occurred in the Longmenshan fault area along the fault strike with logarithmic time since in 10 years following the main shock of the Wenchuan earthquake.

and 2600–3800 years by fault slip rate [52]. A study in an exploratory trench before the Wenchuan earthquake indicated that the strong earthquake recurrence interval of a single fault in the Longmenshan fault belt was estimated to be 2000–3000 years. The seismic wave inversion and GPS rate after the Wenchuan earthquake indicate that the average recurrence interval of strong earthquakes with magnitude  $M_s = 8.0$  is 2000–10000 years [45]. The matter of multiple faults being involved and the inadequacies of measurements in the region lead to a wide range in calculation results.

It should be noted that the Lushan earthquake is located at the Y-shaped intersection point of the northeast Longmenshan fault belt, northwest Xianshuihe Fault belt, and north-south Anninghe Fault belt. The Lushan earthquake is the largest earthquake since the Wenchuan earthquake in this area. The occurrence of the Lushan earthquake may directly lead the underground stress condition change and ground surface ruptures in the Xianshuihe Fault belt and the Anninghe Fault belt, as well as in the rupture blank zone between the epicentres of the Wenchuan earthquake and the Lushan earthquake, as illustrated in Figure 1. Attention should be paid to the stress change in these areas, and more studies should be conducted in the future. Underground stress observation techniques, which do not depend on seismic records, can be a meaningful method for earthquake disaster mitigation in this area.

## 6. Conclusions

The spatiotemporal evolution of earthquakes in Longmenshan fault and adjacent area is analysed in this study. Several main conclusions can be drawn:

- (1) The earthquake activity over the 10 years before the Wenchuan earthquake remained stable, the seismicity attenuated suddenly in the first year following the main shock, and the magnitude of earthquakes before the Wenchuan earthquake decreased gradually thereafter.

- (2) The seismogenic zone of the Wenchuan earthquake was smaller than the earthquake stricken area.
- (3) The earthquakes that occurred in the Longmenshan fault area and adjacent area in the study period were mainly shallow earthquakes, with focal depths of less than 60 km.
- (4) In the 6 months following the Wenchuan earthquake, the focal depths of the earthquakes fluctuated dramatically within the range from 0 to 30 km and then gradually stabilized, mainly within the range from 10 to 16 km.
- (5) The earthquakes in the study area mainly distributed with an along-dip distance of 0–20 km, and the earthquakes occurred uniformly over a logarithmic time scale during the 10 years following the Wenchuan earthquake. The earthquakes were distributed uniformly along the fault strike.

## Data Availability

The test data used to support the findings of this study are included within the article.

## Conflicts of Interest

The authors declare that there are no conflicts of interest regarding the publication of this paper.

## Acknowledgments

This research was financially supported by the National Natural Science Foundation of China (No. 41907247) and the Open Fund of State Key Laboratory of Geohazard Prevention and Geoenvironment (No. SKLGP2021K008).

## References

- [1] P.-Z. Zhang, “Beware of slowly slipping faults,” *Nature Geoscience*, vol. 6, no. 5, pp. 323–324, 2013.
- [2] R. J. Zhou, Y. Li, A. L. Densmore et al., “Active tectonics of the Longmen Shan region on the eastern margin of the Tibetan Plateau,” *Acta Geologica Sinica-English Edition*, vol. 81, pp. 593–604, 2007.
- [3] S. P. Pei, H. J. Zhang, J. R. Su, and Z. X. Cui, “Ductile gap between the Wenchuan and Lushan earthquakes revealed from the two-dimensional Pg seismic tomography,” *Scientific Reports*, vol. 4, Article ID 6489, 2017.
- [4] S. Toda, J. Lin, M. Meghraou, and R. S. Stein, “12 May 2008  $M=7.9$  Wenchuan, China, earthquake calculated to increase failure stress and seismicity rate on three major fault systems,” *Geophysical Research Letters*, vol. 35, Article ID L17305, 2008.
- [5] Z. Peng and P. Zhao, “Migration of early aftershocks following the 2004 Parkfield earthquake,” *Nature Geoscience*, vol. 2, no. 12, pp. 877–881, 2009.
- [6] X. Qin, Q. Chen, M. Wu, C. Tan, C. Feng, and W. Meng, “In-situ stress measurements along the Beichuan-Yingxiu fault after the Wenchuan earthquake,” *Engineering Geology*, vol. 194, pp. 114–122, 2015.
- [7] Y. Zhang, J. Shi, P. Sun et al., “Surface ruptures induced by the Wenchuan earthquake: their influence widths and safety

- distances for construction sites,” *Engineering Geology*, vol. 166, pp. 245–254, 2013.
- [8] C. B. Hu, Y. E. Cai, and Z. M. Wang, “Effects of large historical earthquakes, viscous relaxation, and tectonic loading on the 2008 Wenchuan earthquake,” *Journal of Geophysical Research*, vol. 117, Article ID B06410, 2012.
- [9] X. Fan, C. H. Juang, J. Wasowski et al., “What we have learned from the 2008 Wenchuan Earthquake and its aftermath: a decade of research and challenges,” *Engineering Geology*, vol. 241, pp. 25–32, 2018.
- [10] H. W. Wang, Y. F. Ren, and R. Z. Wen, “Source parameters, path attenuation and site effects from strong-motion recordings of the Wenchuan aftershocks (2008–2013) using a non-parametric generalized inversion technique,” *Geophysical Journal International*, vol. 212, pp. 872–890, 2016.
- [11] S. Zhang, Z. Wu, and C. Jiang, “Signature of fault healing in an aftershock sequence? The 2008 wenchuan earthquake,” *Pure and Applied Geophysics*, vol. 173, no. 1, pp. 73–84, 2016.
- [12] X. Lin, D. Dreger, H. Ge et al., “Spatial and temporal variations in the moment tensor solutions of the 2008 Wenchuan earthquake aftershocks and their tectonic implications,” *Tectonics*, vol. 37, pp. 989–1005, 2018.
- [13] C. Wang, C. Song, Q. Guo, J. Mao, and Y. Zhang, “New insights into stress changes before and after the Wenchuan Earthquake using hydraulic fracturing measurements,” *Engineering Geology*, vol. 194, pp. 98–113, 2015.
- [14] K. G. Zhu, C. Q. Chi, Z. N. Yu et al., “Extracting borehole strain precursors associated with the Lushan earthquake through principal component analysis,” *Annals of Geophysics*, vol. 61, Article ID SE447, 2018.
- [15] P. Xiong, X. H. Shen, X. F. Gu et al., “Seismic infrared anomalies detection in the case of the Wenchuan earthquake using bi-angular advanced along-track scanning radiometer data,” *Annals of Geophysics*, vol. 58, Article ID S0217, 2015.
- [16] Y. Liu, T. Chen, F. Xie et al., “Analysis of fluid induced aftershocks following the 2008 Wenchuan Ms 8.0 earthquake,” *Tectonophysics*, vol. 619–620, pp. 149–158, 2014.
- [17] X. Z. Yin, J. H. Chen, Z. Peng et al., “Evolution and distribution of the early aftershocks following the 2008 Mw 7.9 wenchuan earthquake in sichuan, China,” *Journal of Geophysical Research: Solid Earth*, vol. 123, no. 9, pp. 7775–7790, 2018.
- [18] J. Wu, D. Yao, X. Meng, Z. Peng, J. Su, and F. Long, “Spatial-temporal evolutions of early aftershocks following the 2013 Mw 6.6 Lushan earthquake in Sichuan, China,” *Journal of Geophysical Research: Solid Earth*, vol. 122, no. 4, pp. 2873–2889, 2017.
- [19] Y. Huang, J. Wu, T. Zhang, and D. Zhang, “Relocation of the M8.0 Wenchuan earthquake and its aftershock sequence,” *Science in China-Series D: Earth Sciences*, vol. 51, no. 12, pp. 1703–1711, 2008.
- [20] L. J. Fang, W. Wu, W. Wang et al., “Relocation of the mainshock and aftershock sequences of Ms 7.0 Sichuan Lushan earthquake,” *Chinese Science Bulletin*, vol. 58, no. 28–29, pp. 3451–3459, 2013.
- [21] F. Omori, “On the aftershocks of earthquakes,” *Journal of the College of Science, Imperial University of Tokyo*, vol. 7, pp. 111–200, 1894.
- [22] A. Kato, J. i. Fukuda, S. Nakagawa, and K. Obara, “Foreshock migration preceding the 2016 Mw 7.0 Kumamoto earthquake, Japan,” *Geophysical Research Letters*, vol. 43, no. 17, pp. 8945–8953, 2016.
- [23] H. K. Hung, R. J. Rau, E. Benedetti et al., “GPS Seismology for a moderate magnitude earthquake: lessons learned from the analysis of the 31 October 2013 ML 6.4 Ruisui (Taiwan) earthquake,” *Annals of Geophysics*, vol. 60, Article ID S0553, 2017.
- [24] R. Lloyd, J. Biggs, and A. Copley, “The decade-long Machaze-Zinave aftershock sequence in the slowly straining Mozambique Rift,” *Geophysical Journal International*, vol. 217, no. 1, pp. 504–531, 2019.
- [25] N. Uchida, S. H. Kirby, N. Umino, R. Hino, and T. Kazakami, “The great 1933 Sanriku-oki earthquake: reappraisal of the main shock and its aftershocks and implications for its tsunami using regional tsunami and seismic data,” *Geophysical Journal International*, vol. 206, no. 3, pp. 1619–1633, 2016.
- [26] E. Valerio, P. Tizzani, E. Carminati, and C. Doglioni, “Longer aftershocks duration in extensional tectonic settings,” *Scientific Reports*, vol. 7, pp. 16403–403, 2017.
- [27] A. Zarola and A. Sil, “Artificial neural networks (ANN) and stochastic techniques to estimate earthquake occurrences in Northeast region of India,” *Annals of Geophysics*, vol. 60, Article ID S0658, 2017.
- [28] K. Richards-Dinger, R. S. Stein, and S. Toda, “Decay of aftershock density with distance does not indicate triggering by dynamic stress,” *Nature*, vol. 467, no. 7315, pp. 583–586, 2010.
- [29] D. Kilb, V. G. Martynov, and F. L. Vernon, “Aftershock detection thresholds as a function of time: results from the ANZA seismic network following the 31 october 2001 ML 5.1 anza, California, earthquake,” *Bulletin of the Seismological Society of America*, vol. 97, no. 3, pp. 780–792, 2007.
- [30] W. J. Bosl and A. Nur, “Aftershocks and pore fluid diffusion following the 1992 Landers earthquake,” *Journal of Geophysical Research*, vol. 107, pp. 2366–2381, 2002.
- [31] C.-H. Chang, Y.-M. Wu, L. Zhao, and F. T. Wu, “Aftershocks of the 1999 chi-chi, taiwan, earthquake: the first hour,” *Bulletin of the Seismological Society of America*, vol. 97, no. 4, pp. 1245–1258, 2007.
- [32] B. Enescu, J. Mori, and M. Miyazawa, “Quantifying early aftershock activity of the 2004 mid-Niigata Prefecture earthquake (Mw6.6),” *Journal of Geophysical Research*, vol. 112, Article ID B04310, 2007.
- [33] O. Lengliné, B. Enescu, Z. Peng, and K. Shiomi, “Decay and expansion of the early aftershock activity following the 2011, Mw 9.0 Tohoku earthquake,” *Geophysical Research Letters*, vol. 39, Article ID L18309, 2012.
- [34] T. Shirzad, “Study of fault plane using the interferometry of aftershocks: case study in the Rigan area of SE Iran,” *Geophysical Journal International*, vol. 217, no. 1, pp. 190–205, 2019.
- [35] X. B. Tan, X. W. Xu, Y. H. Lee et al., “Late Cenozoic thrusting of major faults along the central segment of Longmen Shan, eastern Tibet: evidence from low-temperature thermochronology,” *Tectonophysics*, vol. 712–713, pp. 145–155, 2017.
- [36] K. Zhang and D. Wei, “Implications from the kinematic pattern of the Longmenshan region,” *Tectonophysics*, vol. 504, no. 1–4, pp. 57–64, 2011.
- [37] M. Ishimoto and K. Iida, “Observations sur les seismes enregistres parle microsismographe construit dernièrement,” *Bulletin of the Earthquake Research Institute*, vol. 17, pp. 443–478, 1939.
- [38] B. Gutenberg and C. F. Richter, “Earthquake magnitude, intensity, energy, and acceleration\*,” *Bulletin of the Seismological Society of America*, vol. 32, no. 3, pp. 163–191, 1942.
- [39] T. C. Hanks, “Bvalues and  $\omega$ - $\gamma$  seismic source models: implications for tectonic stress variations along active crustal fault zones and the estimation of high-frequency strong ground motion,” *Journal of Geophysical Research*, vol. 84, no. B5, pp. 2235–2242, 1979.

- [40] D. J. Andrews, "A stochastic fault model: 1. Static case," *Journal of Geophysical Research: Solid Earth*, vol. 85, no. B7, pp. 3867–3877, 1980.
- [41] S. Wiemer and W. Wyss, "Minimum magnitude of completeness in earthquake catalogs: examples from Alaska, the Western United States, and Japan," *Bulletin of the Seismological Society of America*, vol. 90, no. 4, pp. 859–869, 2000.
- [42] D. Kilb, J. Gomberg, and P. Bodin, "Triggering of earthquake aftershocks by dynamic stresses," *Nature*, vol. 408, no. 6812, pp. 570–574, 2000.
- [43] S. Das and C. H. Scholz, "Theory of time-dependent rupture in the Earth," *Journal of Geophysical Research: Solid Earth*, vol. 86, no. B7, pp. 6039–6051, 1981.
- [44] S. Zhu, "Is the 2013 lushan earthquake (Mw=6.6) a strong aftershock of the 2008 wenchuan, China mainshock (Mw=7.9)?" *Journal of Geodynamics*, vol. 99, pp. 16–26, 2016.
- [45] B. C. Burchfiel, L. H. Royden, R. D. van der Hilst et al., "A geological and geophysical context for the Wenchuan earthquake of 12 May 2008, Sichuan, People's Republic of China," *Geological Society of America Today*, vol. 18, no. 7, pp. 4–11, 2008.
- [46] T. Utsu, "A statistical study on the occurrence of aftershocks," *Geophysical Magazine*, vol. 30, pp. 521–605, 1961.
- [47] A. Douglas, D. Bowers, P. D. Marshall, J. B. Young, D. Porter, and N. J. Wallis, "Putting nuclear-test monitoring to the test," *Nature*, vol. 398, no. 6727, pp. 474–475, 1999.
- [48] L. Han, Z. Wu, C. Jiang, and J. Liu, "Properties of three seismic events in September 2017 in the northern Korean Peninsula from moment tensor inversion," *Science Bulletin*, vol. 62, no. 23, pp. 1569–1571, 2017.
- [49] Z. Wu, P. J. Barosh, Z. Zhang, and H. Liao, "Effects from the wenchuan earthquake and seismic hazard in the longmenshan Mountains at the eastern margin of the Tibetan plateau," *Engineering Geology*, vol. 143–144, pp. 28–36, 2012.
- [50] Q. Xu, S. Zhang, and W. Li, "Spatial distribution of large-scale landslides induced by the 5.12 Wenchuan Earthquake," *Journal of Mountain Science*, vol. 8, no. 2, pp. 246–260, 2011.
- [51] K. Jia, S. Zhou, J. Zhuang, and C. Jiang, "Possibility of the independence between the 2013 lushan earthquake and the 2008 wenchuan earthquake on longmen Shan fault, sichuan, China," *Seismological Research Letters*, vol. 85, no. 1, pp. 60–67, 2014.
- [52] Y. Wang, F. Wang, M. Wang, Z.-K. Shen, and Y. Wan, "Coulomb stress change and evolution induced by the 2008 wenchuan earthquake and its delayed triggering of the 2013 Mw 6.6 lushan earthquake," *Seismological Research Letters*, vol. 85, no. 1, pp. 52–59, 2014.

## Research Article

# Research on Intelligent Evaluation Model of Railway Internationalized Earthquake Emergency Rescue Talents Based on Analytic Hierarchy Process and Fuzzy Theory

Jin Jing , Yang Yu, and Jiang Yuxin

China Academy of Railway Sciences Group Co. Ltd., Beijing 100000, China

Correspondence should be addressed to Jin Jing; 278946257@qq.com

Received 7 May 2021; Revised 15 July 2021; Accepted 29 July 2021; Published 11 October 2021

Academic Editor: Roberto Nascimbene

Copyright © 2021 Jin Jing et al. This is an open access article distributed under the Creative Commons Attribution License, which permits unrestricted use, distribution, and reproduction in any medium, provided the original work is properly cited.

Earthquakes occur frequently in the 21st century and cause a large number of casualties; induced secondary geological disasters will cause more serious casualties. How to reasonably deal with the earthquake disaster to carry out emergency rescue work is becoming increasingly urgent; the ability level of earthquake disaster emergency rescue personnel is directly related to the follow-up relief effect. Based on this, aiming at the emergency rescue ability of nationalized railway management talents in high-intensity earthquake areas around the world, this paper will use the methods of analytic hierarchy process and fuzzy theory to construct an intelligent evaluation model of railway international earthquake emergency rescue personnel ability. In addition, this paper carries out a questionnaire survey of experts in related fields and model empirical research and puts forward optimization measures and suggestions for the personnel training of railway international earthquake emergency rescue in high-intensity seismic areas based on the results of model evaluation.

## 1. Introduction

The “National Medium and Long-term Education Reform and Development Plan Outline (2010–2020)” pointed out that international talents refer to talents who have an international vision, are familiar with international rules, and can participate in international affairs and international competition. Earthquakes occur frequently in the 21st century and will directly cause railway deformation (see Figures 1(a) and 1(b)), causing a lot of economic losses and casualties; induced secondary geological disasters will cause more serious casualties. How to reasonably deal with the earthquake disaster to carry out emergency rescue work is becoming increasingly urgent; the ability level of earthquake disaster emergency rescue personnel is directly related to the follow-up relief effect [1–5]. With the deepening of overseas railway projects, there are a large number of lines located in high-intensity earthquake areas, such as Indonesia Yawan high-speed railway (see Figures 2 & 3), earthquakes occur frequently and do great harm (see Figures 4–7) [6–10], and the talent team cannot meet the needs of rapid growth in

terms of scale or quality. This paper constructs a model for evaluating the ability of railway international earthquake emergency rescue talents based on fuzzy theory, analytic hierarchy process, expert investigation, and other methods. Based on the model analysis, the key ability elements and training optimization measures for railway international emergency rescue personnel in high-intensity earthquake areas are put forward.

*1.1. Overview of Research on Emergency Rescue Capability.* “Competency” is usually called “emergency rescue capability” in high-speed railway response to earthquake disasters, which reflects the expression of the comprehensive ability of emergency rescue personnel to deal with earthquake disasters, which will be studied systematically in this paper. The concept of “competency” originated in the field of American psychology. It is one of the methods to replace traditional intelligence tests to measure personal work ability and performance. It is widely used in education, business, and other fields. In 1953, David McClelland, a professor of



FIGURE 1: The earthquake paralyzed the railway system.

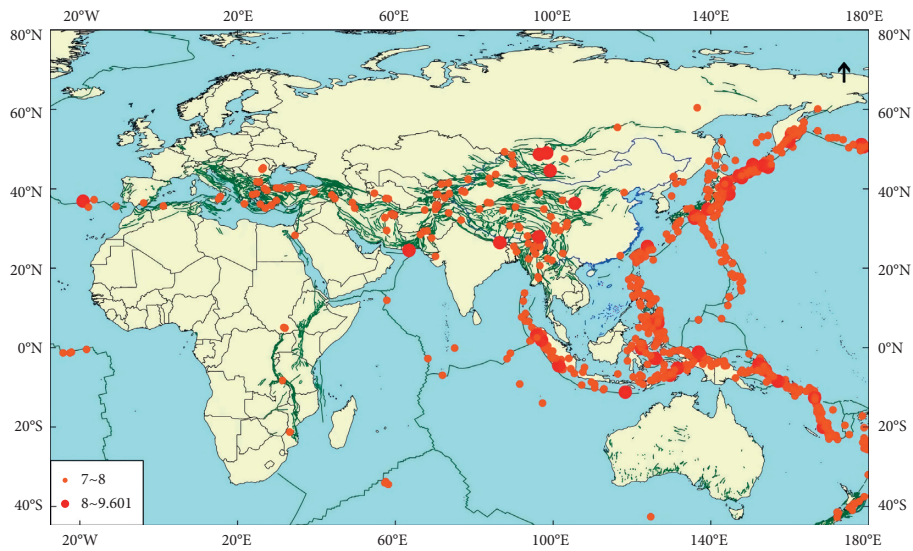


FIGURE 2: Distribution diagram of historical earthquakes with magnitude 7 and above in the world.

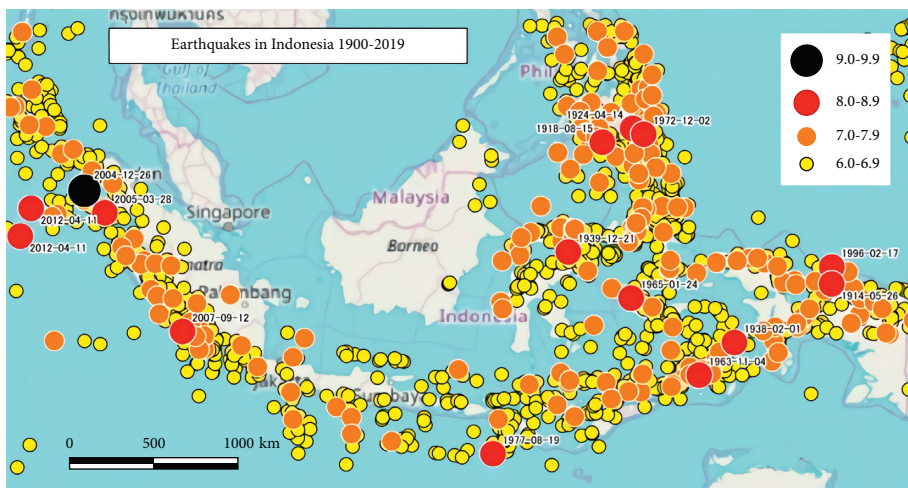


FIGURE 3: Seismic intensity distribution along the Yawan high-speed railway in Indonesia.





FIGURE 4: The armed police are carrying out emergency rescue during the May 12, 2008, Wenchuan earthquake.



FIGURE 5: Rescue workers in a collapsed building after the earthquake in Christchurch, New Zealand, February 23, 2011.



FIGURE 6: Dam damage caused by earthquake.



FIGURE 7: Landslide caused by earthquake to form dammed lake.

psychology at Harvard University, proposed in the paper “testing for competence rather than for intelligence” [11] that academic talent and knowledge structure in the traditional sense are important factors to measure academic ability, but it is difficult to evaluate work ability or performance. He believes that the measurement of work ability is an implicit and lasting personal trait, which is called “competency.” In 1982, Richard Boyatzis applied the competency probability to the business field. In his book “Competent Managers” [12], he defined competence as a potential personal trait of high efficiency and outstanding performance at work, including motivation, characteristics, skills, personal image, social role, and knowledge system. Hornby and Thomas [13] and Jacobs [14] apply competence to the field of human resource management, believing that competence is the embodiment of effective management ability in the work environment and believes that this ability is observable. Spencer and Spencer [15] pointed out that competence is a potential characteristic possessed by excellent employees, including motivation, personal traits, self-awareness, knowledge, and skills. Brown [16] further elaborated that competency is the ability required to meet the goals of a certain position in the workplace environment. It can be standardized and evaluated as the entry screening condition, which is also the basis of training and professional certification.

## 2. Construction of an Index System for the Ability of Earthquake Emergency Rescue Personnel

*2.1. Identification of Emergency Rescue Capability Elements.* Taking railway internationalized operation and management talents as the object, through literature research, recruitment case analysis, and expert interviews, the competency indicators are screened and classified to form the key elements of the competence for international talents.

Based on the literature research method, it sorts out more than 30 international talents’ competency research literature on HowNet, extracts and conceptualizes competency features, and counts the frequency of competency features.

Similarly, based on the case analysis method, through sorting out Worry-Free Recruitment, Zhilian Recruitment, and other websites, recruitment requirement of 41 international project managers from many railway construction and emergency equipment manufacturing companies such as Siemens, Alstom, China Railway, China Railway Engineering, CRRC, China Communications, and China Hydropower is collected. For management positions, competency characteristics are extracted and the frequency of occurrence is counted, as shown in Table 1:

*2.2. The Ability Index System of Emergency Rescue Talents.* On the basis of identifying the ability characteristics of international emergency rescue talents based on literature research and recruitment case analysis and through investigating more than 30 middle and senior managers participating in railway overseas projects, the

TABLE 1: Statistical frequency of emergency rescue capability characteristics.

Competency index	Frequency of literature statistics	Recruitment statistics index frequency	Subtotal
Professional knowledge	10	38	48
International perspective	9	34	43
Communication skills	15	27	42
Management ability of emergency rescue project	10	28	38
Sense of responsibility	12	19	31
Integrity and confidence	9	19	28
Compressive ability	12	15	27
Teamwork	6	14	20
Political literacy	5	15	20
International business knowledge of emergency rescue	4	14	18
Emergency rescue capability	6	8	14
Information acquisition and processing capabilities	8	5	13
Ability to learn quickly in local customs	4	5	9

competence characteristics of the indicator system for international talents are listed and optimized, the indicator definitions are clarified, and the categories are sorted and integrated, as shown in Figure 8, categorizing to form three first-level indicators of knowledge, skills, and professionalism and 15 second-level indicator systems details as follows:

- (1) Knowledge: the professional knowledge of emergency rescue that employees must possess for a specific job
- (2) Skills: the ability to master and apply certain professional knowledge of emergency rescue to complete specific tasks
- (3) Professionalism: the ideology, ethics, awareness, and behavior habits that employees should possess when engaging in a specific position of emergency rescue

Definition and description of competency index:

- (i) Railway engineering knowledge: master and understand all links and procedures in railway engineering construction, be familiar with construction process, engineering materials, and construction technology, and know technical specifications and quality inspection and control procedures.
- (ii) Knowledge of earthquake risk prevention and control: understand the laws and regulations on target market access, foreign investment approval, foreign exchange supervision, national security review, and employment.
- (iii) Knowledge of emergency rescue fund management: master international financial management, foreign exchange management, corporate finance, international investment management, international taxation, etc.
- (iv) International perspective: familiar with international practices, with the international frontier knowledge of emergency rescue of this major, with the ability to operate internationally, and with experience in overseas engineering project development of emergency rescue.

- (v) International emergency rescue legal knowledge: including international trade, foreign investment, international finance, international business negotiation, international etiquette, and other knowledge systems, familiar with the work process of overseas project bidding, business negotiation, contract writing, etc.
- (vi) Communication skills: individuals can correctly listen to the voices of the rescued and emergency rescue teams, feel their feelings, needs, and opinions, and have the ability to respond appropriately, to listen, speak, read, and write in at least one international common language, and to communicate across cultures.
- (vii) Information acquisition and processing capabilities: obtain the new technical information of emergency rescue through the Internet and interpersonal network, fully understand the new technical information, and use the information to speed up the development of emergency rescue work.
- (viii) Emergency rescue ability: employees can quickly understand the intentions of their superiors at work and then form goals and formulate concrete and feasible action plans, rationally use relevant resources, implement the plan, and achieve the work goals.
- (ix) Emergency rescue project management ability: employees plan the project schedule, organize, and implement project management according to the project schedule plan and do a good job in project quality, safety, risk, contract, cost, and other management tasks.
- (x) Ability to learn rapidly in local customs: master the customs of the place where the disaster occurred and be able to quickly adjust and adapt according to their own characteristics.
- (xi) Sense of responsibility: employees are responsible for what they do, take responsibility for others, and consciously perform their obligations to the organization.

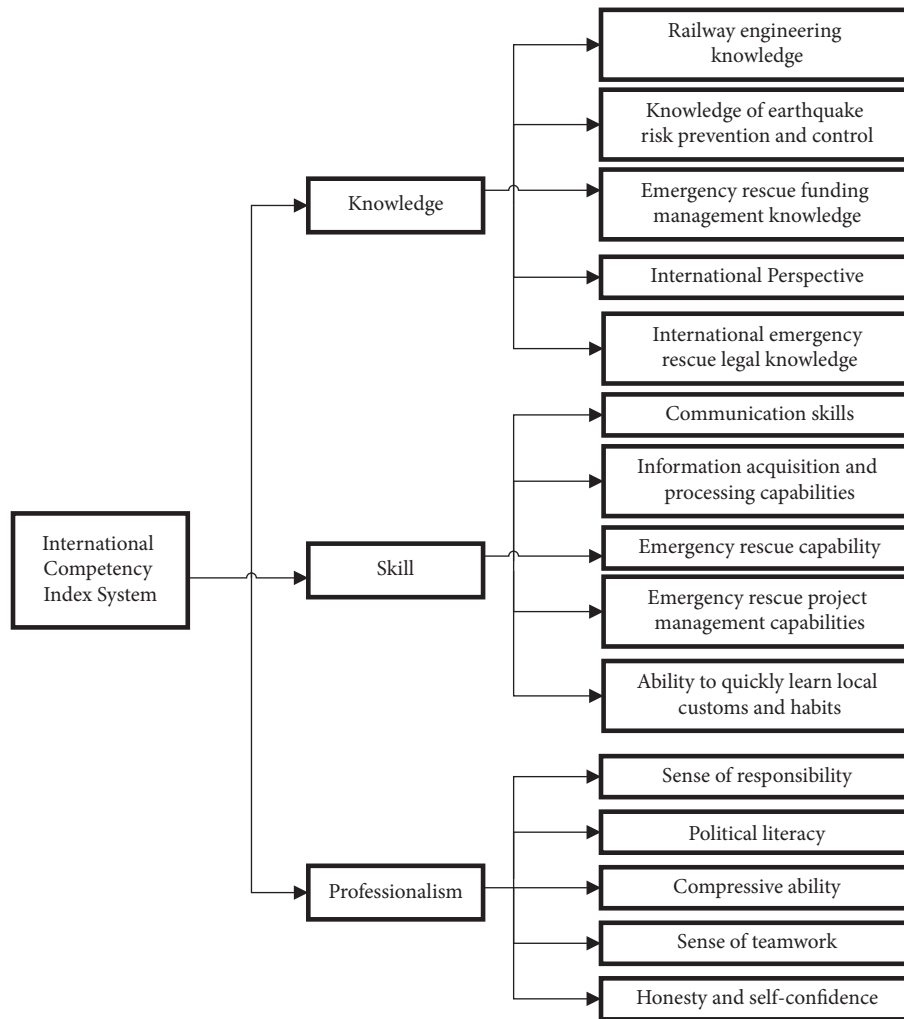


FIGURE 8: Ability index system of railway international emergency rescue personnel in high-intensity earthquake area.

- (xii) Political literacy: employees are loyal to the country, trust in their work, team, and organization, and are aware of the importance of the country and collective interests in key events
- (xiii) Compressive ability: the strength of adaptability, tolerance, endurance, and ability to overcome adversity overseas earthquake disasters.
- (xiv) Teamwork literacy: have a holistic view, be able to obey commands, cooperate with others according to the needs of work goals, coordinate various relationships, mobilize the enthusiasm of all parties, and be able to deal with and solve various problems in the work in a timely manner.
- (xv) Integrity and confidence: good conduct, honesty, and decent, self-belief in one's own views, decisions,

and tasks, and the ability to solve problems effectively. The first priority is to save the safety of life and property in the process of earthquake.

### 3. Construction of Competency Model Based on Fuzzy Analytic Hierarchy Process

The analytic hierarchy process is a system qualitative and quantitative analysis method. The basic principle is to decompose the research object into a hierarchical structure according to the system composition, establish a hierarchical multilevel structure model, and systematically clarify the relationship between various factors that affect the evaluation. Then, adopting the Delphi method, relative importance of each factor at the same level is compared and justified according to the corresponding scoring rules, and finally, the relevant index weight is obtained.

However, in the traditional analytic hierarchy process, when constructing the judgment matrix based on the expert score, the only specific value is obtained, and the constructed matrix is an ideal situation that does not allow deviation. In the actual index comparison process, people often have fuzzy feelings in their judgments, and the true value is often within an interval range. In order to reflect the cognitive information of experts more comprehensively and obtain a more scientific evaluation result, the triangular fuzzy function theory is incorporated in the construction of the judgment matrix, and the traditional single importance value is converted into fuzzy numerical intervals with upper and lower bounds which is helpful to scientifically and quantitatively deal with information problems in fuzzy environments [17].

**3.1. Triangular Fuzzy Number.** Define if the membership function of fuzzy number  $A$  is

$$\mu_A x = \begin{cases} \frac{x}{m-l} - \frac{l}{m-l}, & x \in [l, m], \\ \frac{x}{m-u} - \frac{u}{m-u}, & x \in [m, u], \\ 0, & x \notin [l, u], \end{cases} \quad (1)$$

where  $x: [l, m]$  is continuous and strictly increasing and  $x: [m, u]$  is continuous and strictly decreasing and satisfies  $l < m < u$  and  $l, m, u \in R$ . Then, the fuzzy number  $A$  is a triangular fuzzy number, denoted as  $A = l, m, u$ . Among them,  $l$  is the lower limit,  $u$  is the upper limit, and  $m$  is the possible value [18].

**3.2. Construct a Triangular Fuzzy Judgment Matrix [19].** With  $n$  evaluation indicators, the constructed judgment matrix is  $B = (b_{ij})_{n \times n}$ , where  $b_{ij} = [l_{ij}, m_{ij}, u_{ij}]$  is a closed interval with  $m_{ij}$  as the median and  $b_{ji} = b_{ij}^{-1} = [u_{ij}^{-1}, m_{ij}^{-1}, l_{ij}^{-1}]$ .

If there are a number of  $K$  experts jointly participating in the judgment, at this time,  $b_{ij}$  is a comprehensive triangular fuzzy number, and its value is obtained by the following formula:

$$b_{ij} = \frac{1}{K} \otimes (b_{ij}^1 + b_{ij}^2 + \dots + b_{ij}^k) \quad (k = 1, 2, \dots, K). \quad (2)$$

After more than 30 experts in railway engineering, railway economics, railway logistics, commerce and trade, transportation planning and management, human resources, and other related fields scored, the four triangular fuzzy judgment matrices  $B_i$  ( $i = 1, 2, 3, 4$ ) are as follows:

$$\begin{aligned} B1 &= \begin{bmatrix} (1, 1, 1) & (4, 5, 6) & (6, 7, 8) \\ \left(\frac{1}{6}, \frac{1}{5}, \frac{1}{4}\right) & (1, 1, 1) & (4, 5, 6) \\ \left(\frac{1}{8}, \frac{1}{7}, \frac{1}{6}\right) & \left(\frac{1}{6}, \frac{1}{5}, \frac{1}{4}\right) & (1, 1, 1) \end{bmatrix}, \\ B2 &= \begin{bmatrix} (1, 1, 1) & (4, 5, 6) & (6, 7, 8) & (5, 6, 7) & (5, 6, 7) \\ \left(\frac{1}{6}, \frac{1}{5}, \frac{1}{4}\right) & (1, 1, 1) & (5, 6, 7) & (6, 7, 8) & (1, 2, 3) \\ \left(\frac{1}{8}, \frac{1}{7}, \frac{1}{6}\right) & \left(\frac{1}{7}, \frac{1}{6}, \frac{1}{5}\right) & (1, 1, 1) & \left(\frac{1}{5}, \frac{1}{4}, \frac{1}{3}\right) & \left(\frac{1}{6}, \frac{1}{5}, \frac{1}{4}\right) \\ \left(\frac{1}{7}, \frac{1}{6}, \frac{1}{5}\right) & \left(\frac{1}{8}, \frac{1}{7}, \frac{1}{6}\right) & (3, 4, 5) & (1, 1, 1) & (1, 2, 3) \\ \left(\frac{1}{7}, \frac{1}{6}, \frac{1}{5}\right) & \left(\frac{1}{3}, \frac{1}{2}, 1\right) & (4, 5, 6) & \left(\frac{1}{3}, \frac{1}{2}, 1\right) & (1, 1, 1) \end{bmatrix}, \\ B3 &= \begin{bmatrix} (1, 1, 1) & (5, 6, 7) & (1, 2, 3) & (6, 7, 8) & (3, 4, 5) \\ \left(\frac{1}{7}, \frac{1}{6}, \frac{1}{5}\right) & (1, 1, 1) & \left(\frac{1}{6}, \frac{1}{5}, \frac{1}{4}\right) & \left(\frac{1}{4}, \frac{1}{3}, \frac{1}{2}\right) & \left(\frac{1}{4}, \frac{1}{3}, \frac{1}{2}\right) \\ \left(\frac{1}{3}, \frac{1}{2}, 1\right) & (4, 5, 6) & (1, 1, 1) & (3, 4, 5) & (3, 4, 5) \\ \left(\frac{1}{8}, \frac{1}{7}, \frac{1}{6}\right) & (2, 3, 4) & \left(\frac{1}{5}, \frac{1}{4}, \frac{1}{3}\right) & (1, 1, 1) & (1, 2, 3) \\ \left(\frac{1}{5}, \frac{1}{4}, \frac{1}{3}\right) & (2, 3, 4) & \left(\frac{1}{5}, \frac{1}{4}, \frac{1}{3}\right) & \left(\frac{1}{3}, \frac{1}{2}, 1\right) & (1, 1, 1) \end{bmatrix}, \\ B4 &= \begin{bmatrix} (1, 1, 1) & (1, 2, 3) & (5, 6, 7) & (7, 8, 9) & (7, 8, 9) \\ \left(\frac{1}{3}, \frac{1}{2}, 1\right) & (1, 1, 1) & (5, 6, 7) & (5, 6, 7) & (7, 8, 9) \\ \left(\frac{1}{7}, \frac{1}{6}, \frac{1}{5}\right) & \left(\frac{1}{7}, \frac{1}{6}, \frac{1}{5}\right) & (1, 1, 1) & (3, 4, 5) & (6, 7, 8) \\ \left(\frac{1}{9}, \frac{1}{8}, \frac{1}{7}\right) & \left(\frac{1}{7}, \frac{1}{6}, \frac{1}{5}\right) & \left(\frac{1}{5}, \frac{1}{4}, \frac{1}{3}\right) & (1, 1, 1) & (2, 3, 4) \\ \left(\frac{1}{9}, \frac{1}{8}, \frac{1}{7}\right) & \left(\frac{1}{9}, \frac{1}{8}, \frac{1}{7}\right) & \left(\frac{1}{8}, \frac{1}{7}, \frac{1}{6}\right) & \left(\frac{1}{4}, \frac{1}{3}, \frac{1}{2}\right) & (1, 1, 1) \end{bmatrix}. \quad (3) \end{aligned}$$

According to the above fuzzy judgment matrix, the fuzzy evaluation factor matrix  $R$  is constructed, and the calculation formula is as follows:

$$R = (r_{ij})_{n \times n} = \begin{bmatrix} 1 & 1 - \frac{u_{12} - l_{12}}{2m_{12}} & \dots & 1 - \frac{u_{1n} - l_{1n}}{2m_{1n}} \\ 1 - \frac{u_{21} - l_{21}}{2m_{21}} & 1 & \dots & \dots \\ \dots & \dots & \dots & \dots \\ 1 - \frac{u_{n1} - l_{n1}}{2m_{n1}} & \dots & \dots & 1 \end{bmatrix}. \quad (4)$$

Calculate and adjust the judgment matrix  $Q$ :

$$Q = M \times R$$

$$= \begin{bmatrix} 1 & m_{12} & \dots & m_{1n} \\ m_{21} & 1 & \dots & \dots \\ \dots & \dots & \dots & \dots \\ m_{n1} & \dots & \dots & 1 \end{bmatrix} \times \begin{bmatrix} 1 & 1 - \frac{u_{12} - l_{12}}{2m_{12}} & \dots & 1 - \frac{u_{1n} - l_{1n}}{2m_{1n}} \\ 1 - \frac{u_{21} - l_{21}}{2m_{21}} & 1 & \dots & \dots \\ \dots & \dots & \dots & \dots \\ 1 - \frac{u_{n1} - l_{n1}}{2m_{n1}} & \dots & \dots & 1 \end{bmatrix}. \quad (5)$$

In the formula, matrix  $M$  is a matrix composed of the median values of all triangular fuzzy numbers in the judgment matrix.

Convert the adjusted judgment matrix  $Q$  into a judgment matrix with a diagonal of  $l$  in columns, and record it as the final judgment matrix  $P$ ; then,  $P = (p_{ij})_{n \times n}$  and  $P_{ij} = 1/p_{ji}$ .

**3.3. Determine the Weight.** Using the tomographic analysis method and combining the triangular fuzzy judgment matrix, the weight is determined and the consistency check is performed [19], the above calculation process is realized through the python language, and the results are as follows:

Hierarchical single sort CR	CR1=0.014187<0.1
	CR2=0.000201<0.1
	CR3=0.015965<0.1
	CR4=0.015583<0.1
Total rank order CR	CR1=0.014187<0.1
	CR2=0.014388<0.1
	CR3=0.030152<0.1
	CR4=0.029770<0.1

The consistency index CR of single-level ranking and total-level ranking are both less than 0.1, indicating that the above judgment matrix has good consistency. According to the model calculation, the weight of each indicator is as follows:

Secondary indicators and weights	Three-level indicator layer	Hierarchical single sort weight	Total ranking weight
Knowledge(Z) W(Z)=0.63	Railway engineering knowledge (Z1)	W(Z1)=0.430	W(Z1)=0.271
	<input type="checkbox"/> Knowledge of earthquake risk prevention and control (Z2)	W(Z2)=0.284	W(Z2)=0.180
	Emergency Rescue funds Management knowledge (Z3)	W(Z3)=0.032	W(Z3)=0.020
	<input type="checkbox"/> International Perspective (Z4)	W(Z4)=0.126	W(Z4)=0.080
	International Emergency Rescue legal knowledge (Z5)	W(Z5)=0.128	W(Z5)=0.081
Skills(J) W(J)=0.30	Communication skills (J1)	W(J1)=0.418	W(J1)=0.126
	Information acquisition and processing capabilities (J2)	W(J2)=0.043	W(J2)=0.013
	Emergency rescue capability (J3)	W(J3)=0.301	W(J3)=0.091
	Emergency Rescue Project Management ability (J4)	W(J4)=0.133	W(J4)=0.040
	Ability to learn rapidly in local customs (J5)	W(J5)=0.105	W(J5)=0.032
Professionalism(Y) W(Y)=0.07	Sense of responsibility (Y1)	W(Y1)=0.383	W(Y1)=0.025
	Political literacy (Y2)	W(Y2)=0.331	W(Y2)=0.022
	Compressive ability (Y3)	W(Y3)=0.190	W(Y3)=0.012
	Teamwork literacy (Y4)	W(Y4)=0.070	W(Y4)=0.005
	Integrity and confidence (Y5)	W(Y5)=0.026	W(Y5)=0.002

According to the expert evaluation results, the second-level index weights are ranked as follows: knowledge (0.63), skills (0.30), and professionalism (0.07). The order of three-level indicator weight is railway engineering knowledge (0.271), knowledge of earthquake risk prevention and control (0.180), emergency rescue funds management knowledge (0.020), international perspective (0.080), international emergency rescue legal knowledge (0.081), communication ability (0.126), information acquisition and processing ability (0.013),

emergency rescue capability (0.091), emergency rescue project management ability (0.040), ability to learn rapidly in local customs (0.032), sense of responsibility (0.025), political literacy (0.022), compressive ability (0.012), sense of teamwork (0.005), and integrity and self-confidence (0.002). From the analysis of indicator weights, it can be seen that the weight ratio of knowledge is the highest, skills are second, and professionalism is the lowest. According to the index weight analysis, the weight proportion of knowledge is the highest, the skill is

the second, and the professional accomplishment is the lowest. Among them, railway engineering knowledge, knowledge of earthquake risk prevention and control, communication ability, information acquisition and processing ability in skill module, sense of responsibility, and political literacy in professional accomplishment module are prominent in the knowledge module. They need to be targeted for personal literacy and existing knowledge base and training.

#### 4. Conclusion

Through the above research, the following conclusions are drawn:

- (1) In this study, the evaluation model of emergency rescue ability of international talents of railway management in high-intensity earthquake area is established, which can cover three types of knowledge, skills, professional accomplishment, and 15 secondary indicators and quantitatively determine the influence weight of different impact indicators. It will point out the direction for the follow-up international earthquake disaster emergency rescue personnel training.
- (2) The construction of the evaluation system of emergency rescue ability is helpful to build a unified talent standard, identify the gap between employee current competency level and job demand, customize the training plan of personnel, enhance the pertinence of training, improve the effectiveness of training, help employees to improve their performance, and realize modular design for the training of earthquake emergency rescue personnel of high-speed railway in high-intensity areas. Then, comprehensively improve the comprehensive quality and level of earthquake emergency rescue personnel.

#### Data Availability

The data used to support the findings of this study are available from the corresponding author upon request.

#### Conflicts of Interest

The authors declare that they have no conflicts of interest regarding the publication of this paper.

#### References

- [1] M. L. Istiyanti, S. Goto, and H. Ochiai, "Characteristics of tuff breccia-andesite in diverse mechanisms of landslides in Oita Prefecture, Kyushu, Japan," *Geoenvironmental Disasters*, vol. 8, no. 1, 2021.
- [2] A. Dille, F. Kervyn, A. L. Handwerger et al., "When image correlation is needed: Unravelling the complex dynamics of a slow-moving landslide in the tropics with dense radar and optical time series," *Remote Sensing of Environment*, vol. 258, Article ID 112402, 2021.
- [3] E. Tondi, A. M. Blumetti, M. Čičak et al., "Conjugate coseismic surface faulting related with the 29 December 2020, Mw 6.4, Petrinja earthquake (Sisak-Moslavina, Croatia)," *Scientific Reports*, vol. 11, no. 1, 2021.
- [4] M. Niño, M. A. Jaimes, and E. Reinoso, "Seismic-event-based methodology to obtain earthquake-induced translational landslide regional hazard maps," *Natural Hazards*, vol. 73, no. 3, pp. 1697–1713, 2014.
- [5] D. M. Tralli, R. G. Blom, V. Zlotnicki, A. Donnellan, and D. L. Evans, "Satellite remote sensing of earthquake, volcano, flood, landslide and coastal inundation hazards," *ISPRS Journal of Photogrammetry and Remote Sensing*, vol. 59, no. 4, pp. 185–198, 2005.
- [6] M. J. Rodríguez-Peces, J. García-Mayordomo, and J. J. Martínez-Díaz, "Slope instabilities triggered by the 11th May 2011 Lorca earthquake (Murcia, Spain): comparison to previous hazard assessments and proposition of a new hazard map and probability of failure equation," *Bulletin of Earthquake Engineering*, vol. 12, no. 5, pp. 1961–1976, 2014.
- [7] F. Guzzetti, A. C. Mondini, M. Cardinali, F. Fiorucci, M. Santangelo, and K.-T. Chang, "Landslide inventory maps: New tools for an old problem," *Earth-Science Reviews*, vol. 112, no. 1–2, pp. 42–66, 2012.
- [8] H. Hong, B. Pradhan, C. Xu, and D. Tien Bui, "Spatial prediction of landslide hazard at the Yihuang area (China) using two-class kernel logistic regression, alternating decision tree and support vector machines," *Catena*, vol. 133, pp. 266–281, 2015.
- [9] H. Singh and S. K. Som, "Earthquake triggered landslide-Indian scenario," *Journal of the Geological Society of India*, vol. 87, no. 1, pp. 105–111, 2016.
- [10] H. Tang, H. Jia, X. Hu, D. Li, and C. Xiong, "Characteristics of landslides Induced by the Great Wenchuan Earthquake," *Journal of Earth Science*, vol. 21, no. 1, pp. 104–113, 2010.
- [11] D. C. McClelland, "Testing for competence rather than for "intelligence."," *American Psychologist*, vol. 28, no. 1, pp. 1–14, 1973.
- [12] H. Gunz, "The competent manager: A model for effective performance, Richard E. Boyatzis," *A Model for Effective Performance*, Wiley, New York, NY, USA, Article ID 247813294, 1983.
- [13] D. Hornby and R. Thomas, "Toward a Better Standard of Management," *Personnel Management*, vol. 21, no. 1, pp. 52–55, 1989.
- [14] R. Jacobs, "Getting the Measure of Management Competence," *Personnel Management*, vol. 21, no. 6, pp. 32–37, 1989.
- [15] L. Spencer and S. Spencer, *Competence at Work: Model for Superior Performance*, John Wiley & Sons, New York, NY, USA, 1993.
- [16] R. B. Brown, "Meta-Competence: A Recipe for Reframing the Competence Debate," *Personnel Review*, vol. 22, no. 6, pp. 25–36, 1993.
- [17] X. Cheng and J. Ji, "A New Priority Method of the Triangle Fuzzy Analytic Hierarchy Process," *Journal of Hainan Normal University*, vol. 23, no. 1, pp. 8–11, 2010.
- [18] L. qiang, J. Han, Y. Wang, and Y. Le, "Risk Evaluation of Railway PPP Project based on AHP," *Railway Transport and economy*, vol. 39, no. 10, pp. 7–11+30, 2017.
- [19] B. Luo, Q. Wang, and J. Zhu, "A Method for Determining Evaluation Index Weight Based on Triangular Fuzzy Number and AHP," *Research on Telecommunication Technology*, vol. 2013, no. 6, pp. 9–16, 2013.

## Research Article

# Study on Dynamic Response Characteristics and Damage Mechanism of Tunnel Lining at Entrance of Shallow Bias Tunnel

Lin Li,<sup>1</sup> Xiaodan Guo,<sup>1</sup> Zuyin Zou ,<sup>1</sup> Zhanyuan Zhu,<sup>1</sup> Zihong Guo,<sup>1</sup> Weimin Xiao,<sup>1</sup> and Deping Guo<sup>2</sup>

<sup>1</sup>School of Civil Engineering, Sichuan Agricultural University, Dujiangyan 611830, China

<sup>2</sup>Sichuan Railway Investment Group Co., Ltd., Chengdu 610094, China

Correspondence should be addressed to Zuyin Zou; 382358357@qq.com

Received 1 July 2021; Revised 19 August 2021; Accepted 26 August 2021; Published 25 September 2021

Academic Editor: Honglue Qu

Copyright © 2021 Lin Li et al. This is an open access article distributed under the Creative Commons Attribution License, which permits unrestricted use, distribution, and reproduction in any medium, provided the original work is properly cited.

The structural damage of the lining structure at the entrance of a tunnel is the most common instability problem. The instability problem may cause dynamic effects such as earthquakes and blasting. Based on the seismic damage data collected from previous major earthquakes at the entrance of shallow-buried tunnel, the shaking table test and numerical simulation are used to analyze dynamic response characteristics and damage evolution characteristics of the tunnel in the shallow-buried hole at 30°. The study revealed the stress characteristics of tunnel lining and the mechanism of structural damage under earthquake excitation. The research results show that the biased tunnel (30°) is susceptible to damage on the unsymmetrical loading side, the biased ground surface leads to acceleration, and high speed also significantly increases the effect. The biased side leg of the tunnel lining cross section is a location with a large internal force distribution. The biased tunnel has a relatively unfavorable internal force value distribution and a larger peak, and the peak at the larger bias side has the largest peak value. The skewback and spandrel portion of the biased tunnel lining load are more likely to be damaged.

## 1. Introduction

The tunnel opening section is an area that is often subject to changing conditions during the transition from the ground to the underground, it is inevitable that the tunnel encounters a bias phenomenon due to insufficient precautions or poor dynamic effects. The so-called unsymmetrical loading tunnel refers to the tunnel with its support being subject to bias load, where its surrounding rock pressure exhibits apparent unevenness caused by topographical factors, geological factors, and engineering factors [1].

The seismic damage at the entrance of an unsymmetrical loading tunnel mainly includes the collapse of the slope at the entrance and cracks in the lining structure [2]. There are many reports about the damage of tunnel openings caused by earthquakes. For example, there was an opening of the tunnel that was damaged during the 1999 Chi-Chi earthquake [3–5] (Figure 1). In 2008, there were a large number of earthquakes in the Wenchuan earthquake in China. Serious

damage occurred at the opening section of the unsymmetrical loading tunnel [6–8] (Table 1 and Figure 2). The characteristics of the epicenter at the opening of the unsymmetrical loading tunnel section became the focus of research and serves as the decisive place for seismic fortification.

The seismic response of underground structures has been studied by many researchers using various methods, including theoretical analysis, numerical simulation, and physical model tests [9–13]. On-site investigation of the Kumamoto earthquake by Zhang et al. [14] showed that the main seismic damage was cracks seen at the entrance of tunnel lining. Genis and Jai et al. [8, 15–17] performed dynamic response analysis on the stability of the tunnel opening. Wang et al. [18] proposed a method for identifying damage indicators of tunnel lining structures based on wavelet residual force vector. Varma et al. [19] established a universal discrete element coding model, proving that shallow-buried tunnel linings are more vulnerable to





FIGURE 1: Lining crack of tunnel in chi-chi earthquake [4].

TABLE 1: Investigation results of seismic damage for tunnels during Wenchuan earthquake.

Tunnel name	Length (m)	Distance to epicenter (km)	Fault amount	Destruction feature
Longxi	3691	0.5–2	1	Rock falls; pavement uplift; lining crack; lining dislocation; cable trench; water leakage
Taoguan	625	15	0	Portal failure; rock falls; headwall damage; lining crack
Longdongzi	1071	2	4	Rock falls; pavement uplift; lining crack; lining dislocation; cable trench; water leakage
Shaohuoping	451	1	1	Portal failure; rock falls; headwall damage; lining crack; lining dislocation; water leakage
Zaojiaowan	1926	5	0	Portal failure; headwall damage; lining crack; lining dislocation; cable trench; water leakage
Caopo	759	20	0	Portal failure; rock falls; lining crack; cable trench; water leakage
Dankanliangzi	1567	24	1	portal failure; rock falls; headwall damage
Zipingpu	4090	5	10	Rock falls; pavement uplift; lining crack; lining dislocation; cable trench



(a)



(b)

FIGURE 2: Damage patterns of tunnel linings during the Wenchuan earthquake 2008, China. (a) Damage at the entrance of Longxi tunnel [8]. (b) Cracking at the portal of Taoguan tunnel [7].

damage under seismic loads. Wang et al. [20] performed a series of shaking table tests on a scaled-up tunnel model under earthquake excitation to identify damage to the tunnel lining. Wang et al. [21] carried out a large-scale shaking table model test of a small-clearance shallow-buried biased tunnel, finding that the acceleration amplification coefficient and change trend of the left-hole lining are quite different compared with the right-hole lining. Most of the previous research studies are designed to verify the analysis method and provide experimental data regarding the ultimate

stability of the tunnel. However, the study has not been extensively performed to the damage mechanism of the earthquake on the tunnel lining of the shallow-buried unsymmetrical loading tunnel.

In this paper, the shaking table test and numerical simulation are combined to study the lining damage mechanism of the shallow-buried tunnel opening section under the condition of  $30^\circ$  bias angle and  $60^\circ$  elevation slope. First, the shaking table model test is used to study the damage characteristics of the tunnel lining of the shallow-

buried bias tunnel. Then, the dynamic finite element analysis method is used to analyze the characteristics, deformation, and internal force response laws of the full-time dynamic response of the tunnel lining of the shallow-buried bias tunnel. Finally, the simulation results are compared with the model test results to prove the rationality of the shaking table test and the reliability of the numerical simulation.

## 2. Test Plan

*2.1. Model Test Device.* The tunnel model is built in a rigid, sturdy box with a length, width, and height of 1.3 m, 1.0 m, and 1.0 m, respectively (Figure 3(b)), which is anchored on a shaking table (Figure 3(c)). The main parameters of the shaking table are shown in Table 2. With the direction perpendicular to the excitation direction, the wall of the box is lined with a molded polystyrene foam board with a thickness of 70 mm. Meanwhile, a smooth PVC film is pasted on the box walls at both ends of the model to reduce friction resistance on the surface where box comes in contact with soil (Figure 3(a)). A layer of crushed stone is laid on the bottom of the model box to increase the frictional resistance on the contact surface, so as to avoid relative sliding of the bottom plate of the model body when excited (Figure 3(b)).

*2.2. Model Material Parameters.* For the model test of rock mass materials, the geometric dimensions, boundary conditions and acting loads of the model, the bulk density, strength and deformation characteristics of the model rock mass, etc. must meet the similarity requirements expressed as follows [22]:

$$\begin{aligned} C_\sigma &= C_l C_\gamma, \\ C_\sigma &= C_E C_\varepsilon, \\ C_\mu &= 1, \\ C_\delta &= C_l C_\varepsilon, \end{aligned} \quad (1)$$

where  $C_\sigma$  is stress similarity ratio,  $C_l$  is geometric similarity ratio,  $C_E$  is elastic modulus similarity ratio,  $C_\mu$  is Poisson's similarity ratio,  $C_\gamma$  is bulk density similarity ratio,  $C_\varepsilon$  is strain similarity ratio, and  $C_\delta$  is deformation similarity ratio.  $C$  is the similarity ratio of physical parameter between the model and the prototype, respectively. Other ratios were calculated according to their relations with the basic ratios, as shown in Table 3.

The subscripts  $m$  and  $p$  represent the model and prototype, respectively, and  $C_b$ ,  $C_\rho$ , and  $C_a$  represent the similarity ratios of geometry, density, and acceleration, respectively. This study takes  $C_l$  and  $C_\rho$  as 1/50 and 1, respectively.

According to the orthogonal test theory, it is determined that the main materials of the surrounding rock are aggregate and cement. The aggregate is composed of fine sand and the cement is composed of gypsum and lime. The fine sand: cement=4:1 and gypsum: lime=7:3. The water content accounts for about 13%. The similar materials for

lining use gypsum with similar mechanical properties as concrete. According to existing research results, water is used. Based on the obtained similarity ratio, water: gypsum=1:1.5. Material mechanical parameters of surrounding rock and lining model: the surrounding rock material has bulk density 17 kN/m<sup>3</sup>, cohesion 2 kPa, internal friction angle 25°, elastic modulus 0.035 Gpa, and Poisson's ratio 0.37 and lining material has bulk density 24 kN/m<sup>3</sup>, elastic modulus 0.56 Gpa, and Poisson's ratio 0.2. The test process is shown in Figure 4.

*2.3. Test Introduction.* In the test, the El-Centro wave is used as the input wave of the shaking table. The input seismic wave is selected, as shown in Figure 5. Before excitation, the white noise is scanned with a peak value of 0.07 g to make the model compact. In each subsequent set of experiments, a white noise scan was also entered to observe the changes in the dynamic characteristics of the system. Load along the cross section of the tunnel increases the input acceleration peak value (0.1 g) step by step. Before each load, a small amplitude (0.07 g) white noise excitation was input, as shown in Table 4.

The sensors used in shake table tests include accelerometers and strain gauges. The accelerometers and strain gauges were used to measure acceleration and strain on and around the tunnel lining, respectively. The sensor arrangement is also different at each test due to different test objectives. Figure 6 shows the arrangement of the instruments during the test phase. The accelerometer A01 is mounted directly on the shake table and keeps a record of the history of the input-based acceleration of the excitation. The accelerometers are arranged at the left- and right-arch shoulders above the tunnel lining; strain gauges are arranged at the left and right spandrel and skewback of the tunnel lining.

## 3. Analysis of Test Results

*3.1. Acceleration Response Characteristics of Lining Structure.* By comparing and analyzing the Fourier spectra of accelerations of the left and right spandrel of the tunnel lining of Figure 7 and 8, it can be found that the Fourier spectra of the tunnels with the same peak acceleration of the left and right spandrel are similar. Compared with the same peak acceleration of the left and right abutments, the right abutment on the biased surface facing the empty slope aggravates the dynamic stress response of the tunnel lining, and the peak value of the Fu-type spectrum is greater than the left abutment value. By analyzing the Fourier spectrum curves of different peak accelerations on the same side, it can be found that the dynamic response of the tunnel lining is positively correlated with the acceleration peak. The larger the acceleration peak, the more intense the Fourier spectrum attenuation, which also increased the peak value.

*3.2. Failure Morphology of Tunnel Lining.* During the test, the high-speed camera was used to record the damage process on the front and side of the tunnel section. After each

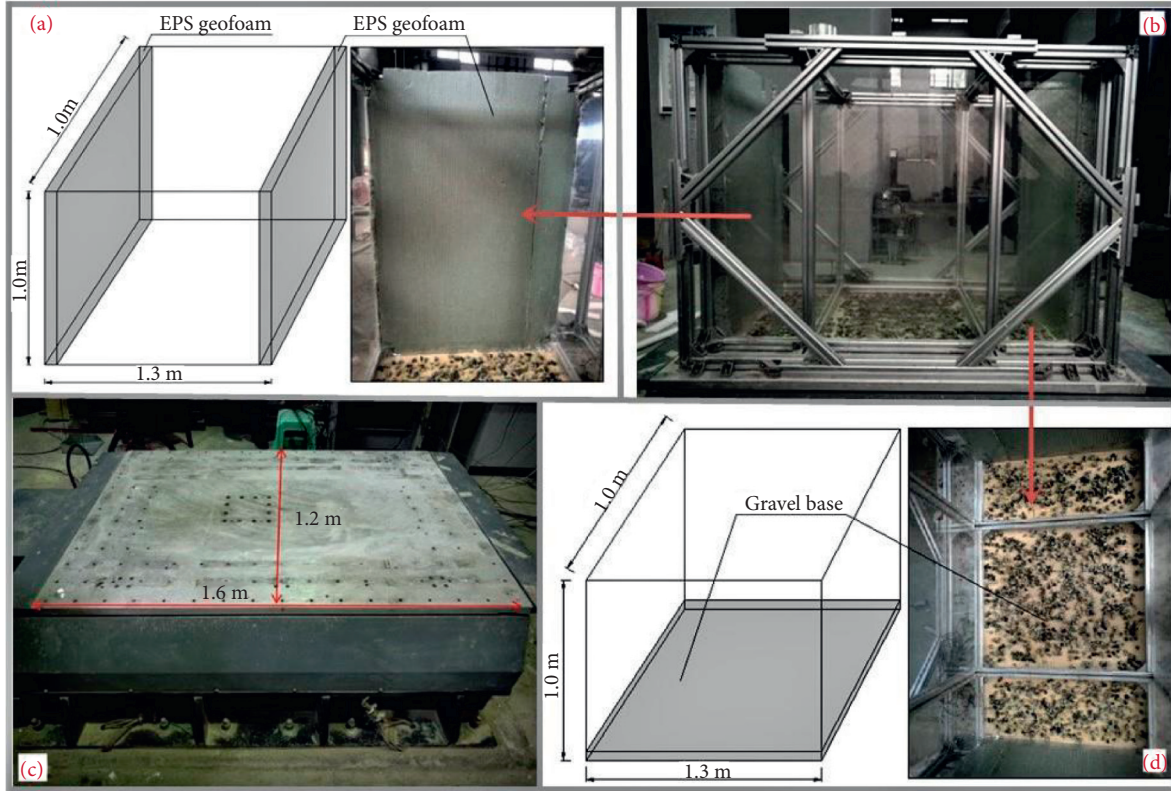


FIGURE 3: Model test device. (a) Polystyrene foam board. (b) Model box. (c) Shaking table. (d) Gravel base.

TABLE 2: Main parameters of the shaking table.

Parameters	Specification
Platform size	1.6 m × 1.2 m
Degree of freedom of motion	Single degree of freedom
Load capacity	1.5 t
Maximum displacement and acceleration	±1.5 m, ±1.0 g
Working frequency	0.01–10 Hz

TABLE 3: The similar constants.

Physical quantity	Similar relation	Similar constants
$L$	$C_L$	1/50
$\rho$	$C_\rho$	1
$E$	$C_E$	1/50
$\nu$	$C_\nu$	1
$t$	$C_t = C_L C_\rho^{0.5} C_E^{-0.5}$	0.141
$a$	$C_a = C_L^{-1} C_\rho^{-1} C_E$	1
$u$	$C_u = C_L C_\epsilon$	1/50
$\sigma$	$C_\sigma = C_E$	1/50
$\epsilon$	$C_\epsilon = C_E^{-1} C_L C_\nu$	1

excitation is completed, each damage status of the tunnel lining under earthquake effect must be checked, and the distribution of cracks must be carefully recorded. Figure 9 shows the crack expansion of a tunnel lining under an

earthquake with increased intensity. Cracks appeared in the tunnel lining at a level of 0.4 g. Subsequently, existing cracks were observed at the shoulder of the tunnel lining and new cracks appeared at a strength level of 0.5 g. The existing cracks were further expanded, and inclined cracks appeared at the strength level of 0.5 g. Figure 8 displays the distribution of final crack and damage details. Cracks appeared at skewback, side wall, and spandrel of tunnel lining under earthquake effect.

**3.3. Structural Damage of Tunnel Lining.** It can be seen from Figure 10 that the peak value of the axial force almost appears at the right skewback. The internal force of the peak right is greater than that of left skewback, and a larger axial force value appears when the pressure is greater. Meanwhile, the axial force values are all pressure effects. The internal force of the bending moment demonstrates positive and negative alternatives, indicating that the tunnel lining is subjected to repeated tensile and compressive cyclic loads under ground motion action. The load is reflected by alternating tensile and compressive stresses. As the fatigue load and the compressive performance of the concrete is far greater than the tensile performance, thus the lining structure is often prone to tensile damage. In summary, it can be seen that the right side of the tunnel lining is the internal force of control section, and the skewback is most likely to be damaged and the damage response of the spandrel is also large under earthquake effect.



FIGURE 4: Model test setup. (a) Lining model. (b) Smoothing of lining. (c) Pouring surrounding rock. (d) Test operating platform.

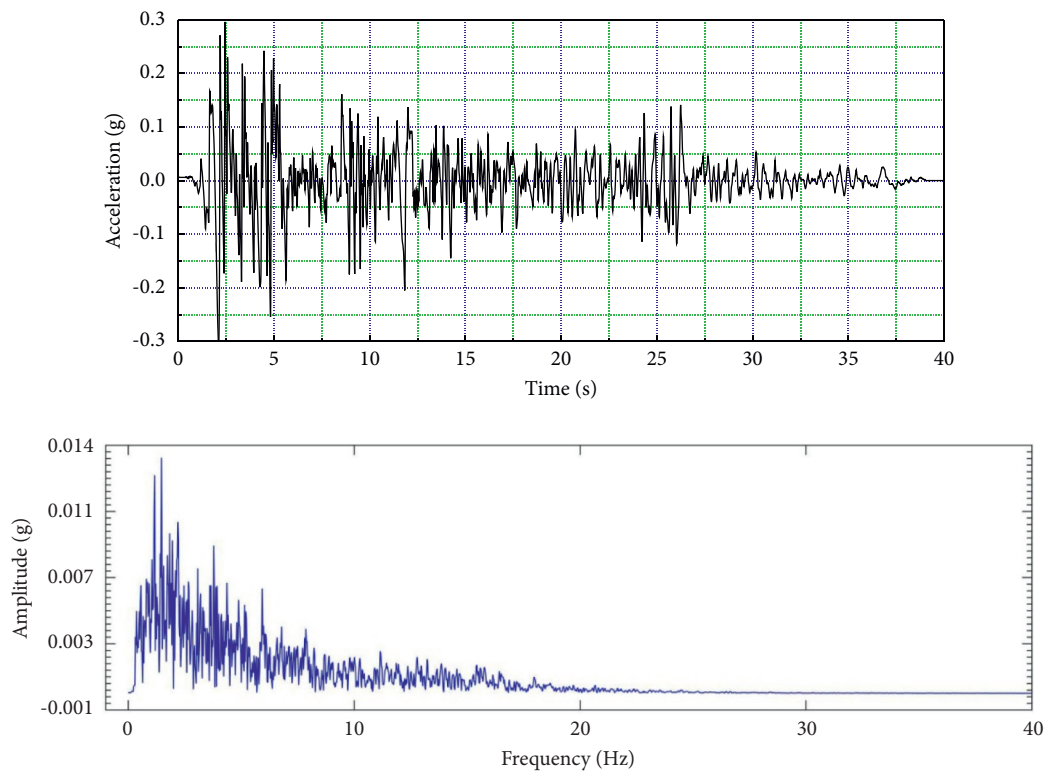


FIGURE 5: EL wave: acceleration-time histories and its corresponding Fourier spectrum.

TABLE 4: Loading sequence for the shaking table tests.

Test ID	Input waveform	PGA (g)
1	EL wave	0.1
2	EL wave	0.2
3	EL wave	0.3
4	EL wave	0.4
5	EL wave	0.5

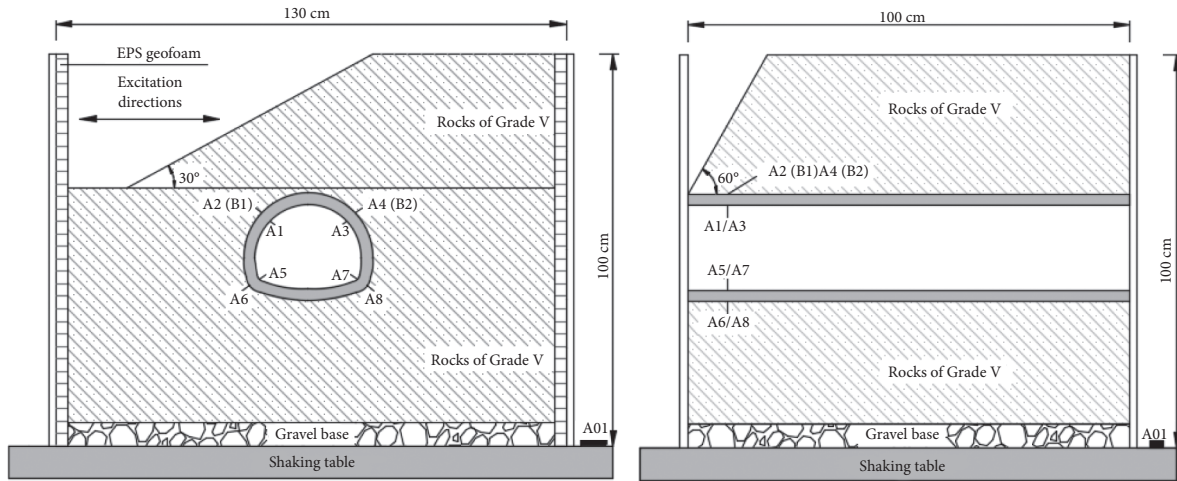


FIGURE 6: Surrounding rock and layout of transducers (B/C), strain gauges; (A), accelerometer).

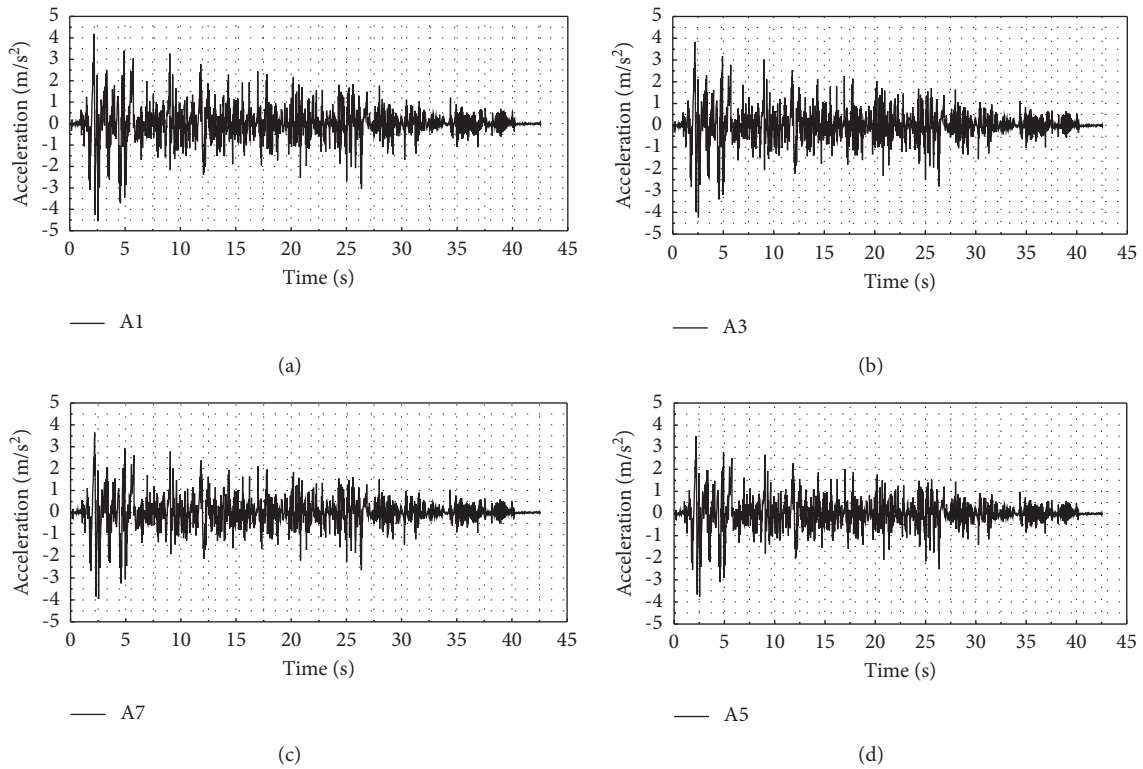


FIGURE 7: Acceleration spectrum curve of different measuring points. (a) 0.3 g A1 acceleration-time history. (b) 0.3 g A3 acceleration-time history. (c) 0.3 g A7 acceleration-time history. (d) 0.3 g A5 acceleration-time history.

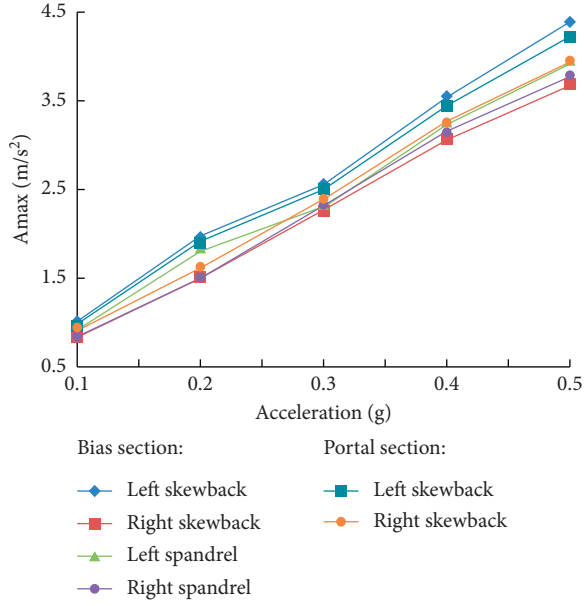


FIGURE 8: Peak contrast.

## 4. Numerical Simulation Analysis

**4.1. Boundary Conditions.** In order to establish an artificial boundary, the infinite continuous medium is cut off, and a continuous spring-damper-centralized mass system is applied at the cutoff, that is, the artificial boundary, as shown in Figure 11.

In order to overcome the inconvenience caused by the actual processing and calculation, we ignore the mass  $M$  and fix one end of the damper connected to the mass  $M$  to form the artificial boundary of the viscous damper + spring. The specific implementation method is shown in Figure 12. As shown in the figure, the coordinates  $X$  and  $Y$  in the figure are tangential to the artificial boundary, and  $Z$  is the normal direction. The parameters of the physical elements on the viscoelastic artificial boundary node in the figure are

$$\begin{aligned}
 K_1 &= K_2 = \frac{2G}{R} \sum_{i=1}^I A_i, \\
 C_1 &= C_2 = \rho c_s \sum_{i=1}^I A_i, \\
 K_3 &= \frac{4G}{R} \sum_{i=1}^I A_i, \\
 C_3 &= \rho c_p \sum_{i=1}^I A_i.
 \end{aligned} \tag{2}$$

Among them,  $\sum A_i$  is the area represented by the nodes on the artificial boundary, and for the case shown in Figure 11,  $I=4$ .

**4.2. Damage Model.** It is difficult to analyze the concrete defect form and damage mechanism and determine the effective force area from the microscopic level, so indirect

methods are needed to determine the material damage. The concrete damage constitutive model is used by Lubliner et al. [23]. The strain equivalence principle is proposed by Lubliner et al. [23]. It is assumed that the strain caused by stress acting on the damaged material is equivalent to the strain caused by effective stress acting on the nondestructive material. According to this principle, the actual constitutive relationship of the damaged material can be obtained from the nominal stress in the nondestructive material:

$$\varepsilon = \frac{\sigma}{\tilde{E}} = \frac{\tilde{\sigma}}{E} = \frac{\sigma}{(1-D)E}, \quad \sigma = (1-D)E\varepsilon. \tag{3}$$

Among them,  $D$  is the elastic modulus damage parameter,  $E$  is the elastic modulus of the material, and  $\tilde{E}$  is the elastic modulus of the damaged material. From (3),

$$D = 1 - \frac{\tilde{E}}{E}. \tag{4}$$

Derivation of (3) gives

$$\frac{d\sigma}{d\varepsilon} = \frac{dE}{d\varepsilon} (1-D)\varepsilon + E(1-D) - E\varepsilon \frac{dD}{d\varepsilon}. \tag{5}$$

When the load is unloaded to a certain value, because the damage is irreversible, that is, the damage value is not reduced during the unloading process, that is,  $dD/d\varepsilon = 0$ , where  $E$  is the constant of the elastic modulus of the material without damage, so (5) can be changed to

$$D = 1 - \frac{1}{E} \frac{dD}{d\varepsilon}. \tag{6}$$

The elastic modulus of the damaged material is the slope of the unloading curve, so it can also be called the unloading modulus so that the elastic modulus of the damaged material can be obtained by unloading.

**4.3. Model Establishment.** The finite element program is used for numerical simulation. The stress and deformation of the biased tunnel are very complicated during the earthquake. It is a three-dimensional stress and deformation problem. In order to improve the accuracy of the simulation results, the three-dimensional problem is dealt with during modeling. The numerical simulation model is shown in Figure 13. This time the biased tunnel is compared with the unbiased tunnel. The elastoplastic constitutive model is adopted for the surrounding rock of the tunnel and the damage constitutive model is adopted for the tunnel lining. Seismic waves are input in the axial direction of the vertical tunnel, and the loading method is the same as the shaking table test.

### 4.4. Damage Evolution and Cracking Mechanism of Tunnel Lining Opening

**4.4.1. Damage Evolution of Tunnel Lining Structure.** According to the damage status of the tunnel lining under the earthquake, Figure 14 shows the damage cloud diagram of the tunnel lining when the damage expands at various

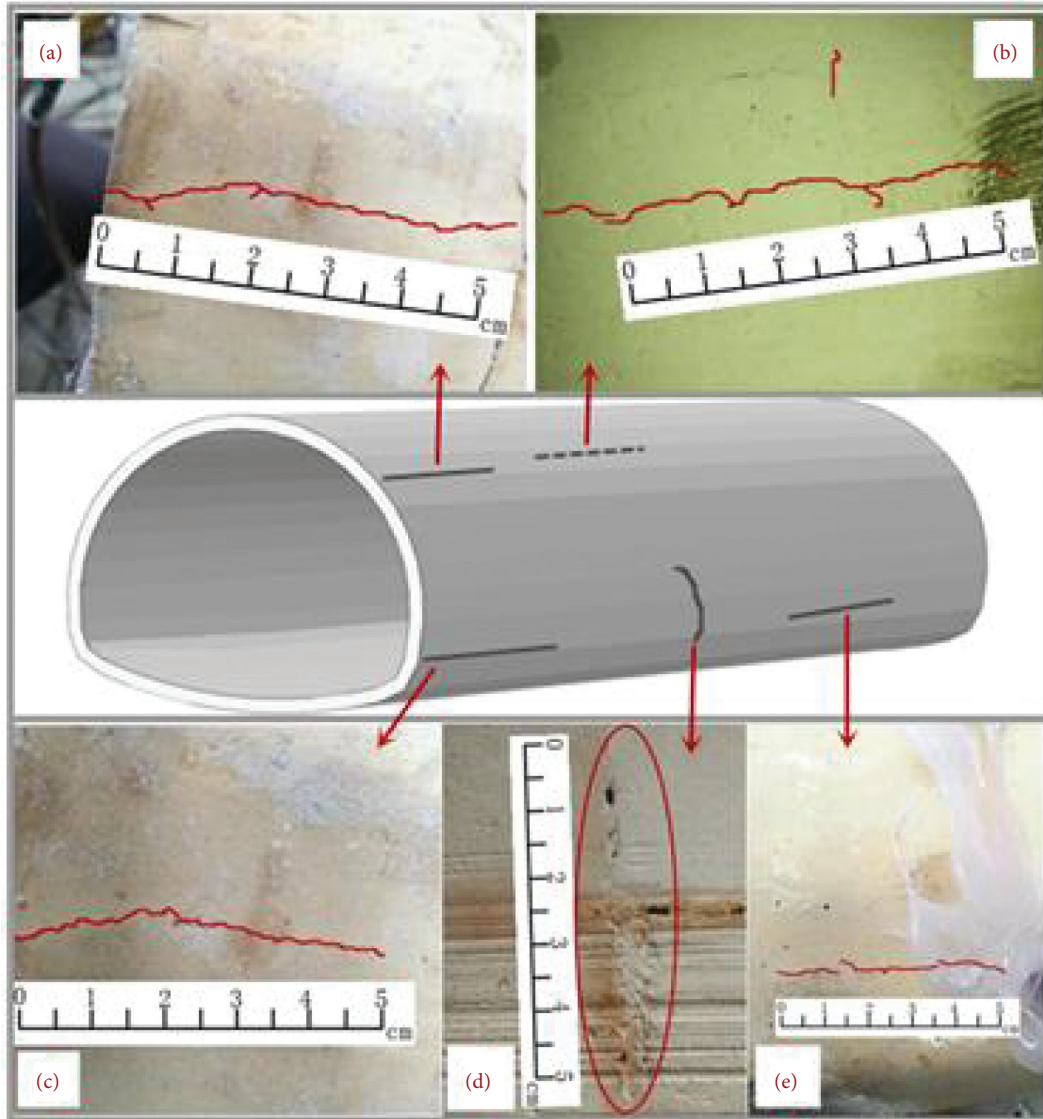


FIGURE 9: Lining crack. (a) Cracks in left skewback of bias section. (b) Cracks in right skewback of bias section. (c) Longitudinal cracks at right spandrel of portal section. (d) Ring crack of right spandrel in bias section. (e) Longitudinal crack of right spandrel in bias section.

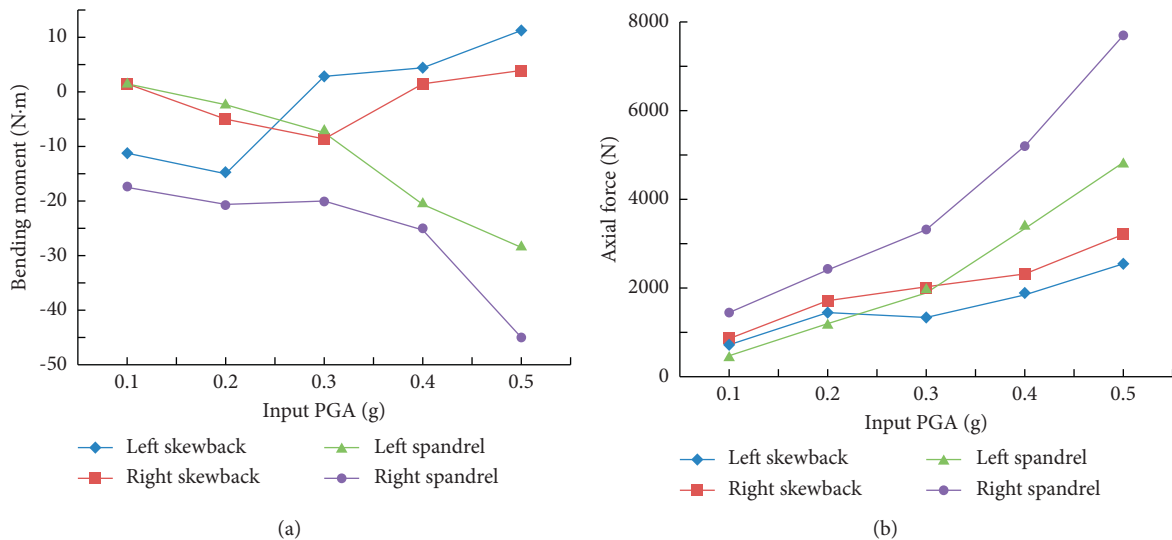


FIGURE 10: Time-history diagram of internal force. (a) Maximum bending moment. (b) Maximum axial force.

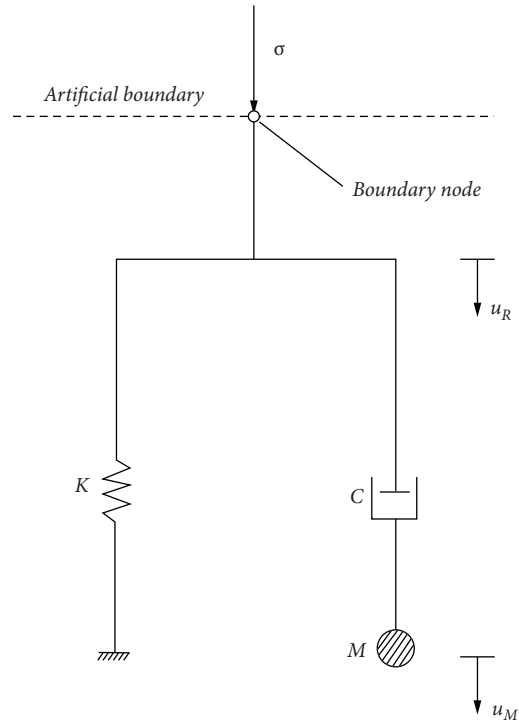


FIGURE 11: Normal boundary.

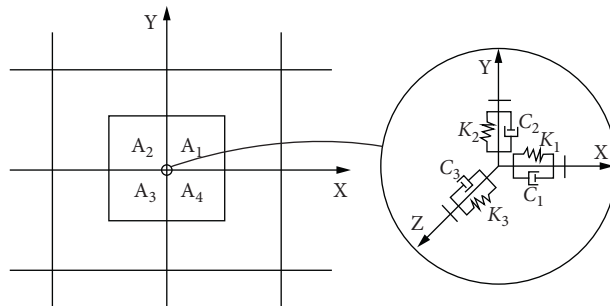


FIGURE 12: Artificial boundary.

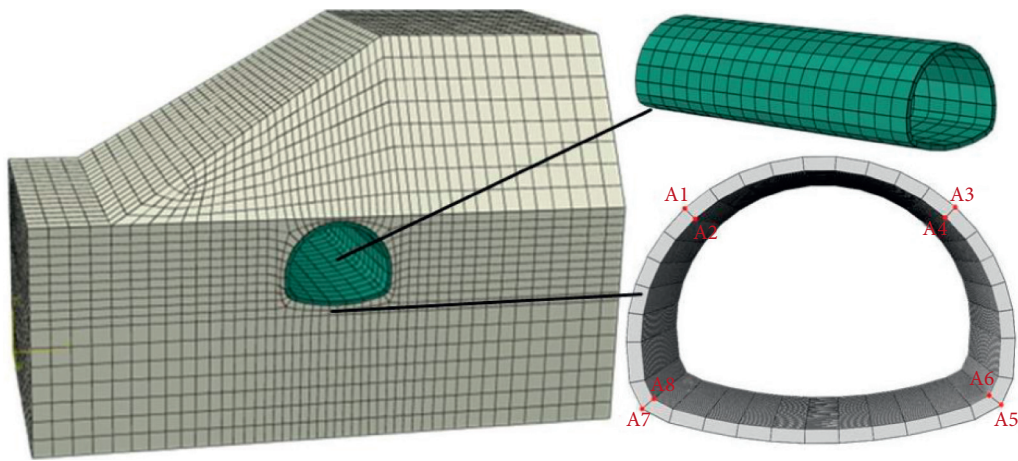


FIGURE 13: 3D bias model.



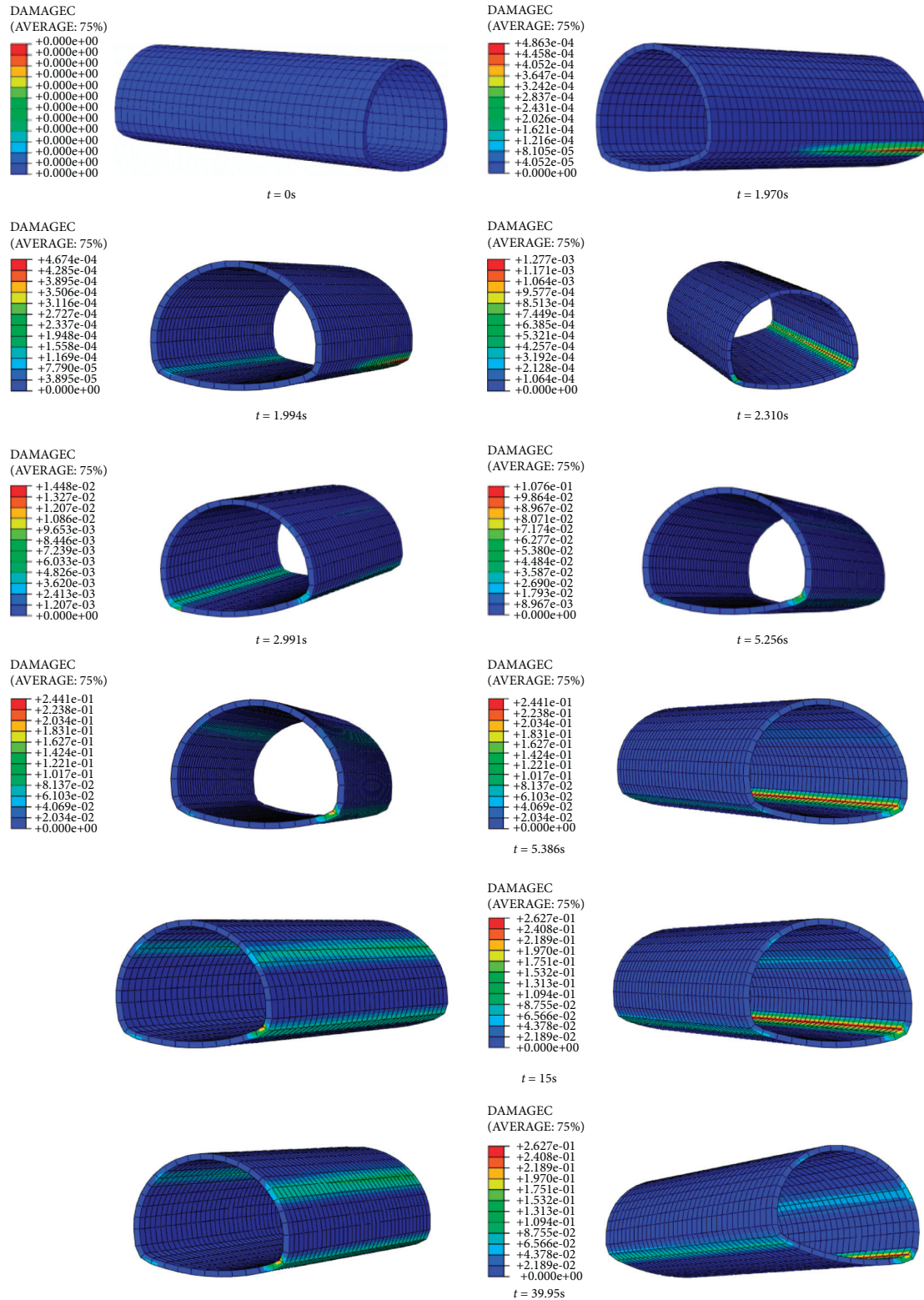


FIGURE 14: Damage map of tunnel lining.

time nodes. The direction of earthquake incidence is the same as the test direction, where damagec is the state variable for compression damage expansion and 1 represents complete damage and cracking of the unit while 0 represents

no damage and cracking of the unit. 0.4 g was adopted as the peak acceleration of seismic waves in this section.

When  $t = 1.970 s$ , it can be seen that the outer edge of the right arch foot at the tunnel opening section first appeared a

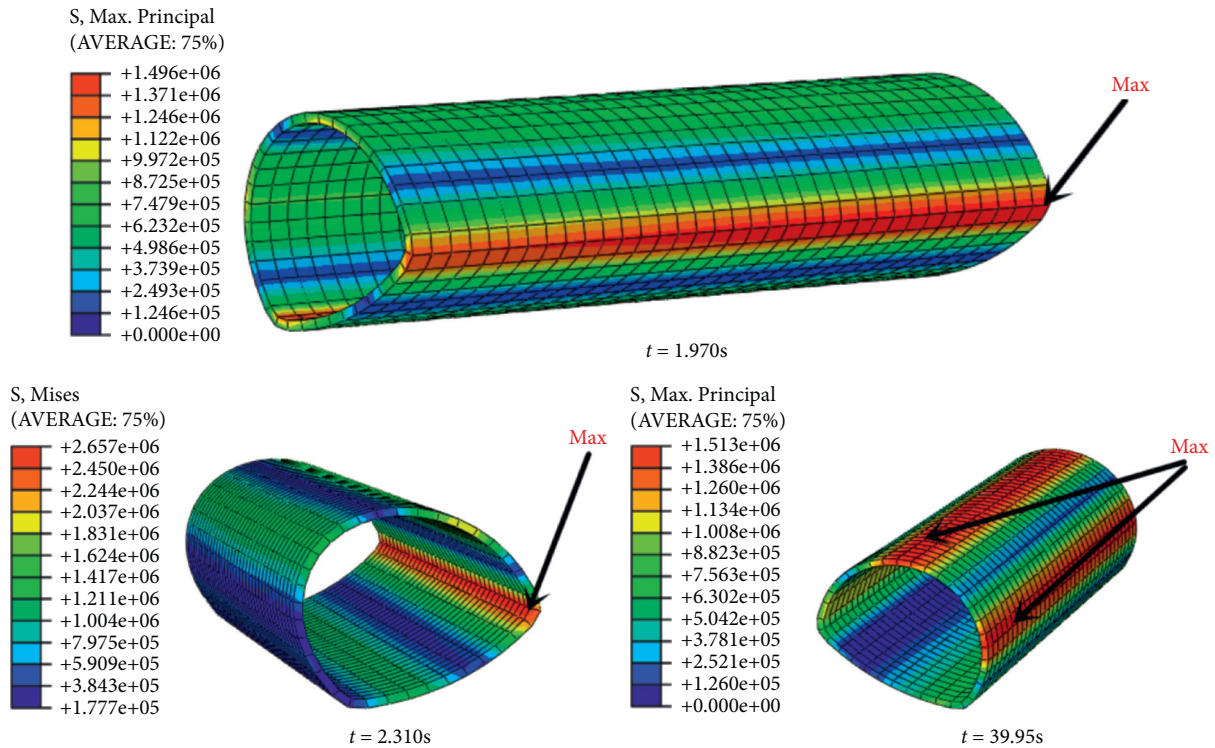


FIGURE 15: Maximum stress.

zone of compression damage under the action of axial ground motion along the tunnel through judging (Figure 14), and the damage was along the outer edge of the tunnel lining which is extend to the inner edge. When  $t = 1.994$  s, the damage area at the right spandrel continues to expand, and there is also a compression damage area at the left spandrel. When  $t = 2.310$  s, the left and right spandrel of the tunnel lining appear throughout the entire tunnel lining in the form of compression damage. When  $t = 2.911$  s, the damage area of the left spandrel of the tunnel lining section appeared, and the damage of the tunnel lining was further expanded until  $t = 5.256$  s, and at this point, the right spandrel of the tunnel lining appeared in the form of the damage. It can be seen at  $t = 5.386$  s that when the left and right spandrel and left and right skewback of the tunnel lining show damage areas with the increase of earthquake time, it shows continuous expansion trend, and the damage area continues to expand until  $t = 15$  s. The damage areas of the left and right spandrel and the left and right spandrel of the tunnel lining became gradually stabilized and no longer expanded. When  $t = 39.95$  s, it is the cloud image of the final compressed damage area presented by the tunnel lining at the end of the earthquake.

In the damage distribution diagram in Figure 14, it is not difficult to find that the left spandrel of the tunnel lining of the tunnel section, the right spandrel, the left skewback, and the right skewback are the areas which are most prone to compressive damage from the beginning to the last compression of damage area under earthquake when tunnel is under a shallow-buried conduction, among which the right arch leg of the tunnel lining has the largest compression

damage. At the same time, it was found the damage of tunnel lining rapidly expanded within 2s under the action of earthquake between  $t = 1.970$  s and  $t = 2.911$  s, which has obvious impact on tunnel lining.

*4.4.2. Analysis of the Maximum Principal Stress Seismic Dynamic Response of the Tunnel Lining Structure.* In order to further study the damage and cracking behavior of the tunnel lining structure, the skewback and spandrel points on the tunnel lining of the opening section are selected as key points (Figure 13). Figure 15 shows the cloud diagrams of maximum principal stress of the tunnel lining structure at the earthquakes of 1.970 s, 2.310 s, and 39.95 s.

When the tunnel lining structure is subjected to damage, namely,  $t = 1.970$  s, the cloud diagram of principal stress cloud diagram of the tunnel lining structure is shown in the figure. At the point, the maximum principle stress appears at skewback along negative direction of X-axis, which was 1.496 MPa. When  $t = 2.310$  s, that is, the maximum principal stress at this moment is 2.657 MPa when the maximum peak intensity of the earthquake action is reached. At this time, the stress value of the tunnel lining structure along the X-axis skewback side basically reaches 2.244 MPa, indicating the maximum principal stress. The damage crack at the maximum position is caused by the concrete tensile strength that reaches the limit value. When  $t = 39.95$  s, the maximum value of the tunnel maximum principal stress is located at the positive abutment position of the X-axis which is 1.513 MPa. At this time, the damage area of the tunnel lining abutment and arch foot tends to be stable, and the maximum principal stress of the tunnel lining structure is fully released.

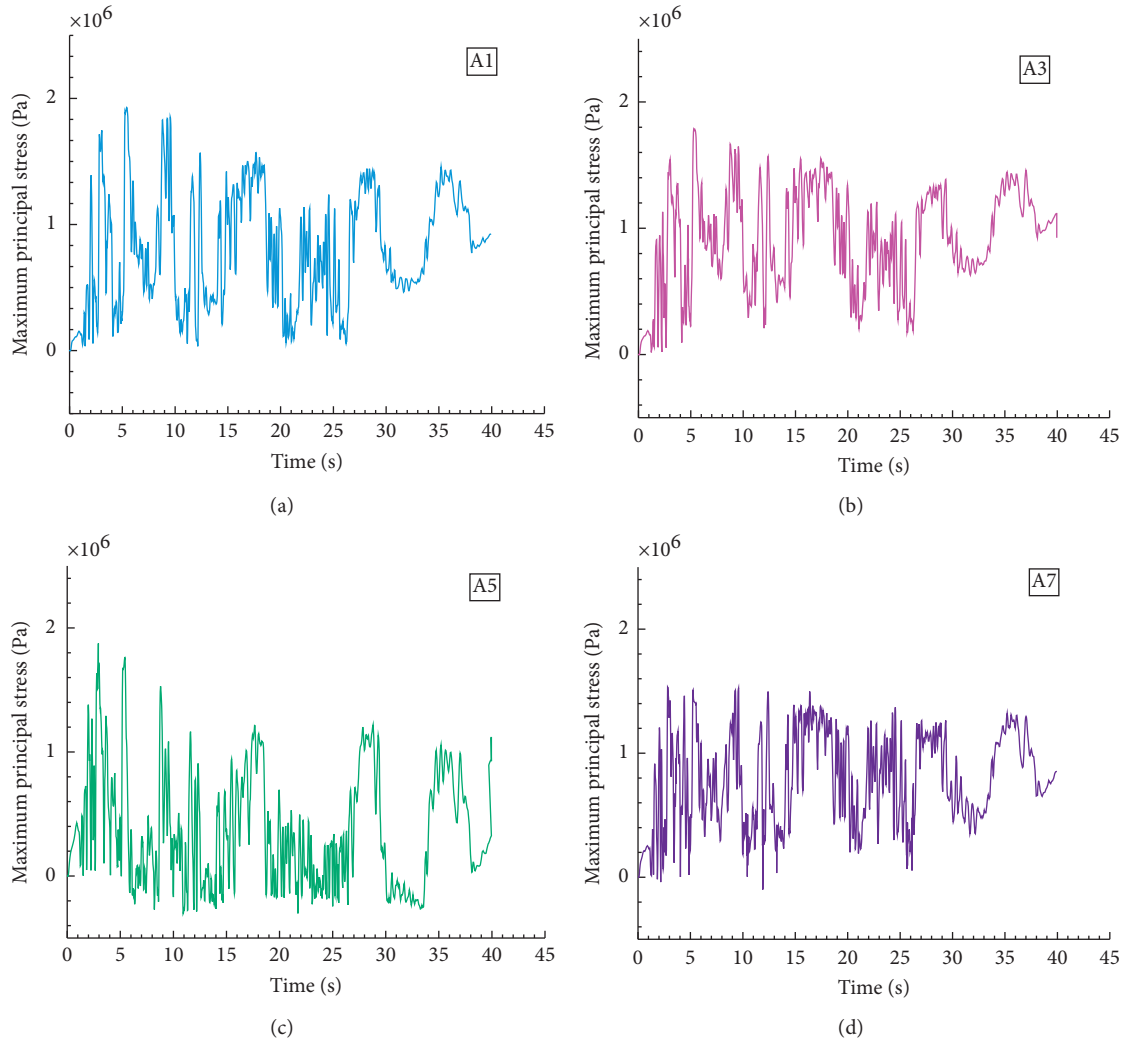


FIGURE 16: Time history of maximum principal stress response.

TABLE 5: Key points A1–A8 maximum principal stress value and corresponding time C25 =1.78.

Key point	A1	A2	A3	A4	A5	A6	A7	A8
Stress (MPa)	1.993	1.838	1.788	1.848	1.875	1.993	1.533	1.951
Time (s)	5.418	9.565	5.289	5.386	2.939	5.321	2.825	9.257

And, the maximum value decreases and a corresponding position shift occurs.

Figure 16 shows the time-history curve of maximum principal stress at key points of the tunnel lining structure. According to Figure 16 and Table 5, it can be seen that the maximum principal stress of 1.57 MPa first appears at point A7 when  $t = 2.825$  s, and when  $t = 2.939$  s, that is, the maximum principal stress of 1.875 appears at the right skewback of the tunnel lining structure. At the moment, the crack is observed at A5, and the maximum principal stress of A3, A6, A4, and A1 reached 1.78 MPa successively in the following 7 seconds. The maximum principal stress of A2 and A8 finally reached 1.78 MPa, and later, crack was witnessed. After the peak value of the seismic wave, the

maximum principal stress of the corresponding key points at the various moments of the damage and crack propagation of the tunnel lining structure in the later period reached the peak value. However, all the principle stresses were less than 1.78 MPa, which indicates that the concrete cracking in the later period can realize the development of crack under less stress, which will cause damage to the concrete. When  $t = 39.95$  s, the maximum principal stresses at A1–A8 key points are all closer to 1.0 MPa when ground motion stops.

4.4.3. Analysis of the Minimum Principal Stress Seismic Dynamic Response of the Tunnel Lining Structure. Figure 17 shows the cloud diagrams of minimum principal stress of the tunnel lining structure at the earthquakes times of

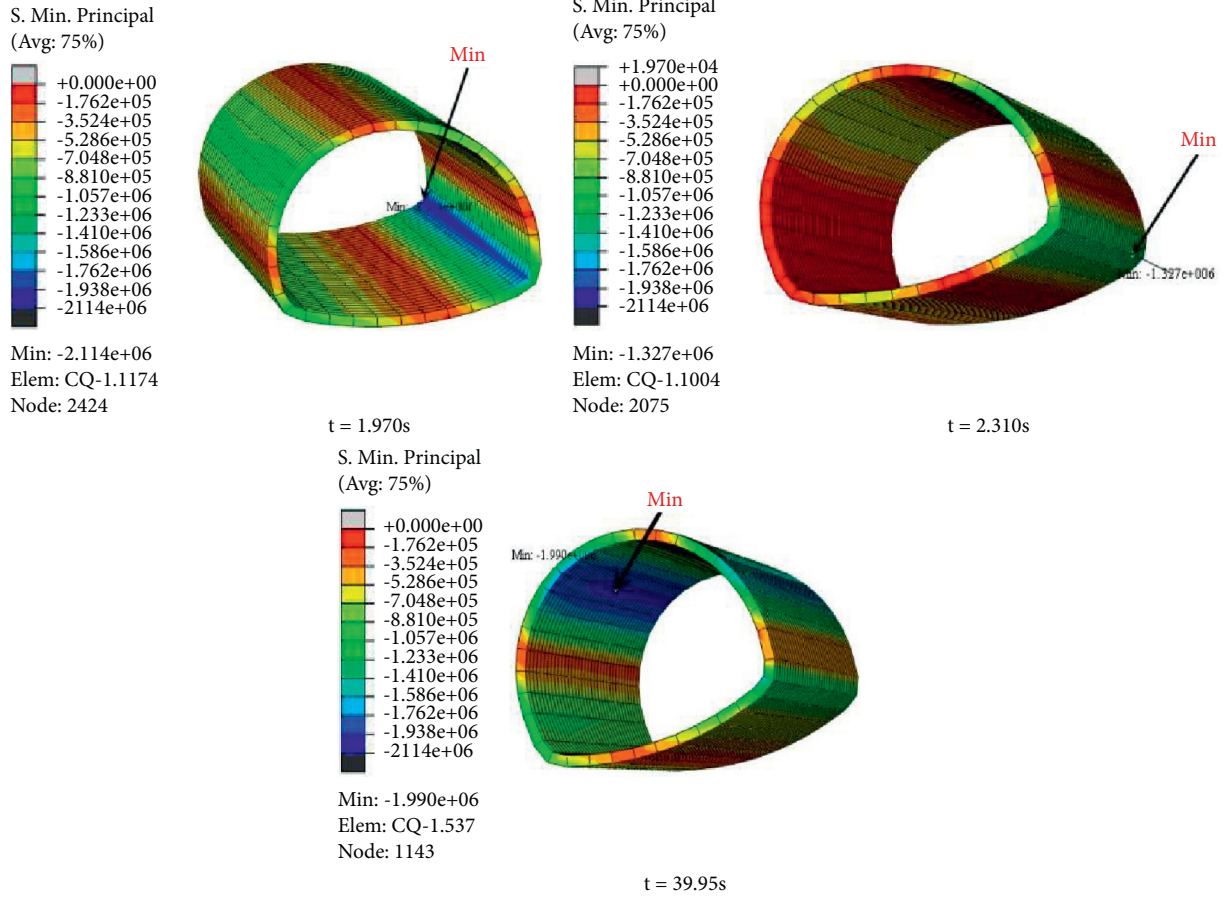


FIGURE 17: Minimum stress.

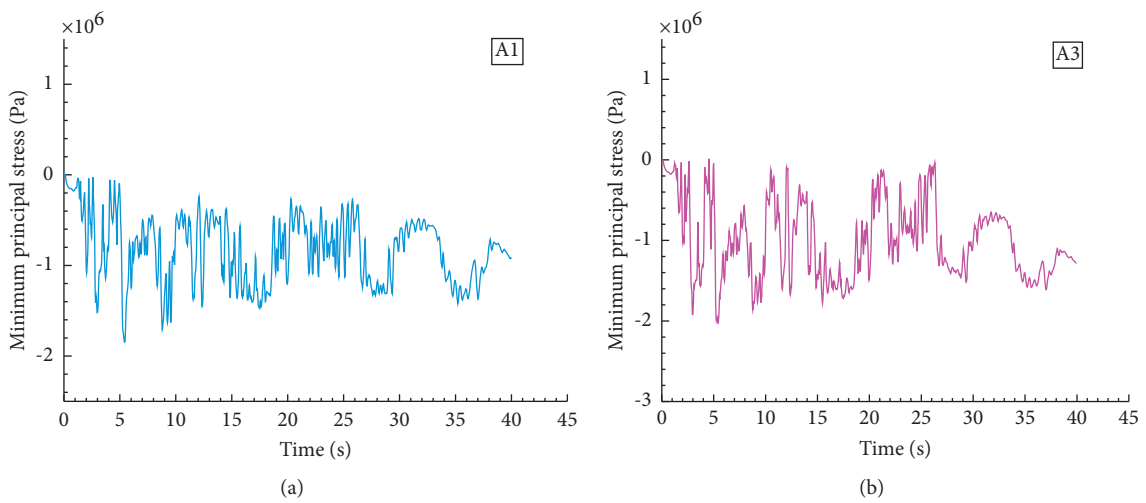


FIGURE 18: Continued.

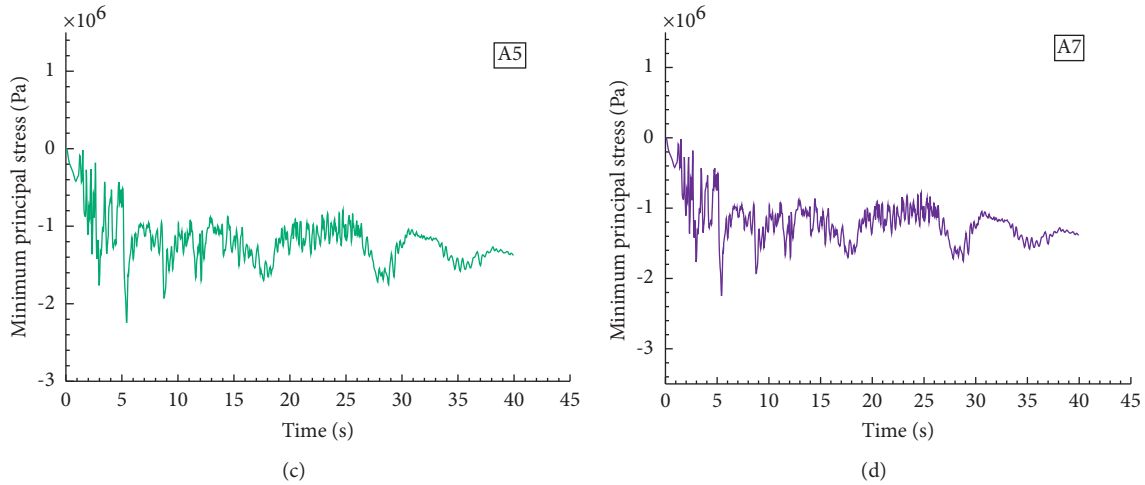


FIGURE 18: Time history of minimum principal stress response.

TABLE 6: Minimum principal stress values at key points A1–A8 and corresponding times  $C_{25} = 1.78$ 

Key point	A1	A2	A3	A4	A5	A6	A7	A8
Stress (MPa)	-1.847	-2.791	-2.029	-1.512	-2.244	-3.501	-2.248	-2.551
Time (s)	5.218	5.450	5.418	5.386	5.328	5.468	5.428	4.388

1.970 s, 2.310 s, and 39.95 s. When  $t = 1.970$  s, a large stress was generated at the right skewback of the tunnel lining structure, and the minimum principal stress reached  $-2.114$  MPa. At this time, the cracking occurred at the skewback of the tunnel lining structure. When  $t = 2.310$  s, the minimum principal stress is  $-1.327$  MPa, and the minimum principal stress witnessed an increment. Since the skewback of the tunnel is under high pressure for a long time, the cracks at the skewback is quickly generated within 1s. When  $t = 39.95$  s, the minimum principal stress was transferred to the arch shoulder, and the minimum principal stress was  $1.990$  MPa.

Figure 18 shows time-history curve of the minimum stress at the key points of the tunnel lining structure A1–A8. By combining Table 6 and Figure 18, it can be seen that the minimum principal stress from A1 to A8 occurs at approximately 5.0 s, and the minimum principal stress of each key point stress is  $-2.791$  MPa. The cure of minimum principal stress at each key point fluctuated slightly but all tended to be stable. It can be seen from the time chart of the minimum principal stress that the stress curve at the right skewback (A5, A6) fluctuates relatively sharply. Meanwhile, it can be found that the tunnel lining structure has a significant bias effect comparing left and right skewback and left and right spandrel at same time.

**4.4.4. Verify Numerical Model.** Combining the results of seismic tunnel damage investigations with model test failure locations is used to verify the maximum and minimum principal stresses and damage locations of the numerical simulation.

## 5. Conclusion

In this paper, a series of shaking table tests and numerical simulations were performed to the shallow-buried biased tunnels under seismic action. And, a detailed description of the design and numerical simulation of the shaking table test are also made. The damage of the tunnel lining is studied by sweep frequency of white noise and combining seismic excitation. The results of the analysis are discussed in terms of lining damage, lining acceleration, and axial force of bending moment, and this research gets these conclusions:

- (1) The lining at entrance of the shallow-buried biased tunnel exhibits a significant biasing effect.
- (2) The biasing effect promotes the unfavorable stress distribution of the tunnel structure.
- (3) Meanwhile, the serious stress concentration occurs at the lining spandrel and skewback. The unfavorable stress distribution is more likely to cause damage to the tunnel. The tunnel lining earthquake damage easily occurs at the spandrel and skewback and gradually expands with the continuous damage of the earthquake.
- (4) Under the action of the earthquake, the axial force of the tunnel structure shows a compressive effect and bending moment demonstrates a cyclic stress of tension and compression, where the bending moment at the right skewback displays the largest internal force, and it is also a serious damage area.

## Data Availability

The data used to support the findings of this study are available from the corresponding author upon request.

## Conflicts of Interest

The authors declare that they have no conflicts of interest.

## Acknowledgments

This study was financially supported by the National Natural Science Foundation of China, under Grant no. 51708373. The authors thank National Natural Science Foundation of China and all who have contributed to this study.

## References

- [1] J. J. Zhang and M. F. Lei, "Safety analysis of biased tunnel construction technology," *Highway Engineer*, vol. 36, no. 5, pp. 144–148, 2011.
- [2] Z. Chen, C. Shi, T. Li, and Y. Yuan, "Damage characteristics and influence factors of mountain tunnels under strong earthquakes," *Natural Hazards*, vol. 61, no. 2, pp. 387–401, 2012.
- [3] Y. M. A. Hashash, J. J. Hook, B. Schmidt, and J. I-Chiang Yao, "Seismic design and analysis of underground structures," *Tunnelling and Underground Space Technology*, vol. 16, no. 4, pp. 247–293, 2001.
- [4] W. L. Wang, T. T. Wang, J. J. Su, C. H. Lin, C. R. Seng, and T. H. Huang, "Assessment of damage in mountain tunnels due to the Taiwan Chi-Chi Earthquake," *Tunnelling and Underground Space Technology*, vol. 16, no. 3, pp. 133–150, 2001.
- [5] D. R. Brunson, R. A. Davey, C. J. Graham et al., "The CHI-CHI, taiwan earthquake OF 21 september 1999," *Bulletin of the New Zealand Society for Earthquake Engineering*, vol. 33, no. 2, pp. 105–167, 2000.
- [6] Z. Wang, B. Gao, Y. Jiang, and S. Yuan, "Investigation and assessment on mountain tunnels and geotechnical damage after the Wenchuan earthquake," *Science in China - Series E: Technological Sciences*, vol. 52, no. 2, pp. 546–558, 2009.
- [7] T. Li, "Damage to mountain tunnels related to the Wenchuan earthquake and some suggestions for aseismic tunnel construction," *Bulletin of Engineering Geology and the Environment*, vol. 71, no. 2, pp. 297–308, 2012.
- [8] H. Yu, J. Chen, A. Bobet, and Y. Yuan, "Damage observation and assessment of the Longxi tunnel during the Wenchuan earthquake," *Tunnelling and Underground Space Technology*, vol. 54, pp. 102–116, 2016.
- [9] Y. M. A. Hashash, D. Park, and J. I.-C. Yao, "Ovaling deformations of circular tunnels under seismic loading, an update on seismic design and analysis of underground structures," *Tunnelling and Underground Space Technology*, vol. 20, no. 5, pp. 435–441, 2005.
- [10] R. J. Bathurst, S. Zarnani, and A. Gaskin, "Shaking table testing of geofoam seismic buffers," *Soil Dynamics and Earthquake Engineering*, vol. 27, no. 4, pp. 324–332, 2007.
- [11] J.-H. Hwang and C.-C. Lu, "Seismic capacity assessment of old Sanyi railway tunnels," *Tunnelling and Underground Space Technology*, vol. 22, no. 4, pp. 433–449, 2007.
- [12] S. Kontoe, L. Zdravkovic, D. M. Potts, and C. O. Menkiti, "Case study on seismic tunnel response," *Canadian Geotechnical Journal*, vol. 45, no. 12, pp. 1743–1764, 2008.
- [13] Z. Y. Chen and H. Shen, "Dynamic centrifuge tests on isolation mechanism of tunnels subjected to seismic shaking," *Tunnelling and Underground Space Technology*, vol. 42, no. 5, pp. 67–77, 2014.
- [14] X. Zhang, Y. Jiang, and S. Sugimoto, "Seismic damage assessment of mountain tunnel: a case study on the Tawarayama tunnel due to the 2016 Kumamoto Earthquake," *Tunnelling and Underground Space Technology*, vol. 71, pp. 138–148, 2018.
- [15] M. Geniş, "Assessment of the dynamic stability of the portals of the Dorukhan tunnel using numerical analysis," *International Journal of Rock Mechanics and Mining Sciences*, vol. 47, no. 8, pp. 1231–1241, 2010.
- [16] L. Tao, S. Hou, X. Zhao et al., "3-D shell analysis of structure in portal section of mountain tunnel under seismic SH wave action," *Tunnelling and Underground Space Technology*, vol. 46, pp. 116–124, 2015.
- [17] J. Lai, H. Fan, B. Liu, and T. Liu, "Analysis of seismic response of shallow large section multi-arch tunnel," *Procedia Engineering*, vol. 15, pp. 5473–5477, 2011.
- [18] S. Wang, J. Li, H. Luo, and H. Zhu, "Damage identification in underground tunnel structures with wavelet based residual force vector," *Engineering Structures*, vol. 178, pp. 506–520, 2019.
- [19] M. Varma, V. B. Maji, and A. Boominathan, "Numerical modeling of a tunnel in jointed rocks subjected to seismic loading," *Underground Space*, vol. 4, 2018.
- [20] Z. Z. Wang, Y.-J. Jiang, C. A. Zhu, and T. C. Sun, "Shaking table tests of tunnel linings in progressive states of damage," *Tunnelling and Underground Space Technology*, vol. 50, pp. 109–117, 2015.
- [21] F. Wang, X. Jiang, and J. Niu, "The large-scale shaking table model test of the shallow-bias tunnel with a small clear distance," *Geotechnical & Geological Engineering*, vol. 35, no. 3, pp. 1093–1110, 2017.
- [22] Q. Xu, P. Cheng, H. Zhu et al., "Experimental study and numerical simulation on progressive failure characteristics of the fault-crossing tunnel surrounding rock," *Chinese Journal of Rock Mechanics and Engineering*, 2016.
- [23] J. Lubliner, J. Oliver, S. Oller, and E. Oñate, "A plastic-damage model for concrete," *International Journal of Solids and Structures*, vol. 25, no. 3, pp. 299–326, 1989.

## Research Article

# Research on Deep-Site Failure Mechanism of High-Steep Slope under Active Fault Creeping Dislocation

Yang Liu <sup>1</sup>, Kaiwen Zhang <sup>1</sup>, Denghang Tian <sup>1</sup>, Liming Qu <sup>1</sup> and Yang Liu<sup>2</sup>

<sup>1</sup>MOE Key Laboratory of High-speed Railway Engineering, College of Civil Engineering, Southwest Jiaotong University, Chengdu 610031, China

<sup>2</sup>Zhongke(Hunan) Advanced Rail Transit Research Institute, Zhuzhou 412000, China

Correspondence should be addressed to Liming Qu; [hustqlm@163.com](mailto:hustqlm@163.com)

Received 19 April 2021; Accepted 4 June 2021; Published 20 August 2021

Academic Editor: Gang Fan

Copyright © 2021 Yang Liu et al. This is an open access article distributed under the Creative Commons Attribution License, which permits unrestricted use, distribution, and reproduction in any medium, provided the original work is properly cited.

The reverse thrust in the deep site causes the upward propagation of stress and displacement in the overlying soil. The displacement field around the fault zone is maximum. As the spatial location becomes shallower, the soil displacement gradually becomes smaller. The deformation of the overlying soil is mainly affected by the vertical dislocation of the fracture zone. The monitoring curve showed no abrupt change value, indicating that the top surface of soil did not rupture, and only the influence of fault on the displacement transfer of the top surface of the soil. When a creeping dislocation occurs in the bottom fracture zone, the maximum principal stress of the upper boundary of the deep site is dominated by compressive stress. The maximum principal stress of the soil on both sides of the fracture zone has a maximum value, and the soil on the right side of the fracture zone has a significant compression effect. The maximum principal stress monitoring curve varies greatly, indicating the plastic failure development of soil, which is the same as the research results of the plastic failure zone in the following paper. When the bottom fracture zone starts to move, the plastic zone first appears at the junction area between the front end of the bottom fracture zone and the overlying soil. As the amount of dislocation of the fracture zone increases, the plastic zone continues to extend into the inner soil. The left and right sides of the fracture zone show tensile failure and compression failure, respectively. The development of the upper envelope curve in the plastic zone of the overlying soil satisfies the Boltzmann equation with a first-order exponential growth, while the development of the lower envelope curve satisfies the Gauss equation with a second-order exponential growth. The development curve equation of the plastic zone is verified according to the residual figures of the fitting result and the correlation parameters.

## 1. Introduction

The stability of the slope under the action of earthquake has always been a research hotspot in slope engineering disaster prevention and mitigation. Dislocation of faults during earthquake will cause huge damage to the slope, induce secondary disasters such as landslides and collapses, and cause huge economic losses [1]. With the deepening of research, slope stability gradually formed some classic calculation theories and methods, such as Bishop method [2], limit analysis method [3], and transfer coefficient method [4]. In addition, some experts and scholars have introduced new research methods for the study of slope stability, such as reliability analysis method [5] and grey theory analysis method [6]. At present, experts on

slope stability research methods have done a lot of research based on model tests and finite element analysis. Sun and Yao [7] summarized the typical failure geological models of rock slopes in China and revealed the deformation failure mechanism of slopes. Soto [8] used the bottom friction theory to carry out the slope rock mass toppling deformation test to study the stability of the rock slope. Bray and Goodman [9] conducted a theoretical analysis on the bottom friction test and concluded that the rock mass is in the limit equilibrium state and the model is similar to the gravity field. Adhykary et al. [10] studied slope dumping and arc shear failure theory through centrifuge tests. Sun et al. [11] combined numerical simulation and laboratory tests to study the influence of normal fault on the Urumqi subway tunnel and found that the results of numerical

simulation and laboratory tests were basically consistent. Ji et al. [12] developed a more complete set of laboratory test equipment based on the advantages and disadvantages of domestic and foreign test devices and verified the reliability of the device. The research results showed that the device was stable and reliable, which could provide a new model test method and research means for future research. Abe et al. [13, 14] used three-dimensional discrete element numerical simulation to describe the improved evolution law of fault gouge, and the results showed that the shape of fault gouge fragments and the resulting interaction determined the friction strength of the fault. Lunn et al. [15] proposed a conceptual model of fault development and numerically simulated the time and space development of geometrically complex fault linkage structures with finite element software. The results showed that the geometry was affected by three key factors: stress ratio, original joint geometry, such as contraction or expansion configuration, and the direction of principal stress. Luan et al. [16] used the strength reduction finite element method to propose a plastic zone criterion for slope instability, which was applied in actual slope engineering. Zheng et al. [17–19] used the strength reduction method to perform finite element calculations on the slope and obtained the failure process of the slope, which provided a new idea for the study of slope stability. Li et al. [20] simulated the entire process of slope instability through real examples and developed a RFPFA system based on the strength reduction method.

The above-mentioned research has important guiding significance for the construction of slope engineering, but it has not obtained a reliable index for how the fault dislocation caused by earthquake affects the stability of the slope and the degree of influence. The failure mode and instability conditions of the slope under fault dislocation need to be further studied. In this paper, based on the finite element analysis software ABAQUS, a calculation model for the deep site of the high-steep slope under the dislocation of the 30° dip angle fracture zone is established. From the deformation propagation of the soil, the distribution of the maximum principal stress of the overlying soil, and the development of the plastic zone during the dislocation of the fracture zone, the failure mechanism of the deep site is studied. According to the range of the plastic zone under the maximum dislocation, the distribution equation of the plastic zone is proposed in order to provide a reference for the instability mechanism of high-steep slopes under fault dislocation.

## 2. Establishment of the Three-Dimensional Finite Element Model

Fault dislocation is divided into creeping dislocation and stick-slip dislocation. The stick-slip dislocation is a kind of rapid fracture movement. The entire process takes a short time and the soil layer is not fully deformed. The creeping dislocation is a slow motion that gradually deforms over time. The creeping dislocation gives the soil time to fully deform [21]. Relevant studies have shown [22] that the creeping dislocation has more significant damage than stick-slip dislocation.

The dislocation of the bottom fracture zone propagates through the deep site to the slope, which leads to the instability of the slope. This paper takes the deep site at the bottom of the slope toe as the research object to study the failure mode of the deep site under the creep of the fracture zone. Combined with previous studies on the accuracy of slope stability safety factor [23]; after many trial calculations, the overall size of the calculation model is 400 m (length) × 50 m (width) × 105 m (height), which is composed of overlying soil and bottom bedrock. The overlying soil is divided into three parts with thicknesses of 20 m, 30 m, and 50 m from top to bottom. The thickness of the bottom bedrock is 5 m, the fracture zone is located in the middle of the bedrock, whose width is 100 m and dip angle is 30°. The schematic diagram of the calculation model is shown in Figure 1.

The main failure mode of the soil under the dislocation of the fracture zone is shear failure, and the deformation during the whole process will show certain nonlinear characteristics. In order to accurately reflect the elastoplastic constitutive relationship of the stress and strain characteristics of the soil layer, the yield criterion is the Drucker–Prager yield criterion. The bottom bedrock is made of mudstone, and the overlying soil is divided into three layers and superimposed by two materials. The three layers of soil are round gravel soil, silty clay, and round gravel soil from top to bottom. The detailed soil parameters are shown in Table 1.

The calculation of the model is divided into two steps: the initial ground stress balance and the application of displacement in the bedrock fracture zone. In the initial ground stress balance calculation, the bottom and side boundary conditions of the calculation model are all normal constraints, and the upper boundary is a free boundary. The contact between the fracture zone and the overlying soil is set as frictional contact, and the initial ground stress predefined field of the soil itself is obtained by applying gravity. After the initial ground stress is balanced, the normal constraint of the fracture zone is released, and the dislocation is realized by applying the displacement load on the bottom fracture zone. The dislocation direction of the fracture zone is X-direction and Z-direction. The displacement load is mainly applied in the Z-direction, and the maximum displacement is 4.0 m. In this paper, considering the influence of the most adverse conditions, the initial dislocation rate of the fracture zone is set to 0.05 m/s. After a certain displacement due to the activity of the fault zone, the dislocation rate is gradually increased until the displacement reaches 4.0 m, and the overlying soil is fully deformed [24, 25]. The displacement load is applied to the meshing nodes of the fracture zone, and the composite direction of the displacement load is consistent with the dip angle. The displacement loading boundary conditions are shown in Figure 2.

Since the model in this paper is an ideal homogeneous soil model, the general static analysis step is iteratively used to determine the solution of the nonlinear problem during the initial ground stress balance, which can improve the solution efficiency. After applying the displacement of the



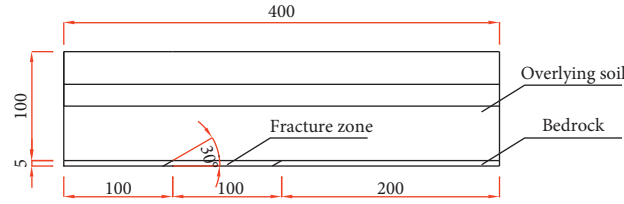


FIGURE 1: The schematic diagram of the calculation model of the deep site.

TABLE 1: Soil parameters of the deep site.

Soil	Density ( $\text{kg}\cdot\text{m}^{-3}$ )	Elastic modulus (MPa)	Poisson ratio	Internal friction angle ( $^\circ$ )	Cohesion (kPa)
Round gravel soil	2100	47	0.25	40.8	4
Silty clay	2010	13.6	0.33	18	21
Mudstone	2470	2500	0.25	—	—

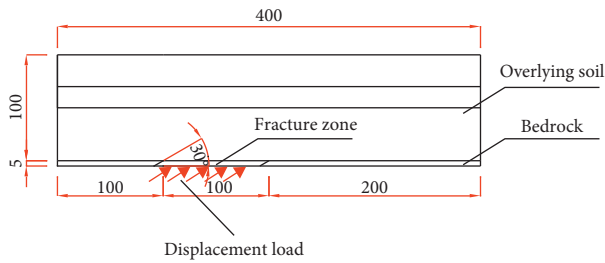


FIGURE 2: Displacement loading diagram of the bottom fracture zone.

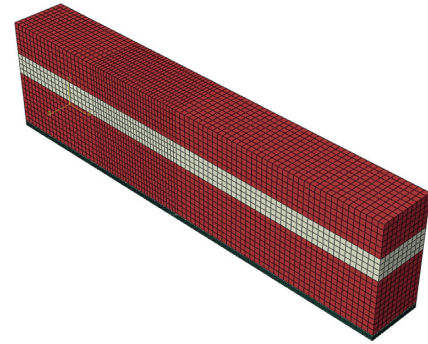


FIGURE 3: Meshing diagram of the calculation model.

fracture zone, the dynamic implicit algorithm can reach the convergence faster. In order to make the calculation converge faster and make the soil deformation caused by fault action closer to the actual situation, the numerical simulation adopted normal constraints around and under the surface, and no constraints were imposed on the top surface.

Due to the relatively regular shape of the calculation model, the overlying soil and the bottom bedrock are all homogeneous materials. The model is divided by eight-node hexahedral structured elements. The meshing diagram of the model is shown in Figure 3.

### 3. Analysis of the Destruction Mechanism of Deep Site under Active Fault Creeping Dislocation

The dislocation of the fracture zone at the bottom of the model is essentially the dislocation of a thrust fault, and the thrust fault is a low-angle fault with large displacement. When the fault movement, it will show significant compression and fragmentation. After the dislocation, fracture structures such as breccia and granular rock will be formed [26], and the displacement value is difficult to obtain in actual engineering. In order to obtain more accurate calculation results, the dislocation range of the fracture zone is set to 0.1~4.0 m in this paper, and a large number of monitoring points are selected from the displacement distribution, stress distribution, and plastic zone distribution of the soil to reveal the failure mechanism of the deep site under the fault dislocation.

*3.1. Analysis of the Displacement Response of the Deep Site under the Creeping Dislocation of the Active Fault.* The area closely related to the deep site and the slope is the upper boundary of the overlying soil. This paper selects the monitoring points of the upper boundary to study the damage of the upper soil through the displacement distribution. The displacement load of the fracture zone is a combination of two directions, so the X- and Z-direction displacement distributions are used for analysis. Figure 4 is the vertical displacement cloud diagram when the fracture zone is displaced by 0.1 m and 4.0 m, and Figure 5 is the displacement distribution curve of the monitoring points on the upper boundary of the deep site in the X-direction and Z-direction under different displacements.

When creeping dislocation occurs in the bottom bedrock fracture zone, the X-direction displacement curve of the overlying soil on the deep site under different displacements is centered symmetrically with a center point of 150 m, and the center point is roughly located in the middle of the fracture zone. The deformation value on the left side of the overlying soil is negative, and the maximum value is approximately at the interface between the front of the fracture zone and the bedrock at 100 m. The deformation value of the soil on the right is positive and the maximum deformation is roughly located at the interface between the back of the fracture zone and the bedrock at 200 m. The distribution range of negative deformation is roughly 0~150 m, the distribution range of positive deformation is roughly

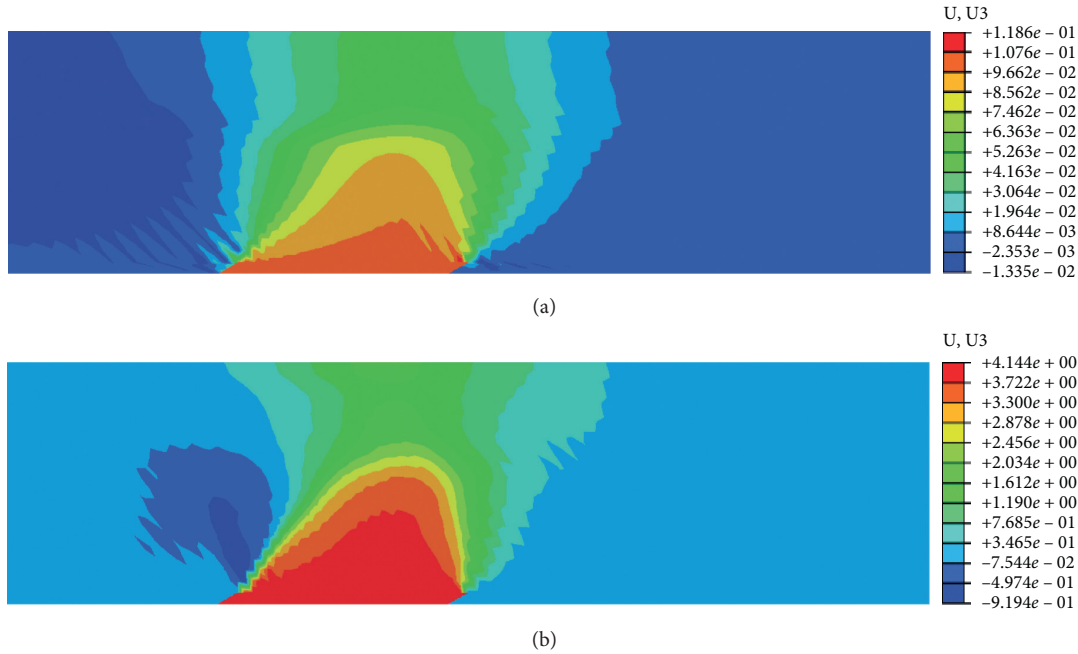


FIGURE 4: Vertical displacement cloud diagram of deep site under different displacements. (a) Vertical displacement cloud diagram when the fracture zone is displaced by 0.1 m. (b) Vertical displacement cloud diagram when the fracture zone is displaced by 4.0 m.

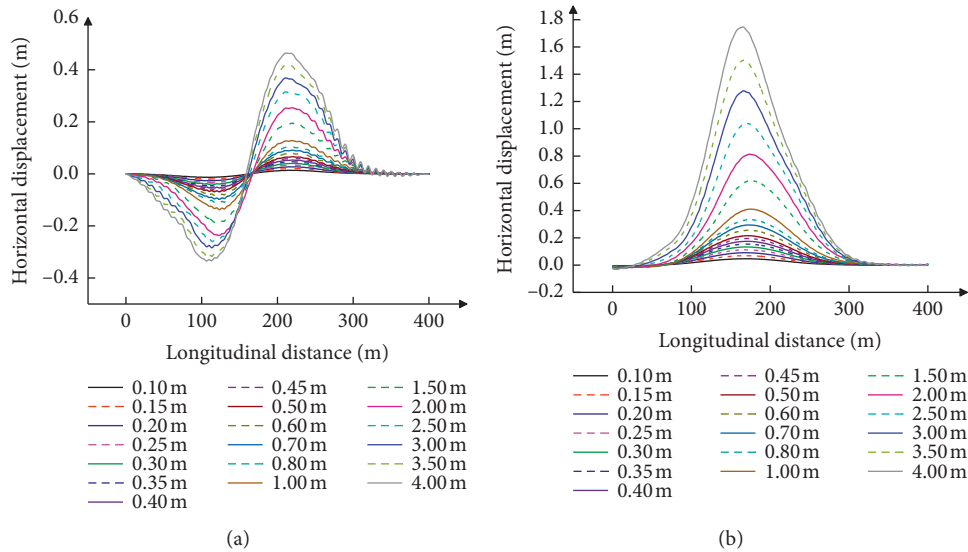


FIGURE 5: Displacement curve in the longitudinal direction of the deep site under different displacements. (a) X-direction displacement curve of the upper boundary. (b) Z-direction displacement curve of the upper boundary.

150~300 m, and the deep-site deformation within 300~400 m is basically zero. When the fracture zone is displaced by 0.1 m, the deep-site displacement is mainly distributed in the range of 50~300 m. With the increase of the displacement amount of the fracture zone, the displacement curve gradually rises, and the slope of the curve at the center point gradually increases.

The Z-direction displacement curve is symmetrically distributed with the axis of symmetry at 150 m. The overall deformation is positive, and the maximum deformation is located at the axis of symmetry. The distribution range of the

deformation along the longitudinal direction is roughly 0~300 m, and the deformation of the soil within the range of 300~400 m is basically 0, which is consistent with the distribution of the X-direction displacement curve along the longitudinal direction. When the fracture zone is displaced by 0.1 m, the maximum deformation value of the overlying soil on the deep site is 0.05 m. With the increase of the dislocation displacement of the fracture zone, the shape of the curve gradually becomes steeper, and the amount of soil deformation gradually increases. When the fracture zone is displaced by 4.0 m, the deformation value of the upper soil is

the largest, which is 1.75 m, and the deformation range reaches the maximum value.

In summary, the deformation range of the overlying soil along the longitudinal length of the deep site during the dislocation of the fracture zone is roughly distributed in the 100 m area before and after the fracture zone, and the upper soil has the most severe deformation. The negative displacement of the  $X$ -direction deformation curve may be due to the forward movement of the left soil body under the pressure of the upper soil body during the dislocation process of the fracture zone. The  $Z$ -direction overall deformation is tensile deformation, and the  $Z$ -direction deformation is larger than the  $X$ -direction deformation under different displacement amounts. With the increase of the dislocation amount of the fracture zone, the maximum displacement in the  $X$ -direction at the boundary of the overlying soil layer is 0.45 m, and the maximum displacement in the  $Z$ -direction is 1.75 m. It can be inferred that the propagation of the fracture zone displacement to the overlying soil layer is mainly determined by the vertical displacement.

*3.2. Analysis of the Stress Response of the Deep Site under the Creeping Dislocation of the Active Fault.* For the upper boundary of the overlying soil, the maximum principal stress distribution is used to measure the damage of its surface. Figure 6 shows the maximum principal stress distribution curve along the longitudinal direction of the upper boundary of the fracture zone with different displacements.

Comprehensive analysis of the maximum principal stress distribution curve of the upper boundary in the above figure shows that the maximum principal stress of the overlying soil is dominated by compressive stress. When the fracture zone just started to move, the maximum principal stress of the soil along the longitudinal length direction increased negatively, and the compressive stress gradually increased. In the area near 100 m, the compressive stress begins to decrease, showing a tendency of tension, but the maximum principal stress value does not show a positive value, and the soil is still in a compressed state. With the increase of the longitudinal distance, the compressive trend becomes more obvious and reaches the maximum compressive stress near 250 m. When the dislocation amount of the fracture zone is 0.1~1.0 m, the shape of the maximum principal stress distribution curve does not change significantly, but as the displacement amount of the fracture zone increases, the value of the maximum principal stress increases as a whole. When the fracture zone is displaced by 1.5 m, the curve changes greatly. The maximum principal stress value of the soil in the area of 100~200 m appears to be a plateau, and its value does not change significantly with the increase of the displacement amount of the fracture zone, while the maximum principal stress on both sides of the fracture zone increases significantly. The fracture zone is displaced to the upper right part of the overlying soil at a dip angle of  $30^\circ$ , and the lower right area of the deep site has a significant compression effect. When the dislocation amount is 2.0 m, 3.0 m, and 4.0 m, it can be seen that the variation trend of the maximum principal stress curve has a great change. The analysis reason is mainly due to the plastic

failure development situation caused by the influence of fault on the soil, which changes in the soft soil layer. The following will focus on the analysis of this change.

*3.3. Analysis of the Development of Plastic Zone under the Creeping Dislocation of the Active Fault.* Related research [27] shows that when calculating slope stability and studying slope instability conditions, the equivalent plastic strain penetration from the toe to the slope can be used as an important criterion for slope instability. The distribution of the plastic zone of the overlying soil layer under the dislocation of the bedrock fracture zone indicates the specific damage range of the soil and the development process of the damage. Since there are many working conditions of the model built, the working conditions with a significant development range of the plastic zone are selected for analysis and research. Figure 7 is the cloud diagrams of the development of the plastic zone of the overlying soil when the bedrock fracture zone is displaced 0.3 m, 0.6 m, 1.0 m, 2.0 m, 3.0 m, and 4.0 m.

The development cloud diagrams of the plastic zone of the overlying soil under the creeping dislocation of the bedrock fracture zone show that when the bottom fracture zone starts to move, the plastic zone first appears at the boundary between the front end of the fracture zone and the overlying soil. With the increase of the displacement amount of the fracture zone, the plastic zone of the overlying soil begins to develop inside the overlying soil at an angle of  $45^\circ$ . When the fracture zone is displaced by 0.6 m, plastic deformation occurs in the boundary area between the rear end of the fracture zone and the overlying soil, and it extends into the soil with the increase of the displacement of the fracture zone. The plastic zone at the front end of the fracture zone begins to extend inner in a horizontal direction, and the plastic strain is concentrated in the boundary area between the front end of the fracture zone and the overlying soil and gradually decreases inward in a disc-shaped during the whole process. The reason for this phenomenon may be due to the fact that the soil on the left side of the fracture zone mainly bears the tensile force, and the right side mainly bears the pressure during the dislocation process. The compressive strength of soil is much better than its own tensile strength. With the increase of displacement, the soil on the left is gradually damaged, and the soil on the right is gradually crushed. During the whole dislocation process of the bottom fracture zone, the plastic zone development law of the overlying soil is obvious. Therefore, it can be inferred that there is a certain connection between the development of the plastic strain of the overlying soil and the dislocation of the fracture zone. As the amount of fault dislocation continues to increase, the soil layer contains a soft clay layer, and a plastic failure zone develops laterally, which is mainly caused by the silty clay layer's soft texture, large cohesive force, and small friction angle, which is easy to be destroyed.

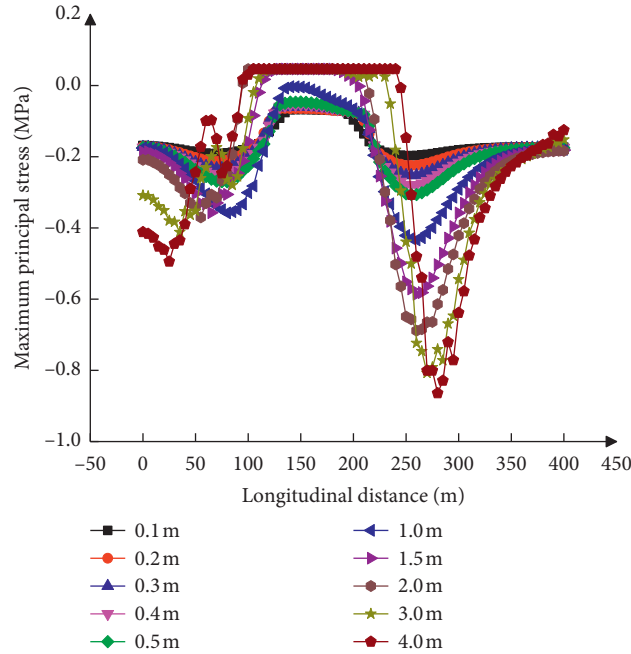


FIGURE 6: The distribution curve of the maximum principal stress along the longitudinal length of the upper boundary.

#### 4. Quantitative Analysis of the Development of Rupture Traces in Deep Site under Active Fault Creeping Dislocation

The development of the plastic zone of the overlying soil is regular in the dislocation process of the fracture zone at the bottom of the deep site. Studying the development of the plastic zone in the dislocation process of fracture zone will provide an important reference for engineering construction and engineering disaster prevention and mitigation [28]. The study in Section 3 of this paper shows that the plastic strain develops more significantly in the area between the overlying soil and the left side of the fracture zone during the fault movement. In order to explore the development law of the plastic zone of the overlying soil, this paper establishes a calculation model for the overlying soil of the uniform round gravel soil and selects the trace of the plastic zone on the left side of the fracture zone under the displacement amount of 4.0 m for quantitative regularity research. Figure 8 shows the cloud diagram of the development of the plastic zone.

When the bottom fracture zone is displaced 4.0 m, the plastic strain in the boundary area between the overlying soil and the front end of the fracture zone is more concentrated. The development area of the plastic zone is divided into an upper envelope and a lower envelope, which is divided into two parts for research.

**4.1. Development Law of the Upper Envelope Curve of the Plastic Zone.** When the fracture zone is displaced 4.0 m, the development range of the plastic zone is roughly 0~50 m. According to the approximate range of the upper envelope when the fracture zone is displaced 4.0 m, some suitable reference points are selected and fitted to obtain the upper

envelope. The fitting result is shown in Figure 9, and the fitting curve equation and related parameters are shown in Table 2.

The fitting function of the envelope curve on the plastic zone selects Boltzmann equation. Boltzmann extended the Maxwell distribution to Maxwell-Boltzmann distribution, and it has been widely used in engineering practice [29, 30]. After bringing the data into the equation, the fitting curve formula of the envelope curve on the plastic zone is obtained:

$$y = \frac{-83.19112}{1 + e^{((x-10.40827)/12.88084)}} + 62.1508. \quad (1)$$

After the fitting curve is obtained, it is determined whether the curve has a good degree of fit according to the residuals and correlation coefficients. The residual figures of the fitting curve are shown in Figure 10.

It can be seen from the fitting curve related parameter table and the fitting curve residual graph that the correlation coefficient  $R^2$  of the fitting curve is 0.9995, and the fitting degree of the reference points and the upper envelope curve is better. The points in the residual graph are distributed on a horizontal band with the origin as the center, and the distribution of scattered points along the horizontal direction is the same, indicating that the residuals are random and the selected regression model is reasonable. Therefore, it can be inferred that the development of the upper envelope curve on the plastic zone of the overlying soil during the fracture zone dislocation process satisfies the Boltzmann equation and exhibits a first-order exponential growth.

**4.2. Development Law of the Lower Envelope Curve of the Plastic Zone.** Consistent with the research method of the

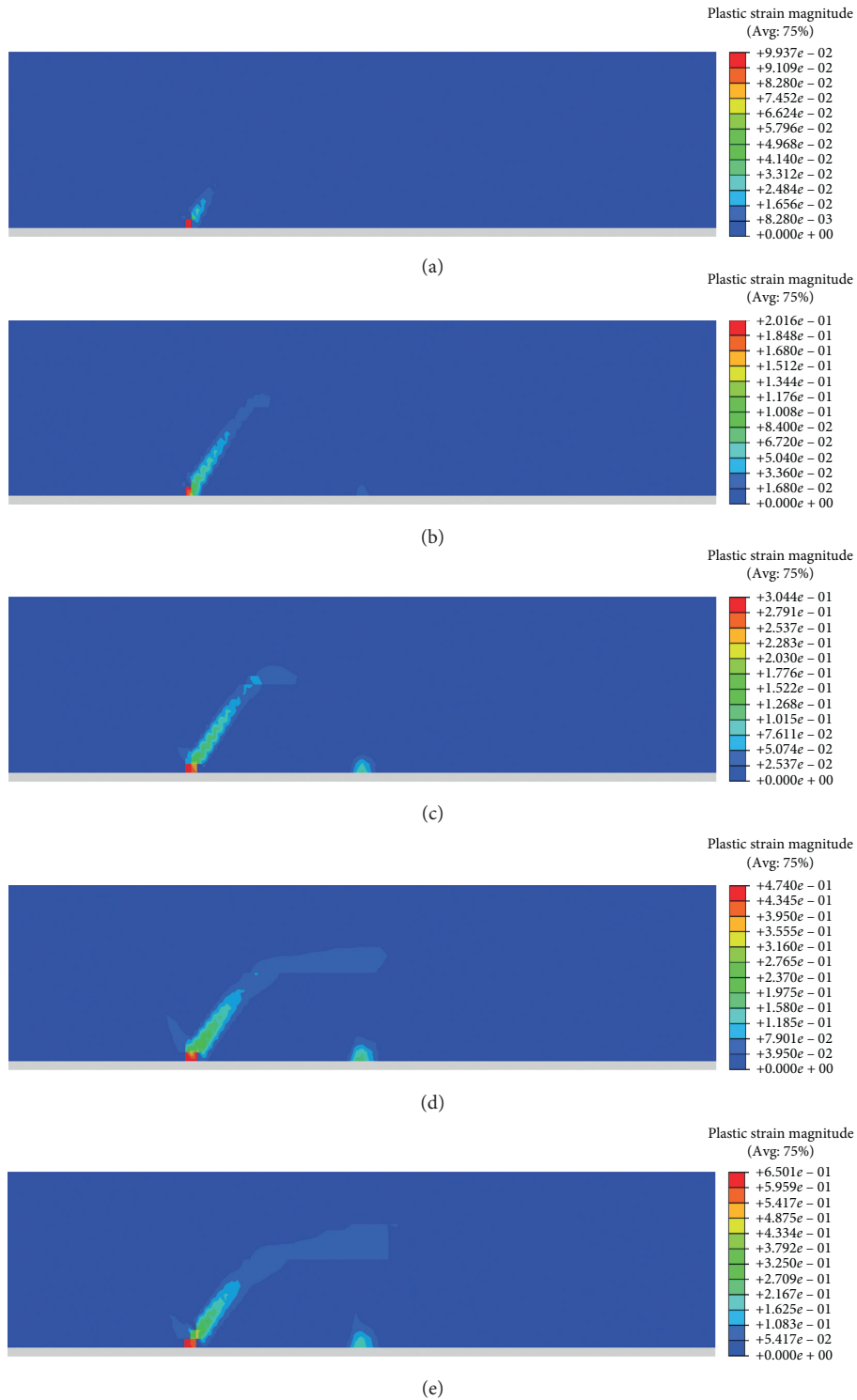


FIGURE 7: Continued.

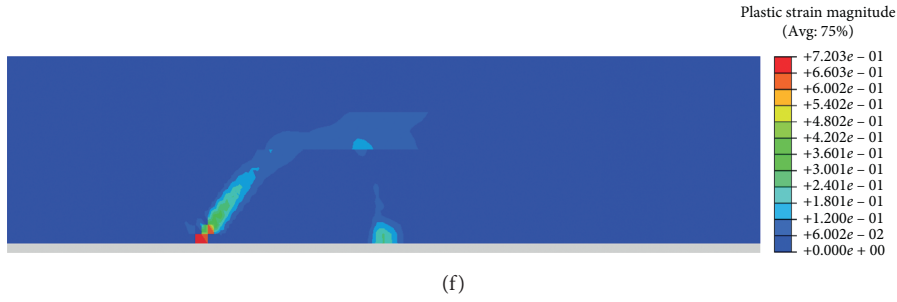


FIGURE 7: The cloud diagrams of the development of plastic zone under different displacements. (a) The cloud diagram of the development of a plastic zone with a displacement of 0.3 m. (b) The cloud diagram of the development of a plastic zone with a displacement of 0.6 m. (c) The cloud diagram of the development of a plastic zone with displacement of 1.0 m. (d) The cloud diagram of the development of a plastic zone with a displacement of 2.0 m. (e) The cloud diagram of the development of a plastic zone with a displacement of 3.0 m. (f) The cloud diagram of the development of a plastic zone with a displacement of 4.0 m.



FIGURE 8: The cloud diagram of plastic zone of uniform round gravel soil model with a dislocation of 4.0 m.

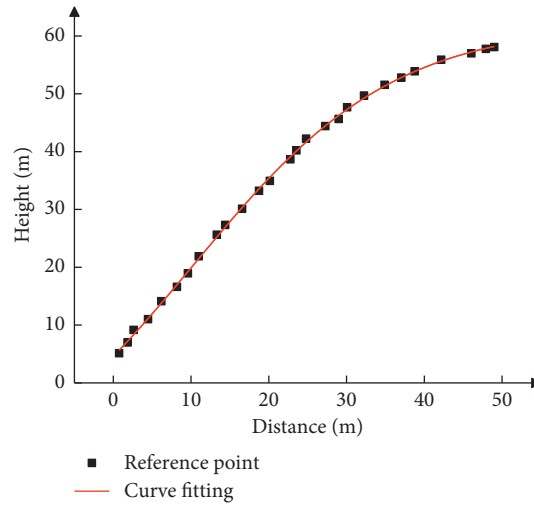


FIGURE 9: Upper envelope fitting curve of the plastic zone.

TABLE 2: Fitting curve equation and related parameters.

Equation	$y = ((A_1 - A_2)/(1 + e^{(x-x_0)/dx})) + A_2$
$A_1$	$-21.04032 \pm 3.1212$
$A_2$	$62.1508 \pm 0.58877$
$x_0$	$10.40827 \pm 0.89537$
$dx$	$12.88084 \pm 0.54026$
$R^2$ (COD)	0.99951
Adjusted $R^2$	0.99945

upper envelope curve of the plastic zone, reference points are selected for curve fitting according to the range of the lower envelope curve when the fracture zone is displaced 4.0 m.

Figure 11 shows the lower envelope curve fitting curve graph, and the relevant parameters of the fitting curve are shown in Table 3.

The fitting function of the lower envelope curve in the plastic zone selects the Gauss equation. After bringing the data into the equation, the fitting curve formula of the lower envelope curve in the plastic zone is obtained. After putting the data into the equation, the following formula is obtained:

$$y = -67.63855 + \frac{1080220}{318.59067 * \sqrt{\pi/2}} e^{-2 * ((x - 447.27807)^2 / 318.59067^2)}. \quad (2)$$

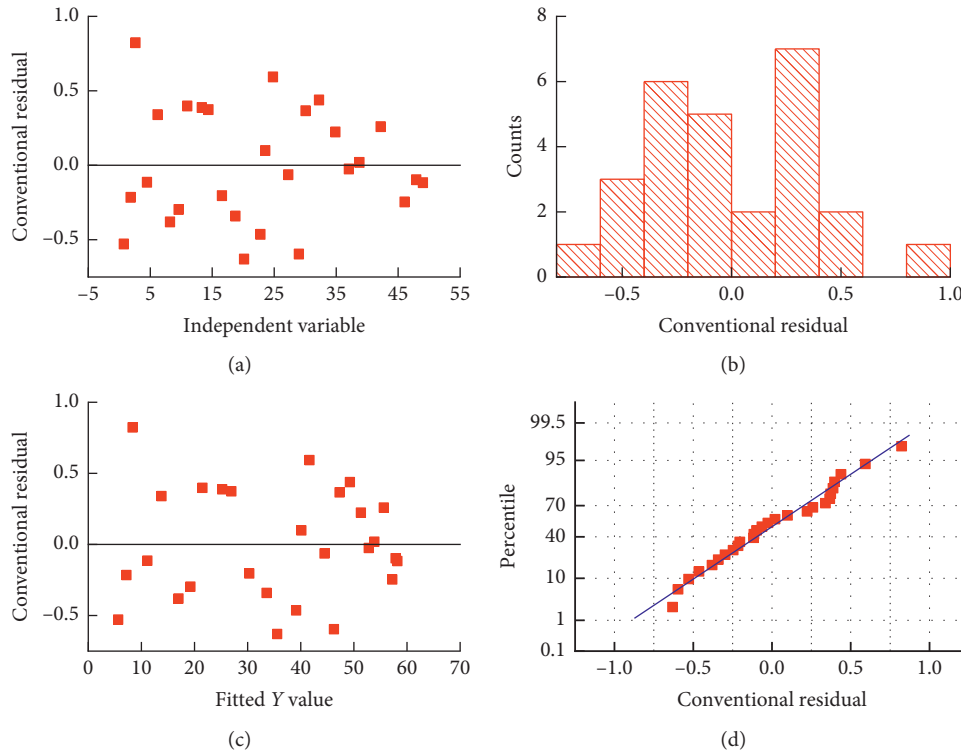


FIGURE 10: The residual figures of the upper envelope fitting curve.

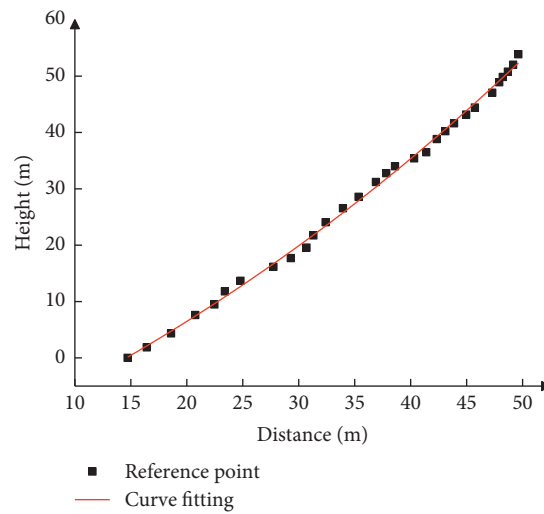


FIGURE 11: Lower envelope fitting curve of the plastic zone.

TABLE 3: Fitting curve equation and related parameters.

Equation	$y = y_0 + (A/\omega\sqrt{\pi/2})e^{-2*((x-x_c)^2/\omega^2)}$
$y_0$	$-67.63855 \pm 159.72034$
$x_c$	$447.27807 \pm 4842.74271$
$\omega$	$318.59067 \pm 2141.81112$
$A$	$1.08022E6 \pm 4.54252E7$
$R^2$ (COD)	0.99784
Adjusted $R^2$	0.99759

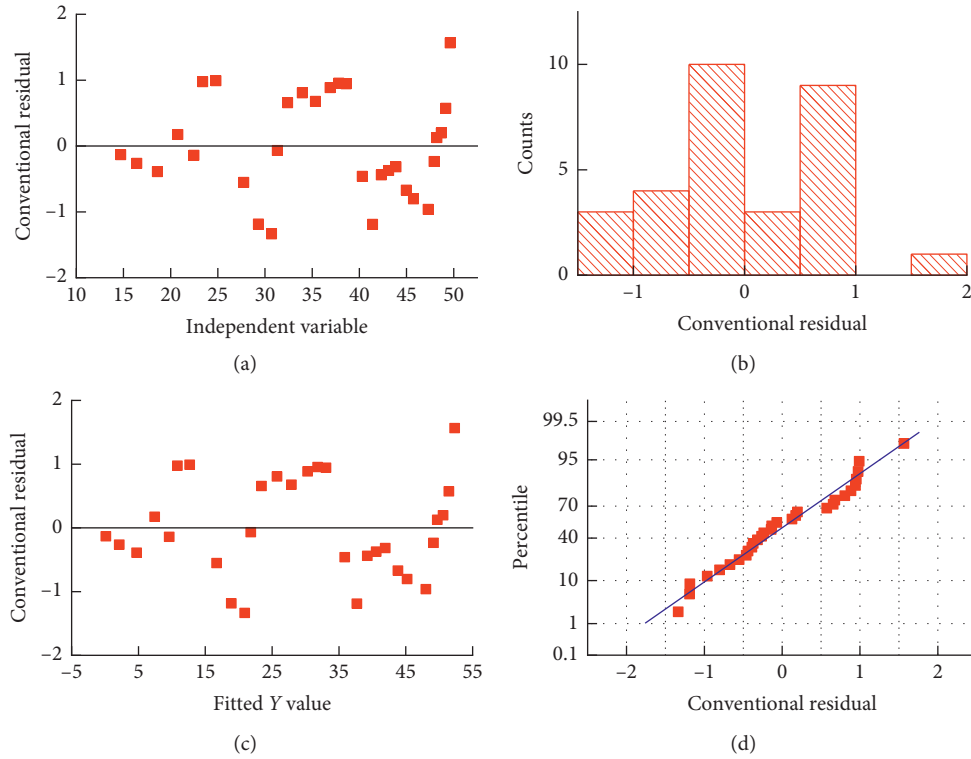


FIGURE 12: The residual figures of the lower envelope fitting curve.

The residual diagram of the lower envelope fitting curve is shown in Figure 12.

The correlation coefficient  $R^2$  of the lower envelope curve fitting curve is 0.9976, and the fitting degree of the reference points and the lower envelope fitting curve of the plastic zone is better. The points in the residual graph are distributed on a horizontal band with the origin as the center, and the distribution of scattered points along the horizontal direction is the same, indicating that the residuals are random and the selected regression model is reasonable. Therefore, it can be inferred that the development of the lower envelope of the plastic zone in the process of fracture zone dislocation satisfies the Gauss equation and exhibits a second-order exponential growth.

## 5. Conclusion

This paper uses the finite element analysis software ABAQUS to establish a three-dimensional finite element deep-site calculation model and studies the dynamic response of the deep site through the displacement distribution, stress distribution, and plastic zone distribution of the upper boundary of the overlying layer on the deep site along the longitudinal direction. At the same time, the contours of the plastic zone in the overlying soil are analyzed and fitted, and the failure mechanism of the deep site under the fault creeping dislocation is revealed. The conclusions are as follows:

- (1) When creeping dislocation occurs in the bottom bedrock fracture zone, the  $X$ -direction deformation

curve of the overlying soil is centered symmetrically at about 150 m, and the center point is roughly located in the middle of the fracture zone. As the bottom fracture zone is squeezed to the right, the soil on the right side of the overlying layer is deformed negatively, and the soil on the left side is positively deformed. With the increase of the dislocation amount of the fracture zone, the development range of soil deformation continues to increase and finally stabilizes in the range of 0~300 m. The  $Z$ -direction deformation curve is approximately symmetrically distributed around 150 m as the axis of symmetry, and the dislocation of the bottom fracture zone drives the overall positive deformation of the soil. As the amount of displacement of the fracture zone increases, the amount of deformation and the deformation range of the overlying soil continue to increase and stabilize in the range of 0~300 m. Due to the large distance between the upper boundary and the bottom fracture zone, the amount of deformation gradually decreases in a disc-shaped form as the deformation propagates upward. The maximum displacement in the  $Z$ -direction is greater than the maximum displacement in the  $X$  direction, and the deformation of the overlying soil is mainly affected by the vertical displacement of the fracture zone. The monitoring curve showed no abrupt change value, indicating that the top surface of soil did not rupture, only the influence of fault on the displacement transfer of the top surface of the soil.



- (2) When creeping dislocation occurs in the bottom fracture zone, the maximum principal stress of the upper boundary of the overlying soil layer on the deep site is dominated by compressive stress. The maximum principal stress of the soil on both sides of the fracture zone has a negative maximum value. Because the entire fracture zone is displaced to the upper right at a dip angle of  $30^\circ$ , the compression effect of the soil on the right side is significant. When the displacement of the fracture zone is less than 1.5 m, the platform range of the maximum principal stress curve is roughly the same as the range of the fracture zone. When the displacement is greater than 1.5 m, the range of the platform expands to 100~250 m. The maximum principal stress monitoring curve shows a great change, indicating the development of plastic failure of soil, which is the same as the result of the plastic failure zone studied later.
- (3) When the bottom fracture zone started to move, the plastic zone first appears at the junction area between the front end of the fracture zone and the overlying soil. With the increase of the amount of dislocation of the fracture zone, the plastic zone of the overlying soil begins to develop inside the overlying soil at an angle of  $45^\circ$ . After the fracture zone is displaced for a certain distance, a plastic zone begins to appear in the boundary area between its rear end and the overlying soil and extends to the upper part of the soil with the increase of the dislocation of the fracture zone, while the plastic zone at the front end extends horizontally inward. The soil on the left side of the fracture zone mainly bears the tensile force, and the right side mainly bears the pressure. The compressive strength of the soil is greater than the tensile strength, so the size of the plastic strain is concentrated in the boundary area between the front end of the fracture zone and the overlying soil and gradually decreases inward in a disc-shaped form. With the increase of the displacement amount of the fracture zone, the soil on the left shows tensile failure, and the soil on the right shows compression failure. As the amount of fault dislocation continues to increase, the soil layer contains a soft clay layer, and a plastic failure zone develops laterally, which is mainly caused by the soft clay layer's soft texture, large cohesive force, and small friction angle, which is easy to be destroyed.
- (4) When the bottom fracture zone is displaced by the maximum distance, the upper envelope of the plastic zone satisfies the Boltzmann equation and exhibits a first-order exponential growth. The lower envelope satisfies the Gauss equation and exhibits a second-order exponential growth. The development curve equation of the plastic zone is verified according to the residual figures of the fitting result and the correlation parameters.

## Data Availability

All the data in this paper are available from the corresponding author upon request.

## Conflicts of Interest

The authors declare that they have no conflicts of interest.

## Acknowledgments

This study was supported in part by Science and Technology Research and Development Plan of China National Railway Corporation Limited (no. K2019G009), National Nature Science Fund Project (no. 52078426), Sichuan Provincial Science and Technology Support Project (nos. 2020YJ0253, 2020YFSY0060, 2019JDR0133, and 2019JDR0134), and China National Railway Group Co. Ltd. Scientific Research Project (nos. SY2016G003 and N2020T004).

## References

- [1] J. Li, S. C. Wu, Y. T. Gao, Y. L. Xie, and M. W. Ji, "Review of slope micro-seismic monitoring in open-pit mine," *Chinese Journal of Rock Mechanics and Engineering*, vol. 33, no. S2, pp. 3998–4013, 2014.
- [2] A. W. Bishop, "The use of the slip circle in the stability analysis of slopes," *Geotechnique*, vol. 45, no. 1, pp. 7–17, 1995.
- [3] Z. Y. Chen, "On Pan's principles of soil and rock stability analysis," *Journal of Tsinghua University (Science and Technology)*, vol. 1, pp. 3–6, 1998.
- [4] J. Lowe and L. Karafath, "Stability of earth dams upon drawdown," in *Proceedings of the 1st Panamer Conference on Soil Mechanics*, pp. 537–552, Mexican Society of Soil, Guadalajara, Mexico, 1960.
- [5] W. J. Guo, *Study on Slope Stability of Deep Foundation Excavation Based on the Gray System Theory*, Huazhong University of Science and Technology, Wuhan, China, 2005.
- [6] S. Lu, "Application of multi-level fuzzy comprehensive evaluation method in stability evaluation of slope rock mass," *Site Investigation Science and Technology*, vol. 1, no. 4, pp. 32–37, 2014.
- [7] Y. K. Sun and B. K. Yao, "Principal geological models of deformation and failure of rock slopes in China," *Chinese Journal of Rock Mechanics and Engineering*, vol. 2, no. 1, pp. 67–76, 1983.
- [8] C. A. Soto, "A comparative study of slope modeling techniques for fractured ground," Master of Science thesis, Department of Mining and Mineral Technology, Royal School of Mines, Imperial College of Science and Technology, London, UK, 1974.
- [9] J. W. Bray and R. E. Goodman, "The theory of base friction models," *International Journal of Rock Mechanics and Mining Sciences & Geomechanics Abstracts*, vol. 18, no. 6, pp. 453–468, 1981.
- [10] D. P. Adhykary, A. V. Dyskin, R. J. Jewell et al., "A study of the mechanism of flexural toppling failure of rock slopes," *Rock Mechanics and Rock Engineering*, vol. 30, no. 2, pp. 75–93, 1997.
- [11] F. Sun, Z. Q. Zhang, and C. Qin, "Research on influence upon tunnel structure of metro line 1 in Urumqi forced by normal fault dislocation," *China Railway Science*, vol. 40, no. 2, pp. 54–63, 2019.

- [12] X. D. Ji, P. Li, S. R. Su, and Y. C. Wang, "Development and application of physical model test device showing evolution process of the reverse fault," *Journal of Xi'an University of Science and Technology*, vol. 33, no. 2, pp. 190–194, 2013.
- [13] S. Abe, J. H. Dieterich, P. Mora, and D. Place, "Simulation of the influence of rate- and state-dependent friction on the macroscopic behavior of complex fault zones with the lattice solid model," *Pure and Applied Geophysics*, vol. 159, no. 9, pp. 1967–1983, 2002.
- [14] S. Abe and K. Mair, "Effects of gouge fragment shape on fault friction: new 3D modelling results," *Geophysical Research Letters*, vol. 36, 2009.
- [15] R. J. Lunn, J. P. Willson, Z. K. Shipton, and H. Moir, "Simulating brittle fault growth from linkage of preexisting structures," *Journal of Geophysical Research-Solid Earth*, vol. 113, no. B7, p. 10, 2008.
- [16] M. T. Luan, Y. J. Wu, and T. K. Nian, "An alternating criterion based on development of plastic zone for evaluating slope stability by shear strength reduction FEM," in *Proceedings of the Sina- Japanese Symposium on Geotechnical Engineering*, pp. 181–188, Geotechnical engineering in urban construction, Beijing, China, October 2003.
- [17] H. Zheng, G. H. Sun, and D. F. Liu, "A practical procedure for searching critical slip surfaces of slopes based on the strength reduction technique," *Computers and Geotechnics*, vol. 36, pp. 1–5, 2009.
- [18] S. Y. Zhao, Y. R. Zheng, and W. D. Deng, "Stability analysis on jointed rock slope by strength reduction fem," *Chinese Journal of Rock Mechanics and Engineering*, vol. 22, no. 2, pp. 254–260, 2003.
- [19] Y. R. Zheng and S. Y. Zhao, "Application of finite element strength reduction method in soil slope and rock slope," *Chinese Journal of Rock Mechanics and Engineering*, vol. 23, no. 19, pp. 3381–3388, 2004.
- [20] L. C. Li, C. A. Tang, and J. Xing, "RFPA simulation analysis of deformation and failure of jointed rock slope," *Journal of Northeastern University*, vol. 27, no. 5, pp. 559–562, 2006a.
- [21] Z. Y. Chen, Y. Zhao, Analysis of tunnel response caused by active reverse fault dislocation. The Geological Society of China," in *Proceedings of the 2019 National Engineering Geology Annual Conference*, pp. 113–118, The Geological Society of China: Editorial Office of Journal of Engineering Geology, Beijing, China, October 2019.
- [22] M. L. Lin, C. F. Chung, and F. S. Jeng, "Deformation of overburden soil induced by thrust fault slip," *Engineering Geology*, vol. 88, no. 1, pp. 70–89, 2006.
- [23] L. Y. Zhang, Y. R. Zheng, S. Y. Zhao, and W. M. Shi, "Study on the accuracy of the finite element strength reduction coefficient method for calculating the safety factor of soil slope stability," *Journal of Hydraulic Engineering*, vol. 1, pp. 21–27, 2003.
- [24] M. L. Lin, C. F. Chung, F. S. Jeng, and T. C. Yao, "The deformation of overburden soil induced by thrust faulting and its impact on underground tunnels," *Engineering Geology*, vol. 92, no. 3, pp. 110–132, 2007.
- [25] J. S. Shi, *Experimental and Numerical Study on the Damage of Overlying Soil and Tunnel Caused by Fault Dislocation*, Zhejiang University, Zhejiang, China, 2017.
- [26] H. L. Song, C. H. Zhang, and G. H. Wang, *Structural Geology*, Geological Publishing House, Beijing, China, 2013.
- [27] M. T. Luan, Y. J. Wu, and T. K. Nian, "A criterion for evaluating slope stability based on development of plastic zone by shear strength reduction FEM," *Journal of Disaster Prevention and Mitigation Engineering*, vol. 23, no. 3, pp. 1–8, 2003.
- [28] G. Q. Chen, R. Q. Huang, Y. C. Shi, and Q. Xu, "Slope stability analysis based on dynamic and overall strength reduction method," *Chinese Journal of Rock Mechanics and Engineering*, vol. 33, no. 2, pp. 243–256, 2014.
- [29] J. Jiang, G. Gao, and Y. Zhang, "Fitting of Q-S curves and bearing capacity calculation of PCC pile," *Journal of China Coal Society*, vol. 34, no. 4, pp. 531–532, 2009.
- [30] Q. Liu and L. Yang, "New model of load transfer function for pile analysis based on disturbed state model," *Journal of Tongji University (Natural Science)*, vol. 34, no. 2, pp. 166–168, 2006.

## Research Article

# Failure Characteristics and Mechanism of Multiface Slopes under Earthquake Load Based on PFC Method

Tao Yang <sup>1</sup>, Yunkang Rao <sup>1</sup>, Huailin Chen <sup>1</sup>, Bing Yang <sup>1</sup>, Jiangrong Hou <sup>1</sup>,  
Zihong Zhou <sup>1</sup> and Haojiang Ding <sup>2</sup>

<sup>1</sup>School of Civil Engineering, Southwest Jiaotong University, Chengdu 610031, China

<sup>2</sup>China Railway Eryuan Engineering Group Co. Ltd., Chengdu 610031, China

Correspondence should be addressed to Bing Yang; yangb@home.swjtu.edu.cn

Received 19 May 2021; Accepted 9 August 2021; Published 19 August 2021

Academic Editor: Honglue Qu

Copyright © 2021 Tao Yang et al. This is an open access article distributed under the Creative Commons Attribution License, which permits unrestricted use, distribution, and reproduction in any medium, provided the original work is properly cited.

Understanding the failure mechanism and failure modes of multiface slopes in the Wenchuan earthquake can provide a scientific guideline for the slope seismic design. In this paper, the two-dimensional particle flow code (PFC<sup>2D</sup>) and shaking table tests are used to study the failure mechanism of multiface slopes. The results show that the failure modes of slopes with different moisture content are different under seismic loads. The failure modes of slopes with the moisture content of 5%, 8%, and 12% are shattering-shallow slip, tension-shear slip, and shattering-collapse slip, respectively. The failure mechanism of slopes with different water content is different. In the initial stage of vibration, the slope with 5% moisture content produces tensile cracks on the upper surface of the slope; local shear slip occurs at the foot of the slope and develops rapidly; however, a tensile failure finally occurs. In the slope with 8% moisture content, local shear cracks first develop and then are connected into the slip plane, leading to the formation of the unstable slope. A fracture network first forms in the slope with 12% moisture content under the shear action; uneven dislocation then occurs in the slope during vibration; the whole instability failure finally occurs. In the case of low moisture content, the tensile crack plays a leading role in the failure of the slope. But the influence of shear failure becomes greater with the increase of the moisture content.

## 1. Introduction

The landslide caused by earthquakes is a common natural disaster in mountain areas [1–3]. Thousands of geological disasters have been triggered by the Wenchuan earthquake ( $M_S = 8.0$ ) in western Sichuan, China, most of which (more than 60,000) were landslides [1, 4]. There are dozens of large-scale landslides ( $>10$  million  $m^3$ ) and more than 100 landslides with an area of more than 50,000  $m^2$  [1, 4]. The landslide triggered by earthquakes is easy to cause a large number of casualties and economic loss. Therefore, it is important to study the failure mode and mechanism of slopes under earthquakes, which is of great significance to carry out earthquake defense and disaster reduction [5, 6].

Gang et al. [7] studied the dynamic failure modes of the bedding slope and counterbedding slope by the shaking table test. The results show that the main dynamic failure modes

of the bedding slope include a vertical tensile crack at the rear of the slope, bedding slide of the strata along the weak intercalation, and rock collapse from the crest of the slope. In contrast, the dynamic failure modes of the counterbedding slope mainly include horizontal and vertical dislocation fissures, weak interlayer extrusion, and breakage at the crest. Liu et al. [8] performed a shaking table test to study the failure mode of slopes with horizontal soft and hard interbeddings under frequent microseisms. The failure mode of the slope is summarized as follows: creep—opening tensile cracks at the shoulder and opening pressing cracks at the slope bottom—developing secondary joints in the back end—developing secondary joints near the slope surface—shearing in soft layers—slope sliding—accumulating blocks at the slope bottom. Li et al. [9] studied qualitatively the failure mechanism of the Hongshiyuan landslide and the stability of the remnant slope combining with the on-site

investigation and unmanned aerial vehicle (UAV) three-dimensional imaging technologies. The failure mechanism is summarized as tension-crushing-shattering-sliding. Deng et al. [10] pointed out that the dynamic failure mode of the bedding rock slope with zigzag asperities is mainly characterized by the vertical tensile crack at the slope rear edge and integral slipping of the slope along the bedding surfaces, and the deformation pattern of the sliding surface was mostly determined by undulating angles and normal stress.

Hou et al. [11] used a two-dimensional particle flow program (PFC<sup>2D</sup>) to investigate the dynamic process and hyperactivity mechanism of the loose deposit slope on the Ya'an-Kangding Expressway. The results show that the porosity of the surface slope generally increases with increasing seismic-wave loading time, while the porosity of the slope remains unchanged. Abe et al. [12] simulated and analyzed the dynamic characteristics of the slope model with different inclined weak interlayers by MPM (material point method). Chang and Tabada [13] used the discrete element model to simulate the avalanche caused by the Jiu-feng-shan earthquake under various assumptions of rock properties, water table height, and boundary shear strength. Tang et al. [14] used the PFC<sup>2D</sup> model to simulate the motion behavior of landslides caused by earthquakes.

The above studies are mainly based on a single free-face. However, there were some slopes damaged with multiple free-faces in the Wenchuan earthquake [15]. Yang et al. [16] simulated the failure process of double-side high and steep slope based on the continuous medium discrete element method (CDEM) combining with shaking table test data. The results show that the stress concentration appears at the top of the sliding mass at first, and then, a part of the tension-shear failure points appears, which expands from the top toward the toe of the sliding mass along the structural plane. Finally, the rupture of the toe leads to a landslide. Through model tests, the dynamic response of double-side slopes under strong earthquakes was studied by Xiao et al. [17]. It is found that the failure of different forms of double-side slopes under seismic waves is mainly caused by the repeated tension-shear effect and co-shear effect in both directions. Yang et al. [4] studied the failure process of a double-side slope with high moisture content under seismic load based on shaking table tests. The test results show that the slope failure has undergone a gradual deformation process, and the slope failure mode is a creeping landslide.

Through the analysis of present studies, it is shown that the failure mechanism of multiface slopes with different moisture content under earthquakes is not clear. The mechanism of crack formation and evolution during slope failure needs to be studied deeply and carefully. In this paper, the seismic instability characteristics and mechanism of three kinds of multiface slopes with different moisture content will be investigated based on PFC<sup>2D</sup> and shaking table test.

## 2. Test Details

To verify the effectiveness of the numerical modeling, a set of shaking table model tests were carried out. A 3 m × 2 m electro-hydraulic servo vibration table was used. The

maximum displacement amplitude of the shaking table is 100 mm, and the effective load is 20 t. It can output acceleration within the range of 0.05 g–1.5 g, and the frequency range is 0.5–100 Hz. The model box used in the test is a self-developed rigid model box with smooth glass on one side, which is 2 m long, 0.8 m wide, and 1.5 m high, as shown in Figure 1. In this paper, the slope with multiple free-faces was simulated by a double-sided slope. In the model box, the double-sided slope is built by layered filling, and the filling height of each layer is 10 cm. In the process of slope filling, the soil is rolled and compacted under constant external force to keep the same porosity in the slope. The final compactness of the model slope is 86.4%, which is medium dense. The height of the double-side slope is 800 mm, the width of the crest of the slope is 360 mm, and the slope angle is 50°. The white sand with vertical zonal distribution is placed on the inner side of the glass wall to observe the deformation of the soil in the test. The test model is shown in Figure 2.

To monitor and study the dynamic characteristics and displacement of the slope, 15 acceleration sensors and 7 displacement sensors are arranged in the slope. At the same time, cameras are set on the front and side of the slope to record the whole process of slope failure, as shown in Figure 3. Sine wave was used to simulate excitation load. The test frequency is controlled at 3 Hz, and the amplitude is increased step by step from 0.1 g to 0.6 g (g is gravity acceleration). The failure of the slope is observed within the loading time of 12 s. If there is no obvious damage, it is found that the slope is stable under this loading amplitude.

## 3. Numerical Models of PFC

The numerical simulation method of particle flow (Particle Flow Code) is based on the discrete element method proposed by Cundall [18]. This method can be used to study the mechanical properties and behavior of media from a microscopic point of view.

*3.1. Constitutive Model and Parameters.* In the two-dimensional PFC model, the particles are represented by a rigid disk, and these discrete particles are subjected to force only in the contact part. When the force acting on the contact point is larger than the contact strength, these particles can be separated from each other, making the model object deformed and displaced. The force and motion of the particles follow the basic principle of Newton's law. The constitutive relation of the soil material can be realized by microcontact and bonding mode between particles. For homogeneous geotechnical materials, a large number of studies have shown that it is more reasonable to use the parallel bonding model [11, 19, 20]. In this regard, the parallel bond model is adopted in this paper, under which the particles have normal strength, tangential strength, normal stiffness, and tangential stiffness. Thus, it has the ability of antitension, antishear, and antitorion. Normal stiffness and tangential stiffness can be expressed as [20]

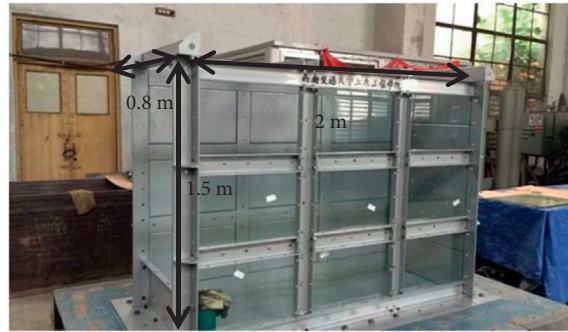


FIGURE 1: Schematic diagram of the model box.

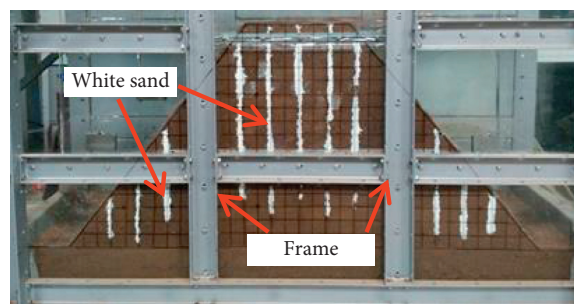


FIGURE 2: Shaking table test model of the double-side slope.

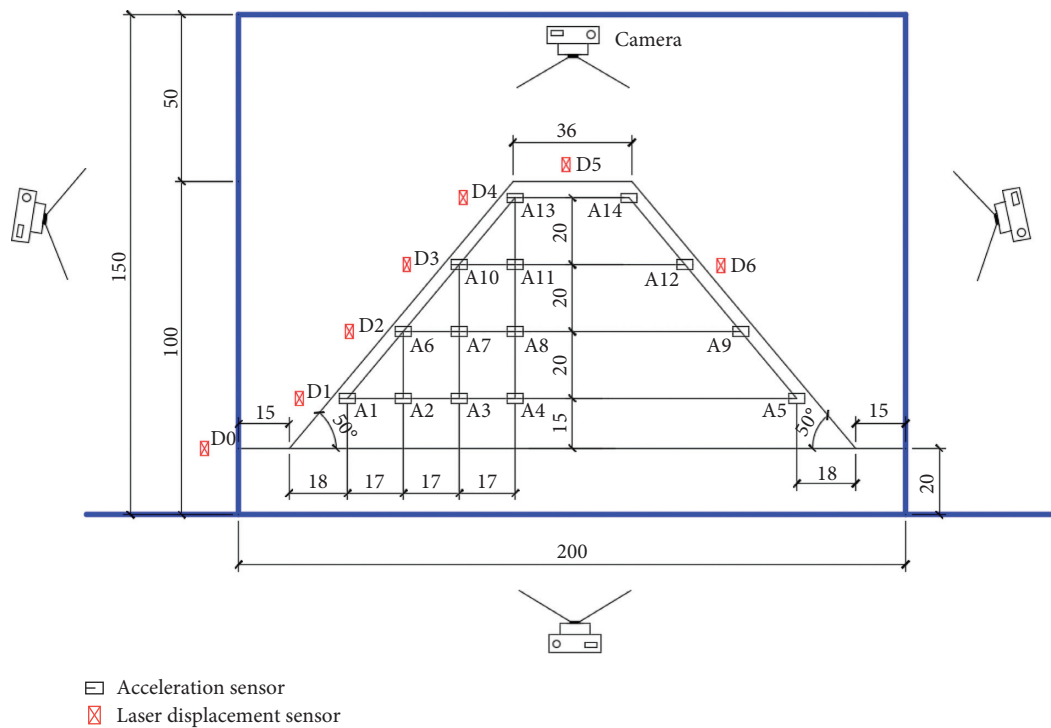


FIGURE 3: Layout of monitoring points.

$$\begin{aligned}
\bar{k}^n &= \frac{\bar{E}_c}{L}, \\
\bar{k}^s &= \frac{12I\bar{E}_c}{AL^3}, \\
\bar{R} &= \bar{\lambda} \min(R^{[A]}, R^{[B]}), \\
A &= \pi\bar{R}^2,
\end{aligned} \tag{1}$$

where  $\bar{k}^n$  is the normal contact stiffness,  $\bar{k}^s$  is the tangential contact stiffness,  $\bar{E}_c$  is Young's modulus of each parallel bond,  $\bar{R}$  is the bond radius,  $\bar{\lambda}$  is the radius multiplier used to set the parallel-bond radius,  $L$  is the bond length, and  $I$  is the moment of inertia.

The soil used in the test is a mixture of fine sand and clay at 1 : 1, with three kinds of moisture content of 5%, 8%, and 12%. The numerical model adopts the same soil parameters as the similar materials mentioned above, and the specific results are shown in Table 1.

**3.2. Boundary Conditions and Ground Motion Input.** In PFC, the wall represented by rigid lines is used as the basic unit. To prevent the dynamic force from reflecting at the boundary of the model, the wall at the bottom of the slope is set with a certain value of damping, and the damping force will be directly substituted into the equation of motion, as shown in equation (2). There are mainly viscous damping and local damping. In this paper, through a large number of trial calculations and sensitivity analyses, it is determined that the tangential and normal viscous damping is 0.157 and the local damping is 0.219:

$$F_{(i)} + F_{(i)}^d = M_{(i)}A_{(i)}, \tag{2}$$

where  $F_{(i)}$ ,  $M_{(i)}$ , and  $A_{(i)}$  are generalized force, mass, and acceleration components, respectively, and  $F_{(i)}^d$  is the damping force.

The field investigation shows that even in the extreme earthquake area of the Wenchuan earthquake, the horizontal seismic force plays a leading role in the instability of roadbed engineering [21]. Therefore, to simplify reasonably, only the horizontal ground acceleration is considered in this paper. A sine wave is used to simulate the excitation load. In PFC, acceleration cannot be applied directly to the slope, so it can only be done by applying velocity. That is, for  $a = A \sin(2\pi ft)$ ,  $v = -A \cos(2\pi f)/2\pi f$ , which is applied to the bottom of the slope. The load frequency is 3 Hz, and the amplitude is in the range of 0.1 g to 0.6 g. The failure of the slope is observed within the loading time of 12 s. If there is no obvious damage, the slope is considered to be stable under this loading amplitude. Two geometric dimensions were used in the numerical model, one is consistent with the model test size, and the other is 10 times larger than the model test size. The numerical model and the location of the monitoring points are shown in Figure 4.

## 4. Results and Discussion

**4.1. Slope Failure Process.** Figure 5 shows the failure process of slopes with different water content under earthquakes. It can be seen from Figure 5 that the numerical simulation results are consistent with the shaking table test results, which shows the effectiveness of the numerical model in this paper. The failure process of the slope with 5% moisture content is that the soil slips along the shallow layer of the slope. A large vertical displacement occurs at the top of the slope, but no obvious horizontal displacement can be observed within the slope, indicating that the shear stress is not the main factor at this time. However, there are two obvious shear slip surfaces in the slope with 8% moisture content, which are almost symmetrical along the middle axis of the slope. When the slope is unstable, the shear failure occurs along the sliding surface. The failure mode can be described as the tension-shear-slip mode, which is the same as the failure mode of Wangjiayan and Daguangbao landslides in the Wenchuan earthquake [15]. With the increase of moisture content of 12%, there is no obvious sliding surface within the slope when the slope fails. However, there are many cracks in the slope and the horizontal displacement in the slope is obvious when loading for 1 s. The slope remains relatively stable until the loading time reached 3 s, and the upper soil collapses and accumulates downward. In this condition, the shattering-collapse slip failure occurs in the slope, which is similar to the failure in the new area of the new Beichuan middle school [15]. Compared with the numerical simulation maps of the slope, it is obvious that, with the increase of moisture content, the distribution range and spacing of slope joints are expanding, and the settlement at the top of the slope is increasing. Based on the analysis of the failure mechanism of three kinds of slopes with different moisture content, it is found that, under the seismic load, the connection between surface soil particles is gradually destroyed, which results in the decreases of the tensile and shear strength. With the continuous vibration, the surface soil slips from the top to the bottom of the slope under the action of seismic force, accumulates at the foot of the slope, and slips on the shallow surface as a whole. Research studies show that, with the increase of soil moisture content, the dynamic shear modulus of soil decreases and the damping ratio is improved. So, the ability of soil to resist plastic deformation increases [22, 23]. Shear failure occurs in the soil of 8% moisture content slope to form a continuous slip surface, and finally, the sliding body slips along the slip surface as a whole. For the slope with 12% moisture content, the dynamic shear modulus of the soil further is decreased, which results in serious damage of the soil by shearing stress. The obvious horizontal uneven dislocation can be seen in Figure 5(e). Consequently, the soil is cut into small pieces under the action of shear, and the stress is redistributed. With the increase of vibration time, instability and collapse occur.

TABLE 1: Physical and mechanical parameters of soil.

Case	Moisture content (%)	Density (g/cm <sup>3</sup> )	Cohesion (kPa)	Internal friction angle (°)	Young's modulus (MPa)	Plastic limit (%)	Liquid limit (%)
1	5.0	1.5	7.5	32	15.1		
2	8.0	1.6	15.5	28	12.6	9	26
3	12.0	1.7	20.0	20	7.7		

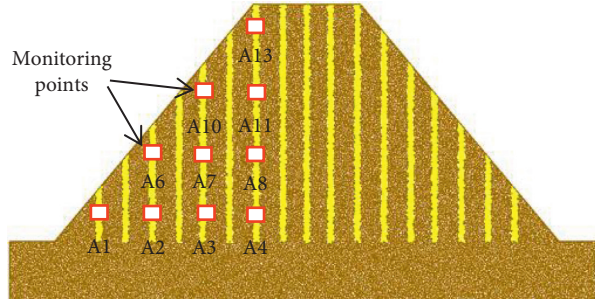


FIGURE 4: Geometrical model in numerical simulation.

**4.2. Dynamic Response of Slope.** To further explore the characteristics of slope failure under seismic load, the dynamic response of the slope was studied based on the surface monitoring points (A1, A6, A10, and A13). The displacement time-history curve and velocity time-history curve for the three groups of working conditions are shown in Figure 6, in which the lines of monitoring point 1, point 6, point 10, and point 13 are represented by black, red, blue, and green curves, respectively.

It can be seen from Figure 6 that the horizontal displacement of the slope with 5% moisture content decreases with the increase of height. At 0.15 s, the displacement and velocity have some changes. The velocity and displacement of monitoring points 1 and 6 were the largest, whose curves have roughly coincided with each other. Furthermore, a peak value occurs in the velocity time-history curve at this time and then decreases gradually, which tends to coincide with the peak value of the upper soil. The curves of monitoring points 10 and 13 are separated, and the displacement and velocity of monitoring point 13 are relatively small. Through the analysis of the time-history curves of velocity and displacement, there is a large slip at monitoring points 1 and 6 and a larger speed at the moment of sliding, and the bond between monitoring points 10 and 13 has been destroyed. The curves of monitoring points 1 and 6 did not separate until 0.8 s, which indicates that although the displacement of the lower soil was larger than that of the upper soil, the loosening time of the internal soil of points 1 and 6 was later than that of the upper soil.

The slope with 8% moisture content is mainly affected by the shear failure, whose displacement and velocity time-history curve abruptly change at 0.25 s, and the velocity and displacement at monitoring point 13 decrease, while the curves of the other three monitoring points remain coincident. Combined with the analysis of Figures 5(c) and 5(d), it can be seen that the lower three points slide along the shear plane in the same sliding body, while the failure of the upper

soil is due to the collapse of the lower soil. The displacement and velocity of monitoring point 1 suddenly increase at 2.25 s, indicating that the soil at monitoring point 1 has slipped out from the original position. Besides, the displacement and velocity time-history curve of monitoring point 6 also increases sharply at 2.6 s, indicating that when the soil at monitoring point 1 slips out from the original position, monitoring point 6 immediately slips out from the original position. It can be seen that the displacement time-history curve for 8% moisture content is much denser than that for 5% water cut slope, which indicates that the damage degree of the bond between particles for 8% moisture content is lower than that for 5%.

The displacement and velocity time history for 12% moisture content almost coincides before 2.25 s, and the displacement increases steadily with the increase of vibration time, which shows that the bond failure between soil particles in the slope with 12% water content is lower. The transmission effect between particles is strong, and the relative sliding is not easy to occur between particles. After 2.25 s, the displacement and velocity at monitoring points 1 and 6 suddenly increase and slip out from the original position, while the displacement and velocity at monitoring points 10 and 13 still maintained a relatively stable development.

By comparing the displacement and velocity time-history curves for the three kinds of moisture content, it can be found that the displacement and velocity for 5% moisture content are significantly smaller than that of 8% and 12%. The displacement of the monitoring point is related to the velocity of nearby soil particles. During the failure of the slope with 5% moisture content, the amplitude of the input sine wave is small, and the whole vibration of the slope is lower. The horizontal seismic force does less work to the soil particles. For this reason, the bond between the soil particles in the shallow topsoil for the 5% moisture content is destroyed into a loose accumulation. In addition, it can be

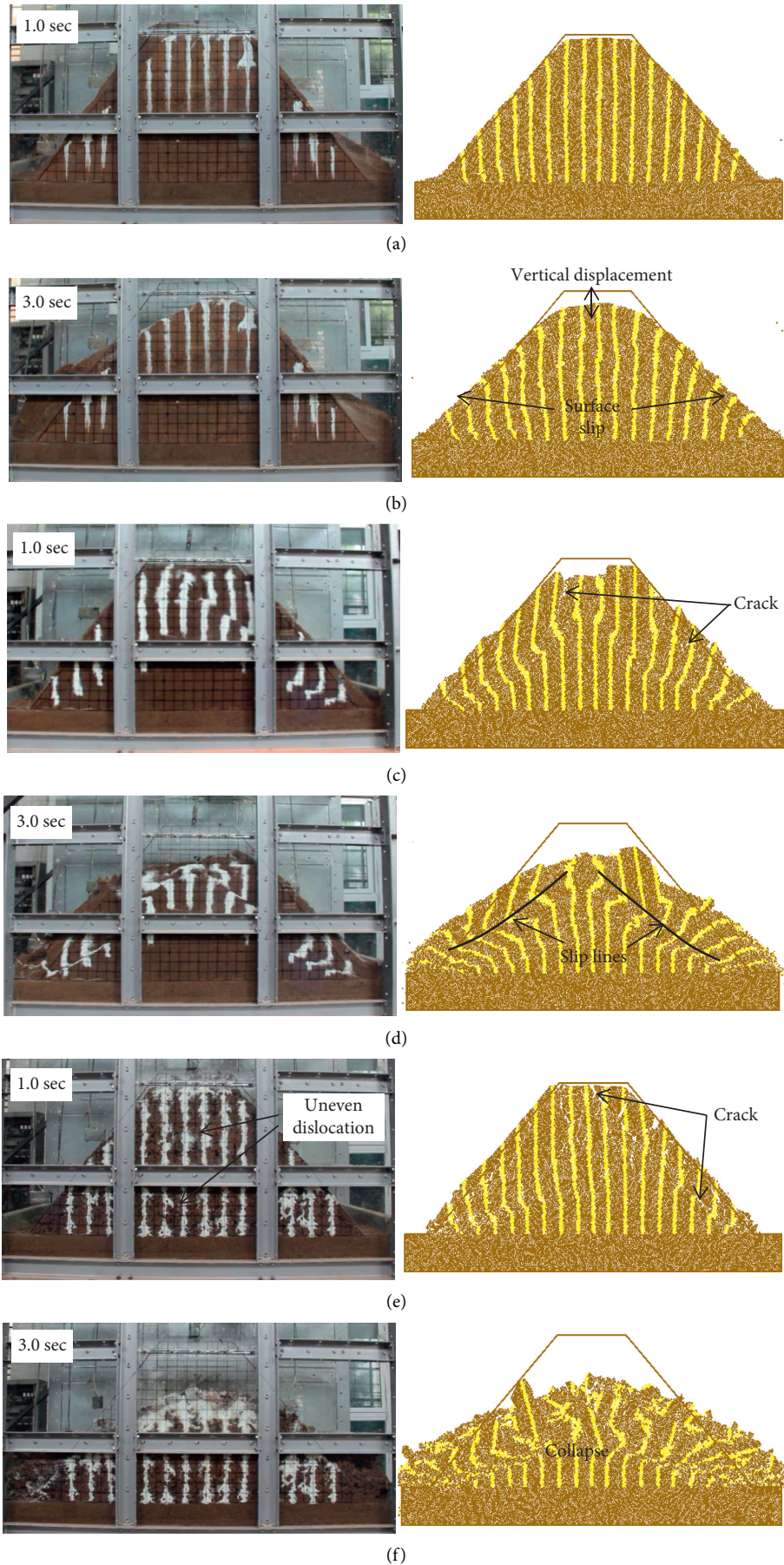


FIGURE 5: Comparison of results by model test and numerical simulation. (a) Failure when loading 1 s (5% moisture content). (b) Failure when loading 3 s (5% moisture content). (c) Failure when loading 1 s (8% moisture content). (d) Failure when loading 3 s (8% moisture content). (e) Failure when loading 1 s (12% moisture content). (f) Failure when loading 3 s (12% moisture content).



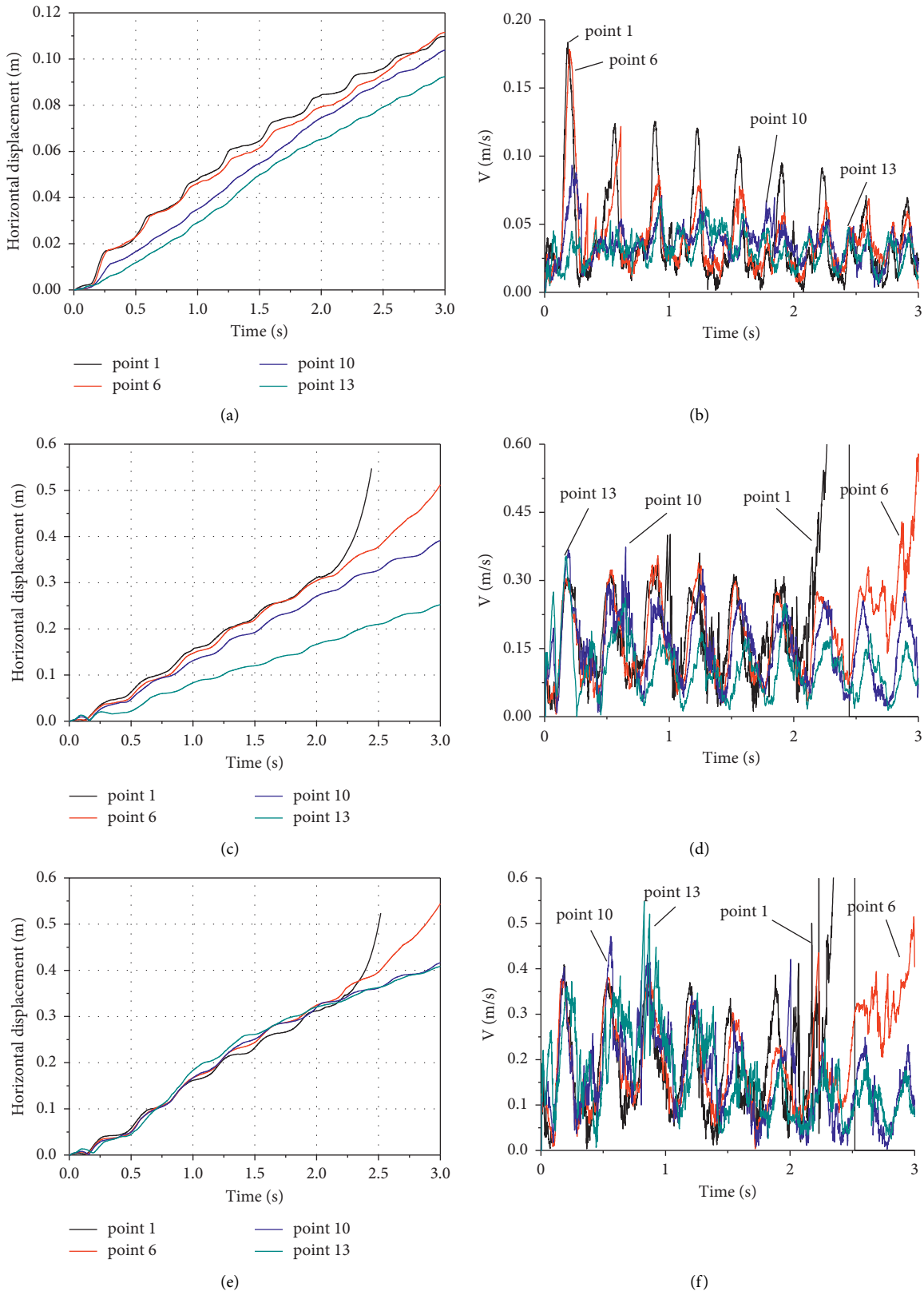


FIGURE 6: Displacement and velocity time history of monitoring points in the slope under different moisture contents. (a) Displacement curve at 5% moisture content. (b) Velocity curve of 5% moisture content. (c) Displacement curve of 8% moisture content. (d) Velocity curve of 8% moisture content. (e) Displacement curve of 12% moisture content. (f) Velocity curve of 12% moisture content.

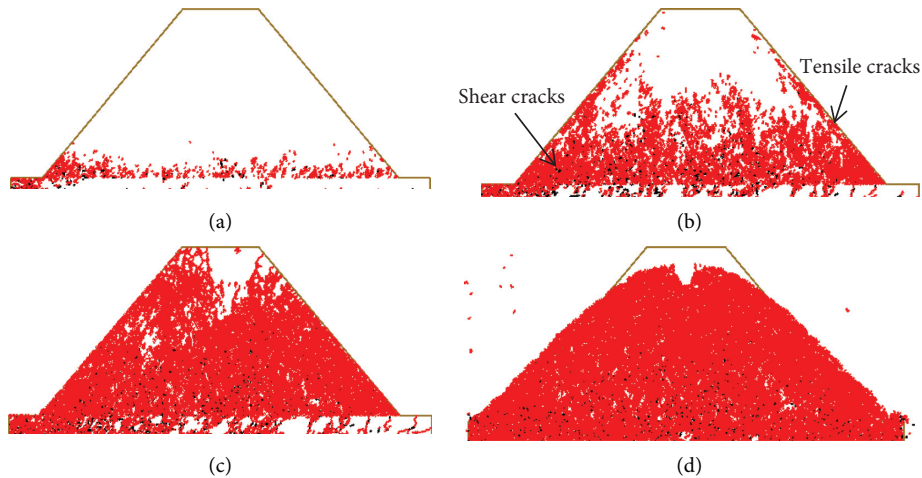


FIGURE 7: Crack development process in the slope with 5% moisture content. (a) At loading 0.1 s. (b) At loading 0.3 s. (c) At loading 0.5 s. (d) At loading 3 s.

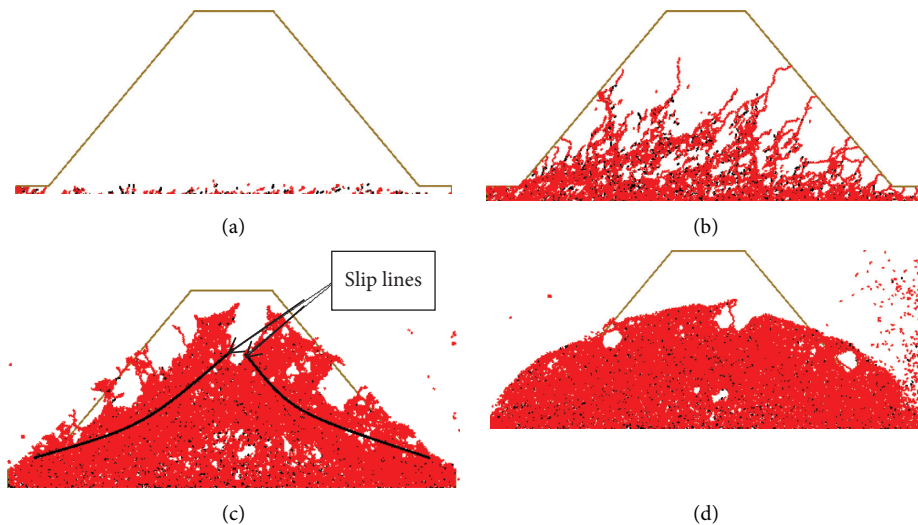


FIGURE 8: Crack development process with 8% moisture content. (a) At loading 0.1 s. (b) At loading 0.5 s. (c) At loading 1 s. (d) At loading 3 s.

seen from Figure 5 that the slope with 5% moisture content has a shallow surface slip, and the interior of the slope is relatively stable.

Based on the above analysis, with the increase of moisture content, the displacement time-history curves of the slope become closer, and the velocity time-history curve before failure is relatively much closer, indicating that the relative motion between particles is reduced.

**4.3. Development Process of Microfissures.** PFC<sup>2D</sup> can simulate the development process of interparticle fracture. The normal bond failure between particles leads to tensile failure, and tangential bond failure leads to shear failure. In this section, black represents the crack caused by shear failure and red indicates the crack caused by tension.

It can be seen from Figure 7 that the cracks in the slope with 5% moisture content develop rapidly, and shear

cracks are mainly in the lower part of the slope. From the previous analysis, the slope began to slide at 0.1 s. There are only tensile cracks in the shallow part of the slope at 0.3 s, and the shear cracks are concentrated at the toe of the slope. The displacement and velocity time-history curves at monitoring points 1 and 6 remain coincident at 0.15 seconds, which shows that the soil at the lower part does not split yet, while the separation of the curves at the upper monitoring points 10 and 13 indicates that the soil around the monitoring point 10 and 13 has become loose due to tension. At 0.5 s, more tensile cracks get developed in the lower shear region, which plays a leading role in the slope failure. The displacement and velocity time-history curves at monitoring points 1 and 6 are separated, which shows that the soil slides under the action of seismic force and self-weight stress. Overall, the slope with 5% moisture content is relatively loose. At the initial stage, the tensile damage of the slope surface is serious. The development of

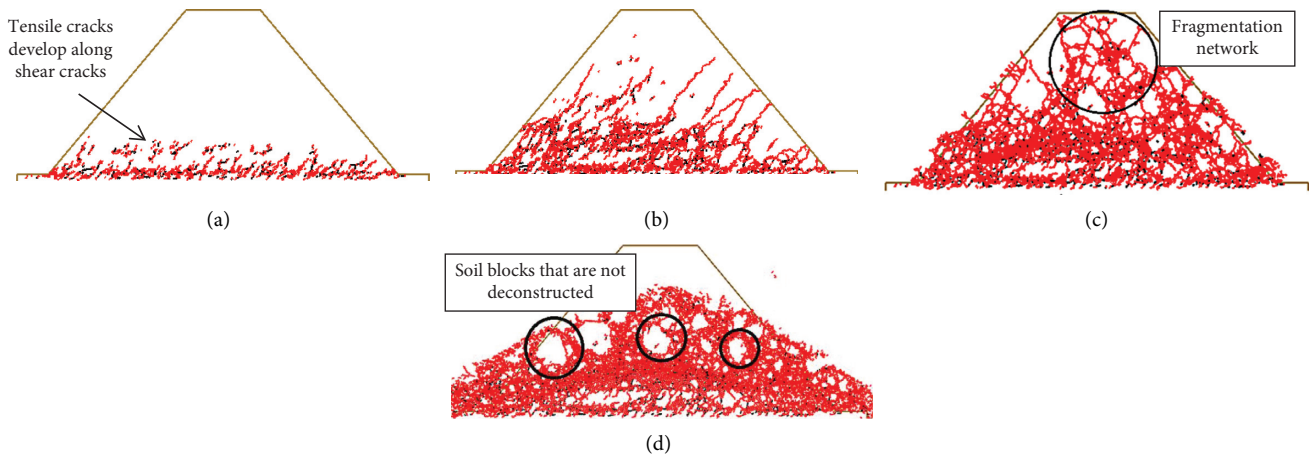


FIGURE 9: Crack development process with 12% moisture content. (a) At loading 0.1 s. (b) At loading 0.5 s. (c) At loading 1 s. (d) At loading 3 s.

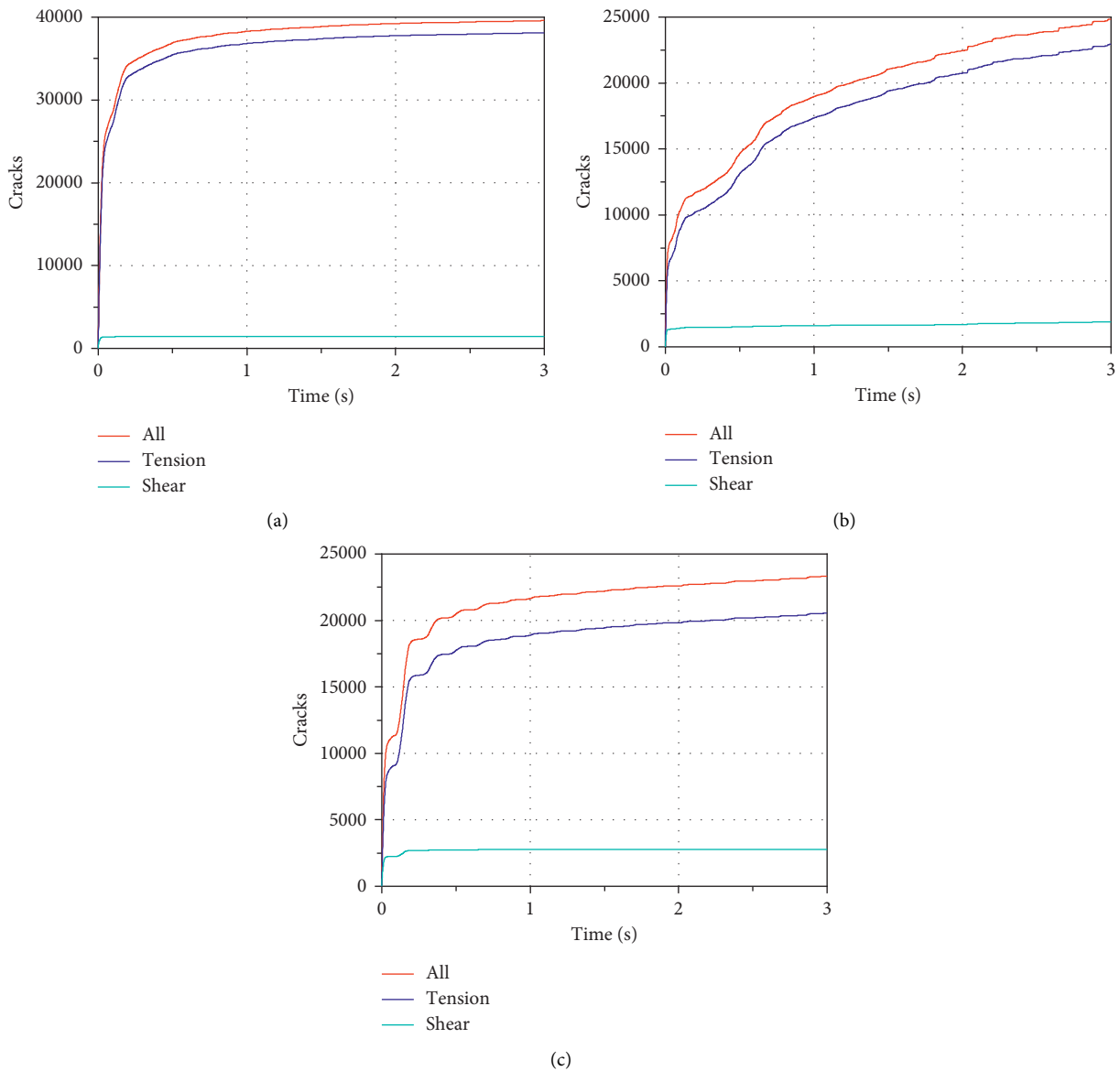


FIGURE 10: Fracture development curve. (a) For 5% moisture content. (b) For 8% moisture content. (c) For 12% moisture content.

tensile cracks in the upper part of the slope causes the damage of the bond between particles, and the soil at the toe of the slope slides as a whole due to local shearing. In a very short time, the development of the tensile cracks at the slope toe and the destruction of the bond between particles lead to slope failure under the action of earthquakes and self-weight stress. The failure mode of the slope with 5% moisture content is shattering-shallow sliding.

From Figure 8, it can be seen that the failure of the slope is related to the connection of the local shear failure surface. When loading for 0.5 s, it can be seen that the small cracks firstly propagate upward, and the tensile cracks develop along the shear cracks. As can be seen from Figure 6(c), at 0.5 s, the displacement time-history curve of monitoring point 13 has been separated from the other three curves, indicating that the overall local shear slip has occurred in the lower part of the slope. At this time, the integrity of the soil at the top of the slope is great, indicating that a small amount of settlement has taken place on the top of the slope. When loading for 1 s, the local shear plane runs through the slope to form the slip surface, and the slip lines intersected at the lower part of the crest of the slope. With the increase of vibration time, the soil on the crest collapses downward with the sliding of the soil on the two sides of the slope.

From Figure 9, it can be seen that the shear cracks develop radially from the bottom of the slope to the top, and the tensile cracks develop along the shear crack. After loading for 1 s, the soil inside the slope breaks up into soil blocks of different sizes, forming a fracture network. It can be seen from Figure 6(e) that the displacement time-history curves of the monitoring points of the slope nearly coincide before failure. With the increase of loading time, uneven dislocation occurs in the interior of the slope, leading to the collapse of the slope.

**4.4. Development of Cracks' Number in Slope.** Fractures include tensile cracks and shear cracks. As can be seen from Figure 10, with the increase of moisture content, the number of fractures and tensile cracks at slope failure gradually decreases, while the shear cracks increase. This shows that tensile cracks mainly developed in the interior of the slope under the action of earthquakes, but are not necessarily the main factor causing damage. The slope with 5% moisture content is relatively loose, and the tensile failure occurs easily under the earthquake. While for 8% and 12% moisture content, the double-sided slopes are damaged mainly by shearing stress. From Figures 10(a) and 10(c), it can be seen that the fractures' number in the slope with 5% and 12% moisture content is relatively stable when loading time is 1 s and increases slowly with the increase of vibration time. The shear slip occurs in the slope with 8% moisture content, and the cracks increase gradually during the sliding of the slope. In short, with the increase of moisture content, the ability of the slope to resist tensile crack increases, so attention should be paid to shear failure in slope reinforcement.

## 5. Conclusions

In this paper, the failure mode and mechanism of multiface slopes with different moisture content under earthquake action were studied by using a two-dimensional particle flow program (PFC<sup>2D</sup>). The following conclusions can be drawn:

- (1) The failure modes of slopes with different moisture content under earthquake action are different. The failure mode of the slope with 5% moisture content is shattering-shallow sliding, and the failure mode of slopes with 8% moisture content is tension-shear-slip, and shattering-collapse slip failure occurs at 12% moisture content.
- (2) The failure of a multiface slope is a gradual failure process under the action of earthquakes. The shallow layer of the slope with 5% moisture content is seriously damaged by tension under the action of earthquakes; the upper part of the slope is unstable due to the damage of the bond between particles. For the slope with 8% moisture content under the action of earthquakes, there are shear cracks developed inside the slope. With the increase of vibration time, the local shear failure plane runs through into a slip plane, and the slope slides along the slip surface. Under the action of earthquakes, a fracture network develops in the slope with 12% moisture content due to shear failure inside the slope.
- (3) With the increase of water content, the fractures and tensile cracks in the slope decrease gradually, while the shear cracks increase gradually. In the case of low moisture content, the tensile cracks play a leading role in the failure of the slope. With the increase of moisture content, the influence of shear failure on slope failure is increasing, and more efforts should be placed on reducing the shear cracks.

## Data Availability

The data used to support the findings of this study are available from the corresponding author upon request.

## Conflicts of Interest

The authors declare that they have no conflicts of interest.

## Acknowledgments

This study was supported by Sichuan Science and Technology Program (2021YFS0323 and 2020YFG0123).




## References

- [1] R. Huang and W. Li, "Development and distribution of geohazards triggered by the 5.12 Wenchuan earthquake in China," *Science in China-Series E: Technological Sciences*, vol. 52, no. 4, pp. 810–819, 2009.
- [2] R. Q. Huang and W. L. Li, "Analysis of the geo-hazards triggered by the 12 May 2008 Wenchuan earthquake, China,"

- Bulletin of Engineering Geology and the Environment*, vol. 68, no. 3, pp. 363–371, 2009.
- [3] J. Wasowski, D. K. Keefer, and C.-T. Lee, “Toward the next generation of research on earthquake-induced landslides: current issues and future challenges,” *Engineering Geology*, vol. 122, no. 1-2, pp. 1–8, 2011.
- [4] B. Yang, F.-p. Gao, and D.-s. Jeng, “Failure mode and dynamic response of a double-sided slope with high water content of soil,” *Journal of Mountain Science*, vol. 15, no. 4, pp. 859–870, 2018.
- [5] J. Huang, M. Zhao, C. Xu, X. Du, L. Jin, and X. Zhao, “Seismic stability of jointed rock slopes under obliquely incident earthquake waves,” *Earthquake Engineering and Engineering Vibration*, vol. 17, no. 3, pp. 527–539, 2018.
- [6] M. Ehteshami-Moinabadi and S. Nasiri, “Geometrical and structural set-ting of landslide dams of the central Alborz: a link between earth- quakes and landslide damming,” *Bulletin of Engineering Geology and the Environment*, vol. 78, 2017.
- [7] G. Fan, J. Zhang, J. Wu, and K. Yan, “Dynamic response and dynamic failure mode of a weak intercalated rock slope using a shaking table,” *Rock Mechanics and Rock Engineering*, vol. 49, no. 8, pp. 3243–3256, 2016.
- [8] X. Liu, C. He, S. Liu, Y. Liu, Y. Lu, and Z. Liu, “Dynamic response and failure mode of slopes with horizontal soft and hard interbeddings under frequent microseisms,” *Arabian Journal for Science and Engineering*, vol. 43, no. 10, pp. 5397–5411, 2018.
- [9] H.-B. Li, X.-W. Li, Y. Ning, S.-F. Jiang, and J.-W. Zhou, “Dynamical process of the Hongshiyuan landslide induced by the 2014 Ludian earthquake and stability evaluation of the back scarp of the remnant slope,” *Bulletin of Engineering Geology and the Environment*, vol. 78, no. 3, pp. 2081–2092, 2019.
- [10] Z. Deng, X. Liu, Y. Liu et al., “Cumulative damage evolution and failure modes of the bedding rock slope under frequent microseisms,” *Arabian Journal of Geosciences*, vol. 13, no. 10, 2020.
- [11] J. Hou, M. Zhang, Q. Chen, D. Wang, J. Akbar, and S. Zhang, “Failure-Mode analysis of loose deposit slope in ya’an-kangding expressway under seismic loading using particle flow code,” *Granular Matter*, vol. 21, no. 1, pp. 1–12, 2019.
- [12] K. Abe, S. Nakamura, H. Nakamura, and K. Shiomi, “Numerical study on dynamic behavior of slope models including weak layers from deformation to failure using material point method,” *Soils and Foundations*, vol. 57, pp. 155–175, 2017.
- [13] K. J. Chang and A. Taboada, “Discrete element simulation of the Jiufengershan rock-and-soil avalanche triggered by the 1999 Chi-Chi earthquake, Taiwan,” *Journal of Geophysical Research: Earth Surface*, vol. 114, pp. 2003–2012, 2009.
- [14] C. L. Tang, J. C. Hu, M. L. Lin et al., “The Tsaoling landslide triggered by the Chi-Chi earthquake, Taiwan: insights from a discrete element simulation,” *Engineering Geology*, vol. 106, no. 1, pp. 1–19, 2009.
- [15] R. Huang, Q. Xu, and J. Huo, “Mechanism and geo-mechanics models of landslides triggered by 5.12 Wenchuan earthquake,” *Journal of Mountain Science*, vol. 8, no. 2, pp. 200–210, 2011.
- [16] Y. Changwei, X. Liu, J. Zhang, Z. Chen, C. Shi, and H. Gao, “Analysis on mechanism of landslides under ground shaking: a typical landslide in the Wenchuan earthquake,” *Environmental Earth Sciences*, vol. 72, no. 9, pp. 3457–3466, 2014.
- [17] R. Xiao, Q. Xu, W. Feng, J. Chen, and Y. Zuo, “Study on deformation and failure mechanism of double slope under strong earthquake conditions by shaking table physical simulation test,” *Journal of Engineering Geology*, vol. 18, no. 6, pp. 837–843, 2010.
- [18] P. A. Cundall and O. D. L. Strack, “A discrete numerical for granular assemblies,” *Geotechnique*, vol. 29, no. 1, pp. 47–65, 1979.
- [19] J. Zhou, P. Cui, and H. Fang, “Dynamic process analysis for the formation of Yangjiagou landslide-dammed lake triggered by the Wenchuan earthquake, China,” *Landslides*, vol. 10, no. 3, pp. 331–342, 2013.
- [20] J. He, X. Li, S. Li, Y. Yin, and H. Qian, “Study of seismic response of colluvium accumulation slope by particle flow code,” *Granular Matter*, vol. 12, no. 5, 2010.
- [21] L. Yao and Q. Chen, “A new topic on seismic technology of line engineering caused by “5.12” Wenchuan earthquake,” *Journal of Sichuan University (Engineering Science Edition)*, vol. 41, no. 3, pp. 43–50, 2009.
- [22] Y. Chen, M. Irfan, T. Uchimura, Q. Meng, and J. Dou, “Relationship between water content, shear deformation, and elastic wave velocity through unsaturated soil slope,” *Bulletin of Engineering Geology and the Environment*, vol. 79, no. 8, pp. 4107–4121, 2020.
- [23] S. Zhao, Y. Zhu, P. He, and D. Wang, “Measurement of dynamic parameters of frozen soil,” *Journal of Rock Mechanics and Engineering*, vol. 22, no. S2, pp. 2677–2681, 2003, in Chinese.

## Research Article

# Analysis of Tunnel Lining Failure Mechanism under the Action of Active Fault

Sujian Ma <sup>1</sup>, Liang Zhang <sup>1</sup>, Dong Wang,<sup>2</sup> XinRong Tan,<sup>2</sup> Sifeng Li <sup>3</sup> and Yang Liu<sup>1</sup>

<sup>1</sup>Department of Civil Engineering, Southwest Jiaotong University, Chengdu 610031, China

<sup>2</sup>China Railway Eryuan Engineering Group Co. Ltd, Chengdu 610031, China

<sup>3</sup>Zhongke (Hunan) Advanced Rail Transit Research Institute Co. Ltd, Zhuzhou 412000, China

Correspondence should be addressed to Sujian Ma; [masujian@my.swjtu.edu.cn](mailto:masujian@my.swjtu.edu.cn) and Liang Zhang; [zhangliangdpme@my.swjtu.edu.cn](mailto:zhangliangdpme@my.swjtu.edu.cn)

Received 4 March 2021; Accepted 1 July 2021; Published 20 July 2021

Academic Editor: Gang Fan

Copyright © 2021 Sujian Ma et al. This is an open access article distributed under the Creative Commons Attribution License, which permits unrestricted use, distribution, and reproduction in any medium, provided the original work is properly cited.

The underground structure that crosses the active fault will cause more serious damage under the dislocation of the active fault. Relying on an actual tunnel in the southwest mountainous area to establish a three-dimensional finite element model, the failure mechanism of the tunnel under strike-slip and thrust fault dislocation is revealed from the lining deformation, stress distribution, and plastic zone distribution, and the results show that the damage range of the lining distributes in the area of the fracture and the damage effect is greatly affected by the movement amount of the active fault. The lining damage under the active fault dislocation is mainly tensile damage, while the lining under the thrust fault dislocation shows compression damage on both sides of the fracture when there is a fracture with a large dip angle. The development range of plastic zone is positively correlated with the dip angle of the fracture and the amount of movement, and the development range is negatively correlated with the dip angle of the fracture and positively correlated with the amount of dislocation. The plastic zone range can be predicted, and the key monitoring range can be set according to the movement form of the active fault, the dip angle of the fracture zone, and the amount of fault movement.

## 1. Introduction

The underground structure has better seismic performance than the above-ground structure due to the restriction of the surrounding rock, but for the tunnel structure that crosses the fault, the degree of earthquake damage will be greatly increased [1–6], and the main reason is that the active fault movement causes the tunnel lining to collapse, which causes substantial economic losses. Relevant regulations [7] stipulate that, to prevent structural damage caused by fault movement, the site selection of buildings should avoid active faults. However, the geological conditions in southwest area of China are relatively complex, and active faults are widely distributed. With the implementation of the Western Development strategy and the development of the “One Belt, One Road” policy, the design and planning of engineering routes are more inclined to functional requirements, which

has increasingly led to the fact that tunnels inevitably cross a large number of faults [8–10].

For tunnels crossing the active fault, domestic and overseas experts have done a lot of research in the fields of model testing, numerical simulation, and statistical analysis. In the field of statistical analysis and research, Toeher [11] used statistical regression methods to establish a statistical relationship between the magnitude of the earthquake and the length of the surface rupture caused by the active fault based on the seismic damage data. Matsuda Tokihiko [12] calculated multiple sets of Japanese earthquake record data and established a statistical relationship between magnitude and surface rupture based on the length of the surface rupture zone caused by an earthquake. In the field of model test analysis, Geng et al. [13] used shaking table tests to study the dynamic response of tunnels traversing fault zones under earthquake action and proposed a reasonable fortification

length of fault-moving tunnels at a specific dip. Liu et al. [14] studied the force characteristics of the lining under the earthquake action and the acceleration amplification effect by controlling the test materials, the similarity ratio, and other parameters through the shaking table comparison test through the fault and, based on this, studied the development of tunnel cracks. Xin [15] carried out seismic shaking table tests on the seismic damage mechanism of the tunnel structure, studied the antivibration effect of the tunnel crossing fault, and established the time history evolution law of the tunnel and surrounding rock model damage. In the field of numerical simulation, Zhou et al. [6] established a three-dimensional finite element model using FLAC3D relying on the tunnel actually traversing the strike-slip fault, studied the mechanical effects of the tunnel lining under the movement of the strike-slip fault, explored the dynamic response law of the tunnel under the action of seismic wave, and obtained the antidistortion and seismic fortification length. Ramaneharla and Meguro [16] used the Applied Element Method and finite element calculation method to simulate and analyze the response of the overlying soil under the action of a tilt-slip fault and found that the greater the amount of bedrock movement, the greater the surface movement produced, and the more developed the soil fractures in high-stress areas. Huang et al. [17–19] make a two-dimensional time-history analysis of the selected soil-tunnel shape through numerical parameter studies and determined the optimal intensity measure in the probabilistic seismic demand model of circular tunnel in soft soil.

The above studies are of important guiding significance for the construction of tunnels crossing the active fault zone, but there are still some deficiencies. Limited by the research conditions at this stage, the data required for statistical analysis is substantial and complex. The size of the model test is generally small, and there are few studies considering the longitudinal direction of the tunnel. Numerical simulation of structural constitutive relationship mostly adopts elastoplastic constitutive, which lacks the analysis of the damage structure of tunnel lining.

Relying on an actual tunnel in China, and using ABAQUS to establish a three-dimensional finite element model, this paper studies the failure of the tunnel lining under two fault movements, strike-slip and thrust under different fault angles and different dislocation amount of active fault, and reveals the failure mechanism of the lining from the three aspects of displacement and deformation, stress distribution, and the development of the plastic zone along the longitudinal lining of the tunnel, to provide a reference for the actual tunnel engineering through the active fault.

## 2. Finite Element Numerical Model Establishment and Parameter Selection

Relying on a domestic actual tunnel project, this paper established three-dimensional finite element models of different dip angles and different fault dislocations under strike-slip and thrust fault based on the finite element analysis software ABAQUS. According to the survey data, in the early stage of the project, the width of the model fracture

is 40 m, and the model is established by taking 180 m before and after the fracture. Since the shape of the tunnel in the actual project is not a perfect circle, the cross-sectional shape of the tunnel is drawn using a five-center circle, with the maximum inner diameter of 10 m, the lining wall thickness of 0.5 m, and the buried depth of 28 m. According to the current experience in tunnel construction, it is believed that the transverse section size should be 5–10 times the tunnel section size. After 5 times, the artificial boundary will have little effect on the calculation results [20]. Therefore, the cross-sectional size of the model is set to 7 times the maximum size of the tunnel. The size of the model is 400 m (length)  $\times$  70 m (width)  $\times$  70 m (height), and the schematic diagram of the calculation model is shown in Figure 1.

Fault dislocation is realized by constraining the boundary conditions of the foot wall area and applying displacement loads to the hanging wall. Considering the most disadvantageous effects, when the fault movement rate is low, the overlying soil will undergo sufficient deformation, which will lead to the maximum damage caused by the fault to the tunnel [21–23]. Therefore, the rate at which the fault starts to move is set to 0.1 m/s. After a certain level, the rate of fault movement increases to give the soil sufficient time to deform.

Although the actual soil is a heterogeneous semi-infinite space, in order to truly simulate the failure process of tunnel lining under active fault dislocation, the model soil layer is assumed to be an ideal elastoplastic material, and the Mohr–Coulomb constitutive is adopted. The soil layer parameters are set according to the actual engineering survey results, as shown in Table 1. The material of the tunnel lining is C55 concrete, and the concrete damage plastic constitutive is adopted in the model. According to the relevant specifications [24], the elastic-plastic stress-strain relationship of lining concrete is defined, and the specific parameters of lining are shown in Table 2. Considering the difference in material properties between the tunnel lining and the surrounding rock and soil, the contact between the two is set as friction, and the friction coefficient is 0.4 [25].

The simulation analysis is divided into three steps. Firstly, the unexcavated rock and soil are balanced by the initial ground stress, so that there is no stress disturbance and deformation under the action of its own weight; that is, the long-term consolidation and deposition of the soil are simulated. Secondly, to simulate the tunnel excavation and lining construction, the surrounding rock loads all act on the lining, and the lining is not allowed to deform. Finally, the displacement load is applied, the restraint of the boundary around the hanging wall is released, the load along the angle of the fracture zone is applied, and the restraint of the foot wall remains unchanged. The displacement load is shown in Figure 2, and the model meshing diagram is shown in Figure 3. In the process of initial ground stress balance and tunnel and lining construction, in order to achieve the simulation consistent with the actual situation, normal constraints are applied at the bottom and lateral boundary of the model, and the three directions of the lining are constrained, as shown in Figure 4(a). When the fault begins to move, the normal constraint on the hanging wall of the fault is released, and a displacement load is applied to realize the movement of the fault, as shown in Figure 4(b).

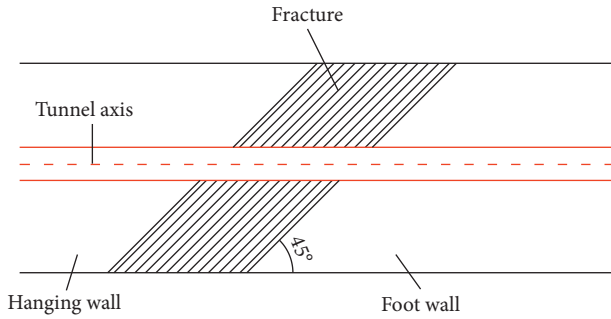


FIGURE 1: Schematic diagram of the model.

### 3. Analysis of Tunnel Lining Safety under Different Dip Angles of Active Faults

Strike-slip faults are large-scale translational faults. The hanging wall moves in translation along the slip surface of the fault zone. The stress source of relative motion is mainly the shear force on both sides. The interruption surface of the movement process is straight and smooth, and the shearing effect is obvious [26]. The damage to the arch waist of the tunnel lining is more serious, so this article focuses on selecting the measurement points at the arch waist for analysis. Thrust fault is a low-angle entry fault with a large displacement distance, showing strong compression and fracture [27], so the dip angle of the fault zone is increased by  $30^\circ$  in the thrust fault model. Since the overall trend of the deformation of the thrust fault is the vertical displacement along the slip surface of the fracture, the main damage area of the tunnel lining in this case is the vault, so this paper focuses on selecting the measurement points on the vault for analysis.

In this paper, the dip angles of the strike-slip fault are  $45^\circ$  ( $\pi/4$ ),  $60^\circ$  ( $\pi/3$ ),  $75^\circ$  ( $5\pi/12$ ), and  $90^\circ$  ( $\pi/2$ ), and the dip angles of the thrust fault are  $30^\circ$  ( $\pi/6$ ),  $45^\circ$  ( $\pi/4$ ),  $60^\circ$  ( $\pi/3$ ),  $75^\circ$  ( $5\pi/12$ ), and  $90^\circ$  ( $\pi/2$ ).

**3.1. Response Analysis of Lining Displacement and Deformation of Tunnels with Different Dip Angles.** The displacement diagram of the arch waist of the tunnel lining along the longitudinal direction under the 3.5 m of the hanging wall of the strike-slip fault is shown in Figure 5(a). The displacement and deformation diagram of the arch waist of the tunnel lining along the longitudinal direction under the 0.8 m movement of the hanging wall of the thrust fault is shown in Figure 5(b).

As can be seen from the lining displacement curve in Figure 5, the fault dislocation drives the lining in the corresponding area to move in the same direction, and the lining displacement curve in the longitudinal direction of the tunnel has a dislocation platform, and the range is roughly the same as the bottom area of the hanging wall. The displacements of the lining platform of the tunnel in the movement direction are 3.5 m and 0.8 m, which are consistent with the amount of fault dislocation. The lining displacement curves under different dip angles of the active faults are similar in shape and distributed in an “S” shape.

The deformation of the lining appears steeply in the fracture along the longitudinal direction of the tunnel. With the change of the dip angle, the range of the steep drop of the curve and the slope of the curve will not change significantly, and the curve moves to the foot wall with the increase of the dip angle of the fracture. The starting point of the steep-descent section of the strike-slip fault at a dip angle of  $45^\circ$  is about 140 m, while the starting point of the steep-descent section of the thrust fault at a dip angle of  $30^\circ$  is about 100 m. With the continuous increase of the dip angle of the fracture, the starting point of the  $90^\circ$  dip of the two active faults is about 180 m. It can be inferred that the failure area of the tunnel passing through the active fault area with different dip angles is roughly concentrated in the fracture, and the deformation has little correlation with the dip angle. In addition, strike-slip faults and thrust faults have similar shapes along the displacement application direction, while the displacement curve of the thrust fault is uplifted in the hanging wall at a dip angle of  $30^\circ$ , which is speculated that it may be caused by the uneven deformation of the upper soil due to the concentrated load at the lower part.

**3.2. Stress Response Analysis of Tunnel Lining with Different Dip Angles.** The lining material is C55 concrete, which can withstand high pressure. Therefore, the maximum principal stress is used to analyze the stress response of the lining under fault movement. The stress distribution of the lining under active fault dislocation with different dip angles is shown in Figure 6.

It can be seen from Figure 6(a) that the maximum principal stress at the hanging wall and foot wall is basically 0 when the strike-slip fault displacement is 3.5 m, and the maximum value of the maximum principal stress along the longitudinal length of the tunnel appears in the fracture. When the dip angle is  $45^\circ$  and  $60^\circ$ , the maximum principal stress of the lining along the longitudinal direction is the tensile stress, and the maximum is concentrated near 200 m; that is, the maximum stress occurs in the middle of the intersection of the fracture and the lining. With the increase of the dip angle, the maximum value of the maximum principal stress is basically unchanged, and the lining in the central area needs to be monitored. When the dip angle is  $75^\circ$  and  $90^\circ$ , the lining appears compressive stress along the longitudinal direction, and the maximum compressive stress appears near 250 m. As the dip angle increases, the stress curve gradually moves to the foot wall, which is consistent with the distribution law of the lining displacement curve.

It can be seen from Figure 6(b) that when the thrust fault displacement is 0.8 m, the maximum principal stress of the lining in the hanging wall and foot wall areas fluctuates slightly and is basically 0. The maximum principal stress along the longitudinal direction of the tunnel appears in the fracture. The maximum principal stress along the longitudinal length of the tunnel is basically the tensile stress. When the dip angle is  $30^\circ$ , the maximum tensile stress is located near 100 m, while the maximum tensile stresses of other dip angles are basically located at the bottom of the intersection of the fault and the hanging wall. It is speculated that the



TABLE 1: Material parameters of surrounding rock.

Model	Density ( $\text{kg/m}^3$ )	Elastic modulus (MPa)	Poisson ratio	Internal friction angle ( $^\circ$ )	Cohesion (kPa)
Fault	2300	$1.6 \times 10^3$	0.4	28	$0.1 \times 10^3$
Surrounding rock	2400	$3.5 \times 10^3$	0.32	35	$0.4 \times 10^3$

TABLE 2: Material parameters of tunnel lining.

Model	Density ( $\text{kg/m}^3$ )	Elastic Modulus (MPa)	Poisson ratio	Compressive yield stress (MPa)	Tensile yield stress (MPa)
Lining	2400	$2.648 \times 10^4$	0.167	32.5	2.64

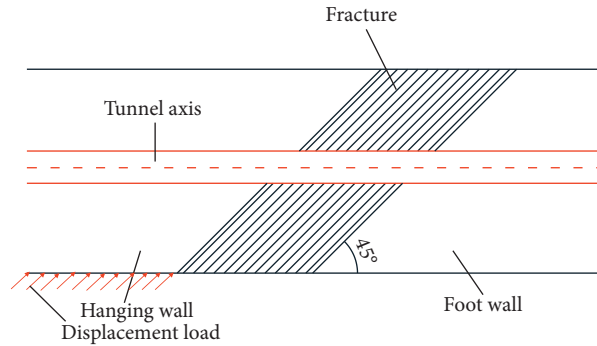


FIGURE 2: Schematic diagram of displacement load.

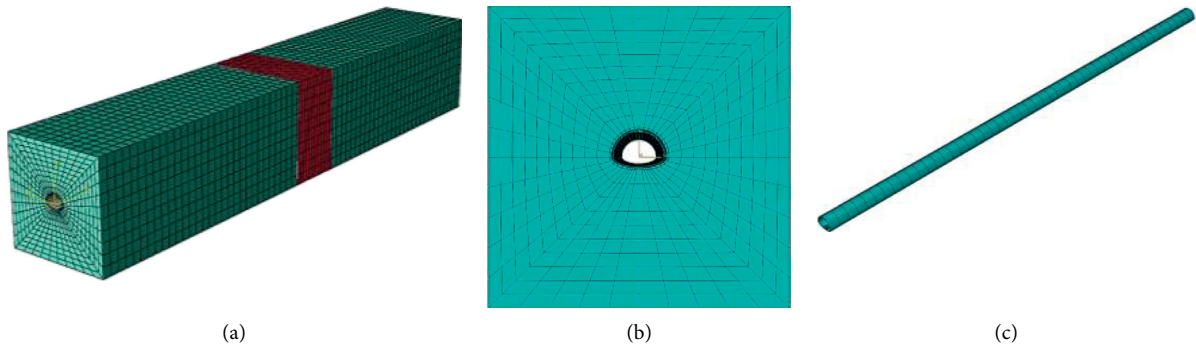


FIGURE 3: The meshing diagrams of each part of the model. The meshing diagram of the (a) model, (b) cross-sectional view of the model, and (c) division of tunnel lining.

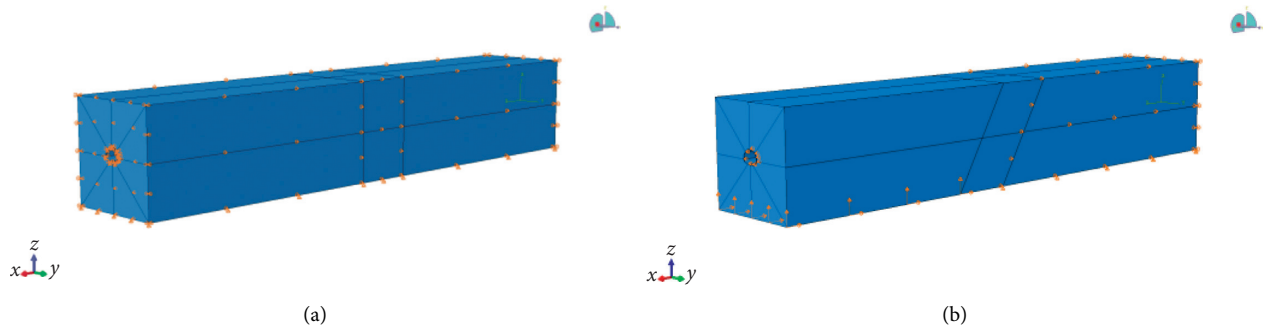


FIGURE 4: Boundary conditions of calculation model. (a) Initial boundary conditions of the model. (b) Boundary conditions of fault movement.

reason the maximum principal stress of the lining at  $30^\circ$  shifts back from the predicted value may be the larger area of the top of the hanging wall, the smaller area of the bottom

bearing displacement load, and uneven overall sliding. With the increase of the dip angle, the maximum tensile stress position gradually shifts from the hanging wall to the foot

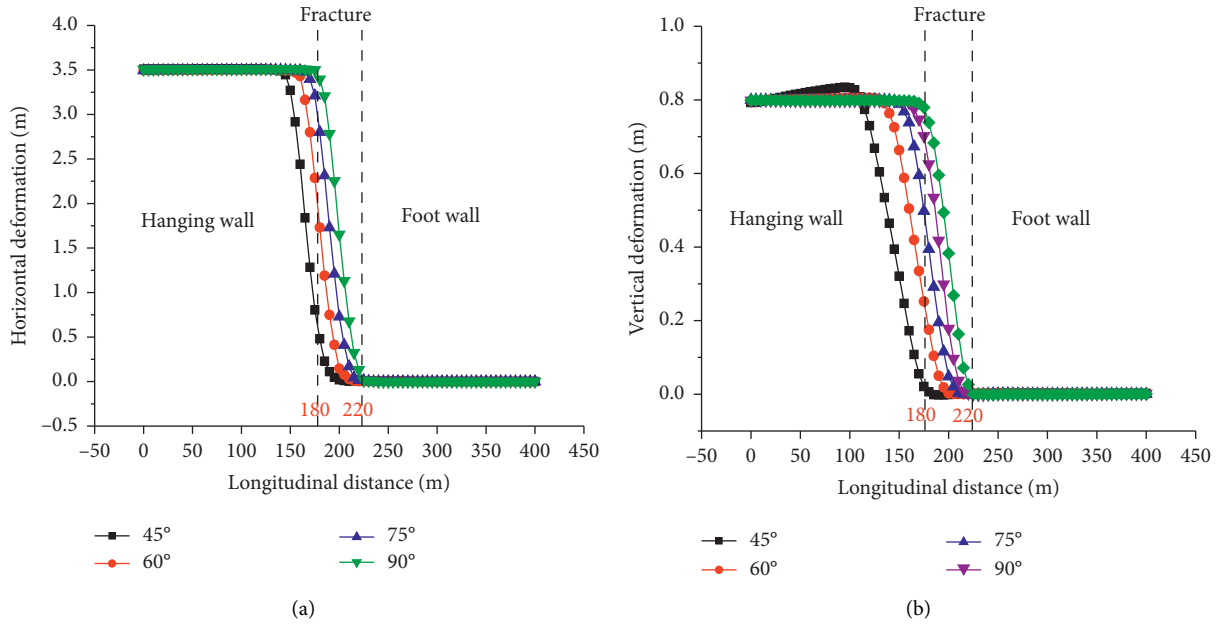


FIGURE 5: Displacement curves of tunnel lining with different dip angles. Lining displacement curves of different dip angles under (a) 3.5 m of strike-slip fault and (b) 0.8 m of thrust fault.

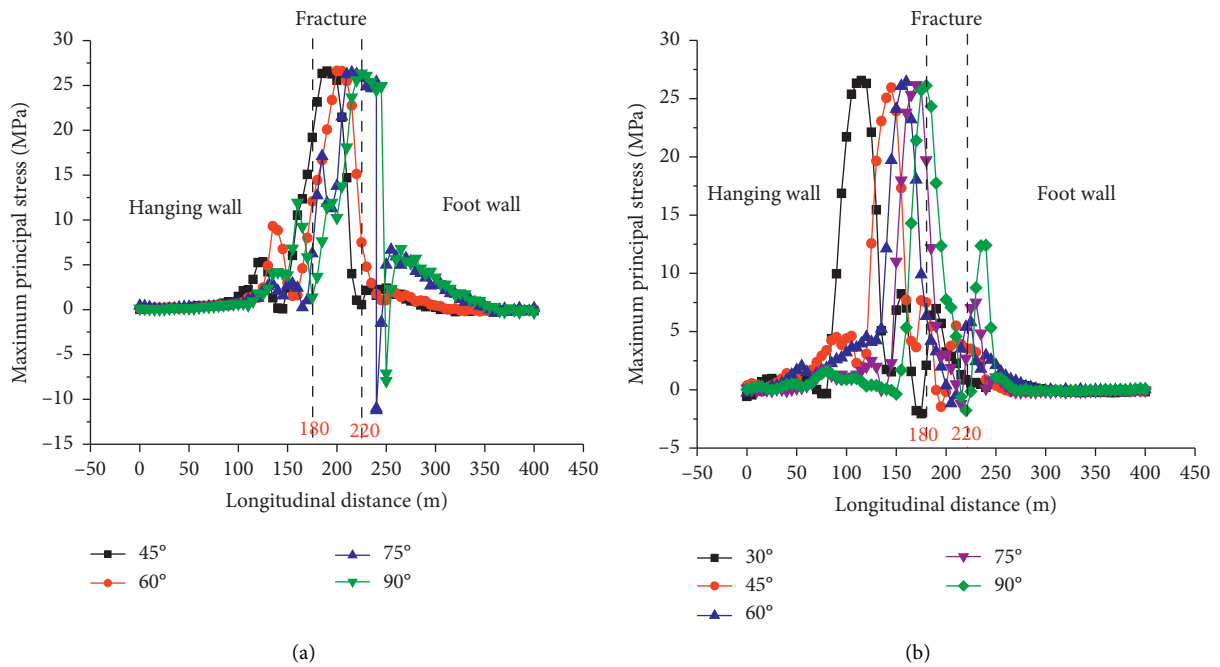


FIGURE 6: Maximum principal stress distribution curves of tunnel lining with different dip angles. The distribution of the maximum principal stress under (a) strike-slip fault and (b) under thrust fault.

wall. The damage position of the tunnel lining under fault movement is mainly determined by the bottom area of the hanging wall under the displacement load.

3.3. Analysis of the Distribution of Plastic Zone in Tunnel Lining with Different Dip Angles. The plastic zone distribution and range of the tunnel lining with strike-slip fault

movement of 3.5 m and thrust fault movement of 0.8 m under 4 kinds of dip angles are analyzed. The cloud diagrams of the lining plastic zone range under strike-slip and thrust fault movement are shown in Figures 7 and 8.

As can be seen from the above figures, when the strike-slip displacement is 3.5 m, the plastic zone of the tunnel lining is concentrated in the vault and the bottom of the arch, whose location is mainly concentrated in the fracture,



FIGURE 7: Plastic zone of lining under strike-slip fault with different dip angles. Cloud diagram of the plastic zone of the strike-slip fault with (a) 45° dip angle, (b) 60° dip angle, (c) 75° dip angle, and (d) 90° dip angle.

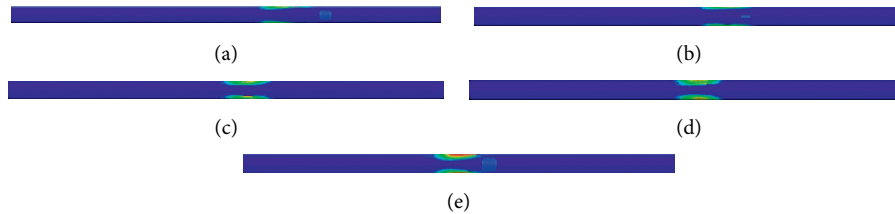


FIGURE 8: Plastic zone of lining under thrust fault with different dip angles. Cloud diagram of the plastic zone range of the thrust fault with (a) 30° dip angle, (b) 45° dip angle, (c) 60° dip angle, (d) 75° dip angle, and (e) 90° dip angle.

and the distribution of the plastic zone is scattered from the central point in a discord shape. When the thrust fault displacement is 0.8 m, the plastic zone of the tunnel lining is concentrated in both sides of the tunnel lining, and the starting position of the plastic zone is roughly located at the intersection of the fracture and the hanging wall. With the increase of the dip angle, the starting position of the plastic zone of the lining gradually moves to the foot wall, which is consistent with the stress distribution law of the tunnel lining. The development area of the plastic zone gradually increases and extends to the vault, and it can be inferred that when the fault moves, the plastic deformation first occurs on the arch side of the tunnel lining, which gradually extends from the arch side to the vault.

The extent of the plastic zone plays a vital role in the key monitoring of the lining after the fault occurs. According to the calculation results, the variation curves of the plastic zone of tunnel lining with the dip angle of fracture are drawn, as shown in Figure 9, the displacement of strike-slip fault is 0.8 m, and the displacement of thrust fault is 3.5 m.

Comprehensive analysis of Figure 9 shows that the plastic zone of the tunnel lining when the strike-slip fault is displaced 3.5 m is linear and positively correlated with the dip angle. The extent of the plastic zone of the lining increases with the increase of dip angle. The plastic zone range of the tunnel lining and the dip angle are logarithmic function and negatively correlated when the thrust fault is dislocated 0.8 m, and the plastic zone range gradually decreases with the increase of dip angle. Therefore, under the dislocation of active faults, the range of the tunnel lining plastic zone can be calculated according to the dip angle and the key monitoring range can be set.

#### 4. Analysis of Tunnel Lining Safety under Different Displacements of Active Faults

Fault movement is mainly divided into stick-slip movement and creeping movement. Stick-slip movement is a sudden rapid rupture movement, and creeping movement is a slow

movement that occurs over time. Studies have shown that the slow movement of the fault gives the soil a sufficient deformation process, and the damage degree is greater than that of the stick-slip movement [28]. The slow movement of the fault has higher damage degree and happened in tunnel engineering. Therefore, this paper analyzes the failure modes of tunnel lining when the creeping movement of the fault occurs.

*4.1. Deformation Response Analysis of Tunnel Lining under Different Movement Amounts of Active Faults.* This paper selects strike-slip and thrust faults 0.8 m, 1.0 m, 1.2 m, 1.4 m, 1.6 m, 2.0 m, 2.5 m, and 3.5 m for analysis, and Figure 9 shows the displacement curve of the tunnel lining vault under different movement amounts when the dip angle is 90°.

It can be seen from Figure 10(a) that when the dip angle is 90°, the tunnel lining displacement curve under different displacements of strike-slip fault is distributed in an “S” shape, and the tunnel lining in the hanging wall moves in the same form with the fault, whose displacement is consistent with the fault movement. The deformation curve of the lining along the longitudinal direction of the tunnel has a steep drop section, and all steep drop sections are located in the fracture. With the increase of the fault displacement, the slope of the displacement curve in the steep drop zone gradually increases. Therefore, the lining damage significant area under strike-slip fault is mainly located in the fracture, and the higher the fault displacement, the more serious the lining damage.

It can be seen from Figure 10(b) that the deformation curve of the tunnel lining under the thrust fault with 90° dip angle has the same shape as the displacement curve under the strike-slip fault in the respective load application directions, and both show “S” shape. The tunnel lining moves in the same form as the hanging wall along the displacement load application direction. Similar to the displacement curve of the strike-slip fault in the load direction, the lining displacement

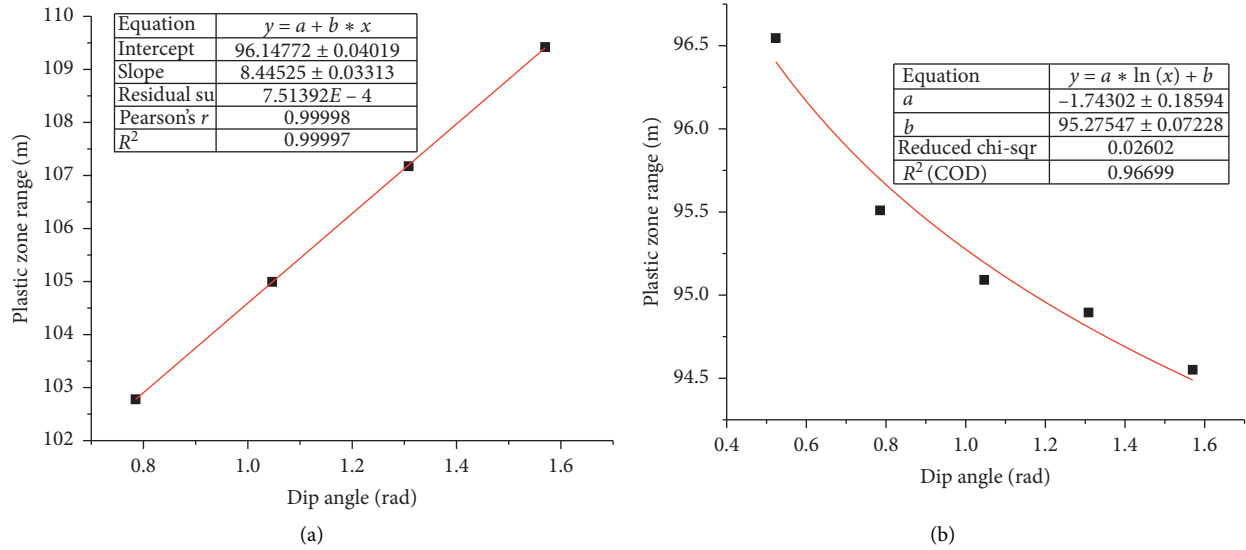


FIGURE 9: The curves of lining plastic zone range with different dip angles under active fault. The curve of plastic zone range under (a) strike-slip fault and (b) thrust fault with different dip angles.

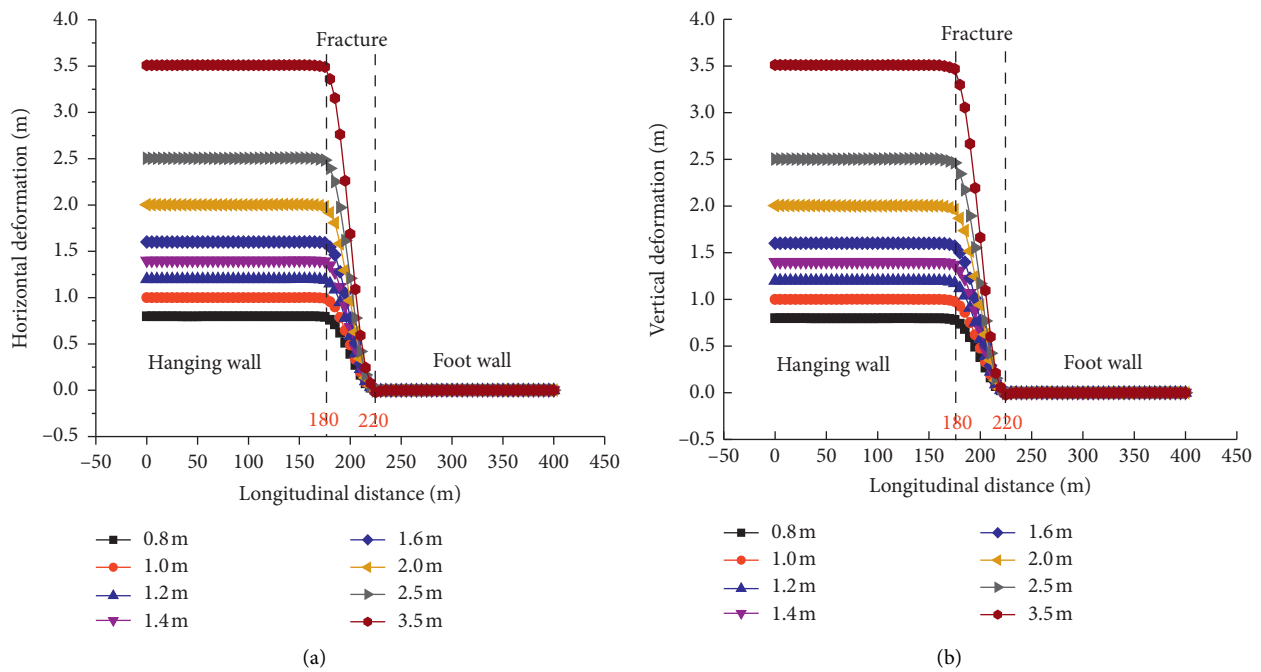


FIGURE 10: Lining deformation curves under different displacements of 90° fault. The lining deformation curves under different displacements of (a) strike-slip fault and (b) thrust fault.

curve has a steep drop in the fault, and all is located in the fracture. As the displacement increases, the slope of the steep-descent curve continues to increase, and the lining located in the fracture zone is more likely to be damaged.

**4.2. Stress Response Analysis of Tunnel Lining under Different Displacements of Fault.** To explore the influence of the stress distribution on the tunnel lining under different faults of strike-slip and thrust, the maximum principal stress distribution along the longitudinal length of the tunnel was

made according to the calculation results, as shown in Figure 11.

It can be seen from Figure 11(a) that the maximum principal stress distribution curves under different strike-slip faults are basically consistent in shape and maximum values. The maximum principal stress of the lining at the hanging wall and foot wall is basically 0, and the maximum principal stress of the lining along the longitudinal length of the tunnel increases first and then decreases. The changing section of the curve as a whole is located between 150 m and 250 m, and the maximum principal stress is located near

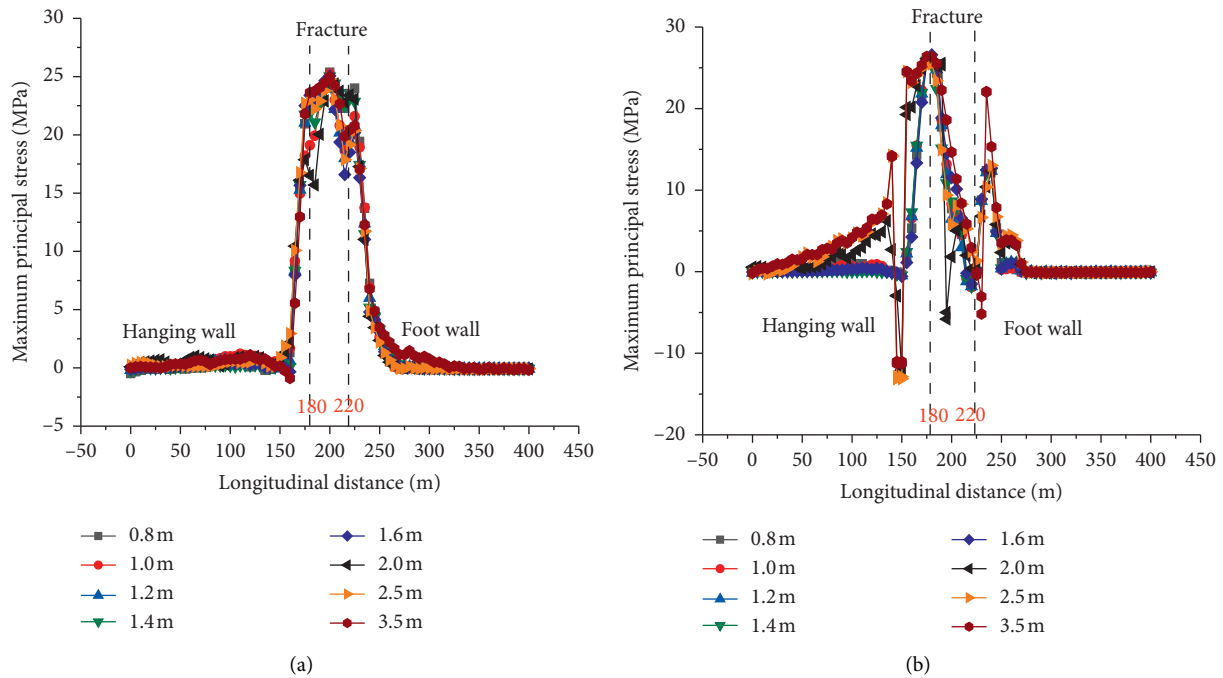


FIGURE 11: The distribution curves of the maximum principal stress of the lining under different displacements of active faults. The maximum principal stress distribution curves of the lining under (a) strike-slip fault and (b) thrust fault.

200 m. The overall curve is symmetrically distributed. Therefore, it can be inferred that the significant damage area of the tunnel lining under the strike-slip fault movement is located 50 m before and after the fracture, and the damage in the middle is the most significant. The maximum principal stress distribution of the tunnel lining under different strike-slip fault is roughly the same. It is speculated that this may be due to the damage to the middle of the tunnel lining before the fault displacement of 3.5 m.

It can be seen from Figure 11(b) that the maximum principal stress distribution curve of the lining under the thrust fault is different from the strike-slip fault movement. The maximum principal stress distribution curves at 0.8 m, 1.0 m, 1.2 m, 1.4 m, and 1.6 m faults are similar, which are roughly symmetrical, while the maximum principal stress distribution curves at 2.0 m, 2.5 m, and 3.5 m are roughly centrally symmetrical. The maximum principal stress of the lining at the hanging wall and foot wall of the thrust fault is basically zero, and the maximum principal stress change section of the lining is basically between 150 m and 200 m, and the maximum stress is near 200 m, which is similar to the stress distribution law of a strike-slip fault. In addition, the maximum principal stress under the thrust fault appears compressive stress, and the maximum compressive stress is at 150 m and 220 m, which is consistent with the area of the fracture zone. Therefore, it can be inferred that the lining located within 50 m before and after the fracture zone undergoes significant tensile failure when the thrust fault is dislocated, and the lining located in the middle of the fracture has the most obvious damage. As the displacement of fault increases, compression failure occurred in the lining 50 m in front of the fracture.

*4.3. Analysis of the Plastic Zone Range of the Tunnel Lining under Different Displacements.* The development of the plastic zone of the tunnel lining under different displacements of the active fault has an important reference value for the key monitoring area of the tunnel crossing the active fault area. According to the calculation results of the model, the development cloud diagram of the plastic zone with different displacements of strike-slip and thrust fault at  $90^\circ$  dip is obtained, as shown in Figure 12.

Comprehensive analysis of Figure 12 shows that the plastic zone of the tunnel lining under strike-slip fault is mainly concentrated in the vault and roughly located in the fracture. As the displacement increases, the plastic zone continues to increase and gradually gathers towards the vault. The distribution of the plastic zone in the vault is roughly the same as the distribution of the maximum principal stress under the strike-slip fault movement, and the damage to the lining in the fracture is the most significant. The plastic zone of the tunnel lining under the thrust fault movement is mainly concentrated in the lining arch waist, and the range is roughly located in the middle fracture. As the displacement increases, the extent of the plastic zone on both sides of the arch waist continues to increase, and the development of plastic zones at different parts of the strike-slip fault appears. Therefore, it can be inferred that the development of the plastic zone of the tunnel lining under the strike-slip fault is gradually extending from both sides of the arch waist to the vault, while the development of the plastic zone of the tunnel lining under the thrust fault gradually extends from the vault to both sides of the vault.

Comprehensive analysis of Figure 13 shows that when the dip angle is  $90^\circ$ , the development of the plastic zone of the



FIGURE 12: The cloud diagrams of plastic zone with different displacements under  $90^\circ$  dip angle. Cloud diagram of plastic zone under strike-slip fault with (a) 0.9 m and (b) 1.1 m. Cloud diagram of plastic zone under thrust fault with (c) 0.9 m and (d) 1.1 m.

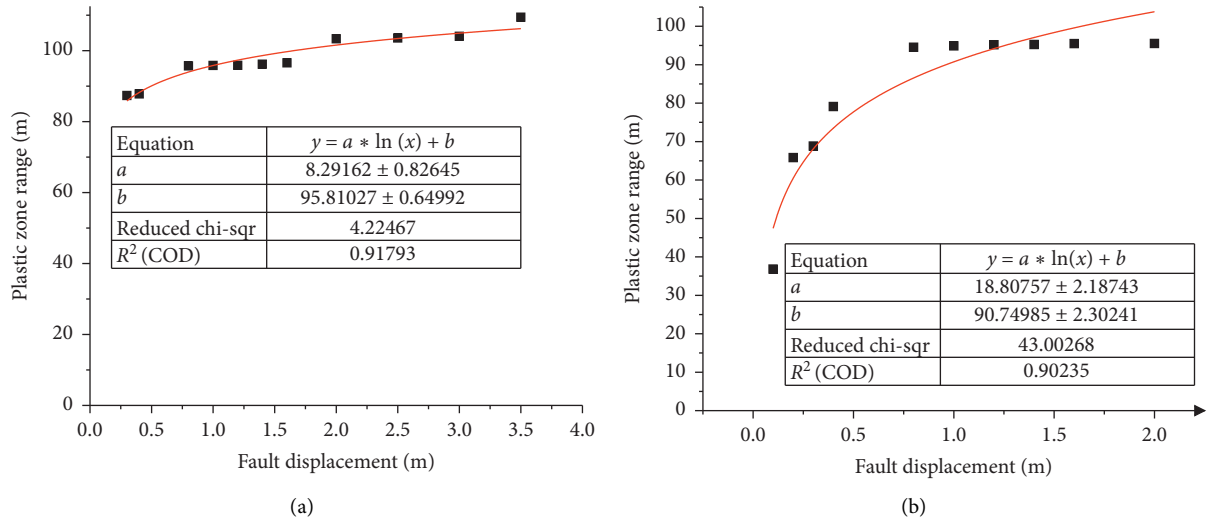


FIGURE 13: The development curves of the plastic zone range under different displacements of the active faults. Plastic zone range under different displacements of (a) strike-slip fault and (b) thrust fault.

active fault is distributed in a logarithmic function, and the development range of the plastic zone is positively correlated with the amount of movement, and with the increase of movement amount, the range of plastic zone gradually increases. Therefore, the key monitoring range of the lining under active fault movement should consider not only the influence of the dip angle of the fracture, but also the influence of the displacement of active fault.

## 5. Conclusion

In this paper, by establishing a three-dimensional finite element tunnel model under strike-slip and thrust fault movement, the tunnel lining displacement, maximum principal stress distribution, and the plastic zone development under different dip angles and different fault movement amounts are discussed. Thus, the damage mechanism of the lining under the active fault movement is revealed, and the conclusions are as follows:

- (1) Under active fault movement, the tunnel lining moves in the same form with the hanging wall, and the displacement curve shows an “S”-shaped distribution. The significant area of failure is roughly located near the fracture. When the dip angle of thrust fault is less, the displacement load will result in uneven displacement upward transmission. The

shape of the deformation curve of the lining under different displacements of the active fault is the same, showing an “S”-shaped distribution. The significant area of lining damage is also located near the fracture, and the damage effect becomes more significant with the increase of fault dislocation.

- (2) The maximum principal stress at the hanging wall and foot wall under the active fault movement is basically 0. The maximum principal stress under the movement of a strike-slip fault occurs in the central area of the fault zone and is mainly tensile failure. The maximum principal stress under the thrust fault movement gradually moves to the foot wall with the increase of the dip angle, and compressive failure also occurs. The significant damage area of the lining under the strike-slip fault is mainly tensile failure, while the compressive failure occurs when the thrust fracture is steep. The damage range is mainly affected by the dip angle of the fracture, while the damage effect is mainly affected by the increase of fault dislocation.
- (3) The plastic zone of the tunnel lining under different dip angles strike-slip fault is concentrated in the fracture and develops from both sides of the arch waist to the arch top and arch bottom. The extent of the plastic zone gradually increases in a logarithmic

function. The plastic zone of the tunnel lining under the thrust fault movement is also concentrated in the fracture zone, but it develops from the vault and arch bottom to both sides of the arch waist. The extent of the plastic zone is similar to the law of development under strike-slip faults, showing a gradual increase in a logarithmic function relationship.

## Data Availability

The data used to support the findings of this study are available from the corresponding author upon request.

## Conflicts of Interest

The authors declare that they have no conflicts of interest regarding the publication of this paper.

## Acknowledgments

This study was supported in part by the Sichuan Provincial Science and Technology Support Project (Nos. 2020YJ0253, 2020YFSY0060, 2019JDRC0133, and 2019JDRC0134); Fundamental Research Funds for the Central Universities-Interdisciplinary Research Project (2682021ZTPY102); National Nature Science Fund Project (No. 52078426); National Key Research and Development Plan (No. 2018YFE0207100); China Railway Eryuan Engineering Group Co. Ltd Scientific Research Project (KYY2019034(19-22) and KYY2019070(19-20)); and China National Railway Group Co. Ltd Scientific Research Project (Nos. SY2016G003 and N2020T004).

## References

- [1] P. Geng, C. He, and Q. X. Yan, "The current situation and prospect of seismic analysis methods for tunnel structure," *China Civil Engineering Journal*, vol. 46, no. S1, pp. 262–268, 2013.
- [2] Z. B. Li, "Analysis on seismic technology of tunnels in areas with high seismic intensity," *Building Technology Development*, vol. 43, no. 5, pp. 88–89, 2016.
- [3] L. M. Qu, X. M. Ding, G. Kouroussis, and C. J. Zheng, "Dynamic interaction of soil and end-bearing piles in sloping ground: numerical simulation and analytical solution," *Computers and Geotechnics*, vol. 134, Article ID 103917, 2021.
- [4] Y. S. Shen, L. Z. Tang, and P. F. Zhou, "Research on anti-seismic technology of Railway tunnel structure crossing soft and hard interface in strong earthquake area," *Railway Standard Design*, vol. 62, no. 10, pp. 123–129, 2018.
- [5] J. S. Shi, *Experimental and Numerical Study on the Damage of Overlying Soil and Tunnel Caused by Fault movement*, Zhejiang University, Hangzhou, China, 2017.
- [6] L. Qu, C. Yang, X. Ding, G. Kouroussis, and C. Zheng, "A continuum-based model on axial pile-head dynamic impedance in inhomogeneous soil," *Acta Geotechnica*, 2021.
- [7] National Standard of the People's Republic of China, *Code for Seismic Design of Buildings (GB50011-2010)*, China Construction Industry Press, Beijing, China, 2010.
- [8] V. A. Kontogianni and S. C. Stiros, "Earthquakes and seismic faulting: effects on tunnels," *Turkish Journal of Earth Sciences*, vol. 12, no. 1, pp. 153–156, 2003.
- [9] M. Russo, G. Germani, and W. Amberg, "Design and construction of large tunnel through active faults a recent application," in *Proceedings of the International Conference of Tunnelling & Under-ground Space Use*, pp. 1–14, Istanbul Turkey, October 2002.
- [10] Y. Zhao, *Seismic Response Analysis of Subway Tunnel in Active Fault area*, Institute of Engineering Mechanics, China Earthquake Administration, Heilongjiang, China, 2014.
- [11] D. Toeher, "Earthquake energy and ground breakage," *Bulletin of the Seismological Society of America*, vol. 48, no. 2, pp. 147–153, 1958.
- [12] M. Toshihiko, *Research on Active Faults*, Seismological Press, Beijing, China, 1983.
- [13] P. Geng, Y. He, C. He, Q. L. Quan, and Q. X. Yan, "Study on the reasonable seismic fortification length of the tunnel crossing the fracture zone," *Chinese Journal of Rock Mechanics and Engineering*, vol. 33, no. 02, pp. 358–365, 2014.
- [14] Y. Liu, J. Lai, J. P. Xin, X. D. Li, and R. J. Xing, "Dynamic comparative test research on seismic response law of tunnel crossing fault," *Rock and Soil Mechanics*, vol. 40, no. 12, pp. 4693–4702, 2019.
- [15] C. L. Xin, *Research on the Mechanism of Ground Motion Damage and Anti-seismic Measures for Tunnels Crossing faults*, Southwest Jiaotong University, Chengdu, China, 2015.
- [16] M. Ramaneharla, *Numerical Modeling of Dip-Slip Faults for Studying Ground Surface deformation*, Bulletin of Earthquake Resistant Structure Research Center, Institute of Industrial Science, The University of Tokyo, Tokyo, Japan, 2001.
- [17] Z.-K. Huang, K. Pitilakis, S. Argyroudis, G. Tsinidis, and D.-M. Zhang, "Selection of optimal intensity measures for fragility assessment of circular tunnels in soft soil deposits," *Soil Dynamics and Earthquake Engineering*, vol. 145, Article ID 106724, 2021.
- [18] Z.-K. Huang, K. Pitilakis, G. Tsinidis, S. Argyroudis, and D.-M. Zhang, "Seismic vulnerability of circular tunnels in soft soil deposits: the case of Shanghai metropolitan system," *Tunnelling and Underground Space Technology*, vol. 98, Article ID 103341, 2020.
- [19] Z.-K. Huang and D.-M. Zhang, "Scalar- and vector-valued vulnerability analysis of shallow circular tunnel in soft soil," *Transportation Geotechnics*, vol. 27, Article ID 100505, 2021.
- [20] W. Zhang, *Research on Seismic Response and Damping Measures of Large-Diameter Shield Tunnel structure*, Wuhan Institute of Rock and Soil Mechanics, Chinese Academy of Sciences, Wuhan, China, 2009.
- [21] Z. Y. Chen and Y. Zhao, "Analysis of tunnel response caused by active reverse fault movement," in *Proceedings of the 2019 National Engineering Geology Annual Conference*, pp. 113–118, The Geological Society of China: Editorial Office of Journal of Engineering Geology, Philadelphia, Pennsylvania, USA, 2019.
- [22] M. L. Lin, C. F. Chung, and F. S. Jeng, "Deformation of overburden soil induced by thrust fault slip," *Engineering Geology*, vol. 88, no. 1-2, pp. 70–89, 2006.
- [23] M.-L. Lin, C.-F. Chung, F.-S. Jeng, and T.-C. Yao, "The deformation of overburden soil induced by thrust faulting and its impact on underground tunnels," *Engineering Geology*, vol. 92, no. 3-4, pp. 110–132, 2007.
- [24] GB 50010-2010, *GB 50010—2010 Code for Design of concrete Structures*, pp. 19-20, China Architecture & Building Press, Beijing, China, 2015, in Chinese.
- [25] H. Huo, *Seismic Design and Analysis of Rectangular Undergroundstructures*, pp. 23–28, School of Civil Engineering, PurdueUniversity, West Lafayette, IN, USA, 2005.

- [26] J. W. Xu, "On the main problems of strike-slip fault," *Frontiers of Earth Science*, vol. 1, no. 02, pp. 125–136, 1995.
- [27] H. L. Song, C. H. Zhang, and G. H. Wang, *Structural Geology*, Geological Publishing House, Beijing, China, 2013.
- [28] X. Z. Liu, X. L. Wang, and L. L. Lin, "Model experimental study on influence of normal fault with 60° dip angle stick-slip movement on mountain tunnel," *China Civil Engineering Journal*, vol. 47, no. 2, pp. 121–128, 2014.



## Research Article

# Influence of Two Cooling Methods on Dynamic Mechanical Properties of High Temperature Sandstone

Qi Ping <sup>1,2,3</sup>, Qi Diao,<sup>2,3</sup> Dezhi Qi,<sup>2,3</sup> Chen Wang,<sup>2,3</sup> and Chuanliang Zhang<sup>2,3</sup>

<sup>1</sup>State Key Laboratory of Mining Response and Disaster Prevention and Control in Deep Coal Mine, Anhui University of Science and Technology, Huainan, Anhui 232001, China

<sup>2</sup>Engineering Research Center of Mine Underground Projects, Ministry of Education, Anhui University of Science and Technology, Huainan, Anhui 232001, China

<sup>3</sup>School of Civil Engineering and Architecture, Anhui University of Science and Technology, Huainan, Anhui 232001, China

Correspondence should be addressed to Qi Ping; [ahpingqi@163.com](mailto:ahpingqi@163.com)

Received 23 April 2021; Accepted 6 July 2021; Published 19 July 2021

Academic Editor: Honglue Qu

Copyright © 2021 Qi Ping et al. This is an open access article distributed under the Creative Commons Attribution License, which permits unrestricted use, distribution, and reproduction in any medium, provided the original work is properly cited.

To study the influence of different cooling methods on dynamic mechanical properties of high temperature rock, both natural cooling and water cooling were used to cool high temperature (100°C~1000°C) coal mine sandstone to room temperature (20°C). Basic physical parameters of sandstone were measured, and impact compression tests were carried out by using the SHPB test device. Comparative analysis shows that the volume expansion rate, mass loss rate, density reduction rate, and P-wave velocity reduction rate of sandstone specimens are positively correlated with the temperature in a quadratic function. The deterioration rate of physical parameters of water cooling sandstone specimens is slightly larger than that of natural cooling. The variation of dynamic stress-strain curves is basically consistent. Compaction stage of water cooling is slightly larger than that of natural cooling. With the increase in temperature, dynamic compressive strength of sandstone specimens first increases, then decreases, and reaches maximum at 300°C. Subsequently, dynamic compressive strength decreases in a quadratic function with the temperature, and dynamic compressive strength of water cooling sandstone specimens is significantly lower than that of natural cooling. The dynamic elastic modulus also first increases and then decreases with the temperature and reaches maximum at 300°C. The dynamic elastic modulus of water cooling sandstone specimens is lower than that of natural cooling, but they are roughly the same at 1000°C. Dynamic strain increases in a quadratic function with the temperature, and dynamic strain of water cooling sandstone specimens is greater than that of natural cooling. The impact failure of sandstone specimens is intensified with the temperature, and the failure degree of water cooling is greater than that of natural cooling.

## 1. Introduction

Rock often experiences long-term high temperature heating and rapid cooling in geotechnical engineering and other fields. During the warring states period in China, Li Bing used the method of first heating rock then rapid cooling with water to excavate mountains for the Dujiangyan Irrigation Project. Modern tunnels and underground caverns may encounter fire and explosion accidents, and the rock walls of tunnels and caverns may experience fire extinguishing and water cooling after long-term high temperature heating. The permeability of water to rocks is bound to affect the self-bearing capacity of tunnels [1, 2]. When the wildfires are

extinguished by planes dropping water, the properties of rock are changed after high temperature. Therefore, studying the physical and mechanical properties of rock after different high temperature treatments has significance for the safe production and disaster prevention.

Some scholars have conducted experimental studies on static and dynamic mechanics of rock under and after high temperature. Sirdesai et al. [3] conducted high temperature heating of fine-grained red sandstone at 50°C~500°C for 5, 10, 15, 20, and 30 days and studied the effects of thermal treatment duration on the physical properties and tensile strength of red sandstone. Yang et al. [4] conducted the Brazilian splitting test and conventional triaxial compression

test for granite with two grain sizes after high temperature treatment and found that the mechanical properties of coarse grain granite are more sensitive to temperature than fine grain granite. Gao et al. [5] carried out 4 grades temperature treatment for Fangshan marble and conducted dynamic compression tests under dry and saturated conditions. Ping et al. [6, 7] studied the dynamic mechanical energy evolution characteristics of limestone under high temperature and carried out the experimental study on dynamic splitting tensile of high temperature sandstone under different loading rates. Experimental studies on wave characteristics and dynamic mechanical properties of granite after different high temperatures were conducted by the ultrasonic analyzer and SHPB device [8]. Zhang et al. [9] carried out uniaxial compression tests under 5 kinds of loading rates for 200°C limestone. The experimental study on dynamic mechanical properties of limestone and sandstone after different high temperatures was carried out by Ping et al. [10, 11]. Liu et al. [12] studied the impact dynamic characteristics of marble after different temperatures treatment. Li et al. [13] conducted high temperature heating treatment of Beishan granite, and then uniaxial and triaxial compression tests were carried out with different impact velocities. The above tests are the experimental study on different kinds of rock after high temperature heating and natural cooling treatment.

Some scholars also have carried out a series of experimental studies on statics, acoustics, and physical properties of high temperature rock after water cooling. Xi and Zhao [14] carried out the uniaxial compression test, tensile test, shear test, and ultrasonic velocity test for high temperature granite within 600°C after water cooling. Physical and mechanical properties, such as porosity, pore size distribution, compressive strength, peak strain, and microstructure, were studied for five temperatures yellow sandstone in Hanzhong area of Shanxi Province after two cooling methods (water cooling and natural cooling) [15]. Zhu et al. [16] heated granite to high temperature within 500°C and tested density, P-wave and S-wave velocities, uniaxial compressive strength, and elastic modulus after water cooling. Experimental analysis of mechanical and wave properties of limestone and marble after high temperature water cooling was conducted by Huang et al. [17, 18]. Han et al. [19] studied the mechanical behaviour of high temperature sandstone after water cooling. Concrete specimens were treated by natural cooling and water cooling after high temperature heating and then the uniaxial compressive test was carried out [20]. Wang et al. [21] conducted 20°C~800°C high temperature heating and rapid water cooling for granite and studied the influence of rapid water cooling on residual mechanical properties of high temperature granite. Shi et al. [22] conducted cyclic heating and water cooling for granite specimens and studied the physical and mechanical properties. The effects of two cooling rates on P-wave velocity, uniaxial compressive strength, tensile strength, and fracture toughness of sandstone were studied by cooling with water and liquid nitrogen after high temperature treatment [23]. The uniaxial compression test, velocity test, acoustic emission test, and electron microscope scanning test were carried

out for 100°C to 800°C sandstone after water cooling, and then the influence of thermal shock caused by rapid cooling on the mechanical properties of sandstone was studied [24]. Rathnaweera et al. [25] studied the influence of natural cooling and water cooling on mechanical behaviour of clay-rich Hawkesbury sandstone after heating from 25°C to 1000°C. With the MTS322 test system, fracture toughness was tested for granite subjected to 1, 5, 10, 15, and 20 cycles of heating and water cooling treatment [26]. Through laboratory tests, the physical and mechanical properties of granite after 1 and 30 cycles of heating and water cooling from 20°C to 500°C were studied [27]. Zhu et al. [28] carried out the impact test of water cooling high temperature granite by using the split Hopkinson pressure bar device. Zhai et al. [29] carried out high temperature heating on C35 concrete under two heating gradients. After natural cooling and water cooling, SHPB impact compression tests under different loading rates were carried out to study the fracture distribution, fractal characteristics, energy dissipation, and dynamic mechanical properties.

At present, the tests and research studies on rock after high temperature water cooling are mostly concentrated in static condition, and the research on dynamic properties of high temperature rock after water cooling is still less. However, in practical engineering, some tunnels and underground caverns after fire may still suffer the impact of traffic accidents, explosions, and earthquakes. Therefore, it is necessary to study the dynamic mechanical properties of high temperature rock after water cooling.

To compare the effects of two cooling methods on the physical and dynamic mechanical properties of high temperature sandstone, common roadway sandstone in coal mine was selected as research object. Sandstone specimens were heated from room temperature (20°C) to 100°C, 200°C, 300°C, 400°C, 500°C, 600°C, 700°C, 800°C, 900°C, and 1000°C and then cooled by water cooling and natural cooling. The basic physical parameters of sandstone were measured, and the variation of mass, volume, density, and P-wave velocity was analyzed. Impact compression tests were carried out for high temperature sandstone specimens after cooling under the same loading conditions by  $\phi 50$  mm SHPB test apparatus. The influence of two cooling methods on dynamic parameters such as dynamic compressive stress-strain curve, dynamic compressive strength, dynamic elastic modulus, dynamic strain, and strain rate was analyzed.

## 2. Materials and Methods

*2.1. Processed Samples.* Sandstone samples were taken from Gubei Coal Mine of Huainan Mining Group. In order to enhance the comparison of test results, tested sandstone specimens were drilled from the same rock block. According to test methods recommended by the International Society of Rock Mechanics (ISRM) [30], sandstone specimens were processed into cylinder with the size of  $\phi 50$  mm  $\times$  25 mm, and the aspect ratio is 0.5 to meet the requirements of stress equilibrium and inertial effect in the SHPB test.

Vertical drilling machine, cutting machine, double-end grinding machine, and other equipment were applied to

core, cut, and polish sandstone specimens to achieve good uniformity and consistency. The roughness of two end of sandstone specimen is less than  $\pm 0.02$  mm, the non-parallelism of the two ends is less than  $\pm 0.05$  mm, and the axis deviation is less than  $\pm 0.25^\circ$ . The mass, volume, and P-wave velocity of all specimens were measured before heating. The density was  $2.605 \text{ g/cm}^3$ , and the P-wave velocity was  $3862 \text{ m/s}$ .

**2.2. Heating and Cooling Treatment of Specimens.** Sandstone specimens were heated by box-type resistance furnace equipped with an electric furnace temperature controller. The highest heating temperature of box-type resistance furnace is  $1200^\circ\text{C}$ . In order to heat the specimen fully and uniformly, the heating rate was set as  $10^\circ\text{C}/\text{min}$  and then the temperature is kept constant for 4h after reaching the target temperature.

After heating, sandstone specimens were taken out from the furnace. For the water cooling method, sandstone specimens were quickly put into the water tank (Figure 1). A piece of toughened glass was put at the bottom of the tank to avoid high temperature sandstone specimens burn the bottom of the tank. The height of ordinary tap water in the tank is about 40 mm to ensure sandstone specimens immersed in water. For the nature cooling method, sandstone specimens were taken out from the furnace to prevent the residual temperature in the furnace from continuously heating the sandstone specimens so as to avoid the large deviation between two cooling methods due to different heating time.

After sandstone specimens were heated and cooled, the mass, volume, and longitudinal wave velocity were measured for the second time so as to study the influence of physical parameters of sandstone after two cooling methods.

**2.3. Impact Compression Test.** SHPB test apparatus in the State Key Laboratory of Mining Response and Disaster Prevention and Control in Deep Coal Mine was adopted for the impact compression test (Figure 2).

Input bar, output bar, and absorption bar of SHPB test apparatus are all made of high-strength alloy steel. The diameter of SHPB test apparatus is 50 mm, the elastic modulus is 210 GPa, and the longitudinal wave velocity is  $5190 \text{ m/s}$ . Spindle-shaped striker was used to generate semisine loading wave, ensure the stress equilibrium during impact process, and prevent the specimen from premature failure. Compressed gas used for impact is nitrogen. The pressure for each impact compression test was set as 0.3 MPa. The spindle-shaped striker was placed in the same position in the launch tube each time to make the gas act on the striker equally, ensure the consistency of impact load, and keep the incident energy within the same range.

### 3. Results and Analysis

**3.1. Results of Basic Physical Parameters.** 11 temperature gradients were set up in this research, which were room temperature ( $20^\circ\text{C}$ ),  $100^\circ\text{C}$ ,  $200^\circ\text{C}$ ,  $300^\circ\text{C}$ ,  $400^\circ\text{C}$ ,  $500^\circ\text{C}$ ,

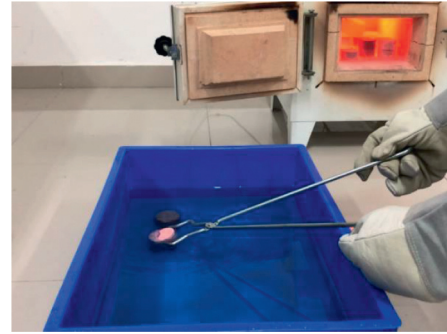


FIGURE 1: Water cooling treatment for heated sandstone.



FIGURE 2: Split Hopkinson pressure bar test apparatus.

$600^\circ\text{C}$ ,  $700^\circ\text{C}$ ,  $800^\circ\text{C}$ ,  $900^\circ\text{C}$ , and  $1000^\circ\text{C}$ . Tables 1 and 2 list the basic physical parameters of sandstone specimens before heating and after two cooling methods, such as volume, mass, density, and longitudinal wave velocity.

**3.2. Variation of Volume, Mass, and Density of Specimens.** Figures 3~5 are the deteriorate rates of volume, mass, and density of high temperature sandstone specimens after two cooling methods.

As seen from Figure 3, volume expansion rate of water cooling sandstone specimens is greater than that of natural cooling, and the volume expansion rate of high temperature sandstone specimens after two cooling methods first decreases slightly and then increases with the heating temperature, and there is a quadratic function between volume expansion rate and temperature. At  $100^\circ\text{C}\sim 500^\circ\text{C}$ , the specimen volume of two cooling methods is less affected by temperature, and there is no obvious expansion. Because the volume expansion of mineral particles within this temperature range only occupies the original micropore and microcrack space inside the specimen, the volume expansion is not obvious. When heated to  $600^\circ\text{C}\sim 1000^\circ\text{C}$ , the specimen volume of two cooling methods begins to expand rapidly. This is because the original micropores and microcracks in the specimen exceed the limit of structural thermal stress. With the continuous thermal expansion of sandstone mineral particles, new microcracks generate inside the sandstone specimen, and the appearance volume expands rapidly. When the heating temperature was  $1000^\circ\text{C}$ , the volume expansion rates for natural cooling and water cooling were 4.47% and 4.69%. The volume expansion rate of

TABLE 1: Basic physical parameters of sandstone before heating and after water cooling.

$T$ (°C)	Samples	Before heating					After water cooling				
		$D$ (mm)	$L$ (mm)	$M$ (g)	$P$ (g·cm <sup>-3</sup> )	$C$ (m·s <sup>-1</sup> )	$D$ (mm)	$L$ (mm)	$M$ (g)	$\rho$ (g·cm <sup>-3</sup> )	$C$ (m·s <sup>-1</sup> )
20	GB11-01	49.96	25.18	127.40	2.582	3934	49.96	25.18	127.40	2.582	3934
	GB11-02	49.78	25.21	127.85	2.606	3939	49.78	25.21	127.85	2.606	3939
	GB11-03	49.69	25.11	126.52	2.599	3923	49.69	25.11	126.52	2.599	3923
100	GB11-09	49.70	25.22	127.67	2.610	3708	49.60	25.14	127.41	2.624	3927
	GB11-13	49.74	25.37	128.77	2.613	3731	49.63	25.37	128.41	2.616	3731
	GB11-15	49.86	25.07	126.22	2.579	3917	49.67	25.00	125.96	2.601	3676
200	GB11-17	49.64	25.14	127.08	2.612	3929	49.68	25.06	126.31	2.601	3481
	GB11-18	49.75	25.08	127.26	2.611	4179	49.69	25.06	126.47	2.603	3685
	GB11-19	49.78	25.13	127.77	2.612	4188	49.71	25.15	127.10	2.604	3930
300	GB11-25	49.85	25.25	127.74	2.592	3945	49.70	25.19	129.45	2.650	3314
	GB11-27	49.67	25.12	126.17	2.593	3693	49.71	25.08	126.44	2.597	3689
	GB11-28	49.79	25.08	127.11	2.603	3918	49.71	25.07	125.59	2.580	3484
400	GB11-33	49.68	25.19	127.77	2.618	4198	49.64	25.17	126.99	2.607	3496
	GB11-35	49.74	24.99	126.10	2.597	4165	49.68	24.98	125.34	2.589	3470
	GB11-36	49.66	25.09	127.53	2.625	3689	49.72	25.07	126.80	2.606	3481
500	GB11-41	49.69	24.90	126.72	2.625	3661	49.71	25.12	125.11	2.567	3305
	GB11-43	49.74	24.93	126.62	2.614	3462	49.75	25.00	124.39	2.560	3289
	GB11-44	49.73	25.22	127.41	2.601	3708	49.78	25.19	125.98	2.570	3403
600	GB11-51	49.77	25.17	126.84	2.591	3495	49.98	25.32	120.53	2.427	2345
	GB11-52	49.76	25.19	126.90	2.591	4198	49.99	25.22	120.81	2.441	2335
	GB11-53	49.91	25.15	127.68	2.595	3929	49.93	25.22	123.14	2.494	2425
700	GB11-61	49.66	25.02	125.83	2.597	3474	50.18	25.26	119.27	2.388	2105
	GB11-62	49.65	25.14	127.47	2.619	3928	50.06	25.41	120.39	2.408	1629
	GB11-63	49.72	25.16	127.36	2.608	3931	50.26	25.35	121.23	2.411	2264
800	GB11-71	49.60	25.18	126.41	2.599	3703	50.00	25.40	117.90	2.365	1716
	GB11-72	49.68	25.20	126.94	2.599	3500	50.10	25.46	119.20	2.376	1872
	GB11-73	49.79	25.23	128.10	2.608	3710	50.19	25.39	118.81	2.366	1983
900	GB11-81	49.72	25.18	127.47	2.608	4196	50.29	25.48	119.32	2.358	1633
	GB11-82	49.80	25.26	128.10	2.604	3946	50.32	25.54	116.45	2.294	1520
	GB11-83	49.53	25.14	126.34	2.608	3697	50.16	25.39	118.32	2.359	1627
1000	GB11-90	49.87	25.19	127.66	2.595	4198	50.48	25.55	119.00	2.327	1452
	GB11-91	49.73	25.17	126.57	2.590	4194	50.52	25.62	117.60	2.291	1489
	GB11-93	49.70	25.05	127.65	2.626	3914	50.46	25.54	116.47	2.281	1485

water cooling is generally slightly larger than that of natural cooling. The reason is that after the high temperature specimen is naturally cooled in the air, the thermal expansion of mineral particles will gradually shrink due to cooling, so the overall volume of the specimen will be smaller than that of the high temperature state after cooling. When the high temperature specimen is cooled in water, there will be a huge temperature difference between the inside and outside of the high temperature specimen, which will cause additional damage to the specimen. The size and number of micropores and microcracks in the specimen increase resulting in a larger volume expansion rate of water cooling than natural cooling.

As illustrated in Figure 4, mass loss rate of high temperature sandstone specimens after two cooling methods is also positively correlated with temperature in a quadratic function. When the temperature is in the range of 100°C~500°C, mass loss rate of two cooling methods is small. The mass loss rates of natural cooling and water cooling are 0.21%~2.66% and 0.23%~1.38%. When heated to 600°C~700°C, the mass loss rates of two cooling methods increase obviously. The mass loss rates of natural

cooling and water cooling are 4.94%~6.24% and 4.44%~5.19%. When heated to 800°C~1000°C, the mass loss rates of natural cooling and water cooling are 6.54%~7.38% and 6.69%~7.54%, and the mass loss rate of two cooling methods is basically the same. It is worth noting that the mass loss rate of water cooling is slightly lower than that of natural cooling when the temperature is between 300°C and 700°C. That is because when high temperature sandstone is cooled in water, the water can enter into the internal pores of sandstone, which increases the mass of sandstone. When the action temperature ranges from 800°C to 1000°C, there are many micropores and microcracks in the specimen, and the pore diameter and crack width are large. Even if water is immersed into the sandstone sample, it will gradually evaporate and drain after being removed from the water. Therefore, the mass loss rate of water-cooled specimen is basically same with that of natural cooling.

Figure 5 illustrates that the density reduction rate of sandstone specimens after two cooling methods is positively correlated with temperature in a quadratic function. At 100°C~500°C, the density reduction rate of two cooling

TABLE 2: Basic physical parameters of sandstone before heating and after natural cooling.

$T$ (°C)	Samples	Before heating					After natural cooling				
		$D$ (mm)	$L$ (mm)	$M$ (g)	$P$ (g·cm <sup>-3</sup> )	$C$ (m·s <sup>-1</sup> )	$D$ (mm)	$L$ (mm)	$M$ (g)	$\rho$ (g·cm <sup>-3</sup> )	$C$ (m·s <sup>-1</sup> )
20	GB11-05	49.90	25.06	127.51	2.602	3916	49.90	25.06	127.51	2.602	3916
	GB11-06	49.85	25.20	127.58	2.594	3937	49.85	25.20	127.58	2.594	3937
	GB11-07	49.74	25.19	127.47	2.604	3936	49.74	25.19	127.47	2.604	3936
100	GB11-12	49.74	25.12	126.78	2.598	3489	49.53	25.21	126.50	2.605	3501
	GB11-14	49.80	25.17	128.04	2.612	4194	49.70	25.18	127.75	2.616	3497
	GB11-16	49.75	25.00	126.91	2.611	3907	49.71	24.90	126.66	2.621	3662
200	GB11-21	49.94	25.19	126.75	2.570	3704	49.55	25.14	125.99	2.599	3307
	GB11-22	49.78	25.13	127.63	2.610	3695	49.71	25.14	126.84	2.600	3492
	GB11-24	49.79	25.16	127.09	2.595	3700	49.61	25.16	126.48	2.602	3494
300	GB11-29	49.79	25.12	127.33	2.604	3925	49.74	25.07	126.36	2.594	3482
	GB11-30	49.97	25.00	126.57	2.581	3676	49.78	24.97	125.59	2.585	3285
	GB11-32	49.72	25.15	127.02	2.602	3698	49.68	25.14	126.10	2.588	3696
400	GB11-37	49.72	25.20	126.66	2.589	3706	49.71	25.07	125.53	2.580	3299
	GB11-38	49.85	25.06	126.16	2.580	3685	49.73	24.97	124.91	2.575	3468
	GB11-39	49.62	25.02	128.47	2.655	3475	49.59	25.00	126.96	2.629	3290
500	GB11-46	49.63	25.23	127.89	2.621	3942	49.68	25.15	124.58	2.556	3309
	GB11-47	49.85	25.16	128.10	2.609	3931	49.77	25.12	124.21	2.542	3306
	GB11-48	49.77	25.18	128.02	2.613	3703	49.72	25.16	125.00	2.559	3311
600	GB11-56	49.76	25.29	127.51	2.593	3719	49.93	25.35	121.85	2.455	2535
	GB11-57	49.76	25.18	126.96	2.593	3702	49.95	25.26	120.05	2.426	2177
	GB11-58	49.65	24.73	127.23	2.657	3637	49.91	24.90	118.28	2.428	2490
700	GB11-64	49.82	25.11	127.11	2.597	3923	50.03	25.28	119.02	2.395	2039
	GB11-66	49.67	25.15	126.40	2.595	3929	50.03	25.34	118.43	2.378	1863
	GB11-67	49.76	25.18	127.11	2.596	3703	49.97	25.37	119.41	2.400	2114
800	GB11-74	49.85	25.10	127.28	2.599	3922	50.21	25.34	118.91	2.371	1712
	GB11-76	49.83	25.10	127.45	2.604	3921	50.16	25.35	118.77	2.372	1760
	GB11-77	49.74	25.22	127.13	2.594	3941	50.08	25.40	119.19	2.383	1814
900	GB11-86	49.89	25.17	127.40	2.590	3932	50.26	25.49	118.82	2.351	1931
	GB11-87	49.70	25.13	126.06	2.586	3695	50.19	25.43	117.98	2.346	1869
	GB11-88	49.74	25.05	126.74	2.604	3684	50.21	25.35	118.59	2.363	1864
1000	GB11-94	49.77	25.15	127.12	2.598	4191	50.37	25.55	117.90	2.316	1935
	GB11-95	49.69	25.16	127.07	2.605	3931	50.50	25.61	117.53	2.291	2001
	GB11-98	49.69	25.12	126.86	2.604	3306	50.31	25.53	118.54	2.335	1934

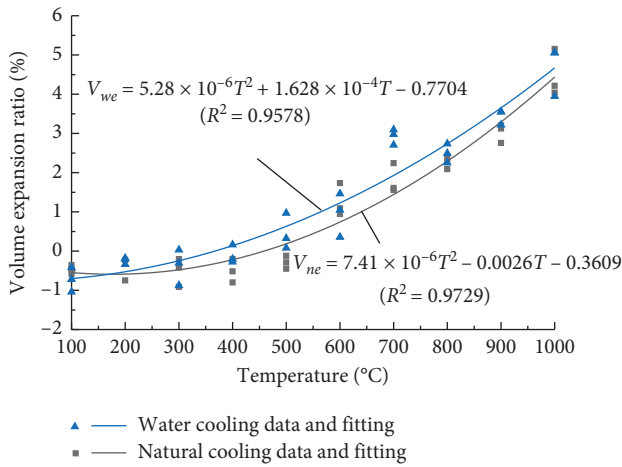


FIGURE 3: Volume expansion rate of high temperature sandstone after two cooling methods.

methods is less affected by temperature. At 500°C, the density reduction rates of natural cooling and water cooling are 2.37% and 1.83%. At 600°C~1000°C, the

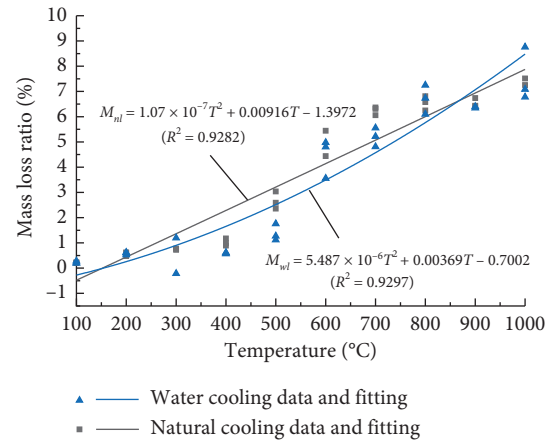


FIGURE 4: Mass loss rate of high temperature sandstone after two cooling methods.

density reduction rate of two cooling methods increases rapidly. The density reduction rates of natural cooling and water cooling are 5.89%~11.09% and 5.34%~11.67%. As

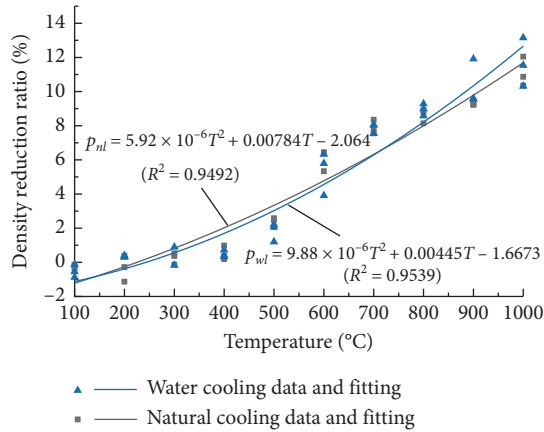


FIGURE 5: Density reduction rate of high temperature sandstone after two cooling methods.

the density is the superposition result of mass and volume, the density reduction rate of two cooling methods is basically the same.

**3.3. P-Wave Velocity Variation.** Figure 6 shows the variation of P-wave velocity of high temperature sandstone specimens after two cooling methods. Pores and cracks can affect the propagation velocity of ultrasonic wave in the medium. Analyzing the variation of P-wave velocity can help to understand the development of pores and cracks in high temperature rock indirectly and then understand the variation of mechanical properties.

As seen from Figure 6, the P-wave velocities of sandstone specimens after two cooling methods decrease with the temperature. At 100°C~500°C, the P-wave velocities of the two cooling methods have little difference and the P-wave velocity of water cooling is slightly larger than that of natural cooling. That is because high temperature sandstone cooled in water can make water enter into the specimen, which improves the density of sandstone specimen.

At 600°C, the P-wave velocity of specimens after two cooling methods decreases significantly, and the drop was about 1000 m/s. There are two reasons for this large drop. On the one hand, the original moisture inside the specimen is evaporated due to high temperature, then the compactness of the specimen is reduced, and the porosity is increased. On the other hand, due to different thermal expansion coefficients of mineral particles in the specimen, the uneven expansion occurs. The expansion leads to the extension and initiation of pores and cracks inside and on the surface of the specimen. The pores and cracks will hinder the P-wave propagation in the specimen. Therefore, the P-wave velocities after two cooling methods decrease significantly.

The P-wave velocity of natural cooling specimens tends to be stable at 700°C~1000°C, indicating that the pores and cracks in the specimen have been fully developed. The wave velocity of water cooling decreases to 1857 m/s at 800°C and further decreased to 1593 m/s and 1475 m/s at 900°C and 1000°C. The P-wave velocity reduction rate of water cooling is slightly bigger than that of natural cooling. When high

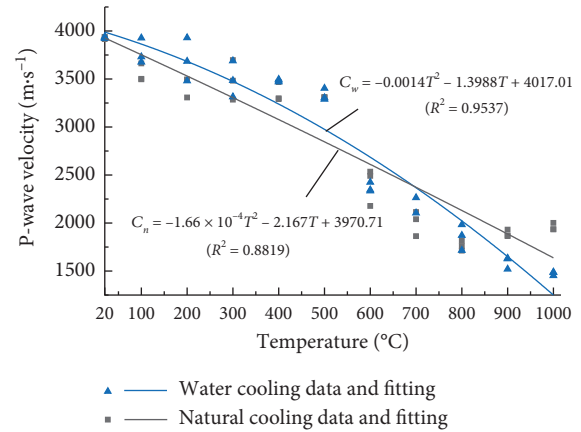


FIGURE 6: P-wave velocity of high temperature sandstone after two cooling methods.

temperature sandstone specimen is cooled in water, there is a large temperature difference between the inner and outer layers of sandstone specimen. At this time, the outer layer of the specimen will shrink, while the inner part of the specimen is still in a state of thermal expansion. Therefore, tensile stress is generated in the outer layer of the specimen, and the tensile stress generated by this temperature difference will gradually emerge from outside to inside with the cooling effect. Developed pores and cracks in the inner and on the surface of the specimen result in further attenuation of P-wave energy. Therefore, the decrease rate of P-wave velocity of water cooling is greater than that of natural cooling.

**3.4. Dynamic Compressive Stress-Strain Curve.** Based on impact compression tests, Figure 7 presents the dynamic compressive stress-strain curves of high temperature sandstone after two cooling methods.

As seen from Figure 7, the dynamic stress-strain curves of high temperature sandstone specimens after two cooling methods have experienced four stages. In the first stage, the stress slowly increases with the strain, called the compaction stage. The slope of stress-strain curve is small, and it is in a state of slow upward. In this stage, the micropores and microcracks in the specimen are compacted and closed under the impact load, and this stage is very short. In the second stage, the slope of stress-strain curve increases and remains constant. The stress-strain curve in this stage is approximately a straight line, and the rock is in an elastic deformation stage. In the third stage, the slope of stress-strain curve begins to decrease, and the curve is in a convex shape, called the plastic strengthening stage. In the fourth stage, the slope of stress-strain curve is negative, called the failure stage. Under the continuous action of impact load, the rock begins to break and the bearing capacity of rock begins to decline.

It can be seen that the dynamic stress-strain curves of two cooling methods are basically consistent. The stress-strain curve of water cooling is lower and wider than that of natural cooling. The reason for this difference is that the compaction stage of water cooling is longer than that of

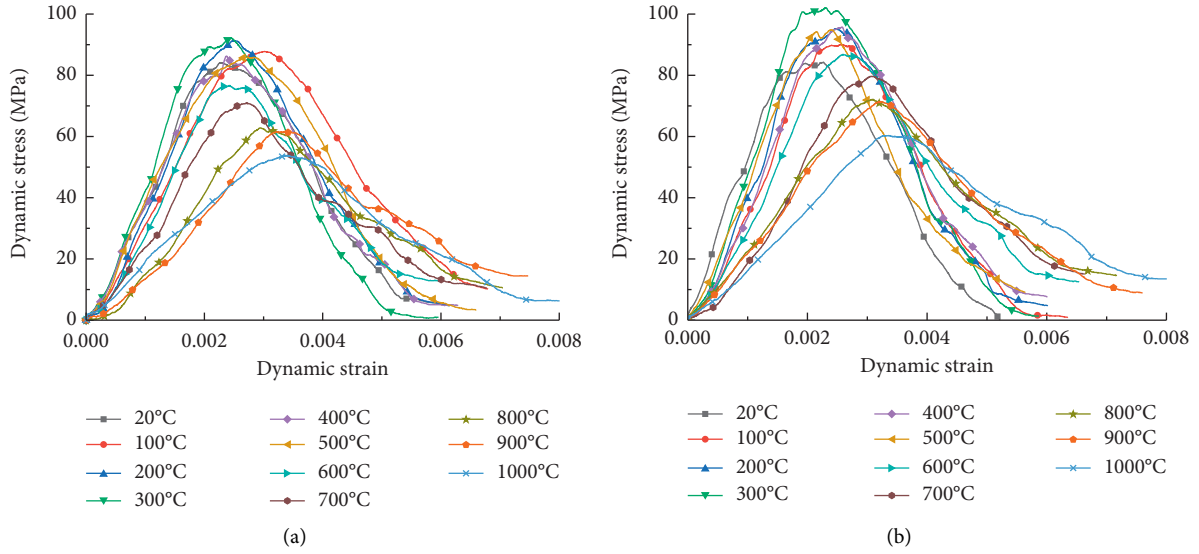


FIGURE 7: Dynamic stress-strain curves of high temperature sandstone after two cooling methods: (a) water cooling; (b) natural cooling.

natural cooling. Rapid cooling of high temperature sandstone specimen in water intensifies the development of micropores and microcracks, and the compression displacement of impact force increases with more pores in the specimen. Therefore, the compaction stage of water cooling is longer than that of natural cooling. In the elastic stage, the slope of stress-strain curves of water cooling is smaller than that of natural cooling, namely, the dynamic elastic modulus of water cooling is smaller than that of natural cooling. In the third stage, the dynamic peak stress of water cooling is lower than that of natural cooling, while the corresponding dynamic strain of water cooling is slightly larger than that of natural cooling.

**3.5. Dynamic Compressive Strength.** Dynamic compressive strength ( $\sigma_d$ ) of high temperature sandstone specimens ranging from room temperature (20°C) to 1000°C after two cooling methods is shown in Figure 8.

As seen from Figure 8, the dynamic compressive strength of water cooling sandstone specimens is significantly lower than that of natural cooling. The dynamic compressive strength of two cooling methods increases first and then decreases with the temperature and reaches the maximum at 300°C. When heating temperature exceeds 300°C, the dynamic compressive strength of two cooling methods decreases in a quadratic function with the temperature, as shown in the following equation:

$$\left. \begin{aligned} \sigma_{wd} &= -9.06 \times 10^{-6}T^2 - 0.044T + 106.58 (R^2 = 0.9801), \\ \sigma_{nd} &= -1.75 \times 10^{-5}T^2 - 0.036T + 114.29 (R^2 = 0.9802) \end{aligned} \right\} \quad (1)$$

where  $\sigma_{wd}$  and  $\sigma_{nd}$  are the dynamic compressive strength of water cooling and natural cooling and  $T$  is the heating temperature.

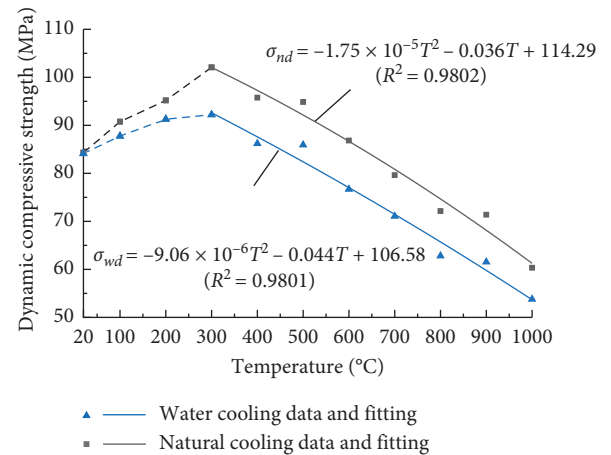


FIGURE 8: Dynamic compressive strength of high temperature sandstone after two cooling methods.

When the temperature is 100°C~300°C, the dynamic compressive strength of two cooling methods increases with the temperature. This is because when the temperature is low, the expansion of heated mineral particles inside the sandstone specimen can fill the original micropores and microcracks, which improve the compactness and dynamic compressive strength of sandstone specimen. Moreover, the evaporation of water will increase the friction force between mineral particles, which also increase the dynamic compressive strength. According to above analysis, water cooling will cause additional damage to high temperature sandstone. During water cooling, the friction between mineral particles is weakened as water enters into the specimen. Therefore, the dynamic compressive strength of water cooling is lower than that of natural cooling.

With the increase in heating temperature, the difference of dynamic compressive strength between water cooling and natural cooling is gradually larger and the difference is the

largest at 800°C and 900°C. The dynamic compressive strength of water cooling is 12.92% and 13.77% lower than that of natural cooling, indicating that water cooling causes an obvious degradation for high temperature sandstone. At 1000°C, the difference between water cooling and natural cooling decreases, indicating that after the high temperature of 1000°C, the thermal damage caused by high temperature gradually becomes the main factor of degradation.

**3.6. Dynamic Elastic Modulus.** As seen from Figure 9, the dynamic elastic modulus of water cooling sandstone specimens is smaller than that of natural cooling. The dynamic elastic modulus of two cooling methods first increases and then decreases with the temperature. The maximum dynamic elastic modulus is at 300°C, and the dynamic elastic modulus of two cooling methods is basically consistent at 1000°C. There is a quadratic function between the dynamic elastic modulus of sandstone and temperature, as shown in the following equation:

$$\left. \begin{aligned} E_{wd} &= -4.55 \times 10^{-5} T^2 + 0.018 T + 43.40 \quad (R^2 = 0.9710), \\ E_{nd} &= -7.14 \times 10^{-5} T^2 + 0.046 T + 42.90 \quad (R^2 = 0.9481) \end{aligned} \right\} \quad (2)$$

where  $E_{wd}$  and  $E_{nd}$  are the dynamic elastic modulus of water cooling and natural cooling and  $T$  is the heating temperature.

When the temperature is 100°C~300°C, the dynamic elastic modulus of two cooling methods increases with the temperature. While when the temperature exceeds 300°C, the dynamic elastic modulus of two cooling methods decreases. With the increase in temperature, the difference of the dynamic elastic modulus between two cooling methods first increases and then decreases. At 500°C, the difference is the largest, and the dynamic elastic modulus value of natural cooling is 28.13% higher than that of water cooling, indicating that water cooling significantly deteriorates the dynamic mechanical properties of high temperature sandstone. At 1000°C, the difference between two cooling methods decreases. The dynamic elastic modulus of natural cooling is 20.09 GPa and the dynamic elastic modulus of water cooling is 18.22 GPa, which are basically consistent. Hence, high temperature gradually becomes the main factor affecting the dynamic mechanical properties of sandstone, but water cooling still has a certain effect.

**3.7. Dynamic Strain and Strain Rate.** Dynamic strain of sandstone specimens after water cooling and natural cooling is shown in Figure 10.

As seen from Figure 10, the dynamic strain of water cooling sandstone specimens is greater than that of natural cooling. The dynamic strain of two cooling methods increases in a quadratic function with the temperature, as shown in the following equation:

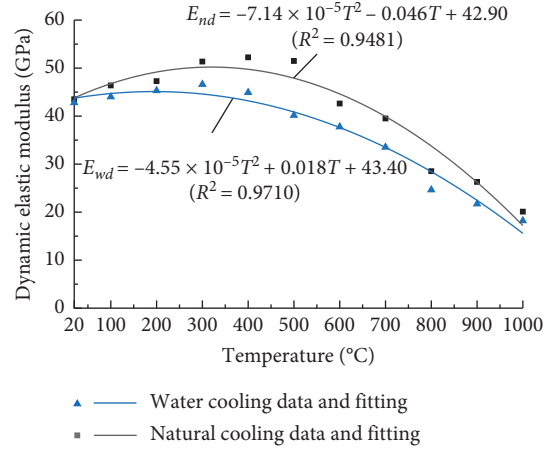


FIGURE 9: Dynamic elastic modulus of high temperature sandstone after two cooling methods.

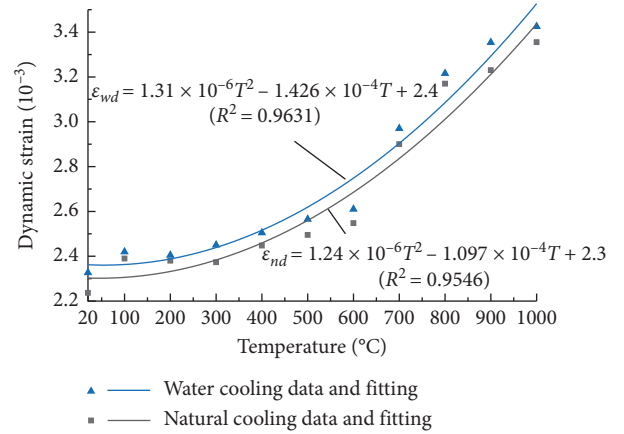


FIGURE 10: Dynamic strain of high temperature sandstone after two cooling methods.

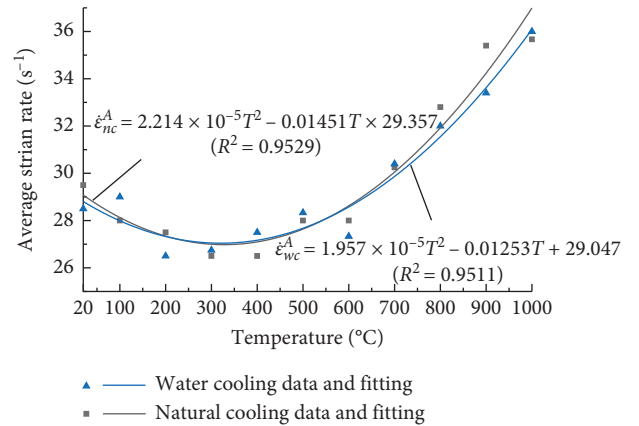























FIGURE 11: Average strain rate of high temperature sandstone after two cooling methods.



TABLE 3: Impact failure modes of high temperature sandstone after two cooling methods.

T (°C)	Water cooling	Natural cooling
20		
100		
200		
300		
400		
500		
600		
700		
800		
900		
1000		

$$\left. \begin{aligned} \varepsilon_{wd} &= 1.31 \times 10^{-6}T^2 - 1.426 \times 10^{-4}T + 2.4 \quad (R^2 = 0.9631), \\ \varepsilon_{nd} &= 1.24 \times 10^{-6}T^2 - 1.097 \times 10^{-4}T + 2.3 \quad (R^2 = 0.9546), \end{aligned} \right\} \quad (3)$$

where  $\varepsilon_{wd}$  and  $\varepsilon_{nd}$  are the dynamic strain of water cooling and natural cooling and  $T$  is the heating temperature.

When the temperature is 100°C~300°C, the dynamic strain of two cooling methods is not significantly affected by temperature. The dynamic strain of natural cooling and water cooling is  $2.24 \times 10^{-3}$ ~ $2.37 \times 10^{-3}$  and  $2.33 \times 10^{-3}$ ~ $2.45 \times 10^{-3}$ . From 400°C, the dynamic strain of two cooling methods begins to increase gradually, and the increase was the largest at 700°C.

Average strain rate of high temperature sandstone after two cooling methods has little difference. With the increase in temperature, the strain rate first decreases and then increases, and there is a quadratic function between strain rate and temperature, as shown in Figure 11.

**3.8. Impact Failure Modes of Specimens.** As seen from the impact failure modes listed in Table 3, the impact failure degree of sandstone specimens increases with the temperature and the impact failure degree of water cooling specimens is significantly greater than that of natural cooling. Corresponding to the variation of dynamic compressive strength and dynamic peak stress, the impact failure degree of two cooling methods first decreases and then increases with the increase in the heating temperature, which is basically consistent with the result of Ping et al. [31].

When the temperature is 400°C~1000°C, the failure degree of water cooling sandstone specimens is obviously greater than that of natural cooling and the degree of fragmentation increases with the increase in heating temperature. When the temperature is 900°C and 1000°C, the number of granular fragments of water cooling increases obviously and the color of fragments of water cooling is darker than that of natural cooling, which is black-brown. It shows that under the combined action of high temperature and water cooling, the iron oxide content in sandstone specimens increases significantly.

## 4. Conclusions

Natural cooling and water cooling are used to cool high temperature sandstone specimens with 11 temperature gradients ranging from room temperature (20°C) to 1000°C. Then, SHPB impact compression tests are carried out for sandstone specimens after heating and cooling under the same loading conditions. The conclusions are drawn as follows:

- (1) The volume expansion rate, mass loss rate, density reduction rate, and P-wave velocity reduction rate of sandstone specimens after two cooling methods are positively correlated with temperature in a quadratic function. The deteriorate rate of physical parameters of water cooling sandstone specimens is slightly larger than that of natural cooling. The P-wave velocity of sandstone decreases with the temperature.

When the temperature is 600°C, the P-wave velocity of specimens after two cooling methods decreases most. When the temperature is 700°C~1000°C, the P-wave velocity of natural cooling sandstone tends to be stable and no obvious decrease occurs while the P-wave velocity of water cooling continues to decrease.

- (2) The dynamic compressive strength of water cooling sandstone specimens is significantly lower than that of natural cooling. The dynamic compressive strength of water cooling and natural cooling first increases and then decreases with the temperature. At 300°C, the dynamic compressive strength of two cooling methods is the largest, and then dynamic compressive strength decreases in a quadratic function with the temperature. At 800°C and 900°C, the difference of dynamic compressive strength between water cooling and natural cooling is the largest, while the difference of dynamic compressive strength decreases at 1000°C. The dynamic elastic modulus of water cooling sandstone specimens is less than that of natural cooling. The dynamic elastic modulus of two cooling methods first increases and then decreases with the temperature. The maximum is at 300°C. At 1000°C, the difference of the dynamic elastic modulus between two cooling methods decreases.
- (3) The dynamic strain of water cooling sandstone specimens is greater than that of natural cooling. The dynamic strain of two cooling methods increases with the temperature. When the temperature is between 100°C and 300°C, the dynamic strain of two cooling methods is not obviously affected by the temperature. From 400°C, the dynamic strain value of two cooling methods begins to increase gradually, and the biggest increase is at 700°C. The average strain rate of two cooling methods is basically consistent, and the average strain rate is positively correlated with temperature in a quadratic function.
- (4) The impact failure degree increases with heating temperature, and the impact failure degree of water cooling sandstone specimens is significantly greater than that of natural cooling. The impact failure degree of two cooling methods first decreases and then increases with the temperature, which corresponds to the variation of dynamic compressive strength. At 900°C and 1000°C, the number of granular fragments of water cooling increases obviously, and the color of fragments of water cooling is darker than that of natural cooling, which is black-brown, indicating that the iron oxide content in sandstone specimens increases significantly under the combined action of high temperature and water cooling.

## Data Availability

The datasets generated and analyzed in the current study are obtained from the corresponding author upon reasonable request.

## Conflicts of Interest

The authors declare that they have no conflicts of interest regarding the publication of this paper.

## Acknowledgments

This research received financial supports from the National Natural Science Foundation of China (nos. 52074005, 52074006, and 51674008), Anhui Provincial Natural Science Foundation (no. 1808085ME134), and Anhui Postdoctoral Science Foundation (no. 2015B058). The authors would like to thank the State Key Laboratory of Mining Response and Disaster Prevention and Control in Deep Coal Mine, Engineering Research Center of Underground Mine Construction, Ministry of Education, and Anhui University of Science and Technology, for providing the experiment conditions.

## References

- [1] J. Yu, W. Yao, K. Duan, X. Liu, and Y. Zhu, "Experimental study and discrete element method modeling of compression and permeability behaviors of weakly anisotropic sandstones," *International Journal of Rock Mechanics and Mining Sciences*, vol. 134, pp. 1–14, Article ID 104437, 2020.
- [2] J. Yu, C. H. Ren, Y. Y. Cai, and W. Yao, "Analytical approach for evaluating the dynamic self-bearing capacity of tunnels," *International Journal of Geomechanics*, vol. 21, no. 8, pp. 1–15, Article ID 04021133, 2021.
- [3] N. N. Sirdesai, T. N. Singh, P. G. Ranjith, and S. Rajesh, "Effect of varied durations of thermal treatment on the tensile strength of red sandstone," *Rock Mechanics and Rock Engineering*, vol. 2017, no. 50, 213 pages, 2017.
- [4] S. Q. Yang, W. L. Tian, and J. P. Dong, "Experimental study on failure mechanical properties of granite with two grain sizes after thermal treatment," *Chinese Journal of Geotechnical Engineering*, vol. 43, no. 2, pp. 281–289, 2021.
- [5] L. S. Gao, Y. Xu, and B. B. Wu, "Dynamic compression strength of thermal damaged Fangshan marble on dry and saturated conditions," *Chinese Journal of Rock Mechanics and Engineering*, vol. 37, no. supp2, pp. 3827–3833, 2018.
- [6] Q. Ping, C. Zhang, H. Su, and H. Zhang, "Experimental study on dynamic mechanical properties and energy evolution characteristics of limestone specimens subjected to high temperature," *Advances in Civil Engineering*, vol. 2020, Article ID 8875568, 12 pages, 2020.
- [7] Q. Ping, M. Wu, P. Yuan, H. Su, and H. Zhang, "Dynamic splitting experimental study on sandstone at actual high temperatures under different loading rates," *Shock and Vibration*, vol. 2020, Article ID 8867102, 12 pages, 2020.
- [8] L. P. Zhi, J. Y. Xu, Z. Q. Liu, and S. Liu, "Research on impacting failure behavior and fluctuation characteristics of granite exposed to high temperature," *Chinese Journal of Rock Mechanics and Engineering*, vol. 32, no. 1, pp. 135–142, 2013.
- [9] L. Y. Zhang and X. B. Mao, "Experimental study of the mechanical effects of loading rates on limestone at high temperature," *Rock and Soil Mechanics*, vol. 31, no. 11, pp. 3511–3515, 2010.
- [10] Q. Ping, H. P. Su, D. D. Ma, H. Zhang, and C. Zhang, "Experimental study on physical and dynamic mechanical properties of limestone after different high temperature treatment," *Rock and Soil Mechanics*, vol. 42, no. 4, pp. 1–12, 2021.
- [11] Q. Ping, M. J. Wu, P. Yuan et al., "Experimental study on dynamic mechanical properties of high temperature sandstone under impact loads," *Chinese Journal of Rock Mechanics and Engineering*, vol. 38, no. 4, pp. 782–792, 2019.
- [12] S. Liu, J. Y. Xu, L. P. Zhi, and T. Chen, "Experimental research on mechanical behaviors of marble after high temperatures subjected to impact loading," *Chinese Journal of Rock Mechanics and Engineering*, vol. 32, no. 2, pp. 273–280, 2013.
- [13] Y. B. Li, Y. Zhai, and C. S. Wang, "Mechanical properties of Beishan granite under complex dynamic loads after thermal treatment," *Engineering Geology*, vol. 267, pp. 1–10, Article ID 105481, 2020.
- [14] B. P. Xi and Y. S. Zhao, "Experimental research on mechanical properties of water-cooled granite under high temperatures within 600°C," *Chinese Journal of Rock Mechanics and Engineering*, vol. 29, no. 5, pp. 892–898, 2010.
- [15] A. B. Jin, S. L. Wang, Y. D. Wei, H. Sun, and L. Wei, "Effect of different cooling conditions on physical and mechanical properties of high-temperature sandstone," *Rock and Soil Mechanics*, vol. 44, no. 11, pp. 3531–3539, 2020.
- [16] Z. N. Zhu, H. Tian, N. N. Dong, and B. Dou, "Experimental study of physico-mechanical properties of heat-treated granite by water cooling," *Rock and Soil Mechanics*, vol. 39, no. s2, pp. 169–176, 2018.
- [17] Z. P. Huang, Y. Zhang, Y. K. Sun, and C. Liu, "Mechanical and acoustic characteristics of high temperature limestone with water cooling treatment," *Journal of Central South University*, vol. 47, no. 12, pp. 4181–4189, 2016.
- [18] Z. P. Huang, Y. Zhang, and W. D. Wu, "Analysis of mechanical and wave properties of heat-treated marble by water cooling," *Rock and Soil Mechanics*, vol. 37, no. 2, pp. 367–375, 2016.
- [19] G. S. Han, H. W. Jing, and H. J. Su, "Experimental research on mechanical behaviors of water-cooled sandstone after high temperature treatment," *Journal of China University of Mining and Technology*, vol. 49, no. 1, pp. 69–75, 2020.
- [20] Y. Zhai, X. Q. Ai, Z. C. Deng, and W. He, "Influences of cooling mode and high temperature on concrete compressive strength," *Journal of Hunan University*, vol. 41, no. 11, pp. 74–80, 2014.
- [21] P. Wang, Y. L. Chen, and X. L. Zhou, "Impact of rapid cooling in water on residual mechanical properties of granite under high temperature," *Journal of Water Resources & Water Engineering*, vol. 24, no. 3, pp. 54–63, 2013.
- [22] X. C. Shi, L. Y. Gao, and J. Wu, "Effects of cyclic heating and water cooling on the physical characteristics of granite," *Energies*, vol. 13, Article ID 2136, 2020.
- [23] Q. Li, T. B. Yin, X. B. Li, and S. Zhang, "Effects of rapid cooling treatment on heated sandstone: a comparison between water and liquid nitrogen cooling," *Bulletin of Engineering Geology and the Environment*, vol. 2020, no. 79, 327 pages, 2020.
- [24] G. S. Han, H. W. Jing, and H. J. Su, "Effects of thermal shock due to rapid cooling on the mechanical properties of sandstone," *Environmental Earth Sciences*, vol. 78, Article ID 146, 2019.
- [25] T. D. Rathnaweera, P. G. Ranjith, X. Gu et al., "Experimental investigation of thermomechanical behaviour of clay-rich sandstone at extreme temperatures followed by cooling treatments," *International Journal of Rock Mechanics and Mining Sciences*, vol. 107, no. 107, pp. 208–223, 2018.
- [26] T. B. Yin, Q. Li, and X. B. Li, "Experimental investigation on mode I fracture characteristics of granite after cyclic heating

- and cooling treatments,” *Engineering Fracture Mechanics*, vol. 222, Article ID 106740, 2019.
- [27] Z. Zhu, H. Tian, G. Mei, G. Jiang, and B. Dou, “Experimental investigation on physical and mechanical properties of thermal cycling granite by water cooling,” *Acta Geotechnica*, vol. 15, no. 7, pp. 1881–1893, 2020.
- [28] Y. L. Zhu, J. Yu, and H. D. Gao, “Effect of water cooling on microscopic damage and dynamic properties of high-temperature granite,” *Explosion and Shock Waves*, vol. 39, no. 8, pp. 083104-1–083104-11, 2019.
- [29] Y. Zhai, Y. Li, Y. Li, W. Jiang, and X. Liu, “Research on the impact loading and energy dissipation of concrete after elevated temperature under different heating gradients and cooling methods,” *Materials*, vol. 11, no. 9, pp. 1–20, Article ID 1651, 2018.
- [30] International Society for Rock Mechanics (Isrm), “Suggested methods for determining tensile strength of rock materials,” *International Journal of Rock Mechanics and Mining Science & Geomechanics Abstracts*, vol. 15, no. 1, pp. 99–103, 1978.
- [31] Q. Ping, M. J. Wu, H. Zhang et al., “Experimental study on dynamic mechanical characteristics of sandstone under actual high temperature conditions,” *Chinese Journal of Underground Space and Engineering*, vol. 15, no. 3, pp. 691–698, 2019.

## Research Article

# Experimental Study on Seismic Response of Buried Oil and Gas Pipeline Soil Layers under Lateral Multipoint Excitation

Jianbo Dai <sup>1</sup>, Li Wang <sup>2</sup>, Chengtao Hu <sup>1</sup> and Guidi Zhang <sup>1</sup>

<sup>1</sup>*Xi'an Shiyu University, Xi'an 710065, China*

<sup>2</sup>*Shaanxi Zhongli Testing and Identification Co., Ltd., Xi'an 710077, China*

Correspondence should be addressed to Jianbo Dai; 184298843@qq.com

Received 7 May 2021; Accepted 1 July 2021; Published 10 July 2021

Academic Editor: Honglue Qu

Copyright © 2021 Jianbo Dai et al. This is an open access article distributed under the Creative Commons Attribution License, which permits unrestricted use, distribution, and reproduction in any medium, provided the original work is properly cited.

The seismic response of buried oil and gas pipelines is mainly influenced by the site soil. In this paper, a bidirectional laminar shear continuum model box is developed for the site response of buried oil and gas pipelines under transverse multipoint seismic excitation. By comparing the acceleration response of the soil and pipeline, monitoring the soil displacement, and analyzing the acceleration coefficient and Fourier spectrum, the seismic response characteristics of the soil at different excitation modes and peak seismic acceleration and its laws were investigated. The test results show that the soil under transverse excitation undergoes the process of soil compaction to nonlinear characteristics and finally soil damage, and the course of multipoint excitation develops faster and causes more serious soil damage. The peak Fourier spectrum of both the pipe and the soil appears at the frequency of 4–6 Hz, and in general, the acceleration of the pipe is greater than that of the soil; the difference between the two gradually decreases with the increase of loading level. Compared with the uniform excitation, the increase in the loading level during the lateral multipoint excitation will result in a decrease of the consistency of the acceleration time history curve at each measurement point and a decrease of the peak of the spectrum. The effect of laminar shear between soil bodies becomes more obvious with the increase of acceleration peaks on the shaking table. It is also found out that the excitation method has little effect on the displacement time history curve, but the multipoint excitation may cause fluctuations in the displacement time history curve.

## 1. Introduction

With the gradual improvement of oil and gas transportation pipeline networks, the local failure of oil and gas transportation pipeline networks caused by earthquakes often results in huge wealth losses. Due to factors such as length routs, multiple and complex geological conditions, and strong uncertainty of earthquakes, the seismic performance of pipelines has been a popular issue by various scholars [1]. Numerous studies have shown that the seismic response of buried oil and gas pipelines is mainly influenced by the vibration of the surrounding soil [2]; therefore, exploring the nonlinear seismic response of the site around buried pipelines is an effective way to study and analyze the design of pipeline seismic damage prevention and control.

Site response under seismic action is the basis for analyzing the seismic response of underground structures [3, 4]. Haydar and Bilge [5] and Yang and Yan [6] investigated the effect of nonlinear properties of soil on-site response and analyzed the influencing factors. Angshuma and Pradipta [7] studied the local effects of the site using nonlinear one-dimensional numerical analysis. Alireza et al. [8] evaluated four known nonlinear equivalence methods based on the seismic design of a subway tunnel in Tehran. Rashidov et al. [9] and Delong et al. [10] carried out numerical simulations of buried pipe-soil interactions to explore the changes in mechanical properties between pipes and soils during seismic action.

In conjunction with studies related to soil nonlinear response, Subramanian et al. [11], Yong et al. [12], and Ouyang et al. [13] carried out shaking table tests for long

tunnels and underground galleries under multipoint excitation to analyze the nonlinear characteristics of the soil around the structures, respectively. Junyan et al. [14] and Yan et al. [15] conducted shaking table tests for underground structures under nonuniform excitation separately in order to analyze the influence of soil type and burial depth of the underground structures on the structural response. They found out that the type of soil and the burial depth of the underground structure had a greater influence on the structural response, and the dynamic response of the site under multipoint excitation was more in line with the actual response during earthquakes than under uniform excitation. Buried pipes are redundant structures with axial dimensions much larger than their radial dimensions, causing different seismic waves to form at different points during earthquake propagation, rather than just a lag in the arrival time of the seismic waves. George et al. [16] conducted research and analysis on a multipoint seismic wave synthesis, providing a method for multipoint seismic wave input in shaking table tests.

Based on the above research, this paper designs a bidirectional laminated shear continuum model box, synthesizes three sets of coherent waves with different vibration waveforms as the input waves of two shakers based on seismic wave synthesis theory, conducts shaking table array tests of buried oil and gas pipelines under transverse multipoint seismic excitation, analyzes the seismic response law of the soil around buried oil and gas pipelines under different ground vibrations, different peak seismic accelerations, and different excitation methods, and provides a reference for subsequent simulation analysis and pipeline design.

## 2. Experimental Investigation

**2.1. Simulate Relationship and Test Material.** The test is a scaled-down model test, with the complete model for the pipe and the ignored gravity model for the soil. Considering the limitations of the test site conditions, a similarity ratio design was carried out for the length ( $l$ ), modulus of elasticity ( $E$ ), density ( $\rho$ ), stress ( $\sigma$ ), strain ( $\epsilon$ ), acceleration ( $a$ ), and gravitational acceleration ( $g$ ) of the model based on the similarity ratio principle and volume analysis [17], and the obtained material similarities are as shown in Table 1.

The cross-sectional size of the prototype pipe was 1422 mm  $\times$  33.3 mm. Combining the dimensions of the model box used and the similar ratio design, it was determined that the pipe was made of L245 type longitudinal resistance welded steel pipe with a cross-sectional size of 14 mm  $\times$  3.0 mm and a length of 3500 mm, and the internal pressure was 8 MPa. The specific parameters of the pipe material are shown in Table 2. The soil used in the test is saturated sand with a density of 1.78 g/cm<sup>3</sup>, the corresponding moisture content is 14.1%, the internal friction angle is 28.5°, and the cohesion is 10.6 kPa.

TABLE 1: Simulate relationship.

Material	$S_l$	$S_E$	$S_\rho$	$S_\sigma$	$S_\epsilon$	$S_f$	$S_\alpha$	$S_g$
Pipeline	1/10	1/10	1	1/10	1	3.16	1	1
Soil	1/10	1/4	1	1/4	1	5	2.5	1

### 2.2. Bidirectional Laminar Shear Continuum Model Box.

The test was carried out on a shaking table at the Hunan Provincial Key Laboratory of Structural Vibration and Wind Resistance, with two shaking tables of 1000 mm  $\times$  1000 mm in size and spacing of 2000 mm between the two adjacent shakers. The shaking table uses a three-parameter servo control system to control the acceleration of the input table, which enables bi-directional four degrees of freedom loading, with a maximum speed of  $\pm$  400 mm/s in the horizontal direction and a maximum displacement of  $\pm$  75 mm in the horizontal direction.

For this test, a bidirectional laminated shear continuum model box [18] was developed, with an outer diameter of 4160 mm  $\times$  840 mm  $\times$  940 mm and an inner diameter of 3900 mm  $\times$  600 mm  $\times$  800 mm. The box is divided into three main sections: each section is connected by an articulated extension device and the left and right sections are placed on the table, with the two ends of the middle section resting on the edge of the table to bear the weight of the middle section. The box is made up of nine layers of independent frames stacked together along the height direction; each layer of the frames is provided with grooves and built-in balls to connect them, to ensure that horizontal laminar shearing can occur during vibration. To prevent excessive deformation of the box when the table surface increases in acceleration, limit plates are provided on each frame layer on both sides of the box and limit ropes are also provided in the middle section of the box. The soil is loaded into the box in four layers, after each layer of soil is loaded, compaction is then carried out and sensors or pipes are buried. The final site layout and model is shown in Figure 1.

**2.3. Measurement Point Arrangement.** To study the seismic response of the soil from top to bottom during the test loading process, three monitoring surfaces were arranged along the length of the box, and three groups of sensors were placed along with the height of the soil in each monitoring surface, with the height of each sensor being 150 mm, 360 mm, and 650 mm, respectively. The acceleration measurement points are M11–M33 and displacement sensors are D11–D33. The measurement points on the pipe (A1–A5) are equipped with three-way acceleration sensors at 750 mm intervals from 250 mm from the end of the pipe to monitor the acceleration changes of the pipeline. The layout of the soil acceleration sensors and displacement meters and pipeline acceleration sensors is shown in Figure 2.

TABLE 2: Mechanical properties of the pipeline.

Material	Diameter (mm)	Thickness (mm)	Yield strength (MPa)	Tensile strength (MPa)	Internal pressurization (MPa)
L245	140	3	245	415	8



FIGURE 1: Design of the test model box. (a) Site layout of the model box. (b) Design of the model box.

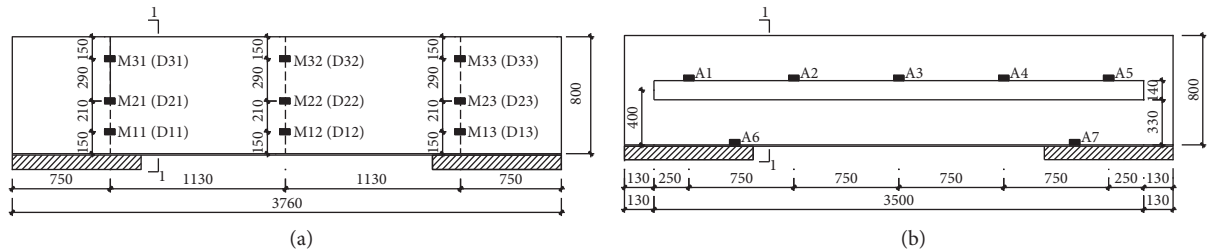


FIGURE 2: Layout of measuring point. (a) Layout of acceleration and displacement sensors in soil. (b) Layout of acceleration sensors in the pipeline.

**2.4. Seismic Wave Selection and Test Conditions.** The EL-Centro wave (E wave) and Wenchuan wave (W wave) were chosen as the original seismic waves in the experiment. Based on the multipoint seismic wave synthesis theory, the reciprocal power spectrum model was applied and the coherence between the two points was used to make corrections in the original seismic waves based on the coherent amplitude and coherent phase angle. This results in a time course of seismic waves at two different locations considering spatial correlation.

The experiment uses artificial randomly synthesized multipoint seismic waves (R-wave) as an approximate transformation relationship based on the response spectrum and power spectrum and generates a mutual power spectrum matrix using the coherence function to form the total power spectrum matrix. The power spectrum matrix is used to generate the Fourier amplitude spectrum at each point, and a fast Fourier transform is performed from the amplitude and phase spectra to obtain the smooth acceleration time course at each point. The smooth time course is then multiplied by the intensity envelope function to obtain the ground shaking time course that satisfies the time-frequency nonsmoothness. Finally, the final acceleration timescale is output by long-period filtering and baseline adjustment. The synthesis of the two multipoint excitation seismic waves was programmed using MATLAB software, and after similar ratio conversion and peak adjustment, seismic waves with

acceleration peaks of 0.25 g, 0.5 g, 1.0 g, and 1.55 g were input to the loading table to simulate 7 degrees', 8 degrees', 9 degrees', and 9 degrees' rare earthquakes, respectively. Figure 3 shows the time course curves of the three multipoint excitation seismic waves with adjusted acceleration peak of 0.25 g.

The two coherent waves were used as input waves for the two shaking tables for multipoint input, while the same seismic waves converted by similarity ratio were input directly at both tables at the same time for uniform input, and the tables were input in the order of gradually increasing amplitude from 0.25 g to 1.55 g to analyze the damage pattern and seismic response of the model at different acceleration peaks. The specific loading conditions are shown in Table 3.

### 3. Test Results and Analysis

**3.1. Experimental Macroscopic Reaction Phenomena.** By comparing the macroscopic response of the soil layer during the uniform and multipoint excitation, it was found that the variation of the model soil box was small for the input table peak acceleration of 0.25 g and 0.50 g under lateral uniform excitation and the soil and box were in a stable vibration state. There was no obvious change on the surface of soil at this time. At the third stage of loading (1.00 g), the movement of the soil box increased, and both top and bottom of

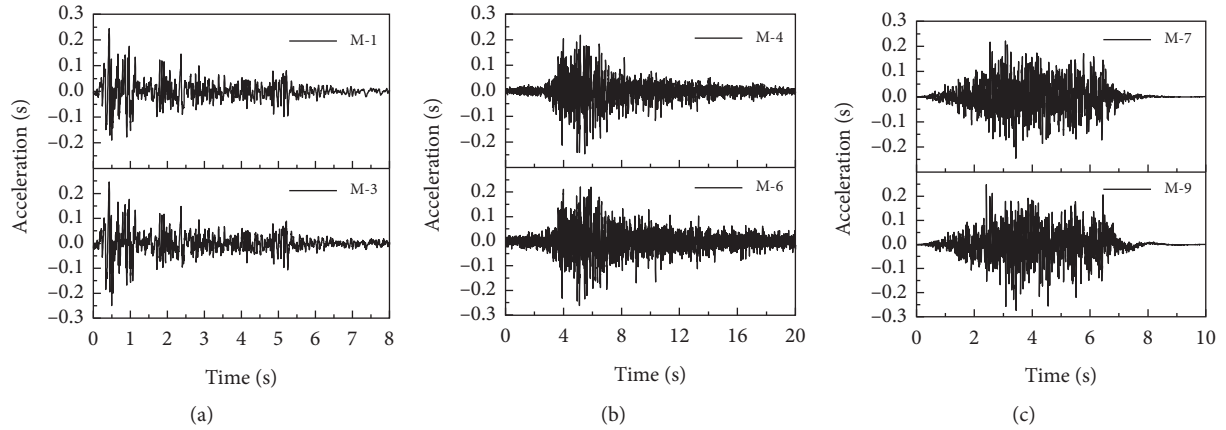


FIGURE 3: Multipoint seismic wave of the platform. (a) EL-Centro waves. (b) Wenchuan waves. (c) Artificial waves.

TABLE 3: Working condition of the test.

Working condition	Uniform excitation			Working condition	Multipoint excitation			Remarks
	Amplitude (g)	Table 1	Table 2		Amplitude (g)	Table 1	Table 2	
1	0.25	M-1	M-1	2	0.25	M-1	M-3	
3	0.25	M-4	M-4	4	0.25	M-4	M-6	7 degrees
5	0.25	M-7	M-7	6	0.25	M-7	M-9	
7	0.50	M-10	M-10	8	0.50	M-10	M-12	
9	0.50	M-13	M-13	10	0.50	M-13	M-15	8 degrees
11	0.50	M-16	M-16	12	0.50	M-16	M-18	
13	1.00	M-28	M-28	14	1.00	M-28	M-30	
15	1.00	M-31	M-31	16	1.00	M-31	M-33	9 degrees
17	1.00	M-34	M-34	18	1.00	M-34	M-36	
19	1.55	M-37	M-37	20	1.55	M-37	M-39	
21	1.55	M-40	M-40	22	1.55	M-40	M-42	9.5 degrees
23	1.55	M-43	M-43	24	1.55	M-43	M-45	

the box began to exhibit large displacement, while the displacement of the central soil body was relatively small due to the constraints of the oil and gas pipeline, at which time the soil cracks appeared and gradually propagated in all directions. At the final stage of loading (1.55 g), the soil gradually loosened due to large shear deformation, and the nonlinear characteristics of the soil gradually became obvious. With the continuous application of the load, local subsidence occurred at the end of the soil box and the soil was damaged.

The macroscopic response phenomena under lateral multipoint seismic excitation are similar to those under uniform excitation. However, the soil deformation under multipoint excitation is significantly larger compared with uniform excitation when the peak acceleration of the table is less than 0.50 g, and fine cracks begin to appear on the surface of the soil. When the peak acceleration of the table is 1.00 g, the soil box has a serpentine motion of each layer of the frame, and the inconsistent motion of each layer of the frame leads to large shear deformation of the soil, and the soil starts to show nonlinear characteristics. When the peak acceleration of the table reaches 1.55 g, the movement of the soil box is huge, and the upper limit bolts of each layer of the soil box frame collide with the limit plate, making a large

sound, and the soil body is seriously damaged. The final damage state of the soil body is shown in Figure 4.

Comparing the macroscopic response phenomena of the soil box and soil under uniform and multipoint excitation, the macroscopic response phenomena observed under different excitation methods are similar, but the deformation of the soil box and soil is relatively more obvious during multipoint excitation. The deformation of the soil box and the soil is relatively obvious during the multipoint excitation. During the first two levels of loading, the deformation of the two boxes is the same and the soil body is in the compaction process, but as the loading level increases, the overall deformation of the model produced by the multipoint excitation is greater than that of the unanimous excitation.

**3.2. Time Course Analysis of the Pipe and Surrounding Soil Acceleration.** In order to analyze the acceleration response of the pipe and the surrounding soil, the seismic response of the Wenchuan wave was used as the research object, and the acceleration time curves and Fourier spectra of the pipe and the soil at the peak acceleration of 0.25 g and 1.55 g on the table were extracted for comparison. The acceleration time curve and Fourier spectrum are shown in Figures 5 and 6.





FIGURE 4: Final failure state of soil. (a) Left side. (b) Right side.

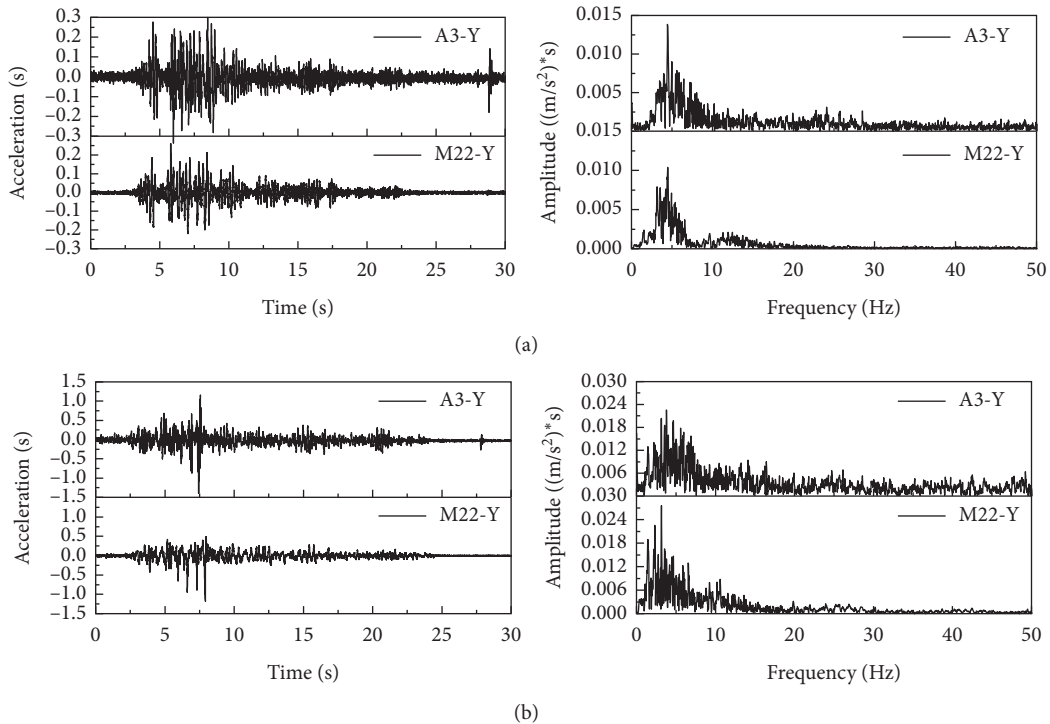


FIGURE 5: Acceleration time history and Fourier spectrum of pipeline and soil under uniform excitation. (a) 0.25 g. (b) 1.55 g.

Figure 5 shows the acceleration time response curves and Fourier spectra of the pipe and the soil for the table acceleration peaks of 0.25 g and 1.55 g under uniform lateral excitation. The peak acceleration of the pipe is slightly greater than the peak acceleration of the soil, at which time the soil in the soil box is in a compacted state, and the pipe moves in concert with the surrounding soil. The Fourier spectra of the pipe and the soil are the same, but the peak point composition of the pipe spectrum is richer than that of the soil. When the peak acceleration of the platform is 1.55 g, due to the large deformation of the soil box and the soil, the shear deformation of the soil is serious. The pipe and soil acceleration time curve is more different and the soil has many peak points while the peak points in the pipe appear in the 6~8 s. The peak acceleration of the pipe is about 1.2 times that for the soil. The peak of the Fourier spectrum is slightly smaller than that of the soil.

Figure 6 shows the acceleration time response curves and Fourier spectra of the pipe and the soil for the table

acceleration peaks of 0.25 g and 1.55 g under multipoint excitation. At the first stage (0.25 g), there is a difference between the acceleration time curves of the pipe and the soil, with multiple peak points in the pipe acceleration, and the peak is significantly larger than the peak of the soil acceleration. At the fourth-stage (1.55 g) loading, the vibration frequency and acceleration peak of the pipe are still relatively large, and the peak size of the Fourier spectrum of the pipe and the soil changes, with the peak point of the soil spectrum exceeding that of the pipe gradually. The reason for this is that at the last stage of loading the soil is loose and the mutual restraint between soil and pipe is weakened, and the pipe is basically in a free vibration state while the soil vibration is still restrained by the acceleration of the table.

Comparing the acceleration response of the pipe and soil at uniform and multipoint excitation, it can be concluded that the pipe acceleration is greater than the soil acceleration at all levels of loading, and this gradually decreases as the peak acceleration of the input table increases. The Fourier

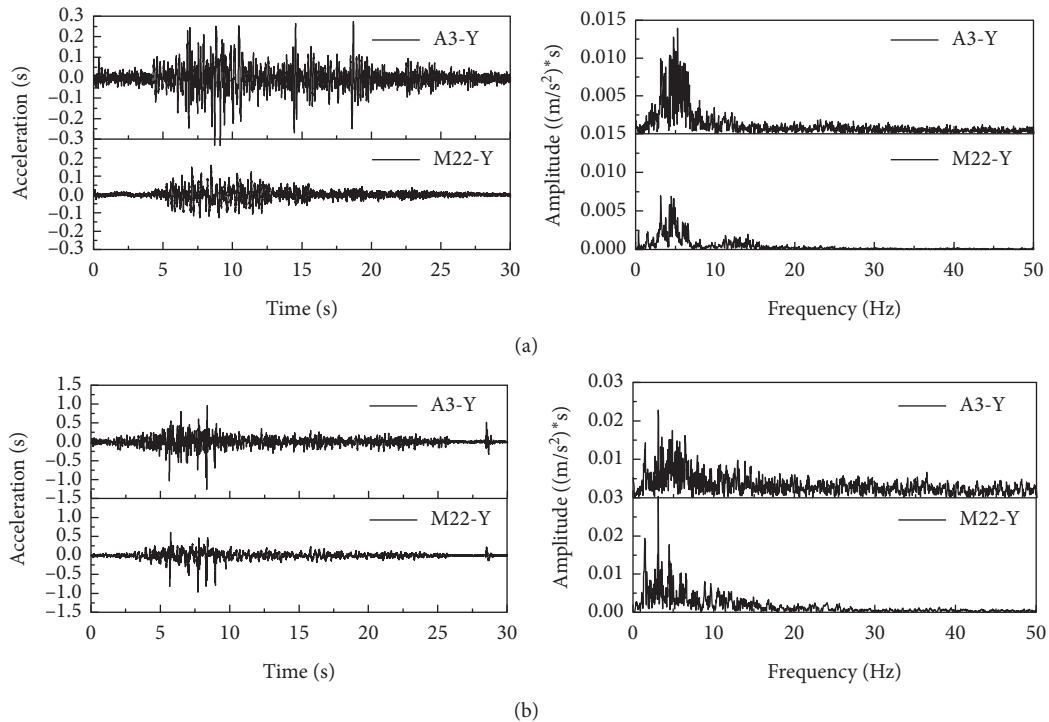


FIGURE 6: Acceleration time history and Fourier spectrum of pipeline and soil under multipoint excitation. (a) 0.25 g. (b) 1.55 g.

spectrum of the pipe is richer than that of the soil, with the peak of the pipe spectrum larger than that of the soil when the peak acceleration of the table is small. As the table becomes large, the peak of the soil spectrum gradually increases and exceeds that of the pipe.

**3.3. Acceleration Amplification Factor.** The study shows that the presence of buried pipes affects the seismic response state of the soil around the pipes. The variation curve of the soil acceleration amplification coefficient of the model soil box when extracting different ground shaking effects is shown in Figures 7 and 8. It can be found that the peak acceleration of the soil with the height of the measurement point shows a tendency to decrease initially and then increase.

Under the uniform excitation, the acceleration amplification coefficients at the bottom measurement points are all around 1 at the first stage of loading. When the height of the measured points increases, the peak acceleration of both E and W waves increases. And the peak acceleration of the soil exceeds that of the table, which is up to 1.26 times the peak acceleration of the table, while the R wave only produces acceleration amplification at the surface of the soil. As the peak acceleration of the table increases, the soil acceleration amplification curve shrinks more significantly at the elevation of the pipe, and the acceleration amplification factor generated by the soil in the box is less than 1 at this time.

The acceleration trends of the soil under different ground vibrations are the same for multipoints excitation. At the first stage of loading, the W and R wave amplification coefficients were similar, both of them converged at the

measurement point where the pipe was laid, the amplification effect of the soil at the bottom and middle of the table under the action of E wave was not obvious, and the acceleration amplification coefficient at the top measurement point was larger due to the loose soil, reaching 1.35. With the increase of the loading level, the acceleration amplification coefficient of the soil decreased compared with the first stage of loading, and the contraction of each measurement point was obvious at the height of 360 mm. The reason for this is that the multipoint excitation causes the two ends of the pipe to vibrate in different directions and with different amplitudes, resulting in greater disturbance of the soil by the pipe and significant changes in the peak acceleration of the soil.

Both the difference in excitation method and type of earthquake and loading level have important effects on the change of acceleration amplification coefficient of the soil. At the same loading level, the acceleration amplification coefficients at each measurement point shrink more significantly at the pipe elevation, indicating that the shear deformation of the soil is greater and more likely to enter the nonlinear development phase. At the same time, the values of acceleration amplification coefficients and their reduction at the central measurement point are significantly greater than at the remaining measurement points, indicating that the burial of the pipe causes the acceleration amplification coefficients of the surrounding soil to contract significantly.

**3.4. The Impact of Buried Pipelines on the Seismic Response of the Site.** In order to further analyze the trend of soil acceleration with the height of the measurement points, the acceleration time courses of acceleration measurement point

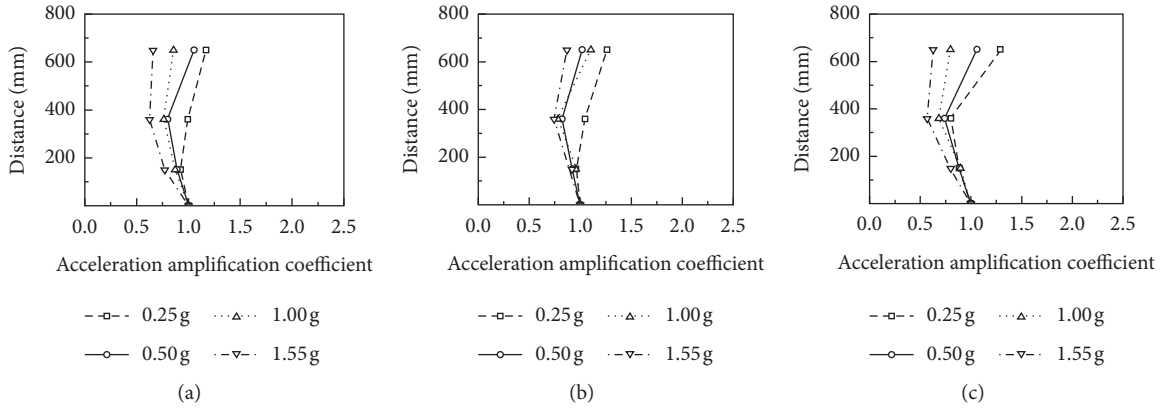


FIGURE 7: Uniform excitation. (a) EL-Centro waves. (b) Wenchuan waves. (c) Artificial waves.

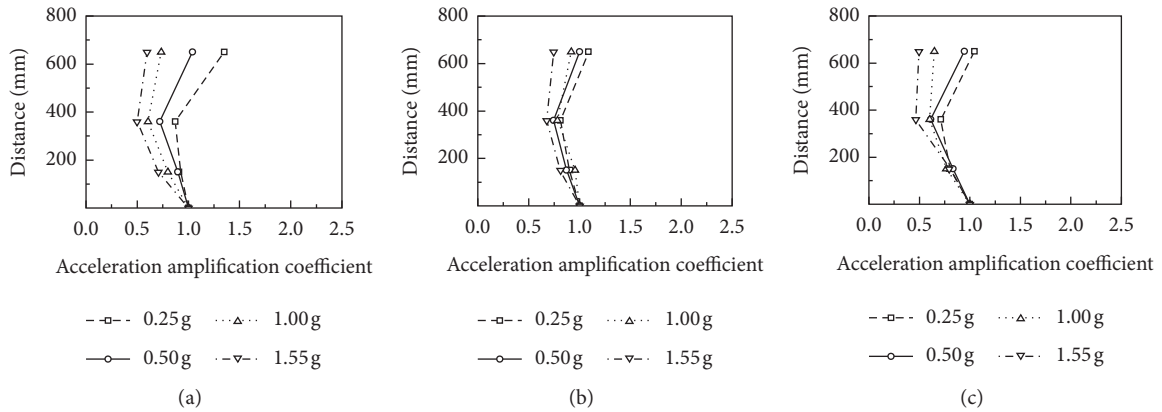


FIGURE 8: Multipoint excitation. (a) EL-Centro waves. (b) Wenchuan waves. (c) Artificial waves.

M11, M21, and M31 were extracted for analysis at uniform and multipoint excitation. Due to the length restrictions of the paper, the authors selected the soil acceleration variation data under the action of W wave for processing and obtained the soil acceleration time course curve and its Fourier spectrum at 0.25 g and 1.55 g loading as shown in Figures 9 and 10.

Figure 9 shows the acceleration time curve and its Fourier spectrum of each measuring point for different loading levels under uniform lateral excitation. It is obvious that the waveforms of the acceleration time course curves at different height measurement points are similar when the first level (0.25 g) is loaded, and the difference between the peak acceleration of the soil and that of the table is not large, about 0.25 g. When comparing the Fourier spectra of the different height measurement points, the peak of the spectrum at the bottom measurement point is generally smaller, while that at the middle and upper measurement points occurs at 4–7 Hz, with the largest value reaching  $0.013 \text{ (m/s}^2) \cdot \text{s}$ . At the last level (1.55 g), the consistency of the acceleration time course curve of each measurement point becomes worse, the difference between the acceleration of the soil at the bottom and that of the table is not large, but the peak acceleration of the soil at the middle and upper

part is smaller than that of the table, and the degree of reduction is obvious. When comparing the Fourier spectra of each measurement point, it was found that the peak Fourier spectra of the soil at the bottom increased significantly with respect to the primary loading, with multiple peaks in the frequency range of 0–20 Hz, while the peak Fourier spectra of the soil in the middle and upper parts of the box showed relatively small increases.

Figure 10 shows the acceleration time curves and their Fourier spectra at each measuring point for peak acceleration of 0.25 g and 1.55 g on the table under lateral multipoint excitation. It can be seen that when the peak acceleration of the table is 0.25 g, the peak acceleration of the soil at the bottom and upper measurement points is close to that of the input table, while the peak acceleration of the soil in the middle is slightly smaller than the other measurement points due to the constraints of the pipe. At this time, the soil is in the compaction process, and the overall change in the acceleration time curve is small. The Fourier spectrum amplitude at the bottom shows multiple peaks, which is different from the Fourier spectrum characteristics of the measurement point during the uniform excitation, indicating that the multipoint excitation will have an amplifying effect on the peak of the soil at the bottom. The middle and upper measurement points of

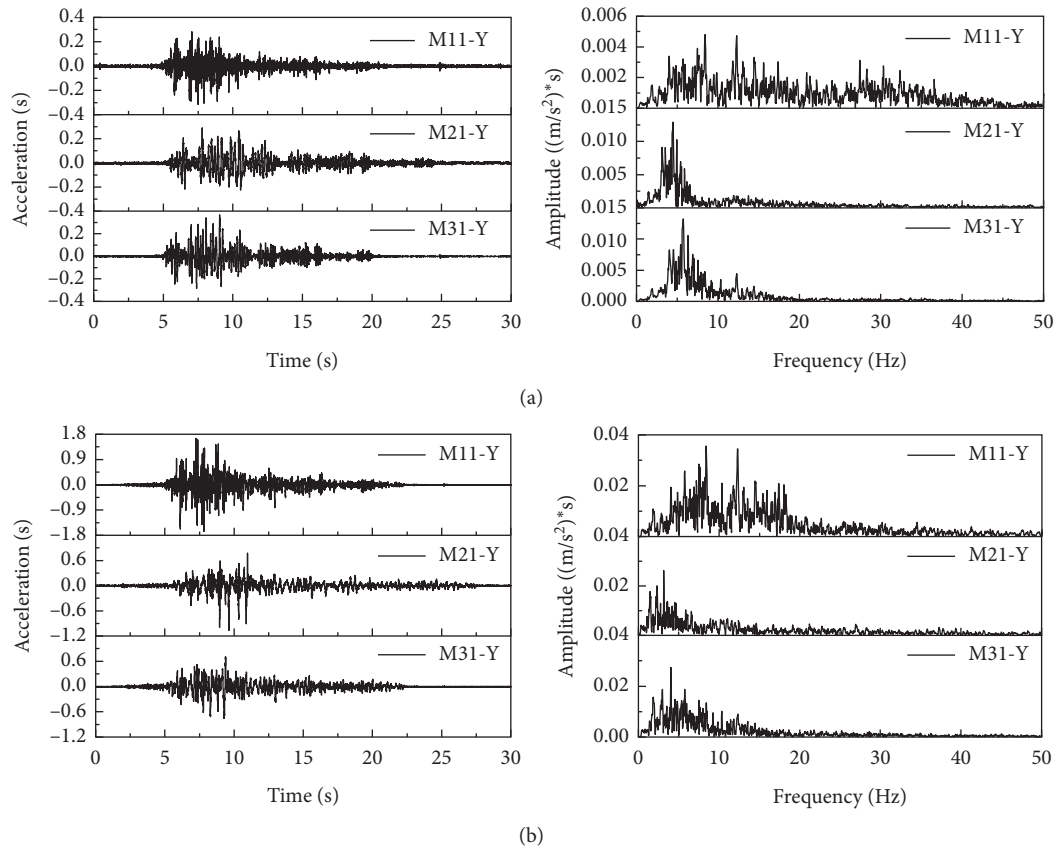


FIGURE 9: Uniform excitation. (a) 0.25 g. (b) 1.55 g.

the soil also show amplifying effect but the Fourier spectrum waveform does not change much compared to the uniform excitation. When the peak acceleration of the table is 1.55 g, the waveforms of the acceleration time curve of the soil at different heights differ greatly, with the increase of the height of the measurement point; the peak acceleration amplification effect of the soil shows a trend of first weakening and then increasing, in which the peak acceleration of the measurement point M21 near the pipe is the smallest. At this time, the Fourier spectrum of the bottom measurement point still maintains the characteristics of multipeak, but the peak of the spectrum is reduced; the peak of the spectrum of the central and upper measurement points slightly increased compared to the low loading level.

Comparing the acceleration peaks and spectrum peaks of each measurement point during uniform and multipoint excitation, it was found that the consistency of the acceleration time curve of each measuring point gradually decreases with the increase of loading level, and this situation is especially obvious during multipoint excitation. When the peak acceleration of the table is small, the peak Fourier spectrum of the uniform excitation is larger than that of the multipoint excitation. At 1.55 g multipoint excitation, the peak acceleration of the soil is generally larger than that of the uniform excitation, and the peak

Fourier spectrum of the multipoint excitation also exceeds that of the uniform excitation.

**3.5. The Displacement Response of the Soil Layer.** The displacement curves with time for different heights of the measurement points within the table acceleration of 0.25 g and 1.55 g are presented in Figures 11 and 12. The distance of measurement points D11, D21, and D31 from the bottom of the soil box is 150 mm, 360 mm, and 650 mm, respectively.

At a peak table acceleration of 0.25 g, the soil is in the compaction process and shows highly holistic. The soil deformation under uniform and multipoint excitation is small, and the overall difference in its peak displacement is not significant, 9 mm and 8 mm, respectively. The displacement time curve formed under multipoint excitation is relatively more fluctuating, and the displacement time curve at the bottom measurement point is different from that at the middle and top, and the soil produces residual displacement in the late stage of the loading. When the peak acceleration of the table increases to 1.55 g, the soil exhibits obvious non-linear characteristics and the displacement time curve waveform is similar to that at low loading levels, but the displacement increases significantly, up to four times that at

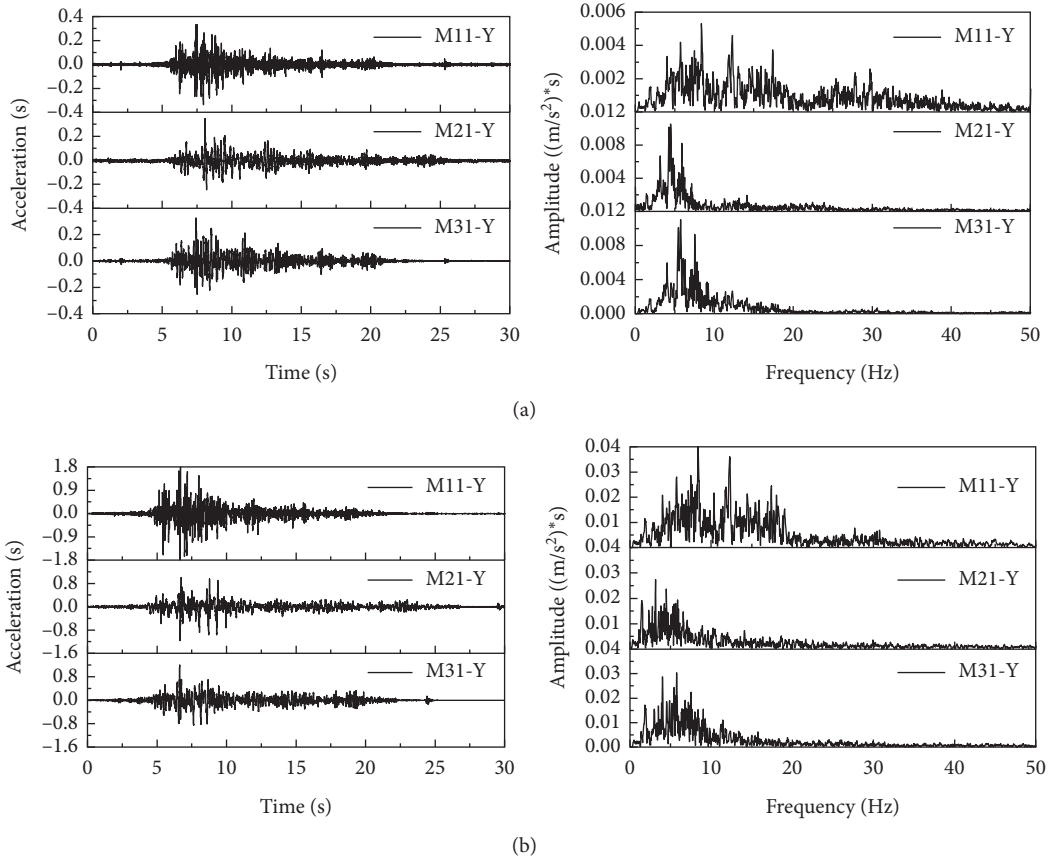


FIGURE 10: Multipoint excitation. (a) 0.25 g. (b) 1.55 g.

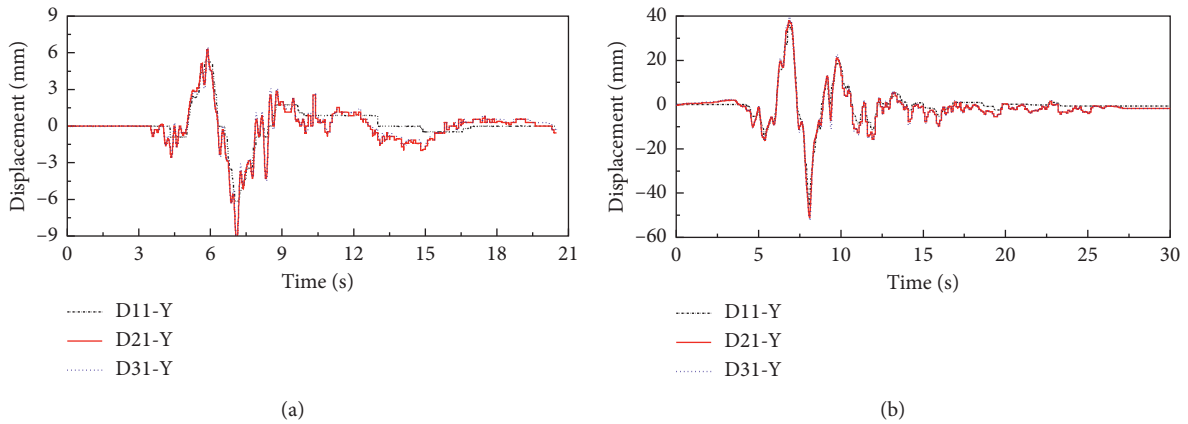


FIGURE 11: Uniform excitation. (a) 0.25 g. (b) 1.55 g.

0.25 g. Comparing the displacement curves of different elevation measurement points at the same time, it was found that, at the early stage of loading, the movement direction of each measurement point was the same and the displacement values did not differ greatly, and the shearing effect between soil layers was weak. With the increase of

loading time, the displacement of each measurement point in the soil gradually increases, and the inconsistent movement speed of each layer causes the soil to undergo laminar shear, and as the peak acceleration of the table increases, the layer shear effect between each measurement point becomes more obvious.

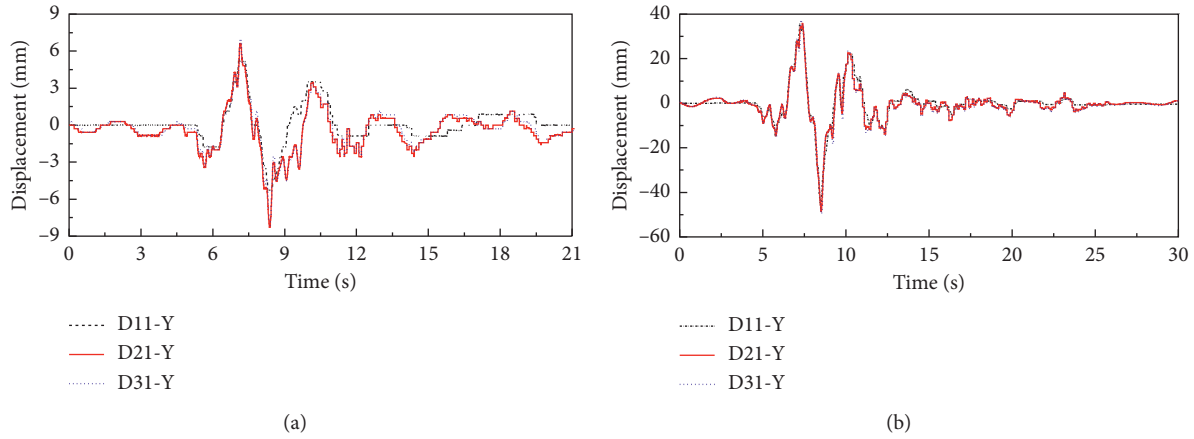


FIGURE 12: Multipoint excitation. (a) 0.25 g. (b) 1.55 g.

#### 4. Conclusion

In this paper, the seismic response of the soil around buried oil and gas pipelines and their variation characteristics are analyzed through shaking table tests of buried pipelines under lateral uniform and multipoint excitation, and the main conclusions obtained are shown as follows:

- (1) The soil exhibits the same trend with increasing loading levels for both lateral uniform and multipoint excitation: the soil undergoes a process of compaction-surface crack development, pronounced nonlinear characteristics, soil damage, with the soil developing faster and causing more serious soil damage during multipoint excitation compared to uniform excitation.
- (2) Compared with uniform excitation, the peak acceleration of the pipe is slightly higher than that of the soil at multiple points of excitation, and the difference between the two decreases as the loading level increases, with the peak acceleration of the soil exceeding that of the pipe at a table acceleration of 1.55 g. The peak Fourier spectrum of both the pipe and soil occurs at frequencies of 4–6 Hz under the loading, and the Fourier spectrum of the pipe is richer than that of the soil.
- (3) The acceleration amplification coefficient of the soil tends to decrease and then increase as the elevation of the measurement point increases; the amplification coefficient of the tube circumference shrinks significantly under multipoint excitation. The increase of loading level will cause the waveform consistency of the acceleration response curve of the soil at different elevations worse. At this time, the peak of the Fourier spectrum at multipoint excitation exceeds that of the uniform excitation, which has a greater impact on the seismic response of the soil.
- (4) The waveforms of the displacement time curves are similar for both uniform and multipoint excitation, and the acceleration time curves at each measurement point do not vary significantly with elevation;

under seismic excitation, the shear effect between the soil layers becomes more obvious with the increase of the peak acceleration at the table. Compared with uniform excitation, the displacement time curves of multipoint excitation show smaller fluctuations, but the overall effect of the excitation method on the soil displacement is not significant [19].

#### Data Availability

The data used to support the findings of this study are available from the corresponding author upon request.

#### Conflicts of Interest

The authors declare that they have no conflicts of interest.

#### Acknowledgments

The authors gratefully acknowledge the National Natural Science Foundation of China (grant no. 51808446) (Research on Disaster Mechanism and Seismic Performance of Long Distance Oil and Gas Pipelines under Multi-Dimensional and Multi-Support Earthquake Excitation) and Key Research and Development Program of Shaanxi (grant no. 2019SF-266) (Research on Stress Detection and Safe Operation Monitoring System for Oil and Gas Pipelines in Service).

#### References

- [1] M. Castiglia, T. Fierro, and F. Santucci de Magistris, "Pipeline performances under earthquake-induced soil liquefaction: state of the art on real observations, model tests, and numerical simulations," *Shock and Vibration*, vol. 2020, Article ID 8874200, 20 pages, 2020.
- [2] P. Burkov, C. Wu, V. Burkov, and S. Burkova, "FEM analysis of soil-pipe interaction," *AIP Conference Proceedings*, vol. 1863, no. 1, pp. 1–4, 2017.
- [3] A. Vishwajit and S. R. Satish Kumar, "Seismic soil-structure interaction: a state-of-the-art review," *Structure*, vol. 16, pp. 317–326, 2018.

- [4] A. Haydar and S. Bilge, "A comparative study on linear and nonlinear site response analysis," *Environmental Geography*, vol. 50, no. 8, pp. 1193–1200, 2006.
- [5] A. Haydar and S. Bilge, "Effect of nonlinearity on site response and ground motion due to earthquake excitation," *Bulletin of Engineering Geology and the Environment*, vol. 69, pp. 287–293, 2010.
- [6] J. Yang and X. R. Yan, "Factors affecting site response to multi-directional earthquake loading," *Engineering Geology*, vol. 107, no. 3-4, pp. 77–87, 2009.
- [7] D. Angshunan and C. Pradipta, "Influence of motion energy and soil characteristic on seismic ground response of layered soil," *International Journal of Civil Engineering*, vol. 18, no. 7, pp. 763–782, 2020.
- [8] R. Alireza, K. Mohanmmadreza, and H. Mir Raouf, "Numerical investigation of closed-form solution for seismic design of a circular tunnel lining (by quasi-static method)," *Civil Engineering Journal*, vol. 4, no. 1, pp. 239–257, 2018.
- [9] T. R. Rashidov, T. Yuldashev, and D. A. Bekmirzaev, "Seismodynamics of underground pipelines with arbitrary direction of seismic loading," *Soil Mechanics and Foundation Engineering*, vol. 55, no. 4, pp. 243–248, 2018.
- [10] H. Delong, T. Aiping, and W. Zhongyue, "Analysis of pipe-soil interactions using goodman contact element under seismic action," *Soil Dynamics and Earthquake Engineering*, vol. 139, Article ID 106290, 2020.
- [11] M. Subramanian, G. Pearce, O. K. Guldu et al., "Multi-point shaking table test of a long tunnel subject to non-uniform seismic loadings," *Bulletin of Earthquake Engineering*, vol. 16, no. 2, pp. 1041–1059, 2018.
- [12] Y. Yong, Y. Haitao, and L. Chong, "Multi-point shaking table test for long tunnels subject to non-uniform seismic loadings-part I: theory and validation," *Soil Dynamics and Earthquake Engineering*, vol. 108, pp. 177–186, 2018.
- [13] Z. Ouyang, J. Cui, R. Luo, and P. Li, "Shaking table test of seismic response of immersed tunnels under the influence of multiple factors," *Shock and Vibration*, vol. 2020, Article ID 8858486, 17 pages, 2020.
- [14] H. Junyan, M. Hesham Ei Naggarb, H. Benwei et al., "Nonlinear soil response under non-uniform seismic excitation form multi-point shaking table teats," *Soil Dynamics and Earthquake Engineering*, vol. 139, Article ID 106342, 2020.
- [15] K. Yan, J. Zhang, Z. Wang, W. Liao, and Z. Wu, "Seismic responses of deep buried pipeline under non-uniform excitations from large scale shaking table test," *Soil Dynamics and Earthquake Engineering*, vol. 113, pp. 180–192, 2018.
- [16] T. George, J. Virieux, and R. Madariaga, "Seismic wave synthesis by Gaussian beam summation: a comparison with finite difference," *Geophysics*, vol. 52, no. 8, pp. 1065–1073, 2012.
- [17] G. Fatih, S. Murat, and C. Erkan, "Small shaking table testing and numerical analysis of free-field site response and soil-structure oscillation under seismic loading," *Bulletin of Engineering Geology and the Environment*, vol. 79, no. 6, pp. 2949–2969, 2020.
- [18] P. C. Li and H. Wang, "A novel strategy for the crossarm length optimization of PSSCs based on multi-dimensional global optimization algorithms," *Engineering Structures*, vol. 238, Article ID 112238, 2021.
- [19] X. Li, X. Wang, L. Li et al., "Design and performance test of 3D laminar shear container for shaking table," *Rock and Soil Mechanics*, vol. 38, no. 5, pp. 1524–1532, 2017.

## Research Article

# Push Plate Test of CRTS II Slab Ballastless Track: Theoretical Analysis, Experiments, and Numerical Simulation

Yu Liu <sup>1,2</sup>, Qianqi Xu <sup>1</sup>, Xiaodan Sun <sup>1</sup>, Guotao Yang <sup>3</sup>, and Guotang Zhao <sup>3</sup>

<sup>1</sup>School of Civil Engineering, Southwest Jiaotong University, Chengdu 610031, China

<sup>2</sup>Key Laboratory of High-Speed Railway Engineering, Ministry of Education, Southwest Jiaotong University, Chengdu 610031, China

<sup>3</sup>Department of Science, Technology and Information Technology, China Railway, Beijing 100844, China

Correspondence should be addressed to Yu Liu; liuyu@swjtu.edu.cn

Received 28 April 2021; Accepted 7 June 2021; Published 21 June 2021

Academic Editor: Honglue Qu

Copyright © 2021 Yu Liu et al. This is an open access article distributed under the Creative Commons Attribution License, which permits unrestricted use, distribution, and reproduction in any medium, provided the original work is properly cited.

Push plate test is a powerful tool to evaluate the interfacial bond performance of China railway track structure type-II slab ballastless track structure (CRTS II SBTS). However, there is still a lack of theoretical explanation of the push plate test. In this paper, a linear proportional distribution method is proposed in terms of a series of analytical formulas to describe the interfacial force-displacement variation of CRTS II SBTS in different damage stages of the horizontal push plate test. The force-displacement relationship established by the linear proportional distribution method agrees well with that observed in full-scale test. The horizontal push plate test is then simulated, in which a bilinear cohesive zone model (CZM) was adopted to simulate the interface within track structure. The parameters of the CZM are calculated based on the force-displacement curves obtained from scale push plate test. Particularly, the normal cohesive parameters are determined based on the scale vertical push plate test instead of the traditional splitting tensile test. The simulation proves that both the maximum affected length in the undamage stage and the maximum damaged length in the damage stage depend rather on the interfacial stiffness and the material parameters of SBTS than the horizontal load. These two lengths given by the simulation are close to those defined by the proposed linear proportional distribution method. This indicates the reliability of the proposed method and the capability of scale push plate test in determining cohesive parameters.

## 1. Introduction

China railway track structure type-II slab ballastless track structure (CRTS II SBTS) is widely used for high-speed railway (HSR) of China because it can provide high rail smoothness and ensure high comfort, stability, and safety of high-speed train. It is firstly applied in the Beijing-Tianjin HSR in 2008 and then utilized in the Beijing-Shanghai HSR in 2011. The total mileage of the CRTS II SBTS application is over 9,000 km, about 26% of the total mileage of China HSR. CRTS II SBTS is a layered structure that consists of the track slab made of reinforced, the cement asphalt mortar (referred to as CA mortar hereinafter) layer, and the base made of concrete, as illustrated in Figure 1. A perfect bond of the interfaces between the CA mortar layer and the track slab as

well as the base is the key to ensure the stability and durability of CRTS II SBTS. However, under the daily cyclic thermal load [1, 2] and the repeated living load of the train [3], the interfacial bond is likely to degrade or fail, leading to the discontinuous and nonuniform distribution of the interfacial stress, and hence the initiation or expansion of delamination [4].

In the early stage of the CRTS II SBTS application, the interfacial bond behavior was evaluated by a single index of interfacial bond strength observed in in-situ push plate test [5]. The bond behavior between the track slab and the CA mortar layer was considered qualified if the interfacial bond strength meets the standard. However, the single index of interfacial bond strength is incapable to explain a large number of interfacial damage and delamination that are



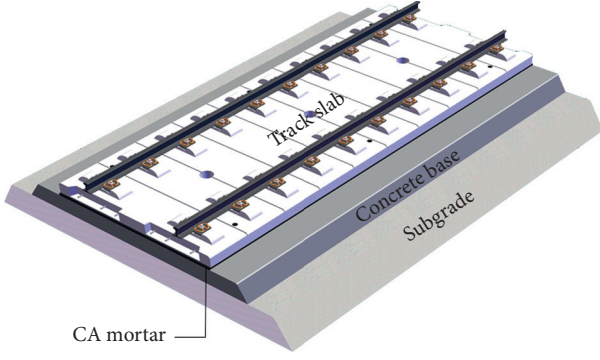


FIGURE 1: Diagram of the CRTS II SBTS on subgrade.

observed in CRTS II SBTS in recent years. Therefore, finite element analysis (FEA) together with fracture mechanics theory has been introduced to interpret the initiation and evolution of the interfacial damage [6, 7]. In the FEA, CRTS II SBTS is regarded as a layered composite structure. The interface between the CA mortar layer and the track slab is simulated by the cohesive zone model (CZM) [8, 9]. The parameters of the CZM are usually determined by the push plate test of CRTS II SBTS. However, because of the high cost and the high requirements for the test site and test equipment, only very rare push plate test are full scale that use real CRTS II SBTS [10, 11]. Most existed experimental studies are scale push plate test [12] which are relatively cheaper, simpler, and practical to be repeated in large quantities. One problem of the scale push plate test is that if the specimen is too small, the interfacial bond may fail too quick after loading to obtain the expected force-displacement relationship curve. Compared to the numerous experimental studies of push plate test, there is no study that presents a theoretical explanation for the interfacial force-displacement variation during push plate test. Considering the cost of the experiment, it is worth trying to establish theoretical formulas to describe the interfacial force-displacement relationship of CRTS II SBTS. In addition, a theoretical solution of the interfacial force-displacement relationship would help to validate whether the commonly used CZM and the cohesive parameters obtained from push plate test are reliable for the use of FEA.

On the other hand, the push plate test carried out so far are all horizontal push plate test that can only provide tangential force-displacement relationship and tangential cohesive parameters. No vertical push plate test has been reported. The normal cohesive parameters used in most simulations are obtained from splitting tensile test [13–16]. In the splitting tensile test, the normal cohesive parameters are determined based on the normal strain at several specific points. The normal cohesive parameter determined in this way has large randomness because it strongly depends on the bond behavior of the CA mortar of the selected local area. It cannot represent the overall bond behavior of the entire interface and the real changing of the force-displacement variation. To make the FEA of the interfacial damage evolution closer to reality, a real normal force-displacement relationship is required to calculate realistic normal cohesive

parameters, which strongly suggests the need to carry out vertical push plate test.

In this paper, the theoretical analysis of the force-displacement variation of the interface during the horizontal push plate test of CRTS II SBTS is conducted. A scale vertical push plate test and a scale horizontal push plate test are carried out to determine the normal and tangential cohesive parameters, respectively. The calculated cohesive parameters are then adopted in the FEA for a CRTS II SBTS model by which the evolution of the interfacial damage is reproduced. The scope of this work is to explore the force-displacement variation during the push plate test, determine the parameters that better describe the interfacial bond behaviour of CRTS II SBTS than the single index of interfacial bond strength, and clarify whether the interfacial parameters obtained from the scale push plate test can be used in the FEA of the full-scale push plate test.

## 2. Theoretical Analysis of Horizontal Push Plate Test

In this section, the CZM used to describe the bond performance of the interface is introduced and a new method in terms of a series of analytical formulas to construct the force-displacement relationship in the push plate test is proposed.

*2.1. Bilinear CZM.* The bilinear CZM in fracture mechanics theory is employed to characterize the force-displacement variation in the entire loading process, as shown in Figure 2. Assume that  $\sigma_n$ ,  $\sigma_t$ , and  $\sigma_s$  are the interfacial stresses in the normal and two tangential directions, respectively. For a tangentially isotropic interface,  $\sigma_t = \sigma_s$ . As seen from Figure 2, the force-displacement curve increases linearly at the early stage of loading, with the slope of the stiffness  $E_n$  and  $E_s$  for the normal and tangential direction, respectively. When the force-displacement curve reaches the peak, the interfacial damage initiates, which can be quantitatively judged by the Quads criterion:

$$\left(\frac{\langle \sigma_n \rangle}{\sigma_n^0}\right)^2 + \left(\frac{\sigma_t}{\sigma_t^0}\right)^2 + \left(\frac{\sigma_s}{\sigma_s^0}\right)^2 \geq 1, \quad (1)$$

where  $\langle \sigma_n \rangle = (\sigma_n + |\sigma_n|)/2$ . The stress for the moment of the damage initiation is called interfacial strength,  $\sigma_n^0$  and  $\sigma_t^0$  for the normal and tangential direction, respectively, while the corresponding displacement is  $\delta_n^0$  and  $\delta_s^0$ , respectively. Therefore,  $E_n = \sigma_n^0/\delta_n^0$  and  $E_s = \sigma_s^0/\delta_s^0$ .

The bilinear CZM also assumes a linear softening evolution after damage initiation. Thus, the stress after damage initiation can be given by

$$\begin{cases} \sigma_n = (1 - D)E_n\delta_n, \\ \sigma_s = (1 - D)E_s\delta_s, \end{cases} \quad (2)$$

where  $D$  represents the overall damage in one cohesive element, which is zero initially and then gradually evolves from 0 to 1 upon further loading [17]:

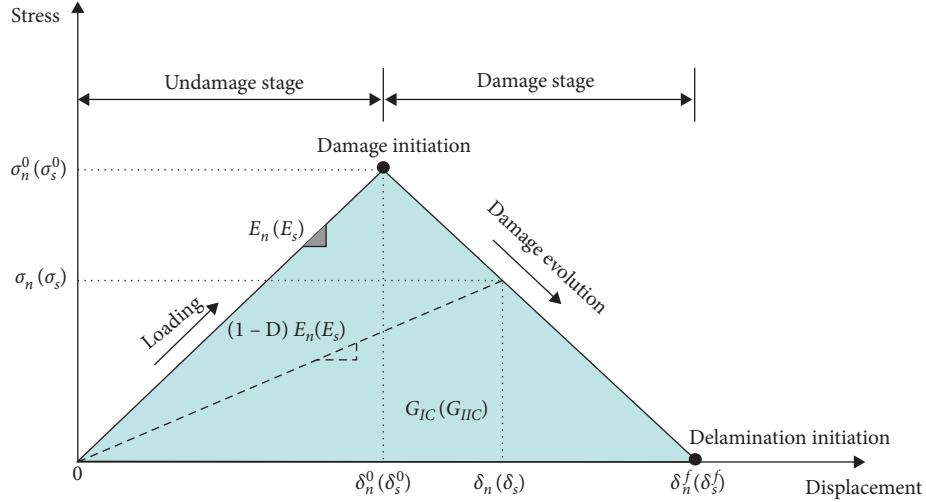


FIGURE 2: Bilinear CZM for the damage evolution.

$$D = \frac{\delta_m^f(\delta_m - \delta_m^0)}{\delta_m(\delta_m^f - \delta_m^0)}, \quad (3)$$

where  $m = n$  for the normal direction and  $m = s$  for the tangential direction. When  $D$  equals to 1, delamination occurs. Assuming  $\delta_n^f$  and  $\delta_s^f$  are the normal and tangential displacement for the moment of the delamination occurrence, respectively the fracture toughness in the normal and tangential direction,  $G_{IC}$  and  $G_{IIC}$ , can be measured by the area of the triangle in Figure 2,  $G_{IC} = (1/2)\sigma_n^0\delta_n^f$  or  $G_{IIC} = (1/2)\sigma_s^0\delta_s^f$ .

**2.2. Force-Displacement Variation in Push Plate Test.** In this section, the force-displacement relationship of CRTS II SBTS during the horizontal push plate test is theoretically analyzed with the aid of the bilinear CZM. A standard single CRTS II SBTS is 6.45 meter long. For this length, the longitudinal compression deformation of the track slab cannot be neglected in the horizontal displacement of the track slab. The zone with longitudinal compression deformation becomes larger as the loading continues. To sufficiently represent the zone that is affected by the load, a scenario long track slab is assumed. Note that, this long track slab is not actually a longitudinally continuous system of several single track slabs. It is uniform and isotropic without any discontinuity. The stress and displacement of the scenario track slab under horizontal load is first calculated. Then, the stress and displacement of a single track slab for different damage stages can be determined by directly taking the part on the scenario track slab that is undamaged, partially damaged, or completely damaged. The details of this method, the linear proportional distribution method, are demonstrated below.

In the horizontal push plate test, the force is applied at the leftmost end of the scenario track slab. When the horizontal push force is low and the maximum tangential stress on the track slab is less than  $\sigma_s^0$ , the scenario track slab will not be damaged. The tangential stress distribution along

the scenario track slab is as shown in Figure 3(a), with the maximum tangential stress appears at the loading end. Both the displacement and the tangential stress vary linearly on the slab. Assuming the length of the slab that is affected by the horizontal load (with nonzero tangential stress, referred to as the maximum affected length hereinafter) to be  $L_0$  and the right end of  $L_0$  to be the origin of coordinates (point O in Figure 3(a)), the cross-section compressive strain for point  $x$  will be

$$\varepsilon_x = \frac{\sigma_x}{E} = \frac{1}{2} \frac{\sigma_s}{E} \frac{x^2}{L_0 h} = \frac{1}{2} \frac{E_s}{E} \frac{x^2}{L_0 h} \delta_s, \quad (4)$$

where  $h$  and  $E$  are the thickness and elastic modulus of the slab, respectively. Therefore, the longitudinal displacement at the left end of the slab can be calculated by

$$\int_0^{L_0} \varepsilon_x dx = \int_0^{L_0} \frac{1}{2} \frac{E_s}{E} \frac{x^2}{L_0 h} \delta_s dx = \frac{1}{6} \frac{E_s}{E} \frac{L_0^3}{L_0 h} \delta_s. \quad (5)$$

At the left end of the slab, equation (5) should be equal to  $\delta_s$ , which gives

$$L_0 = \sqrt{\frac{6Eh}{E_s}}. \quad (6)$$

As seen from equation (6),  $L_0$  relates only to  $E$ ,  $h$ , and  $E_s$  and is not horizontal load dependent.

Once the maximum tangential stress exceeds  $\sigma_s^0$ , damage is initiated at the loading end and the stress at the loading end starts to decrease. As the loading continues, the damage extends towards the other end of the slab and the location of the maximum stress moves towards the other end. At the moment, when the tangential stress at the loading end reduces to zero and the displacement at the loading end equals to  $\delta_s^f$ , delamination occurs. At this moment, the damage extends to a certain point where the tangential stress equals  $\sigma_s^0$  and the displacement equals  $\delta_s^0$ . Taking this point as the origin of coordinates (point O in Figure 3(b)), the left of point O is the maximum damaged zone within which the

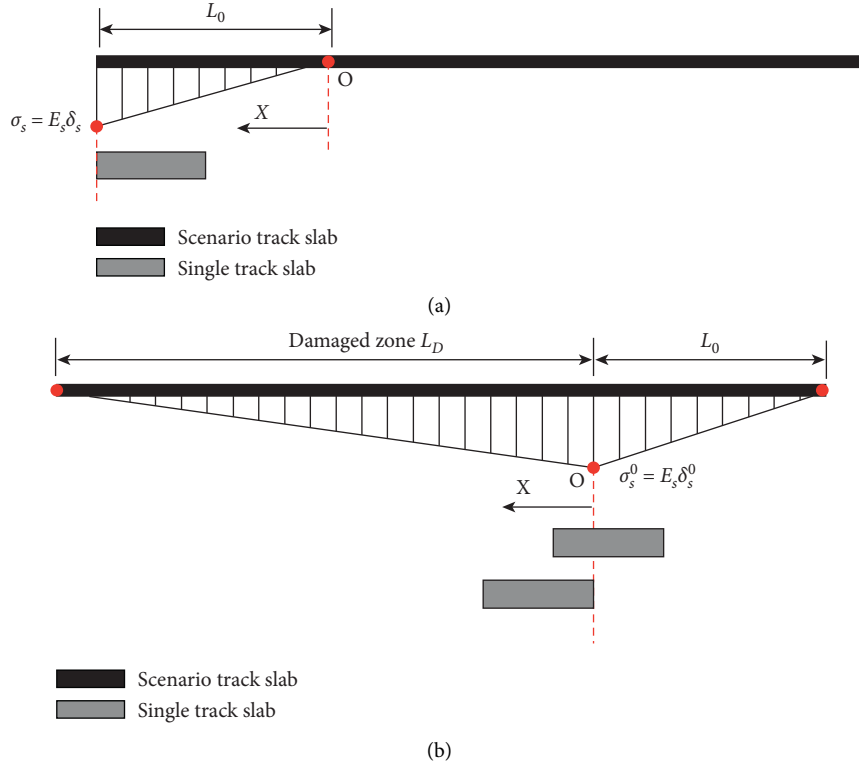


FIGURE 3: Linear proportional distribution of stress of a single track slab.

stress linearly decreases to zero at the loading end. The right part of point O is not damaged, within which the stress also linearly decreases to zero. The maximum damaged length is assumed to be  $L_D$ .

According to the bilinear CZM in Figure 2, the tangential stress in the damage stage is  $\sigma_s = \sigma_s^0 \cdot (\delta_s^f - \delta_s) / (\delta_s^f - \delta_s^0)$ . At the loading end,  $\delta_s = \delta_s^f$ ; thus,  $\sigma_s = 0$ . For any  $x$  between the loading end and point O, the tangential stress is

$$\sigma_{s-x} = \left(1 - \frac{x}{L_D}\right) \sigma_s^0. \quad (7)$$

Taking the right portion of point O as the analytical object, the cross-section compressive stress at point O is

$$\sigma_{c-o} = \frac{\sigma_s^0 L_0}{2h}. \quad (8)$$

Taking the left portion of point O as the analytical object, the cross-section compressive stress at  $x$  is

$$\sigma_{c-x} = \sigma_{c-o} + \frac{\sigma_{s-x} + \sigma_s^0}{2} \cdot x. \quad (9)$$

Hence, the compressive deformation at the loading end can be calculated by

$$\int_0^{L_D} \frac{\sigma_{c-x}}{E} dx = \frac{1}{E} \int_0^{L_D} \left\{ \sigma_{c-o} + \frac{\sigma_{s-x} + \sigma_s^0}{2} \cdot x \right\} dx = \frac{\sigma_s^0}{2Eh} \left( L_0 \cdot L_D + \frac{2}{3} L_D^2 \right). \quad (10)$$

The longitudinal displacement at the loading end equals the sum of the longitudinal displacement at point O and the compressive deformation at the loading end:

$$\delta_s^f = \delta_s^0 + \frac{\sigma_s^0}{2Eh} \left( L_0 \cdot L_D + \frac{2}{3} L_D^2 \right). \quad (11)$$

Equation (11) gives

$$\frac{2}{3} L_D^2 + L_0 \cdot L_D = (\delta_s^f - \delta_s^0) \frac{2Eh}{\sigma_s^0}. \quad (12)$$

Assuming that  $\lambda = L_D/L_0$ , equation (12) can be further simplified as

$$\frac{2}{3} \lambda^2 + \lambda = \frac{1}{L_0^2} (\delta_s^f - \delta_s^0) \frac{2Eh}{\sigma_s^0}. \quad (13)$$

According to equation (6),  $L_0$  is fixed for constant  $E$ ,  $E_s$ , and  $h$ ; thus, equation (13) turns to be

$$\frac{2}{3} \lambda^2 + \lambda - \frac{1}{3} \frac{\delta_s^f - \delta_s^0}{\delta_s^0} = 0, \quad (14)$$

which gives

$$\lambda = \frac{1}{4} \left[ -3 + \sqrt{9 + \frac{8(\delta_s^f - \delta_s^0)}{\delta_s^0}} \right]. \quad (15)$$

As seen from equation (15),  $L_D$  is also horizontal load independent. It only depends on  $E$ ,  $h$ ,  $E_s$ ,  $\delta_s^0$ , and  $\delta_s^f$ .

Using equations (6) and (15),  $L_0$ ,  $L_D$ , and the displacement and tangential stress at any point on the scenario slab can be determined. On the basis of this, the displacement and stress of a single track slab for different damage stages can be calculated by locating the single track slab on the scenario track slab according to the condition of whether the single track slab is undamaged, partially damaged, or completely damaged.

A single track slab that is not damaged can be considered as being located entirely in the undamaged zone of the scenario track slab, as illustrated in Figure 3(a). The tangential stresses at the left and right end of the single track slab  $\sigma_{sl}$  and  $\sigma_{sr}$  are

$$\begin{aligned} \sigma_{sl} &= E_s \delta_s, \\ \sigma_{sr} &= \frac{L_0 - L}{L_0} E_s \delta_s, \end{aligned} \quad (16)$$

where  $L$  is the length of the single track slab. The horizontal load is then calculated by

$$F_H = \frac{2L_0 - L}{2L_0} E_s \delta_s \cdot LB. \quad (17)$$

A single track slab that is damaged can be considered as being located partially or fully in the damaged zone of the scenario track slab, as illustrated in Figure 3(b). For a partially damaged single track slab,  $\sigma_{sl}$  and  $\sigma_{sr}$  are

$$\begin{aligned} \sigma_{sl} &= \frac{L_D - x}{L_D} E_s \delta_s^0, \\ \sigma_{sr} &= \frac{L_0 - (L - x)}{L_0} E_s \delta_s^0, \end{aligned} \quad (18)$$

where  $x$  is the length of the portion on the single track slab that is damaged,  $x = ((\delta_s - \delta_s^0)/(\delta_s^f - \delta_s^0))L_D$ ; then, the horizontal load is given by

$$F_H = E_s \delta_s^0 \cdot \left[ L - \frac{x^2}{2L_D} - \frac{(L - x)^2}{2L_0} \right] B. \quad (19)$$

If the single track slab is completely damaged, it can be considered as being located entirely in the damaged zone of the scenario slab. Then,  $\sigma_{sl}$  and  $\sigma_{sr}$  are

$$\begin{aligned} \sigma_{sl} &= (1 - D) E_s \delta_s, \\ \sigma_{sr} &= \frac{L_D}{L_D - L} (1 - D) E_s \delta_s, \end{aligned} \quad (20)$$

and the horizontal load will be

$$F_H = \frac{2L_D - L}{2(L_D - L)} (1 - D) E_s \delta_s \cdot LB. \quad (21)$$

The flowchart of the use of the linear proportional distribution method is illustrated in Figure 4. For any single track slab with given  $E$ ,  $E_s$ , and  $h$  and cohesive parameters of  $\delta_s^0$  and  $\delta_s^f$ ,  $L_0$  and  $L_D$  can be determined; hence, the force-displacement relationship can be constructed using equations (17), (19), and (21). The force-displacement curve constructed by this method is compared to that observed in the full-scale push plate test. Two full-scale test are used for the comparison. One is carried out by the Max Bögl company and the other is presented in [10]. The comparison of the force-displacement curves is shown in Figure 5. In general, the theoretical curve constructed by the linear proportional distribution method agrees well with the tested curve. Differences could be observed for the displacement less than 0.5 mm in Figure 5(a). This is not surprising considering the linear assumption of the stress variation in the undamage stage of the bilinear CZM. Differences are also seen between the displacement range of (0.02 mm, 0.32 mm) in Figure 5(b). This may indicate that when the interfacial stiffness (the slope of the curve in the undamage stage) is large, a greater horizontal load than the theoretical estimation is needed to make the damage initiate. Note that, both of the two tested curves exhibit three stages that differ from the two-stage assumption in the bilinear CZM. There is an apparent stage between the undamage stage and damage stage, in which the track slab is partially damaged due to the existence of the longitudinal compression deformation, as revealed in [10]. This stage is well defined by equation (19), which makes the proposed analytical formulas an effective and reliable tool for the quantitative analysis of the entire evolution process of the interfacial damage in the horizontal push plate test.

### 3. Scale Push Plate Tests for CZM Parameters

The horizontal push plate test is then simulated using the finite element analysis (FEA). In the FEA, the interface between the track slab and the CA mortar layer is simulated using cohesive elements. To determine the cohesive parameters of the CZM, two-scale push plate test are carried out, including a scale vertical push plate test and a scale horizontal push plate test for the determination of the normal and tangential cohesive parameters, respectively. Figure 6(a) shows the scheme and in-situ setup of the scale vertical push plate test. The test is carried out 28 days after the CA mortar is grouted into the track structure. The track slab is lifted vertically with the load applied at the midpoint of the track slab. Two dial gauges are placed 20 cm away from the midpoint at each side. The thicknesses of the track slab and the CA mortar layer are 20 cm and 3 cm, respectively, which are the same as the real track structure. The base is integrally poured with a thickness of 30 cm. In order to meet the requirements of the minimum loading area of the jack in the vertical push plate test and ensure the uniform distribution of the load, a 20 cm by 20 cm loading area is reserved in the middle of the specimen. At each side of the loading

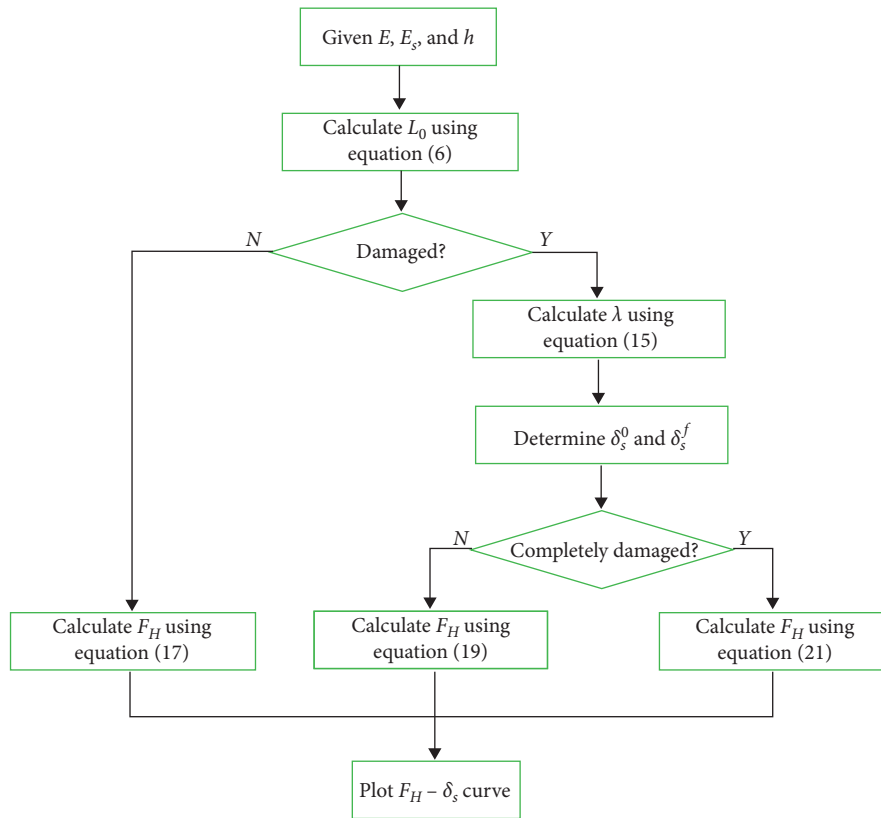


FIGURE 4: Flowchart of the use of the linear proportional distribution method.

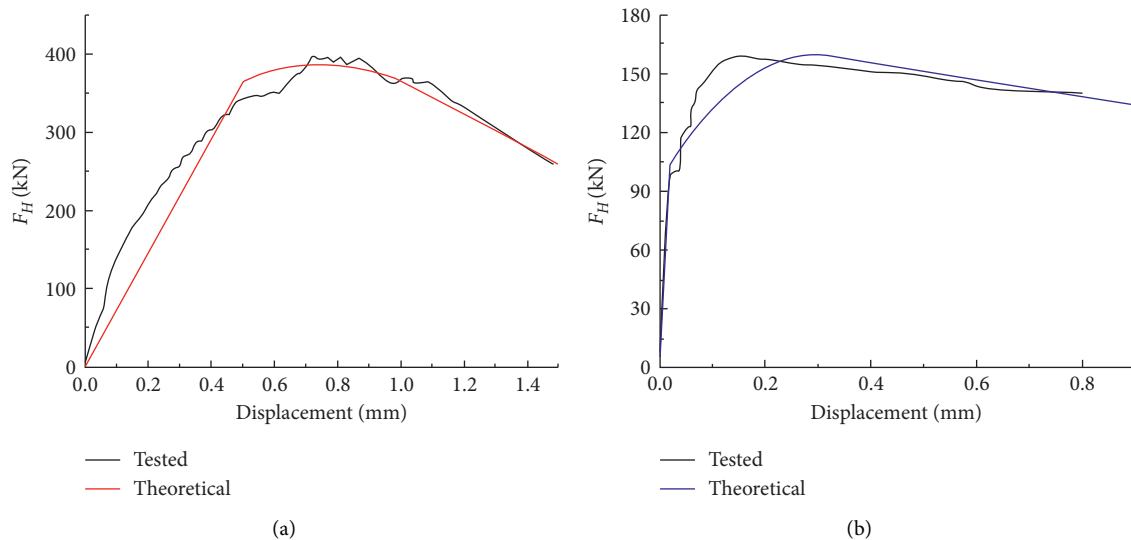


FIGURE 5: Comparison of force-displacement relationships constructed by the proposed method and full-scale test. (a) Max Bögl company; (b) [10].

area, an area of 20 cm by 20 cm is designed for the track slab to be bonded with the base so that the stress of the interface is uniform and symmetrical. Therefore, the total length of the track slab is 60 cm and the width is 20 cm. Figure 6(b) shows the scheme and in-situ setup of the scale horizontal

push plate test. The size of the specimen is the same as that used in the vertical push plate test. The load is horizontally applied at the center of the cross section at one end, and two dial gauges are arranged horizontally at both two ends of the specimen. The relative displacement between the track slab

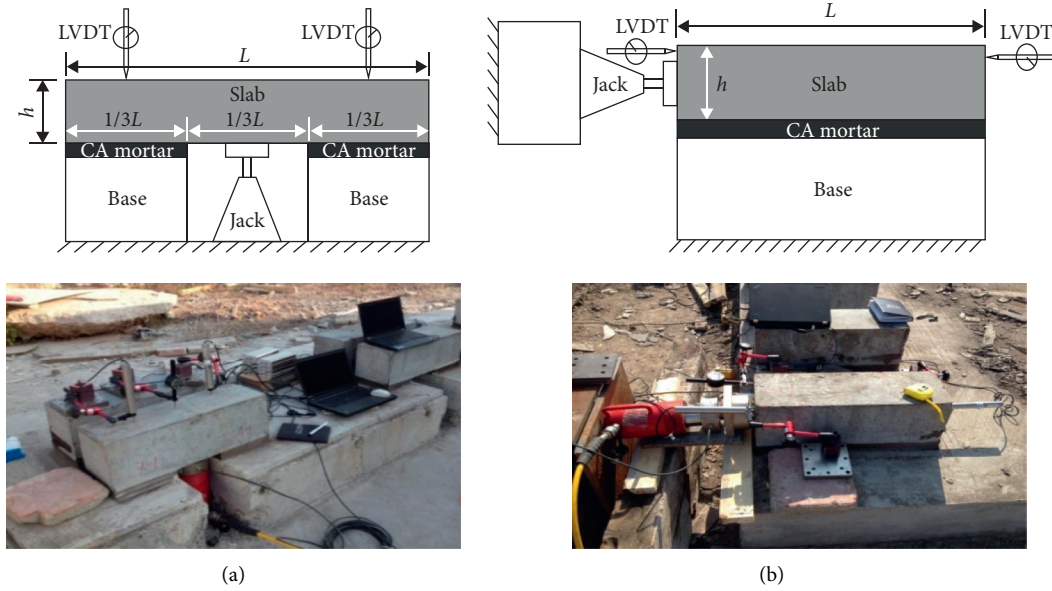


FIGURE 6: Scheme and setup of the scale push plate tests. (a) Scale vertical push plate test. (b) Scale horizontal push plate test.

and the base was tested using LVDTs. The jack works synchronously by an automation control system to provide a constant-rate increased load.

Figure 7 shows the force-displacement curve obtained in the scale tests.  $\sigma_n^0$  and  $\sigma_s^0$  can be determined by the peak stress of the vertical and horizontal force-displacement curve, respectively.  $\delta_n^0$  and  $\delta_s^0$  are then identified corresponding to  $\sigma_n^0$  and  $\sigma_s^0$ , respectively. Afterwards,  $E_n$  and  $E_s$  can be calculated using  $E_n = \sigma_n^0 / \delta_n^0$  and  $E_s = \sigma_s^0 / \delta_s^0$ .  $\delta_n^f$  and  $\delta_s^f$  are visually picked as the displacement after which there is slight fluctuation in the force-displacement curve. Based on  $\delta_n^f$  and  $\delta_s^f$ ,  $G_{IC}$  and  $G_{IIC}$  can be calculated using  $G_{IC} = (1/2) \sigma_n^0 \delta_n^f$  or  $G_{IIC} = (1/2) \sigma_s^0 \delta_s^f$ . The determined cohesive parameters are also indicated in Figure 7.

#### 4. Simulation of Horizontal Push Plate Test

In this section, the entire evolution of the interfacial damage during the horizontal push plate test is simulated using FEA. The finite element model of CRTS II SBTS, as shown in Figure 8, consists of a 6.45-meter-long track slab, a base of the same length, and a CA mortar layer between the track slab and the base. The track slab, CA mortar layer, and base are established using solid elements. The interface between the track slab and the CA mortar layer is simulated using 1-mm-thick cohesive elements with the parameters illustrated in Figure 7. The elastic modulus for the track slab, CA mortar layer, and base is  $3.60 \times 10^4$  MPa,  $1 \times 10^4$  MPa, and  $2.20 \times 10^4$  MPa, respectively. The corresponding density is  $2500 \text{ kg/m}^3$ ,  $1950 \text{ kg/m}^3$ , and  $2400 \text{ kg/m}^3$ , respectively. The initial state of the interface is assumed to be perfectly bonded (no damage), and the nodes at the bottom of the base are fully constrained. In the FEA, the load is applied by gradually increasing the displacement from 0 to 1 mm with an interval of 0.005 mm at one end of the track slab.

Figure 9 shows the simulated interfacial tangential stress  $\sigma_s$  and total stiffness damage  $D$  along the track slab for seven selected loading displacements, 0.025 mm, 0.04 mm, 0.05 mm, 0.1 mm, 0.15 mm, 0.6 mm, and 1 mm, respectively. In Figure 9,  $\sigma_s$  and  $D$ , for the same loading displacement, are plotted in the same color. Solid lines represent  $\sigma_s$ , while dashed lines denote  $D$ . Figures 9(a)–9(c) are for the undamage stage, partial damage stage, and complete damage stage, respectively. The undamage stage corresponds to the stage when the loading displacement is less than 0.04 mm. Two loading displacements of 0.025 mm and 0.04 mm are selected in the undamaged stage. As seen from Figure 9(a),  $\sigma_s$  gradually decreases from the loading end to the other end of the track slab, with increasing peak values for larger loading displacements.  $D$  keeps zero for both of the two cases because no damage occurs. When the loading displacement is larger than 0.04 mm, the damage will occur firstly at the loading end and then gradually extends to the other end as the loading displacement increases. Figure 9(b) shows  $\sigma_s$  and  $D$  for three selected loading displacements of 0.05 mm, 0.1 mm, and 0.15 mm. In each  $\sigma_s$  curve, the whole track slab includes two zones: one is the damaged zone from the loading end to a certain point, where  $\sigma_s$  is very close to  $\sigma_s^0$ . The rest zone of the track slab is the zone without damage. In the damaged zone, a slight reduction of  $\sigma_s$  from  $\sigma_s^0$  and the attenuation of  $D$  from the loading end can be observed. In the undamaged zone,  $D$  keeps zero and  $\sigma_s$  gradually decreases. The larger the loading displacement, the longer the length of the damaged zone, and hence the greater the maxima of  $D$ . The distribution of  $\sigma_s$  and  $\delta_s$  on the entire track slab for the three loading displacements is plotted in Figure 10 which exhibits the development of the interfacial displacement from the loading end to the entire track slab. When the loading displacement reaches 0.15 mm, the damage extends to the whole interface. Afterward,  $\sigma_s$  shows an overall reduction, whereas  $D$  shows an overall increase for

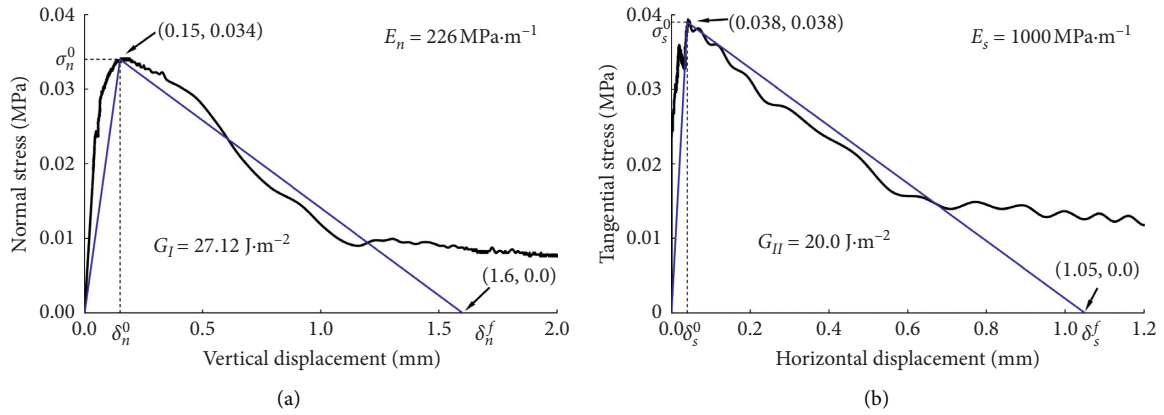


FIGURE 7: Force-displacement curve of the vertical (a) and horizontal push plate test (b).

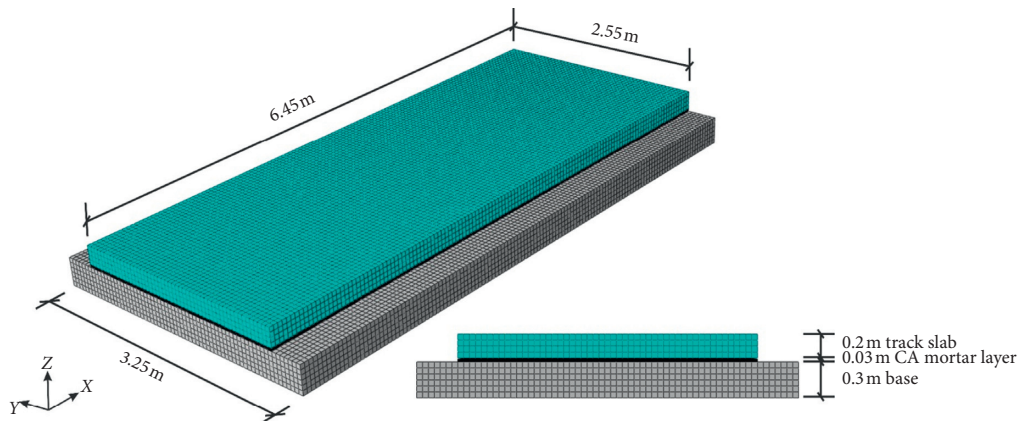


FIGURE 8: Finite element model of CRTS II SBTS.

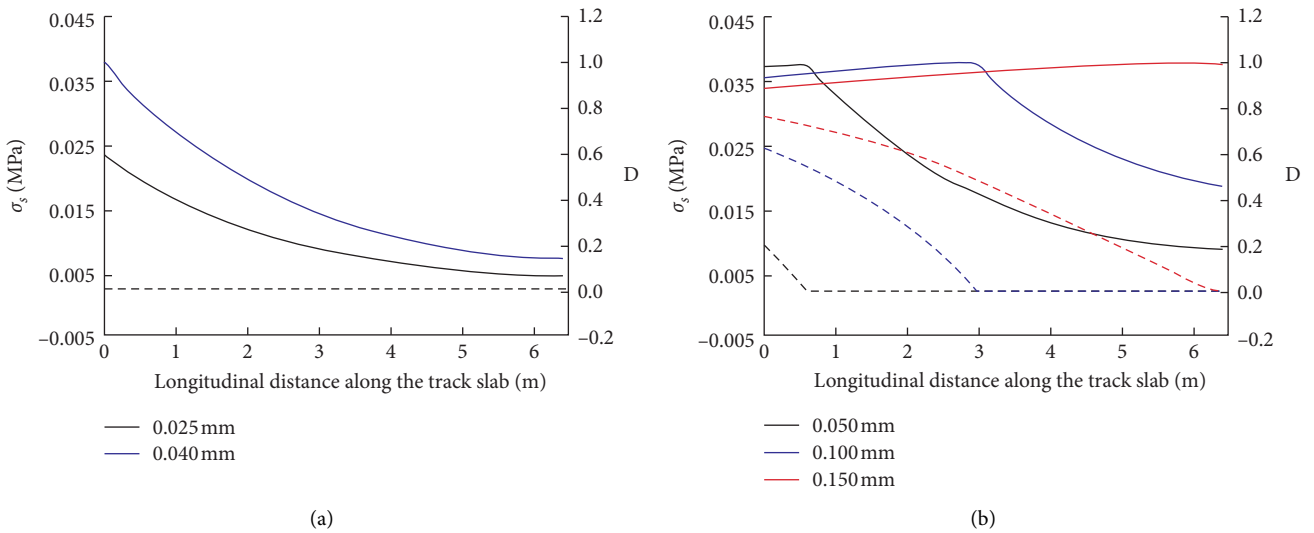


FIGURE 9: Continued.

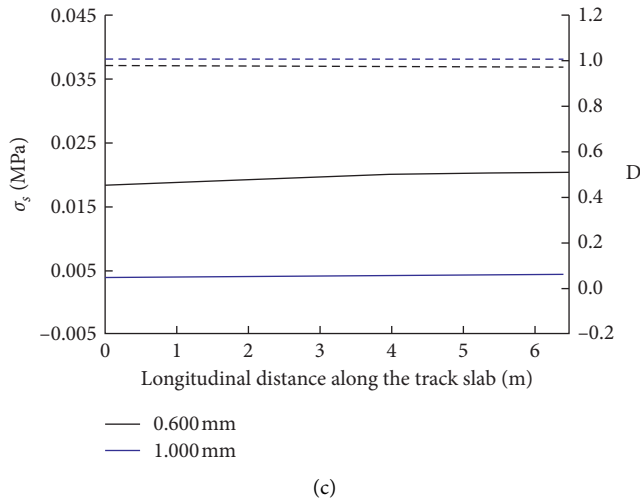


FIGURE 9: Distribution of  $\sigma_s$  and  $D$  on the track slab. (a) Undamage stage. (b) Partial damage stage. (c) Complete damage stage.

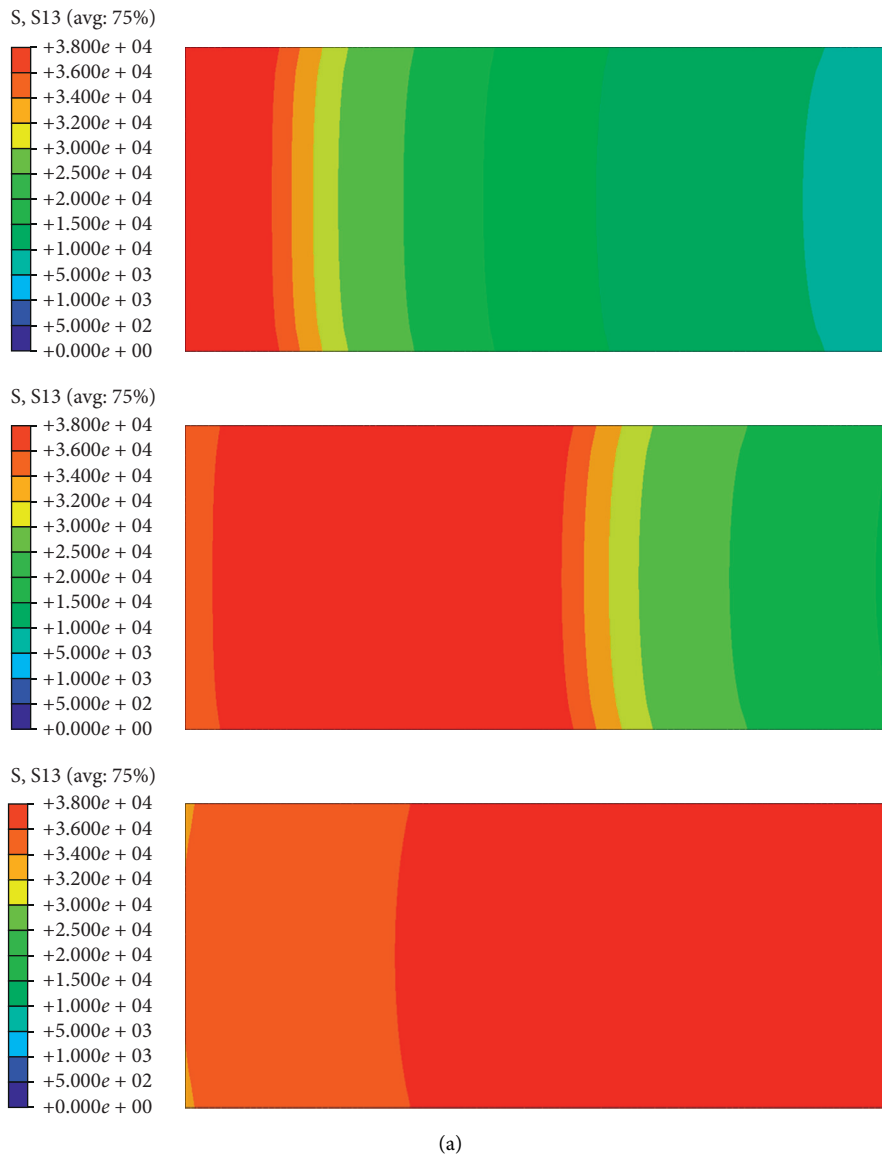


FIGURE 10: Continued.



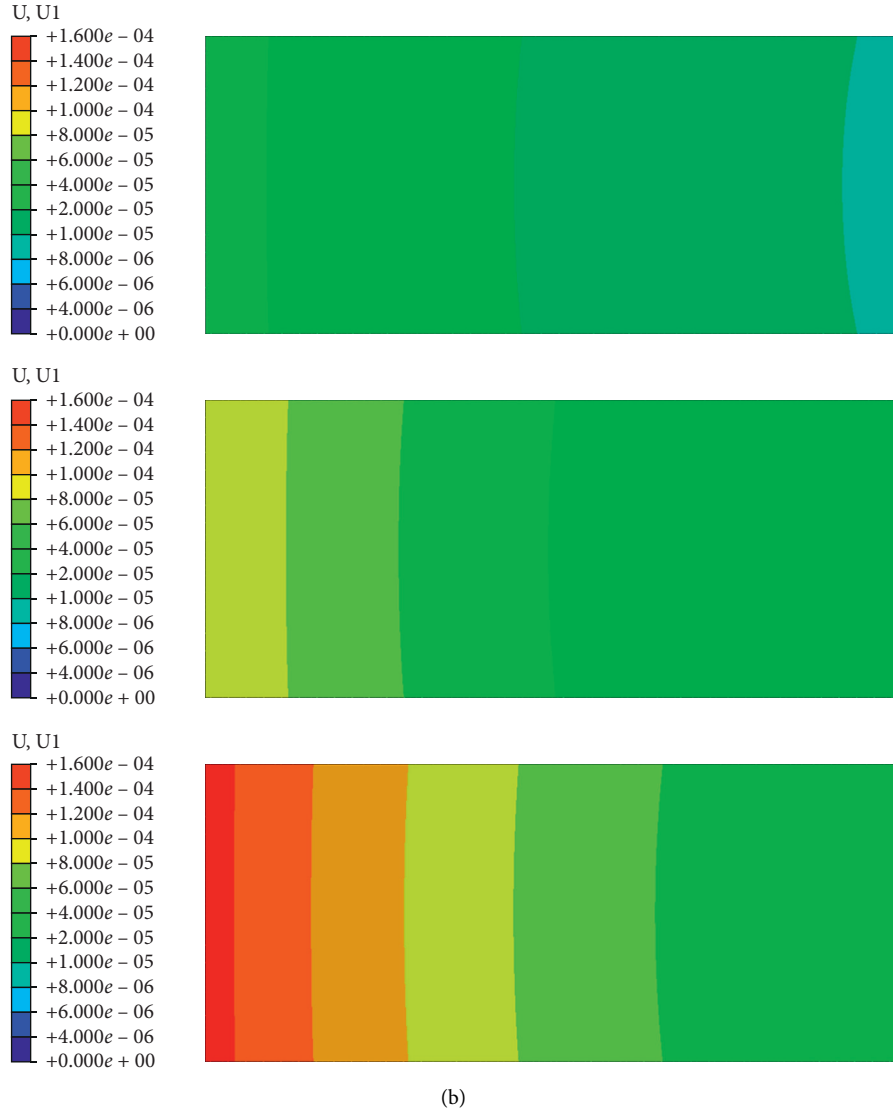


FIGURE 10: The interfacial tangential stress and displacement on the track slab. (a) Development of interfacial tangential stress. (b) Development of interfacial tangential displacement.

TABLE 1: Comparison of the theoretical and simulated  $L_0$  for various  $E_s$ .

$E_s$ (MPa $\cdot$ m $^{-1}$ )	Theoretical (m)	FEA (m)	Error (%)
30	37.42	38.00	1.6
100	20.49	18.50	9.7
1000	6.48	6.10	5.9
5000	2.90	2.90	0.0

larger loading displacements (Figure 9(c)). When the loading displacement reaches 1 mm,  $\sigma_s$  is close to zero, and  $D$  is approximately 1, which indicates the occurrence of delamination.

To verify the reliability of the linear proportional distribution method,  $L_0$  and  $L_D$  are simulated for various  $E_s$  and  $G_{IIC}$ . To represent the scenario long track slab, the finite element model in Figure 8 is enlarged to be 50 meter long.  $L_0$  for  $E_s$  of 30, 100, 1000, and 5000 MPa/m is first simulated

TABLE 2: Comparison of the theoretical and simulated  $L_D$  for various  $G_{IIC}$ .

$G_{IIC}$ (J $\cdot$ m $^{-2}$ )	$\lambda$	Theoretical (m)	FEA (m)	Error (%)
5	1.04	6.71	6.50	3.1
10	1.76	11.42	10.70	6.3
20	2.79	18.11	16.00	11.7
40	4.26	27.58	22.50	18.4

with fixed  $\sigma_s^0$  of 0.038 MPa and  $G_{IIC}$  of 20 J/m $^2$ . The simulated  $L_0$  is compared with the theoretical  $L_0$  calculated using equation (6), as listed in Table 1. From Table 1,  $L_0$  from the FEA is very close to the theoretical  $L_0$ .  $L_0$  decreases as  $E_s$  increases. For  $E_s$  of 30 MPa/m,  $L_0$  is approximately six times the length of a single track slab and 5.6 times of  $L_0$  for  $E_s$  of 1000 MPa/m.  $L_D$  for  $G_{IIC}$  of 5, 10, 20, and 40 J/m $^2$  are then simulated with fixed  $\sigma_s^0$  of 0.038 MPa and  $E_s$  of 1000 MPa/m. The simulated  $L_D$  is listed in Table 2 together with the

theoretical  $L_D$  calculated based on  $\lambda$  of equation (15). From Table 2,  $L_D$  from the FEA is generally closed to the theoretical  $L_D$ . The difference between the theoretical and simulated  $L_D$  becomes larger as  $G_{IIC}$  increases. The agreement between the theoretical and simulated solutions in Tables 1 and 2 indicates that the linear proportional distribution method is effective to analyze the force-displacement variation for a single track slab.

## 5. Conclusions

In this paper, the push plate test of CRTS II SBTS is investigated by theoretical analysis, experiments, and numerical simulation. In the theoretical analysis, a series of analytical formulas of the force-displacement relationship is derived. In the numerical simulation, a bilinear CZM is adopted to simulate the interface within CRTS II SBTS. The parameters of the CZM are determined by scale push plate test. Particularly, a scale vertical push plate test instead of the traditional splitting tensile test is carried out to determine the normal cohesive parameters. The simulation exhibits the variation of the interfacial tangential stress  $\sigma_s$  and total stiffness damage  $D$  during the entire loading process. The results are as follows:

- (1) The force-displacement curve constructed by the linear proportional distribution method agrees well with those obtained from full-scale test. This proves the reliability of the proposed method in analyzing the force-displacement variation of CRTS II SBTS in the horizontal push plate test.
- (2) The simulation indicates that there is a partial damage stage between the undamage stage and the complete damage stage. This three-stage variation of the interfacial bond properties differs from the two-stage assumption of the bilinear CZM. However, the three-stage assumption is closer to the real force-displacement variation observed in the full-scale push plate test, and the linear proportional distribution method proposed in this paper is capable to reproduce this three-stage variation of the interfacial bond properties.
- (3) The maximum affected length on the track slab in the damage stage,  $L_0$ , and the maximum damaged length in the undamage stage,  $L_D$ , are independent of the horizontal load. They only depend on the elastic modulus  $E$ , the interfacial stiffness  $E_s$ , the height of the track slab  $h$ , and the cohesive parameters  $\delta_s^0$  and  $\delta_s^f$ .  $L_0$  and  $L_D$  given by the FEA are very close to those defined by the proposed linear proportional distribution method. This proves the reliability of the proposed method and the capability of scale push plate test in determining the cohesive parameters.

However, this does not imply that the full-scale push plate test can be replaced fully by the scale push plate tests. The full-scale push plate test is of high cost and complicated, but it can minimize the effects from the construction quality, specimen size, loading condition, and other factors. A

practical way to determine tangential cohesive parameters is to carry out a certain amount of scale test with the validation of several full-scale test. For the determination of the normal cohesive parameters, the scale vertical push plate test is the most practical way so far due to the challenge of setting up a full-scale vertical push plate test with uniform interfacial force during the entire loading process.

The size of the specimen in the scale test in this paper is estimated based on engineering experience with the aid of several times of trial test, which ensures that delamination will not occur too early during the test. The size effect is not involved considering that the scope of this paper is rather in building an integrated analysis approach using theoretical, experimental, and numerical tools than specifically discussing any of the three tools. In the future work, the effect of changing the specimen size on the test results would be investigated [18]. The parameters of the CZM are actually temperature dependent. However, for the bilinear CZM used in this paper, there is no existing research that reports the temperature variability of the key parameters (the interfacial stiffness, the interfacial strength, and the fracture toughness). In future works, push plate test under the load of time-varying temperature could be conducted by the use of a large scale temperature cabinet, from which the temperature variability of the parameters of the CZM could be investigated. The interface bond behavior is likely to degrade under the daily repeated living load of the train. This will increase the possibility of damage initiation and expansion. However, the fatigue of the interfacial bond behavior is out of the evaluation of push plate test and could be investigated in the future with the aid of fatigue test of CRTS II SBTS [19, 20].

## Data Availability

The data used to support the findings of this study are available from the corresponding author upon request.

## Conflicts of Interest

The authors declare no conflicts of interest with respect to the research, authorship, and/or publications of this article.

## Acknowledgments

The research was financially supported by the National Natural Science Foundation of China (Grants nos. 51708459 and 51878578) the Project of Science and Technology Research and Development of China Railway Co., Ltd. (Grant no. K2020G007), and the Open Foundation of Undergraduate-Oriented Engineering Practice Project of Key Laboratory of Southwest Jiaotong University (ZD2020010035).

## References

- [1] Y. Li, J. Chen, J. Wang, X. Shi, and L. Chen, "Study on the interface damage of CRTS II slab track under temperature load," *Structure*, vol. 26, pp. 224–236, 2020.
- [2] G. Dai, H. T. Su, W. S. Liu, and B. Yan, "Temperature distribution of longitudinally connected ballastless track on

- bridge in summer,” *Journal of Central South University*, vol. 48, no. 4, pp. 1073–1080, 2017.
- [3] G. Zhao, L. Gao, L. Zhao, and Y. L. Zhong, “Analysis of dynamic effect of gap under CRTS II track slab and operation evaluation,” *Journal of the China Railway Society*, vol. 39, no. 1, pp. 1–10, 2017.
- [4] G. Zhao and Y. Liu, “Mechanism analysis of delamination of CRTS II slab ballastless track structure,” *Journal of the China Railway Society*, vol. 42, no. 7, pp. 117–126, 2020.
- [5] J. Liu, X. Wen, Z. Zhang, S. Li, and Z. Zeng, “Influence of the stabilizer on interfacial bonding behavior of cement asphalt mortar in slab ballastless track,” *Journal of Materials in Civil Engineering*, vol. 30, no. 10, Article ID 04018245, 2018.
- [6] J. Ren, J. Wang, X. Li, K. Wei, H. Li, and S. Deng, “Influence of cement asphalt mortar debonding on the damage distribution and mechanical responses of CRTS I prefabricated slab,” *Construction and Building Materials*, vol. 230, Article ID 116995, 2020.
- [7] Y. Zhong, L. Gao, P. Wang, and S. Liang, “Mechanism of interfacial shear failure between CRTS II slab and CA mortar under temperature loading,” *Engineering Mechanics*, vol. 5, no. 2, pp. 230–237, 2018.
- [8] J. Zhang, S. Zhu, C. Cai, M. Wang, and H. Li, “Experimental and numerical analysis on concrete interface damage of ballastless track using different cohesive models,” *Construction and Building Materials*, vol. 263, Article ID 120859, 2020.
- [9] Y. Zhang, K. Wu, L. Gao, X. Cai, and S. Yan, “Comparison of viscoelastic and elastic analysis of slab track under temperature gradient loading,” *Journal of Central South University*, vol. 51, no. 7, pp. 2028–2038, 2020.
- [10] G. Dai and M. Su, “Full-scale field experimental investigation on the interfacial shear capacity of continuous slab track structure,” *Archives of Civil and Mechanical Engineering*, vol. 16, no. 3, pp. 485–493, 2016.
- [11] X. Chen, Y. Zhu, D. Cai, G. Xu, and T. Dong, “Investigation on interface damage between cement concrete base plate and asphalt concrete waterproofing layer under temperature load in ballastless track,” *Applied Sciences*, vol. 10, no. 8, p. 2654, 2020.
- [12] D. Li, *Performance of CRTS II slab ballastless track on the high speed railway bridge*, Ph.D. thesis, China Academy of Railway Science, Beijing, China, 2016.
- [13] X. Liu, C. Su, D. Liu, F. Xiang, C. Gong, and P. R. Zhao, “Research on the bond properties between slab and CA mortar and the parameters study of cohesive model,” *Journal of Railway Engineering Society*, vol. 34, no. 3, pp. 22–28, 2017.
- [14] Q. Shen, W. Chen, C. Liu, W. Zou, and L. Pan, “The tensile strength and damage characteristic of two types of concrete and their interface,” *Materials*, vol. 13, no. 1, pp. 16–34, 2019.
- [15] S. Zhu, M. Wang, W. Zhai et al., “Mechanical property and damage evolution of concrete interface of ballastless track in high-speed railway: experiment and simulation,” *Construction and Building Materials*, vol. 187, pp. 460–473, 2018.
- [16] Y. Xu, D. Yan, W. Zhu, and Y. Zhou, “Study on the mechanical performance and interface damage of CRTS II slab track with debonding repairment,” *Construction and Building Materials*, vol. 257, Article ID 119600, 2020.
- [17] D. Ranz, J. Cuartero, L. Castejon, R. Miralbles, and H. Malon, “A cohesive zone model approach in interlaminar behavior of carbon/epoxy laminated curved beams,” *Composite Structures*, vol. 238, Article ID 111983, 2020.
- [18] J. Liu, W. Yu, and X. D., “Size effect on static splitting tensile strength of concrete experimental and numerical studies,” *Journal of Materials in Civil Engineering*, vol. 32, no. 10, Article ID 04020308, 2020.
- [19] Z. Zeng, J. Wang, S. Shen, P. Li, A. Shuaibu, and W. Wang, “Experimental study on evolution of mechanical properties of CRTS III ballastless slab track under fatigue load,” *Construction and Building Materials*, vol. 210, pp. 639–649, 2019.
- [20] L. Zhou, L. Yang, Z. Shan, X. Peng, and A. Mahunon, “Investigation of the fatigue behaviour of a ballastless slab track-bridge structural system under train load,” *Applied Sciences*, vol. 9, no. 17, Article ID 3625, 2019.

## Research Article

# Dynamic Response of Parallel Overlapped Tunnel under Seismic Loading by Shaking Table Tests

Tao Yang <sup>1</sup>, Yunkang Rao <sup>1</sup>, Honggang Wu <sup>2</sup>, Junyun Zhang <sup>1</sup>, Hao Lei <sup>3</sup>,  
and Haojiang Ding <sup>4</sup>

<sup>1</sup>School of Civil Engineering, Southwest Jiaotong University, Chengdu 610031, China

<sup>2</sup>Northwest Research Institute Co., Ltd. of C.R.E.C, Lanzhou, Gansu 730000, China

<sup>3</sup>School of Civil Engineering, Lanzhou Jiaotong University, Lanzhou, Gansu 730000, China

<sup>4</sup>China Railway Eryuan Engineering Group Co. Ltd., Chengdu 610031, China

Correspondence should be addressed to Honggang Wu; 271462550@qq.com

Received 12 April 2021; Accepted 29 May 2021; Published 8 June 2021

Academic Editor: Honglue Qu

Copyright © 2021 Tao Yang et al. This is an open access article distributed under the Creative Commons Attribution License, which permits unrestricted use, distribution, and reproduction in any medium, provided the original work is properly cited.

Potential earthquake-induced damage to overlapped tunnels probably occurs during the operation and maintenance of mountain tunnel engineering, especially in the seismically active zone. This study investigated the dynamic response and the failure characteristics of the parallel overlapped tunnel under seismic loadings by employing shaking table tests. The failure mode of the parallel overlapped tunnels was analyzed through macroscopic test phenomena. The dynamic responses of the surrounding rock and tunnel lining were evaluated by acceleration and dynamic strain, respectively. In particular, wavelet packets were used to investigate the spectrum characteristics of the tunnel structure in depth. The failure process of the model can be divided into three stages. The upper-span and the under-crossing tunnels showed different failure characteristics. Additionally, the lining damage on the outer surface of the tunnel mainly occurred on the right side arch waist and the left side wall, whereas the lining damage on the inner surface of the tunnel mainly appeared on the crown and invert. Wavelet packet energy results showed that the energy characteristic distributions of the upper-span and the under-crossing tunnels were not consistent. Specifically, the energy eigenvalues of the crown of the upper-span tunnel and the invert of the under-crossing tunnel were the largest, which should be considered to be the weak parts in the seismic design.

## 1. Introduction

Earthquakes and rainfall are two important factors often considered in the studies of engineering structure stability [1, 2], and the structural dynamic response caused by earthquakes has been paid more attention. The overlapped tunnel has been widely used in engineering because of the limitation of terrain and route selection [3]. According to the relative relationship of space and structure in the cross tunnel, Li et al. and Liu et al. [4, 5] divided the cross tunnel into two types: structural cross and spatial cross. Moreover, the structural cross tunnel was divided into structural bifurcation, structural connection channel, and structural wind types; the spatial cross tunnel was divided into spatial orthogonal, spatial parallel, and spatial oblique types, as

shown in Figure 1. As the traffic arteries pass through complex mountainous areas, more overlapped tunnels are built-in high-intensity earthquake areas, which often face the problems of earthquake damage [6]. Therefore, it is necessary to study the seismic response of overlapping tunnels in high-intensity earthquake areas.

In previous studies on overlapped tunnels, scholars mainly discussed the construction mechanical characteristics of overlapped tunnels and have already made some achievements in the statics of the cross tunnel in terms of the distribution of mechanical characteristics, reinforcement technology, and monitoring and measurement [7–17]. Some scholars have analyzed the mechanical characteristics and stability of the surrounding rock of the cross tunnel with a small clear distance through different numerical software;

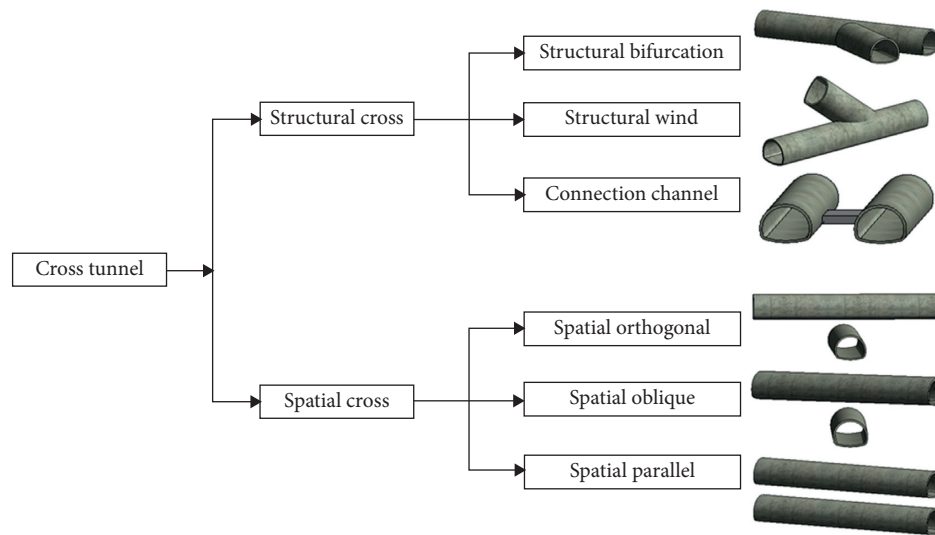


FIGURE 1: Classification of cross tunnels.

the results showed that the maximum displacement at the crown was caused by the construction disturbance and the release of the stress of the crown [10, 11]. Liu et al. and Lin et al. [12, 13] conducted a theoretical analysis and numerical simulation study on the construction process of the overlapped subway tunnel with a small clear distance. They pointed out that when a new tunnel was constructed over the span, the additional stress generated was mainly concentrated in the original tunnel area at the intersection of the tunnel. Other scholars have put forward suggestions for the reinforcement of overlapped tunnels. For example, Zhang et al. and Liu et al. [14, 15] used compensation grouting to reinforce the rock column between the existing tunnel and the new tunnel to reduce the settlement of the existing tunnel. Furthermore, the strength of the surrounding rock and the existing tunnel can be improved together by controlling the specific grouting pressure. In terms of monitoring and measurement of overlapped tunnels, the superposition method was used to monitor the surface settlement of the existing tunnel and the new tunnel. Fang et al. and Jin et al. [16, 17] found that the settlement of the existing tunnel and the surface section shows different shapes; that is, the settlement of the existing tunnel section is in the shape of “W,” whereas the settlement of the surface section is in the shape of “U.”

Owing to the characteristics of multieffect coupling, load reciprocating superposition, and complex deformation of overlapped tunnels under dynamic loading, the degree and scope of structural damage are aggravated, which poses a great potential safety risk for the construction and operation of the overlapped tunnel [18]. At present, some scholars have studied the dynamics of the overlapped tunnel, mainly focusing on the effects of blasting vibration, train loading, and seismic loading [19, 20]. The blasting excavation of overlapped tunnels has specific unique characteristics, which not only ensures that the original tunnel structure and support system will not be damaged during blasting but also considers the self-stability of surrounding rock after multiple

vibrations [21]. Zhao et al. [22] used field monitoring tests and finite element numerical methods to study the blasting vibration velocity and frequency of existing tunnels. Moreover, they used different indicators to evaluate the impact of blasting during the construction of new tunnels.

Additionally, the vibration of long-term train load can cause damage and cracking of the tunnel structure and even cause severe damage to the tunnel lining, which is easy to cause large deformation of the structure and bring great hidden danger to the operation safety of the overlapped tunnel. Some scholars carried out field tests and model tests to study the effect of train loading and draw some valuable conclusions on the overlapped tunnel [23, 24]. The overlapped tunnel structure will produce the superposition of seismic waves under the action of seismic loading, and the loading generated by the seismic effect is greater than the other two dynamic loadings, so it is often the most severely damaged under the action of seismic load [25]. Wu et al. and Lei et al. [26, 27] carried out shaking table tests to study the seismic response of orthogonal and oblique overlapped tunnels, respectively, and preliminarily discussed and analyzed the acceleration response and lining strain response of the upper-span and under-crossing tunnels.

Through the above studies, it is found that previous studies on the overlapped tunnel mainly focused on the static aspects such as construction mechanics. Although the dynamics of the overlapped tunnel have also made some progress, the dynamic response characteristics of the overlapped tunnel under seismic loading have not made a substantial breakthrough, and the study on the parallel overlapped tunnel is even less. To study the dynamic response and spectrum response of the parallel overlapped tunnel under seismic loadings, the dynamic damage of the tunnel lining and the acceleration response of the surrounding rock was analyzed through the shaking table tests. Additionally, the mathematical tool of wavelet packet was introduced to discuss the characteristics of seismic waves in the time-frequency domain. The results are expected to

provide a theoretical reference for the response to the dynamic rationality study of this type of the overlapped tunnel.

## 2. Shaking Table Tests

**2.1. Shaking Table System.** This test used the RC-3000 vibration control system, which used a structure that directly integrates the LAN bus and the embedded DSP. Moreover, this system had a full range of one-way vibration test functions. The main technical parameters of this shaking table system are shown in Table 1.

The shaking table system was equipped with a rigid model box with dimensions of 175 cm (length)  $\times$  30 cm (width)  $\times$  120 cm (height). The mainframe of the rigid model box was welded with 4080L alloy aluminum material, as shown in Figure 2. To meet the requirements of rigidity and visual test, both sides of the inner side were made of 10 mm thick PP sheet to facilitate the observation of failure phenomena, and the inner side of the model box was a steel plate. The model box was rigidly fixed on the shaking table by surrounding bolts, which is a commonly used device for studying soil-structure dynamic characteristics in shaking table tests.

The rigid model box may cause errors in the test data due to the boundary effect [28]. Therefore, three measures were taken to deal with the boundary effect-caused errors: (1) to reduce the influence of the boundary effect, a 50 mm thick polystyrene foam board with a density of  $15 \text{ kg/m}^3$  was used to paste the inner side of the model box to reduce the friction between the side wall of the model box and the soil. The polystyrene foam plastic board was always in a linear elastic state during the test loading process and had good compression properties (Dynamic elastic modulus  $E_d = 4.13 \text{ MPa}$ ); (2) to reduce the reflection of waves on the boundary surface, a layer of polystyrene foam board was also laid on the two sides parallel to the tunnel; (3) to ensure good adhesion between the model soil and the bottom of the box, a layer of 5 cm thick gravel soil with the size of 1 cm was laid on the bottom of the model box to increase the friction; thus, the bottom plate was treated as a friction boundary to limit the relative displacement between the bottom of the box and the soil. The effectiveness of the above treatment of the boundary effect of the model box has been verified in previous experiments [26].

**2.2. Design and Construction of the Model.** Taking into account the size of the shaking table model box and the possible application of this model in some actual construction projects, this experiment used the geometric similarity ratio  $C_l$  of 100 to design the tunnel combined with the previous tunnel construction practice of relevant specifications [29]. Taking geometry, density, and acceleration as the basic physical parameters, the geometric similarity ratio was determined to be 1 : 100; the similarity ratios of density and acceleration were both 1 : 1; the similarity ratios of other physical quantities were derived based on the Buckingham  $\pi$  theorem [30], as shown in Table 2.

TABLE 1: Parameters of shaking table system.

Parameters	Technical specification
Table size (m)	$3 \times 2$
Loading direction	Horizontal (X)
Working frequency (Hz)	0.2~50
Maximum load (t)	0.5
Maximum acceleration (g)	1.0
Maximum overturning moment (kN·m)	10
Maximum eccentric moment(kN·m)	5
Maximum velocity (m/s)	2
Maximum displacement (mm)	51

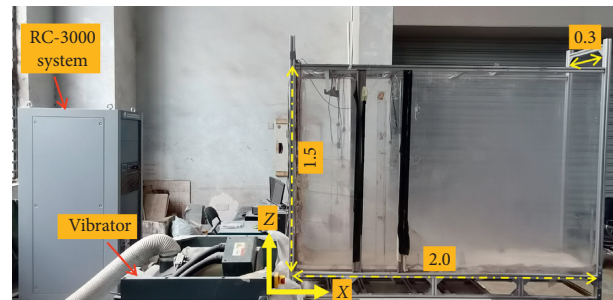


FIGURE 2: Shaking table system and model box (unit: m).

The selection of model materials was mainly based on previous study [29]. The parameter preparation was carried out according to the Chinese criterion “Code for Design of Highway Tunnels (JTG 3370.1-2018)” taking the IV grade surrounding rock as an example. According to the model design parameters and the test results of multiple sets of materials, it was finally determined that quartz sand was the main material; gypsum powder and talc powder were used as auxiliary materials; and red clay, cement, and water were used as bonding materials. The sample test process is shown in Figure 3. The specific similar parameters are shown in Table 3. Moreover, in the process of the test, considering that the earthquake may induce a landslide, which may affect the dynamic response of the tunnel structure, the sliding surface was set in advance in the model design.

The lining section of the tunnel adopted the standard section of the three-lane highway composite tunnel lining at a speed of 120 km/h, with a design grade of C30 and thickness of 60 cm. Additionally, the lining model, which was mainly made by mixing gypsum powder and water in a certain proportion, had a maximum span of 19.3 cm, a height of 14.6 cm, and a thickness of 0.6 cm according to the geometric similarity. Furthermore, the steel wire mesh with a diameter of 0.2 mm was used to approximate the circumferential main reinforcement and distributed reinforcement in the lining structure, as shown in Figure 4.

During the model filling process, similar materials were filled into the model box with a layer of 10 cm thick by layered filling. Moreover, each soil layer was compacted in the same way to ensure that the model was filled evenly. During the filling of the similar materials, acceleration sensors and strain gauges were arranged, as shown in Figures 5(a) and 5(b).

TABLE 2: Similarity relations and ratios.

	Physical parameters	Symbol and relational expression	Similarity ratio
Geometric parameters	Length ( $L$ )	$C_L$	1/100
	Linear displacement ( $x$ )	$C_x = C_L$	1/100
Material parameters	Density ( $\rho$ )	$C_\rho$	1
	Stress ( $\sigma$ )	$C_\sigma = C_E$	1/100
	Strain ( $\epsilon$ )	$C_\epsilon$	1
	Poisson's ratio ( $\mu$ )	$C_\mu$	1
	Internal friction angle ( $\phi$ )	$C_\phi$	1
	Cohesion ( $c$ )	$C_c = C_E$	1/100
	Elastic modulus ( $E$ )	$C_E = C_L C_a C_p$	1/100
Dynamic parameters	Acceleration ( $a$ )	$C_a$	1
	Frequency ( $f$ )	$C_f = C_L^{-1/2} C_a^{1/2}$	1/0.1
	Velocity ( $v$ )	$C_v = C_L^{1/2} C_a^{1/2}$	1/10
	Time ( $t$ )	$C_t = C_L^{1/2} C_a^{-1/2}$	1/10

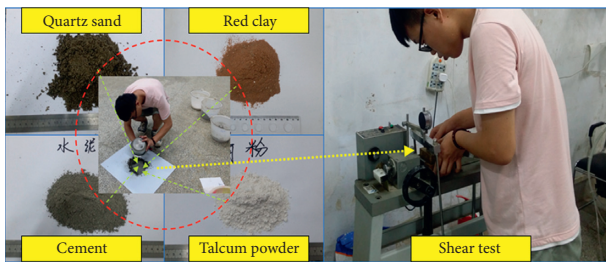


FIGURE 3: Similar material acquisition.

**2.3. Design of the Loading Conditions.** Since the response spectrum of the El-Centro seismic wave is in good agreement with the design response spectrum of the Chinese seismic code (Code for seismic design of buildings GB50011-2010), the El-Centro seismic wave was selected as the input wave for the shaking table test. Additionally, the seismic waves input in this test was all horizontal. When a  $0.1g$  seismic wave was loaded, the acceleration time history and frequency spectrum curve of the vibration table was collected, as shown in Figure 6. To meet the seismic design requirements of frequent, fortified, and rare earthquakes of the prototype area, the peak values of input waves were 0.1, 0.2, 0.3, and  $0.4g$ , respectively. Additionally, to explore the failure mode of the tunnel model under extreme earthquakes,  $0.6g$  was designed and loaded, as presented in Table 4. Furthermore, to test the natural frequency of the model, a  $0.2\sim 50$  Hz sine wave was inputted into the model before the start of the test to explore the initial dynamic characteristics of the model.

### 3. Test Results

#### 3.1. Deformation and Failure Characteristics of the Model.

The macroscopic test is the most intuitive means to analyze the deformation and failure of the model. During the entire process of the test from the beginning to the end, the subsequent loading continues to be loaded based on the previous working condition, without human intervention to restore the model to its original state. Therefore, the overall process of the model changes dynamically with the working conditions.

Through the observation of the deformation and failure process of the model, the failure process can be roughly divided into three stages: (1) in Case 1-2, the model has no obvious failure phenomenon; (2) in Case 3-4, the generation and development of cracks on the top of the slope and around the tunnel, named the deformation stage; and (3) in Case 5-6, the model has large deformation, name the failure stage.

When the amplitude of the seismic wave is  $0.1g$ , there is no crack around the spatial parallel overlapped tunnel and the slope surface. With the increase of the input seismic amplitude, a slight transverse crack appears at the side wall of the upper-span tunnel in Case 2, as shown in Figure 7. Therefore, the model can be considered in the elastic stage in Case 1-2. Owing to the constraints of the surrounding rock on the tunnel structure, the soil-structure combination is relatively close, which is generally considered to be the structure with the best seismic performance; thus, the model is generally not prone to damage and deformation under the action of micro- and small earthquake loadings.

When the peak acceleration of the seismic wave is  $0.2g$  in Case 3, the model has gradually begun to deform and destroy because the seismic inertia force and the amplitude of the input seismic wave increase. First, a transverse crack extending to the potential sliding surface appears at the top of the landslide slope. Then, some small cracks appear on the top and surface of the slope, which is dominated by transversal arc-shaped cracks. Additionally, cracks also appear in the intersection of the overlapped tunnel along the direction of the potential sliding surface. These phenomena are due to the horizontal tension caused by the horizontal seismic wave, which makes cracks on the top of the slope first. Furthermore, in Case 4, the existing cracks in the slope begin to spread and develop, and some new cracks appear near the potential sliding surface and the top of the slope, as shown in Figure 8. The occurrence and development of cracks indicate that local damage may have occurred in the surrounding rock at this time, resulting in enhanced absorption of seismic waves by the soil; thus, the model begins to enter the stage of deformation.

With the continuous increase of the input seismic wave amplitude, more notable model failure occurs. When the

TABLE 3: Similarity relations and ratios.

Material	Mass mix ratio (%)				$\Gamma$ (kN·m <sup>-3</sup> )	$E$ (GPa)	$C$ (kPa)	$\Phi$ (°)	$\sigma_t$ (MPa)	$\sigma_c$ (MPa)
	Quartz sand	Red clay	Cement	Gypsum powder						
Surrounding rock	—	—	—	—	20–23	1.72–5.69	200–700	27–39	—	2–20
	70	30	5	3	17.5	0.04	6.9	32	—	0.15
Sliding body	—	—	—	—	19	—	16.39	23.15	—	—
	70	—	20	3	17.2	—	4.6	22	—	—
Sliding belt	—	—	—	—	19.5–20	—	5	32	—	—
	27	52	—	—	17.2	—	6.6	25	—	—
Lining structure	—	—	—	—	—	30.8	—	—	2.0	23.2
	—	—	—	1.1	—	0.77	—	—	0.05	0.58



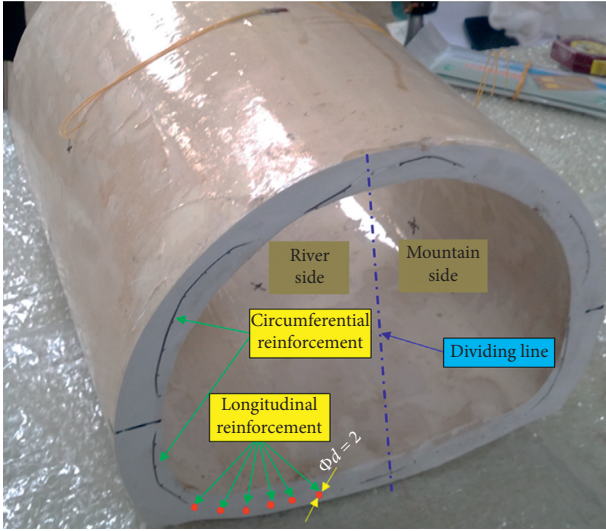


FIGURE 4: Tunnel model.

peak acceleration of loadings is  $0.4$  and  $0.6g$ , the transverse cracks on the top and surface of the slope have penetrated. Owing to the consumption of seismic energy, the filtering effect of the surrounding rock is gradually intensified, leading to the gradual development of cracks. In Case 5, the cracks at the crown of the upper-span tunnel penetrate to the slope and “tore” the slope, causing a large amount of displacement. This occurs because that the stiffness of the surrounding rock and soil mass decreases and the damping ratio increases. Additionally, the cumulative damage of the model increases, indicating that the model is in the plastic strengthening stage of crack development. After loading the  $0.6g$  seismic wave, a large number of blocks at the place where the slope was pulled apart collapsed and slipped, and accumulated at the foot of the slope, as shown in Figure 9. The model has undergone major deformation and collapse and shows the characteristics of strong earthquake failure at the failure stage.

**3.2. Damage of the Tunnel Lining.** To clearly understand the dynamic strain changes and distribution laws of the tunnel lining in the circumferential direction under different seismic loading conditions, the dynamic strain peak value of the model is analyzed in the time domain, as shown in Figure 10.

The analysis of the peak dynamic strain on the outer surface of the upper-span tunnel lining shows that the peak strain at the crown ( $S1$ ), the right arch waist ( $S2$ ), the invert ( $S5$ ), and the right side wall ( $S2$ ) are larger, with the peak strain at the mountainside inverted arch being the largest, as shown in Figure 10(a). Moreover, the strain peaks at these four locations ( $S1$ ,  $S2$ ,  $S4$ , and  $S5$ ) form a “rectangle” and are parallel to the sliding direction of the slope, which also reveals the reason why the strain peaks at these four locations are larger. Figure 10(b) shows the peak dynamic strain on the inner surface of the upper-span tunnel lining. The inner surface of the lining shows the maximum tensile stress at the left arch waist ( $S6'$ ). In contrast, the right arch waist

( $S2'$ ) shows the maximum compressive stress. The stress of the remaining parts is stable, and the difference in the peak dynamic strain under each case is small.

Figure 10(c) shows the peak dynamic strain on the outer surface of the under-crossing tunnel lining. When the seismic excitation is  $0.1\sim 0.3g$ , the difference between the peak values of dynamic strain at each point of the tunnel lining under various cases is small, and the entire tunnel gradually transits from a stable state to a small deformation stage. However, when the seismic excitation reaches  $0.4g$ , the dynamic strain peak value of each measuring point changes drastically, which indicates that the slope of the under-crossing tunnel has structural damage at  $0.4g$ . Additionally, from the point of view of the degree of change of the strain peak, the strain change of the crown ( $S7$ ) is the most drastic, and the strain change of the right side wall ( $S9$ ) is the most stable. This indicates that the under-crossing tunnel crown is likely to become a weak link in the seismic design. As seen from Figure 10(d), the peak dynamic strain is at the crown ( $S7'$ ), the right arch waist ( $S8'$ ), and the invert ( $S10'$ ) in the inner surface of under-crossing tunnel lining. Similar to the response of the outer surface lining, the strain peak value of each measuring point on the inner surface changes drastically in Cases 5 and 6.

By comparing the dynamic strain peak changes of the upper-span and under-crossing tunnel linings, it can be seen that for the upper-span tunnel, the peak strain of the tunnel lining (whether the inner surface or the outer surface) changes drastically after Case 3 ( $0.2g$ ). This indicates that the internal structure of the slope has changed after the input seismic amplitude of  $0.2g$ , and the effect of seismic waves on the slope and tunnel reconstruction is enhanced. However, for the under-crossing tunnel, the strain peak of the tunnel lining changes drastically after Cases 5-6. This also shows that under the action of the seismic waves, the under-crossing is more stable than the upper-span tunnel. Note that this is also related to the changing form of the slope. From the previous test phenomenon, it can be inferred that the landslide is sliding. The trailing edge of the slope is damaged first, and then the sliding body slides down to exert a force on the lower slope and the tunnels.

Furthermore, the maximum stresses on the outer surface of the upper-span and under-crossing tunnel lining are both on the right arch waist ( $S2$ ,  $S8$ ) and the left side wall ( $S5$ ,  $S11$ ). However, the maximum stress on the inner surface of the upper-span and under-crossing tunnel linings is different. The upper-span tunnel appears at the left side of the arch ( $S6'$ ), whereas the under-crossing tunnel appears at the right arch waist ( $S8'$ ), the crown ( $S7'$ ), and the invert ( $S10'$ ). This phenomenon indicates that the forces on the inner and outer surfaces of the tunnel lining are different, and the right arch waist and the left side wall should be considered to be weak parts in the seismic design.

**3.3. Dynamic Response of the Surrounding Rock.** To clarify the seismic response distribution law of surrounding rock and tunnel crown and invert at the cross-center section, the acceleration response of the  $A1\text{--}A6$  is analyzed. To more

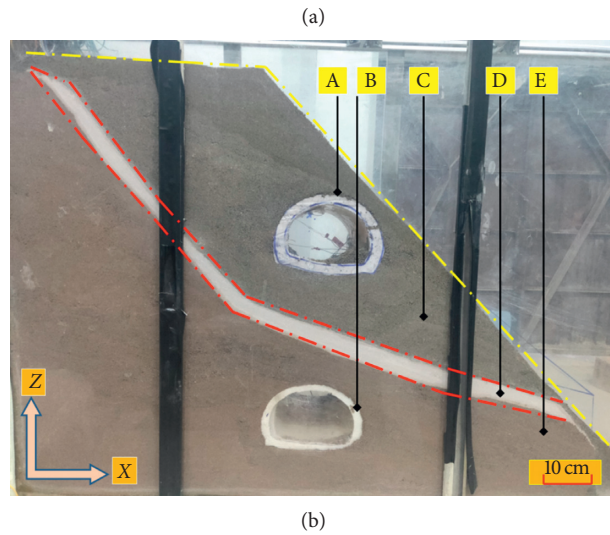
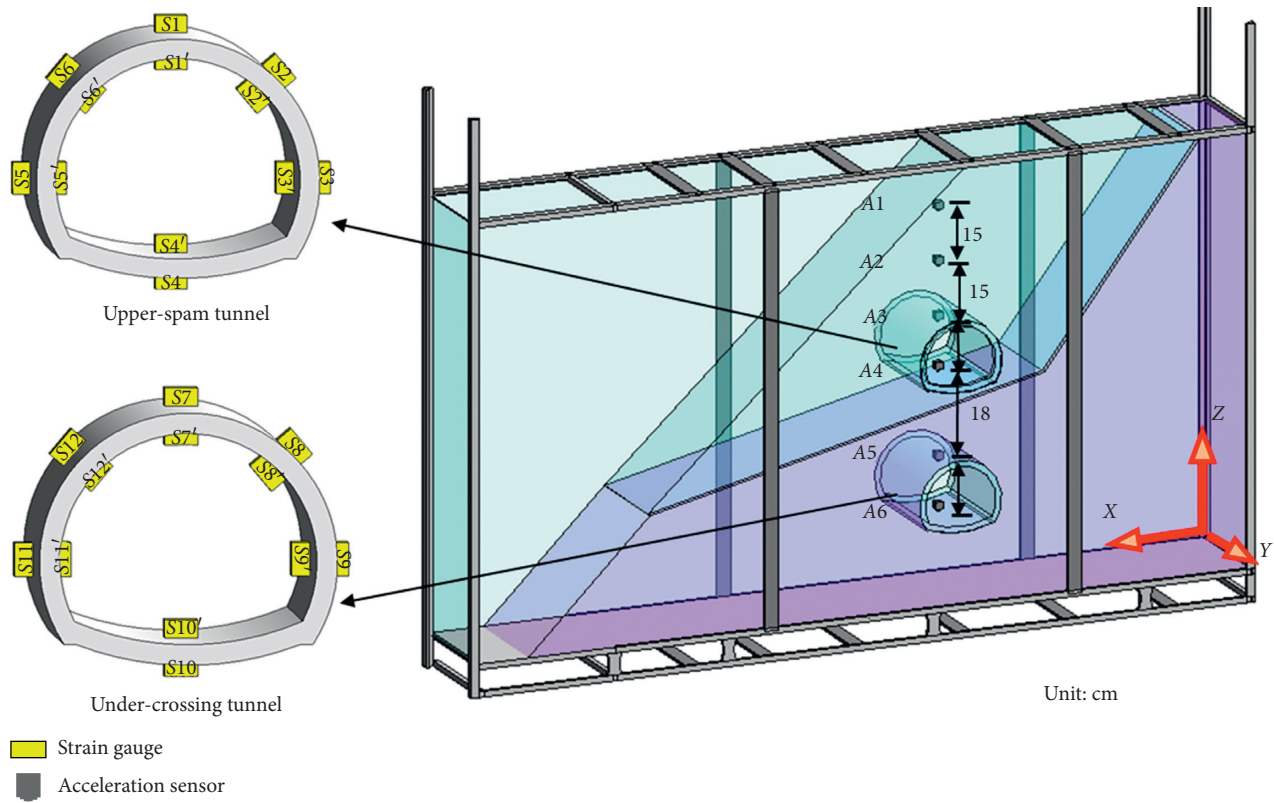


FIGURE 5: Arrangement of the sensors and layout of the model. A denotes the upper-span tunnel, B denotes the under-crossing tunnel, C denotes the slip body, D denotes the artificial boundary (potential sliding surface), and E denotes the surrounding rock. (a) Arrangement of the sensors. (b) The layout of the test model.

clearly explain the changing trend of the acceleration response of the tunnel structure and surrounding rock under different loading cases, the acceleration amplification factor is defined as the peak acceleration ratio of the measuring point under each case to the  $0.1g$  (Case 1), as shown in Figure 11.

The acceleration magnification coefficient of each measuring point along the elevation direction shows obvious regularity, which is an obvious magnification effect along the elevation. However, for the parallel overlapped tunnel, the

acceleration response at the crown and invert of the tunnel is significantly different from that of a single-hole tunnel. Owing to the spatial effect and mutual influence of the intersection, the existence of the upper-span tunnel has a certain weakening of the seismic response of the under-crossing tunnel. This weakening effect is more obvious for the crown (A5) of the under-crossing tunnel.

Furthermore, the acceleration amplification factor has obvious stages. When the input seismic wave is  $0.15\text{--}0.2g$ , the acceleration amplification factor of each measuring point

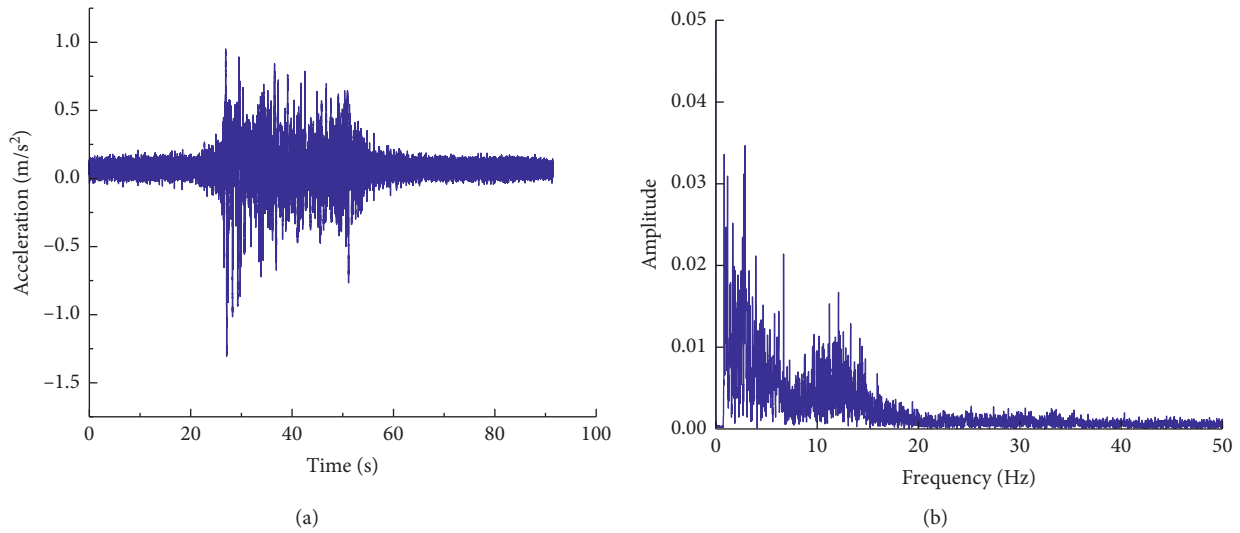


FIGURE 6: The curve of the time history and frequency spectrum of El-Centro. (a) Time history. (b) Fourier spectrum.

TABLE 4: Loading conditions.

	Input motion	Direction	Peak acceleration ( $g$ )
Case 0	Sine wave	X	0.05
Case 1	El-Centro	X	0.1
Case 2	El-Centro	X	0.15
Case 3	El-Centro	X	0.2
Case 4	El-Centro	X	0.3
Case 5	El-Centro	X	0.4
Case 6	El-Centro	X	0.6

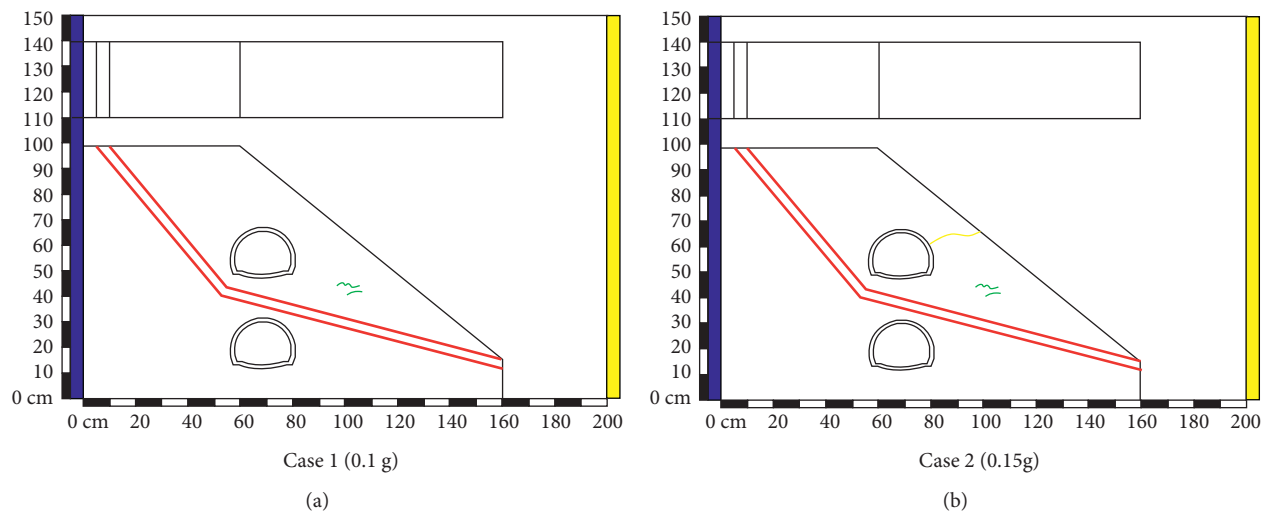


FIGURE 7: Deformation and failure in Cases 1-2.

shows a linearly decreasing trend with the increase of the input amplitude of a seismic wave, indicating that the model is in an elastic state at this time. When the input seismic wave is 0.2-0.3 $g$ , the acceleration amplification factor gradually transits from the elastic characteristic to the plastic stage, and the acceleration amplification factor begins to increase, which indicates that the dynamic shear modulus of soil decreases and the damping ratio increases in this process.

When the input seismic wave is 0.3-0.4 $g$ , the acceleration amplification factor presents a “serrated” distribution state and cracks gradually increase. Moreover, the filtering effect becomes more intensified. These indicate that the model may be in the plastic enhancement stage. When the input seismic wave is 0.4-0.6 $g$ , the acceleration amplification factor has increased significantly, especially at the A1 measurement point. This indicates that the slope top may

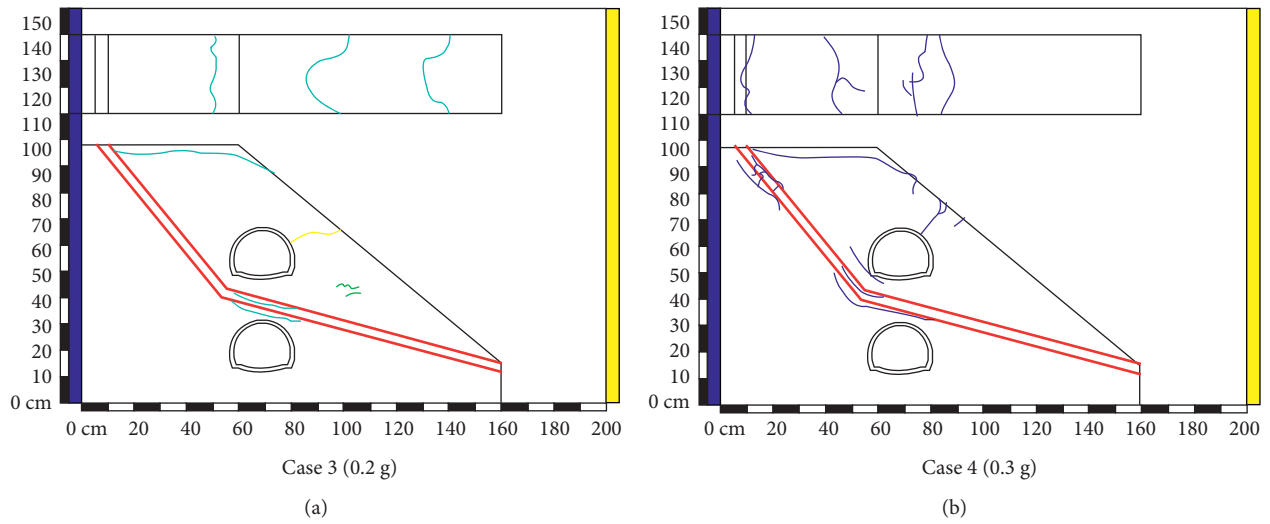


FIGURE 8: Deformation and failure in Cases 3-4.

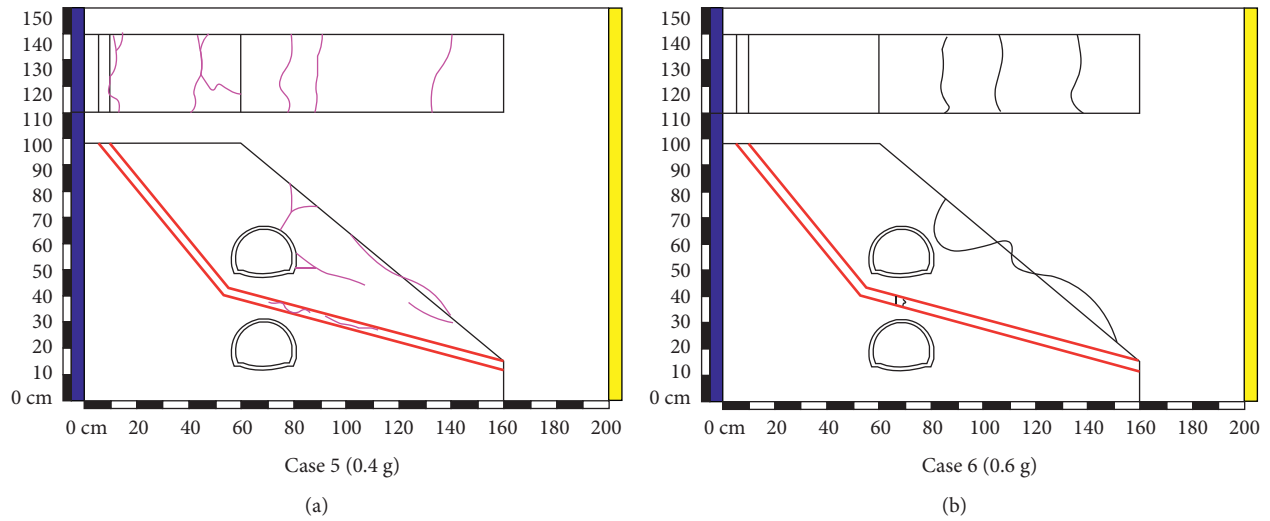


FIGURE 9: Deformation and failure in Cases 5-6.

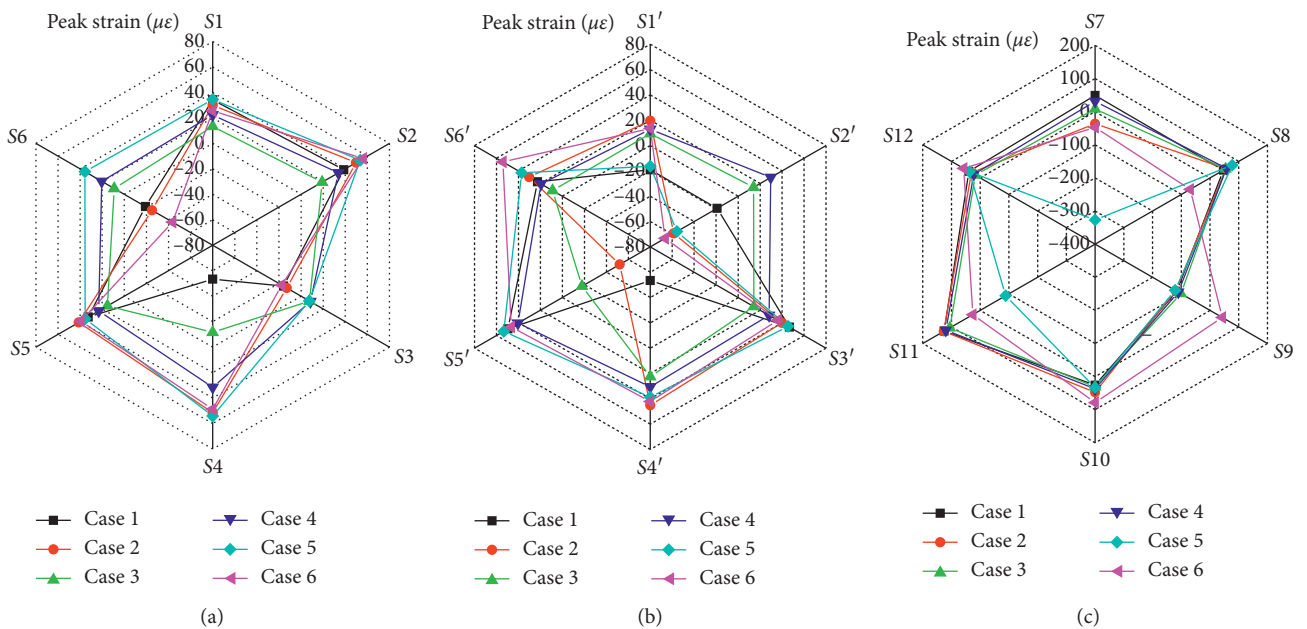


FIGURE 10: Continued.

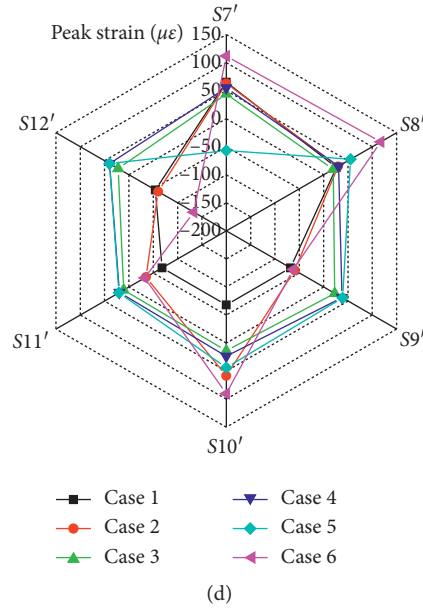


FIGURE 10: Damage of the tunnel lining. The strain gauge is tensioned as positive and compression is negative. (a) The outer surface of the upper-span tunnel. (b) The inner surface of the upper-span tunnel. (c) The outer surface of the under-crossing tunnel. (d) The inner surface of the under-crossing tunnel.

have loosened or even collapsed. Moreover, the integrity of the model has been destroyed, and its bearing capacity has been significantly weakened.

Through the above analysis, it is found that the model is basically in the critical failure stage in Case 5, so the acceleration response analysis is carried out with  $0.4g$  as an example. Figure 12 presents the acceleration time history curves of the A1–A6 in Case 5 ( $0.4g$ ). Under the action of  $0.4g$  seismic wave, the time of the peak acceleration of each measuring point is the same, which is about 30 s. Additionally, as the height of the measuring points increases, the peak acceleration also increases. The peak acceleration values of A1–A6 are 8.07, 6.22, 4.63, 3.68, 2.72, and 2.47  $\text{m/s}^2$ , respectively, and the peak acceleration values are 1.30, 1.34, 1.26, 1.35, and 1.10 times of the latter, respectively. This also confirms that the overlapped tunnel structure has a certain amplification effect on seismic waves.

## 4. Discussion

**4.1. Wavelet Packet Analysis.** It is necessary to analyze the frequency spectrum to avoid the resonance of seismic waves with the structure in the main frequency band in engineering. Through analysis, we can obtain relevant information of excellent frequencies and frequency bands to understand the frequency and periodic distribution characteristics of the seismic wave propagation process more clearly and provide relevant theoretical references for engineering practice. Therefore, the wavelet packet analysis method is introduced to analyze the seismic energy and spectral characteristics of the intersection of the two tunnels.

To further subdivide the local characteristics of acceleration signal in the time domain and frequency domain, wavelet packet, which can reflect the characteristics of both frequency packet and time domain based on wavelet analysis [30], is used to analyze the ground motion response signal. The effective frequency range of the input seismic wave of the shaking table test is 0.1~50 Hz, and the number of decomposition layers of the acceleration signal can meet the requirements by taking 3 layers considering the requirements of refinement and resolution. The analysis adopts the Meyer wavelet with good regularity, fast attenuation, and compact support in the frequency domain as the mother wavelet, and the acceleration signal is decomposed by discrete wavelet transform. The frequency band number and frequency range of the decomposed wavelet packet is shown in Figure 13.

Taking the  $0.4g$  acceleration response under Case 5 as an example, the wavelet packet transform method is used to analyze and change the upper-span tunnel invert (A4) and the under-crossing tunnel crown (A5), and the obtained acceleration response wavelet component diagrams in each frequency band are shown in Figure 14.

It is seen from Figure 14 that with the wavelet packet decomposition frequency band increases, the acceleration response gradually decreases, and the acceleration response of the first and second frequency bands is significantly larger than that of the other frequency bands. Furthermore, the main frequency bands that affect the acceleration response are the first frequency band wavelet component (0.2~6.27 Hz) and the second frequency band wavelet component (6.27~12.52 Hz), which also shows that the

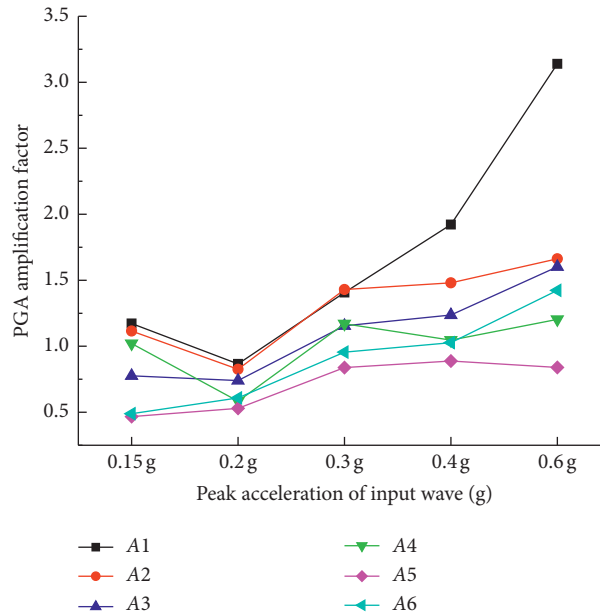


FIGURE 11: Distribution of acceleration amplification factor.

surrounding rock has a certain dissipation and filtering effect on the energy of seismic waves with medium and high frequency (above 12.52 Hz). Additionally, it can be seen that after the wavelet packet decomposition of the acceleration response, the dynamic response of each frequency band at the A4 is greater than that of the A5, which indicates that the acceleration response may have a superposition effect at the invert of the upper-span tunnel.

**4.2. Frequency Band Energy Ratio Analysis.** It can be seen from Figure 13 that, in the shaking table test, the seismic waves in the 1st and 2nd frequency bands (0.2~6.27 and 6.27~12.52 Hz) play a major role in the three-dimensional crossing tunnel, but the proportion of seismic wave energy in each frequency band cannot be clearly expressed. To quantitatively reflect the proportion of seismic wave energy in the total energy in each frequency band, the MATLAB software is used to extract the energy characteristic values in each frequency band, as shown in Table 5.

For the energy eigenvalues of each frequency band of the tunnel crown and invert, the energy eigenvalues of the 5th frequency band account for almost 0 in the total energy, indicating that the 25.02~31.27 Hz seismic wave has little effect on the crown and invert of the parallel overlapped tunnel. Except for A4 under the action of 0.2g and 0.4g seismic waves, the energy eigenvalues of the 1st frequency band of all measuring points are more than 70% of the total energy under other cases. However, the energy eigenvalues of the 2nd frequency band vary significantly in the

proportion of the total energy, and it can be obtained that under the action of seismic waves in the three cases, the average value of the energy characteristic of the 2nd frequency band at each measurement point accounts for about 14.9% of the total energy. This also shows that the main effects on the crown and invert of the tunnel are the 1st frequency band (0.2~6.27 Hz) and the 2nd frequency band (6.27~12.52 Hz) seismic waves, and the 1st frequency band seismic wave plays a leading role.

When the peak value of the input wave is 0.2, 0.4, and 0.6g, the maximum sum of the energy eigenvalues of the 1st and the 2nd frequency band is 96.65%, 98.11%, and 98.51%, and the minimum is 94.70%, 89.66%, and 88.84%, respectively. With the increase of the peak value of the input wave, the proportion of the sum of the energy eigenvalues of the 1st and the 2nd frequency band to the total energy is increasing, which is caused by the gradual increase of the proportion of the energy eigenvalues of the 2nd frequency band. Furthermore, this shows that as the peak value of the input wave increases, the influence of the energy eigenvalue of the 1st frequency band is gradually reduced, while the influence of the 2nd frequency band is increasing.

For the sum of the energy eigenvalues of the 1st and 2nd frequency band seismic waves, the energy eigenvalues of the upper-span tunnel crown are all larger than those of the invert, while the energy eigenvalues of the under-crossing tunnel crown are gradually smaller than those of the invert with the increase of the seismic wave loading

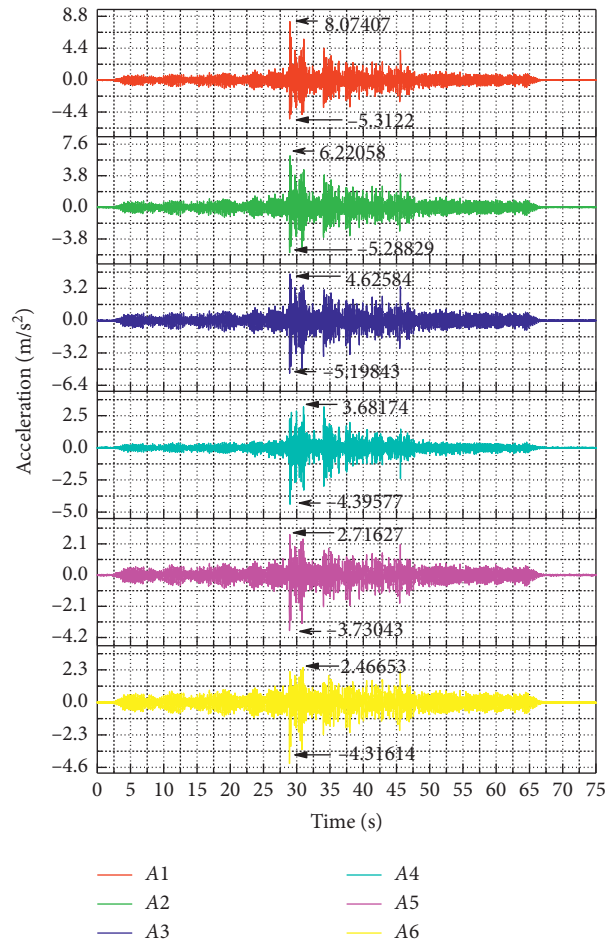


FIGURE 12: Time history of the acceleration of the central section under the action of 0.4g seismic wave.

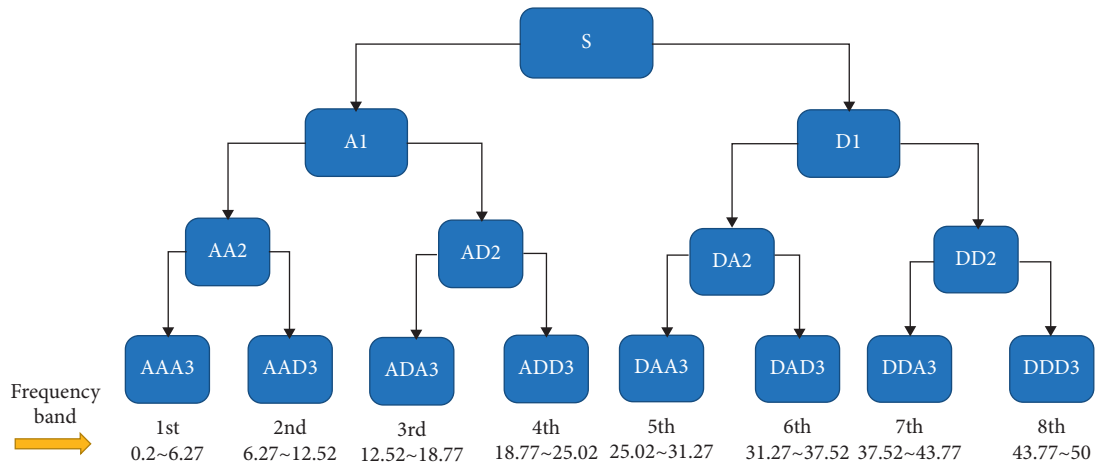


FIGURE 13: Decomposed wavelet packet frequency band number and frequency range. *Note.* S is the original input signal, A is an approximate signal, and D is the detailed signal (relatively high frequency). The width of each frequency band is  $50/8 = 6.23$  Hz, and the corresponding lowest frequency band is  $0.2 \sim 0.6$  Hz.

peak value. This phenomenon indicates that under the action of seismic loadings, the energy distribution characteristics of the upper-span and under-crossing tunnels

are inconsistent, and the main weak position of the upper-span tunnel is the crown while the under-crossing tunnel is the invert.

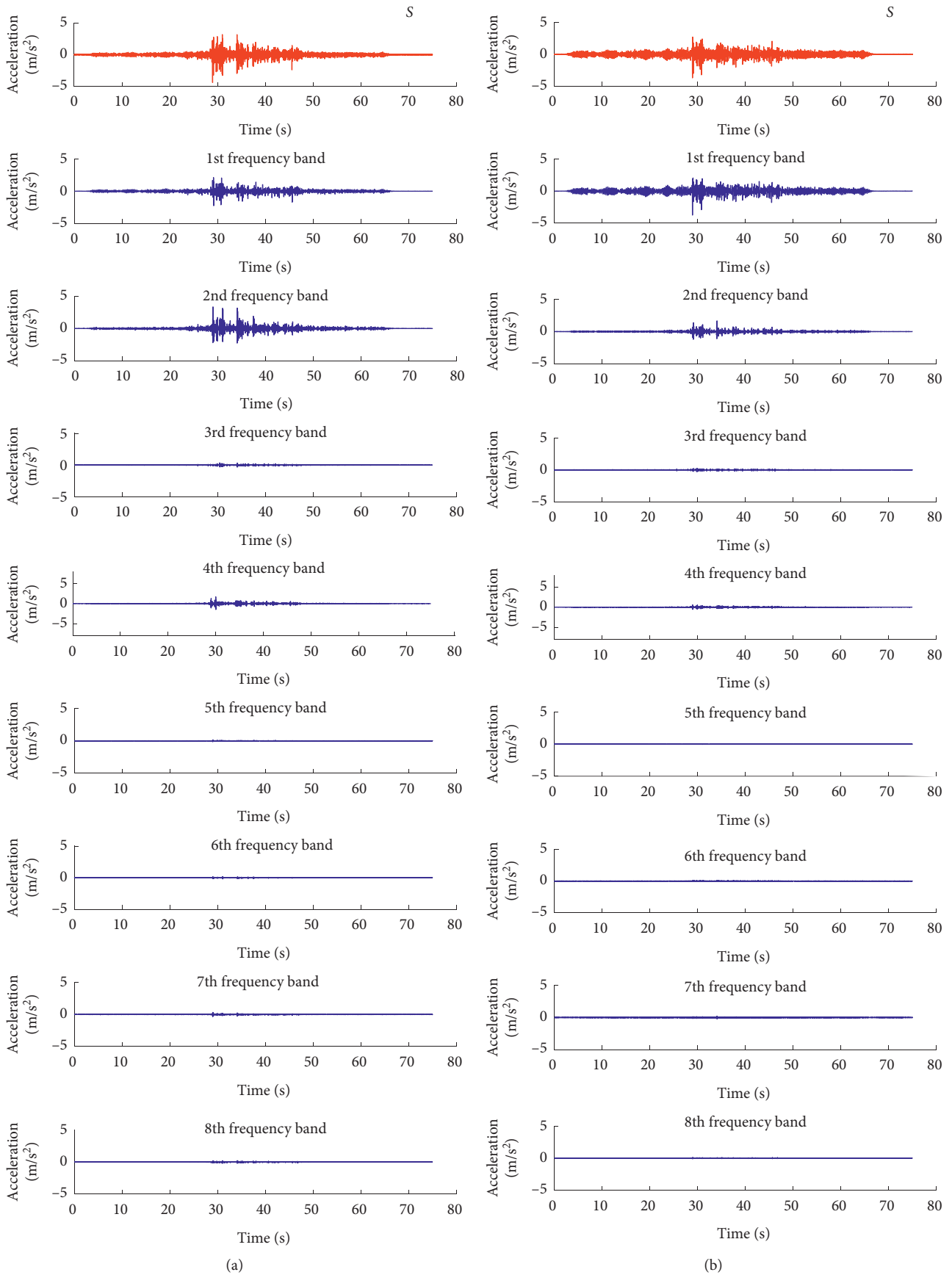


FIGURE 14: Wavelet component of acceleration response under the action of 0.4g seismic wave. The red curve denotes the original dynamic acceleration time-domain curve, and the blue curves from top to bottom denote the wavelet components of the 1st to 8th frequency bands. (a) A4. (b) A5.



TABLE 5: Acceleration energy ratio of the crown and invert under different amplitude seismic waves.

Monitoring point	0.2g				0.4g				0.6g				
	A3	A4	A5	A6	A3	A4	A5	A6	A3	A4	A5	A6	
Energy ratio of each frequency band (%)	E1	79.71	80.60	89.94	77.33	78.10	48.14	87.16	89.96	74.33	48.93	80.52	83.56
	E2	16.94	14.10	6.67	18.58	19.64	40.70	10.28	8.55	22.83	40.73	16.47	14.55
	E3	0.65	0.79	0.67	1.51	0.67	1.36	0.60	0.55	0.81	1.26	0.78	0.65
	E4	1.53	2.79	1.08	1.22	1.28	8.77	1.45	0.52	1.58	7.99	1.78	0.83
	E5	0.06	0.08	0.07	0.06	0.02	0.05	0.02	0.01	0.02	0.05	0.02	0.02
	E6	0.43	0.60	0.57	0.13	0.05	0.23	0.05	0.04	0.07	0.24	0.06	0.04
	E7	0.29	0.43	0.54	0.99	0.18	0.33	0.35	0.33	0.23	0.43	0.29	0.27
	E8	0.39	0.61	0.56	0.17	0.07	0.42	0.10	0.05	0.12	0.37	0.09	0.06

## 5. Conclusion

- (1) The failure process of the model can be roughly divided into three stages, no obvious failure stage (0.1~0.15 g), deformation stage (0.2~0.3g), and failure stage (0.4~0.6g). First, the model appeared cracks on the crown of the upper-span tunnel, and the top of the slope and the intersection of the overlapped tunnel were damaged with the increase of the input seismic wave. Then, the cracks at the top of the upper-span tunnel penetrated and “tore” into the slope, causing a large amount of displacement. Finally, a large number of blocks at the place where the slope was pulled, collapsed and slipped, and the model was completely destroyed.
- (2) According to the peak dynamic strain response of the tunnel, the lining damage on the outer surface of the upper-span and under-crossing tunnels mainly occurred on the right arch waist and the left side wall. Additionally, the lining damage on the inner surface of the upper-span tunnel was mainly reflected on the left arch waist, while the under-crossing tunnel was mainly manifested on the right waist arch, the crown, and the invert.
- (3) For the parallel overlapped tunnel, the acceleration response at the crown and invert of the tunnel is significantly different from that of a single-hole tunnel. Owing to the spatial effect and mutual influence of the intersection, the existence of the upper-span tunnel has a certain weakening of the seismic response of the under-crossing tunnel, and this weakening effect is more obvious for the crown of the under-crossing tunnel.
- (4) From energy eigenvalues of seismic waves, the main influences on the crown and invert of the tunnel were in the 1st frequency band (0.2~6.27 Hz) and the 2nd frequency band (6.27~12.52 Hz) seismic waves, and the 1st frequency band seismic wave played a leading role. Furthermore, the energy distribution characteristics of the upper-span and under-crossing tunnels were inconsistent, and the main weak position of the upper-span tunnel was the crown while the under-crossing tunnel was the invert.

## Data Availability

The data used to support the findings of this study are available from the corresponding author upon request.

## Conflicts of Interest

The authors declare that there are no conflicts of interest regarding the publication of this article.

## Acknowledgments

The authors gratefully acknowledge the financial support by the National Key R&D Program of China (no. 2018YFC1504901), Natural Science Foundation of Gansu Province (no. 145RJZA068), Science and Technology Development Project of China Railway Research Institute Co. Ltd (2017-KJ008-Z008-XB), and Sichuan Provincial Science and Technology Plan Project (nos. 2021YFS0323, 2020YJ0253, and 2020YFSY0060).

## References

- [1] B. Yang, J. Hou, Y. Liu, and Z. Zhou, “Dynamic response and failure characteristics of slope with weak interlayer under action of near-fault ground motion,” *Shock and Vibration*, vol. 2021, p. 18, Article ID 5595278, 2021.
- [2] B. Yang, Z. Zhou, and L. Zhuo, “Experimental study on instability characteristic and bearing capacity of slope with bedrock under the action of rainfall,” *Journal of Southwest Jiaotong University*, (in Chinese), 2020.
- [3] M. S. Islam and M. Iskander, “Twin tunnelling induced ground settlements: a review,” *Tunnelling and Underground Space Technology*, vol. 110, Article ID 103614, 2021.
- [4] Y. Li, L. Peng, and M. Lei, “Research progress in the design and construction technology of crossing tunnels,” *Journal of Railway Science and Engineering*, vol. 11, no. 1, pp. 67–73, 2014, in Chinese.
- [5] C. Liu, L.-M. Peng, M.-F. Lei et al., “Research on crossing tunnels’ seismic response characteristics,” *Korean Society of Civil Engineers*, vol. 23, no. 11, 2019.
- [6] H. Lei, H. Wu, Q. Meng et al., “Study on seismic dynamic response of oblique overlapped tunnels,” *Tunnel Construction*, vol. 41, no. 1, p. 88, 2021, in Chinese.
- [7] L. Kang, C. Shi, L. Peng et al., “Study on the influence factors of crossing tunnel based on orthogonal experiment,” *Journal of Railway Science and Engineering*, vol. 9, no. 4, pp. 70–74, 2012, in Chinese.

- [8] M. Yin, H. Jiang, Y. Jiang, Z. Sun, and Q. Wu, "Effect of the excavation clearance of an under-crossing shield tunnel on existing shield tunnels," *Tunnelling and Underground Space Technology*, vol. 78, pp. 245–258, 2018.
- [9] X. G. Li and D. J. Yuan, "Response of a double-decked metro tunnel to shield driving of twin closely under-crossing tunnels," *Tunnelling and Underground Space Technology*, vol. 28, pp. 18–30, 2012.
- [10] H. Kuriyama, T. Koga, T. Ogata et al., "The design and construction of pillar reinforcement at horizontal twin tunnels," *Journal of Tunnel Engineering JSCE*, vol. 10, pp. 125–130, 2011.
- [11] J. Gong, C. Xia, and X. Lei, "Analysis of field measurement and theoretical calculation on rock pressure in shallow-buried twin tunnels with small spacing," *Chinese Journal of Rock Mechanics and Engineering*, vol. 29, no. S2, pp. 4139–4145, 2010.
- [12] B. Liu, Z. Yu, Y. Han, Z. Wang, R. Zhang, and S. Wang, "Analytical solution for the response of an existing tunnel induced by above-crossing shield tunneling," *Computers and Geotechnics*, vol. 124, Article ID 103624, 2020.
- [13] Q. Lin, D. Lu, C. Lei, Y. Tian, Q. Gong, and X. Du, "Model test study on the stability of cobble strata during shield under-crossing," *Tunnelling and Underground Space Technology*, vol. 110, Article ID 103807, 2021.
- [14] C. Zhang, X. Zhang, and Q. Fang, "Behaviors of existing twin subway tunnels due to new subway station excavation below in close vicinity," *Tunnelling and Underground Space Technology*, vol. 81, pp. 121–128, 2018.
- [15] H. Y. Liu, J. C. Small, J. P. Carter, and D. J. Williams, "Effects of tunnelling on existing support systems of perpendicularly crossing tunnels," *Computers and Geotechnics*, vol. 36, no. 5, pp. 880–894, 2009.
- [16] Q. Fang, D. Zhang, Q. Li, and L. N. Y. Wong, "Effects of twin tunnels construction beneath existing shield-driven twin tunnels," *Tunnelling and Underground Space Technology*, vol. 45, pp. 128–137, 2015.
- [17] Y.-F. Jin, B.-Q. Zhu, Z.-Y. Yin, and D.-M. Zhang, "Three-dimensional numerical analysis of the interaction of two crossing tunnels in soft clay," *Underground Space*, vol. 4, no. 4, pp. 310–327, 2019.
- [18] Y. Li, L. Peng, and M. Lei, "Dynamics issues regarding high-speed railway crossing tunnels," *Modern Tunnelling Technology*, vol. 52, no. 2, pp. 8–15, 2015, in Chinese.
- [19] H. Yi, T. Qi, W. Qian, Y. Yu, Y. Liu, Z. Li et al., "Influence of long-term dynamic load induced by high-speed trains on the accumulative deformation of shallow buried tunnel linings," *Tunnelling and Underground Space Technology*, vol. 84, pp. 166–176, 2019.
- [20] Y. Xia, N. Jiang, C. Zhou, and X. Luo, "Safety assessment of upper water pipeline under the blasting vibration induced by Subway tunnel excavation," *Engineering Failure Analysis*, vol. 104, pp. 626–642, 2019.
- [21] J. Lai, H. Fan, J. Chen et al., "Blasting vibration monitoring of undercrossing railway tunnel using wireless sensor network," *International Journal of Distributed Sensor Networks*, vol. 2015, pp. 1–9, 2015.
- [22] H.-B. Zhao, Y. Long, X.-H. Li, and L. Lu, "Experimental and numerical investigation of the effect of blast-induced vibration from adjacent tunnel on existing tunnel," *KSCE Journal of Civil Engineering*, vol. 20, no. 1, pp. 431–439, 2016.
- [23] X. Zhang, Zhoushunhua, C. He et al., "Experimental Investigation on train-induced vibration of the ground railway embankment and under-crossing subway tunnels," *Transportation Geotechnics*, vol. 26, Article ID 100422, 2020.
- [24] W. Yang, C. Zhang, D. Liu, Q. Yan, Y. Fang, C. He et al., "The effect of cross-sectional shape on the dynamic response of tunnels under train induced vibration loads," *Tunnelling and Underground Space Technology*, vol. 90, pp. 231–238, 2019.
- [25] T. Grigorios, S. Filomena de, A. Ioannis et al., "Seismic behaviour of tunnels: from experiments to analysis," *Tunnelling and Underground Space Technology*, vol. 90, Article ID 103334, 2020.
- [26] H. Lei, H. Wu, and T. Lai, "Shaking table tests for seismic response of oblique overlapped tunnel," *Shock and Vibration*, vol. 2021, Article ID 8816755, 19 pages, 2021.
- [27] H. Wu, H. Lei, and T. Lai, "Shaking table tests for seismic response of orthogonal overlapped tunnel under horizontal seismic loading," *Advances in Civil Engineering*, vol. 2021, Article ID 6633535, 19 pages, 2021.
- [28] T. Zhang, B. Gao, K. Fan et al., "Study on flexible material in the sidewall of rigid model box in shaking table test," *Chinese Journal of Rock Mechanics and Engineering*, vol. 37, no. 10, pp. 2415–2424, 2018, in Chinese.
- [29] H. Wu, X. Chen, and A. Hui, "Research on the force exerting mode model test of tunnel-landslide orthogonal system," *Journal of Railway Engineering Society*, vol. 33, no. 3, pp. 1–28, 2016, in Chinese.
- [30] A. Grinsted, J. C. Moore, and S. Jevrejeva, "Application of the cross wavelet transform and wavelet coherence to geophysical time series," *Nonlinear Processes in Geophysics*, vol. 11, no. 5–6, pp. 561–566, 2004.

## Research Article

# Vibration Response Characteristics and Application of Existing Railway Subgrade

Junyun Zhang , Zhuoling He , Siyuan Chen , and Le Zhang 

*School of Civil Engineering, Southwest Jiaotong University, Chengdu 610031, China*

Correspondence should be addressed to Junyun Zhang; [zjywxjfb@swjtu.edu.cn](mailto:zjywxjfb@swjtu.edu.cn)

Received 31 March 2021; Accepted 18 May 2021; Published 28 May 2021

Academic Editor: Gang Fan

Copyright © 2021 Junyun Zhang et al. This is an open access article distributed under the Creative Commons Attribution License, which permits unrestricted use, distribution, and reproduction in any medium, provided the original work is properly cited.

The existing conventional methods of subgrade disease assessment are not suitable for the existing lines. There are many research studies on the vibration response and attenuation law of the railway subgrade, but few research studies focus on the vibration response and attenuation law caused by the weak subgrade. In this study, vibration response tests were carried out at different positions and depths of the subgrade before and after reinforcement improvement. The results show that vibration response near the ballast is obvious, and it attenuates with the increase of the horizontal distance from the rail; the vibration acceleration response of the subgrade after reinforcement changes greatly; the vibration response curve of the reinforced section is spindle shaped, and the vertical vibration acceleration response attenuates obviously at the depth of 6.5 m, only about 10% to 30% of the surface; the vibration acceleration of the subgrade with reinforcement at the depth of 4.5 m attenuates to 60% of the surface; the vibration acceleration of the subgrade without reinforcement at the depth of 4.5 m attenuates to 50%–60% of the surface.

## 1. Introduction

At present, the conventional methods for evaluating subgrade diseases mainly include the stiff-plate bearing test [1, 2], cone penetration test [3, 4], dynamic penetration test [5–8], and ground-penetrating radar [9–14]. Among them, the stiff-plate bearing test and the penetration test could affect the normal operation of the train, and the test point is single, which cannot represent the subgrade state of the section. The ground-penetrating radar could determine the structural layers of the subgrade quickly and soil layers such as ballast bags, but it cannot quantitatively analyze the physical and mechanical indexes of the subgrade. These disease detections for existing line have limitations, not applicable to disease detection of existing lines.

Researchers have carried out a lot of theoretical analysis, numerical simulation test, indoor model test, and field test on vibration response characteristics and attenuation law of the railway subgrade [15–24]. In the early study of the subgrade vibration response, scholars considered the influence of thickness [5], grouping form [25], train speed [26], and properties of soil [27] on

subgrade vibration response characteristics and attenuation law. Previous research usually focused on indoor model test and numerical simulation. But as the most direct method for subgrade vibration response characteristics, field tests conducted in China [28, 29], France [30], Germany [31], and UK [32] provided an important basis for the study of subgrade vibration response characteristics. However, there are few field test studies on the vibration response and attenuation law of the diseased subgrade, and the characteristics of the vibration response of the diseased subgrade for a railway line are not definite at present.

Based on Baoji-Zhongwei Railway improvement project, the monitoring results of vibration response difference between the weak subgrade and improved subgrade are compared. And the acceleration in the maximum value, mean value, and effective value are discussed to research the attenuation law of the weak subgrade and improved subgrade. In addition, the selection of monitoring point location is analyzed. The comparison before and after the reinforcement may provide reference for the detection method of the weak subgrade.

## 2. General Situation of Test Site

Baoji-Zhongwei Railway, built in the 1990s, is a single-line multipurpose railway, as shown in Figure 1. The research site is located in section K329–K331, 20 km away from the Guyuan City. The diseased subgrade lies among farmland, and water content in loess at a certain depth of the surface is high due to irrigation. The subgrade shows soft plastic or flow plastic shape, leading to subgrade settlement under the action of train dynamic load. The monitoring section is a typical northwest seasonal frozen region in China, freezing in winter and thawing in summer. As the surrounding farmland is irrigated, the maximum freezing depth is 1.4 m–3 m.

## 3. Principle

The subgrade has a certain plasticity. The measured displacement is lagging (Figure 2), and the measured vibration value is affected by many factors. Therefore, the displacement is not suitable for vibration test and analysis. In most of the subgrade vibration response monitoring, the monitoring target train is fast and the frequency is high, and the vibration acceleration is often used as the detection index. Considering the on-site monitoring results and engineering practice, the vibration acceleration is taken as the detection index in this research.

The relationship between vibration acceleration and subgrade stiffness is explained by theoretical derivation of the vibration response of the subgrade surface under moving load, as shown in the following equation:

$$(\lambda + G)\nabla(\nabla \cdot \vec{u}) + G\nabla^2 \vec{u} + \vec{X} = \rho \frac{\partial^2 \vec{u}}{\partial t^2}, \quad (1)$$

Where  $\vec{u} = \vec{u}(\vec{x}, t) = (u(x, y, z, t), v(x, y, z, t), w(x, y, z, t))$  is the displacement of viscoelastic half-space;  $\vec{X} = \vec{X}(\vec{x}, t) = (X_x(x, y, z, t), X_y(x, y, z, t), X_z(x, y, z, t))$  is the body force of viscoelastic half-space;  $\lambda$  and  $G$  are the Lamé parameters of viscoelastic half-space;  $\rho$  is the density of viscoelastic half-space;  $\nabla$  is the Hamilton operator; and  $\nabla^2$  is the Laplace operator.

At present, viscoelastic half-space is widely used to simulate subgrade. The governing equation of the ideal model of viscoelastic half-space expressed is as follows.

For the basic governing equations, there are many ways to solve them. At present, the commonly used methods are the green function method and direct integral change method [33].

According to the geometric equation and physical equation of viscoelastic dynamics, Fourier transform is carried out with respect to the spatial variables  $x$  and  $y$ , as shown in the following equation:

$$\begin{aligned} \sigma_{zz} &= \left[ (\lambda + 2G) \frac{\partial^2}{\partial z^2} - \lambda(k_1^2 + k_2^2) \right] \Phi - 2iGk_2 \frac{\partial \psi_1}{\partial z} + 2iGk_1 \frac{\partial \psi_2}{\partial z}, \\ \tau_{zx} &= G \left[ 2ik_1 \frac{\partial \Phi}{\partial z} + k_1 k_2 \Psi_1 - \left( k_1^2 + \frac{\partial^2}{\partial z^2} \right) \psi_2 \right], \\ \tau_{zy} &= G \left[ 2ik_1 \frac{\partial \Phi}{\partial z} + k_1 k_2 \Psi_1 - \left( k_1^2 + \frac{\partial^2}{\partial z^2} \right) \psi_2 \right], \end{aligned} \quad (2)$$

where  $\Phi$  is the scalar function;  $\psi_1$  and  $\psi_2$  are vector functions;  $\lambda$  and  $G$  are the Lamé constants of viscoelastic half-space;  $\rho$  is the density of viscoelastic half-space; and  $k_1$  and  $k_2$  are the wave numbers along the directions of  $x$  and  $y$ .

Stress boundary condition of viscoelastic questions is imported, as shown in the following equation:

$$\begin{aligned} z &= 0, \\ \sigma_{zz} &= -F, \\ \tau_{zx} &= 0, \\ \tau_{zy} &= 0. \end{aligned} \quad (3)$$

Considering the above formula, the acceleration can be obtained as

$$\begin{aligned} a &= -\frac{Pc^2}{4\pi^2 G} \int_{-\infty}^{+\infty} \int_{-\infty}^{+\infty} \frac{k_1^2}{\Delta} \left[ B_p (k_1^2 + k_2^2 + B_s^2) e^{-B_p z} \right. \\ &\quad \left. - 2B_p (k_1^2 + k_2^2) e^{-B_s z} e^{i(k_1 x + k_2 y - k_1 ct)} \right] dk_1 dk_2, \end{aligned} \quad (4)$$

where  $P$  is the value of load,  $\delta(\cdot)$  is the load action function,  $f(t)$  is the load function which changes over time,  $B_{p,s}^2 = k_1^2 + k_2^2 - k_{p,s}^2$ ,  $k_{p,s} = \omega/c_{p,s}$ ,  $\omega$  is the vibrational frequency, and  $k_1$  and  $k_2$  are the wave numbers along the directions of  $x$  and  $y$ .

It can be seen from the above formulas that the vibration acceleration of the subgrade can reflect the stiffness characteristics of the subgrade to a certain extent. The stiffness properties of the subgrade before and after treatment are obviously different. Hence, it is reasonable that vibration acceleration is used to reflect the stiffness properties of the subgrade in this research.

## 4. Monitoring Scheme

**4.1. Vibration Response Monitoring Equipment.** An 891-2 vibration pickup developed by the Institute of Engineering Mechanics, CEA, was used in this test, as shown in Figure 3. Moreover, an amplifier and an acquisition instrument were adopted for monitoring, and the connection among the instruments is shown in Figure 4. The vibration pickup was connected to the amplifier to amplify the collected vibration response signal by a certain multiple. And then it was connected to the data acquisition instrument. The data acquisition instrument was connected with the computer to directly analyze and sort out the test signal.

**4.2. Reinforcement Scheme.** Sections K329+530 and K330+990 were reinforced by rotary jet grouting piles from December 3, 2016, to December 15, 2016, as shown in Figure 5. Rotary jet grouting piles were used to reinforce this section of subgrade. The distance between the rotary jet grouting piles was 2 m, arranged crosswise.

**4.3. Arrangement of Measuring Points.** Three representative sections were selected for vibration monitoring in this monitoring, K329+530, K330+990, and K331+315, to comprehensively analyze the vibration response

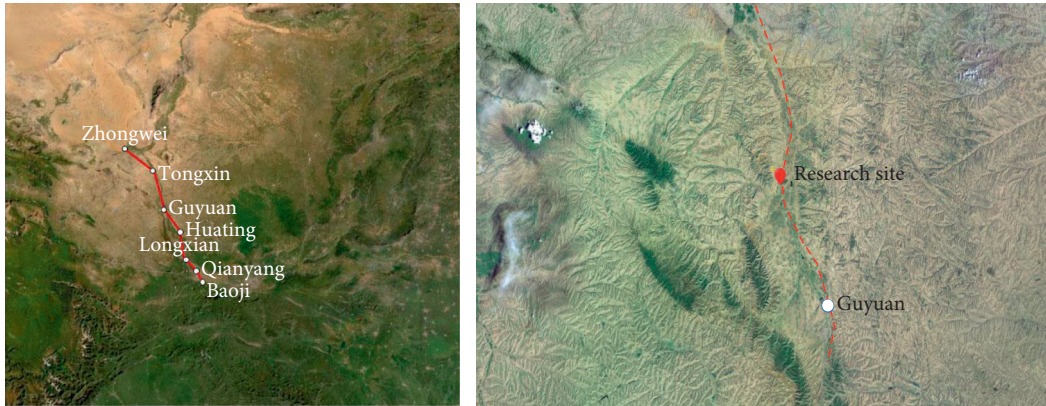


FIGURE 1: The location of research site.

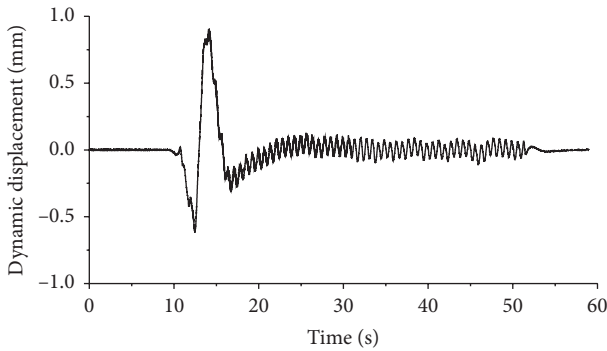


FIGURE 2: Time history diagram of dynamic displacement.



FIGURE 4: Connection among the instruments.



FIGURE 3: 891-2 vibration pickup.

characteristics of existing railway subgrade. K331 + 315 is weak subgrade, and the other two are improved subgrades. And the vibration acceleration of the subgrade adjacent to ballast, foot of subgrade, and subgrade underneath the foundation were monitored, respectively. Three directions are specified, of which the X direction is parallel to the rail direction (longitudinal), the Y direction is perpendicular to the rail direction (transverse), and the Z direction is vertical, as shown in Figure 6(a).

Measuring point C1 and measuring point C2 were arranged in section K329 + 530, to monitor the response characteristics of subgrade vibration at different locations. In this test, two measuring points were set on the surface

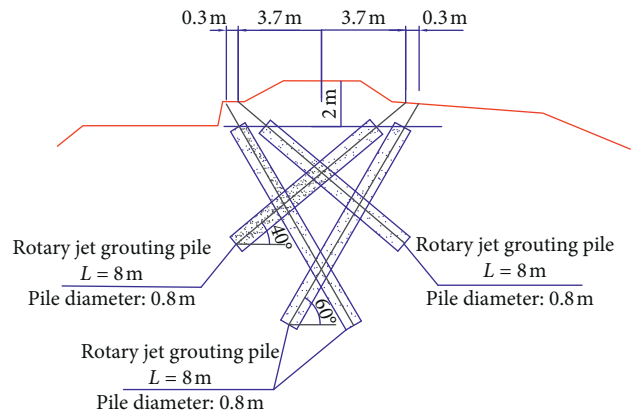


FIGURE 5: Plane layout of existing railway subgrade strengthened by inclined rotary jet grouting pile.

perpendicular to the direction of embankment. Measuring point C1 was set at the ballast and measuring point C2 was set at the bottom of embankment, as shown in Figure 6(b).

In order to research the propagation and attenuation law of the vibration response along soil depth before and after subgrade reinforcement treatment as well as the seasonal variation, measuring points were arranged in sections K330 + 990 and K331 + 315. Considering the communication optical cable along the railway, the measuring points

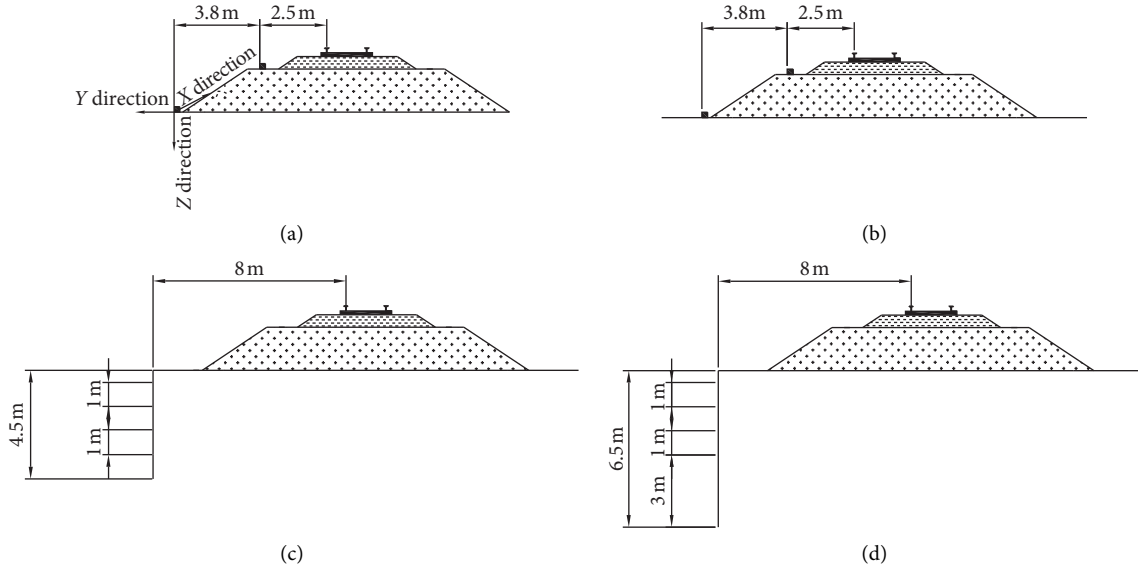


FIGURE 6: Schematic diagram of the layout of the vibrator pickup. (a) The layout direction of the vibrator. (b) Section K329 + 530. (c) Section K330 + 990. (d) Section K331 + 315.

were arranged at a distance of 8 m from the rail horizontal distance. The specific layout depths of K330 + 990 section after subgrade reinforcement were 0.5 m, 1.5 m, 2.5 m, 3.5 m, and 6.5 m, respectively, as shown in Figure 6(c). The specific layout depths of section K331 + 315 section before subgrade reinforcement treatment were 0.5 m, 1.5 m, 2.5 m, 3.5 m, and 4.5 m, respectively, as shown in Figure 6(d).

## 5. Results and Analysis

**5.1. Selection of Vibration Direction and Value.** The response of subgrade vibration influenced by train passing is a complex forced composite action. In order to elaborate this response more reasonably, different physical representative values need to be taken for analysis. In this paper, the characteristic values of vibration acceleration are defined as follows: the average value of the absolute maximum acceleration, in which 5 maximum acceleration values and 5 minimum acceleration values are calculated; the effective value while the train passes; and the average value while the train passes. The expression of the three is shown in equations (5)–(7).

$$|a_i|_{\max} = \frac{\sum_{j=1}^N |a_i|_{\max}}{N} \quad (5)$$

· (i = X, Y, Z; j = 1, 2, 3, ..., N = 10),

$$|a_i|_{\text{val}} = \frac{1}{N} \sqrt{\sum_{j=1}^N |a_i|^2} \quad (6)$$

· (i = X, Y, Z; j = 1, 2, 3, ..., N),

$$|a_i|_{\text{ave}} = \frac{\sum_{j=1}^N |a_i|}{N} \quad (i = X, Y, Z; j = 1, 2, 3, \dots, N). \quad (7)$$

From Figure 7, it can be seen that among the three directions of vibration acceleration, the largest is vertical vibration acceleration (Z direction) and the smallest is Y direction. In addition, the mean and the effective values are more obvious than the maximum, and the mean and the effective values in Z direction are more significant than those in other two directions. Therefore, the mean and effective values of vertical vibration acceleration are taken as the indexes to study the attenuation law of vibration acceleration of damaged subgrade.

**5.2. Vibration Response along Horizontal Distance of Subgrade.** It can be seen from Figures 8 and 9 that before foundation reinforcement, the peak vertical, longitudinal, and transverse vibration accelerations near ballast are 8.45 mm/s<sup>2</sup>, 14.4 mm/s<sup>2</sup>, and 22.3 mm/s<sup>2</sup>, respectively, while the peak vertical, longitudinal, and transverse vibration accelerations of the foot of the subgrade are 6.85 mm/s<sup>2</sup>, 6.37 mm/s<sup>2</sup>, and 3.06 mm/s<sup>2</sup>, respectively; the vibration response decreases with the increase of the horizontal distance from rails. The vibration response of C1 measuring point is more obvious, and it is suitable to study the vibration response characteristics before and after subgrade reinforcement if considering the actual situation.

### 5.3. Vibration Response before and after Subgrade Reinforcement

**5.3.1. Time-Domain Curve.** Figure 10(a) shows a time history diagram of vibration acceleration at K331 + 315

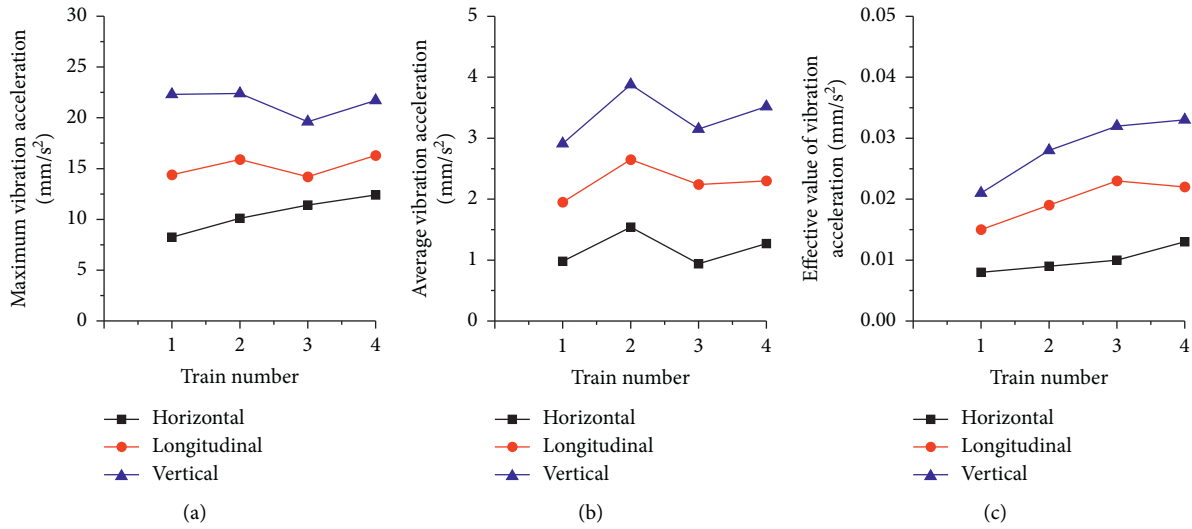


FIGURE 7: Vertical vibration acceleration at K329 + 530 C1 measuring point. (a) Maximum before reinforcement. (b) Average acceleration before reinforcement. (c) Effective value before reinforcement.

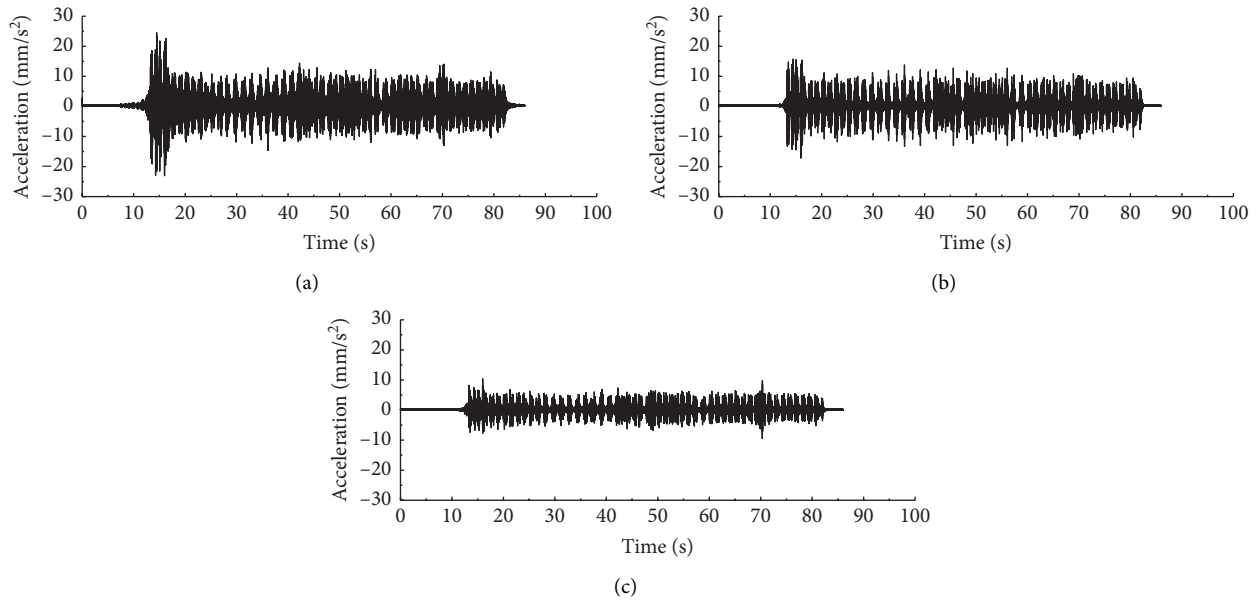


FIGURE 8: Time-domain curves of vibration acceleration of C1 measuring point before subgrade reinforcement-truck in different directions: (a) Z direction. (b) Y direction. (c) X direction.

measuring point when a truck passes by. The vibration response at various depths and the vibration acceleration caused by wheel pairs at different depths at the same time can be clearly seen in the diagram. The vibration acceleration response at 0.5 m away from the surface is greater than that at 1.5–3.5 m, and the vibration acceleration attenuation at 4.5 m is obvious. Figure 10(b) shows the response time history diagram of subgrade vibration acceleration at K330 + 990 measuring point. It can be seen in the diagram that the response of vibration acceleration caused by train passing is consistent from top to bottom. The response time history curve of subgrade vibration acceleration caused by train passing shows periodic variation characteristics with obvious peak and oscillation

characteristics, which are excited directly by periodic wheel and axle forces of the train. The peak and valley of the vibration acceleration response at 6.5 m underground are not obvious, and the time history curve is close to the spindle shape. Refraction and reflection occur when the vibration wave reaches this depth, which leads to non-periodicity of vibration.

**5.3.2. Vibration Attenuation Law.** According to the result of vibration direction, the mean and the effective values in Z direction are more significant than those in other two directions. Therefore, the vibration attenuation law of vertical vibration was studied, as seen in Figures 11 and 12.

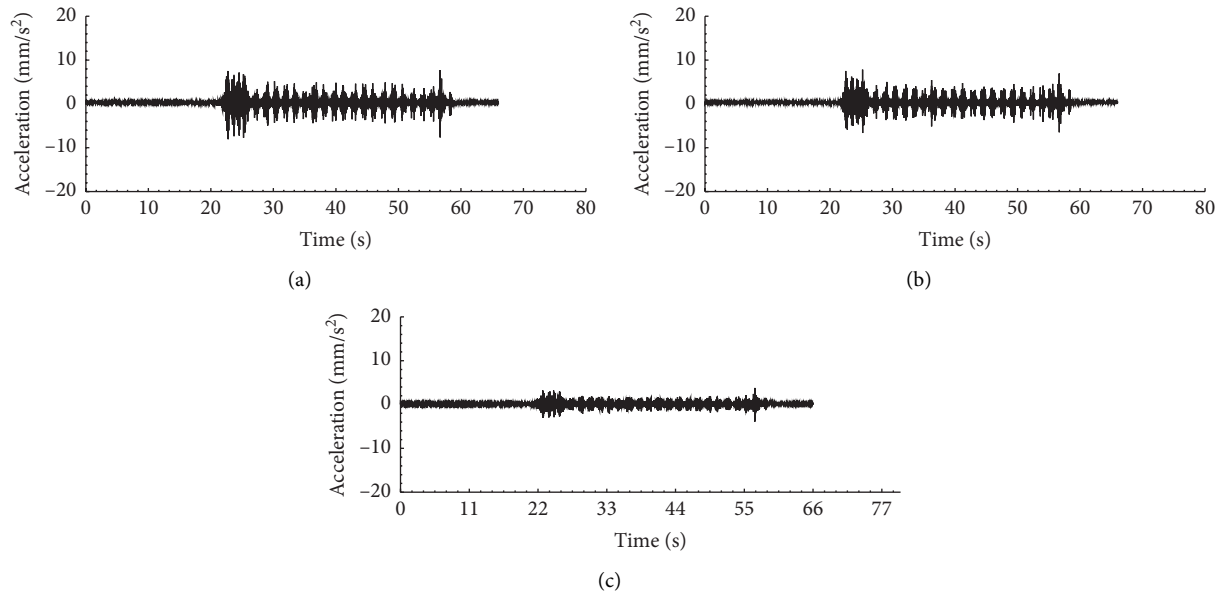


FIGURE 9: Time-domain curves of vibration acceleration of C2 measuring point before subgrade reinforcement-truck in different directions: (a) Z direction. (b) Y direction. (c) X direction.

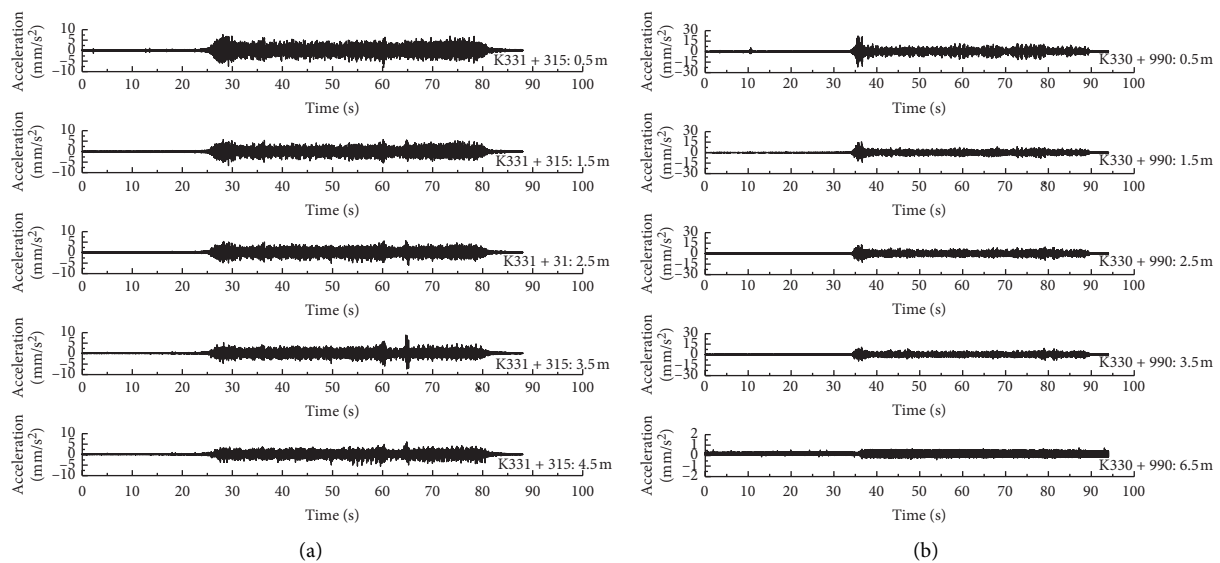


FIGURE 10: Time-domain diagram of vertical vibration acceleration. (a) K331 + 315. (b) K330 + 990.

- (1) The average value of vibration acceleration at the K330 + 990 subgrade shallow layer ( $Z=0.5$  m) is  $2.45 \text{ mm/s}^2$ , while the corresponding average value of vibration acceleration at the subgrade deep layer ( $Z=6.5$  m) is only  $0.15 \text{ mm/s}^2$ , which reflects the attenuation process of vibration propagation in soil. Due to the dissipation of vibration energy by soil material damping and geometric damping, the vibration acceleration of soil gradually decreases with the increase of depth.
- (2) Maximum of time history curve of soil vibration acceleration corresponds to load-force time history curve, which reflects the loading characteristics of moving loads of trains. Among them, 0.5–4.5 m has obvious loading characteristics of vibration acceleration time history curve due to its shallow distance to the ground surface, while 6.5 m has no obvious loading characteristics due to its deep distance to the vibration source.
- (3) The vibration response of different measuring points differs greatly, and the vibration response of the reinforcement section is larger than that of the non-reinforcement section as a whole. For K330 + 990 measuring point, the vibration attenuation is



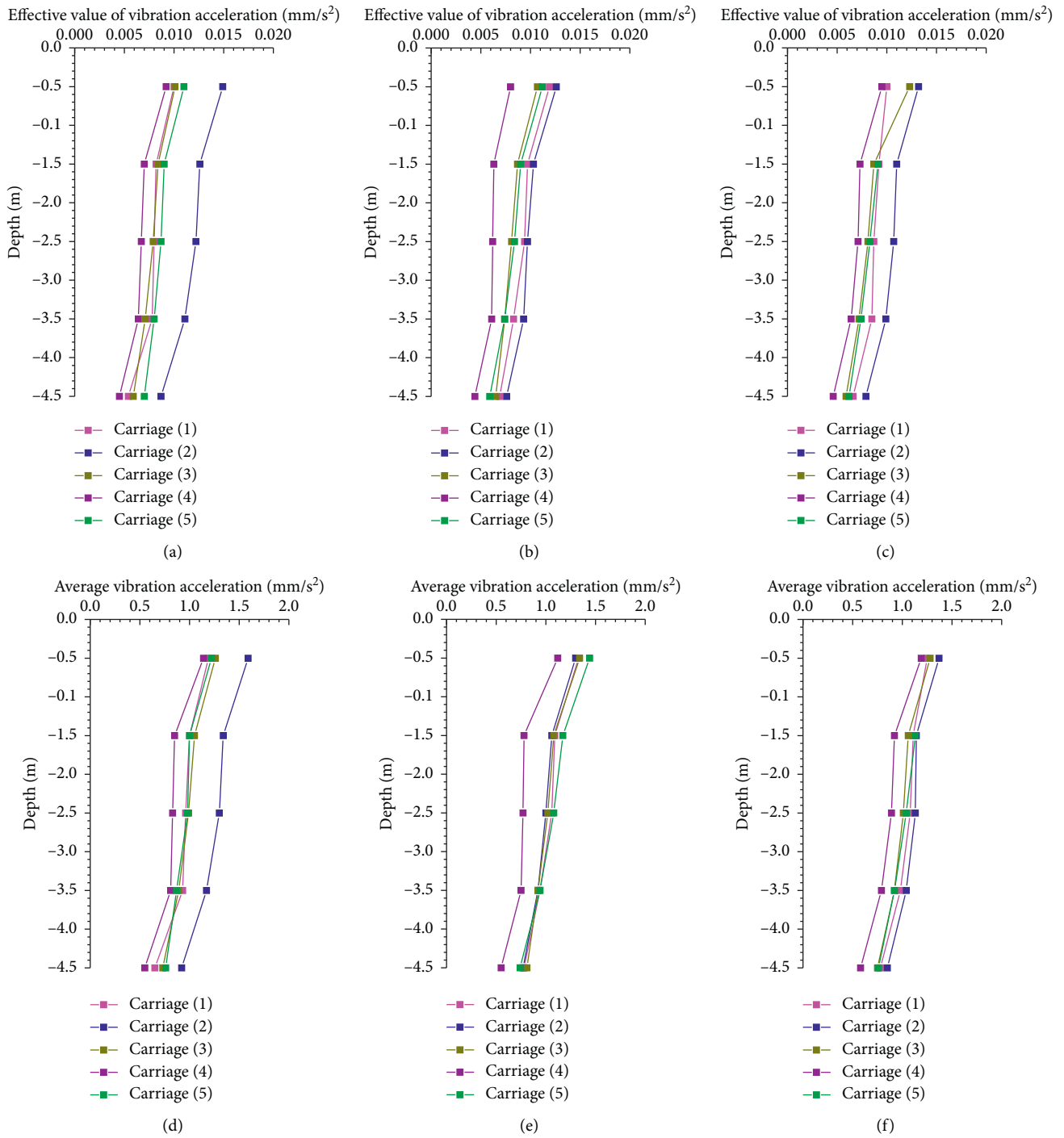


FIGURE 11: Effective value and average value of vertical vibration acceleration at K331 + 315 measuring point. (a) Effective value attenuation curve in September 24th. (b) Effective value attenuation curve in October 10th. (c) Effective value attenuation curve in October 24th. (d) Average attenuation curve in September 24th. (e) Average attenuation curve in October 10th. (f) Average attenuation curve in October 24th.

obvious. At 6.5 m depth, the vibration acceleration attenuates to one tenth of the surface; at K331 + 315 measuring point, at 4.5 m depth, the vibration acceleration attenuation is only 50%–60% of the surface.

## 6. Discussion

The results of needle subgrade treatment project and on-site monitoring show that the response of vibration acceleration is obviously different before and after subgrade

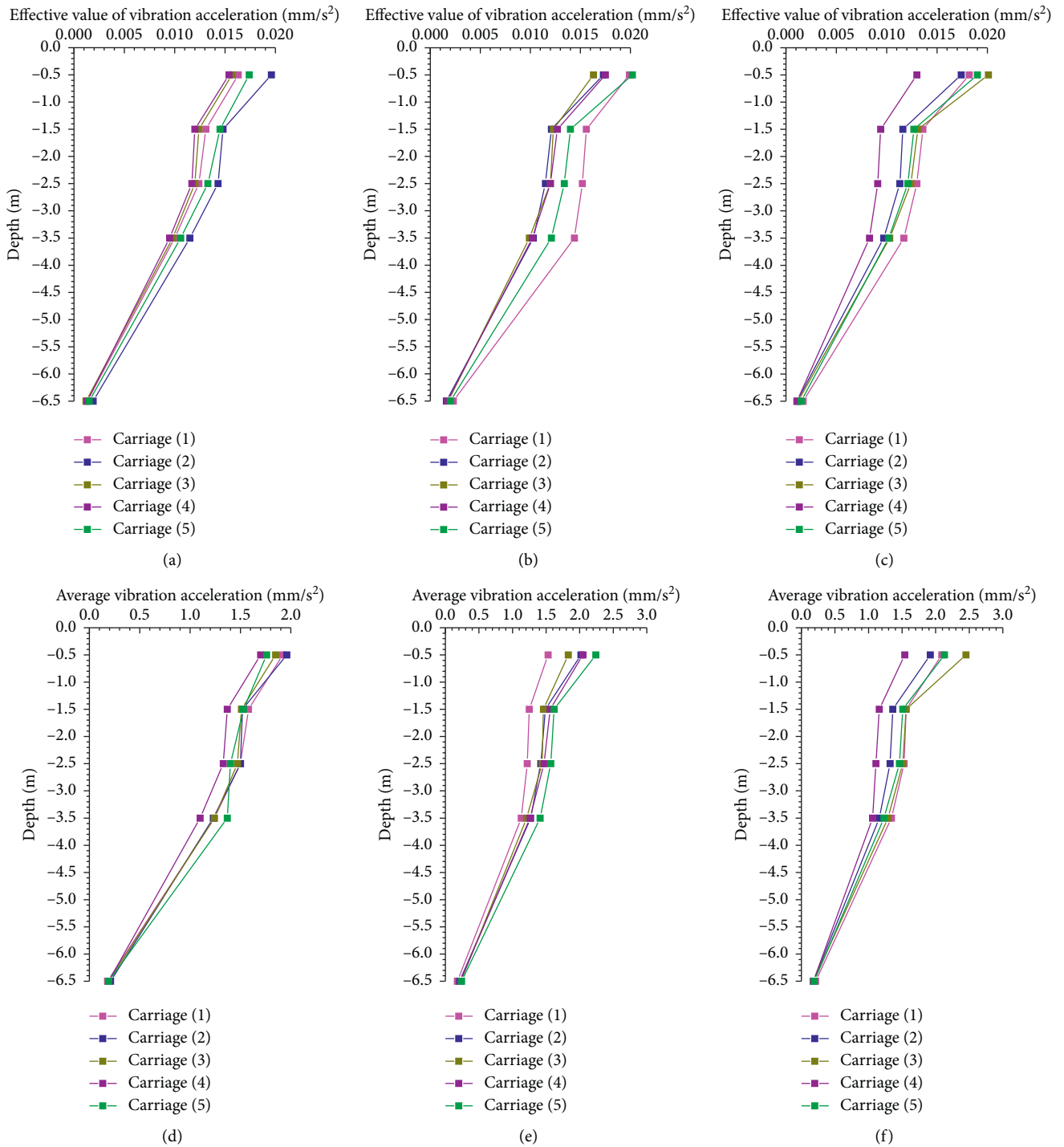


FIGURE 12: Effective value and average value of vertical vibration acceleration at K330+990 measuring point. (a) Effective value attenuation curve in September 23rd. (b) Effective value attenuation curve in October 11th. (c) Effective value attenuation curve in October 22nd. (d) Average attenuation curve in September 23rd. (e) Average attenuation curve in October 11th. (f) Average attenuation curve in October 22nd.

reinforcement. At the same time, the monitoring of the reinforced section and unreinforced diseased section shows that the vibration response of the reinforced section is generally larger than that of the unreinforced section in the same period. Based on the above results, the method of vibration response detection is discussed to detect subgrade diseases.

- (1) The vibration response near the ballast is obvious and decreases with the increase of the horizontal distance from the rail. Therefore, the ballast can be taken as the measuring point. Considering the actual field conditions such as the width of ballast rail and whether there is a stone shoulder, this position can be taken as a point from the ballast to the middle of

the stone shoulder. And the distance is 2.5 m which is more in line with actual engineering.

- (2) Among the three directions of vibration acceleration, the transverse vibration acceleration is the smallest, followed by the longitudinal vibration acceleration, and the vertical vibration acceleration is the largest. The vibration response curve of the reinforced section is spindle shaped, and the vertical vibration acceleration response attenuates obviously at 6.5 m depth, only about 10% to 30% of the surface. The vibration acceleration of the subgrade at 4.5 m decreases to more than 60% of the surface, while that of the unreinforced section attenuates to 50%–60% of the surface at 4.5 m.

## 7. Conclusion

At present, the conventional methods for evaluating subgrade diseases mainly include the stiff-plate bearing test, cone penetration test, dynamic penetration test, and ground-penetrating radar. But these disease detections have limitations for the disease detection of existing line. In this paper, vibration response tests were carried out at different positions and depths of the damaged subgrade of the existing railway before and after reinforcement improvement, and some conclusions are as follows:

- (1) The vibration response near the ballast is obvious and decreases with the increase of the horizontal distance from the rail. Considering the actual situation, it is reasonable to take 2.5 m distance from rail as the measuring point.
- (2) The response of vibration acceleration before and after subgrade reinforcement changes significantly.
- (3) The vibration acceleration of the reinforced subgrade at 4.5 m decreases more than 60% of the surface, while that of the vibration acceleration of the unreinforced section attenuates to only 50%–60% of the surface.

## Data Availability

The test data used to support the findings of this study are included within the article.

## Conflicts of Interest

The authors declare that there are no conflicts of interest regarding the publication of this paper.

## Acknowledgments

This research was supported by the Sichuan Province Science and Technology Support Program (grant nos. 2021YFS0321, 2020YJ0253, and 2020YFSY0060). The authors also gratefully acknowledge Southwest Jiaotong University for support. The authors appreciate all the institutions and individuals that have provided support for this study.

## References

- [1] L. Bertulienė, A. Laurinavičius, and A. Vaitkus, "Research and evaluation of methods for determining deformation modulus of a base course of road pavement," *The Baltic Journal of Road and Bridge Engineering*, vol. 5, no. 2, pp. 110–115, 2010.
- [2] L. Bertulienė, A. Laurinavičius, and O. Lapinskienė, "Research of strength measurement methods on subgrade of experimental road pavement," *The Baltic Journal of Road and Bridge Engineering*, vol. 07, no. 3, pp. 228–236, 2012.
- [3] G. Q. Wang, "Engineering features and foundation division of rock and soil masses in Hefei city," *Chinese Journal of Rock Mechanics and Engineering*, vol. 18, no. 6, pp. 694–698, 1999.
- [4] G. Q. Wang, W. Xu, D. X. Wu et al., "Characteristics of environmental geology and geological disasters of Anhui province," *Chinese Journal of Rock Mechanics and Engineering*, vol. 23, no. 1, pp. 164–169, 2004.
- [5] M. Brough, A. Stirling, G. Ghataora, and K. Madelin, "Evaluation of railway trackbed and formation: a case study," *NDT&E International*, vol. 36, no. 3, pp. 145–156, 2003.
- [6] Y. Byun and J. Lee, "Instrumented dynamic cone penetrometer corrected with transferred energy into a cone tip: a laboratory study," *Geotechnical Testing Journal*, vol. 36, no. 4, pp. 533–542, 2013.
- [7] R. Salgado and S. Yoon, "Dynamic cone penetration test (DCPT) for subgrade assessment," Technical Summary, Joint Transportation Research Program, Indiana Department of Transportation and Purdue INDOT Research FHWA/IN/JTRP-2002/30, West Lafayette, IN, USA, 2003.
- [8] Y. H. Byun, H. K. Yoon, Y. S. Kim et al., "Active layer characterization by instrumented dynamic cone penetrometer in Ny-Alesund," *Svalbard*, *Cold Regions Science And Technology*, vol. 104–105, pp. 45–53, 2014.
- [9] K. M. Hinkel, J. A. Doolittle, J. G. Bockheim et al., "Detection of subsurface permafrost features with ground-penetrating radar," *Barrow, Alaska*, *Permafrost and Periglacial Processes*, vol. 12, no. 2, pp. 179–190, 2001.
- [10] B. J. Moorman, S. D. Robinson, and M. M. Burgess, "Imaging periglacial conditions with ground-penetrating radar," *Permafrost and Periglacial Processes*, vol. 14, no. 4, pp. 319–329, 2003.
- [11] Y. Z. Ma, Y. S. Zhang, S. Zubrzycki et al., "Hillslope-Scale variability in seasonal frost depth and soil water content investigated by GPR on the southern margin of the sporadic permafrost zone on the Tibetan plateau," *Permafrost and Periglacial Processes*, vol. 26, no. 4, pp. 321–334, 2015.
- [12] A. V. Titov and S. S. Krylov, "Physical and mathematical modeling approaches for GPR investigation of underground ice in the permafrost zone," in *Proceedings of the SAGEEP 2015-28th Annual Symposium On the Application Of Geophysics To Engineering And Environmental Problems*, Austin, TX, USA, 2015.
- [13] J. P. Xiao and L. B. Liu, "Permafrost subgrade condition assessment using extrapolation by deterministic deconvolution on multifrequency GPR data acquired along the Qinghai-Tibet railway," *IEEE Journal of Selected Topics in Applied Earth Observations and Remote Sensing*, vol. 9, no. 1, pp. 83–90, 2016.
- [14] E. Léger, B. Dafflon, F. Soom et al., "Quantification of Arctic soil and permafrost properties using Ground-Penetrating radar and electrical resistivity tomography datasets," *IEEE Journal of Selected Topics in Applied Earth Observations and Remote Sensing*, vol. 10, no. 10, pp. 4348–4359, 2017.

- [15] V. V. Krylov, "Generation of ground vibrations by superfast trains," *Applied Acoustic*, vol. 44, no. 2, pp. 149–164, 1995.
- [16] H. Takemiya and X. C. Bian, "Substructure simulation of inhomogeneous track and layered ground dynamic interaction under train passage," *Journal of Engineering Mechanics*, vol. 131, no. 7, pp. 699–711, 2005.
- [17] L. Yang, W. Powrie, and J. A. Priest, "Dynamic stress analysis of a ballasted railway track bed during train passage," *Journal of Geotechnical and Geoenvironmental*, vol. 135, no. 5, pp. 680–689, 2009.
- [18] X. Bian, Y. Chen, and T. Hu, "Numerical simulation of high-speed train induced ground vibrations using 2.5 D finite element approach," *Science China Physics, Mechanics & Astronomy*, vol. 51, no. 6, pp. 632–650, 2008.
- [19] X. Bian, W. Jin, and H. Jiang, "Ground-borne vibrations due to dynamic loadings from moving trains in subway tunnels," *Journal of Zhejiang University-SCIENCE B*, vol. 13, no. 11, pp. 870–876, 2012.
- [20] H. Mei, W. Leng, R. Nie et al., "Random distribution characteristics of peak dynamic stress on the subgrade surface of heavy-haul railways considering track irregularities," *Soil Dynamics and Earthquake Engineering*, vol. 116, pp. 205–214, 2019.
- [21] Y. Momoya, E. Sekine, and F. Tatsuoka, "Deformation characteristics of railway roadbed and subgrade under moving-wheel load," *Soils and Foundations*, vol. 45, no. 4, pp. 99–118, 2005.
- [22] Z. He, J. Y. Zhang, and T. Sun, "Influence of maximum particle diameter on the mechanical behaviour of Soil-Rock Mixtures," *Advances in Civil Engineering*, vol. 2020, no. 3, Article ID 8850221, 9 pages, 2020.
- [23] J. Y. Zhang, Z. L. He, and X. Yu, "Three-dimensional finite element modeling of soft rock tunnel with large section: a case study," *Frontiers in Physics*, vol. 8, Article ID 577787, 2020.
- [24] Z. L. He and J. Y. Zhang, "Compaction quality inspection method of soil-rock filled embankment based on continuous compaction control technology," *Advances in Civil Engineering*, vol. 2021, no. 3, Article ID 8894042, 12 pages, 2021.
- [25] X. Sheng, C. J. C. Jones, and M. Petyt, "Ground vibration generated by a load moving along a railway track," *Journal of Sound and Vibration*, vol. 228, no. 1, pp. 129–156, 1999.
- [26] G. Lombaert and G. Degrande, "Experimental validation of a numerical prediction model for free field traffic induced vibrations by in situ experiments," *Soil Dynamic and Earthquake Engineering*, vol. 21, no. 6, pp. 485–497, 2001.
- [27] A. M. Kaynia, C. Madshus, and P. Zackrisson, "Ground vibration from high-speed trains: prediction and countermeasure," *Journal of Geotechnical and Geoenvironmental Engineering*, vol. 126, no. 6, pp. 531–537, 2000.
- [28] L. Wang, "Vibration characterization of fully-closed high speed railway subgrade through frequency: sweeping test," *Soil Dynamics and Earthquake Engineering*, vol. 88, pp. 33–44, 2016.
- [29] J. Xiao, B. Wang, C. Liu et al., "Influences of subgrade form and ground stiffness on dynamic responses of railway subgrade under train loading: field testing case study," *Procedia Engineering*, vol. 143, pp. 1185–1192, 2016.
- [30] D. P. Connolly, P. A. Costa, G. Kouroussis et al., "Large scale international testing of railway ground vibrations across Europe," *Soil Dynamics and Earthquake Engineering*, vol. 71, pp. 1–12, 2015.
- [31] P. Galvín and J. Domínguez, "Experimental and numerical analyses of vibrations induced by high-speed trains on the Cordoba –Malaga line," *Soil Dynamics and Earthquake Engineering*, vol. 29, no. 4, pp. 641–657, 2009.
- [32] P. A. Costa, R. Calçada, and A. S. Cardoso, "Track-ground vibrations induced by railway traffic: in-situ measurements and validation of a 2.5 D FEM-BEM model," *Soil Dynamics and Earthquake Engineering*, vol. 32, no. 1, pp. 111–128, 2012.
- [33] H. Zhou, *Study On Dynamic Response Of Structures And Ground Subjected To Moving Loads*, Zhejiang University, Hangzhou, China, 2005.

## Research Article

# Rapid Assessment and Classification for Seismic Damage of Mountain Tunnel Based on Concentric Circle Method

Hua Xu <sup>1</sup>, Jingsong Xu,<sup>1,2</sup> Runfang Sun,<sup>1</sup> Hefu Pu,<sup>3</sup> and Yin Cheng<sup>1</sup>

<sup>1</sup>Key Laboratory of Transportation Tunnel Engineering, Ministry of Education, School of Civil Engineering, Southwest Jiaotong University, Chengdu 610031, China

<sup>2</sup>Yunnan Communications Investment & Construction Group CO.LTD, Kunming 650100, China

<sup>3</sup>School of Civil Engineering and Mechanics, Huazhong University of Science and Technology, Wuhan 430074, China

Correspondence should be addressed to Hua Xu; xuhua@swjtu.edu.cn

Received 11 March 2021; Accepted 15 May 2021; Published 27 May 2021

Academic Editor: Honglue Qu

Copyright © 2021 Hua Xu et al. This is an open access article distributed under the Creative Commons Attribution License, which permits unrestricted use, distribution, and reproduction in any medium, provided the original work is properly cited.

Concentric circle method (CCM), a new method based on analytic hierarchy process (AHP) and numerical discretization of 40 mountain tunnels damaged by Wenchuan earthquake in China, is proposed to rapidly assess the seismic damage level (SDL) of mountain tunnels. The new method consists of four components. First, according to the type and degree of seismic damage of tunnel, the whole tunnel is divided into a number of successive sections. Second, four factors (i.e., slope and portal damage, lining damage, pavement damage, and earthquake collapse) are selected as the main controlling factor set, and then multilevel factor sets are proposed to establish the assessment system. Third, the discretized assessment indexes and classification criteria are established for the rapid assessment of SDL of mountain tunnel. Finally, based on the comprehensive analysis on the SDL of each section, the SDL of the whole tunnel is calculated in terms of the seismic damage index and synthetic radius. With the assessment results shown on a straightforward concentric circle diagram, the proposed CCM method can rapidly and reliably assess the SDL of mountain tunnel to win over precious time for emergency rescue and provide references for the repair of damaged tunnel. In addition, the accuracy and applicability of the proposed method is verified by using a case study of Longxi tunnel located at the epicenter of the Wenchuan earthquake in China.

## 1. Introduction

A significant number of tunnels and underground structures have been damaged during earthquakes. In particular, the mountain tunnels located in high-intensity seismic area are more prone to serious damage because of closing to fracture zone. For example, 16% of the railway mountain tunnels located within the disaster area were seriously damaged during Hyogoken-Nambu earthquake occurred in Japan in 1995 [1]; 26% of the 50 mountain tunnels located within 25 km of the earthquake fault were severely damaged, and 22% moderately damaged during the Chi-Chi earthquake occurred in Central Taiwan in 1999 [2]; 65% of the 40 mountain tunnels near the epicenter were damaged during the Wenchuan earthquake occurred in 2008 in Sichuan, China [3]. In addition, mountain tunnels suffered from

extremely severe seismic damage usually blocked the traffic almost entirely, resulting in substantial difficulty in emergency rescue and disaster relief. Therefore, a rapid assessment of seismic damage level (SDL) after earthquake would have significant importance on timely and efficient operation of emergency rescue and remedial measures in mountain tunnels.

Recently, an increasing number of researchers and engineers have carried out field investigation and mechanism analysis on seismic damage of tunnels and underground structures during earthquakes [4–11]. Regarding the current research on the seismic damage assessment, most researchers mainly focused on the identification of risk factors and evaluation of seismic damage of tunnels, but less attentions were paid to the SDL assessment. Wang et al. [2] conducted a systematic statistics and assessment of damage

in mountain tunnels resulted from the 1999 Taiwan Chi-Chi earthquake and analyzed the potential factors. Using the least square method according to tunnel's traffic function and damage description based on the site investigation, Fang et al. [12] proposed an equation for the evaluation of tunnel seismic damage. Jiang et al. [13] analyzed the tunnel damage caused by the 2004 Mid Niigata Prefecture earthquake using Hayashi's quantification theory type II. Wang et al. [14] proposed a new classification criterion to classify the seismic damage and a risk-based assessment technique to quantify the seismic risk. Zang et al. [15] summarized the main influencing factors and put forward a fuzzy comprehensive evaluation method to study the seismic risk level of tunnel portals. Nevertheless, there are still some shortages so far. For instance, owing to the complex multi-index system, complicated calculations, and single assessment result, these methods stated above are not so simple, resulting in great difficulty in applying the rapid assessment to tunnel seismic damage. Moreover, the assessment methods mentioned above do not take the slope and portal damage into comprehensive consideration. As a result, the crews and vehicles for emergency rescue and disaster relief cannot pass through the damaged tunnels, whose accessibility is not assessed and guaranteed, but have to seek detours, which significantly slows down the emergency rescue.

Therefore, combining analytic hierarchy process (AHP) with numerical discretization, a new method called concentric circle method (CCM) is proposed to allow for rapid assessment of the SDL of mountain tunnels. Although the concept of CCM has been applied in different fields, such as camera calibration [16], the principle of those differs from the CCM in this paper. Besides, the CCM has not been introduced to the seismic damage assessment of mountain tunnels so far. The idea of AHP is to treat the object of interest as a system for deciding online with the way of thinking, viz., decomposition, comparative judgment, and comprehensive analysis [17, 18]. The idea of the numerical discretization is dividing continuous values into several intervals, using mathematical methods [19, 20]. Because of the conciseness and practicality, the two methods have been widely applied in various engineering fields, such as risk assessment of tunnel engineering and slope stability classification [14, 21].

With the assessment results shown on a straightforward concentric circle diagram, the proposed method can rapidly and accurately assess the SDL of mountain tunnel to win over precious time for emergency rescue and provide references for the repair of damaged tunnel. Moreover, the accuracy and applicability of the proposed method was illustrated using the field data of damaged mountain tunnels in the 2008 Wenchuan earthquake, China.

## 2. Statistical Analysis on the Seismic Damage Type of Mountain Tunnels

Tens of mountain tunnels suffered from some degree of seismic damage during the 2008 Wenchuan earthquake in China. The typical seismic damages in the mountain tunnels include collapse and slide of slope, collapse of lining and

surrounding rock, cracks of tunnel portal, cracks and displacement of lining, upheaval and cracks of tunnel invert [3, 9, 14, 22]. A field investigation into 11 tunnels on the new Dujiangyan-to-Wenchuan highway found that 8 tunnels located near the epicenter were severely damaged. In particular, the Longxi tunnel suffered from destructive damage, involving extensive large-scale lining cracks, severely distorted steel arch and bar, large-scale lining peeling-off, lining collapse up to tens of meters, significant crack and upheaval as high as 120 cm from tunnel pavement, and totally five large-scale collapses in the whole tunnel. Thereby, the statistical analyses on field investigation data of 40 damaged mountain tunnels during Wenchuan earthquake [3, 9, 14, 21] have been carried out with regard to the types and degrees of seismic damage of mountain tunnels. The main seismic damage types of mountain tunnels are summarized in Table 1, which may provide a useful reference for establishing the seismic damage assessment system and selecting the appropriate assessment indexes.

The tunnel portal section is generally more prone to seismic damage than the tunnel tube section, because of less confining force from the surrounding rock and larger seismic inertial force. In particular, the tunnel portal slope is prone to severe seismic damage due to the action of seismic surface wave and the ground acceleration amplification effect. The main types of seismic damage at the tunnel portal slope include rock falls, collapse, and landslide, which are likely to damage the portal structure or even block the tunnel portal, significantly hindering the emergency rescue after earthquake. According to the report about statistical analysis of the field investigation data of damaged mountain tunnels in the 2008 Wenchuan earthquake by Highway Planning, Survey, Design, and Research Institute of Sichuan Provincial Department [23], the seismic damage of portal slope and portal structure in the tunnel portal section is the most common type and occurred for 97.18% of all the seismic damages of this section (Figure 1). Therefore, the damage of portal slope and portal structure should be taken into careful consideration in establishing the assessment and classification system and in selecting assessment indexes.

The seismic damage types and characteristics of tunnel tube are different from those of the tunnel portal due to different influencing factors, the surrounding rock conditions, and seismic inertial force. The mountain tunnels located on two highways (i.e., Dujiangyan-Yingxiu Highway and Dujiangyan-Yingxiu section of National Highway No. 213) near the epicenter suffered from extensive seismic damage during the Wenchuan earthquake. Statistical analyses of the seismic damage types and proportions of the damaged tunnel tube for these two highways showed that the main damage types are lining damages and road pavement damages (Figure 2). The lining damages mainly include cracks (longitudinal, transverse, oblique, and radial), peeling-off, falling, collapsing, water leakage, and shear displacement, and the road pavement damages mainly include upheaval and cracks (longitudinal and transverse). The lining damages greatly reduce the strength and safety of tunnel. For the road pavement damages, the rescue vehicles may not pass through the damaged tunnel, which will

TABLE 1: Main seismic damage types of mountain tunnels during Wenchuan earthquake.

Tunnel section	Main damage types
Portal	Slope: mountain chipping, crack, collapse, landslide, rock falls Portal: crack, tilt, sink, buried, tunnel opencut punctured
	Lining: crack, aliquation, peeling-off, falling, collapse, dislocation, water seepage, construction joint crack and dislocation
Tube	Lining: crack, aliquation, exfoliating, falling, collapse, dislocation, water seepage, construction joint crack and dislocation
	Road or invert: crack, fracture, upheaval
	Surrounding rock: collapse
	Others: decorative surface drop, groove, and other facility damage

significantly delay emergency rescue. Therefore, the lining damages and the road pavement damages are typical and severe in the seismic damage of tunnel tube and should be taken into significant consideration in establishing the assessment and classification system and in selecting the assessment indexes.

The collapse of surrounding rock is the most severe damage type among all seismic damages for tunnels. Once happened, it hinders or even completely blocks the rescue vehicles, and also it takes high economic cost and long time to repair the collapsed surrounding rock. In Longxi tunnel during the Wenchuan earthquake, for example, it took tens of millions of RMB and duration of 3 months to repair five locations of the collapsed surrounding rock. It is recommended that the collapse of surrounding rock be given the highest level of seismic damage in the assessment and classification system for tunnels.

Some other seismic damages of tunnel, including dropping of decorative surface layer, road groove damage, accessory equipment damage, and others, are also introduced in Table 1. Because these seismic damages have lesser impact on the safety of tunnel structure and the rescue remedy, they are not taken into consideration in the rapid assessment system.

### 3. Rapid Assessment and Classification Based on CCM

**3.1. Assessment and Classification System of Tunnel Seismic Damage.** The tunnel is a linear system with certain length, consisting of the tunnel lining structure and surrounding rock. After earthquake, the type and degree of seismic damage are different at various sections of the tunnel due to varying properties of surrounding rock and supporting structure. Therefore, based on the type and degree of seismic damage, the whole tunnel is divided into successive sections with certain length in longitudinal direction ( $l_1, l_2, l_3, \dots, l_n$ ) using the numerical discretization, with each section having uniform seismic damage.

The influence of each index on the result can be quantified via a weight, to allow an explicit process. Based on the idea of AHP and statistical analysis on the field investigation data of 40 damaged mountain tunnels during Wenchuan earthquake, four main factors, i.e., the slope and portal damage, the lining damage, the pavement damage, and the earthquake collapse, are selected as the controlling factor sets of level 1 in the rapid assessment and classification system. Each controlling factor set is divided into secondary

factor sets, which are then further divided into the next level factor sets. Finally, a set of effective assessment and classification system covering complete multilevel factor sets and specific quantitative parameters is established as shown in Figure 3.

Level-1 factor set: the assessment and classification for seismic damage of the whole tunnel is comprehensive analysis on the SDL of each tunnel section from entrance to exit. According to the type and degree of seismic damage, the damaged tunnel is divided into successive sections with certain length in longitudinal direction so as to establish the level-1 factor set as follows:

$$U = \{U_{l_1}, U_{l_2}, U_{l_3}, \dots, U_{l_n}\}, \quad (1)$$

where  $U$  is the seismic damage of the tunnel as a whole and  $U_i$  ( $i = l_1, l_2, l_3, \dots, l_n$ ) is the seismic damage of the respective tunnel section.

Level-2 factor set: the main seismic damage types at various sections include the portal and slope damage, the lining damage, the road pavement damage, and the earthquake collapse, which have significant effect on the safety of tunnel structure and postearthquake emergency rescue, as described in Section 2. As a result, they are selected as the level-2 factor set as follows:

$$U_{li} = \{u_1, u_2, u_3, u_4\}, \quad (2)$$

where  $u_1, u_2, u_3$ , and  $u_4$  are the portal and slope damage, the lining damage, the road pavement damage, and the earthquake collapse, respectively.

Level-3 factor set: the main type of portal and slope damage ( $u_1$ ) includes crack, collapse, landslide and rock falls from slope, crack, and tilt of tunnel portal; the main type of tunnel lining damage ( $u_2$ ) includes crack, peeling-off, water leakage, and shear displacement; the main type of pavement damage ( $u_3$ ) include crack and upheaval; earthquake collapse ( $u_4$ ) is surrounding rock collapse induced by earthquake. Herein, this study only takes the lining damage ( $u_2$ ) as an example to establish the level-3 and level-4 factor sets, while other factor sets ( $u_1, u_3, u_4$ ) of level 3 and level 4 are shown in Figure 3:

$$u_2 = \{u_{21}, u_{22}, u_{23}, u_{24}\}, \quad (3)$$

where  $u_{21}, u_{22}, u_{23}$ , and  $u_{24}$  are crack, peeling-off, water leakage, and shear displacement, respectively.

Level-4 factor set: it is obvious that different damage types have different characteristics, and thus, in order to reflect the attribute values of different damage types, the

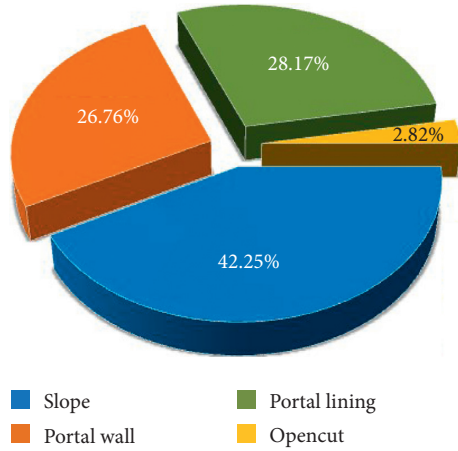


FIGURE 1: Percentage distribution of different seismic damage types in tunnel portal section.

level-4 factor set is established to reflect the degree of the same seismic damage type. For example,  $u_{21}$  can be expressed as follows:

$$u_{21} = \{n_1, n_2, n_3, n_4\}, \quad (4)$$

where  $n_1$ ,  $n_2$ ,  $n_3$ , and  $n_4$  are the length, width, density, and direction of crack, respectively.

**3.2. Development of CCM.** The rapid assessment and classification of tunnel seismic damage based on the CCM is carried out according to the following thoughts. First, the seismic damage level (SDL) is discretized and quantified into five levels with the corresponding seismic damage descriptions and discrete values (0, 1, 2, 3, and 4), such that the initial CCM diagram is drawn with different radius (=1, 2, 3, and 4). Second, according to the type and degree of seismic damage, the to-be-assessed tunnel is divided into a number of sections with different lengths, and the length is proportionally allocated as an arc in the CCM diagram. Third, the SDL of each section (i.e., the radius in CCM diagram) is calculated according to the parameters of assessment indexes. Finally, based on the comprehensive analysis on the SDL of each section, the SDL of the tunnel as a whole is calculated by the seismic damage index and synthetic radius introduced in later section below, and then the assessment result can be clearly shown on the CCM diagram in a straightforward way. The procedure of establishing the CCM is described in detail as follows:

Step 1: draw the initial CCM diagram.

On the basis of statistical analysis of the data from the field investigation of tunnel seismic damage, the SDL is quantified to 5 levels (i.e., undamaged, slight, moderate, severe, and extremely severe) with their corresponding seismic damage description and discrete value (i.e., 0, 1, 2, 3, and 4) introduced in Section 4.5. As such, the initial CCM diagram is drawn with radius of 1, 2, 3, and 4, with the larger radius representing a greater SDL (Figure 4).

Step 2: divide the whole damaged tunnel into sections. Using discretization, the whole tunnel ( $l$ ) is divided to  $n$  successive sections. The type and degree of seismic damage are almost the same for one section. The length of the  $i$ th section is denoted as  $l_i$ , which gives

$$l = l_1 + l_2 + l_3 + \dots + l_i + \dots + l_n, \quad (5)$$

where  $l$  is the total length of the tunnel and  $n$  is the total number of the divided sections.

Step 3: allocate the angle and arc of each section.

In the CCM diagram, the linear tunnel is treated as a  $360^\circ$  circle, so the  $i$ th section tunnel can be represented by an angle  $\theta_i$ , where  $\theta_i$  is the ratio of the length of the  $i$ th section to the total length of tunnel (equation (2)) and  $l_i$  is the length of the  $i$ th section (not the length of the corresponding arc of  $\theta_i$  in CCM diagram):

$$\theta_i = \frac{l_i}{l} \times 2\pi, \quad i = 1, 2, 3, \dots, n, \quad (6)$$

where  $n$  is the total number of tunnel sections.

In this way, we can successively assess and classify the seismic damage of each section using the idea of AHP. Once the sector domain with a specific angle  $\theta_i$  in the CCM diagram is allocated to the  $i$ th section (Figure 5), the contribution of SDL of the  $i$ th section to the overall assessment and classification of tunnel seismic damage can be further confirmed. At the beginning of the whole assessment and classification process, the  $x$ -axis positive half shaft  $0^\circ$  is treated as the entrance portal of the tunnel. With the increase of counterclockwise angle, the longitudinal assessment for tunnel seismic damage is continuously carried out in the order of sections divided beforehand to the  $x$ -axis positive half shaft  $360^\circ$ , which is treated as the exit portal of the tunnel.

Step 4: determine the radius for the SDL of each section.

The radius is determined by the SDL of each section. According to the seismic damage investigation data for the  $i$ th section, together with multilevel factor sets and specific quantitative parameters, the radius for the SDL of the  $i$ th section is calculated and denoted as  $r_i$ .

To illustrate how to calculate the radius in detail, the  $i$ th section of the tunnel is taken as an example. First, it is very important to sort out the field investigation damage data according to the four main seismic damage types and multilevel factor sets. Second, based on the sorted data, the indexes of four main seismic damage types are determined for the multilevel factor sets of the  $i$ th section. As a result, the level of four main seismic damage types is independently assessed as five possible damage levels which, respectively, correspond to five discrete values (i.e., 0, 1, 2, 3, and 4). Finally, due to the independence of four main seismic damage types in the assessment system, the highest damage level among four types should be regarded as the damage level of the  $i$ th section and the discrete value corresponding to the highest damage level is then adopted as



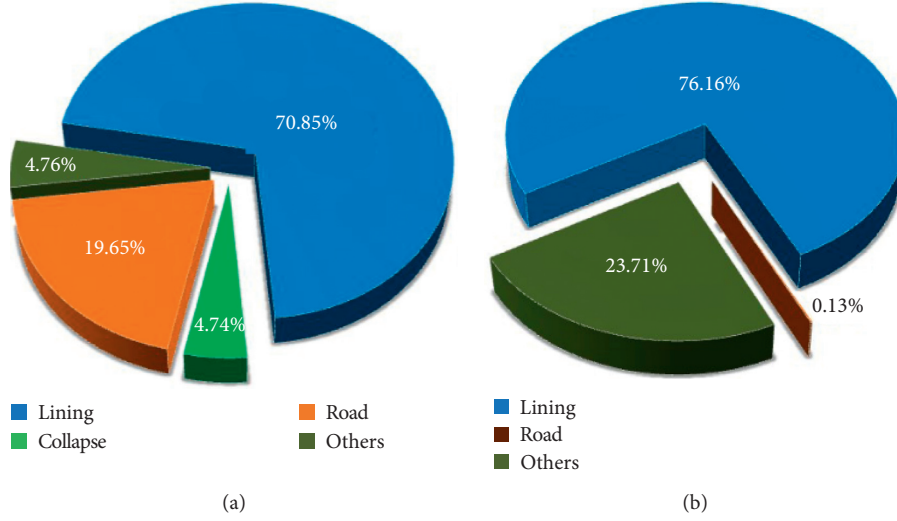


FIGURE 2: Percentage distribution of different seismic damage types in the tunnel tube of two highways: (a) Du-Ying Highway; (b) Du-Ying section of National Highway No. 213.

the radius ( $r_i$ ). In other words, if the damage level of anyone seismic damage type for the  $i$ th section is assessed as extremely severe damage, this section should be regarded as extremely severe damage, and the damage level of other seismic damage types for this section is only a supplement to the damage level.

This method can not only take full consideration of the characteristics of tunnel seismic damage but also meet the need of rescue crews for urgently passing the damaged tunnel. Therefore, the determined radius  $r_i$  is calculated by

$$r_i = \|x\|_{\infty}, \quad (7)$$

where the vector  $x = (P_i, L_i, R_i, C_i)$ ,  $i = 1, 2, 3, \dots, n$ , and  $n$  is the total number of the divided tunnel sections;  $P_i$ ,  $L_i$ ,  $R_i$ , and  $C_i$  are the discrete values of four main factors corresponding to the portal and slope damage, the lining damage, the road pavement damage, and the earthquake collapse, respectively; “ $\|x\|_{\infty}$ ” represents “ $\infty$ -norm” of the vector  $x$  and is calculated by  $\|x\|_{\infty} = \max_{1 \leq j \leq m} \{|x_j|\}$ , where  $m$  is the total number of elements in the vector  $x$ .

Step 5: draw the sector domain of each section.

Drawing the sector domain is necessary for comprehensive assessment and classification, as it reflects the contribution of each divided section to the SDL of the whole tunnel; i.e., larger sector domain reflects more severe seismic damage of tunnel. Based on Steps 3 and 4, the sector domain of each section can be drawn easily in the CCM diagram. The area  $S_i$  of each sector domain is calculated as

$$S_i = \frac{1}{2} \theta_i r_i^2, \quad i = 1, 2, 3, \dots, n, \quad (8)$$

where  $r_i$  is the damage level of the  $i$ th tunnel section;  $\theta_i$  is the ratio of the length of the  $i$ th section to the total length of the tunnel; and  $n$  is the total number of sections.

Step 6: assess the SDL of the whole tunnel.

To obtain a more reasonable assessment for the SDL of the whole tunnel, all sector domains of each section in the CCM diagram should be comprehensively analyzed. Herein, another parameter, the sum of effective area ( $\Delta S$ ), is introduced to reflect the seismic damage of the tunnel as a whole. Clearly,  $\Delta S$  is obtained by accumulating all the sector domains of each section as follows:

$$\Delta S = \sum_{i=1}^n S_i = \frac{1}{2} \sum_{i=1}^n (\theta_i r_i^2) = \frac{\pi}{l} \sum_{i=1}^n (l_i r_i^2). \quad (9)$$

$\Delta S$  is a geometrical meaning that can be shown in the CCM diagram as a shadow area in Figure 6. In the CCM diagram, each concentric circle represents a seismic damage level, and, if  $\Delta S$  is located between two concentric circles, the SDL of the tunnel is regarded as the lower level represented by the inner circle. Therefore, another parameter,  $\alpha$ , which is the seismic damage index, is introduced to achieve the rapid assessment of SDL and is expressed as

$$\alpha = \frac{\Delta S}{S} = \frac{\pi}{16l} \sum_{i=1}^n (l_i r_i^2) = \frac{1}{16l} \sum_{i=1}^n (l_i r_i^2), \quad (10)$$

where  $S$  is the area of the largest circle with radius 4 in concentric circle diagram ( $S = \pi \cdot r_{\max}^2 = 16\pi$ ). If  $\Delta S = S = 16\pi$ , the whole tunnel is extremely severely damaged and likely to threaten the safety of the crews and vehicles for emergency rescue. The corresponding relationship between seismic damage index and seismic damage level is shown in Table 2. In addition, the detailed



FIGURE 3: Structural diagram of AHP for the rapid assessment of the seismic damage level of tunnels.

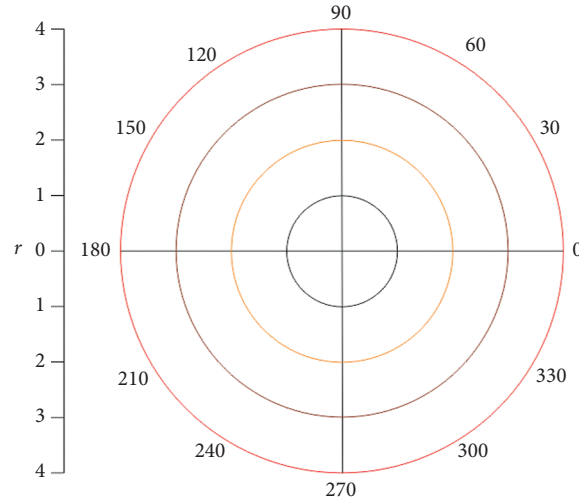


FIGURE 4: SDL initial diagram based on CCM.

classification criterion of tunnel seismic damage is described in Section 4.5.

In particular, to visually display the classification result, an important parameter called synthetic radius of the SDL ( $R_s$ ) is introduced and expressed as follows:

$$R_s = \sqrt{\frac{\Delta S}{\pi}}. \quad (11)$$

With the parameter  $R_s$ , not only the assessment and classification result can be visually displayed in the CCM diagram, but also the close degree with higher level in the same level be obtained by comparing  $R_s$  value. A sample CCM diagram displaying an assessment result of the SDL is shown in Figure 6.

#### 4. Discretized Assessment Indexes and Classification Criterion

Selecting appropriate indexes is important for the assessment of the SDL of mountain tunnel, and therefore, some criteria for index selection are quite essential. First of all, the extremely important indexes which directly reflect characteristics of seismic damage and its degree should be selected. Second, the potential factors that can induce severe disaster after an earthquake should also be selected. According to the statistical analysis in the 2nd section on the damage types of mountain tunnels in Wenchuan earthquake, four main seismic damage types, i.e., the portal and slope damage ( $P$ ), the lining damage ( $L$ ), the road pavement damage ( $R$ ), and the earthquake collapse ( $C$ ), are selected to set up the damage index system. This system covers the main controlling factors affecting the safety of the tunnel structure and emergency rescue after earthquake. Moreover, the independency among indexes is taken into elaborative consideration.

Based on numerical discretization of continuous variables [7, 20], the attribute value for the index of each seismic damage type is discretized into several different ranges which, respectively, correspond to the different assessment

levels with designated discrete values. The index of each seismic damage type is assessed as five damage levels (i.e., extremely severe, severe, moderate, slight, and undamaged), corresponding to the discrete value of 4, 3, 2, 1, and 0. In detail, once an index (such as “ $P$ ”) for the  $i$ th section tunnel is assessed as certain damage level (e.g., “severe”), the corresponding discrete value (e.g., 3) is assigned to  $P_i$  (e.g.,  $P_i = 3$ ). In the same way other indexes (e.g.,  $L_i$ ,  $R_i$ , and  $C_i$ ) are also determined, and then  $r_i$  is calculated using equation (4). The seismic damage level can be identified by the seismic damage description and specific quantitative parameters.

**4.1. Portal and Slope Damage ( $P$ ).** The portal and slope damage always occurs at the entry or exit part of tunnel. Due to its location on the ground surface, the tunnel portal structure is subjected to strong earthquake inertial force and thus prone to be damaged. The seismic damage of the portal slope involves collapse, rock fall, landslide, and others and can easily block the tunnel portal and seriously hinder the emergency rescue. On the basis of the present study on the seismic damage of tunnel portal and slope [14, 15], the index of seismic damage of tunnel portal and slope ( $P$ ) is discretized by quantitatively and qualitatively assessing the degree of slope collapse, the volume of rock fall and landslide, and the seismic damage situation of the tunnel portal structure, as shown in Table 3.

**4.2. Lining Damage ( $L$ ).** The lining damage mainly includes crack, peeling-off, falling, and collapse. The quantitative characteristics of the damage reflect the seismic damage degree of the lining, and they are described by the density, the width and length of cracks, the scale and range of peeling-off, and collapse. On the basis of the present study on lining damage assessment [9, 14], the index of seismic damage of the lining ( $L$ ) is discretized by quantitatively and qualitatively assessing the length, width and density of crack, the scale and degree of peeling-off, the falling and collapse [24], and the situation of groundwater, as shown in Table 4.

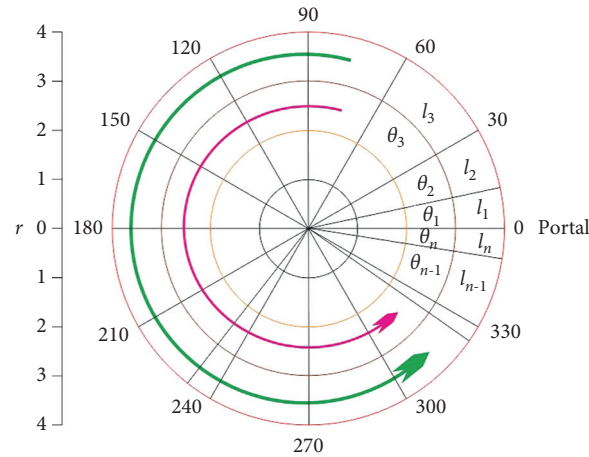


FIGURE 5: The sample diagram of CCM after determining the angle and arc.

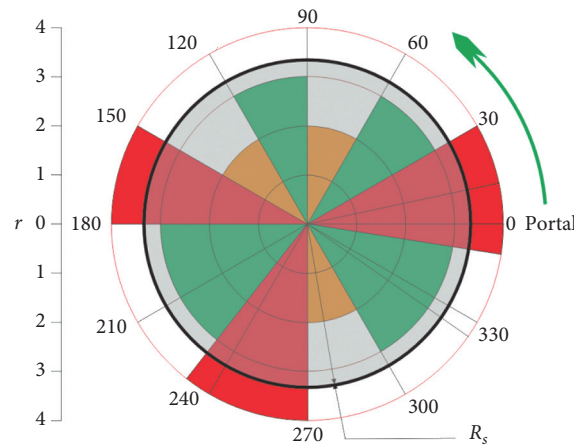


FIGURE 6: A sample CCM diagram with synthetic radius displaying an assessment result.

**4.3. Road Pavement Damage ( $R$ ).** The road pavement damage, including crack and upheaval, can seriously hinder the emergency rescue and disaster relief after earthquakes. Reflecting the severity of the pavement damage, the quantitative characteristics of the damage includes the width, the length and extension direction of cracks, the upheaval height, and others. According to the field investigation data and the present study on seismic damage assessment of pavement [2, 6], the index of seismic damage of road pavement ( $R$ ) is discretized by quantitatively and qualitatively assessing the width, length and direction of crack, the height of upheaval [14, 15, 24], and the situation of ponding water, as shown in Table 5. Note:  $l$  = length of crack,  $w$  = width of crack or dislocation, and  $h$  = height of upheaval or dislocation.

**4.4. Earthquake Collapse ( $C$ ).** The tunnel collapse triggered by earthquake is the most severe damage type among all tunnel seismic damages and can hinder and even completely block the rescue vehicles and crews. It takes high cost and long time to repair the collapse of tunnel and surrounding rock. Based on the present study on tunnel earthquake

collapse [25–29], the index of tunnel earthquake collapse ( $C$ ) is discretized by quantitatively and qualitatively assessing the volume, the type and characteristics of collapse, the groundwater situation, and the degree of weathering or fracture of rocks, as shown in Table 6.

**4.5. Classification Criterion of Tunnel Seismic Damage.** Although some criteria were introduced in different literature studies, up until now, to the knowledge of authors, there lacks a unified standard for the classification of tunnel seismic damage. Dowding and Rozan [30] classified three damage levels, i.e., no damage, minor damage, and damage. Huang et al. [28] and Wang et al. [2] improved the study of Dowding and Rozan's classification by further dividing the minor damage into slight damage and moderate damage. Since the 2008 Wenchuan earthquake, some new classification studies were proposed because extremely severe damages in mountain tunnels, including earthquake collapse and dislocation, have been reported [3, 9]. As a result, a new five-level damage classification system (i.e., extremely severe, severe, moderate, slight, and undamaged) was proposed [2, 9, 14]. Based on the abovementioned studies on the

TABLE 2: Relationship between seismic damage index and seismic damage level of tunnel.

Level	Extremely severe	Severe	Moderate	Slight	Undamaged
Index	$\alpha = 1$	$9/16 < \alpha < 1$	$4/16 < \alpha < 9/16$	$1/16 < \alpha < 4/16$	$0 \leq \alpha < 1/16$

\* Standard value of 0, 1/16, 4/16, 9/16, and 1 is the area ratio of the concentric circles with different radius (0, 1, 2, 3, and 4) to the largest concentric circle with radius 4.

TABLE 3: Discretized assessment index and description of portal and slope damage.

Damage level	Seismic damage description	Discrete value
Extremely severe	Extensive failure of slope; extremely severe mountain collapse, landslide and rock fall; completely buried tunnel portal; extremely severe damage of portal structure (extensive cracks, extremely severe tilt, and subsidence); completely impassable traffic	4
Severe	Local failure of slope; large-scale mountain collapse, landslide and rock fall; most part of tunnel portal is buried; severe damage of portal structure (local cracks, severe tilt, and subsidence); impassable traffic	3
Moderate	Notable cracks of slope; medium-scale rock fall; massive gravel or large stone piles up in front of portal; moderate damage of portal structure (local cracks, moderate tilt, and subsidence); passable traffic after small-scale remediation	2
Slight	No crack on slope surface; small-scale rock fall; sparse gravels or small stones piles up in front of tunnel portal; slight damage of portal structure (slight cracks and tilt); passable traffic	1
Undamaged	Undamaged tunnel portal and slope; smooth traffic; no abnormal phenomenon	0

TABLE 4: Discretized assessment index and description of lining damage.

Damage level	Seismic damage description	Discrete value
Extremely severe	Intensive crack or dislocation ( $l > 10$ m, $w > 10$ mm); developing deformation; cracked vault lining is likely to fall; crushed vault lining range $S > 3$ m <sup>2</sup> ; extremely severe falling of secondary lining, even massive collapse to threaten traffic safety; intruding groundwater	4
Severe	Crack or dislocation ( $5$ m $< l < 10$ m, $5$ mm $< w < 10$ mm), cracked vault lining is likely to fall; crushed vault lining range $1$ m <sup>2</sup> $< S < 3$ m <sup>2</sup> ; continuously inflowing groundwater	3
Moderate	Crack or dislocation ( $l < 5$ m, $1$ mm $< w < 5$ mm); small-scale lining peeling-off; crushed vault lining range $S < 1$ m <sup>2</sup> ; dripping groundwater	2
Slight	Crack or dislocation ( $w < 1$ mm) but not further development; no crushed vault; slight seepage of groundwater	1
Undamaged	No cracks or crush; no groundwater seepage; no abnormal phenomenon	0

Note:  $L$  = length of crack,  $w$  = width of crack, and  $S$  = area of crushed range.

assessment and classification of tunnel seismic damage and referred to the Chinese railway and highway industry standards for tunnel performance degradation [12, 24, 31], the SDL of mountain tunnel is discretized in this study as shown in Table 7.

## 5. Application of CCM

The Wenchuan earthquake caused severe damages to tens of mountain tunnels. Due to the lack of rapid and accurate assessment of tunnel seismic damage, the emergency rescue and damage repair after the earthquake were seriously hindered. In order to demonstrate the applicability and accuracy of the rapid assessment method of CCM proposed in this study, we chose the Longxi tunnel as an example to assess and classify the seismic damage. Longxi tunnel is located near the epicenter of Wenchuan earthquake as shown in Figure 7, being in the south of Chaping Mountain between Yingxiu Town and Longxi Town and to the left bank of the Minjiang River in Sichuan Province of China. The

tunnel axis direction is northwest (NW), and mountain ridge direction is northeast (NE), namely, there exists a large intersection angle between the two axes. The distance between the tunnel exit and the Wenchuan earthquake epicenter (i.e., Yingxiu Town) is only 4 km.

Because of its typical geographical location and representative seismic damage type of Longxi tunnel during the Wenchuan earthquake, some scholars have investigated the seismic damage characteristics of Longxi tunnel and the associated mechanisms [3, 9, 32–37]; however, systematic assessment and classification study on seismic damage of Longxi tunnel was rarely conducted. Although Longxi tunnel is a double-line tunnel, the field investigation on the right line tunnel could not be carried out as the right line encountered severe earthquake collapse during Wenchuan earthquake. Therefore, only the left line of the tunnel is used here to conduct the SDL assessment, and the length to be assessed is 3492 m.

Based on the field investigation data for the left line of Longxi tunnel after earthquake, the relevant parameters of

TABLE 5: Discretized assessment index and description of pavement damage.

Damage level	Seismic damage description	Discrete value
Extremely severe	Extensive and intensive cracks ( $l > 20$ m, $w > 5$ cm); pavement upheaval ( $h > 50$ cm); local dislocation ( $w > 5$ cm, $h > 10$ cm); extremely severe damage to pavement; pavement covered by deep and extensive ponding water; impassable traffic	4
Severe	Intensive cracks ( $10$ m $< l < 20$ m, $1$ cm $< w < 5$ cm); pavement upheaval ( $10$ cm $< h < 50$ cm); local dislocation ( $1$ cm $< w < 5$ cm, $5$ cm $< h < 10$ cm); severe damage to pavement; extensive ponding water; cautiously passable traffic with high risk	3
Moderate	Local cracks ( $5$ m $< l < 10$ m, $0.5$ cm $< w < 1$ cm); pavement upheaval ( $h < 10$ cm); local dislocation ( $w > 1$ cm, $1$ cm $< h < 5$ cm); small-scale damage to pavement; local pavement covered by ponding water; cautiously passable traffic by safety measures	2
Slight	Local cracks ( $l < 5$ m, $w < 0.5$ cm); no pavement upheaval; few dislocation ( $w < 0.5$ cm, $h < 1$ cm); little damage to pavement; local pavement covered by less ponding water; passable traffic but maintenance still needed	1
Undamaged	No crack or upheaval; passable traffic; no abnormal phenomenon	0

TABLE 6: Discretized assessment index and description of tunnel collapse.

Damage level	Seismic damage description	Discrete value
Extremely severe	Collapse ( $v > 5000$ m <sup>3</sup> ); extensive and massive groundwater inrush; strong weathering or severe fractures of rock, extremely unstable collapse cavity; necessary measures should be taken immediately	4
Severe	Collapse ( $1000$ m <sup>3</sup> $< v < 5000$ m <sup>3</sup> ); local groundwater inflow; strong weathering or severe fractures of rock, unstable collapse cavity; necessary measures should be taken	3
Moderate	Collapse ( $300$ m <sup>3</sup> $< v < 1000$ m <sup>3</sup> ); local groundwater dripping; moderate weathering or a number of fractures of rock; poor stability of collapse cavity; measures should be taken as early as possible	2
Slight	Collapse ( $v < 100$ m <sup>3</sup> ); local groundwater leakage or seepage; good stability of collapse cavity; slight weathering or few fractures of rock; measures should be taken in time	1
Undamaged	No collapse or groundwater; no abnormal phenomenon	0

Note:  $v$  = volume of tunnel collapse.

different tunnel sections are calculated using the proposed CCM rapid assessment (Table 8).

Based on the seismic damage description and discretized assessment parameters of SDL as shown in Table 8, the rapid assessment of SDL for the left line of Longxi tunnel is carried out according to the following procedure:

Step 1: draw the initial CCM diagram.

Step 2: divide the Longxi tunnel into 62 different sections (Table 8) according to the type and degree of seismic damage, namely,

$$l = l_1 + l_2 + l_3 + \dots + l_i + \dots + l_{62}. \quad (12)$$

Step 3: assign proportional angle and arc for each section according to its length (Figure 8).

Step 4: calculate the SDL ( $r_i$ ) of each section using equation (3) according to the comprehensive assessment system and indexes ( $P$ ,  $L$ ,  $R$ , and  $C$ ) proposed in this paper, and the  $r_i$  values are shown in Table 8.

Step 5: draw each sector domain in the CCM diagram to represent the seismic damage situation of each tunnel section.

Step 6: calculate the seismic damage index ( $\alpha$ ) and synthetic radius ( $R_s$ ) by equations (6) and (7), respectively, which are equal to 0.584 and 3.06. It is clear that the value of  $\alpha$  is located between 9/16 and 1 according to Table 2, which shows that the seismic damage of the left line of Longxi tunnel is severe. Namely, severe performance degradation of tunnel structure occurred and traffic safety was threatened, and remedial measures should be taken as soon as possible. The synthetic radius for the classification of seismic damage is labelled in the CCM diagram, and the result is visualized in Figure 9.

According to the field investigation data, the left line of Longxi tunnel suffered from severe seismic damage during Wenchuan earthquake, including slope collapse, rock falls, crack and collapse of lining, crack and upheaval of invert, large-scale surrounding rock collapse, and others (Figure 10). The seismic damage significantly lowered the tunnel structural safety and traffic safety and hindered rescue and remedial work after the earthquake. Shown in this case study, the assessment results from the CCM are consistent with those of the field investigation, which verifies the

TABLE 7: Discretized SDL and description of mountain tunnel.

SDL	Seismic damage description	Discrete value
Extremely severe	Extremely severe degradation and damage of tunnel structure; completely impassable traffic; necessary measures should be taken immediately, otherwise further aggravating SDL	4
Severe	Severe degradation and damage of tunnel structure; traffic safety threatened severely; measures should be taken as early as possible, otherwise further aggravating SDL	3
Moderate	Moderate degradation and damage of tunnel structure; traffic safety threatened moderately; measures should be taken in time, otherwise further aggravating SDL	2
Slight	Slight degradation and damage of tunnel structure; traffic safety guaranteed slightly, normal usage unaffected; targeted and key monitoring necessary	1
Undamaged	Undamaged tunnel; no abnormal phenomenon	0

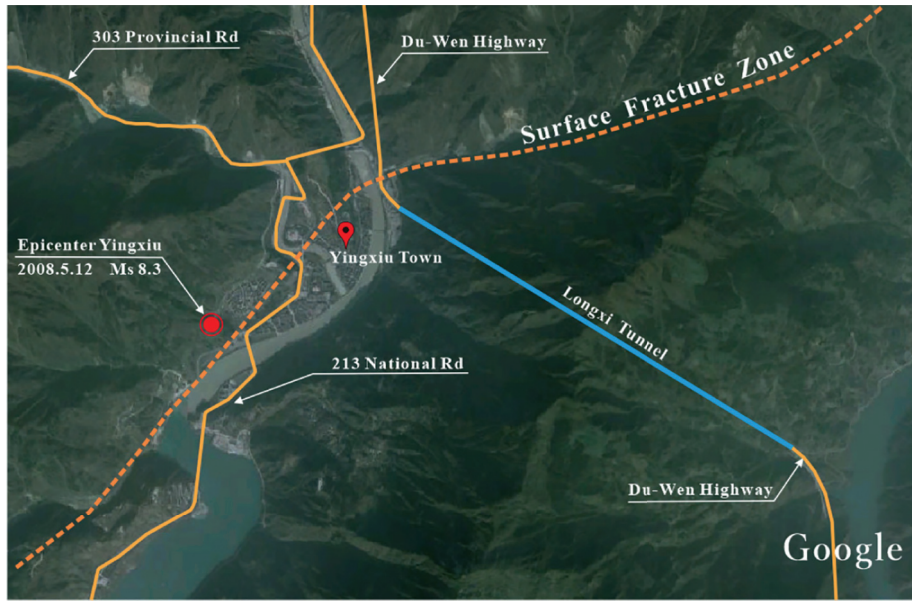


FIGURE 7: The geographical location of Longxi tunnel and the epicenter of Wenchuan earthquake (from Google Map).

TABLE 8: The seismic damage description and assessment parameters of SDL for the left line of Longxi tunnel.

Section	Stake	$l_i$ (m)	Seismic damage description	Index value				
				$P_i$	$L_i$	$R_i$	$C_i$	$r_i$
1	LK21 + 420 ~ 470	50	Intensive crack of pavement at entry portal; intensive and dense cracks ( $1\text{ mm} < w < 10\text{ mm}$ ) on secondary lining in different directions; large-scale secondary lining peeling-off, falling and collapse; local leakage of groundwater; construction joints dislocation ( $h = 10\text{ cm}$ ).	4	4	3	0	4
2	LK21 + 470 ~ 575	105	Intense upheaval of pavement is as high as about 1.2 meter; intensive and dense cracks ( $1\text{ mm} < w < 10\text{ mm}$ ) on secondary lining in different directions; large-scale secondary lining peeling-off, falling and collapse; local leakage of groundwater; construction joints dislocation ( $h = 10\text{ cm}$ ) (Figures 10(a), and 10(b)).	4	4	4	0	4
3	LK21 + 575 ~ 620	45	Large-scale earthquake collapse of surrounding rock; secondary lining collapse; invert upheaval ( $h = 10\text{ cm}$ ).	0	4	2	4	4
4	LK21 + 620 ~ 670	50	Extensive collapse of secondary lining; primary support grid exposed, deformed and distorted.	0	4	0	4	4
5	LK21 + 670 ~ 695	25	Large-scale earthquake collapse; secondary lining collapse; invert upheaval ( $h = 120\text{ cm}$ ) (Figure 10(c)).	0	4	4	4	4
6	LK21 + 695 ~ 755	60	Cracks ( $w = 3\text{ cm}$ ) and peeling-off of secondary lining; invert upheaval ( $h = 80\text{ cm}$ ).	0	3	4	0	4
7	LK21 + 755 ~ 780	25	Invert upheaval ( $h = 80\text{ cm}$ ).	0	0	4	0	4
8	LK21 + 780 ~ 880	100	Dense cracks; several peeling-off and collapse occurred at vault of secondary lining; invert upheaval ( $h = 80\text{ cm}$ ).	0	4	4	0	4
9	LK21 + 880 ~ 890	10	Invert upheaval ( $h = 80\text{ cm}$ ).	0	0	4	0	4

TABLE 8: Continued.

Section	Stake	$l_i$ (m)	Seismic damage description	Index value				
				$P_i$	$L_i$	$R_i$	$C_i$	$r_i$
10	LK21 + 890 ~ LK22 + 285	395	Secondary lining collapse; intense invert upheaval ( $h = 80$ cm) to triangle in shape.	0	4	4	0	4
11	LK22 + 285 ~ 320	35	Invert dislocation ( $h = 15$ cm); longitudinal crack of pavement above central drainage ditch.	0	0	4	0	4
12	LK22 + 320 ~ 335	15	Collapse and transverse cracks ( $w = 1$ cm) of secondary lining; invert dislocation ( $h = 15$ cm)	0	4	4	0	4
13	LK22 + 335 ~ 385	50	Undamaged; no abnormal phenomenon.	0	0	0	0	0
14	LK22 + 385 ~ 470	85	Local collapse of secondary lining; longitudinal crack ( $l > 70$ m, $w = 2$ cm) of pavement above central drainage ditch.	0	3	3	0	3
15	LK22 + 470 ~ 590	120	Undamaged; no abnormal phenomenon.	0	0	0	0	0
16	LK22 + 590 ~ 680	90	Intense invert upheaval ( $h = 30$ cm) to almost triangle in shape; longitudinal crack ( $w = 1$ cm) of pavement above central drainage ditch.	0	0	3	0	3
17	LK22 + 680 ~ 754	74	Longitudinal cracks ( $l > 40$ m, $1$ cm $< w < 3$ cm) on secondary lining; extensive falling of secondary lining; intense invert upheaval ( $h = 30$ cm) to almost triangle in shape; longitudinal crack ( $w = 1$ cm) of pavement above central drainage ditch.	0	4	3	0	4
18	LK22 + 754 ~ 845	91	Invert upheaval ( $h = 30$ cm), intense deformation to almost triangle in shape; longitudinal crack ( $w = 1$ cm) of pavement above central drainage ditch.	0	0	3	0	3
19	LK22 + 845 ~ 877	32	Invert upheaval ( $h = 30$ cm), intense deformation to almost triangle in shape; longitudinal crack ( $w = 1$ cm) of pavement above central drainage ditch.	0	0	3	0	3
20	LK22 + 877 ~ 902	25	Primary support collapse; steel arch exposed, severe deformation and distortion; invert upheaval ( $h = 30$ cm), intense deformation to almost triangle in shape; longitudinal crack ( $w = 1$ cm) of pavement above central drainage ditch.	0	4	3	0	4
21	LK22 + 902 ~ 915	13	Undamaged; no abnormal phenomenon.	0	0	0	0	0
22	LK22 + 915 ~ LK23 + 010	95	Large-scale collapse of primary support; steel arch exposed, severe deformation and distortion.	0	4	0	0	4
23	LK23 + 176~330	154	Severe damage of primary support; severe deformation and distortion of steel arch; large-scale falling of spray concrete.	0	4	0	0	4
24	LK23 + 330~340	10	Undamaged; no abnormal phenomenon.	0	0	0	0	0
25	LK23 + 340 ~ 570	230	Extensive and dense ring cracks ( $1$ mm $< w < 3$ mm); longitudinal cracks on pavement ( $w = 8$ mm); several cracks of construction joints.	0	3	1	0	3
26	LK23 + 570 ~ 625	55	Undamaged; no abnormal phenomenon.	0	0	0	0	0
27	LK23 + 625 ~ 675	50	Extensive cracks, water leakage and collapse of primary support; severe deformation and distortion of steel arch.	0	3	0	0	3
28	LK23 + 675 ~ 680	5	Secondary lining peeling-off occurred at construction joints.	0	3	0	0	3
29	LK23 + 680 ~ 695	15	Undamaged; no abnormal phenomenon.	0	0	0	0	0
30	LK23 + 695 ~ 701	6	Transverse cracks ( $w = 4$ mm) on secondary lining.	0	0	1	0	1
31	LK23 + 701 ~ 865	164	Undamaged; no abnormal phenomenon.	0	0	0	0	0
32	LK23 + 865 ~ 895	30	Cracks ( $w = 4$ mm) of secondary lining; invert upheaval ( $h = 15$ cm).	0	2	3	0	3
33	LK23 + 895 ~ LK24 + 245	350	Undamaged; no abnormal phenomenon.	0	0	0	0	0
34	LK24 + 245 ~ 275	30	Large-scale falling and collapse at lining vault.	0	4	0	0	4
35	LK24 + 275 ~ 310	35	Undamaged; no abnormal phenomenon.	0	0	0	0	0
36	LK24 + 310 ~ 350	40	Longitudinal cracks ( $l > 10$ m, $w = 4$ mm) on secondary lining vault; long invert upheaval ( $l > 12$ m).	0	2	3	0	3
37	LK24 + 350 ~ 365	15	Undamaged; no abnormal phenomenon.	0	0	0	0	0
38	LK24 + 365 ~ 370	5	Transverse cracks ( $w = 4$ mm) on pavement.	0	0	1	0	1
39	LK24 + 370 ~ 390	20	Undamaged; no abnormal phenomenon.	0	0	0	0	0
40	LK24 + 390 ~ 395	5	Cracks ( $w = 2$ mm) on secondary lining; transverse cracks ( $w = 2$ cm) on pavement.	0	2	3	0	3
41	LK24 + 395 ~ 405	10	Undamaged; no abnormal phenomenon.	0	0	0	0	0
42	LK24 + 405 ~ 410	5	Transverse cracks ( $w = 5$ cm) of invert.	0	0	4	0	4
43	LK24 + 410 ~ 450	40	Undamaged; no abnormal phenomenon.	0	0	0	0	0
44	LK24 + 450 ~ 550	100	Large-scale falling and collapse of secondary lining vault.	0	4	1	0	4
45	LK24 + 550 ~ 565	15	Transverse cracks ( $3$ mm $< w < 4$ mm) on secondary lining.	0	3	0	0	3
46	LK24 + 565 ~ 690	125	Slight cracks on secondary lining.	0	2	0	0	2
47	LK24 + 690 ~ 715	25	Large-scale falling and collapse at secondary lining vault.	0	4	0	0	4
48	LK24 + 715 ~ 730	15	Undamaged; no abnormal phenomenon.	0	0	0	0	0
49	LK24 + 730 ~ 735	5	Slight cracks on secondary lining.	0	2	0	0	2
50	LK24 + 735 ~ 755	20	Undamaged; no abnormal phenomenon.	0	0	0	0	0



TABLE 8: Continued.

Section	Stake	$l_i$ (m)	Seismic damage description	Index value				
				$P_i$	$L_i$	$R_i$	$C_i$	$r_i$
51	LK24 + 755 ~ 760	5	Cracks ( $w = 6$ mm) on secondary lining.	0	3	0	0	3
52	LK24 + 760 ~ 790	30	Undamaged; no abnormal phenomenon.	0	0	0	0	0
53	LK24 + 790 ~ 806	16	Cracks ( $4 \text{ mm} < w < 10 \text{ mm}$ ) on secondary lining; transverse cracks ( $w = 3$ cm) of invert.	0	2	3	0	3
54	LK24 + 806 ~ 835	29	Transverse cracks ( $w = 3$ cm) of invert.	0	0	3	0	3
55	LK24 + 835 ~ 840	5	Cracks ( $w = 5$ mm) on secondary lining; transverse cracks of invert.	0	3	2	0	3
56	LK24 + 840 ~ 868	28	Transverse cracks ( $w = 2$ cm) of invert.	0	0	3	0	3
57	LK24 + 868 ~ 870	2	Cracks ( $w = 10$ mm) on secondary lining.	0	3	2	0	3
58	LK24 + 870 ~ 890	20	Large-scale collapse of secondary lining; cracks of the pavement above central drainage ditch.	0	4	2	0	4
59	LK24 + 890 ~ 965	75	Extensive peeling-off and falling on secondary lining; transverse cracks of invert.	0	3	3	0	3
60	LK24 + 965 ~ LK25 + 010	45	Cracks ( $w = 10$ mm) on secondary lining; cracks of the pavement above central drainage ditch.	0	3	2	0	3
61	LK25 + 010 ~ 048	38	Extensive and dense oblique cracks ( $w$ up to 30 mm), falls and collapse of lining vault; cracks and dislocation ( $w$ up to 4 cm) of invert.	0	4	3	0	4
62	LK25 + 048 ~ 078	30	Extensive and dense oblique cracks ( $w$ up to 30 mm), falls and collapse of lining vault; cracks and dislocation ( $w$ up to 4 cm) of invert; mountain collapse, a large amount of huge stone piled up in front of portal (Figure 10(d)).	4	4	3	0	4

Note:  $h$  = height of upheaval or dislocation,  $l$  = length of crack or upheaval, and  $w$  = width of crack or dislocation.

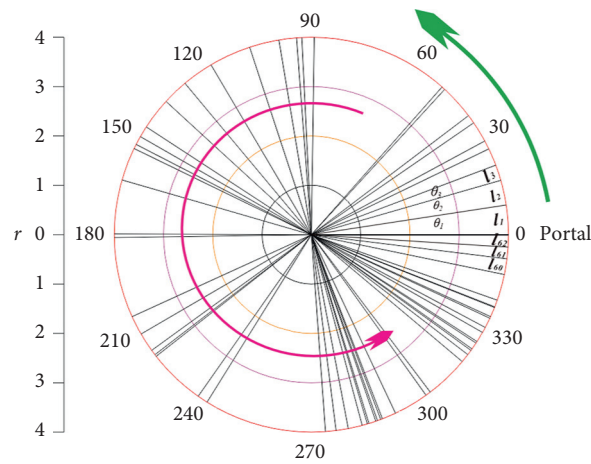


FIGURE 8: Concentric circle model diagram with proportional angle and arc length.

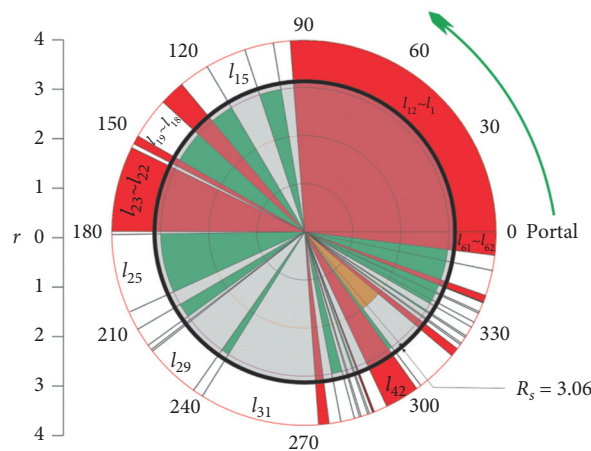


FIGURE 9: The CCM diagram for the SDL of the left line of Longxi tunnel.

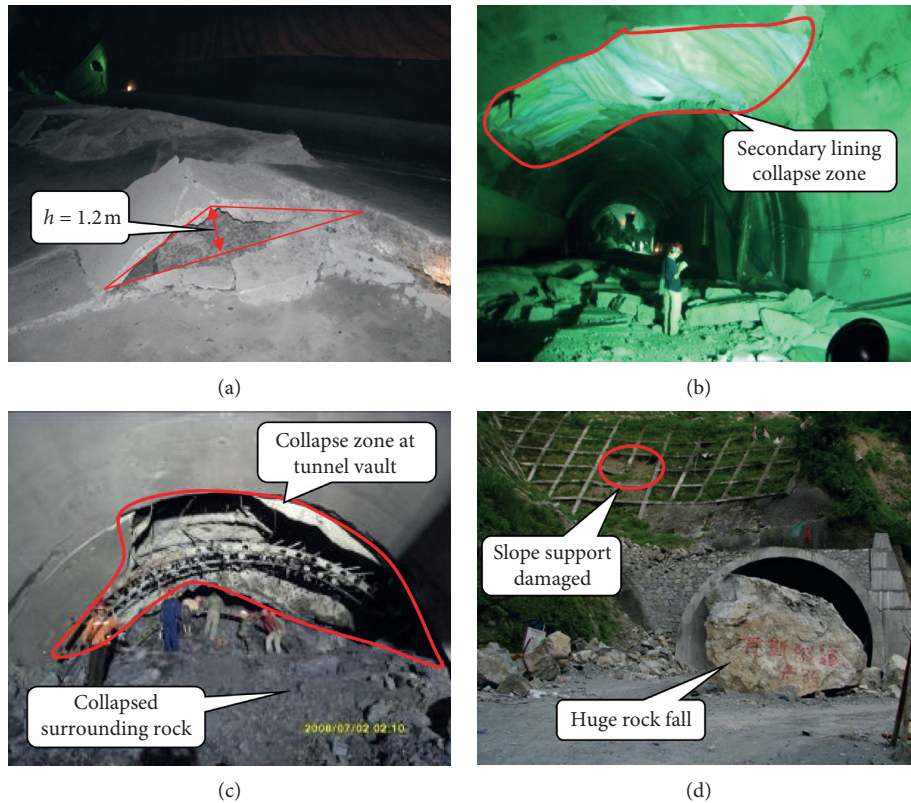


FIGURE 10: The main seismic damage of the left line of Longxi tunnel: (a) severe upheaval and tensile fractures of the invert arch pavement at LK21 + 521~552, (b) collapse of the arch secondary lining at LK21 + 540~558, (c) collapse of surrounding rock and lining at LK21 + 670~695, and (d) huge rock falls at Longxi tunnel.

accuracy and applicability of the CCM assessment method for the seismic damage level.

## 6. Conclusions

Based on the techniques of analytic hierarchy process (AHP) and numerical discretization, the concentric circle method (CCM) is proposed to rapidly assess the seismic damage level (SDL) of mountain tunnel. The proposed method can rapidly and accurately assess the SDL of mountain tunnel to win over precious time for emergency rescue and provide references for the repair of damaged tunnel.

According to the statistical analysis on the damage characteristics and types of 40 mountain tunnels during Wenchuan earthquake, a set of effective assessment and classification system covering complete multilevel factor sets and specific quantitative parameters is established. Four main damage types, including the slope and portal damage, the lining damage, the road pavement damage, and the earthquake collapse, are defined as the level-1 controlling factor sets. To target the feature of rapidity for the assessment of SDL of mountain tunnel, the discretized assessment index and classification criterion are introduced and fully considered in this study.

Using the proposed concentric circle method (CCM), the SDL of the left line of Longxi tunnel after Wenchuan earthquake is used as an example and is identified to be severe damage. The assessment results from the proposed rapid assessment method are consistent with the field investigation data, verifying the accuracy and applicability of the CCM for rapid assessment of seismic damage of mountain tunnel.

## Data Availability

The data used to support the findings of this study are included within the article.

## Conflicts of Interest

The authors declare that they have no conflicts of interest.

## Acknowledgments

This study was financially supported by the National Key Research and Development Program of China (2016YFB1200401-102D), Western Construction Project of the Ministry of Transport (grant no. 2015 318 J29 040), and the Open Foundation of State Key Laboratory of Geohazard

Prevention and Geoenvironment Protection (Chengdu University of Technology, grant no. SKLGP2011K014).

## References

- [1] K. Yashiro, Y. Kojima, and M. Shimizu, "Historical earthquake damage to tunnels in Japan and case studies of railway tunnels in the 2004 Niigataken-Chuetsu earthquake," *Quarterly Report of RTRI*, vol. 48, no. 3, pp. 136–141, 2007.
- [2] W. L. Wang, T. T. Wang, J. J. Su, C. H. Lin, C. R. Seng, and T. H. Huang, "Assessment of damage in mountain tunnels due to the Taiwan Chi-Chi Earthquake," *Tunnelling and Underground Space Technology*, vol. 16, no. 3, pp. 133–150, 2001.
- [3] T. Li, "Damage to mountain tunnels related to the Wenchuan earthquake and some suggestions for aseismic tunnel construction," *Bulletin of Engineering Geology and the Environment*, vol. 71, no. 2, pp. 297–308, 2012.
- [4] S. Senzai, O. Hajime, and M. Takashi, "A study of the damage of subway structures during the 1995 Hanshin-Awaji earthquake," *Cement and Concrete Composites*, vol. 19, no. 3, pp. 223–239, 1997.
- [5] K. F. Ma, C. T. Lee, Y. B. Tsai, T. C. Shin, and J. Mori, "The Chi-Chi, Taiwan earthquake: large surface displacements on an inland thrust fault," *Eos, Transactions American Geophysical Union*, Transactions American Geophysical Union, vol. 80, no. 50, pp. 605–620, 1999.
- [6] Y. B. Tsai and M. W. Huang, "Strong ground motion characteristics of the chichi, taiwan, earthquake of september 21, 1999," *Earthquake Engineering and Engineering Seismology*, vol. 2, no. 1, pp. 1–21, 2000.
- [7] A. Kurose and P. Berest, *Analytical Methods for Dynamic Response of Underground Structures*, VI Colloque National AFPS, Palaiseau, France, 2003.
- [8] O. Naoto, H. Kiyomi, Y. Takemine et al., "Dynamic behavior of a underground motorway junction due to large earthquake," in *Proceedings of the 13th World Conference on Earthquake Engineering*, pp. 1215–1223, Vancouver Canada, August 2004.
- [9] Y. Shen, B. Gao, X. Yang, and S. Tao, "Seismic damage mechanism and dynamic deformation characteristic analysis of mountain tunnel after Wenchuan earthquake," *Engineering Geology*, vol. 180, pp. 85–98, 2014.
- [10] D. Wu, B. Gao, Y. Shen, J. Zhou, and G. Chen, "Damage evolution of tunnel portal during the longitudinal propagation of Rayleigh waves," *Natural Hazards*, vol. 75, no. 3, pp. 2519–2543, 2015.
- [11] H. Xu, T. Li, L. Xia, J. X. Zhao, and D. Wang, "Shaking table tests on seismic measures of a model mountain tunnel," *Tunnelling and Underground Space Technology*, vol. 60, pp. 197–209, 2016.
- [12] X. Q. Fang, J. Q. Lin, X. L. Zhou et al., "Damage evaluation of tunnels in earthquakes," in *Proceeding of the 14th World Conference on Earthquake Engineering*, pp. 1–9, Beijing China, October 2008.
- [13] Y. Jiang, C. Wang, and X. Zhao, "Damage assessment of tunnels caused by the 2004 Mid Niigata Prefecture Earthquake using Hayashi's quantification theory type II," *Natural Hazards*, vol. 53, no. 3, pp. 425–441, 2010.
- [14] Z. Z. Wang and Z. Zhang, "Seismic damage classification and risk assessment of mountain tunnels with a validation for the 2008 Wenchuan earthquake," *Soil Dynamics and Earthquake Engineering*, vol. 45, no. 1, pp. 45–55, 2013.
- [15] W. J. Zang and Z. Z. Wang, "Seismic damage rules and seismic risk of tunnel portals based on fuzzy comprehensive evaluation method," in *Proceedings of the Second International Conference on Geotechnical and Earthquake Engineering*, pp. 498–506, Chengdu China, October 2013.
- [16] J. S. Kim, H. W. Kim, and I. S. Kweon, "A Camera calibration method using concentric circles for vision application," in *Proceedings of the 5th Asian Conference on Computer Vision*, pp. 1–6, Melbourne Australia, January 2002.
- [17] T. L. Saaty, "How to make a decision: the analytic hierarchy process," *European Journal of Operational Research*, vol. 48, no. 1, pp. 9–26, 1990.
- [18] A. Melvin, "Decision-making using the analytic hierarchy process (AHP) and SAS/IML," *SESUG, SD-4*, pp. 1–12, 2012.
- [19] A. Remi, "Numerical discretization of boundary conditions for first order hamilton-jacobi equations," *Siam Journal of Numerical Analysis*, vol. 41, no. 6, pp. 2233–2261, 2003.
- [20] S. T. Li, *Spatial Discretization*, Los Alamos National Laboratory, Los Alamos, NM, USA, 2007.
- [21] M. N. Wang, G. Y. Cui, and G. J. Lin, "Investigation and preliminary analysis on tunnel seismic damage in wenchuan earthquake district," *Southwest Highway*, vol. 4, pp. 41–46, 2009.
- [22] K. Getachew, D. H. Chen, and G. Peng, "Seismic performance evaluation of RC frame designed using Ethiopian and Chinese seismic codes," *Advances in Civil Engineering*, vol. 2020, Article ID 8493495, , 2020.
- [23] 2008 Highway planning, survey, design and research institute of Sichuan provincial department HPSDRISPD, Investigation report of highway earthquake damage in Wenchuan seismic disastrous area. Chengdu, China.
- [24] 1997 The professional standards compilation group of people's Republic of China, Deterioration Evaluation standard of railway bridge and tunnel building (DESRBTB). TB/T 2820.1-2820.8.
- [25] J. H. Shin, I. K. Lee, Y. H. Lee, and H. S. Shin, "Lessons from serial tunnel collapses during construction of the Seoul subway Line 5," *Tunnelling and Underground Space Technology*, vol. 21, no. 3-4, pp. 296–297, 2006.
- [26] A. S. Osman, R. J. Mair, and M. D. Bolton, "On the kinematics of 2D tunnel collapse in undrained clay," *Géotechnique*, vol. 56, no. 9, pp. 585–595, 2006.
- [27] H.-S. Shin, Y.-C. Kwon, Y.-S. Jung, G.-J. Bae, and Y.-G. Kim, "Methodology for quantitative hazard assessment for tunnel collapses based on case histories in Korea," *International Journal of Rock Mechanics and Mining Sciences*, vol. 46, no. 6, pp. 1072–1087, 2009.
- [28] T. H. Huang, T. Y. Ho, and C. T. Chang, *Quick Investigation and Assessment on Tunnel Structure after Earthquake, and the Relevant Reinforced Methods*, Report for Public Construction Commission, Taipei, Taiwan.
- [29] C. Qin and S. C. Chian, "2D and 3D stability analysis of tunnel roof collapse in stratified rock: a kinematic approach," *International Journal of Rock Mechanics and Mining Sciences*, vol. 100, pp. 269–277, 2017.
- [30] C. H. Dowding and A. Rozan, "Damage to rock tunnels from earthquake shaking," *Journal of the Geotechnical Engineering Division*, vol. 104, no. 2, pp. 175–191, 1978.
- [31] L. S. Chen, *Report on Highways' Damage in the Wenchuan Earthquake*, China Communications Press, Beijing, China, 2012.
- [32] H. Wu, H. Lei, and T. Lai, "Shaking table tests for seismic response of orthogonal overlapped tunnel under horizontal

- seismic loading,” *Advances in Civil Engineering*, vol. 2021, Article ID 6633535, , 2021.
- [33] Z. Z. Wang, L. Jiang, and Y. Gao, “Shaking table test of seismic response of immersed tunnels under effect of water,” *Soil Dynamics and Earthquake Engineering*, vol. 116, pp. 436–445, 2019.
- [34] J. Yu and Z. Z. Wang, “The dynamic interaction of the Soil-Tunnel-Building system under seismic waves,” *Soil Dynamics and Earthquake Engineering*, vol. 144, Article ID 106686, 2021.
- [35] J. S. Xu, H. Xu, R. F. Sun, X. W. Zhao, and Y. Cheng, “Seismic risk evaluation for a planning mountain tunnel using improved analytical hierarchy process based on extension theory,” *Journal of Mountain Science*, vol. 17, no. 1, pp. 244–260, 2020.
- [36] Z. F. Fan, J. C. Zhang, H. Xu, and J. Cai, “Transmission of normal P-waves across a single joint based on  $g - \lambda$  model,” *Shock and Vibration*, vol. 2019, Article ID 8240586, , 2019.
- [37] H. Xu, Z. F. Fan, J. C. Zhang et al., “Transmission and application of a P-wave across joints based on a modified  $g - \lambda$  model,” *International Journal of Rock Mechanics and Mining Sciences*, in Press, 2021.

## Research Article

# Shaking Table Test on the Seismic Responses of a Slope Reinforced by Prestressed Anchor Cables and Double-Row Antisliding Piles

Zuo-ju Wu <sup>1</sup>, Zhi-jia Wang <sup>2</sup>, Jun-wei Bi <sup>3</sup>, Xiao Fu <sup>4</sup>, and Yong Yao <sup>1</sup>

<sup>1</sup>School of Civil Engineering and Architecture, Southwest University of Science and Technology, Mianyang, Sichuan 621010, China

<sup>2</sup>College of Civil Engineering and Architecture, Hainan University, Haikou, Hainan 570228, China

<sup>3</sup>College of Civil Engineering, Tongji University, Shanghai 200092, China

<sup>4</sup>School of Civil Engineering, Southwest Jiaotong University, Chengdu, Sichuan 611756, China

Correspondence should be addressed to Zuo-ju Wu; 706805410@qq.com

Received 3 April 2021; Accepted 4 May 2021; Published 11 May 2021

Academic Editor: Honglue Qu

Copyright © 2021 Zuo-ju Wu et al. This is an open access article distributed under the Creative Commons Attribution License, which permits unrestricted use, distribution, and reproduction in any medium, provided the original work is properly cited.

The combined retaining structure has gradually received considerable attention in the slope engineering, due to its good reinforcement effects. However, most of the published research studies were focused on the seismic responses of the single-formal supporting structure only. The investigations of dynamic responses of the combined retaining structures are scarce, and the current seismic design is conducted mainly based on experiences. In this work, a series of large-scale shaking table tests were conducted to investigate the seismic responses of the combined retaining structures (i.e., prestressed anchor cables and double-row antisliding piles) and the reinforced slope under seismic excitations, including amplification effect of internal and surface acceleration of the reinforced slope, distribution and change of prestress of the anchor cable, dynamic response of soil pressure behind the antisliding pile, and horizontal displacement of the reinforced slope surface. Test results show that, supported by the reinforcement of composite support system, the slope with the multilayer weak sliding surface can experience strong ground motion of 0.9 g. The load of the antisliding pile has reached 80% of its bearing capacity, and the load of the anchor cable has reached 75.0% of its bearing capacity. When the seismic intensity reaches 0.5 g, the slope surface has an obvious downward trend, which will make the corresponding soil pressure suddenly increase after the antisliding pile. At the potential sliding zone, the axial force of the anchor cable will increase suddenly under the action of earthquake; after the earthquake, the initial prestress of the anchor cable will be lost, with the loss range of 17.0%~23.0%. These test results would provide an important reference for the further study of the seismic performance of such composite support structure.

## 1. Introduction

There are many mountains in Southwest China, so there are many slopes. Particularly, most slope projects in Sichuan Province are located in the areas with high seismic intensity. When strong earthquakes occur, these supporting structures (such as anchor cables and antisliding piles) are often damaged [1–3]. Therefore, the seismic research of the slope-supporting structure is of great significance.

As an important mean to study the seismic performance of supporting structures, the shaking table test has been

developing rapidly in the past decade. Lai et al. [4] conducted shaking table tests to research the seismic responses of a slope reinforced by double-row antisliding piles, which indicates that the double-row antisliding piles could effectively resist the combination of tension and shear during earthquake. Jiang et al. [5] performed a series of shaking table model tests of the slope supported by anchor cables to deeply study the responses and characteristics of the reinforced slope under earthquake action. Ye et al. [6] investigated the seismic behavior of a slope reinforced by prestressed anchor cables through the shaking table test, in

which the antislip mechanism of the prestressed anchor cables is well analyzed. Lin et al. [7] conducted experimental and numerical investigations and researched the seismic behavior of an anchoring frame beam under earthquakes. Through model tests, Zheng et al. [8] investigated the seismic-induced damage and deformation patterns of a rock slope reinforced by prestressed cables. Xu et al. [9] conducted a shaking table test to determine the load transfer mechanism and dynamic response characteristics of a slope supported by adaptive anchor cables. Ma et al. [10] used the shaking table test to study the distribution and variation of the dynamic soil pressures acting on supporting structures, including the antisliding pile and the prestressed anchor slab-pile wall. Through a series of shaking table tests, Ding et al. [11] investigated the seismic behavior and performance of the slopes reinforced by concrete-canvas and composite reinforcement. Zhou et al. [12] analyzed the seismic damages of road slopes in Wenchuan earthquake and pointed out that the prestressed anchor cable and antisliding pile have good earthquake resistance performance. Currently, the combined retaining structures are more and more widely applied, especially for large-scale slope and landslide projects. Lin et al. [13] performed shaking table tests and investigated the dynamic responses of a slope which is reinforced by prestressed anchor cables and single-row antisliding piles. More recently, Fan et al. [14] conducted experimental investigations to study the dynamic behavior of a slope reinforced by double-row antisliding piles and prestressed anchor cables under Wenchuan seismic excitations.

The above studies mainly focus on the seismic response of the single-formal support structure. However, the dynamic response of the slope reinforced by the composite support structure under earthquake action is very limited. Moreover, investigations related to the seismic responses of the slope reinforced by prestressed anchor cables and double-row antisliding piles are rather scarce, and the corresponding design method for such combined retaining structure is still unclear. Therefore, further in-depth study on the dynamic responses of prestressed anchor cables and double-row antisliding piles under the earthquake loadings must be available to improve the current seismic design.

To address these issues, a series of large-scale shaking table tests were conducted to investigate the seismic responses of a slope reinforced by prestressed anchor cables and double-row antisliding piles. Some meaningful conclusions and recommendations are obtained based on the analysis of test results.

## 2. Engineering Background

Figure 1 shows the prototype slope that is located in Sichuan, China. The height and width of the slope are about 150.00 m and 325.00 m, respectively, and the elevation of the slope toe is 606.00 m. A typical cross section for the shaking table test is selected, as shown in Figure 2. According to the site exploration, the slip bed of the prototype slope mainly formed in intact celadon shale, and the sliding mass mainly consists of the highly weathered shale and Quaternary alluvial deposit. There are two slip surfaces inside the slope,

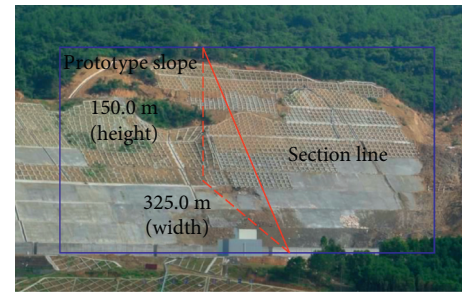


FIGURE 1: Overlook of the prototype slope.

which the potential sliding zones consist of the silty clay with minor gravels. The parameters of the prototype slope are listed in Table 1. In reference to Seismic Ground Motion Parameters Zonation Map of China [15], the seismic design intensity of the prototype site is 7.00. Therefore, taking consideration of the significance of the prototype slope, the effects of seismic loadings should not be neglected. According to the results of stability analyses, the safety factor of the prototype slope under earthquakes is 1.03, and the value of which under the pseudostatic conditions is 0.90. The peak ground acceleration and seismic influence coefficient in the horizontal direction are 0.15 g and 0.24, respectively. The calculations show that the residual sliding force of prototype slopes is extremely large; thus, the original design of single-row antisliding piles and prestressed anchor cables could not meet the needs of stability. Therefore, the slope is designed to be reinforced by prestressed anchor cables and double-row antisliding piles.

## 3. Shaking Table Tests

**3.1. Shaking Table Device.** The shaking table facility used for the tests allows input of three directions of earthquake records with independent control. The shaking table has 6 degrees of freedom, including 3 degrees of translation and 3 degrees of rotation, and the dimensions of which are 6.0 m by 6.0 m. At full load, the maximum acceleration could reach 1.0 g in the horizontal direction and 0.8 g in the vertical direction. The maximum displacements of the shaking table in the horizontal and vertical direction are  $\pm 150.0$  mm and  $\pm 100.0$  mm, respectively, and the loading frequency range of which is 0.1 Hz~80.0 Hz. Additionally, a data acquisition system with 128 channels is adopted, which the maximum error can be controlled within 5.0%.

**3.2. Similitude Law.** According to the scaling laws, three controlling parameters were selected, which are the dimension  $L$ , density  $\rho$ , and acceleration  $a$ , respectively. Limited by the dimensions and bearing capacity of the shaking table facility, the similar constants of dimension ( $C_L$ ), density ( $C_\rho$ ), and acceleration ( $C_a$ ) were set to be  $C_L = 100.0$ ,  $C_\rho = 1.0$ , and  $C_a = 1.0$  for this shaking table test, leading to the model slope height of 200.0 cm. Based on the Buckingham  $\pi$  theorem [16], the similarity ratios of other parameters for this model test could be obtained, as

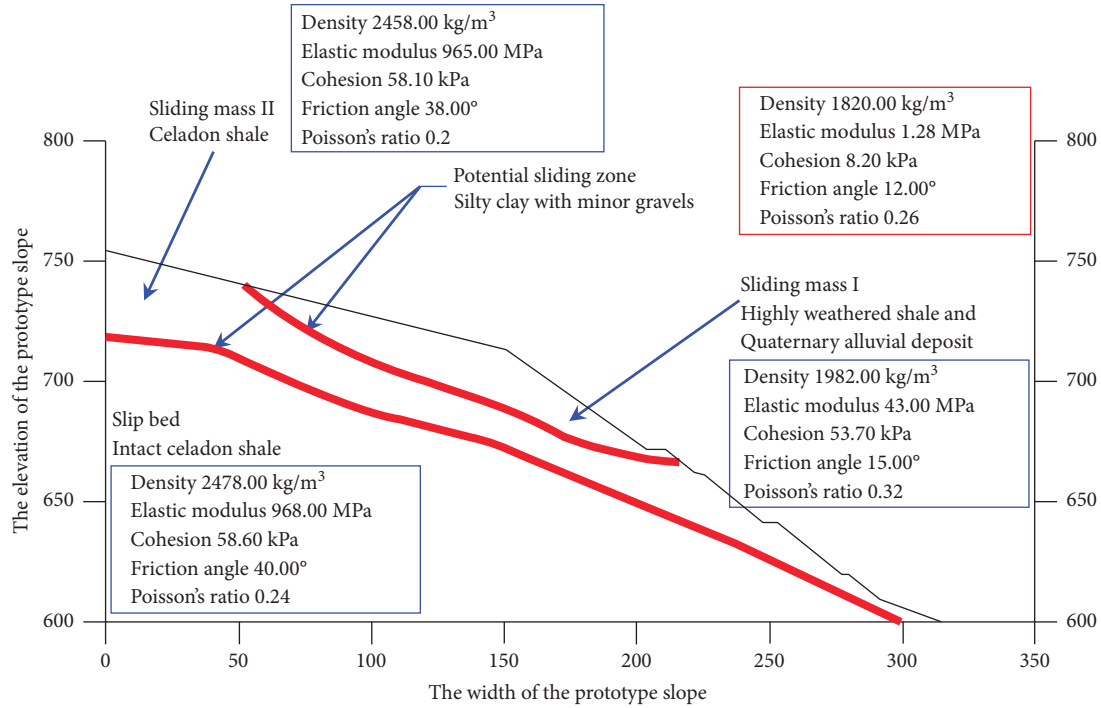


FIGURE 2: The typical section of the prototype slope.

TABLE 1: Material parameters for the prototype slope.

Components	Density $\rho$ (kg/m <sup>3</sup> )	Elastic modulus $E$ (MPa)	Cohesion $c$ (kPa)	Friction angle ( $^{\circ}$ )	Poisson's ratio $\mu$
Slide bed	2478.00	968.00	58.60	40.00	0.24
Sliding mass II	2458.00	965.00	58.10	38.00	0.25
Sliding mass I	1982.00	43.00	53.70	15.00	0.32
Potential sliding zone	1820.00	1.28	8.20	12.00	0.26

illustrated in Table 2, and the detailed derivation of which could be found in Ref. [17].

**3.3. Test Model.** The slope model was placed in a rigid box container with waterproof treatment which fixed on the shaking table, and the dimensions of the box are 325.0 cm  $\times$  150.0 cm  $\times$  250.0 cm (length  $\times$  width  $\times$  height), as shown in Figure 3. The slope model was built layer by layer, in which the height of each layer is 20.0 cm. Based on the required thickness and density of each layer, similar materials with a certain quality would be placed into the model box and then compacted to the desired thickness. After each layer was compacted, the cutting ring method was applied to ensure whether the unit weight meets the requirements or not. For the potential sliding zones, the similar materials were obtained from the prototype slope and remodeled for the shaking table tests. After the test model was built, the slope model is saturated through the pipes preinstalled in the model slope. Additionally, for each component of the model slope, samples were collected, and soil mechanics tests (i.e., cutting ring method, resonant column test, direct shear test, uniaxial compression test, and triaxial test) were performed to obtain the physical parameters. The mechanical parameters of the test model are presented in Table 3.

After the model slope was completed, the prestressed anchor cables and double-row antisliding piles were used to reinforce the slope through the reserved holes. Considered to be rigid, the antisliding piles were made of concrete with a section of 2.0 cm by 3.0 cm, and the bending deformation of which were ignored in this work. As shown in Figure 4, a row of antisliding piles labeled the Pile A were installed at the waist of the model slope, and the other row of piles named the Pile B were located at the slope toe. The height of the Pile A and B are 20.0 cm and 16.0 cm, respectively. Due to the limitation of the model size, it is difficult to install too many rows of prestressed anchor cables in the mode slope. It should be pointed out, in this work, the adjacent six rows of prestressed anchor cables are merged to be one row. Therefore, three rows of prestressed anchor cables numbered 1#, 2#, and 3# were installed above the Pile A, as can be seen in Figure 4; the other four rows were installed between the Pile A and B, which were numbered with 4#, 5#, 6#, and 7#.

For the prestressed anchor cables, as presented in Figure 5(a), the construction holes were reserved using PVC pipes with diameter of 8.0 cm. The prefabricated anchor cables were inserted into the reserved holes. Then, with pulling the PVC pipes out, the reserved holes were filled with sand simultaneously. The depth of sand was determined by the designed length of the anchorage segment of the anchor

TABLE 2: Similarity ratios of the shaking table test.

Parameters	Dimensions	Similarity ratio
Physical dimension ( $L$ )	[L]	$C_L = 100$
Density ( $\rho$ )	[M][L] <sup>-3</sup>	$C_\rho = 1$
Acceleration ( $a$ )	[L][T] <sup>-2</sup>	$C_a = 1$
Elasticity modulus ( $E$ )	[M][L] <sup>-1</sup> [T] <sup>-2</sup>	$C_E = 100$
Stress ( $\sigma$ )	[M][L] <sup>-1</sup> [T] <sup>-2</sup>	$C_\sigma = 100$
Strain ( $\varepsilon$ )	1	$C_\varepsilon = 1$
Force ( $F$ )	[M][L][T] <sup>-2</sup>	$C_F = 1000000$
Velocity ( $v$ )	[L][T] <sup>-1</sup>	$C_v = 10$
Time ( $t$ )	[T]	$C_t = 10$
Displacement ( $u$ )	[L]	$C_u = 100$
Angular displacement ( $\theta$ )	1	$C_\theta = 1$
Frequency ( $\omega$ )	[T] <sup>-1</sup>	$C_\omega = 0.1$
Damping ratio ( $\lambda$ )	1	$C_\lambda = 1$
Internal friction angle ( $\varphi$ )	1	$C_\varphi = 1$



FIGURE 3: The rigid box container for the shaking table test.

cable. In this shaking table test, the length of the anchorage segment is 8.0 cm. The cable material is steel with the diameter of 2.0 cm. The inclined angle of the prestressed anchor cable is set to 20.0°. According to the designed pulling resistance and the similarity ratio, the filled sand in reserved holes was manually compacted for a given number of times, which was determined by the previous compaction test in the laboratory, as presented in Figure 5(d). The prestress of the anchor cable was applied by rotating the nut on the screw which was fixed on the lattice beam, and the applied prestress was close to real-time values measured by the axial force monitoring. It should be noted that utilizing the sand to fill the reserved holes does not seem to match the in situ field situation. However, by controlling and monitoring the prestress strictly, the specific physical significance of anchor cables in this shaking table test agrees well with that in the in situ field situation. In addition, to attenuate the wave reflection from the steel box during shaking, the expanded polystyrene boards with a thickness of 10.0 cm were placed between the slope model and test box [18, 19].

**3.4. Sensor Layout.** As shown in Figure 4, a total of 14 three-dimensional accelerometers were installed inside the model slope and on the slope surface to measure accelerations in

the horizontal and vertical directions. For the horizontal direction, the sensitivity of accelerometers is 173.46 mv/g, which is 192.08 mv/g in the vertical direction. To measure the displacements on the slope surface, six laser displacement meters with the range of 30.00 cm were installed at different locations throughout the slope height, and the sensitivity of which was 33.33 mv/mm. For the prestressed anchor cables, as shown in Figure 5(b), axial force sensors installed at the tension segment were employed to measure the axial force. The sensitivity of the axial force sensor was 1.50 mv/v. Additionally, the dynamic earth pressure acting on the back of antisliding piles was measured by the earth pressure cells with the measuring range of 0.00 MPa~0.80 MPa. As illustrated in Figure 5(c), five earth pressure cells were installed on the Pile B and numbered with 1#~5#; the other five ones for the Pile A were numbered with 6#~10#.

All the abovementioned sensors are new, and calibration of which was conducted before the shaking table test. Moreover, to attenuate the boundary effect on the test results, all the earth pressure cells and axial force sensors were installed on the middle column of antisliding piles and prestressed anchor cables, and all the accelerometers and laser displacement meters were also installed in the middle section.

**3.5. Seismic Loadings and Shaking Sequence.** The seismic loading used in this shaking table test was the El Centro earthquake record which has been widely used in the earthquake engineering. Two simultaneous loading directions of seismic excitations were applied in this shaking table test, namely, the X and Z direction, for which the corresponding time histories of the input seismic motions can be seen in Figure 6. Based on the similarity criteria, the input earthquake records were compressed in the time axis with a compression ratio of 10.00 (the similarity ratio of Time  $t$ ). Six different horizontal peak accelerations of the input seismic loadings (i.e., 0.15 g, 0.30 g, 0.40 g, 0.50 g, 0.70 g, and 0.90 g) were selected. As highlighted in Refs. [20–22], the vertical peak acceleration is generally two-thirds of the horizontal peak acceleration. Additionally, before the excitation of the El Centro earthquake record, the model was scanned by the 0.05 g white noise. The loading sequence of the shaking table tests is listed in Table 4.

## 4. Results and Discussions

**4.1. Acceleration Responses.** The slope would have obvious nonlinear responses under strong seismic motions [23]. According to Ref. [24], the acceleration amplification behavior of the prototype slope could be well revealed by the shaking table test. In this study, the baseline corrected and band-pass filtered are adopted to the measured signals before calculating amplification factors. The peak values of horizontal accelerations are obtained by taking the maximum absolute values from the acceleration time histories.

In this section, the ratio of the peak horizontal acceleration obtained on the slope surface or inside the slope to



TABLE 3: Material parameters for the test model.

Material	Density $\rho$ (g/cm <sup>3</sup> )	Elastic modulus $E$ (MPa)	Friction angle ( $^\circ$ )	Cohesion $c$ ( $10^{-4}$ MPa)	Poisson's ratio $\mu$	
Slope	M 1	2.50	9.80	40.00	6.00	0.25
	M 2	1.95	0.40	15.00	5.50	0.30
Rock base	2.70	10.10	42.00	7.40	0.25	
Potential sliding zone	1.80	$1.20 \times 10^{-2}$	12.00	0.75	0.25	
Antisliding pile	2.70	301.00	Elastic material		0.20	
Anchorage segment	2.50	290.00				

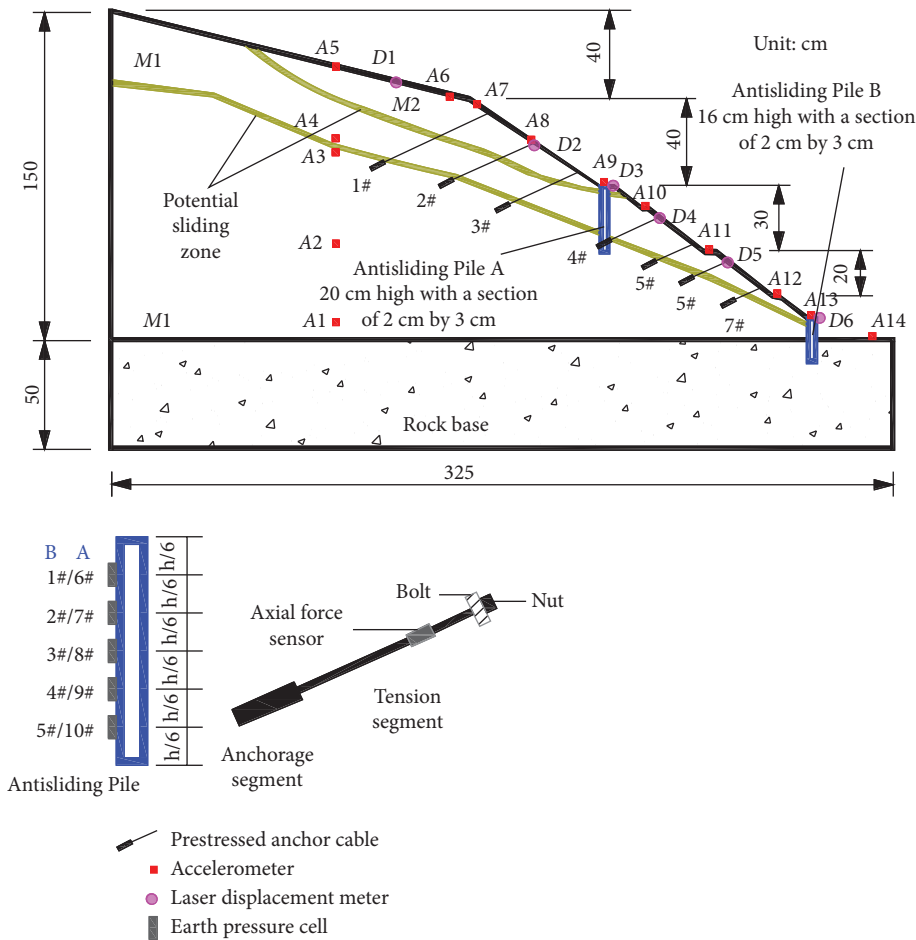


FIGURE 4: Layout of sensors and detailed views of the antisliding pile and prestressed anchor cable.

that collected by A14 is defined as the amplification factor. Figure 7 presents the variations of the amplification factor of horizontal acceleration on the slope surface and inside the slope. As shown in Figure 7(a), comparing with the slope mass above the Pile A, the amplification factors on the slope surface between the Pile A and B are smaller. This indicates that the existence of the Pile A weakens the seismic responses of the slope effectively. However, for the slope mass above 1# anchor cable, the acceleration amplification factor increases rapidly along the slope height because of the reason that this part of the slope is not reinforced by any supporting

structures. Based on the above analysis, the prestressed anchor cables and double-row antisliding piles could effectively reduce the dynamic responses of the slope surface under earthquakes. It can be seen from Figure 7(b) that the amplification factor of horizontal acceleration inside the slope increases generally with the slope height, whereas the acceleration amplification factor decreases when the seismic waves pass through the potential sliding zone from the bottom to the top. It indicates that some of the energy carried by earthquake waves could be dissipated by the potential sliding zone.

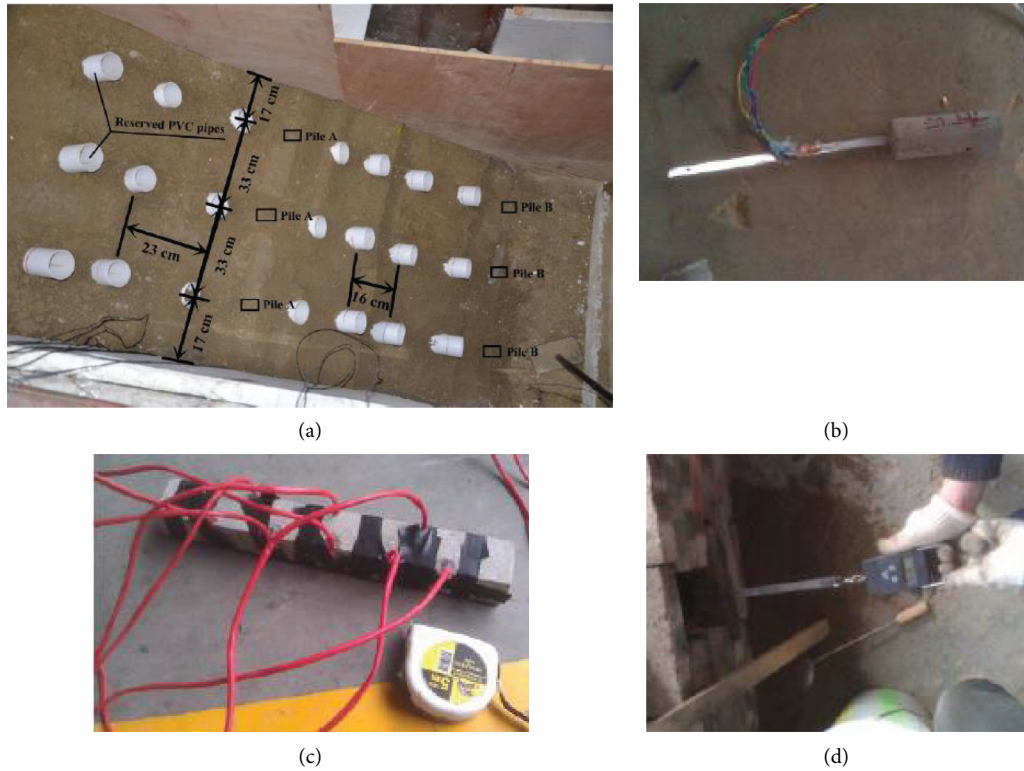


FIGURE 5: The model slope and the retaining structures. (a) Schematic diagram of the model slope. (b) Prestressed anchor cable. (c) Antisliding pile. (d) Compaction test for the anchor cable.

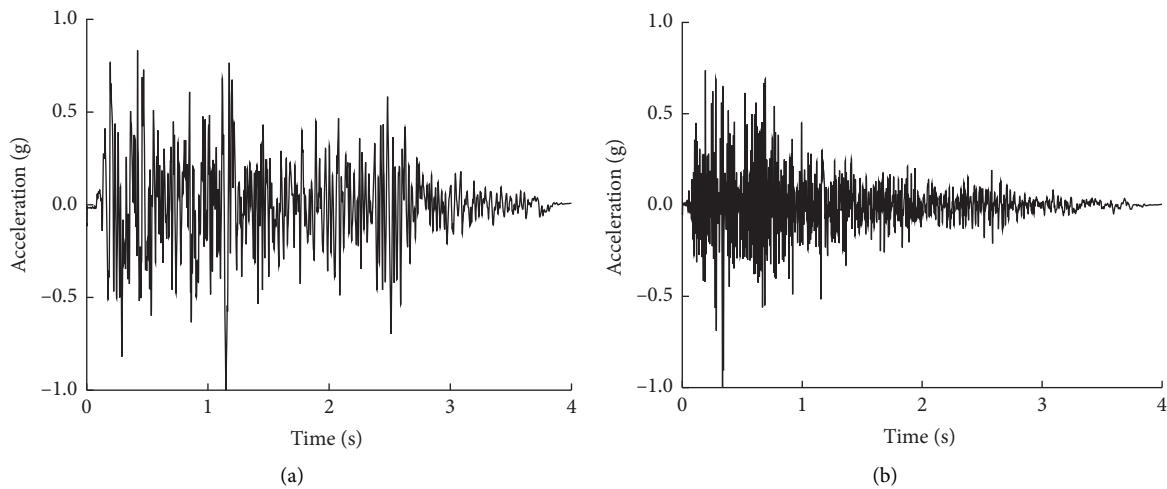


FIGURE 6: The input El Centro earthquake motions. (a) The horizontal seismic excitation. (b) The vertical seismic excitation.

**4.2. Axial Force of the Prestressed Anchor Cables.** To research the seismic responses of prestressed anchor cables, the axial force of each anchor cable was measured, and the initial values of which before each excitation are listed in Table 5. For 2# prestressed anchor cable, the time histories of the axial force under the El Centro seismic loading with different amplitudes are plotted in Figure 8. From the figure, the variations of axial forces are similar to the time history of the input excitation (in Figure 6). The peak values of axial force occur at around the same

time for that of the input earthquake motion. In this work, to well discuss the seismic responses of the prestressed anchor cables, the peak values and residual values of the axial force are analyzed separately.

**4.2.1. Peak Values of the Axial Force.** Figure 9 shows that the peak values of the axial force of prestressed anchor cables increase with the amplitudes of the input seismic loadings, especially when the input amplitude is larger than 0.5 g. It

TABLE 4: Loading sequence for the shaking table test.

No.	Seismic input	Amplitude (g)
1	White noise	0.05
2	El Centro wave	0.15
3	El Centro wave	0.30
4	El Centro wave	0.40
5	El Centro wave	0.50
6	El Centro wave	0.70
7	El Centro wave	0.90

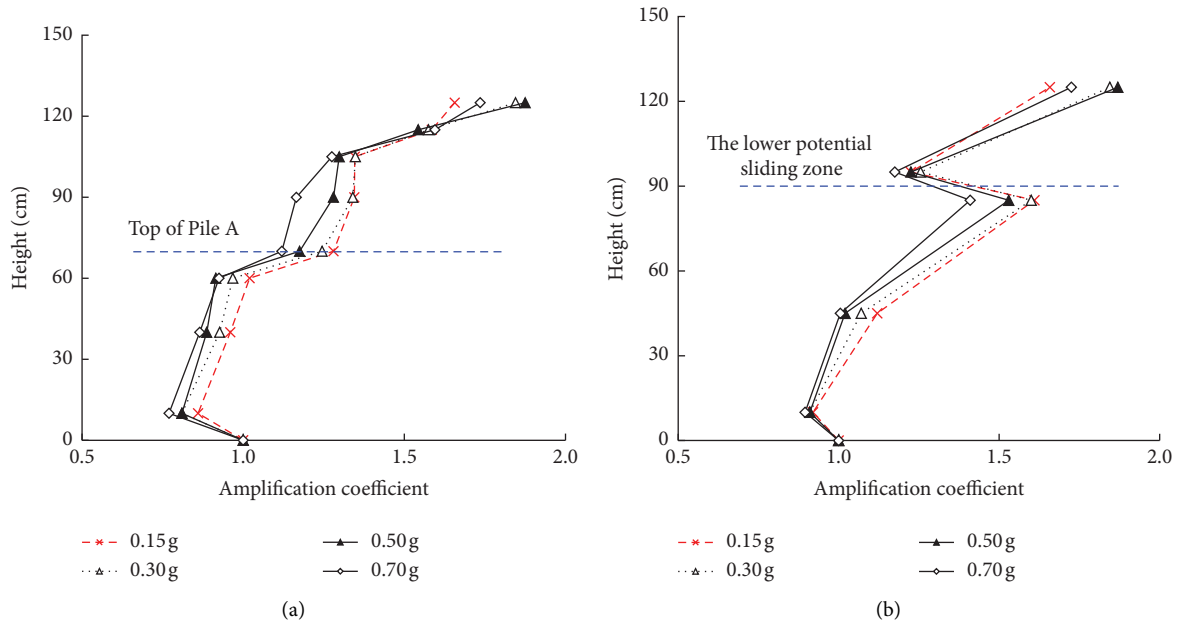


FIGURE 7: Amplification factors of the horizontal acceleration. (a) At the slope surface. (b) Inside the slope.

TABLE 5: Initial prestress values of the prestressed anchor cables before each seismic excitation (Unit: N).

No.	Amplitude					
	0.15 g	0.30 g	0.40 g	0.50 g	0.70 g	0.90 g
1	35.20	30.60	30.90	30.80	27.50	24.10
2	26.50	21.40	22.50	22.40	20.70	17.80
3	25.40	19.20	20.70	20.90	20.40	18.60
4	22.70	18.50	19.00	21.10	21.60	19.80
5	16.10	10.20	10.60	12.00	13.50	14.30
6	23.50	18.40	17.60	18.40	18.60	18.30
7	17.60	17.00	18.60	18.20	20.10	22.00

indicates that the performance of the anchor cable is taken full advantage when the amplitude of excitation is greater than 0.5 g. As presented in Figure 4, seven rows of prestressed anchor cables can be divided into two parts by the Pile A. The maximum increment of the axial force occurs in 2# prestressed anchor cable. The increment of the peak axial force of 1# anchor cable is larger than that of 3# anchor cable, especially when the input amplitude of seismic motion is larger than 0.4 g. It indicates that stronger dynamic responses occur on the upper part of the slope. Under earthquake loadings, the sliding force is firstly undertaken by

the anchor cables located in the upper part of the slope, and the rest of which is undertaken by other anchor cables. For the prestressed anchor cables located between the Pile A and B, the increment of the peak axial force increases generally with the slope height. However, the increment of the peak axial force in 7# anchor cable is larger than 5# and 6# anchor cables and smaller than 4# anchor cable. This is due to that, with a shorter free segment, the seismic responses of the axial force of 7# anchor cable are mainly influenced by the anchor cable length.

To further reveal the relationship between the initial axial force and the variation of axial force during shaking, the notation  $\alpha$  is defined in this section as the increase rate of axial force, which is expressed as follows:

$$\alpha = \frac{(A_2 - A_1)}{A_1}, \quad (1)$$

where  $A_1$  is the initial axial force of the anchor cable and  $A_2$  denotes the peak value of axial force during earthquake loadings.

The increase rates of the axial force of anchor cables under the El Centro earthquake motions with different amplitudes are depicted in Figure 10. It can be seen from the figure that, under 0.50 g, 0.70 g, and 0.90 g seismic

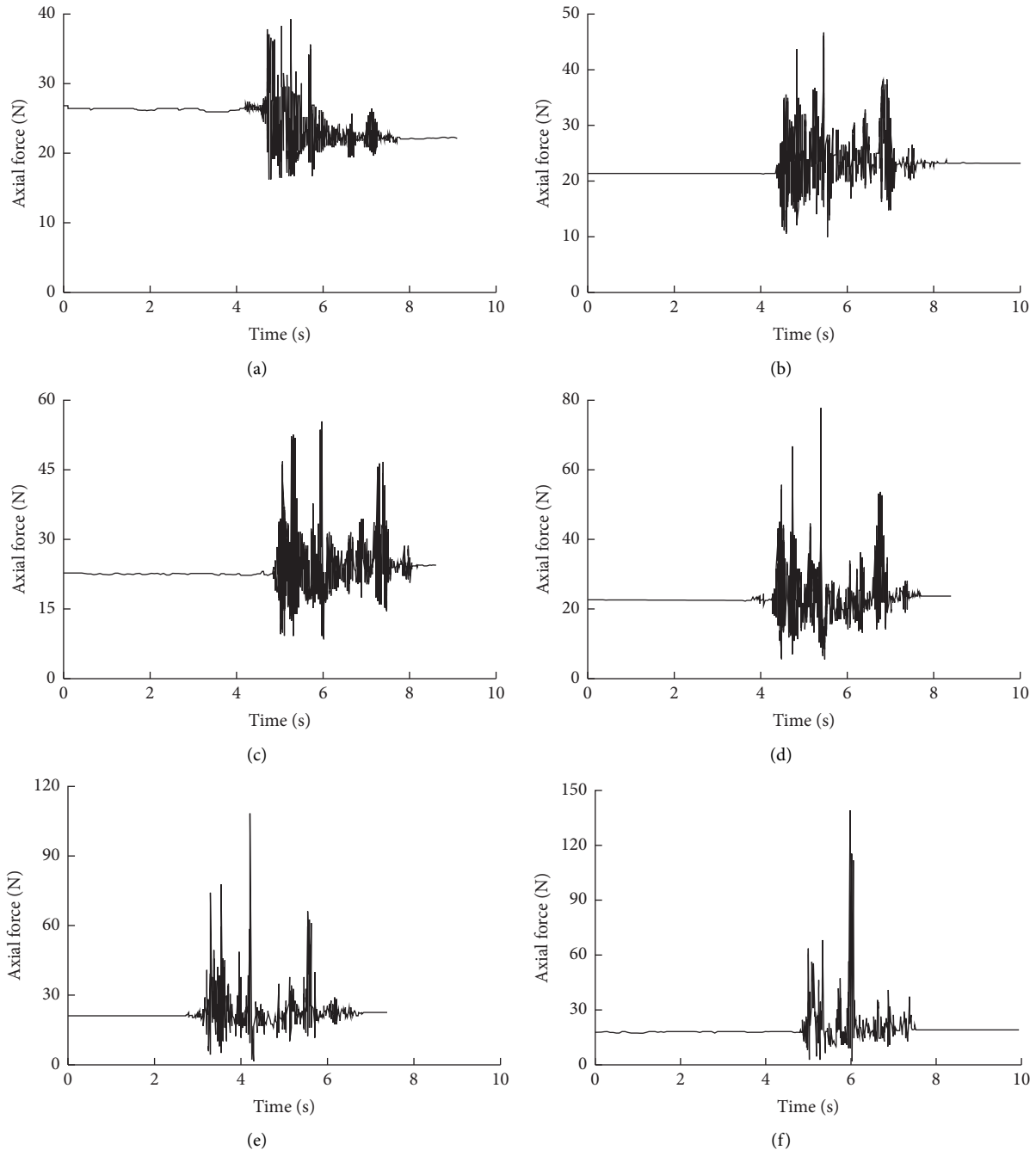


FIGURE 8: Time histories of 2# anchor cable under seismic motions with the amplitude of (a) 0.15 g; (b) 0.30 g; (c) 0.40 g; (d) 0.50 g; (e) 0.70 g; (f) 0.90 g.

excitations, the increase rates of axial force for 2# anchor cable are 2.49, 4.22, and 6.79, respectively, which is the maximum among the prestressed anchor cables. For the other anchor cables, the increase rates are smaller than 2.00 when the amplitude of earthquake loading is not larger than 0.70 g, and in the range of 0.83~3.30 under 0.90 g seismic motions. In reference to the current seismic design method, the safety factor of the calculation of the section area for the prestressed anchor cable is 2.20, in which only static condition is considered. It can be highlighted that the

performance of the prestressed anchor cable under dynamic conditions should be taken into consideration in the seismic design.

The occurrence time of the peak axial force for seven prestressed anchor cables under different excitations is shown in Figure 11. To ensure the integrity of the data collected in the shaking table tests, the data acquisition starts some time before the input of each excitation. Therefore, it is meaningless to compare the occurrence time of the peak axial force with time history of the input

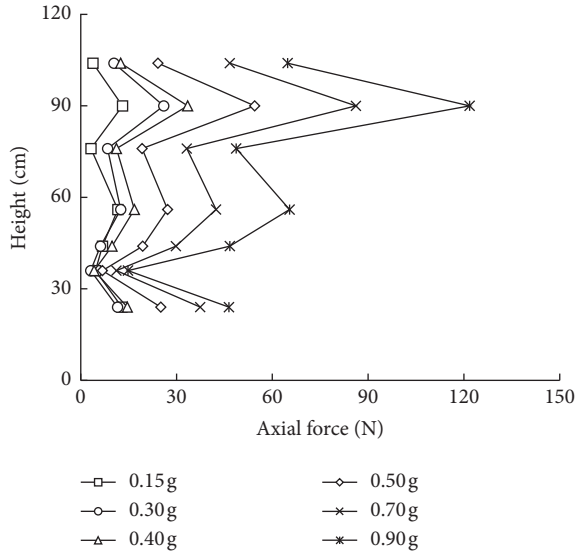


FIGURE 9: Distribution of the peak axial force for all seven anchor cables under seismic motions with different amplitudes.

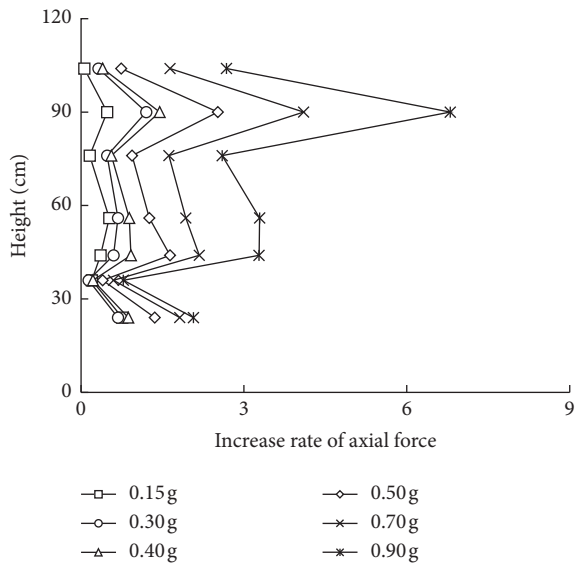


FIGURE 10: Variations of the increase rate of axial force under seismic motions with different amplitudes.

El Centro seismic motion, and the comparison of the occurrence time of peak axial force between different prestressed anchor cables would be discussed in this work. It can be seen from Figure 11 that the most anchor cables get their peak vibration values almost at the same time under each seismic excitation, which indicates that all the prestressed anchor cables work together during shaking. However, under 0.15 g earthquake motion, the occurrence time of the peak axial force for the anchor cables located in the upper part of the slope is somewhat earlier than those in the lower part. This is mainly because that the slope mass is compacted during the seismic excitations, which affects the propagation of the earthquake wave in the slope.

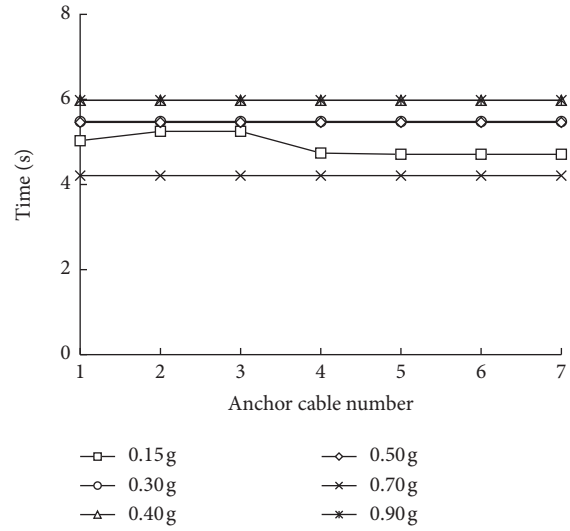


FIGURE 11: The occurrence time of the peak axial force of all seven anchor cables.

**4.2.2. Residual Values of Axial Force.** For the seismic design of the prestressed anchor cable, the prestress loss and the residual value of axial force after earthquake are of great significance. In this work, the notation  $\beta$  is defined as the changing rate of axial force, which is expressed as

$$\beta = \frac{(A_3 - A_1)}{A_1}, \quad (2)$$

in which  $A_1$  is the initial axial force of the anchor cable and  $A_3$  denotes the residual value of axial force after each seismic excitation.

The changing rates of axial force for each anchor cable under seismic excitations are presented in Figure 12. When subjected to 0.15 g seismic motions, the loss of prestress for 1#, 2#, and 3# anchor cables are 11.00%, 16.00%, and 22.00%, respectively. Under the excitations with amplitudes in the range of 0.30 g~0.70 g, the prestress of 1# anchor cable is lost by 4.00% approximately, and by 21.00% under 0.90 g seismic motion. Both for 2# and 3# anchor cables, the prestress increases under 0.30 g~0.90 g seismic excitations. The maximum increment of prestress in 2# anchor cable is about 10.00%, which is greater than that in 3# anchor cable. The loss of prestress for 4#, 5#, and 6# anchor cables are 21.00%, 23.00%, and 19.00% under 0.15 g earthquake excitation, whereas there is almost no prestress loss in 7# anchor cable. When subjected to 0.30 g excitation, the residual axial forces of prestressed anchor cables between the Pile A and B are mainly identical with the initial values. In addition, under the seismic motions with other amplitudes, the prestress of these four anchor cables increases about 10.00%. According to the analysis above, since the maximum of prestress loss is about 23.00% in this test, it is suggested that the initial axial force of the prestressed anchor cable could be raised by 1.20~1.30 times in the seismic design.

The test results show that the axial forces of the prestressed anchor cables in different slope areas are significantly different. It indicates that, for the current seismic

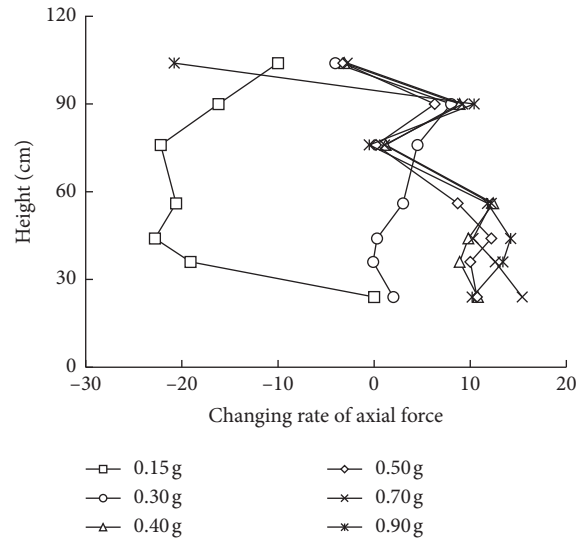


FIGURE 12: Variations of the changing rate of axial force under seismic motions with different amplitudes.

design method, all the prestressed anchor cables are assumed to sustain the same load is inaccurate and uneconomic. In practice, the failure of one anchor cable can cause the failures of adjacent ones because of the chain reaction, which could lead to the slope failure. Therefore, the seismic response differences between anchor cables located in different areas should be fully taken into consideration in the seismic design. Additionally, to ensure the reliability of the prestressed anchor cables and the slope stability, specific design considerations should be adopted in the areas with different geological conditions.

**4.3. Lateral earth Pressure on the Antisliding Piles.** The lateral earth pressures acting on the back of the antisliding Pile A and B under the excitations of El Centro earthquakes are shown in Figure 13. It should be noted that the lateral earth pressure plotted in Figure 13 is the dynamic earth, and the static pressure is not considered in this section. Both for the Pile A and B, the lateral earth pressure increases with the increasing input amplitude. Comparing with the Pile A, the lateral earth pressure acting on the back of the Pile B is much greater, especially for the location with relative height of 0.17 and 0.50. Under the excitations with the amplitude of 0.15 g and 0.30 g, the distribution curves of earth pressure acting on the Pile A are similar to the Pile B. However, when the input amplitude becomes larger than 0.50 g, the lateral earth pressure acting on the Pile A decreases first and then increases along the height, and the minimum of which occurs near the location with relative height of 0.67. It can be seen from Figure 14(b), for the Pile A, the earth pressure acting on the pile toe is larger than that acting on the pile top. As highlighted in Reference [25], the earth pressure measured behind the piles can be equivalent to the earth pressure used in the traditional pseudostatic design, due to the piles are assumed to be rigid. Hence, the major cause of this phenomenon is that the plastic

strain happens in the surrounding soil near the top and toe of the pile under strong earthquake motions. Note that, comparing with the soils, the model piles in this test are of infinite strength and stiffness, leading to rigid rotation and translation of piles during seismic loading. In addition, the difference of the distribution of earth pressure between the Pile A and B is mainly contributed that the Pile B is embedded much deeper than the Pile A and behaving nearly as a fixed pile.

For the seismic responses of double-row antisliding piles, few studies were related to the load-sharing ratio. The ratios between the peak lateral earth pressure acting on the back of the Pile B and A are depicted in Figure 14. It can be seen from the figure that the ratios change mainly in the range of 2.0~5.0, implying that there is a large difference on the load-sharing ratios between the Pile A and B. The earth pressure acting on the back of the Pile B is much larger than that of the Pile A. As highlighted in Refs. [15, 26], the seismic design intensity scale of most areas in China is not larger than 9.0, and the corresponding design acceleration of which is smaller than 0.4 g. The test results in this work have an important practical significance for China and also can provide a reference for other countries and regions in the world.

**4.4. Horizontal Displacements on the Slope Surface.** The horizontal displacements on the slope surface were measured by the laser displacement meters located at different locations throughout the slope height. In this work, the horizontal displacement towards the slope is defined as negative and that away from the slope is defined as positive. In Figure 15, the peak horizontal displacements during seismic excitations and the postearthquake permanent displacements are presented. The figure shows that, when the input amplitude is not larger than 0.50 g, the permanent lateral displacements on the slope surface are small which indicates that the reinforced slope is of good overall stability.

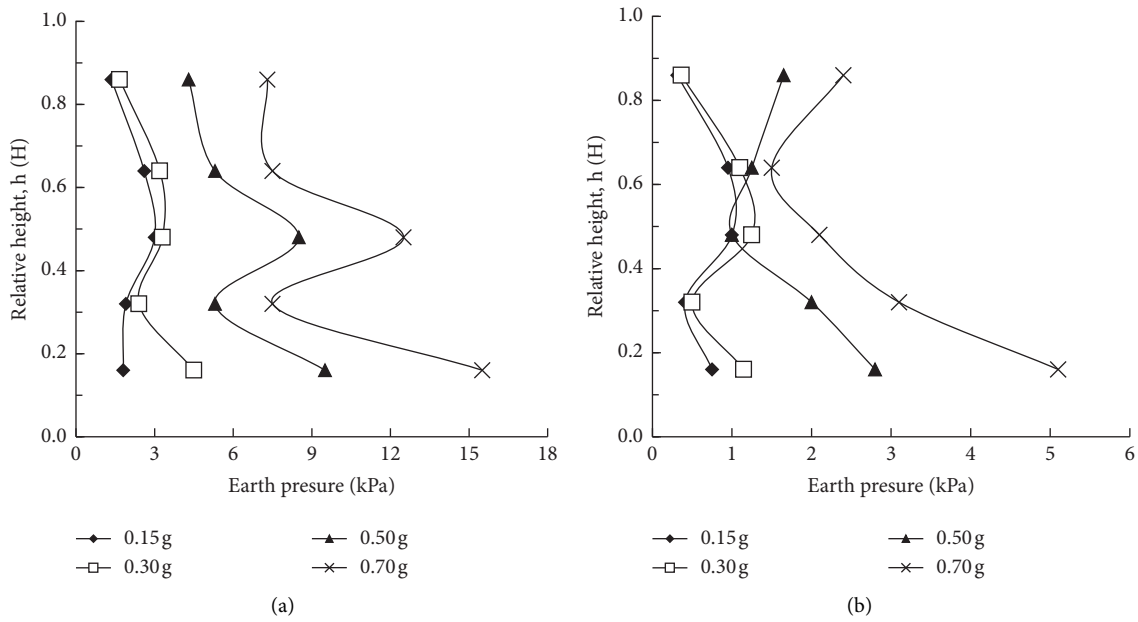


FIGURE 13: Lateral earth pressure acting on the back of (a) the pile B and (b) Pile A under the El Centro earthquake excitations.

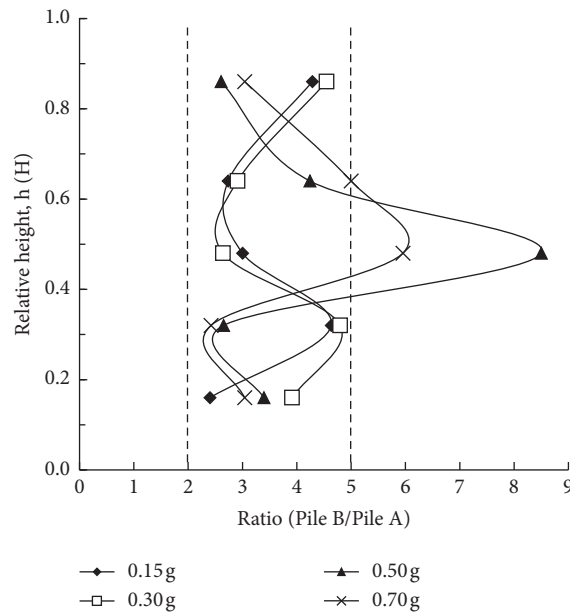


FIGURE 14: The load-sharing ratios between the pile B and A under El Centro earthquake motions.

The peak displacement and permanent displacement on the slope surface increase with the increasing amplitude of the input seismic motions. The slope could be divided into two parts by the Pile A, and the horizontal displacements on the slope surface both for the upper and lower parts of the slope

increase with the elevation. Additionally, it should be noted that the negative permanent displacements on the slope surface occur under 0.15 g El Centro earthquake motion. It is mainly because of that the slope mass is compacted somewhat under the dual actions of seismic motion and

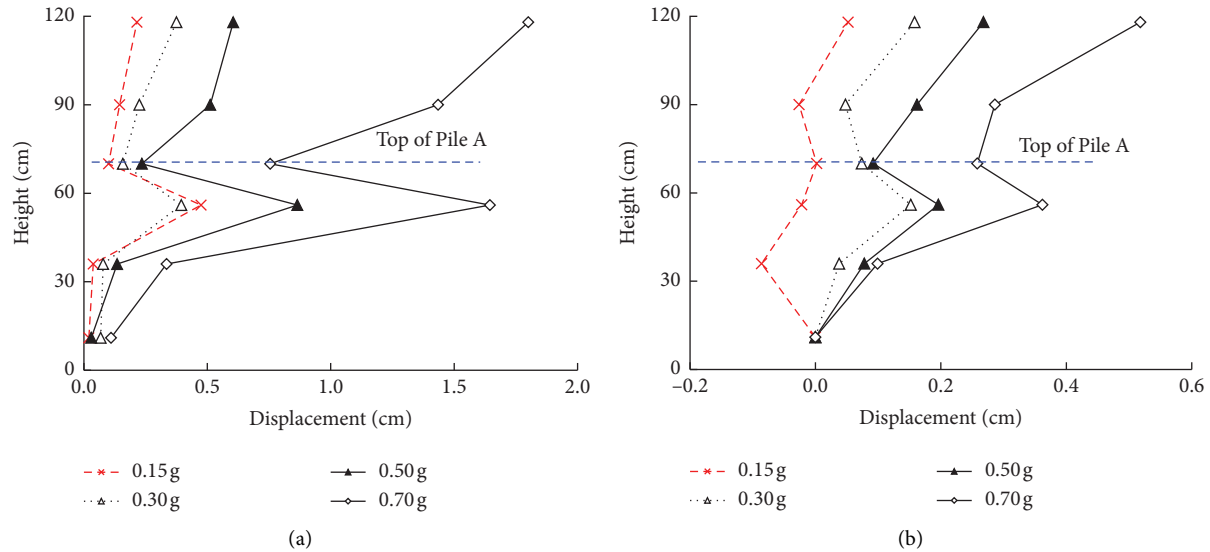


FIGURE 15: Horizontal displacements on the slope surface under the excitations of El Centro earthquake motion. (a) Peak displacement, (b) Permanent displacement.

retaining structures, and this phenomenon is in accordance with the prestress loss of anchor cables under 0.15 g seismic motion.

## 5. Conclusions

According to the test results, several conclusions can be drawn:

- (1) Comparing with the unreinforced part of the slope, the value and the increase rate of the acceleration amplification factor can be effectively controlled by the reinforcements of prestressed anchor cables and double-row antisliding piles, especially for the slope mass between the Pile A and B.
- (2) The maximum of prestress loss is 23.00%. When subjected 0.30 g~0.90 g excitations, the maximum increment of axial force is 15.00%. It can be highlighted that the initial prestress of the anchor cable is suggested to be raised by 1.20~1.30 times in the seismic design for the slope with high requirements of deformation control.
- (3) The lateral earth pressures acting on the back of the Pile A and B increase with the increasing amplitude of the input seismic motions. Comparing with the Pile B located at the slope toe, the earthquake loading undertaken by the Pile A located at the slope waist is obviously smaller, and the load-sharing ratios between the Pile A and B mainly changed in the range of 2.0~5.0.
- (4) Under the seismic excitations, especially the input amplitude not larger than 0.5 g, the lateral displacements on the slope surface can be controlled by the combined retaining structures well. It can be concluded that, reinforced by prestressed anchor

cables and double-row antisliding piles, the slope would have a good overall stability.

## Data Availability

The data used to support the findings of this study are available from the corresponding author upon request.

## Conflicts of Interest

The authors declare that they have no conflicts of interest.

## Acknowledgments

This work was supported by the National Natural Science Foundation of China (Grant no. 51808466) and Young Talents' Science and Technology Innovation Project of Hainan Association for Science and Technology (QCXM201807).

## References


- [1] G. Behrouz, J. A. Danial, and H. Mohsen, "Prediction of seismic slope stability through combination of particle swarm optimization and neural network," *Engineering with Computers*, vol. 32, pp. 85–97, 2016.
- [2] H. B. Seed and R. V. Whitman, "Design of retaining structures for dynamic loads," in *Proceedings of the ASCE Specialty Conference Lateral Stress In the Ground and Design of Earth Retaining Structures*, pp. 103–145, Ithaca, NY, USA, June 1970.
- [3] M. Kamon, T. Wako, K. Isemura et al., "Geotechnical disasters on the waterfront," *Soils and Foundations*, vol. 36, pp. 137–147, 1996.
- [4] J. Lai, Y. R. Zheng, Y. Liu, and X. D. Li, "Shaking table tests on double-row anti-slide piles of slopes under earthquakes," *Chinese Journal of Geotechnical Engineering*, vol. 36, no. 4, pp. 680–686, 2014.



- [5] L. W. Jiang, L. K. Yao, Z. X. Hu, and Q. H. Yang, "Experimental study on slope's superficial dynamic effect and anchoring prevention mechanism under earthquake disturbance," *Journal Of Sichuan University (Engineering Science Edition)*, vol. 42, no. 5, pp. 164–174, 2010.
- [6] H. L. Ye, Y. Y. Zheng, A. H. Li, and X. L. Du, "Shaking table test studies of prestressed anchor cable of slope under earthquake," *Chinese Journal of Rock Mechanics and Engineering*, vol. 31, no. S1, pp. 2847–2854, 2012.
- [7] Y.-l. Lin, Y.-x. Li, G.-l. Yang, and Y. Li, "Experimental and numerical study on the seismic behavior of anchoring frame beam supporting soil slope on rock mass," *Soil Dynamics and Earthquake Engineering*, vol. 98, pp. 12–23, 2017.
- [8] D. Zheng, F.-z. Liu, N.-p. Ju, J. D. Frost, and R.-q. Huang, "Cyclic load testing of pre-stressed rock anchors for slope stabilization," *Journal of Mountain Science*, vol. 13, no. 1, pp. 126–136, 2016.
- [9] M. Xu, Y. Tang, X. Liu, H. Yang, and B. Luo, "A shaking table model test on a rock slope anchored with adaptive anchor cables," *International Journal of Rock Mechanics and Mining Sciences*, vol. 112, pp. 201–208, 2018.
- [10] N. Ma, H. Wu, H. Ma, X. Wu, and G. Wang, "Examining dynamic soil pressures and the effectiveness of different pile structures inside reinforced slopes using shaking table tests," *Soil Dynamics and Earthquake Engineering*, vol. 116, pp. 293–303, 2019.
- [11] G. Ding, L. Zhou, J. Wang, Y. Xu, X. Geng, and X. Li, "Shaking table tests on gravel slopes reinforced by concrete canvas," *Geotextiles and Geomembranes*, vol. 48, no. 4, pp. 539–545, 2020.
- [12] D. P. Zhou, J. J. Zhang, and Y. Tang, "Seismic damage analysis of road slopes in Wenchuan earthquake," *Chinese Journal of Geotechnical Engineering*, vol. 29, no. 3, pp. 565–576, 2010.
- [13] Y. L. Lin, G. L. Yang, and X. Yang, "Response of gravity retaining wall with anchoring frame beam supporting a steep rock slope subjected to earthquake loading," *Soil Dynamics and Earthquake Engineering*, vol. 92, pp. 622–649, 2017.
- [14] G. Fan, J.-j. Zhang, S.-c. Qi, and J.-b. Wu, "Dynamic response of a slope reinforced by double-row anti-sliding piles and prestressed anchor cables," *Journal of Mountain Science*, vol. 16, no. 1, pp. 226–241, 2019.
- [15] General Administration of Quality Supervision, "Inspection and quarantine of the People's Republic of China & standardization administration of People's Republic of China," *Seismic Ground Motion Parameters Zonation Map of China (GB 18308-2015)*, General Administration of Quality Supervision, Beijing, China, 2015.
- [16] E. Buckingham, "On physically similar systems; illustrations of the use of dimensional equations," *Physical Review*, vol. 4, no. 4, pp. 345–376, 1914.
- [17] G. Fan, J. Zhang, J. Wu, and K. Yan, "Dynamic response and dynamic failure mode of a weak intercalated rock slope using a shaking table," *Rock Mechanics and Rock Engineering*, vol. 49, no. 8, pp. 3243–3256, 2016.
- [18] R. J. Bathurst, S. Gaskin, and A. Gaskin, "Shaking table testing of geofoam seismic buffers," *Soil Dynamics and Earthquake Engineering*, vol. 27, no. 4, pp. 324–332, 2007.
- [19] M.-f. Lei, B.-c. Zhou, Y.-x. Lin, F.-d. Chen, C.-h. Shi, and L.-m. Peng, "Model test to investigate reasonable reactive artificial boundary in shaking table test with a rigid container," *Journal of Central South University*, vol. 27, no. 1, pp. 210–220, 2020.
- [20] N. N. Ambraseys and J. Douglas, "Near-field horizontal and vertical earthquake ground motions," *Soil Dynamics and Earthquake Engineering*, vol. 23, no. 1, pp. 1–18, 2003.
- [21] Z. H. Wang, T. Su, H. Konietzky, Y. L. Tan, and G. L. Zhou, "Hydraulic properties of Beishan granite after different high temperature treatments," *Bulletin of Engineering Geology and the Environment*, vol. 80, no. 4, pp. 2911–2923, 2021.
- [22] N. P. Theodulidis and P.-Y. Bard, "Horizontal to vertical spectral ratio and geological conditions: an analysis of strong motion data from Greece and Taiwan (SMART-1)," *Soil Dynamics and Earthquake Engineering*, vol. 14, no. 3, pp. 177–197, 1995.
- [23] H.-x. Liu, Q. Xu, and Y.-r. Li, "Effect of lithology and structure on seismic response of steep slope in a shaking table test," *Journal of Mountain Science*, vol. 11, no. 2, pp. 371–383, 2014.
- [24] M.-L. Lin and K.-L. Wang, "Seismic slope behavior in a large-scale shaking table model test," *Engineering Geology*, vol. 86, no. 2-3, pp. 118–133, 2006.
- [25] H. I. Ling, Y. Mohri, D. Leshchinsky, C. Burke, K. Matsushima, and H. Liu, "Large-scale shaking table tests on modular-block reinforced soil retaining walls," *Journal of Geotechnical and Geoenvironmental Engineering*, vol. 131, no. 4, pp. 465–476, 2005.
- [26] Ministry of Housing and Urban-Rural Development of the People's Republic of China, *Code for Seismic Design of Building (GB50011-2010)*, Ministry of Housing and Urban-Rural Development, Beijing, China, 2010.

## Research Article

# Dynamic Response and Failure Characteristics of Slope with Weak Interlayer under Action of Near-Fault Ground Motion

Bing Yang <sup>1</sup>, Jiangrong Hou <sup>1</sup>, Yifei Liu <sup>1,2</sup> and Zihong Zhou <sup>1</sup>

<sup>1</sup>School of Civil Engineering, Southwest Jiaotong University, Chengdu 610031, China

<sup>2</sup>College of Civil and Transportation Engineering, Shenzhen University, Shenzhen 51800, China

Correspondence should be addressed to Yifei Liu; [yfliu@szu.edu.cn](mailto:yfliu@szu.edu.cn)

Received 3 March 2021; Revised 7 April 2021; Accepted 17 April 2021; Published 3 May 2021

Academic Editor: Chuanbin Zhu

Copyright © 2021 Bing Yang et al. This is an open access article distributed under the Creative Commons Attribution License, which permits unrestricted use, distribution, and reproduction in any medium, provided the original work is properly cited.

Investigations into the Wenchuan earthquake (2008, China) demonstrated that landslides were concentrated in the near-fault areas, and numerous large-scale landslides occurred in slopes with weak interlayers. A mathematical model was established based on the shear beam theory, while a numerical model was developed based on the discrete element method which perfectly matched layer boundary theory. Through a theoretical analysis and numerical simulation, the dynamic response and failure modes of the slope with a weak interlayer under the near-fault ground motion were studied. It was found that a combined effect took place between the near-fault ground motion and the weak interlayer, causing the slope near a fault to be destroyed more easily. The coupling between the near-fault ground motion and the weak interlayer leads to a maximum amplification effect of the slope. The existence of a weak interlayer induces nonconforming vibration between the upper and the lower rock masses of the interlayer. The variation in the amplification effect along the slope elevation is related to the ratio of the input seismic period to the natural slope period. Under horizontal ground motion, weak interlayers will be subjected to impacting and shearing action. The failure mode of the slope with a weak interlayer under near-fault ground motion can be expressed as a trailing edge tension crack, as well as weak interlayer impacting and shearing failure.

## 1. Introduction

Post-earthquake surveys have demonstrated that damages are evidently concentrated in the epicentral area, regardless of the engineering structure or geological body. The damage amount and degree generally exhibit a negative correlation with the distance from the fault, with a nonlinear attenuation. At a small distance from the fault (near-fault), the amount of destruction accounts for more than 70% of the total [1–3]. For example, in the Wenchuan earthquake, 81.2% of the total landslides occurred within 5 km from the fault [4]. Several strong earthquakes at the end of the 20<sup>th</sup> century, such as the 1994 Northridge earthquake in the United States, 1995 Kobe earthquake in Japan, 1999 Izmit earthquake in Turkey, and 1999 Chi-Chi earthquake in Taiwan, China, have provided a large number of near-fault ground motion records. It has been proven that a certain correlation exists between the near-fault ground motion and the disaster concentration [5]. The analysis of these near-

fault ground motion records shows that near-fault ground motions exhibit certain characteristics that are evidently different from those of far-field ground motions [6].

The characteristics of near-fault ground motion can be summarized as the following effects: the rupture directivity, fling step, hanging wall, and vertical effects. Among these, the rupture directivity and fling step effects will induce a long-period and large-amplitude velocity pulse. The generating principle of the rupture directivity and fling step effects are illustrated in Figure 1. Taking a strike-slip fault as an example, when the near-fault site is at the end of the fault along the fracture strike, the energy produced by each rupture will be superimposed. Thus, a velocity pulse will appear, which is produced by the rupture directivity effect, and its direction is perpendicular to the fault strike. The characteristic of the velocity pulse produced by the rupture directivity effect is that the pulse appears at the initial stage of ground motion and is bidirectional [7]. In Burks and Baker's study, the bidirectional pulse generated by the direction

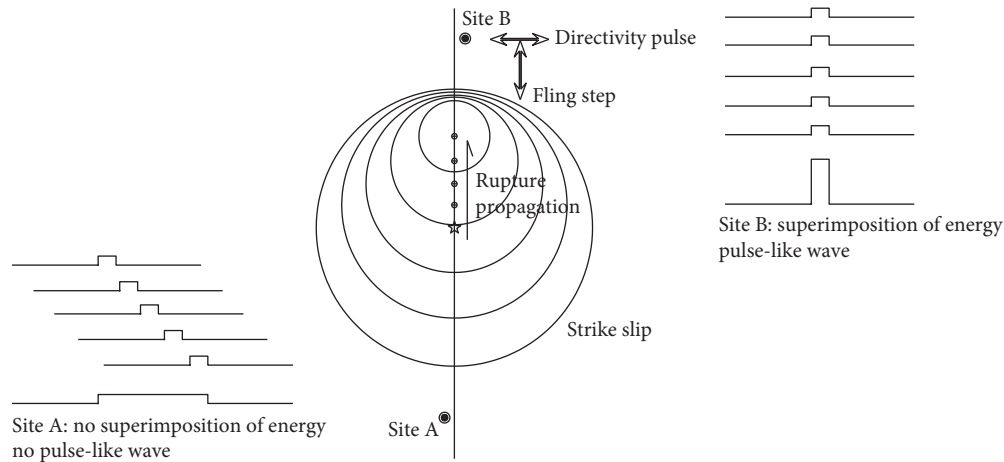


FIGURE 1: Schematic of causes of fling step and directivity pulse effects.

effect is referred to as the directivity pulse. On the strike parallel to the fault rupture, the dislocation between the two earthquake plates will result in a large permanent displacement of ground. This permanent displacement will induce a long-period, unidirectional large pulse, which is the fling step effect in the near-fault effect [8] (see Figure 1). The unidirectional pulse generated by the fling step effect is referred to as the fling step in this study. Two typical velocity waveforms about the fling step effect and near-fault rupture directivity effect recorded in an earthquake are illustrated in Figure 2, which are the fling step recorded in the 1995 Kobe earthquake (Fukiai) and the directivity pulse recorded in the 1999 Chi-Chi earthquake in Taiwan, China (TCU-068), respectively.

Wen et al. [9] analyzed 64 groups of ground motion records within a distance of 200 km from the fault in the 2008 Wenchuan earthquake, and they found that seven ground motions within a distance of 30 km from the fault were pulse-like ground motions. The pulse velocity amplitude measured at Qingping station in Mianzhu county, which is the closest to the fault, was up to 1.26 m/s. An investigation demonstrated that there were five concentrated areas of large landslides in the Wenchuan earthquake [9, 10], as illustrated in Figure 3. If the rupture directivity effect exists, the largest number of landslides should be near the end of the fault, that is, in areas *E* and *C*. In fact, large landslides do exhibit the greatest distribution in these two areas, accounting for 34.8% and 28.6% of the total large-scale landslides, respectively (Figure 4) [2].

As mentioned previously, the two pulse effects mainly affect the parallel and vertical fault directions. Statistical results regarding the direction of large-scale landslides in the Hongshihe basin of Qingchuan county following the Wenchuan earthquake are presented in Figure 5 [2]. From the figure, it can be observed that the sliding directions of the landslides are mainly parallel to and perpendicular to the fault, which further confirms the contribution of the near-fault pulse-like ground motion to the landslides.

The weak interlayer is a layer with a certain thickness, composed of relatively soft materials. In engineering practice, if a weak interlayer exists in the slope, most of the slopes

will exhibit stability problems. The weak interlayer is often the controlling factor for the slope instability [11]. Under the action of ground motion, a slope with a weak interlayer will exhibit several different response characteristics compared to a homogeneous slope [12, 13]. To date, various researchers have studied the seismic response of the slope with a weak interlayer. Huang [14] studied the influence of the elastoplastic parameters of the weak interlayer on the amplification effect by means of the theoretical analysis method. Liu et al. [15] analyzed the influence of a weak interlayer thickness, dip angle, and buried depth on the slope displacement and acceleration using the finite element method. Xu et al. [16] analyzed the stability of a slope with three large-scale weak interlayers using  $FLAC^{3D}$ . Deng et al. [17] studied the failure mode of a slope with a thin sandy layer in the 2004 Niigata Ken Chuetsu earthquake. Huang et al. [18] studied the rotation-translation mechanisms of a slope with a weak interlayer by means of the upper bound stability theory. Chen et al. [11] and Fan et al. [19] studied the seismic response and failure mode of a slope with a weak interlayer using a large-scale shaking table test.

Existing studies on the seismic response of a slope with a weak interlayer have mainly focused on the failure mode, amplification effect, and spectral characteristics of the slope [20]. However, the effect of near-fault ground motion, which exhibits special characteristics, on the weak interlayer has been of less concern, with only few relevant research studies available in the literature.

Near-fault ground motion has many different characteristics from far-field ground motion, and the slope with a weak interlayer also exhibits numerous special dynamic response characteristics compared with the homogeneous slope under the action of ground motion. Postdisaster investigations following the Wenchuan earthquake proved that many of the near-fault landslides triggered by the Wenchuan earthquake contained weak interlayers [2]. For example, in the Daguangbao landslide (at a 4.8 km distance from the fault), the largest landslide triggered by the Wenchuan earthquake, it was found that the slip zone was the interlayer dislocation zone, and the strength and stiffness of which were smaller than those of

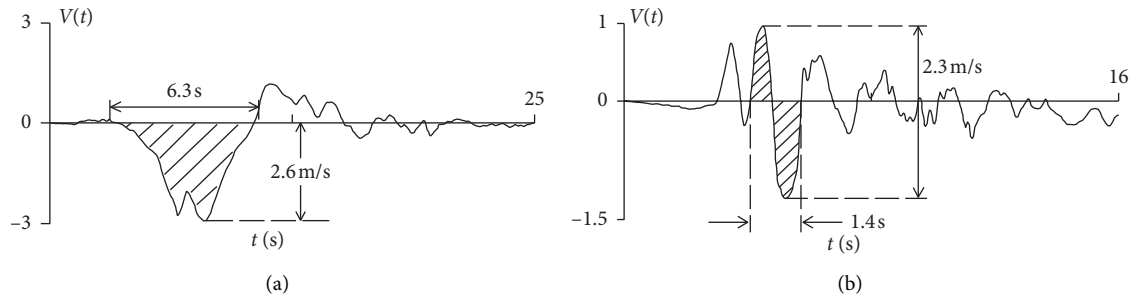


FIGURE 2: Typical velocity records of fling step and directivity pulse. (a) Fling step (Kobe earthquake, 1995). (b) Directivity pulse (Chi-Chi earthquake, 1999).

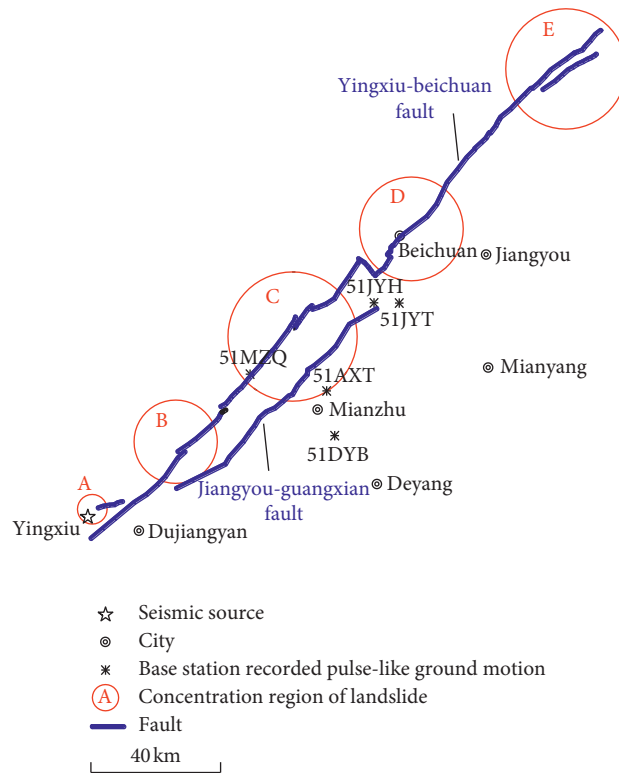


FIGURE 3: Distribution of near-fault pulse-like ground motion records and large-scale landslides in Wenchuan earthquake [9, 10].

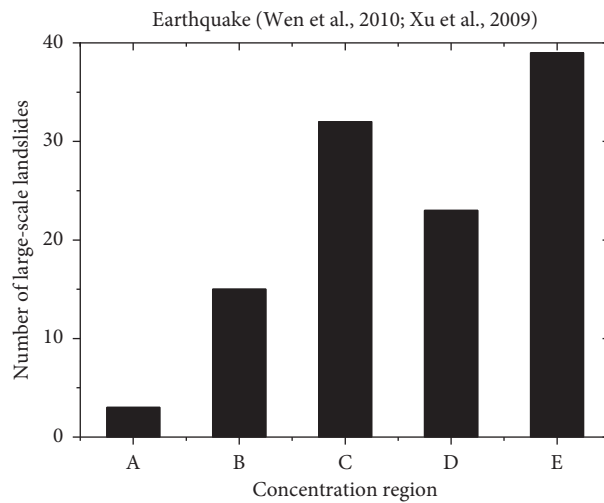


FIGURE 4: Number of large-scale landslides in different concentration regions [2].

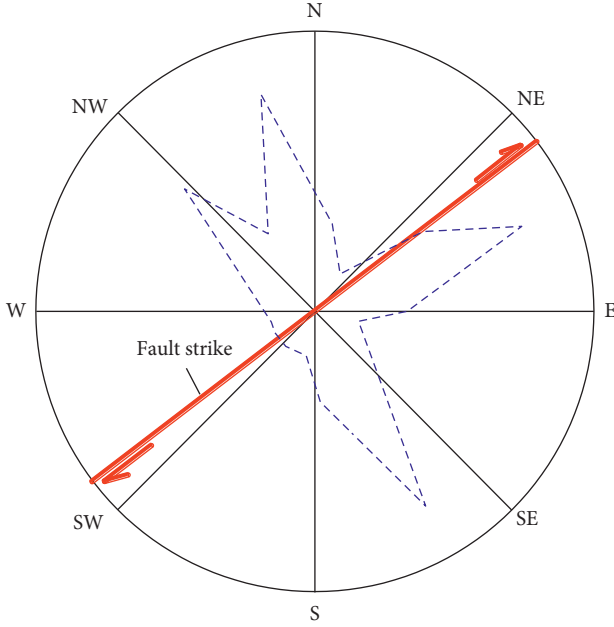


FIGURE 5: Rosette diagram of sliding directions of large-scale landslides in Hongshih basin of Qingchuan county [2].

the rock mass at the upper and lower sides of the slip zone [21]. The strength and rigidity of the rock mass in the sliding zone of the Donghekou landslide in the Wenchuan earthquake (at a 300 m distance from the fault) were also smaller than those of the rock masses above and below the slip zone [22].

When a slope with a weak interlayer is located near the fault, owing to the particularity of the weak interlayer and fault, the question is whether the combination effect of both, which will amplify the slope destruction, will be induced. In this study, this combination effect is investigated. The dynamic response of the slope with a weak interlayer under the action of near-fault pulse-like ground motion is discussed. Moreover, the failure mechanism induced by the combined effect is studied.

## 2. Theoretical Analysis

**2.1. Theoretical Model.** The dynamic response of a slope with a weak interlayer under the action of horizontal ground motion was considered. Furthermore, a mathematical model for the dynamic response of a slope with a weak interlayer was established.

To develop the model, the following assumptions were made: (1) an infinitely long trapezoidal slope is situated on a rigid foundation, and no relative sliding occurs between the slope and foundation, as indicated in Figure 6. (2) Only the horizontal displacement caused by the earthquake is considered, and the shear stress is uniformly distributed in any horizontal plane. The displacement of each point in the same horizontal plane is the same. (3) The slope is divided into three layers by the weak interlayer (Figure 6), and the physical properties of the materials of each layer are consistent.

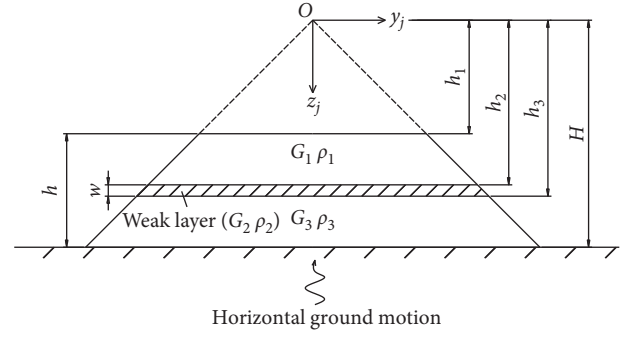


FIGURE 6: Model diagram.

For any slope, taking a thin layer (the microsegment) from the slope (Figure 7), the equilibrium equation in the horizontal direction can be expressed as

$$\frac{\partial^2 u_j}{\partial t^2} dm_j + \tau_j b(z_j) = \left( \tau_j + \frac{\partial \tau_j}{\partial z_j} \right) \left( b(z_j) + \frac{\partial b(z_j)}{\partial z_j} dz_j \right) + F(z_j), \quad (1)$$

where  $dm_j$  is the microsegment mass,  $t$  is the time,  $u_j$  is the horizontal displacement,  $\tau_j$  is the shear stress uniformly distributed in any horizontal section,  $b(z_j)$  is the microsegment width,  $F(z_j)$  is the horizontal external force acting on the microsection, and the subscript  $j = 1, 2, 3$  (1 refers to the layer above the weak layer, 2 refers to the weak layer, and 3 refers to the layer below the weak layer). Moreover,  $dm_j = \rho_j b(z_j) dz_j$ ,  $b(z_j) = \alpha z_j$  (let the slope angle be  $\theta$ ,  $\alpha = 1/\tan \theta$ ; here,  $\theta = 45^\circ$ , namely,  $\alpha = 1$ ),  $\tau_j = G_j (\partial u_j / \partial z_j)$ , and  $F(z_j) = (d^2 u_0 / dt^2) dm_j$ . Substituting the above parameters into equation (1), the equation of slope vibration under the action of horizontal ground motion can be written as

$$\frac{\partial u_j^2}{\partial t^2} - \frac{G_j}{\rho_j} \left( \frac{\partial^2 u_j}{\partial z_j^2} + \frac{1}{z_j} \frac{\partial u_j}{\partial z_j} \right) = \frac{d^2 u_0}{dt^2}, \quad (2)$$

where  $\rho_j$  is the density of each layer material and  $G_j$  is the shear modulus of each layer material.

Let the right-hand side of equation (2) be equal to 0. Then, a linear homogeneous equation can be obtained, which can be solved by the separation variables' method. Suppose that

$$u_j(z_j, t) = \phi_j(z_j) T(t). \quad (3)$$

Substituting equations (3) into (2), and letting both sides of the equation be equal to  $-c_j^2$ ,

$$\frac{d^2 T(t)}{dt^2} + \frac{G_0 c_j^2 T(t)}{\rho} = 0, \quad (4)$$

$$\frac{d^2 \phi_j(z_j)}{dz_j^2} + \frac{1}{z_j} \frac{d\phi_j(z_j)}{dz_j} + c_j^2 \phi_j(z_j) = 0. \quad (5)$$

The general solution of equation (4) is as follows:

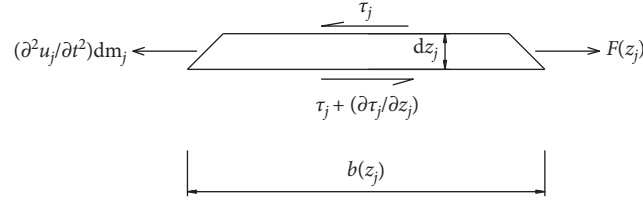


FIGURE 7: Force analysis of the element.

$$T(t) = T(0)\cos(\omega t) + \frac{T(0)}{\omega}\sin(\omega t), \quad (6)$$

where  $\omega$  is the angular frequency:

$$\omega = \frac{G_j c_j^2}{\rho_j}. \quad (7)$$

From equation (7), it can be concluded that

$$c_j = \omega \sqrt{\frac{\rho_j}{G_j}}. \quad (8)$$

Let  $Z_j = c_j z_j$ ; then, equation (5) can be reduced to a 0-order Bessel equation:

$$Z_j^2 \frac{d^2 \phi(Z_j)}{dZ_j^2} + Z_j \frac{d\phi(Z_j)}{dZ_j} + Z_j^2 \phi(Z_j) = 0. \quad (9)$$

The solution to equation (9) can be expressed by the Bessel function:

$$\phi(Z_j) = Z_j^0 [A_j J_0(Z_j) + B_j Y_0(Z_j)], \quad (10)$$

where  $J_0(Z_j)$  and  $Y_0(Z_j)$  are the first and second types of 0-order Bessel functions, respectively, while  $A_j$  and  $B_j$  are the parameters to be calculated.

The boundary condition of the slope with a weak interlayer (see Figure 6) can be expressed as follows: (1) the shear stress at the top of the slope is 0; (2) the shear displacement at the bottom of the slope is 0; and, (3) the shear displacement and stress satisfy the continuity condition at the interlayer interface. The mathematical form can be written as

$$\begin{aligned} G_1(z_1)u_1'(z_1)|_{z_1=h_1} &= 0, \\ G_1(z_1)u_1'(z_1)|_{z_1=h_2} - G_2(z_2)u_2'(z_2)|_{z_2=h_2} &= 0, \\ u_1(z_1)|_{z_1=h_2} - u_2(z_2)|_{z_2=h_2} &= 0, \\ G_2(z_2)u_2'(z_2)|_{z_2=h_3} - G_3(z_3)u_3'(z_3)|_{z_3=h_3} &= 0, \\ u_2(z_2)|_{z_2=h_3} - u_3(z_3)|_{z_3=h_3} &= 0, \\ G_3(z_3)u_3'(z_3)|_{z_3=H} &= 0. \end{aligned} \quad (11)$$

Substituting equations (10) into (11), the following algebraic equation can be obtained:

$$EC = 0, \quad (12)$$

in which

$$E = \begin{bmatrix} G_1 J_{-1}(c_1 h_1) & G_1 Y_{-1}(c_1 h_1) & 0 & 0 & 0 & 0 \\ G_1 J_{-1}(c_1 h_2) & G_1 Y_{-1}(c_1 h_2) & -G_2 J_{-1}(c_2 h_2) & -G_2 Y_{-1}(c_2 h_2) & 0 & 0 \\ J_0(c_1 h_2) & Y_0(c_1 h_2) & -J_0(c_2 h_2) & -Y_0(c_2 h_2) & 0 & 0 \\ 0 & 0 & G_2 J_{-1}(c_2 h_3) & G_2 Y_{-1}(c_2 h_3) & -G_3 J_{-1}(c_3 h_3) & -G_3 Y_{-1}(c_3 h_3) \\ 0 & 0 & J_0(c_2 h_3) & Y_0(c_2 h_3) & -J_0(c_3 h_3) & -Y_0(c_3 h_3) \\ 0 & 0 & 0 & 0 & J_0(c_3 H) & Y_0(c_3 H) \end{bmatrix}, \quad (13)$$

$$C = \begin{bmatrix} A_1 \\ B_1 \\ A_2 \\ B_2 \\ A_3 \\ B_3 \end{bmatrix}.$$

If equation (12) has a nonzero solution, it is necessary to let the coefficient determinant of the equation be equal to 0, and then,

$$|E| = 0. \quad (14)$$

The natural frequencies  $\omega_i$  ( $i = 1, 2, 3, \dots$ ) of the slope can be obtained by solving equation (14). Let  $A_1 = 1$ , and the values of  $B_1, A_2, B_2, A_3$ , and  $B_3$ , represented by  $A_1$ , can be obtained according to equation (12). Thus, the main vibration modes of each order can be written as

$$\varphi_i(z) = \begin{cases} Z_1^0 [A_1 J_0(Z_1) + B_1 Y_0(Z_1)], & \left( Z_1 = \omega_i \sqrt{\frac{\rho_1}{G_1}} z, h_1 \leq z < h_2 \right), \\ Z_2^0 [A_2 J_0(Z_2) + B_2 Y_0(Z_2)], & \left( Z_2 = \omega_i \sqrt{\frac{\rho_2}{G_2}} z, h_2 \leq z < h_3 \right), \\ Z_3^0 [A_3 J_0(Z_3) + B_3 Y_0(Z_3)], & \left( Z_3 = \omega_i \sqrt{\frac{\rho_3}{G_3}} z, h_3 \leq z \leq H \right). \end{cases} \quad (15)$$

The main vibration mode corresponding to each order frequency has thus been obtained, and the vibration equations corresponding to each order frequency under the action of ground motion can be determined by the mode decomposition method.

Define the  $i^{\text{th}}$ -order generalized mass as

$$m_i = \sum_{j=1}^3 \int_{h_j}^{h_j^+} \rho_j(\alpha z) [\varphi_i(z)]^2 dz. \quad (16)$$

The generalized load of the  $i^{\text{th}}$  order is

$$P_i(t) = -\frac{du_0^2}{dt^2} \sum_{j=1}^3 \int_{h_j}^{h_j^+} \alpha z \rho_j [\varphi_i(z)]^2 dz. \quad (17)$$

For each vibration mode, the vibration equations can be expressed as

$$m_i \frac{dY_i^2(t)}{dt^2} + \omega_i^2 m_i Y_i(t) = P_i(t). \quad (18)$$

The vibration function can be obtained by applying the Duhamel integral:

$$u(z, t) = \sum_{i=1}^{\infty} \frac{1}{m_i \omega_i} \varphi_i(z) \int_0^t P_i(s) \sin[\omega_i(t-s)] ds, \quad (19)$$

where  $s$  is the integral time of the Duhamel integral, and  $0 \leq s \leq t$ .

**2.2. Characteristics of Natural Frequency and Vibration Mode of the Slope with the Weak Interlayer.** Considering a trapezoidal slope with a height of 30 m (Figure 6), the slope is homogeneous and has no interlayer. The shear modulus of the rock mass is set to  $G_1 = G_2 = G_3 = 200$  MPa, and the density is assumed to be  $2650 \text{ kg/m}^3$ . According to the frequency equation (equation (14)), the first-order natural frequency of the homogeneous slope is calculated as 2.62 Hz. When a weak interlayer exists in the middle of the slope, the

thickness of the soft interlayer is set to 4 m, and the shear modulus of the rock mass is assumed to be  $G_2 = G_1/4 = 50$  MPa (Figure 6). According to the frequency equation, the first-order natural frequency of the slope with a weak interlayer is 1.87 Hz. It can be observed that the existence of a weak interlayer evidently reduces the first natural frequency of the slope. This means that a slope with a weak interlayer has a longer period (lower frequency) compared to that of a homogeneous slope. In the example above, the period of the slope with a weak interlayer is 1.44 times longer than that of the homogeneous slope.

Suppose that the shear modulus of the rock mass above and below the weak interlayer  $G_1 = G_3 = 200$  MPa, and the shear modulus of the weak interlayer material is  $G_2$ . The weak interlayer thickness is assumed to be  $w$ , and the weak interlayer is located in the middle of the slope. With the variation in the shear modulus and thickness of the weak interlayer, the ratio of the first-order natural period ( $T$ ) of the slope with a weak interlayer to the first-order natural period ( $T_0$ ) of the homogeneous slope is illustrated in Figure 8. It can be observed from the figure that the period ratio  $T/T_0$  increases with an increase in  $G_1/G_2$  and  $w/h$ .

As mentioned previously, the near-fault ground motion has a longer period and larger pulse, which will lead to greater damage to long-period structures [23]. The existence of the weak interlayer causes the first-order natural period of the slope to be longer. Therefore, the existence of a weak interlayer coupled with near-fault ground motion will cause greater damage.

The formula provided by Bray [24] is used to estimate natural period of nine large-scale landslides within a 5 km distance from the fault in the Wenchuan earthquake, in which the nine large-scale landslides are regarded as a homogeneous slope. The estimation formula is presented in equation (20), and the estimated results are displayed in Table 1 as follows:

$$T_s = 4 \frac{H_m}{v_s}, \quad (20)$$

where  $T_s$  is the estimated natural period of the slope regarded as a homogeneous mass,  $v_s$  is the shear wave velocity, and  $H_m$  is the slope height.

The period  $T_i = 6.52$  s, that is, the minimum pulse period of the pulse-like ground motion measured in the Wenchuan earthquake [10] is taken as the dynamic input, and the distribution of the period ratio ( $T_i/T_s$ ) for the above nine large landslides is illustrated in Figure 9. As can be observed from Figure 9, the pulse period of the Wenchuan earthquake is approximately 1.5 to 2.5 times the natural period of the slope regarded as a homogeneous mass. However, Figure 8 demonstrates that the existence of the weak interlayer increases the natural period of the slope. Compared to the homogeneous slope, the natural period of the slope with a weak interlayer is closer to the pulse period of the near-fault ground motion, so it will cause greater damage.

According to equation (15), the displacement diagram of the first four vibration modes for different shear modulus ratios is presented in Figure 10, when the weak interlayer is in the middle of the slope and  $w/h = 0.13$ . It can be observed from the vibration mode diagram that the vibration

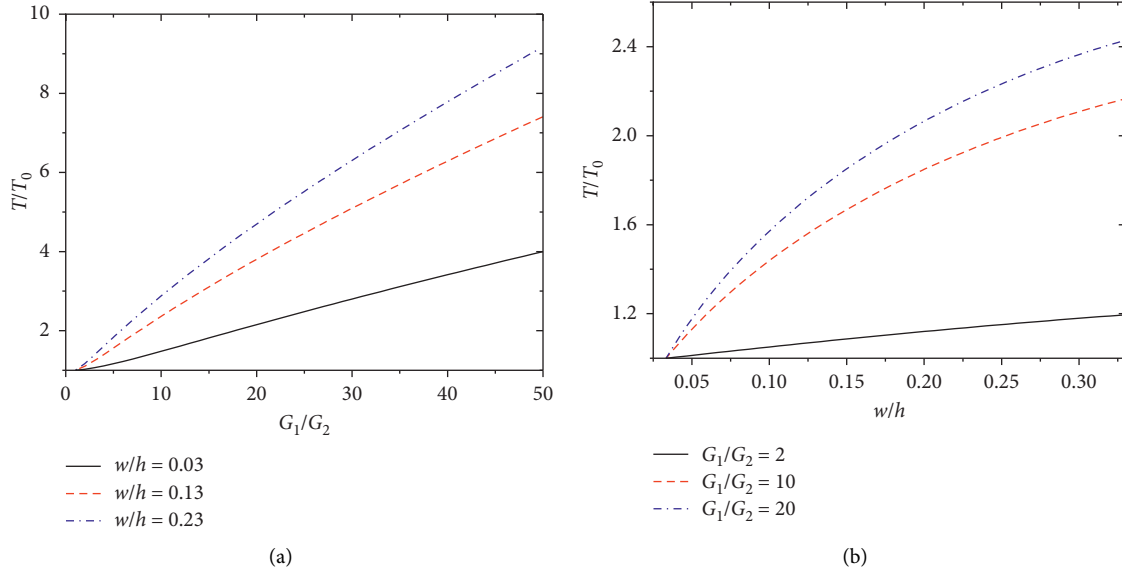


FIGURE 8: Variation in the period ratio  $T/T_0$  with shear modulus and thickness. (a) Shear modulus ratio. (b) Thickness ratio.

TABLE 1: Estimated natural period of large-scale landslides in Wenchuan earthquake.

Name	Distance from fault (km)	Slope height (m)	Shear wave velocity (m/s)	Estimated period (s)
Daguang Bao landslide	4.8	1800	1200	3.9
Guantan landslide	0.5	700	800	3.5
Eagle Rock landslide	1.1	900	1000	3.6
Tangjiashan landslide	2.8	800	1200	2.7
Wang Jiayan landslide	0.4	400	800	2
Donghekou landslide	0.3	800	1200	2.7
Wo qian landslide	0.2	600	1200	2
Shibangou landslide	2.4	300	1000	1.2
Wenjiagou landslide	3.9	600	1000	2.4

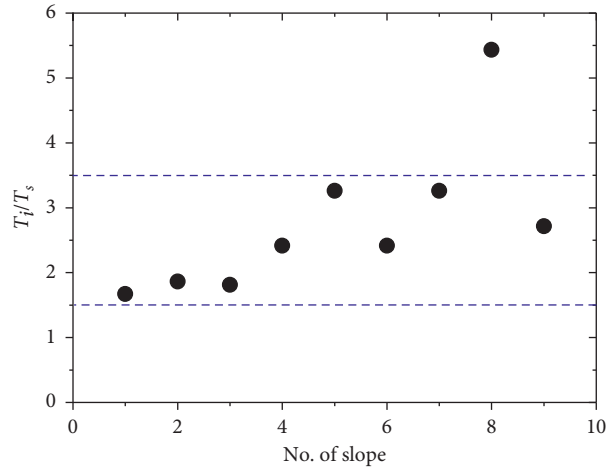


FIGURE 9: Ratio of the pulse-like ground motion period to the natural period of the large-scale landslide regarded as a homogeneous mass in Wenchuan earthquake.

displacement has an inflection point at the intersection of the layers, and the shear strain is discontinuous at this point. Moreover, the first two-order vibration modes vary in nearly the same manner along the slope elevation. From the third mode, the vibration mode along the slope elevation varies

significantly between the different shear modulus ratios (Figures 10(c) and 10(d)). The first vibration mode makes the greatest contribution to the final dynamic response. The figure indicates that a smaller shear modulus of the inter-layer (that is, a higher ratio of  $G_1/G_2$ ) results in a greater



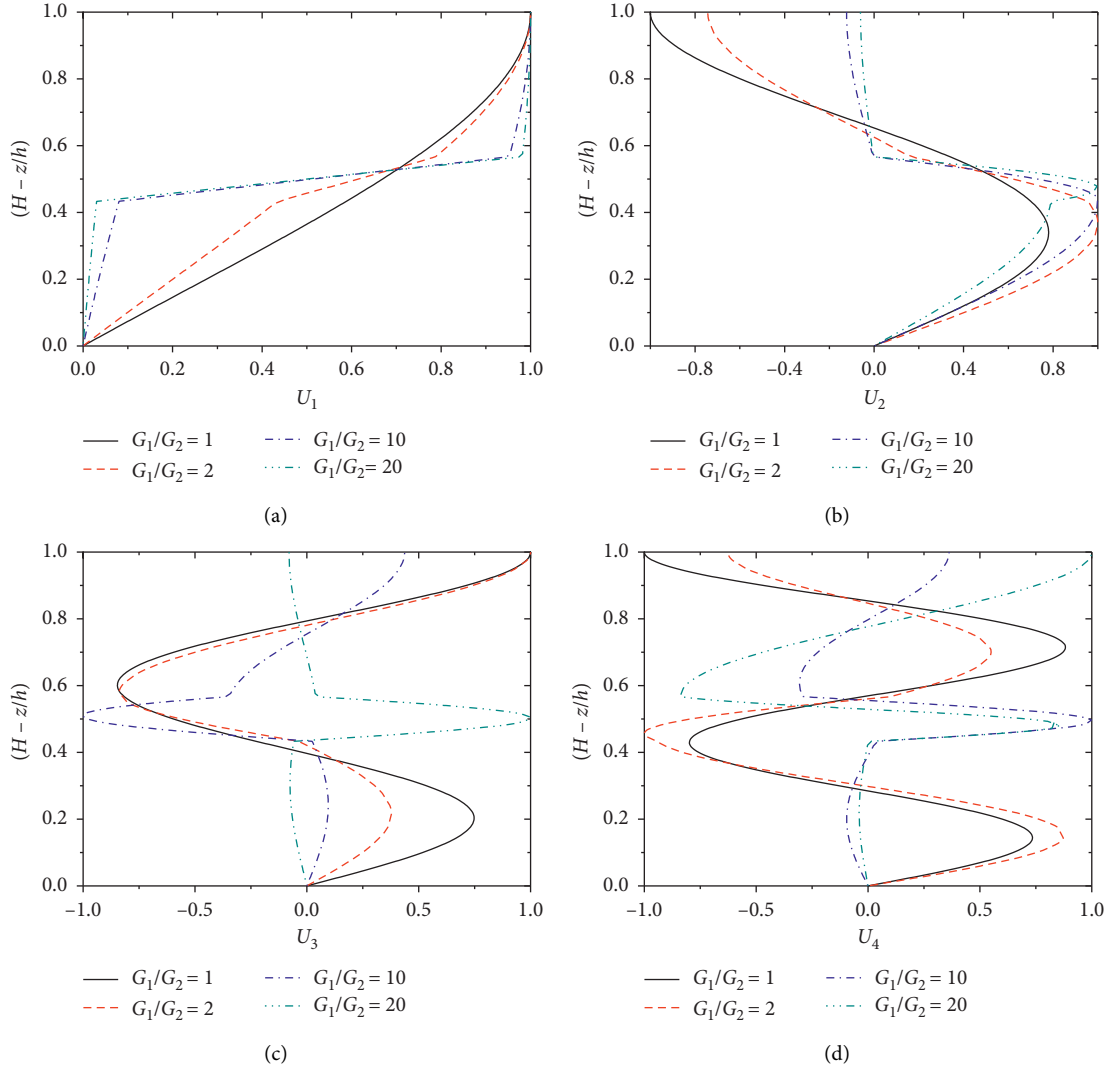


FIGURE 10: Displacement functions of first four vibration modes under different natural periods. (a) First vibration mode. (b) Second vibration mode. (c) Third vibration mode. (d) Fourth vibration mode.

difference between the displacements of the rock mass above and below the interlayer. This delamination phenomenon will lead to evidently nonconforming vibration, which will amplify the damage degree.

### 2.3. Dynamic Response of the Slope with the Weak Interlayer.

The homogeneous model and weak interlayer slope model described in Section 2.2 are taken as an example. A sine wave is selected to simulate the seismic waves, which offers the advantages of single frequency and uniform amplitude. Therefore, certain laws may be investigated more easily. A low-frequency horizontal sinusoidal vibration with a frequency of 2 Hz and an amplitude of  $1 \text{ m/s}^2$  and a high-frequency horizontal sinusoidal vibration with a frequency of 10 Hz and an amplitude of  $1 \text{ m/s}^2$  are exerted at the bottom of the slope. Equation (19) is used to calculate the dynamic response of the slope. The calculated maximum relative displacement (relative to the slope bottom), maximum relative velocity (relative to the slope bottom), and

maximum absolute acceleration along the slope elevation are illustrated in Figure 11.

It can be observed from Figure 11 that the displacement, velocity, and acceleration responses of the slope with or without a weak interlayer are close to the first-order vibration mode at a low-frequency input and second-order vibration mode at a high-frequency input. This indicates that the dynamic response of the slope along the slope elevation is mainly related to the input ground motion frequency and natural frequency of the slope. When the frequency of the ground motion is low and therefore closer to the first-order natural frequency of the slope, the slope vibration is close to its first-order vibration mode. The amplification factor exhibits an increasing trend from the bottom to the top. Moreover, it can be observed from Figure 11 that the amplification effect of the two slopes (with and without an interlayer) does not differ significantly at a high frequency, but the amplification effect of the slope with an interlayer is much greater than that of the homogeneous slope at a low frequency.

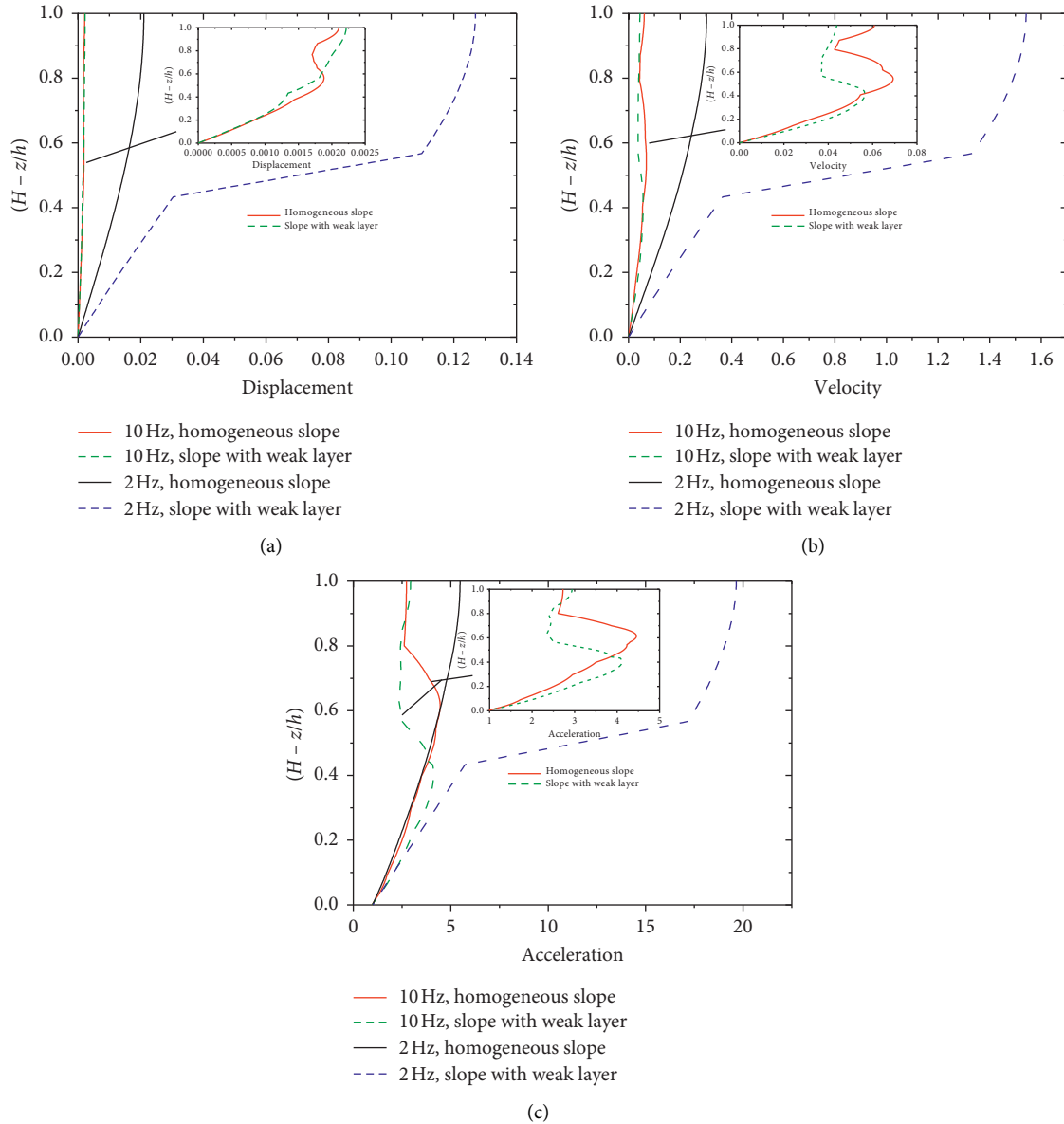


FIGURE 11: Dynamic responses at low and high frequencies. (a) Displacement. (b) Velocity. (c) Acceleration.

The pulse-like ground motion is characterized by a long period and low frequency. The maximum relative velocity along the elevation of the homogeneous slope and the slope with a weak interlayer under pulse-like and pulseless ground motions (the waveforms of the two-ground motion are indicated in Figure 12) calculated by equation (19) are illustrated in Figure 13. It can be observed that the results of the pulse-like ground motion are consistent with those of the low-frequency simple harmonic vibration, while the results of the pulseless ground motion are similar to those of the high-frequency simple harmonic vibration. Therefore, the conclusions obtained from the simple harmonic vibration can be also applied to the analysis of pulse-like ground motion.

As the near-fault pulse-like ground motion is a low-frequency ground motion, the coupling between the pulse-like ground motion and weak interlayer will lead to a greater elevation amplification effect. It can also be observed from

Figures 11 and 13 that a significant velocity difference exists between the upper and lower rock masses of the weak interlayer. This means that a distinct incompatible vibration occurs between the rock masses above and below the interlayer. Figure 14 presents the velocity time history of the measuring points above and below the interlayer under the condition of low-frequency simple harmonic vibration. For a homogeneous slope, the velocity difference between the two measuring points is not evident; however, a significant difference exists for the slope with a weak interlayer. In the vibration process, the velocity difference between the rock masses at the top and bottom of the interlayer will cause the weak interlayer to be subjected to impacting and shearing action, resulting in the weak interlayer being damaged more easily.

The amplification effect of the slope and the impacting and shearing effects caused by the velocity difference between the rock masses at the top and bottom of the weak

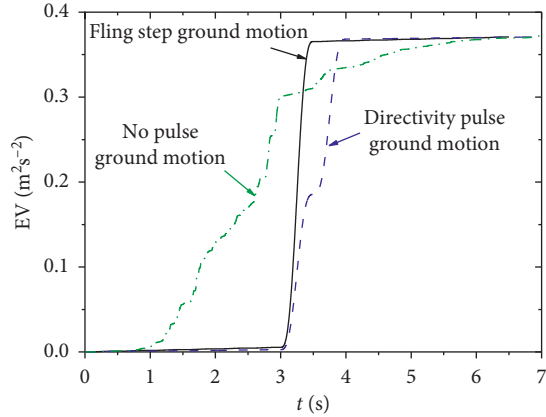


FIGURE 12: Variation in generalized energy with time.

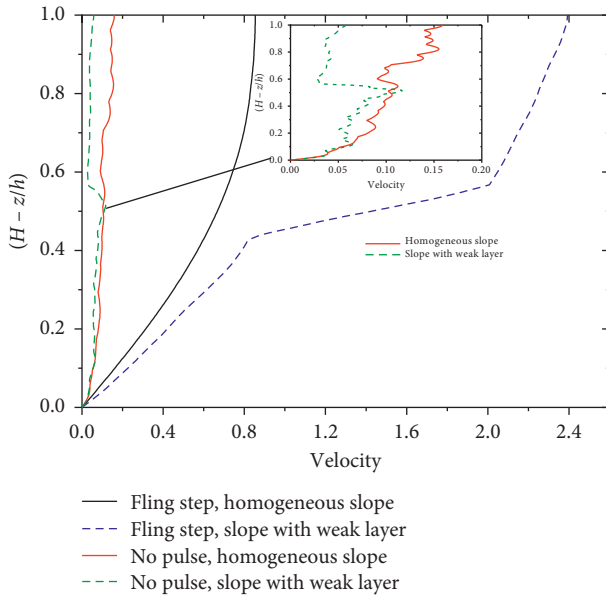


FIGURE 13: Comparison of analytical solutions of pulse-like and pulseless ground motions.

interlayer may be the main reasons for the failure of the weak interlayer. In this study, the peak ground acceleration (PGA) amplification factor at the top of the slope and maximum velocity difference between the rock masses at the top and bottom of the interlayer are used to investigate the two effects. The variations in the PGA and velocity difference with the weak interlayer thickness, shear modulus, and position are presented in Figures 15 and 16.

In Figure 15, the interlayer is in the middle of the slope, and the interlayer thickness and shear modulus are changed. It should be noted that  $T_p$  is the period of input ground motion, while  $T_s$  is the natural period of the slope. It can be observed from Figure 15 that the effects of the interlayer thickness and shear modulus on both the PGA amplification factor and maximum velocity difference are realized by changing the first-order natural period of the slope. When the period of the input vibration is the same as the natural period of the slope ( $T_p/T_s = 1$ ), the PGA amplification factor and maximum velocity difference are the greatest. A larger

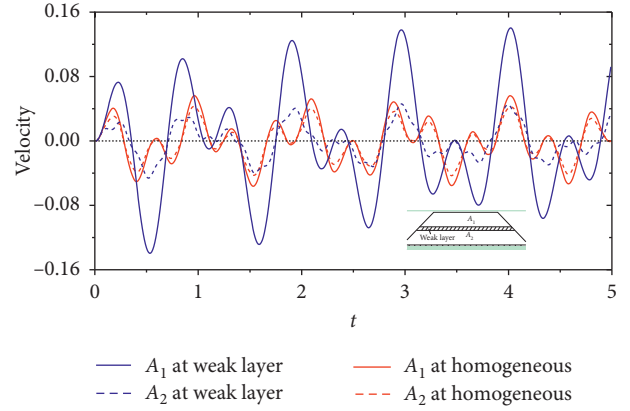


FIGURE 14: Velocity time history of measuring points above and below the interlayer.

difference between the two periods results in a smaller PGA amplification factor and maximum velocity difference. Figure 9 illustrates that the existence of the weak interlayer causes the natural period of the slope to be close to the period of ground motion in the Wenchuan earthquake, which indicates that the ratio ( $T_p/T_s$ ) becomes close to 1 more easily owing to the existence of the weak interlayer in the slope damaged by the Wenchuan earthquake. Therefore, greater damage is caused for the large-scale landslides with a weak interlayer in the Wenchuan earthquake.

Figure 16 illustrates the variations in the PGA amplification factor and maximum velocity difference with the change in  $T_p/T_s$  when the weak interlayer is located at different positions of the slope. It can be observed from the figure that the PGA amplification factor is mainly related to the ratio of the input vibration period to the natural period. For the maximum velocity difference, in addition to the period ratio, the interlayer position has little effect. When the period ratio is the same, the maximum velocity difference is greatest when the interlayer is at the upper part of the slope.

### 3. Numerical Simulation

To provide further understanding of the failure characteristics of the slope with a weak interlayer under near-fault ground motion, it is necessary to establish a numerical model for numerical analysis.

**3.1. Discrete Element Method Model of the Slope with the Weak Layer.** The discrete element method (DEM) was proposed by Cundall and Strack [25]. Compared to the traditional finite element method, the DEM exhibits no deformation coordination problems and can simulate large deformation, rupture, and inversion of rock and soil.

In this study, a computational model was generated using the software PFC<sup>2D</sup>. The contact bond model was used to simulate the adhesion between particles. The height of the slope was set to 40 m, and the angle was set to 45° (Figure 17). The macroparameters of the slope were set as follows: shear modulus  $G_1 = 80$  MPa, Poisson's ratio  $\nu = 0.3$ , density

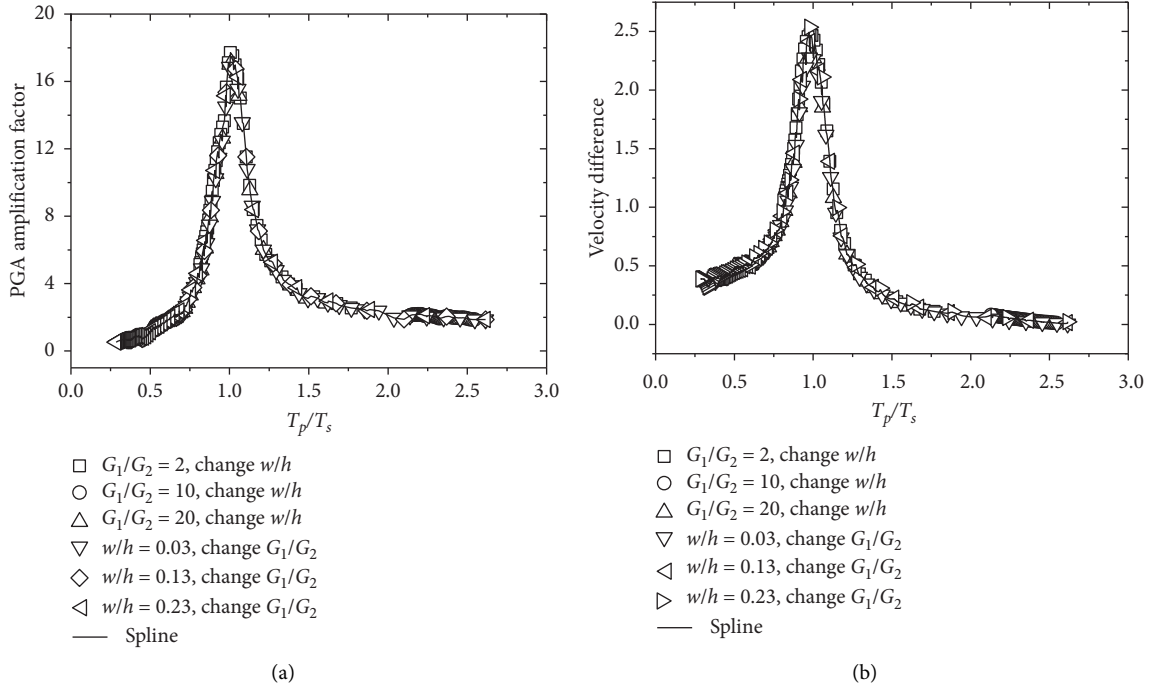


FIGURE 15: Relationship between dynamic response and  $T_p/T_s$ . (a) PGA amplification factor at the top of the slope. (b) Maximum velocity difference between the top and bottom of the interlayer.

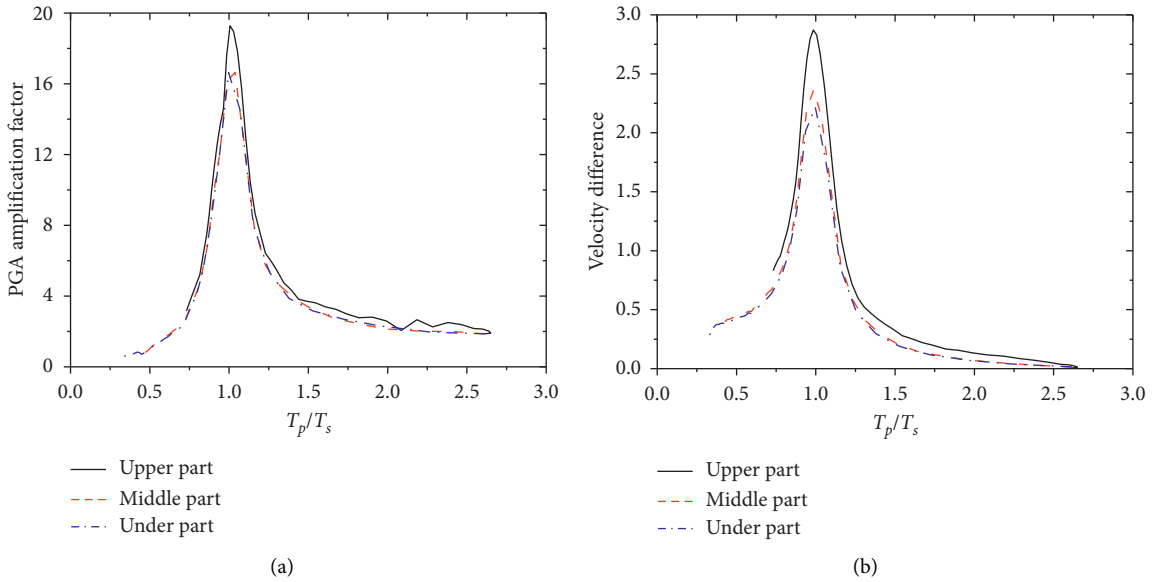


FIGURE 16: Influence of the interlayer position in the slope on the PGA amplification factor and maximum velocity difference.

$\rho = 2650 \text{ kg/m}^3$ , cohesion of the rock mass  $c = 500 \text{ kPa}$ , and internal friction angle  $\phi = 30^\circ$ . According to the static biaxial test, the mesoscopic parameters obtained, corresponding to the macroscopic parameters, are presented in Table 2.

A weak interlayer was set in the middle and lower parts of the slope ( $z/h = 3/8$ ). The weak interlayer thickness was 3 m (Figure 17), and the shear modulus was taken as 1/10 of that of the rock masses above and below the interlayer. The strength was taken as 1/5 of that of the rock mass. The other parameters were the same as those of the rock mass. The

corresponding mesoscopic parameters of the weak interlayer are presented in Table 2.

According to the research by He et al. [26], local damping can better model the energy consumption, and it was therefore used in this study. The damping coefficient was 0.157. For the pulse-like ground motion, the damping coefficient had little effect on the results. Several calculations show that when the local damping coefficient was not very large, the calculation results for the different local damping coefficients were basically the same.

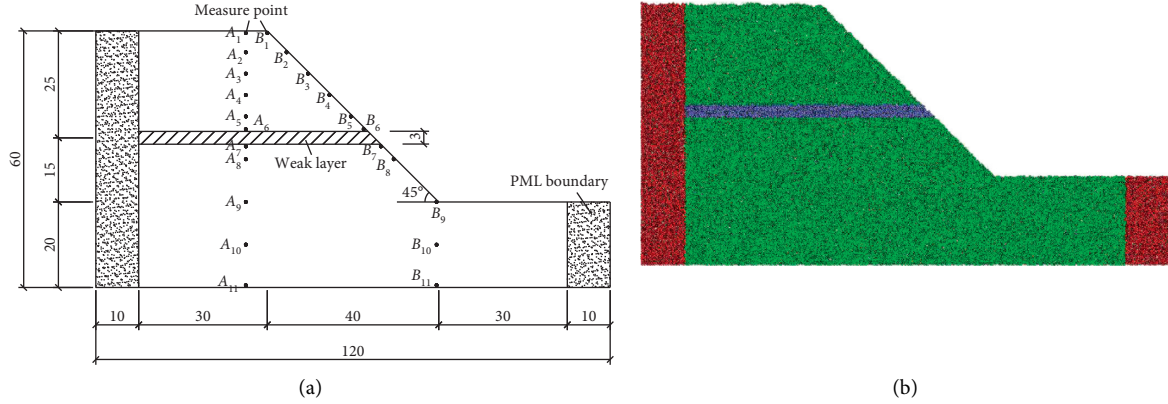


FIGURE 17: Schematic of the calculation model and PFC2D model.

TABLE 2: Mesoscopic parameters of the DEM model.

Symbol	Specific description	Value (rock mass/interlayer)
$\rho$	Density ( $\text{kg/m}^3$ )	2650/2650
$n_0$	Initial porosity	0.18/0.18
$k_n$	Normal contact stiffness (Pa)	$45 \times 10^7 / 45 \times 10^6$
$k_s$	Tangential contact stiffness (Pa)	$15 \times 10^7 / 15 \times 10^6$
$\sigma_c$	Contact bond normal strength (Pa)	$5.0 \times 10^5 / 1.0 \times 10^4$
$\tau_c$	Contact bond tangential strength (Pa)	$5.0 \times 10^5 / 1.0 \times 10^4$
$f_c$	Friction coefficient	0.8/0.8

3.2. *Boundary Condition.* In dynamic problems, the boundary condition has a significant influence on the dynamic analysis results [27] owing to the presence of reflected waves.

The absorbing layer boundary was applied in this study. The boundary of the absorbing layer absorbs the transmission wave by applying an energy-consuming buffer zone outside the calculation area, which is also known as the damping layer. At present, the most representative absorbing boundary is the perfectly matched layer (PML) absorbing boundary. The PML boundary can cause the incident wave to attenuate exponentially, and the false reflection on the boundary can rapidly be attenuated to zero.

In this study, the absorbing effect of the PML was verified by simulating the propagation process of the longitudinal wave in a one-dimensional rock column. As illustrated in Figure 18, a sine wave was applied at the left end, while a PML boundary was set at the right end. The computational results at the measuring point in Figure 19 are illustrated in Figure 18. It can be observed from the figure that the amplitude of the reflection wave was less than 10% of that of the original incident wave, which indicates that the boundary absorption effect was strong. In this study, the damping absorption layer of the PML boundary set as the slope model boundary is illustrated in Figure 17.

3.3. *Ground Motion Input.* To judge whether the ground motion is a pulse-like ground motion, Mukhopadhyay and Gupta [28] proposed a method using the ratio of the half-cycle pulse energy to the total ground motion energy to identify the pulse records. The formula for calculating the maximum half-

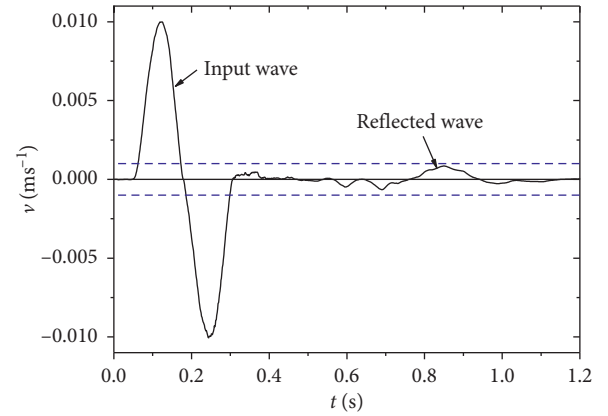


FIGURE 18: Absorption effect of the boundary.

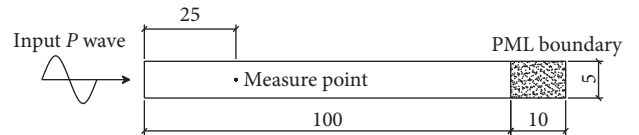


FIGURE 19: Test model of the boundary.

cycle energy ratio between two zeros in a velocity-time curve is presented in equation (21), where  $a$  is the time corresponding to the first zero, that is, the time at which the half cycle begins, while  $b$  is the time corresponding to the second zero point, that is, the time at which the half cycle ends. The parameter (PI) defined in equation (22) is used for judgment. If the value of PI is greater than 0.5, the velocity curve between the two zeros is a component of the velocity pulse in the seismic wave recording:

$$\text{FracEn}(1) = \frac{\int_a^b v^2(t) dt}{\int_0^T v^2(t) dt}, \quad (21)$$

$$\text{PI} = \frac{1}{1 + e^{7.64 - 27 \text{FracEn}(1)}}. \quad (22)$$

The velocity waveform of the ground motion used in this study is illustrated in Figure 20, in which the fling step ground motion is simulated by the half cycle of a harmonic pulse wave, and directivity pulse one is modeled by one cycle of a harmonic pulse. The pulseless ground motion is obtained by compressing and modulating the amplitude of the wave measured at the Songpan base station in the Wenchuan earthquake, which is 99 km away from the fault. The calculated PI values for the fling step and directivity pulse waveform are all greater than 0.9, meeting the definition of pulse-like ground motion. The PI value of the modified wave from the Songpan station is less than 0.3, indicating that it is pulseless ground motion. For comparison, the generalized energy  $E_v$  is used here, and the definition of which is as follows:

$$E_v(t) = \int_0^t v^2(s) ds, \quad (0 \leq s \leq t). \quad (23)$$

Let the generalized energy of the fling step, directivity pulse, and pulseless ground motion be equal. The variation in the generalized energy of the three ground motion types with time is illustrated in Figure 12.

**3.4. Slope Failure Process and Mechanism.** The spatial distribution of the failure points inside the slope under different ground motions is presented in Figure 21. The cumulative rupture process inside the slope over time is illustrated in Figure 22. It can be observed from the figure that the number of ruptures caused by the near-fault pulse-like ground motion is substantially larger than that caused by the pulseless ground motion under the condition of the same excitation energy. The coupling between the near-fault pulse-like ground motion and the slope with a weak interlayer produces the largest number of ruptures. From the rupture type, shear failure accounts for a certain proportion of the failure inside the slope with a weak interlayer; however, for the homogeneous slope, the shear failure proportion is very small. From the spatial distribution of the rupture, for the slope with a weak interlayer, the shear failure is concentrated in the weak interlayer, while the tensile failure is concentrated in the rock mass above the interlayer. For the homogeneous slope, shear failure mainly occurs at the foot of the slope. From the cumulative process of rupture over time, it can be observed from Figures 20 and 21 that ruptures occur only at the steep part of the energy curve. For near-fault ground motion, the ruptures almost all appear in the time period affected by the pulse. The shear and tensile failure inside the slope with a weak interlayer occur synchronously, and the shear failure inside the homogeneous slope lags slightly behind the tensile failure.

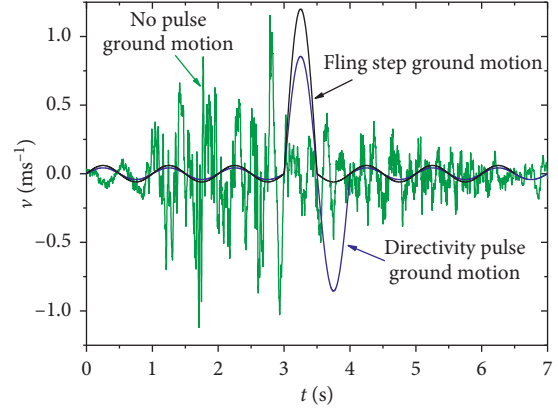


FIGURE 20: Velocity history.

Based on the above analysis, it can be concluded that the most serious damage occurs in the slope with a weak interlayer under near-fault pulse-like ground motions.

Different failure modes occur in the slope with a weak interlayer and homogeneous slope. For the slope with a weak interlayer, the shear failure zone mainly occurs in the weak interlayer, while the tensile failure zone appears in the rock mass above the interlayer. A sliding surface is formed when the tensile failure zone is connected to the shear failure zone. It can be observed from Figure 23(a) that the sliding mass is separated from the slope by the shear and tensile failure zones. For the homogeneous slope, the tensile failure appears at the upper part, while the shear failure mainly occurs at the foot of the slope. Only when the locking segment is cut off, can the sliding surface be penetrated, and the sliding mass can slide down. Compared to the homogeneous slope, the slope with a weak interlayer provides a shear opening for the sliding mass, and no locking segment exists in the slope. Therefore, the slope with a weak interlayer is more likely to be destroyed than the homogeneous slope.

In the aforementioned theoretical analysis, it was proven that the existence of the weak interlayer will lead to impacting and shearing effects in the interlayer owing to uncoordinated vibration. The velocity time history of the measuring points above and below the interlayer was recorded, as illustrated in Figure 24. It can be observed from the figure that the velocity difference between the rock masses at the upper and lower sides of the weak interlayer under the near-fault pulse-like ground motion is evident owing to the amplification effect and phase difference. The velocity difference for the homogeneous slope under the pulse-like ground motion is not large owing to the small phase difference (Figure 24(a)). The slope with a weak interlayer under pulseless ground motion (Figure 24(b)) exhibits a large phase difference and uncoordinated vibration, but the velocity difference is not as evident as that of the pulse-like ground motion owing to the small amplification effect. The time at which shear failure of the weak interlayer occurs is consistent with the time at which the large velocity difference appears. The large velocity difference induced by the coupling between the pulse-like ground motion and weak interlayer causes the weak interlayer to be subjected to

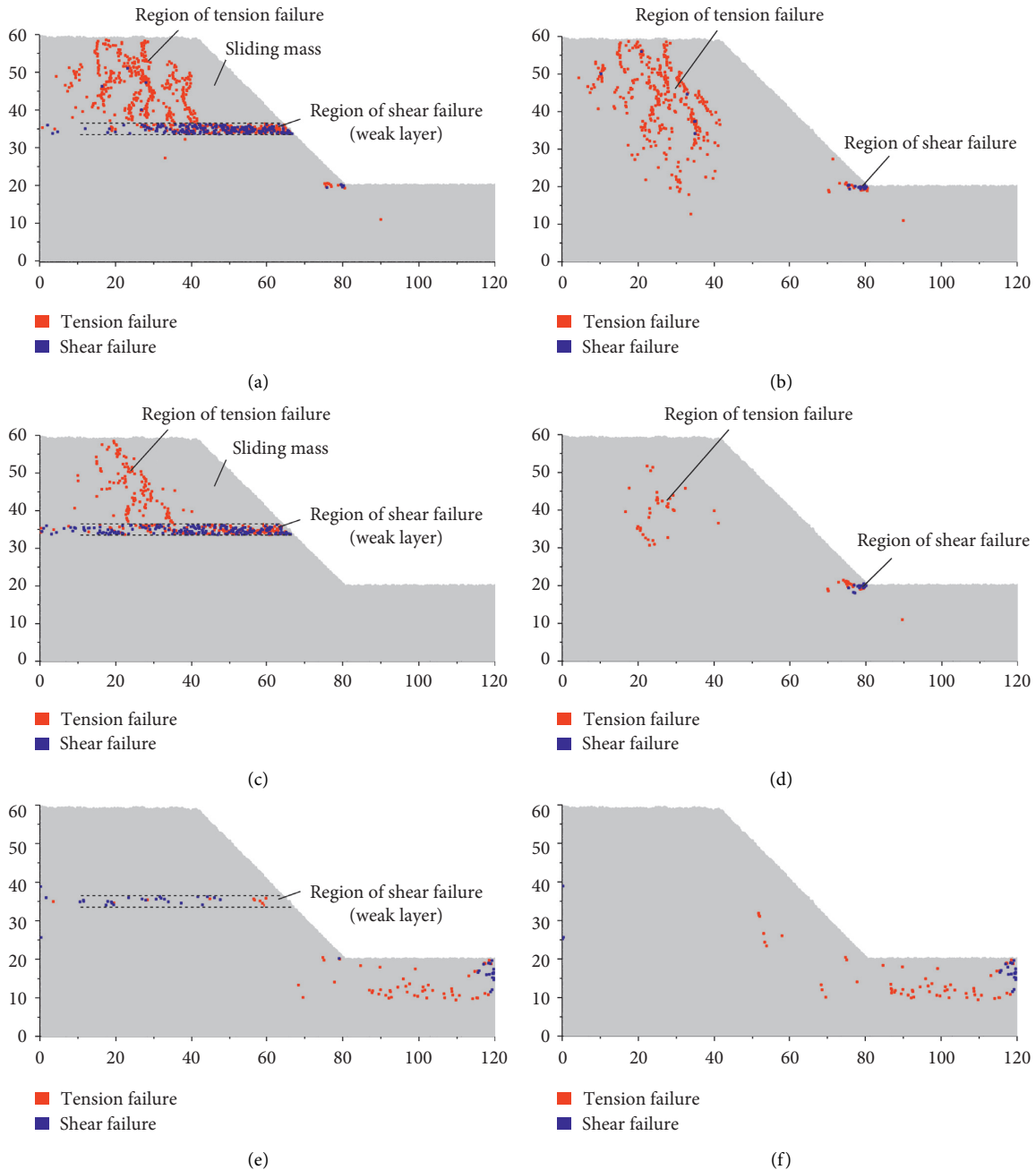


FIGURE 21: Spatial distribution of failure points inside slopes under different ground motions. (a) Slope with a weak interlayer under fling step ground motion. (b) Homogeneous slope under fling step ground motion. (c) Slope with a weak interlayer under directivity pulse ground motion. (d) Homogeneous slope under directivity pulse ground motion. (e) Slope with a weak interlayer under pulseless ground motion. (f) Homogeneous slope under pulseless ground motion.

the impacting and shearing effects, which leads to impacting and shearing damage of the slope.

In the Wenchuan earthquake, the Daguangbao landslide was located near the fault (4.8 km), and the shear modulus and strength of the rock mass in the slip zone were smaller than those of the rock masses on both sides, so it was a slope with a weak interlayer. A scanning electron microscope was used to study the microscopic characteristics of the rock mass fragment in the sliding zone of the Daguangbao landslide by Huang et al. [29]. It was found that impacting

failure of the rock mass occurred in the sliding zone (Figure 25). This verifies that the coupling between the near-fault pulse-like ground motion and weak interlayer will lead to impacting and shearing effects and cause the slope to be destroyed more easily.

In summary, the pulse-like near-fault ground motion coupled with a weak interlayer in the slope will induce impacting and shearing effects and a larger elevation amplification effect, causing the slope to reach failure more easily. The failure characteristics of a slope with a weak

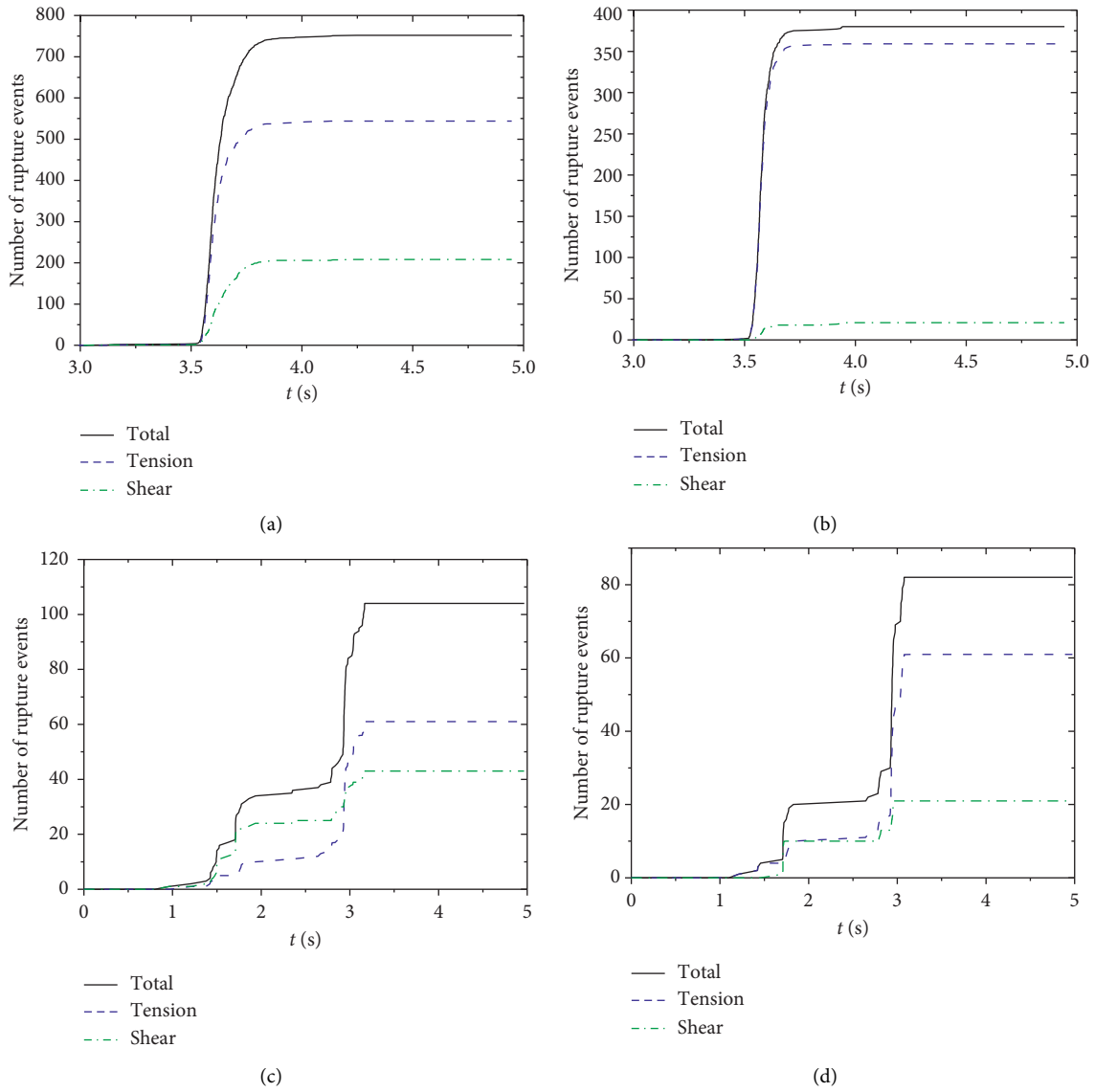


FIGURE 22: Cumulative failure process over time. (a) Slope with a weak interlayer under fling step ground motion. (b) Homogeneous slope under fling step ground motion. (c) Slope with a weak interlayer under pulseless ground motion. (d) Homogeneous slope under pulseless ground motion.

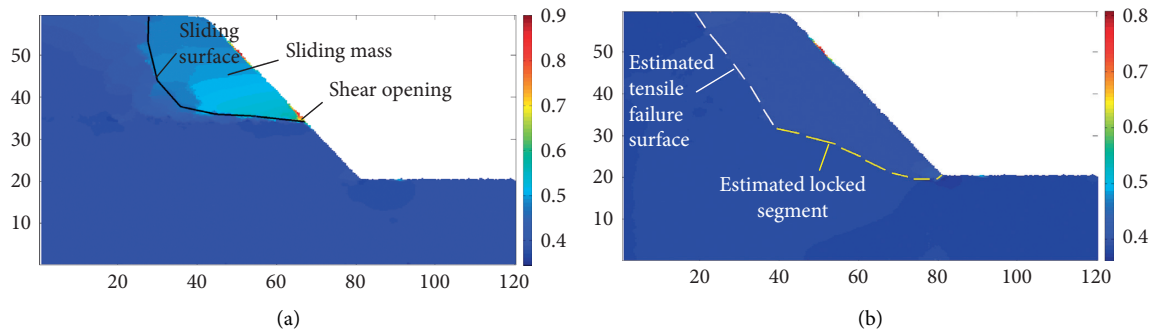


FIGURE 23: Contour of displacement. (a) Slope with a weak interlayer under fling step. (b) Homogeneous slope under fling step.



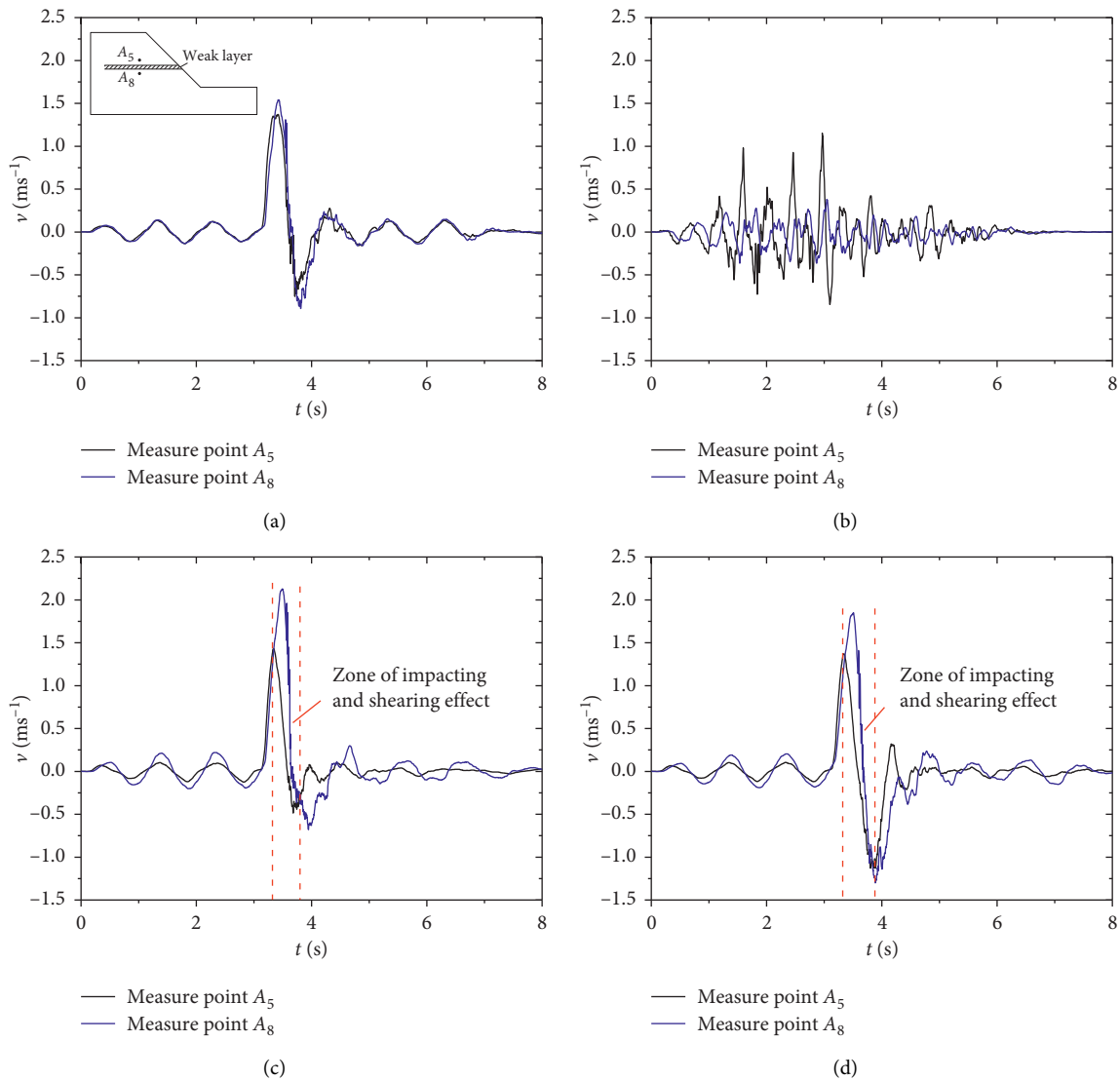


FIGURE 24: Velocity time history of measuring points above and below the weak interlayer. (a) Homogeneous slope under fling step. (b) Slope with a weak interlayer under pulseless ground motion. (c) Slope with a weak interlayer under fling step. (d) Slope with a weak interlayer under directivity pulse.

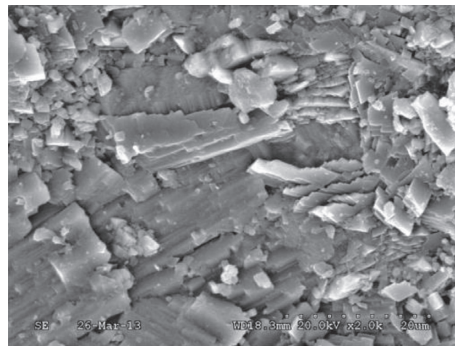


FIGURE 25: Microscopic image of impact failure of the rock mass in the slip zone of the Daguangbao landslide [29].

interlayer under pulse-like ground motion can be described as follows: the weak interlayer is destroyed by the impacting and shearing effects, and then, the tensile crack in the upper

rock mass is induced by elevation amplification. Finally, the sliding mass slips out when the tension and shearing surface is penetrated. Therefore, in practical engineering, a slope

with a weak interlayer near the fault should receive special attention, as it will be the most vulnerable slope. The shear strength of the weak interlayer and tension strength of the upper rock mass should be considered in the engineering design.

#### 4. Conclusions

A mathematical model to investigate the dynamic response of a slope with a weak interlayer was established based on the shear beam theory. Moreover, a two-dimensional numerical model to study the failure process of a slope with a weak interlayer was established based on the DEM and PML boundary theory. Through the theoretical analysis and numerical simulation, the dynamic response and failure mode of the slope with a weak interlayer under the near-fault ground motion were studied. The following conclusions can be drawn:

- (1) The weak interlayer in the slope will increase the first-order natural period of the slope evidently. A smaller shear modulus or larger thickness of the interlayer results in a longer natural period of the slope. The weak interlayer will cause the natural period of the slope to become closer to the period of pulse-like ground motion, leading to greater damage. The influences of the thickness and shear modulus of the interlayer on the dynamic response of the slope are achieved by changing the natural period of the slope.
- (2) The variation in the amplification effect with the elevation is mainly related to the ratio of the seismic period to the natural period of the slope. At low frequencies (below or close to the first-order natural frequency of the slope), the dynamic response of the slope with or without a weak interlayer is close to the first-order vibration mode of the slope, and the amplification effect of the slope with a weak interlayer is substantially larger than that of the homogeneous slope. At high frequencies (far greater than the first-order natural frequency of the slope), the dynamic response of the slope with or without a weak interlayer is close to the second-order vibration mode of the slope, and the amplification effect of the slope with a weak interlayer is not significantly different from that of the homogeneous slope. Moreover, the interlayer has a vibration isolation effect on the high-frequency ground motion, which means that the amplification effect at the rock mass above the interlayer is smaller.
- (3) Under the action of horizontal ground motion, the weak interlayer will be subjected to impacting and shearing action. Under near-fault pulse-like ground motion, the impacting and shearing effects of the weak interlayer are substantially greater than those of pulseless ground motion.
- (4) The failure characteristics of the slope with a weak interlayer under pulse-like ground motion can be

expressed as follows: the weak interlayer is destroyed by the impacting and shearing effects, following which a tension crack in the rock mass above the interlayer is induced by the elevation amplification. Finally, the sliding mass slips out when the tension and shearing surface is penetrated.

In practical engineering, a slope with a weak interlayer near the fault will be the most vulnerable slope. The shear strength of the weak interlayer and tension strength of the rock mass above the interlayer should be considered in the engineering design.

#### Data Availability

The data used to support the findings of this study are available from the corresponding author upon request.

#### Conflicts of Interest

The authors declare that they have no conflicts of interest.

#### Acknowledgments

This study was supported by the National Natural Science Foundation of China (no. 10902112), Fundamental Research Funds for the Central Universities (2682017QY02), Key R&D Projects in Sichuan Province (2021YFS0323 and 2020YFG0123), Applied Basic Research of Science and Technology Plan projects in Sichuan Province (2021YJ0039), and Sichuan International Cooperation Project (2020YFH0017).

#### References

- [1] R. Huang and W. Li, "Development and distribution of geohazards triggered by the 5.12 wenchuan earthquake in China," *Science in China Series E: Technological Sciences*, vol. 52, no. 4, pp. 810–819, 2009.
- [2] Q. Xu, X. J. Pei, R. Q. Huang et al., *Large-Scale Landslides Induced by Wenchuan Earthquake*, Science Press, Beijing, China, 2009.
- [3] B. Zhao, F. Taucer, and T. Rossetto, "Field investigation on the performance of building structures during the 12 May 2008 Wenchuan earthquake in China," *Engineering Structures*, vol. 31, no. 8, pp. 1707–1723, 2009.
- [4] Q. Xu, S. Zhang, and W. Li, "Spatial distribution of large-scale landslides induced by the 5.12 Wenchuan earthquake," *Journal of Mountain Science*, vol. 8, no. 2, pp. 246–260, 2011.
- [5] M. D. Trifunac, "The role of strong motion rotations in the response of structures near earthquake faults," *Soil Dynamics and Earthquake Engineering*, vol. 29, no. 2, pp. 382–393, 2009.
- [6] G. P. Mavroedis and A. S. Papageorgiou, "A mathematical representation of near-fault ground motions," *Bulletin of the Seismological Society of America*, vol. 93, no. 3, pp. 1099–1131, 2003.
- [7] L. S. Burks and J. W. Baker, "A predictive model for fling-step in near-fault ground motions based on recordings and simulations," *Soil Dynamics and Earthquake Engineering*, vol. 80, pp. 119–126, 2016.
- [8] J. D. Bray and A. Rodriguez-Marek, "Characterization of forward-directivity ground motions in the near-fault region,"

- Soil Dynamics and Earthquake Engineering*, vol. 24, no. 11, pp. 815–828, 2004.
- [9] Z. Wen, J. Xie, M. Gao, Y. Hu, and K. T. Chau, “Near-source strong ground motion characteristics of the 2008 Wenchuan earthquake,” *Bulletin of the Seismological Society of America*, vol. 100, no. 5, pp. 2425–2439, 2010.
- [10] Q. Han, X. Du, J. Liu, Z. Li, L. Li, and J. Zhao, “Seismic damage of highway bridges during the 2008 Wenchuan earthquake,” *Earthquake Engineering and Engineering Vibration*, vol. 8, no. 2, pp. 263–273, 2009.
- [11] Z.-L. Chen, X. Hu, and Q. Xu, “Experimental study of motion characteristics of rock slopes with weak intercalation under seismic excitation,” *Journal of Mountain Science*, vol. 13, no. 3, pp. 546–556, 2016.
- [12] B. Yang, Y. Luo, D. Jeng, and J. Feng, “Effects of moisture content on the dynamic response and failure mode of unsaturated soil slope subjected to seismic load,” *Bulletin of Seismological Society of America*, vol. 109, no. 2, pp. 489–504, 2019.
- [13] B. Yang, F. Gao, and D. Jeng, “Failure mode and dynamic response of a double-sided slope with high water content of soil,” *Journal of Mountain Science*, vol. 15, no. 4, pp. 859–870, 2018.
- [14] R. Huang, “Modelling of the effects of properties of a buried weak layer on seismic waves,” *Journal of Engineering Geology*, vol. 11, no. 3, pp. 312–317, 2003.
- [15] L. P. Liu, S. J. Yang, and L. I. Ying-Min, “Influence of soft soil layer on dynamic characteristic of the slope,” *Journal of Chongqing University*, vol. 30, no. 5, pp. 31–34, 2007.
- [16] B. Xu, Q. Qian, C. Yan et al., “Stability and strengthening analyses of slope rock mass containing multi-weak interlayers,” *Chinese Journal of Rock Mechanics and Engineering*, vol. 28, no. s2, pp. 3959–3964, 2009.
- [17] J. Deng, H. Kameya, Y. Miyashita, J. Kuwano, R. Kuwano, and J. Koseki, “Study on a failed dip slope with a thin sandy layer in 2004 Niigata-ken Chuetsu earthquake,” *Engineering Geology*, vol. 123, no. 4, pp. 302–314, 2011.
- [18] M. Huang, H. Wang, D. Sheng, and Y. Liu, “Rotational-translational mechanism for the upper bound stability analysis of slopes with weak interlayer,” *Computers and Geotechnics*, vol. 53, no. 13, pp. 133–141, 2013.
- [19] G. Fan, J. Zhang, J. Wu, and K. Yan, “Dynamic response and dynamic failure mode of a weak intercalated rock slope using a shaking table,” *Rock Mechanics & Rock Engineering*, vol. 49, no. 8, pp. 1–14, 2016.
- [20] B. Yang, Z. Zhou, and L. Zhou, “Experimental study on instability characteristic and bearing capacity of slope with bedrock under the action of rainfall,” *Journal of Southwest Jiaotong University*, 2020, in Chinese.
- [21] S. Cui, X. Pei, and R. Huang, “Effects of geological and tectonic characteristics on the earthquake-triggered Daguangbao landslide, China,” *Landslides*, vol. 15, no. 8, pp. 1–19, 2017.
- [22] X. P. Zhou and H. Cheng, “Stability analysis of three-dimensional seismic landslides using the rigorous limit equilibrium method,” *Engineering Geology*, vol. 174, no. 8, pp. 87–102, 2014.
- [23] Z. Chang, X. Sun, C. Zhai, J. X. Zhao, and L. Xie, “An improved energy-based approach for selecting pulse-like ground motions,” *Earthquake Engineering & Structural Dynamics*, vol. 45, no. 14, pp. 2405–2411, 2016.
- [24] J. D. Bray, “Simplified seismic slope displacement procedures,” *Geotechnical, Geological and Earthquake Engineering*, pp. 327–353, 2007.
- [25] P. A. Cundall and O. D. L. Strack, “A discrete numerical model for granular assemblies,” *Geotechnique*, vol. 29, no. 30, pp. 331–336, 2008.
- [26] J. He, X. Li, S. Li, Y. Yin, and H. Qian, “Study of seismic response of colluvium accumulation slope by particle flow code,” *Granular Matter*, vol. 12, no. 5, pp. 483–490, 2010.
- [27] G. D. Zhang, “Effect of different boundary conditions and seismic waves on seismic response of a slope,” *Journal of Vibration & Shock*, vol. 30, no. 1, pp. 102–105, 2011.
- [28] S. Mukhopadhyay and V. K. Gupta, “Directivity pulses in near-fault ground motions-I: identification, extraction and modeling,” *Soil Dynamics and Earthquake Engineering*, vol. 50, no. 6, pp. 1–15, 2013.
- [29] R. Huang, X. Pei, and S. Cui, “Cataclastic characteristics and formation mechanism of rock mass in sliding zone of daguangbao landslide,” *Chinese Journal of Rock Mechanics & Engineering*, vol. 35, no. 1, pp. 1–15, 2016.